

Selective Averaging
in High Resolution Liquid-State NMR:
Application to Coherence Transfer
and Homonuclear Decoupling

Selective Averaging in High Resolution Liquid-State NMR:
Application to Coherence Transfer and Homonuclear Decoupling.

Zur Erlangung des akademischen Grades eines

DOKTORS DER NATURWISSENSCHAFTEN

(Dr. rer. nat.)

von der KIT-Fakultät für Chemie und Biowissenschaften
des Karlsruher Instituts für Technologie (KIT)
genehmigte

DISSERTATION

von

M. Sc. Jens Daniel Haller



Dekan:

Prof. Dr. M. Wilhelm

Referent:

Prof. Dr. B. Luy

Korreferentin:

Prof. Dr. G. Guthausen

Tag der mündlichen Prüfung:

21. Juli 2021



This work is licensed under the Creative Commons Attribution-ShareAlike 4.0 International License (<http://creativecommons.org/licenses/by-sa/4.0/>).

Acknowledgements

I would like to express my gratitude to *all* people who have supported me during my PhD thesis and with whom I enjoyed the time very much. Also, I wish to acknowledge the help provided by technical services, administration and the executive board of the Institute of Organic Chemistry, the Institute of Biological Interfaces and the Karlsruhe Institute of Technology. Furthermore, I would especially like to thank ...

- ... Prof. Dr. Burkhard Luy for guiding me through an adventurous time, discovering the mysteries of NMR and recording the story on paper. It will always be an unforgettable time for which I am deeply grateful.
- ... Prof. Dr. Gisela Guthausen for her helpful, scientific support as second reviewer.
- ... PD Dr. Claudia Muhle-Goll and Dr. Pavleta Tzvetkova for many assistant discussions, helpful hints and various maintenance services on the spectrometers.
- ... Dr. Andrea Bodor for all her valuable contributions to various projects, the pleasant hours in the NMR lab and not to forget Szilvás Betyár.
- ... Dr. Davy Sinnaeve for many bright thoughts and ideas, as well as the enjoyable time in Lyon.
- ... Prof. Dr. László Nyitray and Dr. Francois-Xavier for the valuable contributions and the common project on selective H α ,C α -correlations.
- ... Prof. Dr. Katalin Kövér, Dr. István Timári and Tamás Gyöngyösi for the possibility to work together on the HSQC-CLIP-COSY experiment.
- ... Prof. Dr. Guido Pintacuda for the opportunity to measure on an ultra high field spectrometer.
- ... Dr. Isabelle Landrieu for the valuable protein samples.
- ... Prof. Dr. Paul Schanda who had introduced me to the NMR community.
- ... the *whole* Luy group including former and recent members with whom I had the pleasure to work, travel, discuss, drink coffee and enjoy the breaks. All your scientific and non-scientific support will make me remember the time together with joy.
- ... my friends and family – in *particular*, Ela, Nora & Ida.

Introduction

Since the seminal discovery of magnetic resonance in a beam of diamagnetic molecules^[1] and later also in ordinary matter,^[2,3] Nuclear Magnetic Resonance (NMR) has evolved to become a well-established method in numerous fields and constitutes the origin of multiple Nobel Prizes.¹ Remarkable, technical advances (e.g. superconducting magnets) as well as the continuous extension of methodological approaches (e.g. Fourier transform and multi-dimensional spectroscopy) have significantly contributed to the circumstance that, today, NMR has become an indispensable, powerful tool. In chemistry and biology, the success of NMR is based on the fact that versatile information on structure, dynamics, molecular interactions and electronic characteristics of investigated compounds is obtained at atomic resolution. Trains of radio frequency (RF) pulses guide nuclear spin dynamics and allow the tailored extraction of desired information. These so-called pulse sequences are in the focus of the dissertation at hand and novel concepts and experimental building blocks are introduced where so far existing approaches fall short. Underlying discussions repeatedly are assisted by the use of *average Hamiltonian theory* (AHT) which constitutes a fundamental concept in the selective modification and averaging of *nuclear spin Hamiltonians*^[4] and a basic introduction with a consistent, particular derivation of key equations is given (Chapter 1). The proposed contributions shall further be classified into two categories which are *coherence transfer* (Chapter 2) and *homonuclear decoupling* (Chapter 3).

The large variety of available NMR experiments, today, rests upon coherence transfer elements with specific spin-spin-coupling evolution. Amongst the most fundamental building blocks are *isotropic* and *planar mixing*, which are used in numerous NMR pulse sequences and originate from the well-known TOCSY-experiment by Ernst & co-workers.^[5] Conventional sequences for isotropic mixing (IM), however, require continuous irradiation and the covered bandwidth is technically limited by the amplitude of applied radio frequency (RF) pulses. With increasing static magnetic fields, larger bandwidths are required and experiments like the ¹³C,¹³C-TOCSY inevitably fail. It is, therefore, of major concern to provide broadband solutions that are able to fill the current void. Here, another approach is pursued that is based on planar mixing (PM) obtained from the so-called *perfect echo*.^[6] In combination with state-of-the-art broadband shaped pulses, TOCSY-type mixing with reduced power is achieved on enormous bandwidths exceeding the limits of conventional IM-sequences by multiple times.

Continuous irradiation, however, comprises another severe issue, that is, energy dissipation and the concomitant high strain on hardware. As a consequence, the potential of many methods are restricted e.g. in *fast-pulsing* ASAP-experiments that operate close to the duty cycle limit. Isotropic mixing at moderate power, on the other hand, could abrogate given limitations and for this reason, in the dissertation at hand an *isotropic perfect echo* (IPE) shall be proposed, that results in low energy isotropic

[1] I. I. Rabi et al. *Physical Review* **1938**, *53*, 318–318.

[2] F. Bloch, W. W. Hansen and M. Packard. *Physical Review* **1946**, *69*, 127.

[3] E. M. Purcell, H. C. Torrey and R. V. Pound. *Physical Review* **1946**, *69*, 37–38.

[4] J. S. Waugh, L. M. Huber and U. Haeberlen. *Physical Review Letters* **1968**, *20*, 180–182.

[5] L. Braunschweiler and R. R. Ernst. *Journal of Magnetic Resonance* **1983**, *53*, 521–528.

[6] K. Takegoshi, K. Ogura and K. Hikichi. *Journal of Magnetic Resonance* **1989**, *84*, 611–615.

¹ Rabi, Physics 1944; Bloch and Purcell, Physics 1952; Ernst, Chemistry 1991; Wüthrich, Chemistry 2002, Mansfield and Lauterbur, Medicine 2003

mixing. The IPE is further applied in *diffusion-ordered spectroscopy* (DOSY)^[7,8] and a fast-pulsing DOSY experiment is obtained. In conventional DOSY, being based on a stimulated echo (STE), undesired echoes are dephased by spoiler gradients and half the signal is irrevocably rejected. Using convection compensation, the STE is applied twice and only $\frac{1}{4}$ of the signal is left – sensitivity is drastically reduced. Moreover, long phase cycles are required for artifact suppression at the cost of long measurement times. In the proposed *fast* DOSY, isotropic mixing from the IPE adopts a rather *unusual* role – instead of *effective* transfer, mixing is used for *spin state preservation* and acquired DOSY spectra are obtained without *J*-modulation and at high sensitivity in less than 30 s.

In many fields of NMR, the use of shaped pulses, be it broadband or band-selective, has been proven essential. Yet, shaped pulses do what they are optimized for and it is not straightforward to predict their effect, if *in silico* and experimental conditions differ. For pulse shape optimizations, in most cases, spin-spin couplings are neglected and so far little is known about the effect of simultaneous coupling evolution. Typically, shaped pulses are one to three orders of magnitude longer than hard pulses and frequently applied to heteronuclei, where large couplings are encountered. While certain pulses, if applied individually, are inherently compensated for *heteronuclear* couplings, in other constellations, e.g. applied in an echo, the compensation breaks down – even more so for homonuclear couplings, where mutually coupled spins are perturbed continuously. Homonuclear *proton-proton* couplings are typically smaller, but can still have an impact considering long pulse lengths (e.g. band-selective pulses). Especially in above proposed planar and isotropic mixing, shaped pulses might occupy a considerable time of the pulse sequence and little is known on how they contribute to mixing. For this purpose, a rigorous examination of existing pulse shapes was undertaken, using a self-derived extension of AHT, that allows a profound choice on pulse shapes for given conditions – remarkable differences are discovered which open up new possibilities for pulse sequence development.

The effect of homonuclear couplings in the strong coupling regime represents a smaller mystery which is based on the fact that the given Hamiltonian is considered *homogeneous* – a correct treatment by the product operator formalism using Cartesian operators in the rotating frame is impeded.^[9] The Hamiltonian of a strongly coupled system can simply be met with basic and well-known mathematical tools that describe so-called *second-order effects*. These tools provide exact calculations for straightforward results, but only little insight about the *origin* of given effects. It is, hence, in the aim of the present thesis to provide a new perspective on a strongly coupled two-spin system using a so-called *double rotating frame*. With only few exceptions, e.g. the just mentioned strong coupling regime, newcomers in NMR are faced with rather simple theory that is based on classical approaches. Certain concepts, however, require a non-classical treatment one of which are so-called *multi-quantum* (MQ) coherences. The evolution of MQ-coherence exhibits interesting, but non-intuitive effects which are best explained following quantum mechanics. One peculiar property signifies that a heteronuclear coupling Hamiltonian of MQ-involved, mutually coupled spins is *without* effect. For this reason, it is conceivable that MQ-coherences can be exploited for *broadband* suppression of *selective* couplings – a concept that shall be transferred to HSQC-type experiments and further used for the extraction of various homo- and heteronuclear couplings.

In biomolecular NMR, the two perpetual issues are sensitivity and resolution. Due to the high gyromagnetic ratio, proton-detection is well-established, however, only moderate ^1H -signal dispersion is given and for biomolecules, being composed of numerous repeating units, signal overlap is regularly encountered. A way to counteract is given by homo- and heteronuclear decoupling where in principle resolution *and* sensitivity is enhanced from collapsing, sometimes *unresolved* multiplets. Yet, the application of so-called *pure shift* methods to *biomolecules* comprises certain aspects that have to be considered carefully. For the *detection of amide protons* a large excess of H_2O is required due to solvent exchange. As a consequence, strong artifacts from radiation damping can be encountered – especially in combination with prevalent high-Q probes, In existing methods, water magnetization had to be saturated from gradients or weak RF-fields in order to achieve solvent suppression and *exchanging* amide protons diminished or completely disappeared. Moreover, in uniformly ^{13}C , ^{15}N -labeled samples, the presence of numerous

[7] E. O. Stejskal and J. E. Tanner. *The Journal of Chemical Physics* **1965**, *42*, 288–292.

[8] K. F. Morris and C. S. Johnson. *Journal of the American Chemical Society* **1992**, *114*, 3139–3141.

[9] M. M. Maricq and J. S. Waugh. *The Journal of Chemical Physics* **1979**, *70*, 3300–3316.

long-range heteronuclear couplings causes additional line broadening. Up to date, these couplings were suppressed by *simultaneous* ^{13}C - and ^{15}N -composite pulse decoupling (CPD) at high risk for the probe – acquisition times had to be strictly reduced. For these reasons, the application of HD was so far confined to non-exchanging amide protons and, due to long-range couplings or RF-power restrictions, the accessible spectral resolution was severely limited. A major aim of the dissertation at hand was, hence, to change the status-quo and provide other means for homonuclear decoupling in the field of biomolecular NMR. It will be shown for an intrinsically disordered (p53TAD) and a small globular protein (human ubiquitin), that, for moderate solvent exchange, the use of a ^{13}C -BIRD-filter lifts given restrictions and high resolution can be obtained from the pure shift detection of amide protons.

Yet, *any* amide detection is impeded if acquired protons undergo solvent exchange in the *fast* regime, where signals are found beneath the water resonance. A protein class where this is most frequently encountered are so-called intrinsically disordered proteins (IDPs) – typically, they are missing tertiary or even secondary structure in big parts and are thus further exposed to water. One possibility is to suppress solvent exchange by decreasing the pH, which, however, abandons near-physiological sample conditions. Another is the detection of *non-exchanging* $\text{H}\alpha$ -protons, which can be achieved at physiological conditions while maintaining high sensitivity. Still, $\text{H}\alpha$ -signals are subject to numerous homo- and heteronuclear couplings which causes severe broadening and in turn low spectral resolution – especially for IDPs with little signal dispersion owing to the lack in secondary structure. Equally, directly attached $\text{C}\alpha$ -nuclei show broad multiplets due to the many homo- and heteronuclear couplings in ^{13}C , ^{15}N -labeled samples. For the acquisition of ^1H , ^{13}C -correlations, the suppression of *carbon-carbon* couplings is typically achieved using a *constant time period*, which fails for *high resolution* given the large number of long-range couplings.^[10] Therefore, in the last part of this thesis the conception of selective $\text{H}\alpha$, $\text{C}\alpha$ -correlations (SHACA) shall be introduced that offers an elegant solution to enhance resolution and sensitivity in *both* dimensions from $\text{C}\alpha$ -band-selective pulses.^[11] The proposed experiments further comprise the use of a real-time pure shift $\text{H}\alpha$ -acquisition, termed BASEREX, that allows homo- and heteronuclear decoupling.^[12] The BASEREX decoupling element, as well as the SHACA approach, are fundamental acquisition concepts and as such applicable to a multitude of band-separable spins, which is finally demonstrated on protein methyl-groups.

^[10] A. Bax, A. F. Mehlkopf and J. Smidt. *Journal of Magnetic Resonance* **1979**, *35*, 167–169.

^[11] A. Bodor et al. *Analytical Chemistry* **2020**, *92*, 12423–12428.

^[12] J. D. Haller, A. Bodor and B. Luy. *Journal of Magnetic Resonance* **2019**, *302*, 64–71.

Contents

Acknowledgements	I
Introduction	III
Contents	VII
1 Theory	1
1.1 Nuclear Spin	1
1.1.1 Solving the Schrödinger Equation	2
1.1.2 Expectation Value in Hilbert Space	3
1.1.3 Hilbert Space for Spin- $\frac{1}{2}$	4
1.2 Nuclear Spin in Liouville Space	6
1.2.1 Spin Density Operator	6
1.2.2 Product Operators	8
1.2.3 Solving the Liouville-von Neumann Equation	9
1.3 Nuclear Spin Hamiltonian	10
1.3.1 Spin Hamiltonian Hypothesis	10
1.3.2 Construction and Truncation of a Nuclear Spin Hamiltonian	10
1.3.3 Zeeman Interaction	12
1.3.4 Radio Frequency Pulse	13
1.3.5 Pulsed Field Gradients	14
1.3.6 Indirect Spin-Spin Coupling	14
1.3.7 Direct Dipole-Dipole Coupling	15
1.4 Product Operator Formalism	16
1.5 Introduction to Frame Transformations	19
1.5.1 Heisenberg Picture	19
1.5.2 Dirac Picture	20
1.5.3 Rotating Frame	22
1.6 Toggling Frame	27
1.6.1 Sequential Transformation	27
1.6.2 Numerical Simulation of the Toggling Frame	29
1.6.3 Toggling Frame: a Graphical Interpretation	32
1.6.4 Toggling Frame: Introducing the Unity Matrix	37
1.7 Average Hamiltonian Theory	38
1.7.1 Piecewise Time-Independent Hamiltonian	38
1.7.2 Dyson Series	39
1.7.3 Magnus Series	41
1.7.4 Numerical Calculation of the Average Hamiltonian	47
1.8 Relaxation	50
1.8.1 Thermal Equilibrium State	50
1.8.2 Random Field Relaxation	50
1.8.3 Dipolar Relaxation in a Two Spin System	51
1.8.4 Cross Correlated Relaxation	53

2	Coherence Transfer Elements	55
2.1	Introduction	55
2.2	Planar Mixing from Perfect Echo	58
2.2.1	Planar Mixing	58
2.2.2	Relayed CLIP-COSY	60
2.2.3	$^{13}\text{C}, ^{13}\text{C}$ -PM-TOCSY	62
2.2.4	Planar Mixing in a 3D (H)CC(CO)NH Experiment	69
2.2.5	Conclusion	73
2.3	Isotropic Mixing from Isotropic Perfect Echo	74
2.3.1	Isotropic Mixing	74
2.3.2	Isotropic Perfect Echo	77
2.3.3	Fast DOSY Using the Isotropic Perfect Echo	85
2.3.4	Conclusion	90
2.4	Pulse Shapes in the Toggling Frame	92
2.4.1	Introduction: Pulse Shape Classification	93
2.4.2	Introduction: Toggling Frame of Shaped Pulses	94
2.4.3	Introduction: Investigation on Common Pulse Shapes	98
2.4.4	Selective 180° Pulse: Q3 (A)	100
2.4.5	Selective 180° Pulse: RE-BURP (A)	102
2.4.6	Selective 180° Pulse: r-SNOB (A)	104
2.4.7	Selective 180° Pulse: I-BURP-2 (B)	106
2.4.8	Selective 90° Pulse: Q5 (A)	108
2.4.9	Selective 90° Pulse: E-BURP-2 (B2)	110
2.4.10	Selective 90° Pulse: e-SNOB (B3)	112
2.4.11	Broadband 180° Pulse: BURBOP-180 (A)	114
2.4.12	Broadband 180° Pulse: Chirped Pulse (B)	116
2.4.13	Broadband 90° Pulse: BURBOP-90 (A)	118
2.4.14	Broadband 90° Pulse: BEBOP (B2)	120
2.4.15	Hard 180° Pulse: Echo	122
2.4.16	Shaped 180° Pulse: IMP (A)	124
2.4.17	Broadband 180° Pulse Sandwich: BUBU (A)	126
2.4.18	Broadband 180° Pulse Sandwich: BUBI (A, B)	129
2.4.19	Broadband 90° Pulse Sandwich: BE ^{tr} BE (B2)	132
2.5	A Different Perspective on Strong Coupling	135
2.5.1	Strong Coupling in the Double Rotating Frame	136
2.5.2	Geometric Phase Induced by Strong Coupling	139
2.5.3	Average Hamiltonian of Strong Coupling	143
2.6	Heteronuclear Ordered Multi-Quantum Correlations	145
2.6.1	Introduction	145
2.6.2	JRES-HOMQC	146
2.6.3	HOMQC-TOCSY	152
2.6.4	Conclusion	157
3	Homonuclear Decoupling	159
3.1	Introduction	159
3.1.1	J -Resolved Experiments	159
3.1.2	Time-Shared Acquisition	160
3.1.3	Pseudo-2D Chunked Acquisition	161
3.1.4	Real-Time Chunked Acquisition	163
3.1.5	Selective Averaging in Real-Time Pure Shift Acquisition	165
3.2	Real-Time Pure Shift Acquisition of Amide Protons	167
3.2.1	Pulse Sequence	168
3.2.2	Water Suppression	169
3.2.3	Application to Globular Proteins	173

3.2.4	Application to Intrinsically Disordered Proteins	179
3.2.5	Conclusion	181
3.3	BIRD-Based Real-Time Pure Shift Acquisition of Uniformly Isotope-Labeled Samples	182
3.3.1	Pulse Sequence	182
3.3.2	Experimental	186
3.3.3	Conclusion	188
3.4	Selective Pure Shift $H\alpha, C\alpha$ -Correlations	189
3.4.1	Pulse Sequence	190
3.4.2	Experimental	191
3.4.3	Conclusion	196
3.5	Selective Pure Shift $H_{\text{Methyl}}, C_{\text{Methyl}}$ -Correlations	197
3.5.1	Pulse Sequence	197
3.5.2	Experimental	199
3.6	Constant Time SHACA-HSQC	200
3.6.1	Pulse Sequence	200
3.6.2	Experimental	201
3.6.3	Conclusion	205
4	Summary	207
5	Appendix	211
5.1	Theory	211
5.1.1	Spin Rotation from Exponential Operator	211
5.1.2	Irreducible Tensor Components	212
5.1.3	Basic Properties of the Trace	213
5.1.4	Basic Properties of the Kronecker Product	214
5.1.5	Transformation of a Propagator	214
5.1.6	In Detail: Transformation to the Toggling Frame	214
5.1.7	Suzuki-Trotter Approximation for Larger Values of θ	216
5.2	Coherence Transfer Elements	217
5.2.1	Numerical Simulations of IPE-1	217
5.2.2	Spin Echo in the Double Rotating Frame	218
5.2.3	Artifacts in the JRES-HOMQC	220
5.3	Homonuclear Decoupling	221
5.3.1	Experimental Setup and Gradient Calibration for Water Suppression	221
5.3.2	Comparison of FHSQC and BEST-TROSY (Comparable Parameters)	224
5.3.3	Artifact Reduction in Real-Time Pure Shift Acquisition	225
5.3.4	BEST-TROSY at Fast Repetition Rates (Ubiquitin)	226
5.4	Pulse Sequences	227
5.4.1	$^{13}\text{C}, ^{13}\text{C}$ -PM-TOCSY	227
5.4.2	3D (H)CC(CO)NH-TOCSY	229
5.4.3	IPE-1-DOSY	234
5.4.4	IPE-2-DOSY	236
5.4.5	JRES-HOMQC	239
5.4.6	HOMQC-TOCSY	242
5.4.7	FHSQC Using ^{13}C -BIRD Pure Shift Amide Proton Detection	245
5.4.8	BEST-TROSY Using ^{13}C -BIRD Pure Shift Amide Proton Detection	249
5.4.9	SHACA-HSQC Using BASEREX	254
5.4.10	SHACA-SIHSQC for Methyl-Groups Using BASEREX	258
5.4.11	CT-SHACA-HSQC Using BASEREX	262
5.5	Numerical Simulations	268
5.5.1	Strong Coupling: Berry-Phase	268
5.5.2	AHT: IPE (Time-Dependence, 1D)	271
5.5.3	AHT: Case 1 and 2 for Shaped Pulses (Offset-Dependence, 1D)	276
5.5.4	AHT: Case 4 for Shaped Pulses (Fast, Offset-Dependence, 2D)	282

List of Publications	291
List of Tables	293
List of Figures	295
List of References	301

Chapter 1

Theory

Nuclear magnetic resonance (NMR) is based on the magnetic property of nuclei that consist of an uneven number of either protons or neutrons. The magnetic property arises from a rather theoretical concept that is known as nuclear spin. The name's origin could be deduced from either a classical picture where a charged particle in an orbit creates a magnetic field or when being exposed to a magnetic field its peculiar similarity to a spinning top in a gravitational field. It might be tempting to believe in such pictures since they are easier to grasp from a macroscopic point of view. However, nuclear spin is a form of angular momentum that is attributed to the particle as one of its intrinsic properties – like mass or charge. One could even think of the nuclear spin as nothing but a mathematical concept that, indeed, very nicely reflects observations from the real world.^[13]

While an ensemble of isolated spins suffice a classical vector treatment using the *Bloch equations*^[14] for coupled spins a quantum mechanical approach is necessary.^[15] The following chapters touch on the quantum mechanical basis for nuclear spin which is extensively used throughout the present dissertation. More elaborate insights can be found in textbooks of different degree of difficulty.^[13,16–18]

1.1 Nuclear Spin

A nuclear spin can be described by a vector \vec{I} that consists of its three orthogonal and Cartesian spin angular momentum operators \hat{I}_x , \hat{I}_y and \hat{I}_z :

$$\vec{I} = \begin{pmatrix} \hat{I}_x \\ \hat{I}_y \\ \hat{I}_z \end{pmatrix} \quad \text{with} \quad |\vec{I}| = \hbar\sqrt{I(I+1)} \quad (1.1.1)$$

where I is the nuclear spin quantum number that defines the number of degenerate states to be $2I + 1$. When subject to an outer magnetic field \vec{B} the degeneracy is lifted and the states are denoted by the magnetic spin quantum number $m_s = I, I - 1, \dots, -I + 1, -I$ as exemplary shown for a spin- $\frac{1}{2}$ in Figure 1.1. The spin's behavior within an outer magnetic field is described by the *Zeeman interaction*^[19] which is further discussed in Section 1.3 and it is based on the spin's magnetic property. The magnetic moment $\vec{\mu}_I$ originating from the nuclear spin \vec{I} is given by:

$$\vec{\mu}_I = \gamma_I \cdot \vec{I} \quad (1.1.2)$$

^[13] M. H. Levitt. *Spin dynamics: Basics of Nuclear Magnetic Resonance, Second Edition*. John Wiley & Sons, 2009.

^[14] F. Bloch. *Physical Review* **1946**, 70, 460–474.

^[15] S. Yun, M. F. Lightstone and M. J. Thomson. *International Journal of Thermal Sciences* **2005**, 44, 421–428.

^[16] J. Keeler. *Understanding NMR spectroscopy*. John Wiley & Sons, 2010.

^[17] R. R. Ernst, G. Bodenhausen and A. Wokaun. *Principles of Nuclear Magnetic Resonance in One and Two Dimensions*. Oxford University Press, 1987.

^[18] F. Schwabl. *Quantenmechanik (QM I)*. Springer Berlin Heidelberg, 2007.

^[19] P. Zeeman. *Verhandlungen der Physikalischen Gesellschaft zu Berlin* **1896**, 15, 128–130.

in which γ_I is the gyromagnetic ratio that determines the strength of the magnetic moment that originates from nuclear spin and has, therefore, an important role in many practical aspects. The gyromagnetic ratio is defined as:

$$\gamma_I = \frac{|\vec{\mu}_I|}{|\vec{I}|} = g_I \cdot \mu_N / \hbar. \quad (1.1.3)$$

in which g_I is a constant of proportionality, called Landé factor, μ_N is the nuclear magneton and \hbar is Planck's constant.

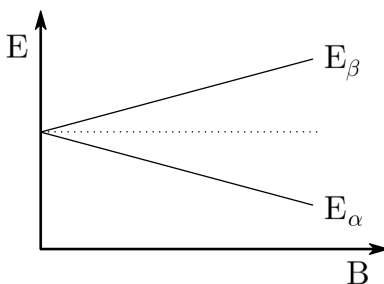


Figure 1.1: Zeeman splitting for nuclear spin $I = \frac{1}{2}$ with positive gyromagnetic ratio as a function of the magnetic field strength B . The eigenstates' energies, E_α and E_β , correspond to quantum numbers of $m_s = +\frac{1}{2}$ and $m_s = -\frac{1}{2}$, respectively.

1.1.1 Solving the Schrödinger Equation

In the present chapter it shall be discussed how the motion of a quantum mechanical system can be determined. The probability for an experimental observation can hereupon be predicted from the expectation value.

The evolution of quantum mechanical systems is determined by the *Schrödinger equation*.^[20] It is a first order linear differential equation where the state's evolution is governed by the total energy operator \hat{H} – it is commonly referred to as the *Hamiltonian*. In principle, it contains all interactions of the considered molecular system. Luckily, in magnetic resonance, only a *reduced spin Hamiltonian* is necessary to describe spin dynamics while interactions to surrounding electrons are considered to occur on a much faster time scale. These interactions normally need to be accounted for by an averaged factor in the *reduced spin Hamiltonian* or, when it comes to time-dependent random molecular motion, are condensed in the relaxation super operator^[21] which causes the magnetization to return to its equilibrium state (Section 1.8.1). Throughout the thesis only the *reduced spin Hamiltonian* is being considered unless denoted otherwise and an introduction to typical Hamiltonians in NMR is found in Section 1.3.

The time-dependent Schrödinger equation which determines quantum dynamics is given as:

$$\frac{\partial}{\partial t} |\psi, t\rangle = -i\hat{H}|\psi, t\rangle \quad \text{and} \quad \frac{\partial}{\partial t} \langle\psi, t| = \langle\psi, t|i\hat{H} \quad (1.1.4)$$

in which $|\psi, t\rangle$ is the *state function* and $\langle\psi, t|$ is its representation in the dual space.² Please note that \hbar is omitted since throughout the dissertation energy eigenvalues are measured in angular frequency units. The state function can be expressed in a complete orthonormal basis which is called the Hilbert space:³

$$|\psi, t\rangle = \sum_{\mathbf{n}} c_{\mathbf{n}}(t)|\mathbf{n}\rangle \quad (1.1.5)$$

^[20] E. Schrödinger. *Physical Review* **1926**, *28*, 1049–1070.

^[21] A. G. Redfield. *Advances in Magnetic and Optical Resonance* **1965**, *1*, 1–32.

² The dual space V^* contains all linear forms that map the vector space V onto its underlying field of scalars. These linear forms of V^* are due to their covariant transformation sometimes referred to as *covectors*.

³ In NMR literature it is frequently stated that a spin state is described by a *state vector* in Hilbert space. However, it is actually described by a whole *set of state vectors* which is called a *state ray*. All vectors being part of the ray differ only by a phase factor λ and $|n'\rangle = \lambda|n\rangle$ with $\lambda = e^{i\varphi}$. Following *Born's law* the probability to find a system $|\psi\rangle$ in state $|n\rangle$

and the system's evolution is reflected in the time-dependent complex coefficients $c_n(t)$. The solution to the Schrödinger equation (1.1.4) is calculated from a Dyson series (Section 1.7.2) – it will result in a unitary rotation whose inverse is given by the adjoint $U^\dagger = U^{-1}$. The unitary rotation is given by:

$$|\psi, t_c\rangle = U(t_c, 0)|\psi, 0\rangle \quad \text{and} \quad \langle\psi, t_c| = \langle\psi, 0|U^\dagger(0, t_c) \quad (1.1.6)$$

$$\text{in which: } U(t_c, 0) = T \exp \left\{ -i \int_0^{t_c} \hat{H}(t) dt \right\}. \quad (1.1.7)$$

We call $U(t_c, 0)$ a propagator that transfers the state function from time $t = 0$ to $t = t_c$ and T is the Dyson Time-Ordering Operator. The operator T is only relevant if we have to deal with a so-called *homogeneous* Hamiltonian^[9] that is *not commuting* with itself at *any* two time points, t' and t'' :

$$[\hat{H}(t'), \hat{H}(t'')] \neq 0. \quad (1.1.8)$$

To solve Equation (1.1.7) for a homogeneous Hamiltonian the reader is referred to Section 1.7. If, on the other hand, the Hamiltonian *commutes* with itself at *any* two time points it is called *inhomogeneous*. In this case, the integral in the exponential of Equation (1.1.7) can be solved with basic math and the propagator is obtained in a rather straight-forward way. It is crucial to note that this holds also for a time-dependent Hamiltonian as long as it is still *inhomogeneous*. If a time-independent Hamiltonian is assumed the situation is further simplified and the propagator is given by:

$$U(t_c, 0) = e^{-i\hat{H}t_c} \quad \text{and} \quad U^\dagger(0, t_c) = e^{+i\hat{H}t_c}. \quad (1.1.9)$$

It might be at first surprising that the formal solution in (1.1.9) is an exponential operator, however, it can be shown that it corresponds to a spin rotation (appendix 5.1.1). For the reason of clarity the time dependence of the propagator is, if not essential, omitted in the following and $U \equiv U(t_c, 0)$.

1.1.2 Expectation Value in Hilbert Space

In quantum mechanics, each experimental observation is associated with the measurement of an Hermitian operator called the *observable*. For an observable \hat{A} multiple different results are conceivable that are all associated with the operator's eigenvalues a . With $|n\rangle$ being the normalized eigenfunctions of \hat{A} the eigenvalues a_n are obtained as follows:

$$\hat{A}|n\rangle = a_n|n\rangle. \quad (1.1.10)$$

Quantum mechanics will fail to predict the exact outcome of a single experiment – even if it is highly controlled – but it can predict the probability to obtain the observable's eigenvalue a_n . Using the state function given in Equation (1.1.5) the probability for the eigenvalue a_n is given from Born's law as:

$$P(a_n) = |\langle n|\psi, t\rangle|^2 = |c_n(t)\langle n|n\rangle|^2 = c_n(t) \cdot c_n^*(t) \quad (1.1.11)$$

Since a single experiment can lead to all possible events it is the observable's expectation value that is of central importance. It can be calculated from:

$$\langle\hat{A}\rangle = \langle\psi|\hat{A}|\psi\rangle \quad (1.1.12)$$

and it can be shown that it is equal to the product of the eigenvalue and the probability of its occurrence:

$$\langle\psi, t|\hat{A}|\psi, t\rangle = c_n(t) \cdot \langle\psi, t|a_n|n\rangle = c_n(t) \cdot c_n^*(t) \cdot a_n \langle n|n\rangle = P(a_n) \cdot a_n \quad (1.1.13)$$

is given by $P(\psi, n') = |\lambda\langle\psi|n\rangle|^2$ where, clearly, the phase factor with $|\lambda| = 1$ is irrelevant. Hence, the vectors belonging to the *same* ray can not be distinguished physically and are ascribed to the same physical state. Instead of the Hilbert space in NMR a *projective Hilbert space* is commonly used (illustrated e.g. in Figure 1.2) in which every “vector” (actually it is a ray) corresponds to an explicit state. Still, the phase factor is of central importance and the time evolution of an eigenstate $|n\rangle$ is determined by a complex phase determined by the eigenstates energy E_n with $|n, t\rangle = \exp\{-iE_n t\} \cdot |n, 0\rangle$. Without further notice the projective Hilbert space shall be used throughout the dissertation.

1.1.3 Hilbert Space for Spin- $\frac{1}{2}$

In NMR, nuclei with spin $I = \frac{1}{2}$ are most frequently encountered and will form the basis of the present dissertation. In principle, for an isolated spin- $\frac{1}{2}$ all orientations in space are equally possible, however, when subject to an outer magnetic field the spin will interact and orientations are no longer degenerate. As discussed earlier, this is based on the Zeeman interaction (Section 1.3) which, in absolute values, is the largest interaction for diamagnetic samples in high resolution NMR. The states are, therefore, commonly represented in the Zeeman eigenbasis with $|\alpha\rangle$ and $|\beta\rangle$ being the two normalized eigenfunctions for a single spin- $\frac{1}{2}$.

Cartesian Operators

If the spin angular momentum operators of Equation (1.1.1) are applied to the Zeeman eigenfunctions $|\alpha\rangle$ and $|\beta\rangle$ one obtains:⁴

$$\begin{aligned} \hat{I}_x|\alpha\rangle &= \frac{1}{2}|\beta\rangle & \hat{I}_y|\alpha\rangle &= -\frac{1}{2i}|\beta\rangle & \hat{I}_z|\alpha\rangle &= \frac{1}{2}|\alpha\rangle \\ \hat{I}_x|\beta\rangle &= \frac{1}{2}|\alpha\rangle & \hat{I}_y|\beta\rangle &= \frac{1}{2i}|\alpha\rangle & \hat{I}_z|\beta\rangle &= -\frac{1}{2}|\beta\rangle \end{aligned} \quad (1.1.14)$$

from which one can derive an operators' matrix representations in the Zeeman eigenbasis to be:

$$\hat{I}_x = \frac{1}{2} \begin{pmatrix} 0 & 1 \\ 1 & 0 \end{pmatrix} \quad \hat{I}_y = \frac{1}{2i} \begin{pmatrix} 0 & 1 \\ -1 & 0 \end{pmatrix} \quad \hat{I}_z = \frac{1}{2} \begin{pmatrix} 1 & 0 \\ 0 & -1 \end{pmatrix} \quad (1.1.15)$$

$$\text{with : } |\alpha\rangle = \begin{pmatrix} 1 \\ 0 \end{pmatrix} \quad \text{and} \quad |\beta\rangle = \begin{pmatrix} 0 \\ 1 \end{pmatrix}. \quad (1.1.16)$$

For a single spin- $\frac{1}{2}$ the operators \hat{I}_x , \hat{I}_y and \hat{I}_z form together with the unity matrix ($\mathbb{1}$) a complete orthogonal matrix space. They are identical to the well-known *Pauli matrices*^[22] ($\hat{\sigma}_x$, $\hat{\sigma}_y$, $\hat{\sigma}_z$ and $\hat{\sigma}_\mathbb{1}$) and satisfy the cyclic commutation relationship:

$$[\hat{I}_i, \hat{I}_j] = \varepsilon_{ijk} \cdot i\hat{I}_k \quad (1.1.17)$$

where ε is the *Levi-Civita symbol*. If (i, j, k) is an even numbered permutation of (x,y,z) then $\varepsilon_{ijk} = +1$ while $\varepsilon_{ijk} = -1$ for an odd numbered permutation.

Shift and Polarization Operators

A transformation of the Cartesian operators and the unity matrix will again lead to a complete matrix space. Its basis operators are the so-called shift (\hat{I}_+ , \hat{I}_-) and polarization operators (\hat{I}_α , \hat{I}_β) which are:

$$\begin{aligned} \hat{I}_+ &= \hat{I}_x + i\hat{I}_y & \hat{I}_- &= \hat{I}_x - i\hat{I}_y & \hat{I}_\alpha &= \frac{1}{2}\mathbb{1} + \hat{I}_z & \hat{I}_\beta &= \frac{1}{2}\mathbb{1} - \hat{I}_z \end{aligned}$$

and vice versa:

$$\hat{I}_x = \frac{1}{2}(\hat{I}_+ + \hat{I}_-) \quad \hat{I}_y = \frac{1}{2i}(\hat{I}_+ - \hat{I}_-) \quad \hat{I}_z = \frac{1}{2}(\hat{I}_\alpha - \hat{I}_\beta) \quad \mathbb{1} = \hat{I}_\alpha + \hat{I}_\beta. \quad (1.1.18)$$

When the shift and polarization operators are applied to the Zeeman eigenfunctions the results are as follows:

$$\begin{aligned} \hat{I}_+|\alpha\rangle &= 0 & \hat{I}_-|\alpha\rangle &= |\beta\rangle & \hat{I}_\alpha|\alpha\rangle &= |\alpha\rangle & \hat{I}_\beta|\alpha\rangle &= 0 \\ \hat{I}_+|\beta\rangle &= |\alpha\rangle & \hat{I}_-|\beta\rangle &= 0 & \hat{I}_\alpha|\beta\rangle &= 0 & \hat{I}_\beta|\beta\rangle &= |\beta\rangle \end{aligned} \quad (1.1.19)$$

^[22] W. Pauli. *Zeitschrift für Physik* **1927**, 43, 601–623.

⁴ Note, Planck's constant \hbar is again omitted since energy eigenvalues shall be given in angular frequency units.

and the operators \hat{I}_+ , \hat{I}_- , \hat{I}_α and \hat{I}_β can likewise be illustrated in the Zeeman eigenbasis as single-entry matrices:

$$\hat{I}_+ = \begin{pmatrix} 0 & 1 \\ 0 & 0 \end{pmatrix} \quad \hat{I}_- = \begin{pmatrix} 0 & 0 \\ 1 & 0 \end{pmatrix} \quad \hat{I}_\alpha = \begin{pmatrix} 1 & 0 \\ 0 & 0 \end{pmatrix} \quad \hat{I}_\beta = \begin{pmatrix} 0 & 0 \\ 0 & 1 \end{pmatrix}. \quad (1.1.20)$$

Superposition States in Bloch Sphere

So far it was assumed that the spin is only in one of its Zeeman eigenstates $|\alpha\rangle$ or $|\beta\rangle$. It might be surprising – since after the measurement a single spin is found either in $|\alpha\rangle$ or $|\beta\rangle$ – but actually it can be in any superposition of these two eigenfunctions. These superposition states are given as:

$$|\psi\rangle = \cos \frac{\theta}{2} |\alpha\rangle + e^{i\phi} \sin \frac{\theta}{2} |\beta\rangle \quad (1.1.21)$$

where θ is the polar and ϕ the azimuthal angle as illustrated by the *Bloch sphere* shown in Figure 1.2. It is noteworthy that the states $|x\rangle$ and $|y\rangle$ are eigenstates of the spin angular momentum operators \hat{I}_x and \hat{I}_y , respectively.

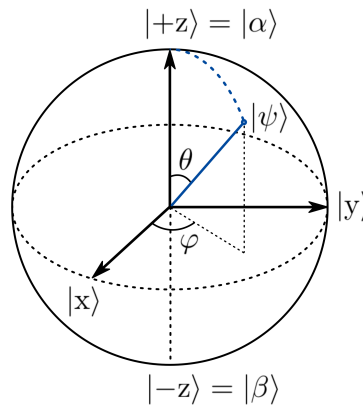


Figure 1.2: Bloch Sphere for nuclear spins with positive gyromagnetic ratio.

1.2 Nuclear Spin in Liouville Space

In the previous section the focus lay on the quantum dynamics of a single spin being in a pure superposition state (Equation 1.1.21). However, in the “real world“ we commonly measure a spin ensemble where each spin of the ensemble is in a superposition of its own – we call it a *mixed state*. To calculate the expectation value for such an ensemble would require to calculate the expectation value of each individual spin which is rather impractical. An elegant solution offers the spin density operator where the ensemble average is already included in the state operator.^[23,24] Since within this formalism the state is no longer expressed as a function, but as an *operator* itself, its quantum dynamics are based on an operator algebra that is commonly referred to as *Liouville space*.^[17]

1.2.1 Spin Density Operator

The spin state of a spin ensemble can be described by a Hermitian spin density operator $\hat{\rho}$ which contains the probabilities p^i for the ensemble to populate one of several possible states. The spin density operator for a mixed state is defined as:

$$\hat{\rho}(t) = \sum_i p^i(t) \cdot |\psi_i, t\rangle\langle\psi_i, t| \quad (1.2.1)$$

and when expressing the state function $|\psi_i, t\rangle$ as a linear combination of eigenfunctions (Equation 1.1.5) it can be shown that averaging over the ensembles' spin states – or more precisely the product of their coefficients $c_n(t)c_m^*(t)$ – can already be done within the state operator:

$$\begin{aligned} \hat{\rho}(t) &= \sum_i p^i(t) \cdot \sum_n \sum_m c_n^i(t)c_m^{i*}(t) \cdot |n\rangle\langle m| \\ &= \sum_n \sum_m \overline{c_n(t)c_m^*(t)} \cdot |n\rangle\langle m|. \end{aligned} \quad (1.2.2)$$

The calculation of the ensemble's expectation value can now be greatly simplified. Starting formally from the sum over all individual expectation values using Equation (1.1.12) we obtain:

$$\begin{aligned} \langle\hat{A}\rangle &= \sum_i p^i(t) \cdot \langle\psi_i, t|\hat{A}|\psi_i, t\rangle \\ &= \sum_i p^i(t) \sum_n \sum_m c_n^i(t)c_m^{i*}(t) \cdot \langle m|\hat{A}|n\rangle \\ &= \sum_n \sum_m \underbrace{c_n(t)c_m^*(t)}_{\rho_{nm}} \cdot \underbrace{\langle m|\hat{A}|n\rangle}_{A_{mn}} \\ &= \sum_n \sum_m \rho_{nm} \text{Tr}\{A|n\rangle\langle m|\} \\ &= \text{Tr}\{A\hat{\rho}(t)\} \end{aligned} \quad (1.2.3)$$

where ρ_{nm} is the time-dependent matrix entry for a density operator $|n\rangle\langle m|$ and for A_{mn} the following identity was used:

$$\text{Tr}\{\hat{A}|n\rangle\langle m|\} = \sum_r \langle r|\hat{A}|n\rangle\langle m|r\rangle = \sum_m \langle r|\hat{A}|n\rangle\delta_{mr} = \langle m|\hat{A}|n\rangle = A_{mn} \quad (1.2.4)$$

Hence, the expectation value of an operator \hat{A} acting on a macroscopic spin ensemble can compactly be calculated from the trace of the operator \hat{A} multiplied by the spin density operator $\hat{\rho}(t)$. It is worth

^[23] J. VON NEUMANN. *Nachrichten von der Gesellschaft der Wissenschaften zu Göttingen* **1927**, 245–278.

^[24] L. LANDAU. *Zeitschrift für Physik* **1927**, 45, 430–441.

noting that the expectation value is calculated in a very similar way to the scalar product⁵ that is given in Liouville space as:

$$\langle \hat{A} | \hat{\rho} \rangle = \text{Tr}\{\hat{A}^\dagger \hat{\rho}\} \quad (1.2.5)$$

What does the Spin Density say?

The content of the spin density operator can best be interpreted when given in the eigenbasis of the Hamiltonian. Its diagonal elements reflect the probability P_m to find the spin system in the eigenstates:

$$\rho_{mm}(t) = \langle m | \hat{\rho}(t) | m \rangle = |\overline{c_m(t)}|^2 = P_m. \quad (1.2.6)$$

which is in close analogy to Equation (1.1.11) for a pure state in Hilbert space. The off-diagonal elements, on the other hand, are directly *associated* with the expectation values of shift operators which can be shown using Equation (1.2.3):

$$\text{Tr}\{|n\rangle\langle m| \hat{\rho}(t)\} = \rho_{mn}(t) \cdot \text{Tr}\{|n\rangle\langle m| m\rangle\langle n|\} = \rho_{mn}(t). \quad (1.2.7)$$

where $|n\rangle\langle m|$ is the shift operator and $\rho_{mn}(t)$ the corresponding off-diagonal element. Hence, the matrix element $\rho_{mn}(t)$ is *related* to the transition between Zeeman eigenfunctions ($|m\rangle$ and $|n\rangle$) and $\rho_{mn}(t)$ can be calculated from:

$$\rho_{mn}(t) = \langle m | \hat{\rho}(t) | n \rangle = \overline{c_m(t)} c_n^*(t). \quad (1.2.8)$$

If the averaged product of coefficients is non-zero ($\overline{c_m(t)} c_n^*(t) \neq 0$) one can say that a *superposition* of Zeeman eigenfunctions $c_m(t)|m\rangle + c_n(t)|n\rangle$ exists *coherently* throughout the spin ensemble. With this regard, the off-diagonal elements are commonly called *coherences* whose time evolution in the *Hamiltonian's eigenbasis* is determined by a single phase:

$$\rho_{mn}(t) = \exp\{-i(E_m - E_n)t\} \rho_{mn}(0) \quad (1.2.9)$$

where E_m and E_n are the energy eigenvalues of the involved eigenfunctions $|m\rangle$ and $|n\rangle$, respectively. Clearly, the time evolution implies that a coherence is never an eigenstate of the Hamiltonian.^[17]

Coherences can further be classified by the value p which reflects the difference in magnetic quantum numbers for the observed transition. One speaks of *p-quantum coherence* and for a coherence represented by an element ρ_{mn} the value p is defined as:

$$p = m_m - m_n \quad (1.2.10)$$

with m_m and m_n being the magnetic quantum numbers of state $|m\rangle$ and $|n\rangle$. Some coherences are of particular interest and are, therefore, given a specified name – these are:

$$\begin{aligned} p = 0 & \rightarrow \text{zero-quantum coherence and zero-spin order} \\ p = \pm 1 & \rightarrow \text{single-quantum coherence} \\ p = \pm 2 & \rightarrow \text{double-quantum coherence.} \end{aligned}$$

It is important to note that per definition only single-quantum coherences associated to $\langle \hat{I}_+ \rangle = \rho_-$ can directly be observed in an experiment.

Matrix Representation of the Spin Density Operator

For an ensemble of isolated spins- $\frac{1}{2}$ the spin density operator in a pure state can be expressed in the general form:

$$\hat{\rho} = |\psi\rangle\langle\psi| = \begin{pmatrix} c_\alpha \\ c_\beta \end{pmatrix} \begin{pmatrix} c_\alpha^* & c_\beta^* \end{pmatrix} = \begin{pmatrix} c_\alpha c_\alpha^* & c_\alpha c_\beta^* \\ c_\beta c_\alpha^* & c_\beta c_\beta^* \end{pmatrix} = \begin{pmatrix} \rho_\alpha & \rho_+ \\ \rho_- & \rho_\beta \end{pmatrix} \quad (1.2.11)$$

⁵ The scalar product of two matrices is given by the *Frobenius inner product* which is a requirement to make the underlying matrix space a Hilbert space.

where the elements ρ_α and ρ_β correspond to the probabilities of populating the states $|\alpha\rangle$ and $|\beta\rangle$, respectively. The elements ρ_+ and ρ_- , on the other hand, are the coherences with $p = +1$ and $p = -1$ according to Equation (1.2.10). Note, the bar over the coefficients denoting the average can be omitted for a pure state.^[17] Clearly, the spin density matrix of Equation (1.2.11) can also be expressed as a linear combination of single-entry matrices:

$$\hat{\rho} = \rho_\alpha \hat{I}_\alpha + \rho_\beta \hat{I}_\beta + \rho_+ \hat{I}_+ + \rho_- \hat{I}_-. \quad (1.2.12)$$

from which is evident that both spin angular momentum operators (Equation 1.1.15) and the spin density of the respective pure state are given by the same matrix *representation*. Despite the similarity they should not be mixed since their origin is fundamentally different. Keeping this in mind, it still seems reasonable to use a notation where the respective state is described by a spin angular momentum operator (e.g. with $\hat{\rho} = \hat{I}_z$). This is commonly done without special notice being taken. For the sake of completeness it shall be mentioned that also *observables* in Liouville space are represented by exactly the same matrix form.

Expectation Value and Scalar Product

It is important to note at that point that an experimental observation is based on the expectation value. Using Equation (1.2.3) for the shift (\hat{I}_+ , \hat{I}_-) and polarization operators (\hat{I}_α , \hat{I}_β) the expectation values are given as:

$$\langle \hat{I}_\alpha \rangle = \rho_\alpha \quad \langle \hat{I}_\beta \rangle = \rho_\beta \quad \langle \hat{I}_+ \rangle = \rho_- \quad \langle \hat{I}_- \rangle = \rho_+ \quad (1.2.13)$$

where $\langle \hat{I}_+ \rangle$ and $\langle \hat{I}_- \rangle$ might not have the expected results. It is the operator \hat{I}_+ that is associated to (-1)-quantum coherence and vice versa for \hat{I}_- . The reason for that is that the expectation value (Equation 1.2.3) and the scalar product (Equation 1.2.5) are calculated in a slightly different manner. Only for Hermitian operators both expectation value and scalar product will lead to the same result. For the Hermitian spin angular momentum operators \hat{I}_x , \hat{I}_y and \hat{I}_z the expectation values are given as:

$$\langle \hat{I}_x \rangle = \frac{1}{2}(\rho_- + \rho_+) \quad \langle \hat{I}_y \rangle = \frac{1}{2i}(\rho_- - \rho_+) \quad \langle \hat{I}_z \rangle = \frac{1}{2}(\rho_\alpha - \rho_\beta). \quad (1.2.14)$$

Note, ρ_+ and ρ_- can be interconverted by complex conjugation with $\rho_+^* = \rho_-$ and $\rho_-^* = \rho_+$. Therefore, the expectation value of the Hermitian operators, $\langle \hat{I}_x \rangle$ and $\langle \hat{I}_y \rangle$, is *always* real.

1.2.2 Product Operators

In the previous chapters only a single spin or a spin ensemble of isolated identical spins was assumed. Honestly, if this was reality it would be a rather boring scenario for an NMR spectroscopist. Luckily, spin-spin interactions (Section 1.3) are in general large enough to be observed and the quantum mechanical description of larger spin systems is required.

The single-spin operator basis consists of matrices of dimension (2×2) , hence, 4 single-entry basis matrices are sufficient to describe the underlying space. In Liouville space the expansion to the operator basis of larger spin systems is done with the Kronecker product (\otimes) of single-spin operators where the matrices' dimensions are increased to $(2^n \times 2^n)$ with n being the number of spins and 4^n is the number of basis operators.^[25] This way, so-called *product operators* are obtained which offer a very convenient way to extend the basis even with Cartesian operators:

$$\begin{aligned} \hat{\sigma}_\gamma \otimes \mathbb{1} &= \hat{I}_{1\gamma} \\ \mathbb{1} \otimes \hat{\sigma}_\gamma &= \hat{I}_{2\gamma} \\ 2\hat{\sigma}_\gamma \otimes \hat{\sigma}_\delta &= 2\hat{I}_{1\gamma}\hat{I}_{2\delta} \end{aligned}$$

^[25] K. Packer and K. Wright. *Molecular Physics* **1983**, 50, 797–813.

where $\hat{\sigma}$ are the Pauli matrices (single-spin operators) with $\gamma, \delta = x, y, z$ and $\hat{I}_{1,2}$ is used to denote the operator for spin 1 or 2 in the expanded basis. For the bilinear operator illustrated in the last line a normalization factor of 2 is required. In the example above it is important to note that the left side of the Kronecker product is associated with spin 1 while the right side is to spin 2. The unity matrix can be considered a place-holder doing nothing to the respective spin. In the last line of the above example a so-called bilinear term is created from two Pauli matrices which is basically identical to the matrix product of the two operators:

$$2\hat{I}_{1\gamma} \cdot \hat{I}_{2\delta} = 2(\hat{\sigma}_\gamma \otimes \mathbb{1}) \cdot (\mathbb{1} \otimes \hat{\sigma}_\delta) = 2\hat{I}_{1\gamma}\hat{I}_{2\delta}. \quad (1.2.15)$$

1.2.3 Solving the Liouville-von Neumann Equation

As was discussed in Section 1.1.1 the time evolution of a quantum mechanical system is determined by the Hamiltonian $\hat{\mathcal{H}}$. In order to determine the dynamics of a spin density operator the Liouville-von Neumann equation has to be applied:

$$\frac{\partial}{\partial t}\hat{\rho}(t) = -i[\hat{\mathcal{H}}, \hat{\rho}(t)]. \quad (1.2.16)$$

The Liouville-von Neumann equation can be derived from the Schrödinger equation (1.1.4) and the definition of the spin density operator for a pure state (Equation 1.2.11):

$$\begin{aligned} \frac{\partial}{\partial t}\hat{\rho}(t) &= \frac{\partial|\psi, t\rangle}{\partial t}\langle\psi, t| + |\psi, t\rangle\frac{\partial\langle\psi, t|}{\partial t} \\ &= -i\hat{\mathcal{H}}|\psi, t\rangle\langle\psi, t| + |\psi, t\rangle\langle\psi, t|i\hat{\mathcal{H}} \\ &= -i(\hat{\mathcal{H}}\hat{\rho}(t) - \hat{\rho}(t)\hat{\mathcal{H}}) \\ &= -i[\hat{\mathcal{H}}, \hat{\rho}(t)]. \end{aligned}$$

From the solution to the Schrödinger equation given in Section 1.1.1 a straight-forward solution to the Liouville-von Neumann equation can be derived:

$$\hat{\rho}(t) = |\psi, t\rangle\langle\psi, t| = U|\psi, 0\rangle\langle\psi, 0|U^\dagger = U\hat{\rho}(0)U^\dagger. \quad (1.2.17)$$

It shall again be mentioned that the propagator U contains the Dyson Time-Ordering operator which can only be omitted for an inhomogeneous Hamiltonian as discussed in Section 1.1.1 and 1.7.2.

1.3 Nuclear Spin Hamiltonian

As we have seen in the previous section, the Hamiltonian $\hat{\mathcal{H}}$ directly determines the system's dynamic and is, therefore, an important attribute of the considered system. Despite the fact that the interaction between the external magnetic field and nuclear spins is comparatively strong, it turns out that in NMR the spin systems can be considered rather solitary with respect to its surroundings which greatly facilitates spin manipulation. In the present section these circumstances shall be further discussed, as well as the origins of various fundamental Hamiltonians of liquid state NMR. As mentioned before, solely spin- $\frac{1}{2}$ nuclei are being considered in the dissertation at hand and, hence, only magnetic interactions will be discussed in the following.⁶

1.3.1 Spin Hamiltonian Hypothesis

The system's full Hamiltonian $\hat{\mathcal{H}}_{\text{full}}$ is composed of all interactions between the systems' electrons and nuclei and, in turn, acts both on space and spin coordinates. For a nuclear magnetic observation, however, electrons move on such a short time scale⁷ that only an average influence is noticeable and we can likewise assume that the energies of spin transitions are too small to have an effect on the motion of the molecule or its electrons.^[13] This is commonly known as the *spin Hamiltonian hypothesis* and the wave function of the full molecular system can be written as the product of two. One of these functions $|\psi_{\text{spin}}\rangle$ depends on spin coordinates and the other $|\phi_{\text{latt}}\rangle$ on all remaining variables which is commonly called the *lattice*:

$$|\Psi_{\text{full}}\rangle = |\phi_{\text{latt}}\rangle \cdot |\psi_{\text{spin}}\rangle. \quad (1.3.1)$$

Formally, we can express a spin Hamiltonian $\hat{\mathcal{H}}_{\text{spin}}$ that depends only on the nuclear (and electronic) spins and averaging over the so-called *lattice* variables is obtained by the partial trace:^[17]

$$\hat{\mathcal{H}}_{\text{spin}} = \sum_{\text{latt}} \langle \phi_{\text{latt}} | \hat{\mathcal{H}}_{\text{full}} | \phi_{\text{latt}} \rangle = \text{Tr}_{\text{latt}} \{ \hat{\mathcal{H}}_{\text{full}} \}. \quad (1.3.2)$$

For the sake of completeness, it shall be mentioned that a restriction to spin variables is likewise possible for the spin density $\hat{\rho}$:

$$\hat{\rho}_{\text{spin}} = \text{Tr}_{\text{latt}} \{ \hat{\rho}_{\text{full}} \} \quad (1.3.3)$$

and the expectation value of an operator \hat{A} which is assumed to be diagonal in the lattice variables:

$$\langle \hat{A} \rangle = \text{Tr}_{\text{spin}} \{ \hat{A} \hat{\rho}_{\text{spin}} \}. \quad (1.3.4)$$

1.3.2 Construction and Truncation of a Nuclear Spin Hamiltonian

The Hamiltonian is sometimes referred to as the total energy operator and in magnetic resonance it can be derived from the classical interaction energy where given variables are replaced by their quantum mechanical analog.^[26] The potential energy of a magnetic moment $\vec{\mu}$ in a magnetic field \vec{B} is known from classical physics and can be calculated from their scalar product:

$$E = -\vec{\mu} \cdot \vec{B}. \quad (1.3.5)$$

The magnetic moment $\vec{\mu}$ can be replaced by its quantum mechanical counterpart $\vec{\mu}_I$ originating from spin \vec{I} which is known from Equation (1.1.2) and (1.1.3) and its interaction in a magnetic field can be written as:⁸

$$\hbar \cdot \hat{\mathcal{H}} = -\vec{\mu}_I \cdot \vec{B}_{\text{eff}} = -\gamma_I \hbar \vec{I} \cdot \vec{B}_{\text{eff}} \quad (1.3.6)$$

^[26] S. A. Smith, W. E. Palke and J. T. Gerig. *Concepts in Magnetic Resonance* **1992**, 4, 107–144.

⁶ The electric charge of nuclei with spin $I \geq 1$ is not spherically symmetric and it can, therefore, interact with an electric field gradient of the surrounding structure – the interaction is called the *quadrupolar coupling*.

⁷ The time scale is considered to be much faster than the *Larmor precession*.

⁸ At this point Planck's constant \hbar shall not be omitted since a direct relation to the classical energy is given.

where $\vec{\mathbf{B}}_{\text{eff}}$ is the effective magnetic field at the spin's location. In general, $\vec{\mathbf{B}}_{\text{eff}}$ can have various origins and it is not necessarily bound to be colinear with its original source. Therefore, an interaction needs to be further specified by a tensor \mathcal{A} which contains the information of the effective magnetic field that is induced by the source at the location of the considered spin $\vec{\mathbf{I}}$. Such a tensor can be regarded a mathematical tool that creates a vector (effective magnetic field) from another vector (source) and depends on the considered interaction. Commonly, one distinguishes *external* interactions of a spin where the source is an *external* magnetic field $\vec{\mathbf{B}}$ (it is controlled by the experimenter) from *internal* spin-spin interactions where the source is a spin $\vec{\mathbf{I}}$ within the considered molecular system. The external and internal Hamiltonian, \mathcal{H}_{ext} and \mathcal{H}_{int} , are said to be *linear* and *bilinear in spin operators*,⁹ respectively, and they can be expressed as:

$$\text{external:} \quad \hat{\mathcal{H}}_{\text{ext}} = \sum_k \vec{\mathbf{I}}_k \mathcal{A}_k \vec{\mathbf{B}} = \sum_k \vec{\mathbf{I}}_k \vec{\mathbf{B}}_{\text{eff}} \quad (1.3.7)$$

$$\text{internal:} \quad \hat{\mathcal{H}}_{\text{int}} = \sum_{k>j} \vec{\mathbf{I}}_k \mathcal{A}_{k,j} \vec{\mathbf{I}}_j = \sum_{k>j} \vec{\mathbf{I}}_k \vec{\mathbf{I}}_{j,\text{eff}} \quad (1.3.8)$$

where k and j are the indices for different spins and \mathcal{A} is considered a general Cartesian rank 2 tensor¹⁰ which contains the information that relates the field $\vec{\mathbf{B}}$ (external) or spin $\vec{\mathbf{I}}_j$ (internal) to spin $\vec{\mathbf{I}}_k$. It is crucial to note that the tensor \mathcal{A} actually acts both ways and e.g. likewise returns the effective field of spin $\vec{\mathbf{I}}_k$ at the location of $\vec{\mathbf{I}}_j$. Further information on tensor \mathcal{A} and its symmetry properties is found in the Appendix 5.1.2.

Expressing the product in Equation (1.3.7) and (1.3.8) by an Einstein notation¹¹ reveals that also the spin and field vectors can be rewritten in a Cartesian tensor \mathcal{T} which is created from their dyadic product¹² and the general Hamiltonian for a *single* interaction can be expressed as:

$$\hat{\mathcal{H}} = \sum_a^3 \sum_b^3 A_{ab} T_{ba} = \mathcal{A} \odot \mathcal{T} \quad (1.3.9)$$

where a and b denote the Cartesian axes (x, y, z) of the Cartesian *components* A (of \mathcal{A}) and T (of \mathcal{T}), the scalar product of tensors is denoted by the operator (\odot) and spin indices (k and j) are omitted. It is important to realize that tensor \mathcal{A} contains only spatial information while spin components are separately contained in tensor \mathcal{T} . In a subsequent step both Cartesian tensors, \mathcal{A} and \mathcal{T} , can be transformed to spherical coordinates and it turns out that the representation as irreducible spherical tensors (Appendix 5.1.2) is particularly helpful if the system undergoes rotational transformation. In terms of irreducible spherical *components* the considered interaction in Equation (1.3.9) can be rewritten:

$$\hat{\mathcal{H}} = \sum_{l=2}^2 \sum_{m=-l}^l (-1)^m A_l^{-m} T_l^m \quad (1.3.10)$$

where l and m are chosen due to the similarity to spherical harmonics. We shall distinguish transformations acting on spatial components A_l^m (e.g. molecular motion) from transformations acting on spin components T_l^m (e.g. z-rotation induced by static magnetic field) – both can result in a truncation of the considered Hamiltonian.

⁹ The quadrupolar coupling is said to be *quadratic* (with $k = j$) which can be considered a special form of bilinearity.

¹⁰ The rank of a tensor is more accurately given by two numbers, r and s , and it describes how the tensor behaves under transformation. A tensor of type (r, s) is composed via the tensor product of r vectors and s covectors (dual space) that transform contra- and covariant, respectively. A bilinear form can be considered a $(0, 2)$ -tensor that maps two vectors onto the space's underlying field while a $(1, 1)$ -tensor creates a vector from a vector.

¹¹ In the Einstein notation different mathematical expression can be written as a sum over indexed coefficients. The above mentioned interaction could, hence, be written as: $\vec{\mathbf{I}} \mathcal{A} \vec{\mathbf{I}} = \hat{I}_a \mathcal{A}_b^a \hat{I}^b = \mathcal{A}_b^a \hat{I}^b \hat{I}_a = \mathcal{A}_b^a \mathcal{T}_a^b$, where in the last step the dyadic product is applied.

¹² The dyadic product describes an operation where a tensor \mathcal{T} is constructed from two vectors, \mathbf{a} and \mathbf{b} , and it can formally be written as $\mathcal{T} = \mathbf{a} \mathbf{b}$. Likewise it can be expressed in terms of a matrix product where the tensor's matrix \mathbf{M} is given as $\mathbf{M} = \mathbf{a} \mathbf{b}^T$. If \mathbf{a} and \mathbf{b} are vectors of dimensions $(n_a \times 1)$ and $(n_b \times 1)$, respectively, the dimension of the resulting matrix is given as $(n_a \times n_b)$.

Molecular Motion

In order to account for molecular motion the coordinates of the spatial tensor components A_l^m need to be transformed from the *principal axes*¹³ (PAS) to the laboratory frame (LAB).¹⁴ For spherical tensors one can use the *Wigner rotation*^[27] matrix elements ($D_{m',m}^l$) to calculate an arbitrary rotation given by three time-dependent *Euler angles* (Ω_t) while the rank of the irreducible tensor is not being changed by the operation.^[26] Hence, a rotation applied to A_l^m will result in a linear combination of the $2l+1$ components $A_l^{m'}$. The transformation to the laboratory frame returns time-dependent components $A_l^{m'}(\text{LAB})$ which can be expressed as:

$$A_l^{m'}(\text{LAB}) = \sum_{m=-l}^l D_{m',m}^l(\Omega_t) A_l^m(\text{PAS}) \quad (1.3.11)$$

where l stays unchanged by the rotation. It turns out that molecular motion in isotropic liquids will cause all spatial components A_l^m with $l > 0$ to vanish due to time-averaging which greatly simplifies common Hamiltonians in liquid state NMR.^[28] Note, the term “vanish” can be misleading – despite the fact that these components are averaged to zero they can still emerge when it comes to relaxation.

Secular Approximation

The spin tensor components T_l^m are given in spin space which, in principle, coincides with the laboratory frame and molecular motion does not impose a transformation on T_l^m (excluding e.g. chemical exchange). However, in high field NMR a z-rotation (U_z) is induced by the static magnetic field and shift operators will acquire a phase while others do not:

$$U_z^\dagger \hat{I}_\pm U_z = \hat{I}_\pm e^{\pm i\omega_z t} \quad (1.3.12)$$

$$U_z^\dagger \hat{I}_z U_z = \hat{I}_z. \quad (1.3.13)$$

Hence, all spin components T_l^m with $m \neq 0$ acquire a periodic time-dependence under the z-rotation and can, therefore, be rejected.^[28] This is what is often referred to as the *secular approximation* and we say the Hamiltonian is truncated. In certain cases also the spin component T_0^0 (where $m = 0$) is further truncated which is shown in Section 2.5.

A detailed step-by-step discussion on the construction of Hamiltonians is given by Smith et al.^[26,29,30] where essential Hamiltonians in liquid state NMR are elaborated. In the following, only truncated Hamiltonians of liquid state NMR will be stated in Cartesian coordinates.

1.3.3 Zeeman Interaction

The Zeeman Hamiltonian $\hat{\mathcal{H}}_Z$ describes the (external) interaction of a spin (\vec{I}_k) with the static magnetic field \vec{B}_0 and since the electronic structure surrounding spin k will alter the effective field at the spin's location the *chemical shielding* tensor σ_k is introduced¹⁵

$$\hat{\mathcal{H}}_Z = - \sum_k \gamma_k \vec{I}_k (\mathbb{1} - \sigma_k) \vec{B}_0 \quad (1.3.14)$$

[27] E. Wigner. *Zeitschrift für Physik* **1927**, 43, 624–652.

[28] U. Haeberlen. *High Resolution NMR in Solids - Selective Averaging*. Academic Press, 1976.

[29] S. A. Smith, W. E. Palke and J. T. Gerig. *Concepts in Magnetic Resonance* **1992**, 4, 181–204.

[30] S. A. Smith, W. E. Palke and J. T. Gerig. *Concepts in Magnetic Resonance* **1993**, 5, 151–177.

¹³ In its principal axes a tensor has a diagonal form – assuming the antisymmetric component of rank 1 is zero.

¹⁴ The transformation to the laboratory frame commonly includes an intermediate step where the principal axis of \mathcal{A} is transformed to arbitrary axes that are aligned with the molecular frame.

¹⁵ Usually, in NMR the measured samples are diamagnetic and the effective field will be slightly weaker than its source which is indicated by $(\mathbb{1} - \sigma)$. One could explain such an effect by a classical analogue, the Lenz's law, which clearly is oversimplified.^[31,32]

where the influence of σ_k is commonly very small and the static field \vec{B}_0 is assumed to point along z. Considering the truncation for liquid state NMR discussed in Section 1.3.2 the Zeeman Hamiltonian can be simplified:

$$\hat{H}_Z = - \sum_k \underbrace{\gamma_k (1 - \sigma_k^{\text{iso}}) B_0}_{-\omega_{0,k}} \hat{I}_{z,k} = \sum_k \omega_{0,k} \hat{I}_{z,k} \quad (1.3.15)$$

where ω_0 is the *Larmor frequency* and σ^{iso} is the *isotropic* chemical shielding. It is calculated from:

$$\sigma^{\text{iso}} = \text{Tr} \{ \boldsymbol{\sigma} \} = \frac{1}{3} (\sigma_{xx} + \sigma_{yy} + \sigma_{zz}) \quad (1.3.16)$$

where σ_{xx} , σ_{yy} and σ_{zz} are the diagonal elements of $\boldsymbol{\sigma}$ given in its principal axes. It is noteworthy that according to Equation (1.3.15) the Larmor frequency for nuclei with $\gamma > 0$ is negative and positive for $\gamma < 0$. In NMR, the spectrum is conventionally illustrated using the *chemical shift* (δ) which is independent of the applied static magnetic field and is expressed in parts per million (ppm). It is defined as:

$$\delta = \frac{\omega_0 - \omega_{\text{int}}}{\omega_{\text{int}}} \quad (1.3.17)$$

where ω_{int} is the frequency of an internal standard with a defined chemical shift δ_{int} (e.g. TMS at 0 ppm). It follows from Equation (1.3.17) that independent of the sign of the gyromagnetic ratio γ a larger δ -value (left side in spectrum) signifies a higher frequency in *absolute values*. The offset frequency ν in the rotating frame (Section 1.5.3) is, on the other hand, calculated as:

$$\nu = \frac{\omega_0 - \omega_{\text{rot}}}{2\pi} \quad (1.3.18)$$

where ω_{rot} is the frequency of the rotating frame which is located in the spectrum's center at $\nu = 0$ Hz. Following Equation (1.3.18) the offset frequency ν for signals with larger δ -values is negative if $\gamma > 0$ and positive if $\gamma < 0$.

1.3.4 Radio Frequency Pulse

The time-dependent perturbation of the radio frequency (RF) pulse $\hat{H}_P(t)$ is given by a linear polarized magnetic field $\vec{B}_1(t)$ in the transverse plain and can be defined in analogy to the Zeeman interaction:

$$\hat{H}_P(t) = - \sum_k \gamma_k \vec{I}_k \vec{B}_1(t) \quad (1.3.19)$$

where $\|\vec{B}_1\| \ll \|\vec{B}_0\|$ and, hence, the chemical shielding tensor of (1.3.14) is assumed to be negligible. The linear polarized magnetic field $\vec{B}_1(t)$ can be decomposed into two counter-rotating circular polarized components ($\hat{H}_{P\pm}$) with half the amplitude (B_1) whereof only the resonant component (\hat{H}_{P+}) needs to be considered:

$$\hat{H}_{P+}(t) = - \sum_k \underbrace{\frac{1}{2} \gamma_k B_1}_{-\omega_1} [\cos(\omega_P t + \phi) \hat{I}_x + \sin(\omega_P t + \phi) \hat{I}_y] \quad (1.3.20)$$

where ω_1 is the *Rabi frequency*^[1], ω_P is the frequency of the pulse¹⁶ and ϕ is the pulse phase for $t = 0$. This is known as the *rotating wave approximation* and shall be discussed thoroughly in section (1.5.3). The transformation to the so-called *rotating-frame* results in a time-independent perturbation^[33] and the pulse is given as:

$$\hat{H}_P = \sum_k \omega_1 [\cos(\phi) \hat{I}_x + \sin(\phi) \hat{I}_y]. \quad (1.3.21)$$

where it is crucial to note that the transformation is performed in a way that the Rabi frequency ω_1 is always positive – independent of the sign of γ .^[13]

[33] I. I. Rabi, N. F. Ramsey and J. Schwinger. *Reviews of Modern Physics* **1954**, 26, 167–171.

¹⁶ The resonant frequency of the pulse ω_P is negative (positive) for nuclei with $\gamma > 0$ ($\gamma < 0$).

1.3.5 Pulsed Field Gradients

During a pulsed field gradient an *inhomogeneous* magnetic field, $\vec{B}_z(t)$, is created along the laboratory frame z-axis.¹⁷ The magnetic field strength is *linearly* dependent on the position within the sample (\vec{r}) and the Hamiltonian can be written as:

$$\begin{aligned}\hat{H}_G(t) &= - \sum_k \gamma_k \vec{B}_z(t) \hat{I}_{z,k} \\ &= - \sum_k \gamma_k G_a(t) r_a \hat{I}_{z,k}\end{aligned}\tag{1.3.22}$$

where r_a is the coordinate along the axes $a = \{x, y, z\}$ and $G_a(t)$ defines the linear field gradient with $G_a(t) = \frac{\partial B_z(t)}{\partial r_a}$. The gradient strength of $G_a(t)$ is commonly given in Gauss or Tesla per meter.

1.3.6 Indirect Spin-Spin Coupling

The indirect spin-spin coupling¹⁸ is an internal spin-spin interaction which was first discussed by Ramsey and Purcell.^[34,35] It is mediated by electrons involved in the chemical bond and its Hamiltonian \hat{H}_J is given as:

$$\hat{H}_J = \sum_{k>j} 2\pi \vec{I}_k \mathcal{J}_{k,j} \vec{I}_j\tag{1.3.23}$$

where $\mathcal{J}_{k,j}$ is the coupling tensor of spin k and j . The factor of 2π accounts for the fact that in isotropic liquids the coupling constant J^{iso} is given in Hertz and the isotropic Hamiltonian is:

$$\hat{H}_J^{\text{iso}} = \sum_{k>j} 2\pi J_{k,j}^{\text{iso}} \vec{I}_k \cdot \vec{I}_j\tag{1.3.24}$$

$$\text{where: } J^{\text{iso}} = \text{Tr}\{\mathcal{J}\} = \frac{1}{3}(J_{xx} + J_{yy} + J_{zz}).$$

For two spins, k and j , with large difference in Larmor frequencies (which is sometimes also referred to as *offset*) the isotropic coupling Hamiltonian \hat{H}_J^{iso} is further truncated to:

$$\hat{H}_J^{\text{weak}} = \sum_{k>j} 2\pi J_{k,j}^{\text{iso}} \hat{I}_{z,k} \hat{I}_{z,j}\tag{1.3.25}$$

and one speaks of weakly coupled spins. If, on the other hand, there is only a small offset for the coupled spins one speaks of strong coupling and it is crucial to note that it is not referred to the size of the coupling constant J^{iso} . In contrast to the Zeeman interaction the Hamiltonian \hat{H}_J is independent of the static magnetic field \vec{B}_0 and second order effects on spectra from strong coupling (for non-identical spins) are reduced in higher magnetic fields. The truncation of the isotropic Hamiltonian shall be discussed in more detail in Section 2.5. It is further worth noting that J is positive if gyromagnetic ratios of involved spins have the same sign and both spins are coupled via one bond. The well-known *Karplus equation*, on the other hand, allows an estimated prediction of J -values for coupled *vicinal* protons that was later generalized empirically.^[36,37]

[34] N. F. Ramsey and E. M. Purcell. *Physical Review* **1952**, *85*, 143–144.

[35] N. F. Ramsey. *Physical Review* **1953**, *91*, 303–307.

[36] M. Karplus. *Journal of the American Chemical Society* **1963**, *85*, 2870–2871.

[37] C. A. Haasnoot, F. A. DE Leeuw and C. Altona. *Tetrahedron* **1980**, *36*, 2783–2792.

¹⁷ Note, in mathematical terms $\vec{B}_z(t)$ is actually not a vector, but a vector field.

¹⁸ There are various expressions for this coupling: *scalar coupling*, *J-coupling*, *indirect dipole-dipole coupling*.

1.3.7 Direct Dipole-Dipole Coupling

The dipolar Hamiltonian $\hat{\mathcal{H}}_D$ can be derived from the classical energy (E_D) of two interacting dipoles $\vec{\mu}$ which are replaced in the Hamiltonian by the quantum mechanical analog ($\vec{\mu} = \gamma\vec{I}$) and from:¹⁹

$$E_D = \sum_{k>j} \frac{1}{r_{kj}^3} \left[\vec{\mu}_k \cdot \vec{\mu}_j - 3 \frac{(\vec{\mu}_k \cdot \vec{r}_{kj})(\vec{\mu}_j \cdot \vec{r}_{kj})}{r_{kj}^2} \right] \quad (1.3.26)$$

$$\text{we obtain: } \hat{\mathcal{H}}_D = \sum_{k>j} \frac{\gamma_k \gamma_j \hbar}{r_{kj}^3} \left[\vec{I}_k \cdot \vec{I}_j - 3 \frac{(\vec{I}_k \cdot \vec{r}_{kj})(\vec{I}_j \cdot \vec{r}_{kj})}{r_{kj}^2} \right] \quad (1.3.27)$$

where \vec{r}_{kj} is a vector of length r_{kj} connecting the spins, \vec{I}_k and \vec{I}_j . Commonly, the dipolar Hamiltonian is written in a condensed form:

$$\hat{\mathcal{H}}_D = \sum_{k>j} b_{kj} \vec{I}_k \mathcal{D}_{kj} \vec{I}_j \quad (1.3.28)$$

where \mathcal{D} is the dipolar coupling tensor with $\text{Tr}\{\mathcal{D}\} = 0$ and prefactors are summarized in a constant b_{kj} :²⁰

$$b_{kj} = \frac{\gamma_k \gamma_j \hbar}{r_{kj}^3}. \quad (1.3.29)$$

For two homonuclear spins, \vec{I}_k and \vec{I}_j , the secular approximation will lead to a truncated Hamiltonian:

$$\hat{\mathcal{H}}_{D,\text{homo}}(\theta_{kj}) = b_{kj} \cdot \frac{1}{2} (3 \cos^2 \theta_{kj} - 1) \cdot (3 \hat{I}_{kz} \hat{I}_{jz} - \vec{I}_k \cdot \vec{I}_j) \quad (1.3.30)$$

where θ is the angle between the static magnetic field vector \vec{B}_0 and the vector \vec{r}_{kj} connecting the two spins. For a heteronuclear spin pair the dipolar Hamiltonian is further truncated and is given by:

$$\hat{\mathcal{H}}_{D,\text{het}}(\theta_{kj}) = b_{kj} \cdot \frac{1}{2} (3 \cos^2 \theta_{kj} - 1) \cdot (2 \hat{I}_{kz} \hat{I}_{jz}). \quad (1.3.31)$$

Since the dipolar coupling tensor \mathcal{D} is symmetric and its trace is zero a tensor decomposition leads to a single second rank tensor. For this reason molecular motion in isotropic liquids will cause the dipolar coupling tensor \mathcal{D} to be averaged to zero.

¹⁹ Note, from replacing the classical magnetic moment $\vec{\mu}$ by its quantum mechanical analog $\gamma\vec{I}$ one would expect that \hbar is squared in the dipolar Hamiltonian. Since in the present dissertation energy eigenvalues are given in angular frequency units, one \hbar is again omitted.

²⁰ The constant b_{kj} is sometimes also extended by the magnetic constant μ_0 over 4π to be given in SI units.^[13]

1.4 Product Operator Formalism

The *Product Operator Formalism* is a helpful tool which offers a fast solution to the Liouville-von Neumann equation (1.2.16) – the Hamiltonian’s effect on a spin density can be calculated from their commutator. It allows an understandable description of many important NMR experiments and is nicely discussed by Sørensen et al.^[38] A short derivation and its general application for Cartesian operators of a two-spin system are being discussed in the following.

Derivation

The formal solution to the Liouville-von Neumann equation is known from (1.2.17) where the state’s evolution is determined by a time-independent Hamiltonian and can be calculated by the propagator U :

$$\hat{\rho}(t) = U\hat{\rho}(0)U^\dagger. \quad (1.4.1)$$

From the Appendix 5.1.1 it is evident that a complex exponential operator can be expressed in a power series and is further given by:

$$U_A = \exp\{-i\theta\hat{A}\} = \cos\frac{\theta}{2}\mathbb{1} - i\sin\frac{\theta}{2}2\hat{A} \quad (1.4.2)$$

where θ is the phase angle of the rotation induced by the operator \hat{A} . If the general exponential operator in Equation (1.4.2) is inserted in (1.4.1) one obtains:

$$U_A\hat{\rho}U_A^\dagger = \exp\{-i\theta\hat{A}\}\hat{\rho}\exp\{+i\theta\hat{A}\} \quad (1.4.3)$$

$$\begin{aligned} &= \left[\cos\frac{\theta}{2}\mathbb{1} - i\sin\frac{\theta}{2}2\hat{A} \right] \hat{\rho} \left[\cos\frac{\theta}{2}\mathbb{1} + i\sin\frac{\theta}{2}2\hat{A} \right] \\ &= \overbrace{\cos^2\frac{\theta}{2}\mathbb{1}\hat{\rho}\mathbb{1} + 4\sin^2\frac{\theta}{2}\underbrace{\hat{A}\hat{\rho}\hat{A}}_{\frac{1}{4}\hat{\rho} + \frac{1}{2}\hat{\rho}}}^{\text{real}} + \overbrace{i\cdot 2\sin\frac{\theta}{2}\cos\frac{\theta}{2}\mathbb{1}\hat{\rho}\hat{A} - i\cdot 2\sin\frac{\theta}{2}\cos\frac{\theta}{2}\hat{A}\hat{\rho}\mathbb{1}}^{\text{complex}} \\ &= \underbrace{\cos^2\frac{\theta}{2}\hat{\rho} + \sin^2\frac{\theta}{2}\hat{\rho}}_{\hat{\rho}} + 2\sin^2\frac{\theta}{2}\hat{\rho} + \underbrace{i2\sin\frac{\theta}{2}\cos\frac{\theta}{2}}_{\sin\theta}[\hat{\rho}, \hat{A}] \\ &= \underbrace{(1 + 2\sin^2\frac{\theta}{2})}_{\cos\theta}\hat{\rho} + i\sin\theta[\hat{\rho}, \hat{A}] \\ &= \cos\theta\hat{\rho} + i\sin\theta[\hat{\rho}, \hat{A}] \end{aligned} \quad (1.4.4)$$

where the identity $\hat{A}\hat{\rho}\hat{A} = \frac{3}{4}\hat{\rho}$ is used in the third line (1.4.4). It is valid if the operators exhibit cyclic commutation properties as described in Equation (1.1.17) and if $\hat{A}^2 = \frac{1}{4}\mathbb{1}$. The identity can be derived from the commutator $[\hat{A}, [\hat{\rho}, \hat{A}]]$ for which can be shown that if both conditions apply:

$$\text{cyclic commutation: } [\hat{A}, [\hat{\rho}, \hat{A}]] = \hat{\rho} \quad (1.4.6)$$

$$\begin{aligned} \text{and if } \hat{A}^2 = \frac{1}{4}\mathbb{1}: \quad &[\hat{A}, [\hat{\rho}, \hat{A}]] = \hat{A}[\hat{\rho}, \hat{A}] - [\hat{\rho}, \hat{A}]\hat{A} \\ &= \hat{A}\hat{\rho}\hat{A} - \underbrace{\hat{A}\hat{A}}_{\frac{1}{4}\mathbb{1}}\hat{\rho} - \hat{\rho}\underbrace{\hat{A}\hat{A}}_{\frac{1}{4}\mathbb{1}} + \hat{A}\hat{\rho}\hat{A} \\ &= 2\hat{A}\hat{\rho}\hat{A} - \frac{1}{2}\hat{\rho}. \end{aligned} \quad (1.4.7)$$

^[38] O. Sørensen et al. *Progress in Nuclear Magnetic Resonance Spectroscopy* **1984**, 16, 163–192.

By Equating (1.4.6) and (1.4.7) and solving for the term $\hat{A}\hat{\rho}\hat{A}$ which is found in Equation (1.4.4) it is obvious that:

$$\hat{A}\hat{\rho}\hat{A} = \frac{3}{4}\hat{\rho}. \quad (1.4.8)$$

Application

We define a general time-independent Hamiltonian $\hat{\mathcal{H}}$ whose rotation axis is given by the operator \hat{A}_H with a rotation frequency ω_H :

$$\hat{\mathcal{H}} = \omega_H \hat{A}_H. \quad (1.4.9)$$

From Equation (1.4.5) we know that the system's evolution under the Hamiltonian $\hat{\mathcal{H}}$ can be described by the following compact result:

$$\begin{aligned} \hat{\rho}(t) &= \exp\{-i\hat{\mathcal{H}}t\} \hat{\rho}(0) \exp\{+i\hat{\mathcal{H}}t\} \\ &= \cos(\omega_H t) \hat{\rho}(0) + i \sin(\omega_H t) [\hat{\rho}(0), \hat{A}_H]. \end{aligned} \quad (1.4.10)$$

Hence, we notice that the rotation around an operator \hat{A}_H will bring the spin density $\hat{\rho}$ to evolve towards the commutator $i[\hat{\rho}, \hat{A}_H]$ and the rotation's angle is given by the product $\omega_H t$. Such a rotation is illustrated for a general case in Figure 1.3 and all possible axes for a system consisting of two spins \hat{I} and \hat{S} are summarized in Table 1.1. In order to describe rotations of this kind the following notation shall be used throughout the dissertation:

$$\hat{\rho} \xrightarrow{\hat{\mathcal{H}}t} \cos(\omega_H t) \hat{\rho} + i \sin(\omega_H t) [\hat{\rho}, \hat{A}_H]. \quad (1.4.11)$$

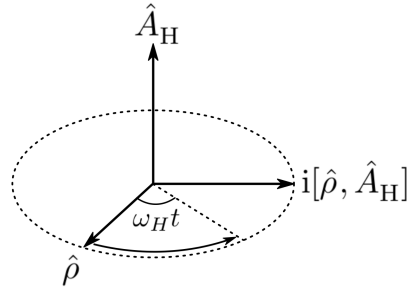


Figure 1.3: General rotation within the product operator formalism (Equation 1.4.10).

Table 1.1: The commutator $([\hat{\rho}, \hat{A}_{\text{H}}])$ is calculated for all combinations of a system consisting of two spins \hat{I} and \hat{S} . An empty field indicates that the two operators commute and, hence, the commutator is zero.

$\hat{A}_{\text{H}} \backslash [\hat{\rho},$	\hat{I}_x	\hat{I}_y	\hat{I}_z	\hat{S}_x	\hat{S}_y	\hat{S}_z	$2\hat{I}_x\hat{S}_x$	$2\hat{I}_y\hat{S}_y$	$2\hat{I}_z\hat{S}_z$	$2\hat{I}_x\hat{S}_y$	$2\hat{I}_y\hat{S}_x$	$2\hat{I}_x\hat{S}_z$	$2\hat{I}_z\hat{S}_x$	$2\hat{I}_y\hat{S}_z$	$2\hat{I}_z\hat{S}_y$
\hat{I}_x			$-\hat{I}_z$	\hat{I}_y											
\hat{I}_y			\hat{I}_z	$-\hat{I}_x$			$2\hat{I}_z\hat{S}_x$	$2\hat{I}_z\hat{S}_y$	$2\hat{I}_z\hat{S}_z$	$2\hat{I}_z\hat{S}_x$	$2\hat{I}_z\hat{S}_y$	$2\hat{I}_z\hat{S}_z$	$2\hat{I}_z\hat{S}_x$	$2\hat{I}_z\hat{S}_y$	$2\hat{I}_z\hat{S}_z$
\hat{I}_z			$-\hat{I}_y$	\hat{I}_x			$-2\hat{I}_y\hat{S}_x$	$2\hat{I}_x\hat{S}_y$		$2\hat{I}_x\hat{S}_y$	$2\hat{I}_x\hat{S}_x$	$-2\hat{I}_y\hat{S}_x$	$2\hat{I}_y\hat{S}_x$	$-2\hat{I}_y\hat{S}_z$	$2\hat{I}_x\hat{S}_z$
\hat{S}_x					$-\hat{S}_z$	\hat{S}_y				$-2\hat{I}_y\hat{S}_z$	$2\hat{I}_z\hat{S}_y$				$2\hat{I}_y\hat{S}_y$
\hat{S}_y					\hat{S}_z	$-\hat{S}_x$				$2\hat{I}_x\hat{S}_z$	$2\hat{I}_z\hat{S}_x$				$-2\hat{I}_y\hat{S}_z$
\hat{S}_z					$-\hat{S}_y$	\hat{S}_x				$-2\hat{I}_x\hat{S}_y$	$2\hat{I}_y\hat{S}_x$				$2\hat{I}_z\hat{S}_z$
$2\hat{I}_x\hat{S}_x$			$-2\hat{I}_z\hat{S}_x$	$2\hat{I}_y\hat{S}_x$											
$2\hat{I}_y\hat{S}_y$			$2\hat{I}_z\hat{S}_y$	$-2\hat{I}_x\hat{S}_y$			$2\hat{I}_y\hat{S}_z$	$2\hat{I}_y\hat{S}_x$	$2\hat{I}_y\hat{S}_y$	$2\hat{I}_y\hat{S}_z$	$2\hat{I}_y\hat{S}_x$	$-2\hat{I}_x\hat{S}_z$	$2\hat{I}_z\hat{S}_x$	$2\hat{I}_z\hat{S}_y$	$-2\hat{I}_x\hat{S}_z$
$2\hat{I}_z\hat{S}_z$			$-2\hat{I}_y\hat{S}_z$	$2\hat{I}_x\hat{S}_z$			$-2\hat{I}_y\hat{S}_y$	$2\hat{I}_x\hat{S}_y$	$2\hat{I}_z\hat{S}_z$	$2\hat{I}_x\hat{S}_y$	$2\hat{I}_y\hat{S}_x$	$-2\hat{I}_y\hat{S}_z$	$2\hat{I}_z\hat{S}_x$	$2\hat{I}_z\hat{S}_y$	$-2\hat{I}_x\hat{S}_z$
$2\hat{I}_x\hat{S}_y$			$-2\hat{I}_z\hat{S}_y$	$2\hat{I}_y\hat{S}_y$			$2\hat{I}_x\hat{S}_z$	$2\hat{I}_x\hat{S}_x$	$2\hat{I}_x\hat{S}_y$	\hat{S}_z	$-2\hat{I}_y\hat{S}_z$	\hat{S}_x	$-\hat{I}_z$	$-\hat{S}_y$	\hat{I}_y
$2\hat{I}_y\hat{S}_x$			$2\hat{I}_z\hat{S}_x$	$-2\hat{I}_x\hat{S}_x$			$-2\hat{I}_y\hat{S}_z$	$2\hat{I}_z\hat{S}_y$	$2\hat{I}_y\hat{S}_x$	\hat{I}_z	$-\hat{S}_z$	\hat{I}_z	$-\hat{S}_z$	\hat{I}_z	\hat{S}_y
$2\hat{I}_z\hat{S}_x$			$-2\hat{I}_y\hat{S}_z$	$2\hat{I}_x\hat{S}_z$			\hat{I}_z	$-\hat{I}_z$	\hat{I}_z	$-\hat{S}_z$	$-\hat{I}_z$	\hat{S}_x	$-\hat{I}_z$	\hat{S}_y	\hat{I}_y
$2\hat{I}_x\hat{S}_z$			$-2\hat{I}_y\hat{S}_z$	$2\hat{I}_y\hat{S}_z$			$-\hat{S}_y$	\hat{I}_y	\hat{S}_x	$-\hat{S}_y$	\hat{I}_x	$-\hat{S}_x$	$-\hat{I}_z$	$-\hat{I}_z$	$-\hat{S}_z$
$2\hat{I}_y\hat{S}_z$			$-2\hat{I}_x\hat{S}_z$	$2\hat{I}_z\hat{S}_z$			$-\hat{S}_x$	\hat{I}_x	\hat{S}_y	$-\hat{S}_x$	\hat{I}_z	$-\hat{S}_y$	$-\hat{I}_z$	$-\hat{I}_z$	$-\hat{S}_z$
$2\hat{I}_x\hat{S}_z$			$-2\hat{I}_y\hat{S}_z$	$2\hat{I}_z\hat{S}_z$			$-\hat{S}_x$	\hat{I}_x	\hat{S}_y	$-\hat{S}_x$	\hat{I}_z	$-\hat{S}_y$	$-\hat{I}_z$	$-\hat{I}_z$	$-\hat{S}_z$
$2\hat{I}_y\hat{S}_z$			$-2\hat{I}_x\hat{S}_z$	$2\hat{I}_z\hat{S}_z$			$-\hat{S}_x$	\hat{I}_x	\hat{S}_y	$-\hat{S}_x$	\hat{I}_z	$-\hat{S}_y$	$-\hat{I}_z$	$-\hat{I}_z$	$-\hat{S}_z$
$2\hat{I}_z\hat{S}_y$			$-2\hat{I}_x\hat{S}_y$	$2\hat{I}_y\hat{S}_y$			$-\hat{S}_y$	\hat{I}_y	\hat{S}_x	$-\hat{S}_y$	\hat{I}_z	$-\hat{S}_x$	$-\hat{I}_z$	$-\hat{I}_z$	$-\hat{S}_z$
$2\hat{I}_z\hat{S}_y$			$-2\hat{I}_x\hat{S}_y$	$2\hat{I}_y\hat{S}_y$			$-\hat{S}_y$	\hat{I}_y	\hat{S}_x	$-\hat{S}_y$	\hat{I}_z	$-\hat{S}_x$	$-\hat{I}_z$	$-\hat{I}_z$	$-\hat{S}_z$
$2\hat{I}_z\hat{S}_y$			$-2\hat{I}_x\hat{S}_y$	$2\hat{I}_y\hat{S}_y$			$-\hat{S}_y$	\hat{I}_y	\hat{S}_x	$-\hat{S}_y$	\hat{I}_z	$-\hat{S}_x$	$-\hat{I}_z$	$-\hat{I}_z$	$-\hat{S}_z$

1.5 Introduction to Frame Transformations

In previous chapters the Schrödinger equation (1.1.4) was used to determine the quantum dynamics of spin systems. In this so-called *Schrödinger picture* the state is in motion and, hence, time-dependent while operators are unaffected by the dynamics imposed by the Hamiltonian. Since the Schrödinger picture coincides with the laboratory frame it is certainly the more intuitive approach. However, it is likewise possible to transfer the time-dependence to the operators leaving the state untouched – the approach is called the *Heisenberg picture* and the equation of motion for operators is called *Heisenberg equation*. A comparable example from the “real world” shall be given: when photographing an object from every angle one can either turn the object or oneself around the object in the opposite direction. One can change from one picture to the other by a unitary frame transformation that is based on the Hamiltonian and in both pictures the same experimental observation (i.e. expectation value) is obtained. It is important to note, that in the same way only a part of the Hamiltonian can be used for the frame transformation leading to a situation where both state and operators are subject to the respective equations of motion – such an approach is known as *Dirac picture* or commonly referred to as an *interaction frame*.^[18] The different pictures are being discussed in the following.

1.5.1 Heisenberg Picture

In the present section the Heisenberg picture shall be derived starting from the Schrödinger picture which was the basic concept for previous sections. As mentioned before, the expectation value of an operator \hat{A} is identical in both pictures. Hence, we can state for a frame transformation:

$$\langle \hat{A} \rangle = \langle \psi_S | \hat{A}_S | \psi_S \rangle = \langle \psi_S | \underbrace{UU^\dagger}_1 \hat{A}_S \underbrace{UU^\dagger}_1 | \psi_S \rangle = \langle \psi_H | \hat{A}_H | \psi_H \rangle, \quad (1.5.1)$$

where the subscripts H and S indicate the Heisenberg and Schrödinger picture, respectively, and the frame transformation is determined by a unitary propagator U with $U^\dagger = U^{-1}$. The state functions and the operators in the respective frames are defined as:

$$\hat{A}_H = U^\dagger \hat{A}_S U, \quad (1.5.2)$$

$$\langle \psi_H | = \langle \psi_S | U \quad \text{and} \quad | \psi_H \rangle = U^\dagger | \psi_S \rangle, \quad (1.5.3)$$

$$U_S = e^{-i\hat{\mathcal{H}}_S t} \quad \text{and} \quad U_S^\dagger = e^{+i\hat{\mathcal{H}}_S t} \quad (1.5.4)$$

where we assume that the Hamiltonian in the Schrödinger picture $\hat{\mathcal{H}}_S$, which determines the frame transformation U_S , is time-independent. Using the Schrödinger equation (1.1.4) it can be shown, that the state in the Heisenberg picture $|\psi_H\rangle$ becomes time-independent:

$$\begin{aligned} \frac{\partial}{\partial t} |\psi_H\rangle &= \frac{\partial}{\partial t} (U_S^\dagger |\psi_S\rangle) \\ &= \frac{\partial}{\partial t} (U_S^\dagger) |\psi_S\rangle + U_S^\dagger \frac{\partial}{\partial t} (|\psi_S\rangle) \\ &= U_S^\dagger (i\hat{\mathcal{H}}_S) |\psi_S\rangle + U_S^\dagger (-i\hat{\mathcal{H}}_S) |\psi_S\rangle = 0. \end{aligned}$$

The equation of motion for operators in the Heisenberg picture \hat{A}_H can be derived using Equation (1.5.2) and (1.5.4). For the reason of clarity $U \equiv U_S$ is used and the Heisenberg equation is obtained:

$$\begin{aligned}
 \frac{\partial}{\partial t} \hat{A}_H &= \frac{\partial}{\partial t} (U^\dagger) \hat{A}_S U + U^\dagger \frac{\partial}{\partial t} (\hat{A}_S) U + U^\dagger \hat{A}_S \frac{\partial}{\partial t} (U) \\
 &= U^\dagger (i\hat{\mathcal{H}}_S) \hat{A}_S U + U^\dagger \frac{\partial}{\partial t} (\hat{A}_S) U + U^\dagger \hat{A}_S (-i\hat{\mathcal{H}}_S) U \\
 &= iU^\dagger \hat{\mathcal{H}}_S \underbrace{U U^\dagger}_1 \hat{A}_S U + U^\dagger \frac{\partial}{\partial t} (\hat{A}_S) U - iU^\dagger \hat{A}_S \underbrace{U U^\dagger}_1 \hat{\mathcal{H}}_S U \\
 &= i\hat{\mathcal{H}}_S \hat{A}_H + U^\dagger \frac{\partial}{\partial t} (\hat{A}_S) U - i\hat{A}_H \hat{\mathcal{H}}_S \\
 &= i[\hat{\mathcal{H}}_S, \hat{A}_H] + U^\dagger \frac{\partial}{\partial t} (\hat{A}_S) U,
 \end{aligned} \tag{1.5.5}$$

where $U^\dagger \hat{\mathcal{H}}_S U = \hat{\mathcal{H}}_S$ since $[U, \hat{\mathcal{H}}_S] = 0$. If the operators in the Schrödinger picture are time-independent ($\frac{\partial}{\partial t} \hat{A}_S = 0$) the solution to the equation of motion for operators (Equation 1.5.5) can be deduced from the solution of the Liouville-von Neumann equation (1.2.17) and is given by:

$$\hat{A}_H(t) = U_S^\dagger \hat{A}_H(0) U_S. \tag{1.5.6}$$

It is important to note that in contrast to (1.2.17) the operators are “backwards” propagated which corresponds to a rotation in the opposite direction (in analogy to the above mentioned example photographing an object by rotating oneself). In many text books a very compact comparison of the Schrödinger and Heisenberg picture is presented as follows:

$$\text{Tr}\{\hat{A}U\hat{\rho}U^\dagger\} = \text{Tr}\{U^\dagger\hat{A}U\hat{\rho}\}. \tag{1.5.7}$$

Here, the cyclic commutation property of the trace (5.1.3) is used to show that the expectation value (see Equation 1.2.3) is equal in both pictures. While on the left side it is the state operator $\hat{\rho}$ that is flanked by the time-dependent propagator U (Schrödinger), on the right side it is the operator \hat{A} that is time-dependent (Heisenberg).

1.5.2 Dirac Picture

The Dirac picture (also known as *interaction frame*) presents another way to look at quantum mechanical systems. In contrast to the Heisenberg picture the frame transformation is undertaken in a way that only a part of the Hamiltonian is transferred to the operators’ dynamics. In many cases this is the large time-independent Hamiltonian $\hat{\mathcal{H}}_{S,0}$ with known eigenfunctions and hence, the smaller time-dependent Hamiltonian $\hat{\mathcal{H}}_{S,1}(t)$ can be subject to perturbation theory. Since both operators and states evolve in time, this frame can be considered as something in between the Schrödinger and the Heisenberg picture. In order to understand the transformation and its consequences, we shall start from the Schrödinger picture, where the Hamiltonian $\hat{\mathcal{H}}_S$ is given as:

$$\hat{\mathcal{H}}_S(t) = \hat{\mathcal{H}}_{S,0} + \hat{\mathcal{H}}_{S,1}(t). \tag{1.5.8}$$

The transformation to the new frame is governed by the time-independent part $\hat{\mathcal{H}}_{S,0}$, while the time-dependent part $\hat{\mathcal{H}}_{S,1}(t)$ is left to state dynamics. Note, in the new frame also $\hat{\mathcal{H}}_{S,1}(t)$ undergoes a transformation and, consequently, the evolution of the transformed state in the Dirac picture is given by the transformed Hamiltonian $\hat{\mathcal{H}}_{D,1}(t)$ where D stands for Dirac. In some cases the transformation is chosen in a way that the time-dependent Hamiltonian $\hat{\mathcal{H}}_{S,1}(t)$ turns out to be time-independent after the transformation. In NMR this is the case when going to the so-called *rotating frame* (Section 1.5.3)

in which the time-dependent Hamiltonian of the radio frequency pulse becomes time-independent. As discussed earlier (Section 1.5.1) the expectation value under transformation mustn't change and hence:

$$\langle A \rangle = \langle \psi_S | \hat{A}_S | \psi_S \rangle = \langle \psi_S | U_{S,0}^\dagger \hat{A}_S U_{S,0} | \psi_S \rangle = \langle \psi_D | \hat{A}_D | \psi_D \rangle, \quad (1.5.9)$$

where the operators and states in the Dirac representation are defined as:

$$\hat{A}_D = U_{S,0}^\dagger \hat{A}_S U_{S,0}, \quad (1.5.10)$$

$$\langle \psi_D | = \langle \psi_S | U_{S,0} \quad \text{and} \quad | \psi_D \rangle = U_{S,0}^\dagger | \psi_S \rangle, \quad (1.5.11)$$

$$U_{S,0} = e^{-i\hat{\mathcal{H}}_{S,0}t} \quad \text{and} \quad U_{S,0}^\dagger = e^{+i\hat{\mathcal{H}}_{S,0}t}. \quad (1.5.12)$$

From here, the equation of motion for operators in the Dirac picture can be derived in a similar way as shown in Equation (1.5.5):

$$\frac{\partial}{\partial t} \hat{A}_D = i[\hat{\mathcal{H}}_{S,0}, \hat{A}_D] + U^\dagger \frac{\partial}{\partial t} (\hat{A}_S) U. \quad (1.5.13)$$

Again, if operators in the original frame are time-independent ($\frac{\partial}{\partial t} \hat{A}_S = 0$) the solution to Equation (1.5.13) is known from the previous section (Equation 1.5.6) and we see that the time evolution of operators in the interaction frame is determined by $\hat{\mathcal{H}}_{S,0}$:

$$\hat{A}_D(t) = e^{i\hat{\mathcal{H}}_{S,0}t} \hat{A}_D(0) e^{-i\hat{\mathcal{H}}_{S,0}t} = U_{S,0}^\dagger \hat{A}_D(0) U_{S,0}. \quad (1.5.14)$$

On the other hand, the equation of motion for the state in the Dirac representation can be derived with the Schrödinger equation and Equation (1.5.11). We obtain the Hamiltonian in the Dirac picture:

$$\begin{aligned} \frac{\partial}{\partial t} | \psi_D \rangle &= \frac{\partial}{\partial t} (U_{S,0}^\dagger | \psi_S \rangle) \\ &= \frac{\partial}{\partial t} (U_{S,0}^\dagger) | \psi_S \rangle + U_{S,0}^\dagger \frac{\partial}{\partial t} (| \psi_S \rangle) \\ &= U_{S,0}^\dagger (i\hat{\mathcal{H}}_{S,0}) \underbrace{U_{S,0} U_{S,0}^\dagger}_{\mathbb{1}} | \psi_S \rangle + U_{S,0}^\dagger [-i\hat{\mathcal{H}}_S(t)] \underbrace{U_{S,0} U_{S,0}^\dagger}_{\mathbb{1}} | \psi_S \rangle \\ &= iU_{S,0}^\dagger \hat{\mathcal{H}}_{S,0} U_{S,0} | \psi_D \rangle - iU_{S,0}^\dagger [\hat{\mathcal{H}}_{S,0} + \hat{\mathcal{H}}_{S,1}(t)] U_{S,0} | \psi_D \rangle \\ &= -iU_{S,0}^\dagger \hat{\mathcal{H}}_{S,1}(t) U_{S,0} | \psi_D \rangle \\ &= -i\hat{\mathcal{H}}_{D,1}(t) | \psi_D \rangle. \end{aligned} \quad (1.5.15)$$

It is clear that the state in the Dirac picture evolves only according to $\hat{\mathcal{H}}_{D,1}$ while the time-independent part $\hat{\mathcal{H}}_{S,0}$ is transferred to the operator's motion. We can derive from the last two lines that the time-dependent perturbation in the new frame is given as:

$$\hat{\mathcal{H}}_{D,1}(t) = U_{S,0}^\dagger \hat{\mathcal{H}}_{S,1}(t) U_{S,0}. \quad (1.5.16)$$

1.5.3 Rotating Frame

In Fourier Transform NMR the sample is set into a static magnetic field and commonly a multitude of radio frequency pulses is applied. In the *laboratory frame* the Hamiltonian $\hat{\mathcal{H}}_L(t)$ during a radio frequency pulse is given as:

$$\hat{\mathcal{H}}_L(t) = \hat{\mathcal{H}}_{L,Z} + \hat{\mathcal{H}}_{L,P}(t), \quad (1.5.17)$$

where $\hat{\mathcal{H}}_{L,Z}$ represents the (time-independent) *Zeeman interaction* of the spins within the static magnetic field (B_0) and $\hat{\mathcal{H}}_{L,P}(t)$ is the time-dependent perturbation of the radio frequency pulse. In order to solve the Schrödinger equation for such a system it is advisable to undergo a transformation to an interaction frame - the so-called *rotating frame*.^[33] This is done in the following by the use of the theory discussed in the previous section (1.5.2) and we find that only a resonant pulse will cause an effective perturbation.

In the previous section we chose the frame transformation in a way that the large time-independent part of the Hamiltonian is transferred to the operator's motion. However, in the rotating frame we do not transfer the entire static Hamiltonian $\hat{\mathcal{H}}_{L,Z}$ but only as much as needed to make the perturbation by the pulse time-independent and the Schrödinger equation obtains a straight-forward solution.

Rotating Wave

The time-dependent perturbation of the pulse (Section 1.3.4) can be described by a linear polarized magnetic field in the transverse plane which can be decomposed into two counter-rotating circular polarized components with half the amplitude. The Hamiltonian of the pulse $\hat{\mathcal{H}}_{L,P}(t)$ with the radio frequency ω_P can, hence, be written as:

$$\hat{\mathcal{H}}_{L,P}(t) = \hat{\mathcal{H}}_{L,P+}(t) + \hat{\mathcal{H}}_{L,P-}(t), \quad (1.5.18)$$

$$\text{and we define: } \hat{\mathcal{H}}_{L,P\pm}(t) = \cos(\pm\omega_P t)\hat{B}_x + \sin(\pm\omega_P t)\hat{B}_y. \quad (1.5.19)$$

where + and - denote the two components with opposite rotation and the operators \hat{B}_x and \hat{B}_y describe the x- and y-components of the pulse. Using Equation (1.3.20) they can be written as:

$$\hat{B}_{x,y} = - \sum_k \underbrace{\frac{1}{2}\gamma_k B_1}_{-\omega_1} \hat{I}_{x,y} \quad (1.5.20)$$

where B_1 is the amplitude of the pulse, γ the gyromagnetic ratio and ω_1 the *Rabi frequency*.^[39] A factor of $\frac{1}{2}$ needs to be considered, since the pulse is decomposed into two counter-rotating parts. Using the so-called *sandwich formula* (it is derived in Section 1.4 and given in Equation 1.4.5) the two components $\hat{\mathcal{H}}_{L,P+}(t)$ and $\hat{\mathcal{H}}_{L,P-}(t)$ can be rewritten with the time-dependent propagator U_P :

$$\hat{\mathcal{H}}_{L,P+}(t) = U_P \hat{B}_x U_P^\dagger \quad \text{and} \quad \hat{\mathcal{H}}_{L,P-}(t) = U_P^\dagger \hat{B}_x U_P, \quad (1.5.21)$$

$$\text{with: } U_P = e^{-i\omega_P I_z t}.$$

Transformation to the Rotating Frame

The transformation from the laboratory to the rotating frame is chosen to be given by U_R and, therefore, the spin state in the rotating frame $|\psi_R\rangle$ is:

$$\langle\psi_R| = \langle\psi_L|U_R \quad \text{and} \quad |\psi_R\rangle = U_R^\dagger|\psi_L\rangle \quad (1.5.22)$$

$$\text{with: } U_R = U_P U_\varphi = e^{-i\omega_P I_z t} \cdot e^{-i\varphi I_z}.$$

^[39] I. I. Rabi et al. *Physical Review* **1939**, *55*, 526–535.

The phase φ depends on the sign of the gyromagnetic ratio with $\varphi = \pi$ for $\gamma > 0$ and $\varphi = 0$ for $\gamma < 0$. By this means the Rabi frequency of the pulse ω_1 is always positive (independent of γ) which is the one and only reason why φ is introduced.^[13] The evolution of the spin state in the rotating frame can be derived similar to Equation (1.5.15) and it should be noted that $[U_R, I_z] = [U_R, \hat{\mathcal{H}}_{L,Z}] = 0$. We obtain the Hamiltonian in the rotating frame as:

$$\begin{aligned}
 \frac{\partial}{\partial t} |\psi_R\rangle &= \frac{\partial}{\partial t} (U_R^\dagger |\psi_L\rangle) + U_R^\dagger \frac{\partial}{\partial t} (|\psi_L\rangle) \\
 &= U_R^\dagger (i\omega_P I_z) |\psi_L\rangle + U_R^\dagger [-i\hat{\mathcal{H}}_L(t)] |\psi_L\rangle \\
 &= U_R^\dagger (i\omega_P I_z) \underbrace{U_R U_R^\dagger}_{\mathbb{1}} |\psi_L\rangle - iU_R^\dagger [\hat{\mathcal{H}}_{L,Z} + \hat{\mathcal{H}}_{L,P}(t)] \underbrace{U_R U_R^\dagger}_{\mathbb{1}} |\psi_L\rangle \\
 &= (i\omega_P I_z) |\psi_R\rangle - iU_R^\dagger [\hat{\mathcal{H}}_{L,Z} + \hat{\mathcal{H}}_{L,P}(t)] U_R |\psi_R\rangle \\
 &= -i \underbrace{(\hat{\mathcal{H}}_{L,Z} - \omega_P I_z)}_{\hat{\mathcal{H}}_{R,Z}} |\psi_R\rangle - i \underbrace{U_R^\dagger \hat{\mathcal{H}}_{L,P}(t) U_R}_{\hat{\mathcal{H}}_{R,P}(t)} |\psi_R\rangle
 \end{aligned} \tag{1.5.23}$$

where after the transformation the Zeeman interaction is given as $\hat{\mathcal{H}}_{R,Z} = \hat{\mathcal{H}}_{L,Z} - \omega_P I_z$ and the two pulse components of Equation (1.5.18) and (1.5.21) are given as:

$$\hat{\mathcal{H}}_{R,P+}(t) = U_R^\dagger \hat{\mathcal{H}}_{L,P+}(t) U_R = U_\varphi^\dagger \underbrace{U_P^\dagger U_P}_{\mathbb{1}} \hat{B}_x \underbrace{U_P U_P^\dagger}_{\mathbb{1}} U_\varphi = U_\varphi^\dagger \hat{B}_x U_\varphi$$

and:

$$\hat{\mathcal{H}}_{R,P-}(t) = U_R^\dagger \hat{\mathcal{H}}_{L,P-}(t) U_R = U_\varphi^\dagger U_P^\dagger U_P^\dagger \hat{B}_x U_P U_P U_\varphi = U_\varphi^\dagger (U_P^\dagger)^2 \hat{B}_x (U_P)^2 U_\varphi$$

where $\hat{\mathcal{H}}_{R,P+}(t)$ has become time-independent while $\hat{\mathcal{H}}_{R,P-}(t)$ now rotates with twice the frequency. If the pulse's frequency ω_P is equal to the Larmor frequency ω_0 the Zeeman interaction is completely removed from the rotating frame ($\hat{\mathcal{H}}_{R,Z} = \hat{\mathcal{H}}_{L,Z} - \omega_0 I_z = 0$) and the pulse is called *on-resonant*. In the following, we shall simply assume that the Rabi frequency ω_1 is positive, independent of the gyromagnetic ratio γ and the propagator U_φ shall, therefore, be omitted.

Effective Hamiltonian of the Radio Frequency Pulse

After the transformation the Hamiltonian is given by the Zeeman interaction $\hat{\mathcal{H}}_{R,Z}$ and the two components of the pulse from Equation (1.5.24):

$$\begin{aligned}
 \hat{\mathcal{H}}_R(t) &= \hat{\mathcal{H}}_{R,Z} + \hat{\mathcal{H}}_{R,P}(t) \\
 &= \underbrace{\hat{\mathcal{H}}_{R,Z} + \hat{B}_x}_{\text{time-independent}} + \underbrace{[U_P^\dagger(t)]^2 \hat{B}_x [U_P(t)]^2}_{\text{time-dependent}}
 \end{aligned} \tag{1.5.25}$$

where the time-dependent part on the right is commonly neglected for high magnetic fields. It can be shown with the theory discussed in Section 1.7 that during one rotation the time-dependent component $\hat{\mathcal{H}}_{R,P-}(t)$ is averaged to zero, if $\|\hat{\mathcal{H}}_R\| \tau_P \ll 2\pi$ where τ_P is the rotation period of $\hat{\mathcal{H}}_{R,P-}(t)$. Hence, the Hamiltonian of the pulse is, to very good approximation, time-independent and the Schrödinger equation can straight-forwardly be solved. In physics this often referred to as the *rotating wave approximation* and the influence of the time-dependent part will be discussed at the end of the present section.

Observation in the Rotating Frame

It was stated at the beginning of Section 1.5.1 and 1.5.2 that a prerequisite for a frame transformation is given by the invariant expectation value. Hence, an observation after a frame transformation would require the application of the Heisenberg equation (it is derived in Equation 1.5.5) in order to adapt the observable's operator as described in Equation (1.5.6). In NMR the radio frequency signal is detected by the probe and prior to digitization the frequency of the analog signal ω_0 needs to be down-converted. This is accomplished by the quadrature receiver which modulates the signal by a reference signal with the frequency ω_{det} (where det stands for detection) and one obtains two signals where one is oscillating at the sum of frequencies ($\omega_0 + \omega_{\text{det}}$) while the other is at the difference ($\omega_0 - \omega_{\text{det}}$). The high frequency signal can be suppressed by an electronic device called *low pass filter* and the low frequency signal can be digitized by the *analog-digital-converter*. The frequency of the reference signal ω_{det} is commonly chosen close to the frequency of the pulse ω_{P} . It turns out that by doing so we electronically (and afterwards digitally) modify the observable in a way that it matches the pulse and, hence, we do not need to adapt the observable's operator. The spectrometer puts us in the rotating frame and we can use the observables *as if* we were still in the laboratory frame.

Off-resonant Perturbation

The rotating frame implies a frame transformation to the resonant component of the pulse, however, it is, in principle, also possible to go to the off-resonant frame, basically, the frame of the counter-rotating component of the pulse. By this means the effects of off-resonant perturbation, namely the so-called Bloch-Siegert Shift can be investigated as shown by Furman and Kadzhaya.^[40] Note, the Bloch Siegert shift, originally derived by Bloch and Siegert^[41], exists even for an on-resonant perturbation and is in this case induced by the counter-rotating field of the linear polarized magnetic field. For the case of an off-resonant perturbation an additional shift is encountered – it is sometimes referred to as Berry phase^[42] or the nucleus being in a *dressed state*. In the following a more intuitive picture of the Berry phase shall be given using spin dynamics induced by a time-dependent perturbation. With this regard, a closer look is taken on a signal that is subject to a weak and slightly off-resonant radio frequency pulse at lower frequency and two thinkable scenarios are shown in Figure 1.4 that are based on a change of frames. We can either detect the signal in the *pulse frame* setting the detector frequency ω_{det} to the frequency of the pulse ω_{P} (Figure 1.4a) or we set the detector to the Larmor frequency of the signal ω_0 which we shall call the *on-resonant frame* (Figure 1.4b).

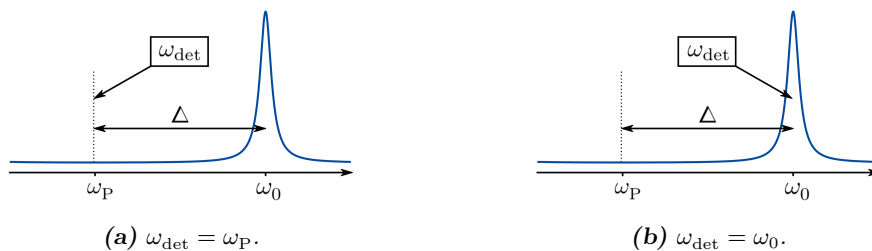


Figure 1.4: Detection in the pulse frame (a) or the on-resonant frame (b) with a frequency offset $\Delta = \omega_0 - \omega_{\text{P}}$. A positive gyromagnetic ratio is assumed.

In the pulse frame we go to a frame that is on-resonant with the off-resonant perturbation ($\omega_{\text{det}} = \omega_{\text{P}}$) which seems paradox. However, we will then end up with a time-independent Hamiltonian whose rotation can be illustrated by a single rotation vector. The effect of the pulse is, therefore, much easier to grasp even though it is not yet the frame in which the effect of off-resonant perturbation shall be observed. In Figure 1.5 (a) and (c) a weak pulse with a nutation frequency $\nu_1 = \frac{\omega_1}{2\pi} = 1$ Hz and an offset $\Delta = 1$ Hz acts on the spin states \hat{I}_x , \hat{I}_y and \hat{I}_z , respectively, and, as expected, a cyclic trajectory around the

^[40] G. B. Furman and I. M. Kadzhaya. *Journal of Magnetic Resonance* **1993**, A105, 7–9.

^[41] F. Bloch and A. Siegert. *Physical Review* **1940**, 57, 522–527.

^[42] M. V. Berry. *Proceedings of the Royal Society of London. A. Mathematical and Physical Sciences* **1984**, 392, 45–57.

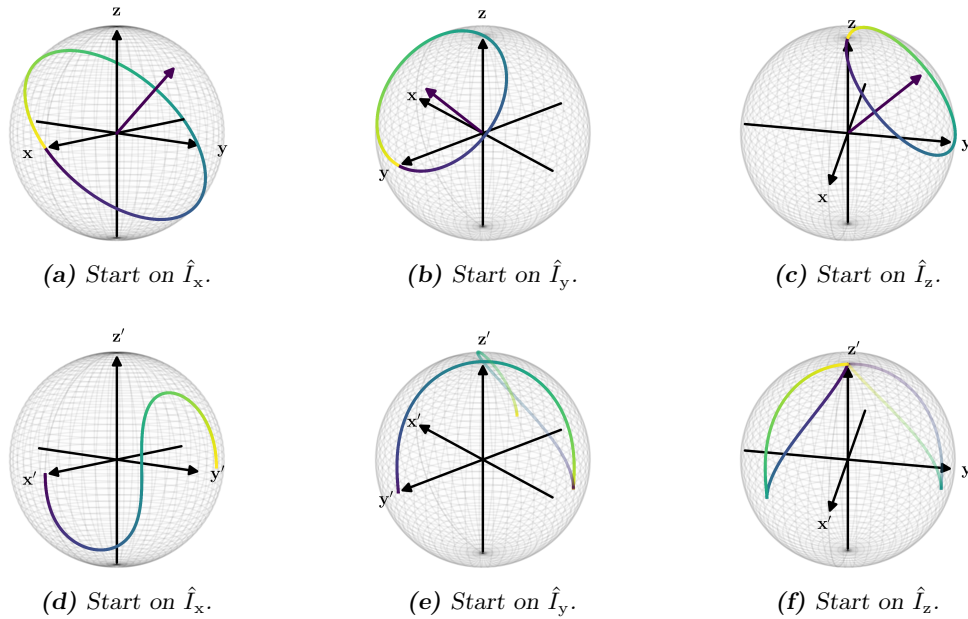


Figure 1.5: The effect of a weak off-resonant pulse is shown within the pulse frame (a-c) and the on-resonant frame (d-f). The pulse's offset $\Delta = \frac{\omega_0 - \omega_P}{2\pi}$ is set to 1 Hz.

Hamiltonian's eigenvector is observed in the pulse frame. The rotation is counter-clockwise which is indicated by the color gradient (purple to yellow). Subsequently, going from the pulse frame back to the on-resonant frame ($\omega_{\text{det}} = \omega_0$) comprises a frame transformation that is rotating the coordinate system (x, y, z) counter-clockwise with the frequency Δ around the z -axis. Within the resulting coordinate system (x', y', z') the Hamiltonian of the off-resonant radio frequency pulse becomes time-dependent and the trajectories of the spin states can be observed in Figure 1.5 (d) and (f) where additional turns are plotted transparently. Clearly, the off-resonant radio frequency pulse has a strong effect on the spectrum including an apparent change in resonance frequency. Without the perturbation the signal would not have acquired any phase within its frame and, hence, the signal experiences an apparent shift to higher frequencies - away from the perturbation's frequency. Note, the signal would likewise move to lower frequencies if the perturbation was at a higher frequency than the signal. A calculation of the acquired shift is described in literature^[43] and is determined by the length of the Hamiltonian's eigenvector in the pulse frame (note, for illustrative reasons the vector in Figure 1.5 is normalized). Likewise, the frequency shift can be approximated by the first order average Hamiltonian as shown by Haeberlen.^[28] When Figure 1.5 (a) and (c) are compared to Figure 1.5 (d) and (f), respectively, it is striking that in both pictures the degree of latitude (north - south) is colorwise identical but only the degree of longitude (east - west) has changed within the respective pictures. The reason for this is given by the fact that the frame transformation comprises a rotation of the sphere about the z -axis. The degree of longitude is, hence, determined by the difference in "horizontal velocity" of the state and the tangential velocity for the respective latitude at which the state is being situated. One should keep in mind that tangential velocity is decreasing for smaller radii at constant angular velocity. Especially, the comparison of Figure 1.5 (a) and (d) will reveal that this is a geometrical issue - it is in close analogy to a satellite's orbit projected on earth.

In Figure 1.6 the calculations are repeated for the offset $\Delta = 2$ Hz and, as expected, the larger the pulse's offset Δ the smaller the off-resonant effect on the spectrum in the on-resonant frame.

^[43] M. Sattler, J. Schleucher and C. Griesinger. *Progress in Nuclear Magnetic Resonance Spectroscopy* **1999**, *34*, 93-158.

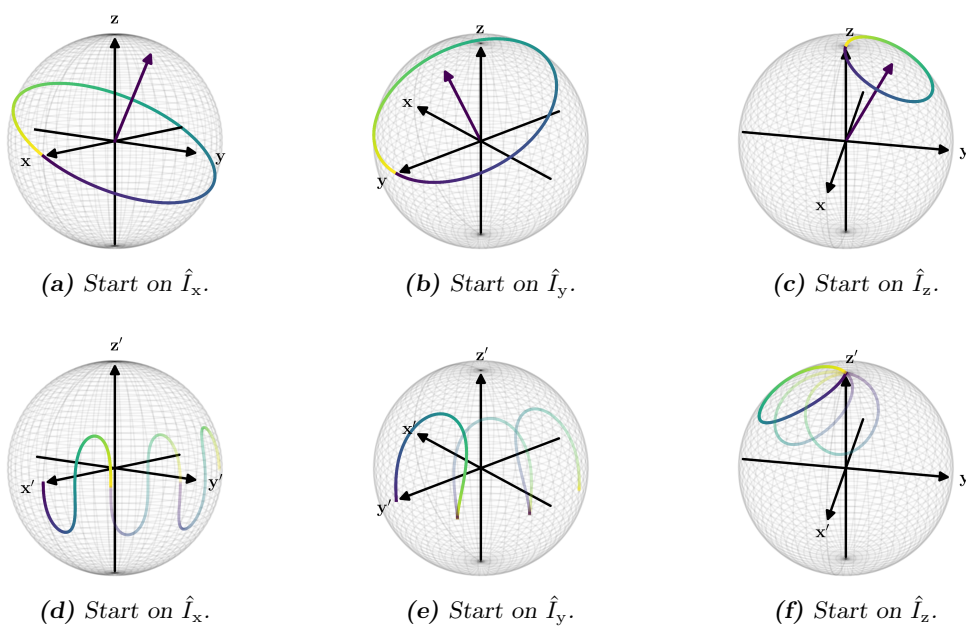


Figure 1.6: The effect of a weak off-resonant pulse is shown within the pulse frame (a-c) and the on-resonant frame (d-f). The pulse's offset $\Delta = \frac{\omega_0 - \omega_P}{2\pi}$ is set to 2 Hz.

1.6 Toggling Frame

As seen in the previous section an interaction frame can be used to modify the Hamiltonian in an opportune way resulting in a time-independent Hamiltonian with convenient solution to the Schrödinger equation. In the so-called *toggling frame*, on the other hand, a frame transformation is used to change the perspective on the Hamiltonian within a pulse sequence. While the transformation from the laboratory frame to the rotating frame removes the Zeeman interaction from state dynamics (or at least parts of it), the transformation from the rotating frame to the toggling frame removes the pulses' Hamiltonians. It turns out, that in contrast to the rotating frame, the transformation to the toggling frame will introduce a time-dependence on the Hamiltonian which, prior to this, is commonly time-independent. At first glance, it seems needless to give oneself a hard time, since the solution to the Schrödinger equation for such a time-dependent Hamiltonian is more complicated even with helpful approaches discussed in Section 1.7. However, the toggling frame is a very useful instrument to elucidate e.g. the effect of coupling during a pulse sequence (Section 1.6.3) and, as a matter of fact, the time-dependence of the Hamiltonian is introduced by the pulses. These are controlled by the operator which leaves full control over the effective Hamiltonian and can be used for pulse sequence design (Section 2.3).

In magnetic resonance the toggling frame is commonly applied in combination with average Hamiltonian theory (Section 1.7) and was first introduced by Waugh, Huber and Haeberlen.^[4]

1.6.1 Sequential Transformation

In the following we assume a Hamiltonian in the rotating frame $\hat{\mathcal{H}}_R(\tau)$ that consists of a coupling Hamiltonian $\hat{\mathcal{H}}_{R,C}$ and the piecewise time-independent Hamiltonian of the pulse sequence $\hat{\mathcal{H}}_{R,P}(\tau)$. It is given:

$$\hat{\mathcal{H}}_R(\tau) = \hat{\mathcal{H}}_{R,P}(\tau) + \hat{\mathcal{H}}_{R,C}, \quad (1.6.1)$$

where the coupling Hamiltonian $\hat{\mathcal{H}}_{R,C}$ is assumed to be an arbitrary bilinear rotation and the piecewise Hamiltonian $\hat{\mathcal{H}}_{R,P}(\tau)$ for a k -spin system can be expressed in n consecutive time steps of length τ_n :

$$\hat{\mathcal{H}}_{R,P}(\tau) = \begin{cases} \hat{\mathcal{H}}_{R,P_1} = \sum_k \omega_k \hat{I}_{k\gamma} & \text{for } \tau_1 \\ \hat{\mathcal{H}}_{R,P_2} = \sum_k \omega'_k \hat{I}_{k\gamma'} & \text{for } \tau_2 \\ \dots & \\ \hat{\mathcal{H}}_{R,P_n} = \sum_k \omega''_k \hat{I}_{k\gamma''} & \text{for } \tau_n \end{cases} \quad (1.6.2)$$

where ω_k is a frequency and $\hat{I}_{k\gamma}$ corresponds to a rotation on spin k around the axes $\gamma = x, y, z$. Classically, the so-called toggling frame describes a frame transformation in which the Hamiltonian of commonly x- and y-pulses is removed. Likewise, a frequency offset can be considered a pulse around z and, if included in the frame transformation, it can be removed. In the following, such a frame shall still be called a toggling frame. Since the Hamiltonian of the pulse in the rotating frame $\hat{\mathcal{H}}_{R,P}$ is a piecewise function for each time step n another transformation $U_{R_n}(\tau)$ is given:

$$U_R(\tau) = \begin{cases} U_{R_1} = \exp\{-i \hat{\mathcal{H}}_{R,P_1} \tau_1\} & \text{for } \tau_1 \\ U_{R_2} = \exp\{-i \hat{\mathcal{H}}_{R,P_2} \tau_2\} & \text{for } \tau_2 \\ \dots & \\ U_{R_n} = \exp\{-i \hat{\mathcal{H}}_{R,P_n} \tau_n\} & \text{for } \tau_n. \end{cases} \quad (1.6.3)$$

It is crucial to note that so far the time-dependent Hamiltonian $\hat{\mathcal{H}}_{R,P}(\tau)$ and the respective transformations $U_R(\tau)$ are given in the rotating frame. When going to the toggling frame, however, each part of the Hamiltonian needs to be transformed to the frame in which it is applied. The transformed Hamiltonian $\hat{\mathcal{H}}_{T,P}(\tau)$ can be deduced from Equation (1.5.15) and (1.5.16) and within the successive toggling frames

it is given as:

$$\hat{\mathcal{H}}_{T,P}(\tau) = \begin{cases} \hat{\mathcal{H}}_{T_1,P_1} = \hat{\mathcal{H}}_{R,P_1} & \text{for } \tau_1 \\ \hat{\mathcal{H}}_{T_2,P_2} = U_{T_1}^\dagger \hat{\mathcal{H}}_{R,P_2} U_{T_1} & \text{for } \tau_2 \\ \dots & \\ \hat{\mathcal{H}}_{T_n,P_n} = U_{T_{n-1}}^\dagger \dots U_{T_1}^\dagger \hat{\mathcal{H}}_{R,P_n} U_{T_1} \dots U_{T_{n-1}} & \text{for } \tau_n \end{cases} \quad (1.6.4)$$

from which the transformations to successive frames $U_T(\tau)$ can be derived in a straight-forward way:

$$U_T(\tau) = \begin{cases} U_{T_1} = \exp\{-i\hat{\mathcal{H}}_{T_1,P_1} \tau_1\} & \text{for } \tau_1 \\ U_{T_2} = \exp\{-i\hat{\mathcal{H}}_{T_2,P_2} \tau_2\} & \text{for } \tau_2 \\ \dots & \\ U_{T_n} = \exp\{-i\hat{\mathcal{H}}_{T_n,P_n} \tau_n\} & \text{for } \tau_n. \end{cases} \quad (1.6.5)$$

It should be noted that the calculation of $\hat{\mathcal{H}}_{T_n,P_n}$ requires the transformation $U_{T_{n-1}}^\dagger$ and, hence, both $\hat{\mathcal{H}}_{T_n,P_n}$ and $U_{T_n}^\dagger$ need to be calculated recursively. This is somehow cumbersome and a more convenient calculation is derived in the following and given at the end of the present section in Equation (1.6.11). Since in previous Sections 1.5.1, 1.5.2 and 1.5.3 different transformations of frames were thoroughly discussed, at this point, I will use preceding results for the transformation to the toggling frame and the more detailed derivation is given in the Appendix 5.1.6. The transformations to the toggling frame are described by $U_T(\tau)$ and the respective spin states $|\psi_T\rangle(\tau)$ are:

$$|\psi_T\rangle(\tau) = \begin{cases} |\psi_{T_1}\rangle = U_{T_1}^\dagger |\psi_R\rangle & \text{for } \tau_1 \\ |\psi_{T_2}\rangle = U_{T_2}^\dagger U_{T_1}^\dagger |\psi_R\rangle & \text{for } \tau_2 \\ \dots & \\ |\psi_{T_n}\rangle = U_{T_{n-1}}^\dagger \dots U_{T_1}^\dagger |\psi_R\rangle & \text{for } \tau_n. \end{cases} \quad (1.6.6)$$

The coupling Hamiltonian in the respective toggling frame $\hat{\mathcal{H}}_{T,C}$ can be derived using the Schrödinger equation as was discussed in Equation (1.5.15) and (1.5.16) and the result is:

$$\hat{\mathcal{H}}_{T,C}(\tau) = \begin{cases} \hat{\mathcal{H}}_{T_1,C} = U_{T_1}^\dagger \hat{\mathcal{H}}_{R,C} U_{T_1} & \text{for } \tau_1 \\ \hat{\mathcal{H}}_{T_2,C} = U_{T_2}^\dagger U_{T_1}^\dagger \hat{\mathcal{H}}_{R,C} U_{T_1} U_{T_2} & \text{for } \tau_2 \\ \dots & \\ \hat{\mathcal{H}}_{T_n,C} = U_{T_{n-1}}^\dagger \dots U_{T_1}^\dagger \hat{\mathcal{H}}_{R,C} U_{T_1} \dots U_{T_{n-1}} & \text{for } \tau_n \end{cases} \quad (1.6.7)$$

where for each of the n time steps a coupling Hamiltonian in a different frame is obtained. However, one can rewrite the Hamiltonian in terms of “propagators created in the rotating frame”, $U_R(\tau)$, that are directly accessible from the pulses’ Hamiltonians in the rotating frame. Using the identity $\exp\{-iU^\dagger \hat{\mathcal{H}} U t\} = U^\dagger \exp\{-i\hat{\mathcal{H}} t\} U$ (a proof hereof is given in the Appendix 5.1.5) and Equation (1.6.4) it is apparent that both $U_R(\tau)$ and $U_T(\tau)$ are interdependent and can be calculated recursively with:

$$\begin{aligned} U_{T_1} &= U_{R_1} \\ U_{T_n} &= U_{T_{n-1}}^\dagger \dots U_{T_1}^\dagger U_{R_n} U_{T_1} \dots U_{T_{n-1}}. \end{aligned} \quad (1.6.8)$$

For the first time step the coupling Hamiltonian in the toggling frame $\hat{\mathcal{H}}_{T_1,C}$ is, hence, simply given as:

$$\begin{aligned} \hat{\mathcal{H}}_{T_1,C} &= U_{T_1}^\dagger \hat{\mathcal{H}}_{R,C} U_{T_1} \\ &= U_{R_1}^\dagger \hat{\mathcal{H}}_{R,C} U_{R_1}. \end{aligned} \quad (1.6.9)$$

Likewise, using Equation (1.6.8), for the second time step the coupling Hamiltonian $\hat{\mathcal{H}}_{T_2,C}$ can be rewritten and one obtains, again, an expression that does not depend on the transformation $U_T(\tau)$

within the toggling frame:

$$\begin{aligned}
 \hat{\mathcal{H}}_{T_2,C} &= U_{T_2}^\dagger U_{T_1}^\dagger \hat{\mathcal{H}}_{R,C} U_{T_1} U_{T_2} \\
 &= \underbrace{U_{T_1}^\dagger U_{R_2}^\dagger U_{T_1}}_{U_{T_2}^\dagger} U_{T_1}^\dagger \hat{\mathcal{H}}_{R,C} U_{T_1} \underbrace{U_{T_1}^\dagger U_{R_2} U_{T_1}}_{U_{T_2}} \\
 &= U_{R_1}^\dagger U_{R_2}^\dagger \hat{\mathcal{H}}_{R,C} U_{R_2} U_{R_1}.
 \end{aligned} \tag{1.6.10}$$

It is crucial to note that rewriting the Hamiltonian has reversed the order of the transformations. If repeated for all consecutive n time steps the coupling Hamiltonian $\hat{\mathcal{H}}_{T,C}(\tau)$ can be given in the piecewise form:

$$\hat{\mathcal{H}}_{T,C}(\tau) = \begin{cases} \hat{\mathcal{H}}_{T_1,C} = U_{R_1}^\dagger \hat{\mathcal{H}}_{R,C} U_{R_1} & \text{for } \tau_1 \\ \hat{\mathcal{H}}_{T_2,C} = U_{R_1}^\dagger U_{R_2}^\dagger \hat{\mathcal{H}}_{R,C} U_{R_2} U_{R_1} & \text{for } \tau_2 \\ \dots & \\ \hat{\mathcal{H}}_{T_n,C} = U_{R_1}^\dagger \dots U_{R_{n-1}}^\dagger \hat{\mathcal{H}}_{R,C} U_{R_{n-1}} \dots U_{R_1} & \text{for } \tau_n \end{cases} \tag{1.6.11}$$

where, again, at each n th step an inversion of the order is observed. Since the order corresponds to the pulses that are applied one after another, the inversion seems to be like an inversion in time. However, the inversion is based on the fact that U_R and U_T are supposed to act on different frames and, therefore, it is basically a geometrical issue which shall be discussed again in the following Section 1.6.3.

1.6.2 Numerical Simulation of the Toggling Frame

In the present section an algorithm shall be discussed that gradually follows the transformation of a Hamiltonian in the toggling frame. The algorithm returns time-dependent coefficients that describe the Hamiltonian decomposed in its basis operators. We assume a time-independent coupling Hamiltonian in the rotating frame $\hat{\mathcal{H}}_{R,C}$ that is given in a general form:

$$\hat{\mathcal{H}}_{R,C} = \omega_C \mathcal{I} \tag{1.6.12}$$

where ω_C is the frequency of the rotation induced by the operator \mathcal{I} that is determined by the coupling. $\hat{\mathcal{H}}_{R,C}$ is transformed to a toggling frame based on the time-dependent Hamiltonian $\hat{\mathcal{H}}_{R,P}(\tau)$ of the pulse sequence and we know from Equation (1.6.11) that the coupling Hamiltonian in the toggling frame $\hat{\mathcal{H}}_{T,C}(\tau)$ can be expressed in a piecewise form:

$$\hat{\mathcal{H}}_{T,C}(\tau) = \begin{cases} \hat{\mathcal{H}}_{T_1,C} = U_{R_1}^\dagger \hat{\mathcal{H}}_{R,C} U_{R_1} & \text{for } \tau_1 \\ \hat{\mathcal{H}}_{T_2,C} = U_{R_1}^\dagger U_{R_2}^\dagger \hat{\mathcal{H}}_{R,C} U_{R_2} U_{R_1} & \text{for } \tau_2 \\ \dots & \\ \hat{\mathcal{H}}_{T_n,C} = U_{R_1}^\dagger \dots U_{R_{n-1}}^\dagger \hat{\mathcal{H}}_{R,C} U_{R_{n-1}} \dots U_{R_1} & \text{for } \tau_n \end{cases}$$

where $U_R(\tau)$ is determined by $\hat{\mathcal{H}}_{R,P}(\tau)$. The transformations are assumed to be split into time steps τ that are much shorter than a rotation induced by the Hamiltonian $\hat{\mathcal{H}}_{R,P}(\tau)$ in order to sample multiple points per rotation – we state:

$$\|\hat{\mathcal{H}}_{R,P}\| \tau \ll 2\pi.$$

The time-dependent coefficients $k(\tau)$ that describe the Hamiltonian within its basis operators \hat{B}_γ can be determined by the use of the projection superoperator that for a general operator A will lead to:

$$\hat{P}_\gamma A = \frac{\langle \hat{B}_\gamma | A \rangle}{\langle \hat{B}_\gamma | \hat{B}_\gamma \rangle} \hat{B}_\gamma = \frac{\text{Tr}\{\hat{B}_\gamma^\dagger A\}}{\text{Tr}\{\hat{B}_\gamma^\dagger \hat{B}_\gamma\}} \hat{B}_\gamma = a_\gamma \hat{B}_\gamma \tag{1.6.13}$$

with $\langle \hat{B}_\gamma | \hat{B}_\gamma \rangle = 1$ for a normalized basis. For each transformation step the time-dependent Hamiltonian $\hat{\mathcal{H}}_{T,C}(\tau)$ is projected on its orthonormal basis operators \hat{B}_γ of the toggling frame and one can define:

$$\hat{\mathcal{H}}_{T,C}(\tau) = \sum_\gamma \hat{P}_\gamma \hat{\mathcal{H}}_{T,C}(\tau) = \omega_C \cdot \sum_\gamma k_C^\gamma(\tau) \hat{B}_\gamma \quad (1.6.14)$$

where ω_C is the frequency of the Hamiltonian $\hat{\mathcal{H}}_{R,C}$ and the coefficients $k_C^\gamma(\tau)$ can be calculated from:

$$k_C^\gamma(\tau) = \frac{1}{\omega_C} \cdot \text{Tr} \left\{ \hat{B}_\gamma^\dagger \hat{\mathcal{H}}_{T,C}(\tau) \right\}. \quad (1.6.15)$$

It is noteworthy that in the superscript of k the variable γ indicates the basis operator in the toggling frame. The coefficients $k_C^\gamma(\tau)$ are defined in a way that they are independent of the coupling frequency ω_C and can be considered a scaling factor ranging from -1 to 1 .²¹ By doing so one obtains more general information of the considered pulse sequence rather than just a particular value for the respective spin system. The step in Equation (1.6.15) can be repeated for all or individual basis operators \hat{B}_γ and the coefficients $k_C^\gamma(\tau)$ are stored numerically.

The calculation of $\hat{\mathcal{H}}_{T,C}(\tau)$ requires that the frame transformations $U_R(\tau)$ are applied in reversed order (Equation 1.6.11) and, hence, one can not simply propagate the Hamiltonian $\hat{\mathcal{H}}_{R,C}$ chronologically.²² However, one could use the cyclic permutation property of the trace to show that the coefficients $k_C^\gamma(\tau)$ can also be obtained from:

$$\begin{aligned} k_C^\gamma(\tau) &= \frac{1}{\omega_C} \cdot \text{Tr} \left\{ \hat{B}_\gamma^\dagger \hat{\mathcal{H}}_{T,C}(\tau) \right\} \\ &= \frac{1}{\omega_C} \cdot \text{Tr} \left\{ \hat{B}_\gamma^\dagger (U_{R_1}^\dagger \dots U_{R_{n-1}}^\dagger \hat{\mathcal{H}}_{R,C} U_{R_{n-1}} \dots U_{R_1}) \right\} \\ &= \frac{1}{\omega_C} \cdot \text{Tr} \left\{ (U_{R_{n-1}} \dots U_{R_1} \hat{B}_\gamma^\dagger U_{R_1}^\dagger \dots U_{R_{n-1}}^\dagger) \hat{\mathcal{H}}_{R,C} \right\} \end{aligned} \quad (1.6.16)$$

and it is clear, that when propagating the basis operators \hat{B}_γ^\dagger instead of the Hamiltonian $\hat{\mathcal{H}}_{R,C}$ the propagators U_R can be applied in chronological order. Even though it might be the most convenient and intuitive way it comes with a small computational penalty: all basis operators need to be propagated instead of only the single Hamiltonian $\hat{\mathcal{H}}_{R,C}$. However, a vast speed up can be obtained if the Hamiltonian in the toggling frame is calculated as described in the following section.

Speeding it up: Calculation in Single Spin Operator Basis

Calculating the interaction in the toggling frame can get costly in terms of calculation time when larger spin systems are assumed. Not only the size of matrices will increase exponentially but also the number of basis operators. However, it is possible to break it down to the calculation of a single spin which can be expanded to the original basis later on. This way, the simulations can also be applied for the calculation of large grids (Section 2.4.3) or, likewise, it could be incorporated in the optimization of pulse shapes. The calculation is based on the following equations where, for bilinear operators, it is shown that the interaction can be subdivided into single operator contributions and, when processed subsequently, the same result is obtained as if the calculation was executed in the original basis. This way the enlarged basis for multi spin systems is circumvented while the subsequent process is based on fast summation and multiplication of scalars – the calculation time is reduced by two to three orders of magnitude.

²¹ Note, some interactions consist of multiple bilinear terms that might be scaled differently (e.g. dipolar coupling). In such a case the coefficients can exceed the limits of -1 and 1 .

²² Still, the calculation in non-chronological order could be undertaken by a few additional lines in the program.

If, for the propagation in the toggling frame, we assume an interaction $\hat{\mathcal{H}}_{R,C}$ that is made up of an arbitrary bilinear coupling term ($\omega_C \cdot 2\hat{T}_{1\delta}\hat{T}_{2\varepsilon}$), it can be shown that its single operator contributions can be propagated individually by the piecewise propagator $U_R(\tau)$. Since product operators can be obtained from matrix multiplication (Section 1.2.2) it can be shown that:

$$\begin{aligned}
 \hat{\mathcal{H}}_{T,C}(\tau) &= U_R^\dagger \hat{\mathcal{H}}_{R,C} U_R \\
 &= \omega_C \cdot U_R^\dagger (2\hat{T}_{1\delta}\hat{T}_{2\varepsilon}) U_R \\
 &= 2\omega_C \cdot U_R^\dagger (\sigma_{1\delta} \otimes \mathbb{1})(\mathbb{1} \otimes \sigma_{2\varepsilon}) U_R \\
 &= 2\omega_C \cdot U_R^\dagger (\sigma_{1\delta} \otimes \mathbb{1}) \underbrace{U_R U_R^\dagger}_{\mathbb{1}} (\mathbb{1} \otimes \sigma_{2\varepsilon}) U_R = 2\omega_C \cdot \underbrace{U_R^\dagger \hat{T}_{1\delta} U_R}_{\hat{T}_{1\delta}} \cdot \underbrace{U_R^\dagger \hat{T}_{2\varepsilon} U_R}_{\hat{T}_{2\varepsilon}},
 \end{aligned} \tag{1.6.17}$$

with $\delta, \varepsilon = (x, y, z)$. For the reason of clarity, we call the individually propagated interaction terms $\hat{T}_{1\delta}$ and $\hat{T}_{2\varepsilon}$. Note, for the subsequent process it is crucial that $U_R(\tau)$ acts on every spin individually, that is, $U_R(\tau)$ must not contain a rotation that is based on a bilinear term. However, since I use the toggling frame to remove the effect of pulses and the Zeeman interaction this condition shall be always met. As discussed for Equation (1.6.14) and (1.6.15) the transformed interaction Hamiltonian $\hat{\mathcal{H}}_{T,C}(\tau)$ in the next step needs to be decomposed into the orthonormal basis \hat{B}_γ of the toggling frame and its respective coefficients. In the following an orthonormal bilinear basis operator $\hat{B}_\gamma = 2\hat{T}_{1\delta'}\hat{T}_{2\varepsilon'}$ is exemplary chosen. Substituting Equation (1.6.17) in (1.6.15) and using basic properties of the trace (Appendix 5.1.3) and the Kronecker product (Appendix 5.1.4) it can be shown that:

$$\begin{aligned}
 k_C^\gamma(\tau) &= \omega_C^{-1} \cdot \text{Tr} \{ \hat{B}_\gamma^\dagger \hat{\mathcal{H}}_{T,C}(\tau) \} \\
 &= \omega_C^{-1} \cdot \text{Tr} \{ (2\hat{T}_{1\delta'}\hat{T}_{2\varepsilon'})^\dagger (\omega_C \cdot 2\hat{T}_{1\delta}\hat{T}_{2\varepsilon}) \} \\
 &= \text{Tr} \{ 4 \cdot (\hat{T}_{1\delta'}\hat{T}_{1\delta})(\hat{T}_{2\varepsilon}\hat{T}_{2\varepsilon'}) \} \\
 &= \text{Tr} \{ 4 \cdot (\hat{\sigma}_{\delta'} \otimes \mathbb{1})(\hat{t}_{1\delta} \otimes \mathbb{1})(\mathbb{1} \otimes \hat{t}_{2\varepsilon})(\mathbb{1} \otimes \hat{\sigma}_{\varepsilon'}) \} \\
 &= \text{Tr} \{ 4 \cdot (\hat{\sigma}_{\delta'}\hat{t}_{1\delta} \otimes \mathbb{1})(\mathbb{1}\mathbb{1} \otimes \hat{t}_{2\varepsilon}\hat{\sigma}_{\varepsilon'}) \} \\
 &= \text{Tr} \{ 4 \cdot (\hat{\sigma}_{\delta'}\hat{t}_{1\delta} \otimes \hat{t}_{2\varepsilon}\hat{\sigma}_{\varepsilon'}) \} \\
 &= \underbrace{2 \text{Tr} \{ \hat{\sigma}_{\delta'}\hat{t}_{1\delta} \}}_{k_\delta^{\delta'}(\tau)} \cdot \underbrace{2 \text{Tr} \{ \hat{\sigma}_{\varepsilon'}\hat{t}_{2\varepsilon} \}}_{k_\varepsilon^{\varepsilon'}(\tau)},
 \end{aligned} \tag{1.6.18}$$

where $\hat{t}_{1\delta}$ and $\hat{t}_{2\varepsilon}$ are the representation of $\hat{T}_{1\delta}$ and $\hat{T}_{2\varepsilon}$ in the reduced single-spin operator basis and $\hat{\sigma}_{\delta'}$ and $\hat{\sigma}_{\varepsilon'}$ correspond to the Pauli matrices (Equation 1.1.15). It now becomes evident that the coefficient k_C^γ for an arbitrary bilinear basis operator can be calculated from the product of two coefficients, $k_\delta^{\delta'}(\tau)$ and $k_\varepsilon^{\varepsilon'}(\tau)$, corresponding to the single-spin operator basis in the toggling frame. It is interesting to note that in contrast to $\hat{t}_{1\delta}$ and $\hat{t}_{2\varepsilon}$ the basis operators, $\hat{\sigma}_{\delta'}$ and $\hat{\sigma}_{\varepsilon'}$, are no longer connected to spin 1 or 2. Hence, in the toggling frame only one set of the single-spin basis operators ($\hat{\sigma}_x, \hat{\sigma}_y, \hat{\sigma}_z$) and its combinations to the single-spin angular momentum operators present in the interaction ($\hat{t}_x, \hat{t}_y, \hat{t}_z$) needs to be calculated resulting in a maximum of 9 trajectories per spin. From these trajectories all possible bilinear basis operators in an expanded basis can be obtained.

Such a separation is also possible when we assume an interaction $\hat{\mathcal{H}}_R$ that is made up of a sum of bilinear terms which can be subdivided into its summands. This is based on the distributive nature of the matrix

product in Liouville space and shown in the following:

$$\begin{aligned}
 \hat{\mathcal{H}}_T &= U_R^\dagger \hat{\mathcal{H}}_R U_R \\
 &= U_R^\dagger (\hat{\mathcal{H}}_\delta + \hat{\mathcal{H}}_\varepsilon) U_R \\
 &= \underbrace{U_R^\dagger \hat{\mathcal{H}}_\delta U_R}_{\hat{\mathcal{H}}_{T,\delta}} + \underbrace{U_R^\dagger \hat{\mathcal{H}}_\varepsilon U_R}_{\hat{\mathcal{H}}_{T,\varepsilon}}.
 \end{aligned} \tag{1.6.19}$$

If we substitute the Hamiltonian in the toggling frame $\hat{\mathcal{H}}_T$ in Equation (1.6.14) assuming normalized basis operators B_γ we obtain:

$$\begin{aligned}
 \hat{P}_\gamma \hat{\mathcal{H}}_T &= \hat{P}_\gamma (\hat{\mathcal{H}}_{T,\delta} + \hat{\mathcal{H}}_{T,\varepsilon}) \\
 &= |B_\gamma\rangle \text{Tr} \{ B_\gamma^\dagger (\hat{\mathcal{H}}_{T,\delta} + \hat{\mathcal{H}}_{T,\varepsilon}) \} \\
 &= |B_\gamma\rangle \text{Tr} \{ B_\gamma^\dagger \hat{\mathcal{H}}_{T,\delta} + B_\gamma^\dagger \hat{\mathcal{H}}_{T,\varepsilon} \} \\
 &= |B_\gamma\rangle \underbrace{\text{Tr} \{ B_\gamma^\dagger \hat{\mathcal{H}}_{T,\delta} \}}_{\omega_\delta \cdot k_\delta^\gamma} + |B_\gamma\rangle \underbrace{\text{Tr} \{ B_\gamma^\dagger \hat{\mathcal{H}}_{T,\varepsilon} \}}_{\omega_\varepsilon \cdot k_\varepsilon^\gamma}
 \end{aligned} \tag{1.6.20}$$

where γ denotes the corresponding basis operator in the toggling frame B_γ and both summands of the interaction ($\hat{\mathcal{H}}_{T,\delta}$, $\hat{\mathcal{H}}_{T,\varepsilon}$) can again be calculated separately.

From Equation (1.6.18) and (1.6.20) it is clear that all kinds of interactions can be decomposed into single spin basis operators. Since the single-spin operator basis consists of only 3 elements and the propagation in the toggling frame is independent of the original basis' size the calculation's speed is considerably enhanced. The python implementation of the calculation discussed in the present subsection is given in the Appendix 5.5.4.

1.6.3 Toggling Frame: a Graphical Interpretation

Another more intuitive way to look at the toggling frame shall be described using an example from literature^[6] which in the following is called the *perfect echo*. In Figure 1.7 the perfect echo pulse sequence is shown whose interesting properties are revealed in the toggling frame and its applications are discussed in more detail in Section 2.2. For the present example we assume a weakly coupled two spin system (Section 1.3.6) and since delays are equally refocused by 180° pulses the spins' frequency offsets are being neglected.

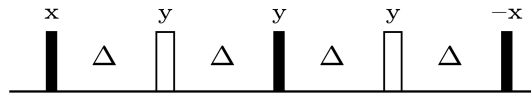


Figure 1.7: Pulse sequence for the so-called perfect echo. Filled black boxes and open white boxes correspond to 90° pulses and 180° pulses, respectively, which are separated by the delay Δ and the pulse's phase is denoted on top.

When going to the toggling frame the Hamiltonian of the pulses are removed from the Schrödinger equation and the coupling Hamiltonian can be calculated from the previous section by Equation (1.6.7) or (1.6.11). Likewise, it is possible to illustrate the sequential transformations to the toggling frame in a graphical way as is shown in Figure 1.8. We shall consider the Hamiltonian in the rotating frame $\hat{\mathcal{H}}_R$ as an object, illustrated in the coordinate system of the rotating frame (x, y, z) , being rotated within the fixed toggling frame (x', y', z') . The rotations $U_R(\tau)$ correspond to the frame transformations that are

directly given by the above shown pulse sequence. For the sequential transformations it is, however, most convenient to use the transformations $U_T(\tau)$ since they are applied in non-reversed order. The rotations $U_T(\tau)$ are applied to the axes (x', y', z') and, as discussed in the previous section (Equation 1.6.8), they need to be calculated recursively from $U_R(\tau)$:

$$\begin{aligned} U_{T_1} &= U_{R_1} \\ U_{T_n} &= U_{T_{n-1}}^\dagger \dots U_{T_1}^\dagger U_{R_n} U_{T_1} \dots U_{T_{n-1}}. \end{aligned} \quad (1.6.21)$$

With respect to Figure 1.8 (a) this implies that in the first frame both transformations are equal with $x = x'$, $y = y'$ and $z = z'$. However, undergoing the sequential transformations the two frames will differ and the rotations $U_R(\tau)$ given by the pulse sequence need to be transformed to the axes in the toggling frame (x', y', z') i.e. $U_T(\tau)$. This turns out to be easier as expected – in Figure 1.8 (a) the rotating frame (x, y, z) is illustrated in the toggling frame (x', y', z') and, hence, the relation between $U_R(\tau)$ and (x', y', z') is directly given – the coordinate system (x, y, z) points in the respective direction of (x', y', z') . Hence, the consecutive rotations U_{R_n} are applied to the axes (x, y, z) in *non-reversed* order which corresponds to the rotations U_{T_n} applied to the axes (x', y', z') . It is crucial to note that a pulse acting on a spin density induces a counter-clockwise rotation (right-hand rule) while for a frame transformation it causes a clockwise rotation (left-hand rule). Since a weakly coupled spin system is assumed the considered Hamiltonian $\hat{\mathcal{H}}_R$ consists only of components along z and, therefore, in Figure 1.8 (a) the z -axis is highlighted in red. In order to obtain the coefficients of the Hamiltonian in the toggling frame, the toggling Hamiltonian $\hat{\mathcal{H}}_T(\tau) = U_T^\dagger(\tau)\hat{\mathcal{H}}_R U_T(\tau)$ is projected onto the axes of the toggling frame (x', y', z') and it shall again be noted that the “toggling Hamiltonian” is only toggling when seen *from* the toggling frame while it is time-independent in the rotating frame.

From a linear Hamiltonian in the rotating frame $\hat{\mathcal{H}}_{R,z}$ (corresponding to the Zeeman interaction with $\hat{\mathcal{H}}_{R,z} = \omega_z \cdot \hat{I}_{1z}$) one obtains a time-dependent Hamiltonian $\hat{\mathcal{H}}_{T,z}(\tau)$ in the toggling frame which can be projected onto its orthonormal basis as calculated in (1.6.14) where:

$$\begin{aligned} \hat{\mathcal{H}}_{T,z}(\tau) &= \sum_{\gamma} \hat{P}_{\gamma} \hat{\mathcal{H}}_{T,z}(\tau) = \omega_z \cdot \sum_{\gamma} k_z^{\gamma}(\tau) \hat{B}_{\gamma} \\ \text{with: } k_z^{\gamma}(\tau) &= \frac{1}{\omega_z} \cdot \text{Tr} \left\{ \hat{B}_{\gamma}^\dagger \hat{\mathcal{H}}_{T,z}(\tau) \right\}. \end{aligned} \quad (1.6.22)$$

and $\gamma = x', y', z'$ being the axes of the toggling frame. In the graphical interpretation shown in Figure 1.8 (a) the calculation in Equation (1.6.22) corresponds to a projection of the red z -vector onto the basis of the toggling frame (x', y', z') . The most dominant time-dependent coefficients, $k_z^{x'}(\tau)$ and $k_z^{y'}(\tau)$ (corresponding to the x' and y' -axis) are plotted in the upper two rows of Figure 1.8 (b).

If a bilinear Hamiltonian in the rotating frame $\hat{\mathcal{H}}_{R,zz}$ (corresponding to a scalar coupling in weak coupling limit i.e. $\hat{\mathcal{H}}_{R,zz} = \omega_{zz} \cdot 2\hat{I}_{1z}\hat{I}_{2z}$) is assumed one can calculate the coefficients of its time-dependent Hamiltonian in the toggling frame $\hat{\mathcal{H}}_{T,zz}(\tau)$ from simple scalar multiplication as was derived in the preceding Section 1.6.2. The coefficient $k_{zz}^{\gamma\gamma'}(\tau)$ corresponding to the bilinear basis operator $\hat{B}_{\gamma\gamma'}$ can, hence, be expressed in terms of the single-spin components, $k_z^{\gamma}(\tau)$ and $k_z^{\gamma'}(\tau)$:

$$\begin{aligned} k_{zz}^{\gamma\gamma'}(\tau) &= \frac{1}{\omega_{zz}} \cdot \text{Tr} \left\{ \hat{B}_{\gamma\gamma'}^\dagger \hat{\mathcal{H}}_{T,zz}(\tau) \right\} \\ &= k_z^{\gamma}(\tau) \cdot k_z^{\gamma'}(\tau) \end{aligned} \quad (1.6.23)$$

with $\gamma, \gamma' = x', y', z'$ being the axes of the toggling frame. It is crucial to note that γ and γ' correspond to the axes of different spins where each might have its individual toggling frame (e.g. Section 2.5).

In the toggling frame of the perfect echo the most significant components of $\hat{\mathcal{H}}_{T,zz}$ are given by $\hat{\mathcal{H}}_{T,zz}^{x'x'}(\tau)$ and $\hat{\mathcal{H}}_{T,zz}^{y'y'}(\tau)$. They are described by:

$$\begin{aligned}\hat{\mathcal{H}}_{T,zz}^{x'x'}(\tau) &= \hat{k}_{zz}^{x'x'}(\tau) \cdot \sum_{k>j} 2\pi J_{k,j} \cdot \hat{I}_{kx} \hat{I}_{jx} \\ \text{and: } \hat{\mathcal{H}}_{T,zz}^{y'y'}(\tau) &= \hat{k}_{zz}^{y'y'}(\tau) \cdot \sum_{k>j} 2\pi J_{k,j} \cdot \hat{I}_{ky} \hat{I}_{jy}\end{aligned}\tag{1.6.24}$$

and their time-dependent coefficients $k_{zz}^{x'x'}(\tau)$ and $k_{zz}^{y'y'}(\tau)$ – calculated from the square of $k_z^{x'}(\tau)$ and $k_z^{y'}(\tau)$, respectively – are shown in the lower two rows of Figure 1.8. While $\hat{\mathcal{H}}_{T,zz}^{y'y'}(\tau)$ is active during the first two delays $\hat{\mathcal{H}}_{T,zz}^{x'x'}(\tau)$ is active during the last two delays. In case of a two spin system the corresponding basis operators for $\hat{\mathcal{H}}_{T,zz}^{x'x'}(\tau)$ and $\hat{\mathcal{H}}_{T,zz}^{y'y'}(\tau)$ are $2\hat{I}_{1x}\hat{I}_{2x}$ and $2\hat{I}_{1y}\hat{I}_{2y}$, respectively, and since these two *predominant* components commute, the time-dependent Hamiltonian $\hat{\mathcal{H}}_{T,zz}(\tau)$ can be considered inhomogeneous²³ to first approximation.

It is, however, interesting to note that on a closer look the weak coupling Hamiltonian in the toggling frame of the perfect echo $\hat{\mathcal{H}}_{T,zz}$ contains further non-zero operators. Some of them are illustrated in Figure 1.9 and, clearly, the considered Hamiltonian $\hat{\mathcal{H}}_{T,zz}(\tau)$ in its *exact* form is no longer inhomogeneous (certain components illustrated in Figure 1.8 and 1.9 do *not* commute). By this means a complete picture on the effect of coupling can be elaborated from the toggling frame for any kind of pulse sequence and, therefore, it represents a helpful tool for the investigation on possible side-effects. Note that all components of the toggling frame Hamiltonian $\hat{\mathcal{H}}_{T,zz}(\tau)$ in Figure 1.9 are non-zero *only* when pulses are applied and it becomes evident that a special focus has to be put on the evolution of coupling *during* RF-pulses (further investigations in Section 2.4).

In the present case all operators other than $\hat{\mathcal{H}}_{T,zz}^{x'x'}$ and $\hat{\mathcal{H}}_{T,zz}^{y'y'}$ are comparatively small and the approximation of $\hat{\mathcal{H}}_{T,zz}$ to an inhomogeneous Hamiltonian is well justifiable. Hence, for a two-spin system it can be shown with the help of average Hamiltonian theory (discussed in Section 1.7) that the zeroth order average Hamiltonian $\bar{\mathcal{H}}_{0,zz}^{\text{PE}}$ of the weak coupling Hamiltonian $\hat{\mathcal{H}}_{R,zz}$ in the perfect echo is given by a *planar mixing* Hamiltonian $\hat{\mathcal{H}}^{\text{PM}}$ of *half* the effective J -coupling:

$$\begin{aligned}\bar{\mathcal{H}}_{0,zz}^{\text{PE}} &\approx \hat{\mathcal{H}}_{T,zz}^{x'x'} + \hat{\mathcal{H}}_{T,zz}^{y'y'} \\ &\approx \frac{1}{2} \hat{\mathcal{H}}^{\text{PM}} = \pi J_{1,2} \cdot (\hat{I}_{1x} \hat{I}_{2x} + \hat{I}_{1y} \hat{I}_{2y}).\end{aligned}\tag{1.6.25}$$

Furthermore, it should be noted that for an n -spin system with $n > 2$ the Hamiltonian $\hat{\mathcal{H}}_{T,zz}$ can no longer be considered inhomogeneous – even if coupling evolution during RF-pulses is neglected. This is based on the fact that bilinear operators corresponding to different couplings no longer commute (i.e. $[\hat{I}_{1x}\hat{I}_{2x}, \hat{I}_{2y}\hat{I}_{3y}] \neq 0$). A planar mixing Hamiltonian can anyway be approximated if the delay Δ is chosen much shorter than the inverse coupling strength and $\|\hat{\mathcal{H}}_{T,zz}\| \cdot 4\Delta \ll 2\pi$. A more detailed discussion about the convergence of the Magnus series and its zeroth order is found in Section 1.7.3.

In contrast to isotropic mixing (IM) where an in-phase to in-phase transfer is obtained for all linear operators of involved spins, planar mixing (PM) provides transfer only for the orthogonal axis that does *not commute* with neither of the two bilinear terms (i.e. transfer from \hat{I}_{1z} to \hat{I}_{2z} for the planar Hamiltonian in Equation 1.6.25). The applications of planar mixing shall be further discussed in Section 2.2.

²³ A further discussion on homogeneous and inhomogeneous Hamiltonians is given in Section 1.1.1 and 1.7.

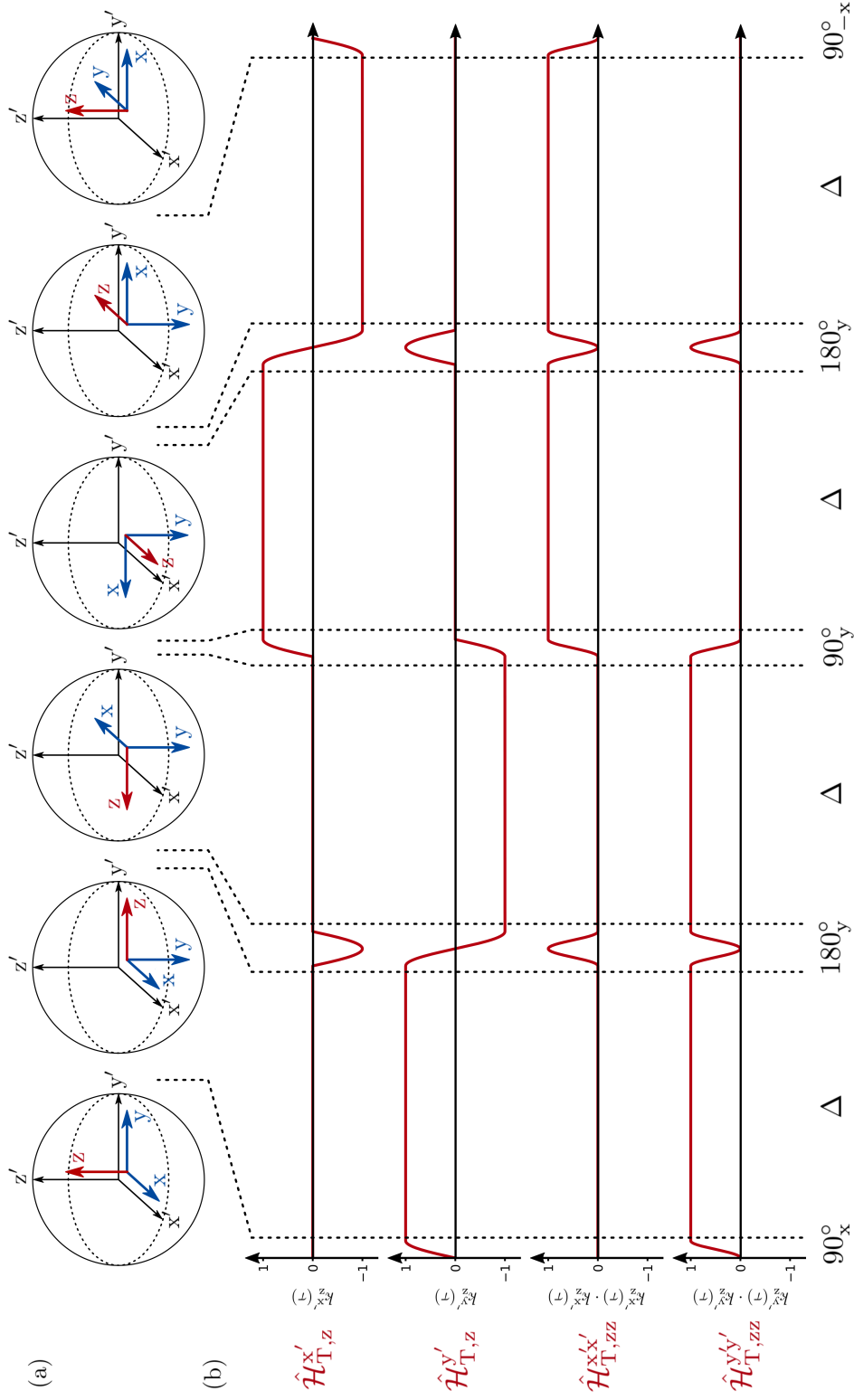


Figure 1.8: The effect of weak scalar coupling during the perfect echo is simulated in the toggling frame. In (a) the transformation is illustrated graphically where the rotating frame (x, y, z) is rotated around the axes (x, y, z) according to the pulse sequence within the fixed toggling frame (x', y', z') . In (b) the time-dependent coefficients of $\hat{\mathcal{H}}_{T,z}^{x'}$, $\hat{\mathcal{H}}_{T,z}^{y'}$, $\hat{\mathcal{H}}_{T,zz}^{x'x'}$ and $\hat{\mathcal{H}}_{T,zz}^{y'y'}$ are plotted against the pulse sequence which are obtained from the projection of \mathbf{z} onto (x', y', z') . The rotations in the rotating frame (x, y, z) are given by the pulse sequence as $U_R(\tau) = \{U_{90}^x; U_{180}^y; U_{90}^y; U_{180}^y; U_{90}^x\}$ while in the toggling frame (x', y', z') they are $U_T(\tau) = \{U_{90}^x; U_{180}^y; U_{90}^y; U_{180}^y; U_{90}^x\}$.

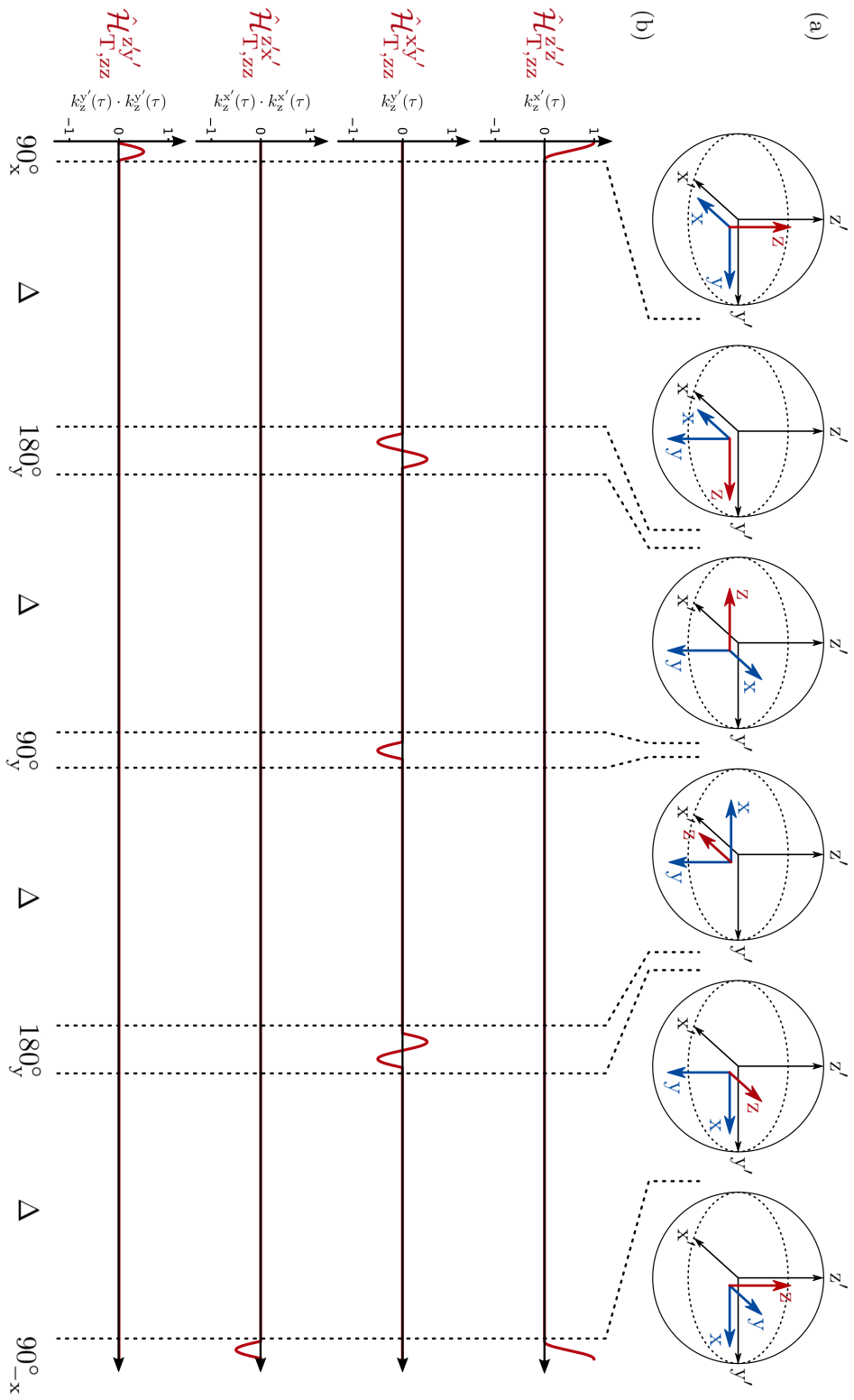


Figure 1.9: The effect of weak scalar coupling during the perfect echo is simulated in the toggling frame. In (a) the transformation is illustrated graphically where the rotating frame (x, y, z) is rotated around the axes (x, y, z) according to the pulse sequence within the fixed toggling frame (x', y', z') . In (b) the time-dependent coefficients of $\hat{H}_{T,zz}^{z'z'}$, $\hat{H}_{T,zz}^{x'x'}$, $\hat{H}_{T,zz}^{y'y'}$ and $\hat{H}_{T,zz}^{x'x'}$ are plotted against the pulse sequence which are obtained from the projection of z onto (x', y', z') . It is crucial to note that only during RF-pulses the illustrated operators are non-zero.

1.6.4 Toggling Frame: Introducing the Unity Matrix

While in previous sections the Hamiltonian undergoes a transformation to the toggling frame another approach is based on subtle juggling with the sequence's propagators. Its aim is to separate the propagators of the pulses from the propagators of the coupling. Since all propagators are modified within the rotating frame it might, therefore, be more intuitive and, non the less, exact. Instead of a (piecewise time-independent) coupling Hamiltonian in the toggling frame (Equation 1.6.11) one obtains its piecewise propagators. The above example of the perfect echo (Figure 1.7) shall, again, be used and its pulse sequence can be rewritten in terms of propagators:

$$U_{\text{PE}} = U_{90}^{-x} U_{\Delta} U_{180}^y U_{\Delta} U_{90}^y U_{\Delta} U_{180}^y U_{\Delta} U_{90}^x \quad (1.6.26)$$

where U_{Δ} is the delay's propagator and all others represent the 90° and 180° pulses with respective phases. Since any unitary transformation approves $U^\dagger U = \mathbb{1}$ the propagator sequence can be modified by introducing the unity matrix $\mathbb{1}$:

$$\begin{aligned} U_{\text{PE}} &= U_{90}^{-x} U_{\Delta} U_{180}^y U_{\Delta} U_{90}^y U_{\Delta} U_{180}^y \underbrace{U_{90}^x U_{90}^{x\dagger}}_{\mathbb{1}} U_{\Delta} U_{90}^x \\ &= U_{90}^{-x} U_{\Delta} U_{180}^y U_{\Delta} U_{90}^y U_{\Delta} U_{180}^y U_{90}^x \underbrace{U_{90}^{x\dagger} U_{\Delta} U_{90}^x}_{U_{\Delta'_1}} \\ &= U_{90}^{-x} U_{\Delta} U_{180}^y U_{\Delta} U_{90}^y \underbrace{U_{180}^y U_{90}^x U_{90}^{x\dagger} U_{180}^{y\dagger}}_{\mathbb{1}} U_{\Delta} U_{180}^y U_{90}^x \underbrace{U_{90}^{x\dagger} U_{\Delta} U_{90}^x}_{U_{\Delta'_1}} \\ &= U_{90}^{-x} U_{\Delta} U_{180}^y U_{\Delta} U_{90}^y U_{180}^y U_{90}^x \underbrace{U_{90}^{x\dagger} U_{180}^{y\dagger} U_{\Delta} U_{180}^y U_{90}^x}_{U_{\Delta'_2}} \underbrace{U_{90}^{x\dagger} U_{\Delta} U_{90}^x}_{U_{\Delta'_1}} \\ &\dots \\ &= \underbrace{U_{90}^{-x} U_{180}^y U_{90}^y U_{180}^y U_{90}^x}_{\text{operator dynamics}} \underbrace{U_{\Delta'_4} U_{\Delta'_3} U_{\Delta'_2} U_{\Delta'_1}}_{\text{toggling frame}} \end{aligned} \quad (1.6.27)$$

from which is evident that the sequential $U_{\Delta'}$ correspond to the coupling propagators in the toggling frame that are completed by the operator dynamics given by the pulses' propagators on the left. Note, again the propagators in the toggling frame $U_{\Delta'}$ are flanked by the sequential transformations in the rotating frame with reversed order as was already found in Equation (1.6.11). While the toggling frame in combination with average Hamiltonian theory is often applied for cyclic transformations $U(\tau) = U(0)$ it is obvious from the result of Equation (1.6.27) that extending the propagator in the toggling frame by the frame's propagator also a valid propagator is obtained for non-cyclic transformations. It shall be noted that the operator dynamics are determined by the Heisenberg equation (1.5.5) which can be illustrated using the calculation of an operator's expectation value and the cyclic properties of the trace:

$$\begin{aligned} \langle \hat{A} \rangle &= \text{Tr} \left\{ \hat{A} (U_{\text{op}} U_{\text{tog}} \hat{\rho} U_{\text{tog}}^\dagger U_{\text{op}}^\dagger) \right\} \\ &= \text{Tr} \left\{ \underbrace{(U_{\text{op}}^\dagger \hat{A} U_{\text{op}})}_{\text{Heisenberg}} \underbrace{(U_{\text{tog}} \hat{\rho} U_{\text{tog}}^\dagger)}_{\text{Schrödinger}} \right\}, \end{aligned} \quad (1.6.28)$$

where U_{op} corresponds to the operator dynamics and U_{tog} to the coupling propagators in the toggling frame. The procedure described in the present section offers a very compact and convenient access to the toggling frame and it shall be further used in Section 2.4.

1.7 Average Hamiltonian Theory

In preceding sections we encountered different types of Hamiltonians that require appropriate treatment. As discussed in Section 1.1.1, surely, the most convenient type is a time-independent Hamiltonian that is consequently also commuting with itself at any two time points (Equation 1.1.8) and is consequently referred to as inhomogeneous^[9]. If time-dependent, the equation of motion can still be solved with basic mathematical tools as long as the Hamiltonian is inhomogeneous. The most generic case – a time-dependent homogeneous Hamiltonian – requires further considerations and shall be in the focus of the current section.

From a homogeneous Hamiltonian one can obtain an *effective* or *average* Hamiltonian that in general is only valid within a defined time step. However, if the Hamiltonian is periodic and stroboscopic observations are made synchronized to the Hamiltonian's period an application to larger time spans is possible – we state for its propagator:

$$U(n \cdot t) = U(t)^n. \quad (1.7.1)$$

If the propagator is available for a defined time step, i.e. via numerical simulations or a *Dyson series*^[44], the effective Hamiltonian can be calculated from the logarithm of the diagonalized propagator. Another elegant solution offers the so-called *Average Hamiltonian Theory* which is based on the *Magnus series*^[45] and was first introduced to magnetic resonance by Waugh, Huber and Haeberlen^[4,46]. Furthermore, it is possible to describe the time-dependent Hamiltonian in a Fourier series making it time-independent in the expanded basis and an exact solution can be found for an infinite basis. This is commonly referred to as *Floquet Theory*^[47,48] and shall here just be noted for completeness – it was shown that the respective orders of the Magnus series and Floquet Theory are identical^[49] and a short summary on this subject is given by Ernst.^[17] Despite the fact that in the following numerical simulations are undertaken, it shall also be stated that just recently a novel method was introduced to the field of magnetic resonance by Giscard and Bonhomme.^[50,51] It is based on path-sums from which *analytical* solutions to a time-dependent Hamiltonian can be obtained.

1.7.1 Piecewise Time-Independent Hamiltonian

In order to obtain a propagator that determines the system's dynamic up to a defined time t_c the most straight-forward ansatz would be to split the Hamiltonian into multiple shorter time steps τ and assume that, if each piece is short enough, the Hamiltonian has become piecewise time-independent. The solution to the Schrödinger equation for a time-independent Hamiltonian is known from Equation (1.1.9) in Section 1.1.1 and the effective propagator U_{eff} for the piecewise time-independent Hamiltonian is given as:

$$\begin{aligned} U_{\text{eff}}(t_c, 0) &= \lim_{\tau \rightarrow 0} U(t_c, t_c - \tau) \dots U(\tau, 0) \\ &= \lim_{\tau \rightarrow 0} \exp\{-i\hat{\mathcal{H}}_n \tau_n\} \dots \exp\{-i\hat{\mathcal{H}}_1 \tau_1\} \\ &= \exp\{-i\hat{\mathcal{H}}_{\text{eff}} t_c\}, \end{aligned} \quad (1.7.2)$$

where τ is approaching zero and the propagation from 0 to t_c is defined by an effective Hamiltonian $\hat{\mathcal{H}}_{\text{eff}}$ – it can be extracted from:

$$\hat{\mathcal{H}}_{\text{eff}} = \frac{1}{(-it_c)} D \log\{U_{\text{diag}}\} D^{-1} \quad (1.7.3)$$

[44] F. J. Dyson. *Physical Review* **1949**, 75, 486–502.

[45] W. Magnus. *Communications on Pure and Applied Mathematics* **1954**, 7, 649–673.

[46] U. Haeberlen and J. S. Waugh. *Physical Review* **1968**, 175, 453–467.

[47] J. H. Shirley. *Physical Review* **1965**, B138, 979–987.

[48] R. Garg and R. Ramachandran. *Journal of Chemical Physics* **2020**, 153, 034106.

[49] M. M. Maricq. *Physical Review* **1982**, B25, 6622–6632.

[50] P.-L. Giscard and C. Bonhomme. *Physical Review Research* **2020**, 2, 023081.

[51] P. L. Giscard et al. *Journal of Mathematical Physics* **2015**, 56, 053503.

where U_{diag} is the diagonalized propagator of U_{eff} in Equation (1.7.2) and D is the transformation into the propagators eigenbasis.²⁴ This is a common approach when numerical simulations are undertaken and with today's computer power a relatively fast result is obtained. However, in contrast to other approaches (e.g. Magnus series^[45]) one has only little insight into the creation of $\hat{\mathcal{H}}_{\text{eff}}$ and the ambiguity of the effective propagator²⁵ often leads to results that have to be interpreted with care.^[52]

1.7.2 Dyson Series

The analytical analog to the numerical solution of the preceding section is given by the *Dyson series*^[44] – it shall be derived in the following assuming again a piecewise time-independent Hamiltonian. A formal derivation of the Dyson series can be found in literature^[18] which is based on time-dependent perturbation theory within an interaction picture (Section 1.5.2), however, in the present section I will rather try to communicate a basic understanding of its genesis – only the first two terms are derived. The propagator of a time-independent Hamiltonian for a time step τ can be expressed in a power series:

$$\begin{aligned} U(\tau) &= \exp \left\{ -i\hat{\mathcal{H}}\tau \right\} \\ &= \mathbb{1} + (-i\hat{\mathcal{H}}\tau) + \frac{(-i\hat{\mathcal{H}}\tau)^2}{2!} + \frac{(-i\hat{\mathcal{H}}\tau)^3}{3!} + \dots \end{aligned} \quad (1.7.4)$$

from which is evident that fast convergence is obtained if $\|\hat{\mathcal{H}}\|\tau$ is small.²⁶ Assuming a time-dependent Hamiltonian that is split into three piecewise time-independent steps τ_n we get three consecutive propagations U_1 , U_2 and U_3 . Using the above power series up to the second order the effective propagator U_{eff} can be calculated as:

$$U_{\text{eff}}(t_c, 0) = U_3 U_2 U_1 \quad (1.7.5)$$

$$\begin{aligned} &\approx \left[\mathbb{1} + (-i\hat{\mathcal{H}}_3\tau_3) + \frac{(-i\hat{\mathcal{H}}_3\tau_3)^2}{2!} \right] \left[\dots \right] \left[\mathbb{1} + (-i\hat{\mathcal{H}}_1\tau_1) + \frac{(-i\hat{\mathcal{H}}_1\tau_1)^2}{2!} \right] \\ &\approx \mathbb{1} \end{aligned} \quad (1.7.6)$$

$$+ (-i) \left[\hat{\mathcal{H}}_1\tau_1 + \hat{\mathcal{H}}_2\tau_2 + \hat{\mathcal{H}}_3\tau_3 \right] \quad (1.7.7)$$

$$+ \frac{(-i)^2}{2!} \left[(\hat{\mathcal{H}}_1\tau_1)^2 + (\hat{\mathcal{H}}_2\tau_2)^2 + (\hat{\mathcal{H}}_3\tau_3)^2 + 2(\hat{\mathcal{H}}_3\hat{\mathcal{H}}_2\tau_3\tau_2 + \hat{\mathcal{H}}_3\hat{\mathcal{H}}_1\tau_3\tau_1 + \hat{\mathcal{H}}_2\hat{\mathcal{H}}_1\tau_2\tau_1) \right] \quad (1.7.8)$$

where in the last line we neglect power terms that are proportional to $(\|\hat{\mathcal{H}}\|\tau)^n$ with $n > 2$. By increasing the number of discrete consecutive propagations in (1.7.5) a continuous Hamiltonian is approximated and one can derive the Dyson series as:

$$U(t_c, 0) = \underbrace{\mathbb{1}}_{\sim \text{Eq. (1.7.6)}} + \underbrace{(-i) \int_0^{t_c} dt \hat{\mathcal{H}}(t)}_{\sim \text{Eq. (1.7.7)}} + \underbrace{(-i)^2 \int_0^{t_c} dt \int_0^t dt' \hat{\mathcal{H}}(t)\hat{\mathcal{H}}(t')}_{\sim \text{Eq. (1.7.8)}} + \dots \quad (1.7.9)$$

where the comparable discrete terms are noted below in braces and the sum over respective orders are replaced by integrals. It should be noted that in analogy to Equation (1.7.8) the two integration limits of the last term stem from the fact that $\hat{\mathcal{H}}(t)$ is always left of $\hat{\mathcal{H}}(t')$ and $t \geq t'$. This is illustrated in

^[52] S. J. Glaser. *Journal of Magnetic Resonance* **1993**, A104, 283–301.

²⁴ For the diagonalization of U_{eff} , first, eigenfunctions $|m\rangle$ need to be calculated from $(U_{\text{eff}} - E\mathbb{1}) \cdot |m\rangle = 0$ where E denotes the eigenvalues. The transformation of U_{eff} to its eigenbasis is then given by $U_{\text{diag}} = D^{-1}U_{\text{eff}}D$ where D consists of all eigenfunctions $|m\rangle$. In eigenbasis of U_{eff} the logarithm is applied to the diagonal elements and a transformation to the original basis is given by D^{-1} .

²⁵ In the considered case the matrix logarithm of the effective propagator U_{eff} is no *single-valued function* and the effective Hamiltonian $\hat{\mathcal{H}}_{\text{eff}}$ calculated from Equation (1.7.3) does not provide a unique solution.

²⁶ The norm of the Hamiltonian $\|\hat{\mathcal{H}}\|$ is considered to be given by its frequency $\omega_{\mathcal{H}}$.

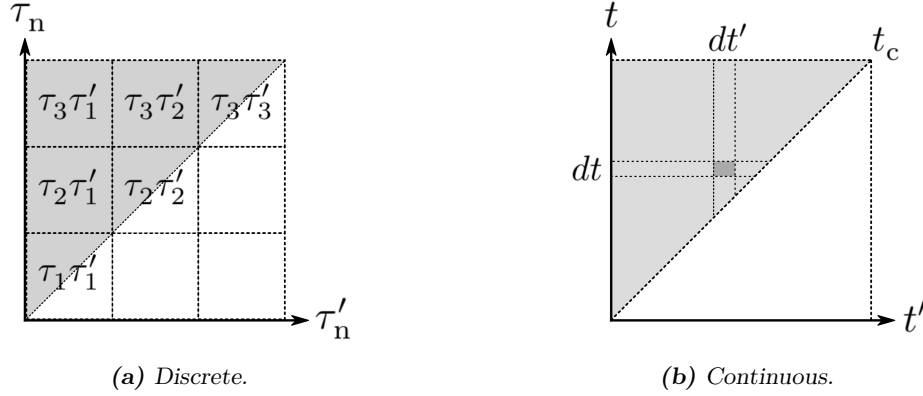


Figure 1.10: The time-dependence of the second order Dyson series is shown for a discrete (1.7.8) and a continuous (1.7.9) Hamiltonian $\hat{H}(t)$. Note in (a), that the diagonal accounts for the relative prefactors of respective terms in Equation (1.7.8).

Figure 1.10 for the case of a discrete (Equation 1.7.8) and a continuous Hamiltonian (Equation 1.7.9). Dyson terms of higher order with $n > 2$ can be derived if also higher orders are considered in the power series of Equation (1.7.4). In order to obtain an approximated effective Hamiltonian \hat{H}_{eff} from Equation (1.7.9) one can proceed as discussed in the preceding section (Equation 1.7.3).

Dyson Series as Exponential Operator

From Equation (1.7.9) again a power series can be reobtained if the integration limits are adjusted to the full time t_c which corresponds to the full square in Figure 1.10 (b). Hence, a factor of $\frac{1}{2}$ needs to be considered and the so-called *Dyson Time Ordering Operator* T ensures that as before the Hamiltonian with the later time argument is always left of the Hamiltonian with an earlier time argument – it acts as described in Equation (1.7.10).

$$T \hat{H}(t)\hat{H}(t') = \begin{cases} \hat{H}(t)\hat{H}(t') & t > t', \\ \hat{H}(t')\hat{H}(t) & t < t'. \end{cases} \quad (1.7.10)$$

Applying the above mentioned changes to Equation (1.7.9) one obtains the power series shown in Equation (1.7.11) which, again, is a *generating function* of an exponential. The propagator of a homogeneous Hamiltonian can, hence, be written as an exponential that is subject to the Dyson Time Ordering Operator T (Equation 1.7.12). Herein, the operator T is an intriguing part since its purpose becomes clear only when being seen as a required operation to obtain an exponential *from* the Dyson series. Therefore, it reveals its rather simple properties only after the exponential is expanded to the power series.

$$\begin{aligned} U(t_c, 0) &= \mathbb{1} + (-i) \int_0^{t_c} dt \hat{H}(t) + (-i)^2 \int_0^{t_c} dt \int_0^t dt' \hat{H}(t)\hat{H}(t') + \dots \\ &= \mathbb{1} + (-i) \int_0^{t_c} dt \hat{H}(t) + (-i)^2 \int_0^{t_c} dt \frac{1}{2} \int_0^{t_c} dt' T \hat{H}(t)\hat{H}(t') + \dots \end{aligned} \quad (1.7.11)$$

$$= T \exp \left\{ -i \int_0^{t_c} \hat{H}(t) dt \right\}. \quad (1.7.12)$$

1.7.3 Magnus Series

While in the previous section the calculation of an effective Hamiltonian $\hat{\mathcal{H}}_{\text{eff}}$ from a homogeneous Hamiltonian was only possible via the detour of calculating the propagator, the *Magnus series*^[45] offers a direct way to obtain $\hat{\mathcal{H}}_{\text{eff}}$. Frequently, it is applied in combination with an interaction frame (Section 1.6) where it leads to an equivalent result as obtained by perturbation theory.^[28] Many commendable textbooks and articles are given in literature that offer further and comprehensible insight to the field.^[4,17,28,46,53]

In order to derive the Magnus series we shall first state an ansatz in which we define the properties that we wish the series to fulfill and in close analogy to the preceding Section 1.7.2 we shall then make use of an intuitive and discrete propagation (Equation 1.7.5) that finally leads to the generic Magnus series. Again only the first two terms of the Magnus series are derived in the same way as described in Haeberlen's book^[28] where, additionally, higher orders of the average Hamiltonian are included. At the end of the section the so-called *Baker-Campbell-Hausdorff Formula* is derived from the Magnus series and the impact of the Hamiltonian's symmetry on the Magnus series is discussed.

Derivation of the Magnus Series

As an ansatz we state that an effective Hamiltonian $\hat{\mathcal{H}}_{\text{eff}}$ can be described as a series where respective orders of the average Hamiltonian $\bar{\mathcal{H}}_n$ are proportional to $(\|\hat{\mathcal{H}}\|t)^{n+1}$:

$$\hat{\mathcal{H}}_{\text{eff}} = \bar{\mathcal{H}}_0 + \bar{\mathcal{H}}_1 + \bar{\mathcal{H}}_2 + \dots \quad (1.7.13)$$

from which is directly clear, that all terms of the Magnus series have to be Hermitian operators and the series can be stopped at any order. Assuming only the first two terms of Equation (1.7.13) the propagator can be expressed in a power series up to the second order and one obtains:

$$\begin{aligned} U_{\text{eff}}(t_c, 0) &= \exp \left\{ -i\hat{\mathcal{H}}_{\text{eff}}t_c \right\} \\ &\approx \exp \left\{ -i(\bar{\mathcal{H}}_0 + \bar{\mathcal{H}}_1)t_c \right\} \\ &\approx \mathbb{1} + (-it_c) \left[\underbrace{\bar{\mathcal{H}}_0}_{\propto(\|\mathcal{H}\|t)} + \underbrace{\bar{\mathcal{H}}_1}_{\propto(\|\mathcal{H}\|t)^2} \right] + \frac{(-it_c)^2}{2!} \left[\underbrace{(\bar{\mathcal{H}}_0)^2}_{\propto(\|\mathcal{H}\|t)^2} + \underbrace{\bar{\mathcal{H}}_0\bar{\mathcal{H}}_1}_{\propto(\|\mathcal{H}\|t)^3} + \underbrace{\bar{\mathcal{H}}_1\bar{\mathcal{H}}_0}_{\propto(\|\mathcal{H}\|t)^3} + \underbrace{(\bar{\mathcal{H}}_1)^2}_{\propto(\|\mathcal{H}\|t)^4} \right] \end{aligned}$$

where in the last line the proportionality to $(\|\mathcal{H}\|t)^n$ is noted below individual terms. We neglect terms that are proportional to $(\|\hat{\mathcal{H}}\|t)^n$ with $n > 2$ and rearrange the rest in a way that equal orders are combined. Rewriting the propagator U_{eff} leads to the following approximation:

$$U_{\text{eff}}(t_c, 0) \approx \mathbb{1} + \underbrace{(-it_c)\bar{\mathcal{H}}_0}_{\propto(\|\mathcal{H}\|t)} + \underbrace{(-it_c)\bar{\mathcal{H}}_1 + \frac{(-it_c)^2}{2!}(\bar{\mathcal{H}}_0)^2}_{\propto(\|\mathcal{H}\|t)^2} \quad (1.7.14)$$

where the order of proportionality is noted below. We shall recall from Equation (1.7.5) that the effective propagator U'_{eff} of a piecewise time-independent Hamiltonian can be approximated by the product of individual propagators U_n or likewise their power series:

$$\begin{aligned} U'_{\text{eff}}(t_c, 0) &= U_3 U_2 U_1 \\ &\approx \mathbb{1} + \underbrace{(-i) \left[\hat{\mathcal{H}}_1\tau_1 + \hat{\mathcal{H}}_2\tau_2 + \hat{\mathcal{H}}_3\tau_3 \right]}_{\propto(\|\mathcal{H}\|t)} \\ &\quad + \underbrace{\frac{(-i)^2}{2!} \left[(\hat{\mathcal{H}}_1\tau_1)^2 + (\hat{\mathcal{H}}_2\tau_2)^2 + (\hat{\mathcal{H}}_3\tau_3)^2 + 2(\hat{\mathcal{H}}_3\hat{\mathcal{H}}_2\tau_3\tau_2 + \hat{\mathcal{H}}_3\hat{\mathcal{H}}_1\tau_3\tau_1 + \hat{\mathcal{H}}_2\hat{\mathcal{H}}_1\tau_2\tau_1) \right]}_{\propto(\|\mathcal{H}\|t)^2} \end{aligned} \quad (1.7.15)$$

^[53] A. Brinkmann. *Concepts in Magnetic Resonance Part A: Bridging Education and Research* **2016**, 45A.

where, again, the order of proportionality is noted below. Comparing the approximations of U_{eff} (Equation 1.7.14) and U'_{eff} (Equation 1.7.15) it becomes clear that respective terms of equal order can be equated. For a discrete approximation of U'_{eff} the zeroth order average Hamiltonian $\bar{\mathcal{H}}_0$ is given as the time-weighted mean in the course of t_c :

$$\bar{\mathcal{H}}_0 = \frac{1}{t_c} (\hat{\mathcal{H}}_1 \tau_1 + \hat{\mathcal{H}}_2 \tau_2 + \hat{\mathcal{H}}_3 \tau_3) \quad (1.7.16)$$

and we realize that these are the linear terms of the propagators' power series. In a similar way the first order average Hamiltonian $\bar{\mathcal{H}}_1$ for the approximation of U'_{eff} can be obtained by equating (1.7.8) to the respective term in Equation (1.7.14). Using the result of the zeroth order in Equation (1.7.16) and solving for $\bar{\mathcal{H}}_1$ we obtain:

$$\begin{aligned} \bar{\mathcal{H}}_1 &= \frac{(\text{Eq. 1.7.8})}{(-it_c)} - \frac{(-it_c)}{2!} (\bar{\mathcal{H}}_0)^2 \\ &= \frac{(-i)}{2t_c} \left[(\hat{\mathcal{H}}_1 \tau_1)^2 + (\hat{\mathcal{H}}_2 \tau_2)^2 + (\hat{\mathcal{H}}_3 \tau_3)^2 + 2(\hat{\mathcal{H}}_3 \hat{\mathcal{H}}_2 \tau_3 \tau_2 + \hat{\mathcal{H}}_3 \hat{\mathcal{H}}_1 \tau_3 \tau_1 + \hat{\mathcal{H}}_2 \hat{\mathcal{H}}_1 \tau_2 \tau_1) \right] \\ &\quad - \frac{(-i)}{2t_c} \left[(\hat{\mathcal{H}}_1 \tau_1)^2 + (\hat{\mathcal{H}}_2 \tau_2)^2 + (\hat{\mathcal{H}}_3 \tau_3)^2 + (\hat{\mathcal{H}}_3 \hat{\mathcal{H}}_2 \tau_3 \tau_2 + \hat{\mathcal{H}}_3 \hat{\mathcal{H}}_1 \tau_3 \tau_1 + \hat{\mathcal{H}}_2 \hat{\mathcal{H}}_1 \tau_2 \tau_1) \right. \\ &\quad \left. + (\hat{\mathcal{H}}_2 \hat{\mathcal{H}}_3 \tau_3 \tau_2 + \hat{\mathcal{H}}_1 \hat{\mathcal{H}}_3 \tau_3 \tau_1 + \hat{\mathcal{H}}_1 \hat{\mathcal{H}}_2 \tau_2 \tau_1) \right] \\ &= \frac{(-i)}{2t_c} \left[(\hat{\mathcal{H}}_3 \hat{\mathcal{H}}_2 \tau_3 \tau_2 + \hat{\mathcal{H}}_3 \hat{\mathcal{H}}_1 \tau_3 \tau_1 + \hat{\mathcal{H}}_2 \hat{\mathcal{H}}_1 \tau_2 \tau_1) - (\hat{\mathcal{H}}_2 \hat{\mathcal{H}}_3 \tau_3 \tau_2 + \hat{\mathcal{H}}_1 \hat{\mathcal{H}}_3 \tau_3 \tau_1 + \hat{\mathcal{H}}_1 \hat{\mathcal{H}}_2 \tau_2 \tau_1) \right] \quad (1.7.17) \end{aligned}$$

$$= \frac{(-i)}{2t_c} \left[[\hat{\mathcal{H}}_3, \hat{\mathcal{H}}_2] \tau_3 \tau_2 + [\hat{\mathcal{H}}_3, \hat{\mathcal{H}}_1] \tau_3 \tau_1 + [\hat{\mathcal{H}}_2, \hat{\mathcal{H}}_1] \tau_2 \tau_1 \right] \quad (1.7.18)$$

and we shall note that the Hamiltonian at later time points, i.e. higher indexing, is always on the left in the commutator. In analogy to the derivation of the Dyson series we can express U'_{eff} by an increasing number (n) of discrete consecutive propagations U_n during t_c . Hereby a continuous Hamiltonian $\hat{\mathcal{H}}(t)$ is approximated and we can express the zeroth and first order average Hamiltonian $\bar{\mathcal{H}}_0$ and $\bar{\mathcal{H}}_1$ by integration:

$$\bar{\mathcal{H}}_0 = \frac{1}{t_c} \int_0^{t_c} dt \hat{\mathcal{H}}(t), \quad (1.7.19)$$

$$\bar{\mathcal{H}}_1 = \frac{(-i)}{2t_c} \int_0^{t_c} dt \int_0^t dt' [\hat{\mathcal{H}}(t), \hat{\mathcal{H}}(t')] \quad (1.7.20)$$

$$\bar{\mathcal{H}}_2 = -\frac{1}{6t_c} \int_0^{t_c} dt \int_0^t dt' \int_0^{t'} dt'' \left([[\hat{\mathcal{H}}(t), \hat{\mathcal{H}}(t')], \hat{\mathcal{H}}(t'')] + [\hat{\mathcal{H}}(t), [\hat{\mathcal{H}}(t'), \hat{\mathcal{H}}(t'')]] \right) \quad (1.7.21)$$

where additionally $\bar{\mathcal{H}}_2$ is just stated without being derived in the present section. Again, the integration limits ensure that $\hat{\mathcal{H}}(t)$ is always left of $\hat{\mathcal{H}}(t')$ in the commutator (and hence, no operator T is required). This is illustrated in Figure 1.11 for a discrete (Equation 1.7.18) and a continuous Hamiltonian (Equation 1.7.20).

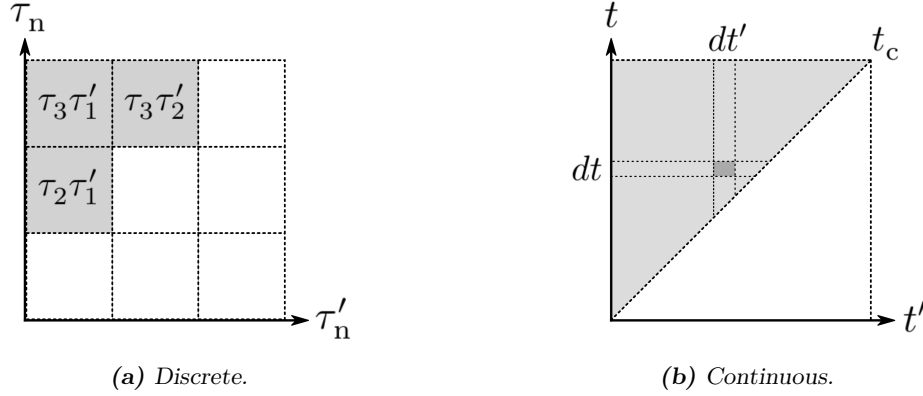


Figure 1.11: The time-dependence of the first order average Hamiltonian $\bar{\mathcal{H}}_1$ is shown for a discrete (1.7.18) and a continuous (1.7.20) Hamiltonian $\hat{\mathcal{H}}(t)$. Note, in (a) the diagonal is not included and τ_n and τ'_n are connected to $[\hat{\mathcal{H}}_n, \cdot]$ and $[\cdot, \hat{\mathcal{H}}'_n]$ respectively.

Baker-Campbell-Hausdorff Formula

The Baker-Campbell-Hausdorff formula can be seen as a special case of the Magnus series, namely, if we assume an effective propagation U_{eff} that consists of two individual time-independent propagations U_A and U_B . We can write:

$$\begin{aligned}
 U_{\text{eff}} &= U_B U_A \\
 &= e^{-iB} e^{-iA} \\
 &= \exp \left\{ \underbrace{-i(A+B)}_{\bar{\mathcal{H}}_0} \underbrace{-\frac{1}{2}[B,A]}_{\bar{\mathcal{H}}_1} \underbrace{+\frac{i}{12}([B,[B,A]] + [[B,A],A])}_{\bar{\mathcal{H}}_2} + \dots \right\}. \quad (1.7.22)
 \end{aligned}$$

Impact of Symmetric Hamiltonians

For the creation of an average Hamiltonian using the Magnus series we find that orders $\bar{\mathcal{H}}_n$ with $n > 0$ clearly depend on the Hamiltonian's development over time. Being aware of this fact it might seem a little less surprising if certain orders are strongly influenced by time-symmetric evolution of the Hamiltonian. It was first discovered by Mansfield^[54] that the first order average Hamiltonian $\bar{\mathcal{H}}_1$ vanishes for a Hamiltonian that is symmetric in time – which was later proven and extended to all odd orders $\bar{\mathcal{H}}_{\text{odd}}$ by Wang & Ramshaw^[55]. For an antisymmetric Hamiltonian, on the other hand, it is shown by Haeberlen^[28] that all orders vanish completely which is commonly of little use and should rather be avoided.

In the following, the properties of the Magnus series of a symmetric and antisymmetric Hamiltonian are calculated for the zeroth and first order average Hamiltonian $\bar{\mathcal{H}}_0$ and $\bar{\mathcal{H}}_1$. For the sake of simplicity we shall again use a discrete Hamiltonian whose results could, in principle, be transferred to a generic continuous one. We can state that the effective propagator U_{eff} for a symmetric piecewise time-independent Hamiltonian is given as:

$$U_{\text{eff}}(t_c, 0) = U_1' U_2 U_1$$

from which the zeroth and first order average Hamiltonian $\bar{\mathcal{H}}_0$ and $\bar{\mathcal{H}}_1$ can be calculated using Equa-

^[54] P. Mansfield. *Physics Letters A* **1970**, 32, 485–486.

^[55] C. H. Wang and J. D. Ramshaw. *Physical Review* **1972**, B6, 3253–3262.

tion (1.7.16) and (1.7.18) and we obtain:

$$\begin{aligned}\bar{\mathcal{H}}_0 &= \frac{1}{t_c} (\hat{\mathcal{H}}_1 \tau_1 + \hat{\mathcal{H}}_2 \tau_2 + \hat{\mathcal{H}}_{1'} \tau_{1'}) \\ \bar{\mathcal{H}}_1 &= \frac{(-i)}{2t_c} \left[\underbrace{[\hat{\mathcal{H}}_{1'}, \hat{\mathcal{H}}_2] \tau_{1'} \tau_2}_{= [\hat{\mathcal{H}}_1, \hat{\mathcal{H}}_2] \tau_1 \tau_2} + \underbrace{[\hat{\mathcal{H}}_{1'}, \hat{\mathcal{H}}_1] \tau_{1'} \tau_1}_{= 0} + \underbrace{[\hat{\mathcal{H}}_2, \hat{\mathcal{H}}_1] \tau_2 \tau_1}_{= -[\hat{\mathcal{H}}_1, \hat{\mathcal{H}}_2] \tau_1 \tau_2} \right] = 0\end{aligned}\quad (1.7.23)$$

where $\hat{\mathcal{H}}_{1'} = \hat{\mathcal{H}}_1$ and the identity $[A, B] = -[B, A]$ is used. From Equation (1.7.23) it is obvious that for any commutator $[\hat{\mathcal{H}}(t_c - \tau_1), \hat{\mathcal{H}}(t_c - \tau_2)]$ with $\tau_1 < \tau_2$ there is another commutator $[\hat{\mathcal{H}}(\tau_2), \hat{\mathcal{H}}(\tau_1)]$ and if a symmetric Hamiltonian is considered it follows that $\hat{\mathcal{H}}(t_c - \tau_1) = \hat{\mathcal{H}}(\tau_1)$ and $\hat{\mathcal{H}}(t_c - \tau_2) = \hat{\mathcal{H}}(\tau_2)$. As an effect for any commutator there is another where the arguments swapped their places and, due to anticommutativity, they cancel and $\bar{\mathcal{H}}_1$ will vanish for any symmetric Hamiltonian. Following the same argumentation this can be extended to higher orders where for any commutator C_{AZ} in the Magnus series with time-ordered arguments from A to Z there is another commutator $C_{Z'A'}$ with time-ordered arguments from Z' to A' :

$$C_{AZ} = [A, [B, \dots [L, [[M, N], O], \dots], Y], Z] \quad (1.7.24)$$

$$C_{Z'A'} = [Z', [Y', \dots [[O', [N', M']], L'], \dots], B'], A'] \quad (1.7.25)$$

For a symmetric Hamiltonian we can state that $(A, B \dots Y, Z) = (A', B' \dots, Y' Z')$ and the commutator $C_{Z'A'}$ shall be modified in a way that a commutator $C_{A'Z'}$ with reversed arguments is obtained. Using again the identity $[A, B] = -[B, A]$ on all nested commutators in $C_{Z'A'}$ will result in $C_{A'Z'}$ whose sign, however, will depend on the number of nested commutators. It turns out, that the odd orders $\bar{\mathcal{H}}_{\text{odd}}$ of the average Hamiltonian contain an odd number of nested commutators while the number for nested commutators in $\bar{\mathcal{H}}_{\text{even}}$ are even and, therefore, we obtain:

$$C_{Z'A'} = \begin{cases} -C_{A'Z'} & \text{for odd orders,} \\ +C_{A'Z'} & \text{for even orders.} \end{cases} \quad (1.7.26)$$

Hence, all odd orders $\bar{\mathcal{H}}_{\text{odd}}$ will vanish since C_{AZ} is canceled by $-C_{A'Z'}$ for a symmetric Hamiltonian.

The prove that an antisymmetric Hamiltonian has no effect can easily be shown when a piecewise time-independent Hamiltonian is assumed where $\hat{\mathcal{H}}_n = -\hat{\mathcal{H}}_{n'}$ and, hence, $U_{n'} = U_n^\dagger$. It can be followed that:

$$\begin{aligned}U_{\text{eff}}(t_c, 0) &= \lim_{n \rightarrow \infty} U_1 U_2 \dots U_{n'} U_n \dots U_2 U_1 \\ &= \lim_{n \rightarrow \infty} U_1^\dagger U_2^\dagger \dots U_n^\dagger U_n \dots U_2 U_1 \\ &= \mathbb{1}\end{aligned}$$

where the effective propagator is given by the unity matrix which is a neutral element.

Convergence

As we have seen in Equation (1.7.19), (1.7.20) and (1.7.21) the n th order of the Magnus series is proportional to $(\|\hat{\mathcal{H}}\|t)^{n+1}$ whose origin lays in the power series (Equation 1.7.4) and it is shown by Maricq^[56] that a sufficient (but not necessary) condition for convergence of the Magnus series is:

$$\int_0^{t_c} \|\hat{\mathcal{H}}\| dt < 2\pi. \quad (1.7.27)$$

However, for practical reasons, it is sometimes more relevant to know up to which value one can neglect all orders higher than $\bar{\mathcal{H}}_0$. This is e.g. the case for the previously mentioned perfect echo in the toggling frame (Section 1.6.3) where to good approximation a planar mixing Hamiltonian is obtained in $\bar{\mathcal{H}}_0$. If applied to a k -spin system with $k > 2$ the Hamiltonian will no longer commute at all times and higher orders $\bar{\mathcal{H}}_n$ with $n > 0$ are no longer zero – they define the *deviation* from the desired behavior. Since the time-dependence of the homogeneous Hamiltonian of the k -spin system stems from the toggling frame transformation we can modify it in a way that the approximation to $\bar{\mathcal{H}}_0$ is sufficient – shortening the delay will achieve that $\|\hat{\mathcal{H}}\|\tau \ll 2\pi$ where τ is the cycle length. The limits for τ can be pushed to longer times if we make use of the symmetry properties discussed above. If we arrange the perfect echo in a super cycle in a way that the homogeneous Hamiltonian will turn out to be symmetric all odd orders will vanish and the deviation to $\bar{\mathcal{H}}_0$ is decreased.

In the following we shall see an illustrative example where the generalized *Suzuki-Trotter formula*^[57] is used to describe the approximated effect of a zeroth order average Hamiltonian $\bar{\mathcal{H}}_0$. With this regard, the process of the Magnus series is basically inverted – we do not approximate a homogeneous Hamiltonian by an average Hamiltonian. Instead from a *zeroth order* average Hamiltonian $\bar{\mathcal{H}}_0$ we approximate a homogeneous Hamiltonian. Assuming a piecewise time-independent propagation for a large number of n the *first approximant* of the exponential given by the Suzuki-Trotter formula can be written as:

$$e^{(A+B)} = \lim_{n \rightarrow \infty} (e^{A/n} e^{B/n})^n = \lim_{n \rightarrow \infty} (U_{A/n} U_{B/n})^n. \quad (1.7.28)$$

which is sometimes referred to as the *Lie product formula*. However, for the reason of consistency the notation by Suzuki shall be used. Clearly, Equation (1.7.28) is based on a simplified Magnus series where only $\bar{\mathcal{H}}_0$ is considered if we define $(A+B) = -i\bar{\mathcal{H}}_0 t$. The *second approximant* of the exponential given by Suzuki reads:

$$e^{(A+B)} = \lim_{n \rightarrow \infty} (e^{A/2n} e^{B/n} e^{A/2n})^n = \lim_{n \rightarrow \infty} (U_{A/2n} U_{B/n} U_{A/2n})^n. \quad (1.7.29)$$

It is crucial to note that independent of the number of cycles n the Suzuki-Trotter approximation of second order will always be symmetric in time and, hence, all odd orders $\bar{\mathcal{H}}_{\text{odd}}$ in the average Hamiltonian created from the right side in Equation (1.7.29) are zero.

As an example consider an off-resonant pulse in the rotating frame which is approximated by consecutive and alternate rotations around x and z. We can state using Equation (1.7.28) and (1.7.29):

$$\text{First approximant:} \quad \exp \left\{ \frac{-i\theta}{\sqrt{2}} (\hat{I}_x + \hat{I}_z) \right\} \approx (U_{x/n} U_{z/n})^n \approx (U_{z/n} U_{x/n})^n \quad (1.7.30)$$

$$\text{Second approximant:} \quad \exp \left\{ \frac{-i\theta}{\sqrt{2}} (\hat{I}_x + \hat{I}_z) \right\} \approx (U_{x/2n} U_{z/n} U_{x/2n})^n \approx (U_{z/2n} U_{x/n} U_{z/2n})^n \quad (1.7.31)$$

where θ is the rotation angle for the normalized Hamiltonian $\frac{1}{\sqrt{2}}(\hat{I}_x + \hat{I}_z)$ and $U_{x/n}$ and $U_{z/n}$ induce a rotation with an angle of $\frac{\theta}{n\sqrt{2}}$ around x and z, respectively.

^[56] M. M. Maricq. *The Journal of Chemical Physics* **1987**, 86, 5647–5651.

^[57] M. Suzuki. *Communications in Mathematical Physics* **1976**, 51, 183–190.

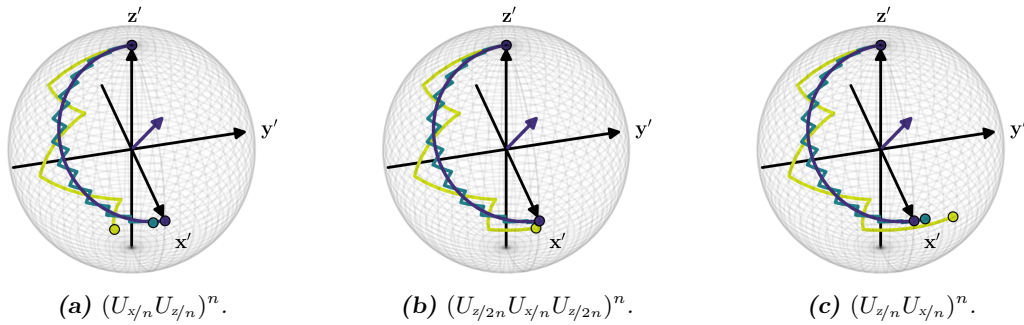


Figure 1.12: Trajectory for an off-resonant pulse in the rotating frame using the Suzuki-Trotter approximation and $\theta = \pi$. In (a) and (c) the first approximatant is simulated, in (b) the second. Green and blue correspond to $n = 3$ and $n = 12$, respectively and purple is the exact rotation.

Experimentally this could be achieved using a DANTE sequence^[58] which consists of a low flip angle pulse train where pulses are equally spaced at constant intervals. In Figure 1.12 the state operator \hat{I}_z is propagated by the approximations given in Equation (1.7.30) and (1.7.31) and the state's evolution is plotted as a trajectory in green ($n = 3$) and blue ($n = 12$). In purple the exact Hamiltonian is plotted and the purple arrow indicates its eigenvector. As expected, the best result is achieved by the second approximatant and, surprisingly, already for very low cycle numbers n a good approximation is obtained which is shown in Figure 1.12 (b).

While Figure 1.12 illustrates an intuitive picture of the quality obtained by the Suzuki-Trotter approximations in Figure 1.13 the variables n and θ are varied systematically and the effective propagator of the exact Hamiltonian is compared to the approximation using the scalar product $\langle U_{\text{exact}} | U_{\text{approx}} \rangle$. It is evident from Figure 1.13 (a) where $\theta = \pi$ that the exact propagator U_{exact} is better approximated for larger numbers of n . For a first order approximation using Equation (1.7.30) the graph is plotted in red and a value of 0.995 is exceeded for $n = 8$. The second order approximation using Equation (1.7.31), on the other hand, is plotted in blue and already for $n = 2$ the value of 0.995 is overstepped. The dependence on θ is shown in Figure 1.13 (b) for $n = 4$ and, clearly, the second approximatant in blue is preferable. It is, however, remarkable that the quality of both approximatants are equally good if full rotations are considered and θ is set to a multiple of 2π as illustrated in Figure 1.13 (c).

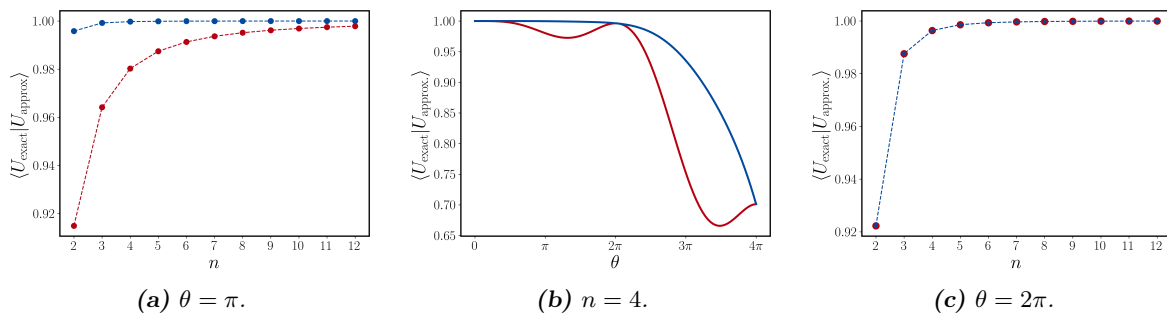


Figure 1.13: The dependency of the Suzuki-Trotter approximatants on n and θ are shown where the first (Equation 1.7.30) and second order (Equation 1.7.31) are plotted in red and blue, respectively. The scalar product $\langle U_{\text{exact}} | U_{\text{approx}} \rangle$ is plotted against n with $\theta = \pi$ in (a) and $\theta = 2\pi$ in (c), and against θ with $n = 4$ in (b).

[58] G. Bodenhausen, R. Freeman and G. A. Morris. *Journal of Magnetic Resonance* **1976**, 23, 171–175.

In order to estimate a rough limit for which an acceptable approximation to $\bar{\mathcal{H}}_0$ can be obtained we consider an evolution over one of n cycles in Equation (1.7.30) and (1.7.31). Using Equation (1.7.27) and the rotation angles of $U_{x/n}$ and $U_{z/n}$ (given by $\frac{\theta}{\sqrt{2n}}$) one can estimate that small rotations and short cycle times are preferable:

$$\sum \|\hat{\mathcal{H}}_{\text{cycle}}\| \tau = \|\hat{\mathcal{H}}_{x/n}\| \frac{\tau}{2} + \|\hat{\mathcal{H}}_{z/n}\| \frac{\tau}{2} = \sqrt{2} \frac{\theta}{n} \ll 2\pi. \quad (1.7.32)$$

The duration of a cycle is given by $\tau = t_c/n$ and a factor of 2 is considered based on the fact that each $U_{x/n}$ and $U_{z/n}$ are applied once per cycle. It is important to note that despite the fact that Equation (1.7.32) is based on Equation (1.7.27) there are two important aspects that need to be considered. First, Equation (1.7.27) describes a sufficient condition and under certain circumstances also for values larger 2π convergence of the Magnus series is obtained. Such a situation is met e.g. for periodic Hamiltonians – if one cycle converges so do all others. For this reason in Equation (1.7.32) only a single cycle is considered. Second, it is only the zeroth order of the Magnus series $\bar{\mathcal{H}}_0$ that shall be approximated and it is, therefore, of no relevance if convergence is obtained from higher orders ($\bar{\mathcal{H}}_1 + \dots$). With this regard, the condition in Equation (1.7.32) has to be modified in a way that the inequality is to some extent increased (\ll). For practical reasons it is commonly more interesting to know a reasonable value for n and, hence, the cycle time $\tau = t_c/n$. In the Appendix 5.1.7 simulations comparable to Figure 1.13 (a) are shown for larger values of θ and convergence is consequently obtained only for larger numbers of n . Examples where the present discussion is of major relevance can be found in Section 2.4, 2.2 and 2.3.

1.7.4 Numerical Calculation of the Average Hamiltonian

The numerical calculation of the average Hamiltonian in the present section shall be explained using a piecewise time-dependent Hamiltonian in the toggling frame $\hat{\mathcal{H}}_T(\tau)$ which is obtained from numerical simulations described in Section 1.6.2. In principle, one wants to describe the effective rotation of the time-dependent Hamiltonian $\hat{\mathcal{H}}_T(\tau)$ by an average Hamiltonian $\bar{\mathcal{H}}$ as described in Section 1.7.3:

$$\bar{\mathcal{H}} = \bar{\mathcal{H}}_0 + \bar{\mathcal{H}}_1 + \dots \quad (1.7.33)$$

where $\bar{\mathcal{H}}_0$ and $\bar{\mathcal{H}}_1$ are the zeroth and first order of the Magnus series, respectively. For numerical simulations it turns out that it is very useful to decompose the Hamiltonian $\hat{\mathcal{H}}_T(\tau)$ into its operator basis $|\hat{B}_\gamma\rangle$ and perform the calculations with real coefficients instead of large matrices. Hence, following Equation (1.6.14) the Hamiltonian in the toggling frame $\hat{\mathcal{H}}_T(\tau)$ can be expressed as:

$$\hat{\mathcal{H}}_T(\tau) = \omega_{\mathcal{H}} \cdot \sum_{\gamma} k^{\gamma}(\tau) \cdot |\hat{B}_{\gamma}\rangle \quad (1.7.34)$$

$$\text{with: } k^{\gamma}(\tau) = \frac{1}{\omega_{\mathcal{H}}} \cdot \text{Tr} \left\{ \hat{B}_{\gamma}^{\dagger} \hat{\mathcal{H}}_T(\tau) \right\}.$$

where $\omega_{\mathcal{H}}$ is the frequency given by the Hamiltonian. Hence, the time-dependence of $\hat{\mathcal{H}}_T(\tau)$ is determined by its coefficients $k^{\gamma}(\tau)$ and the discrete calculation of the zeroth order average Hamiltonian $\bar{\mathcal{H}}_0$ can be deduced from Equation (1.7.19) and (1.7.34). Expressed by its basis operators $\bar{\mathcal{H}}_0$ can be written as:

$$\bar{\mathcal{H}}_0 = \omega_{\mathcal{H}} \cdot \sum_{\gamma} \bar{k}_0^{\gamma} \cdot |\hat{B}_{\gamma}\rangle \quad (1.7.35)$$

$$\text{with: } \bar{k}_0^{\gamma} = \frac{1}{t_c} \sum_i k^{\gamma}(\tau_i) \cdot \tau_i$$

where \bar{k}_0^{γ} can be considered the *zeroth order average coefficient* for the respective basis operator \hat{B}_{γ} and $t_c = \sum \tau_i$. Keeping in mind the discussion about convergence of the Magnus series (Section 1.7.3) one can state that the zeroth order average Hamiltonian $\bar{\mathcal{H}}_0$ in many cases leads to surprisingly good approximations. Still, one could also include higher order terms of the Magnus series which, however, for numerical simulations might get costly in terms of computing time.

First Order Average Hamiltonian

For the numerical calculation of the first order average Hamiltonian $\bar{\mathcal{H}}_1$ one could, in principle, create the time-dependent Hamiltonian of (1.7.34) and brute force calculate its commutator with itself as illustrated in Figure 1.11 (a). However, this would require an immense number of matrix multiplications and in most cases it is advisable to apply a semi-automated algorithm where in the first step only commutators are chosen for calculation that are non-zero. As the toggling frame is reasonably used to elucidate the evolution of coupling during a pulse sequence it is clear that the Hamiltonian in the toggling frame consists of only bilinear terms and, *for a two spin system*, all commutators with itself result in linear terms (see Table 1.1). Hence, it should be noted that the first order average Hamiltonian $\bar{\mathcal{H}}_1$ in such a case will only lead to a shift in phase around respective linear axes. The numerical calculation of $\bar{\mathcal{H}}_1$ can be deduced from Equation (1.7.20):

$$\bar{\mathcal{H}}_1 = \frac{(-i)}{2t_c} \sum_{i>j} \tau_i \cdot \tau_j \cdot [\hat{\mathcal{H}}_T(\tau_i), \hat{\mathcal{H}}_T(\tau_j)]. \quad (1.7.36)$$

As shown in Equation (1.7.34) the Hamiltonian $\hat{\mathcal{H}}_T(\tau)$ is expressed in its basis operators \hat{B}_γ . For two arbitrary basis operators, denoted \hat{B}_δ and \hat{B}_ϵ , the Hamiltonian's commutator with itself is given as:

$$[\omega_{\mathcal{H}} k^\delta(\tau) \hat{B}_\delta, \omega_{\mathcal{H}} k^\epsilon(\tau) \hat{B}_\epsilon] = \varepsilon_{\delta\epsilon\kappa} \cdot i\omega_{\mathcal{H}}^2 k^\delta(\tau) k^\epsilon(\tau) \hat{B}_\kappa \quad (1.7.37)$$

where ε is the *Levi-Civita symbol* which depends on the permutation of $(\delta, \epsilon, \kappa)$ and it is assumed that $\varepsilon_{\delta\epsilon\kappa} = +1$ and $\varepsilon_{\epsilon\delta\kappa} = -1$. The operators \hat{B}_δ and \hat{B}_ϵ in $\hat{\mathcal{H}}_T(\tau)$ will, hence, lead to a contribution to $\bar{\mathcal{H}}_1$ that is given by the operator \hat{B}_κ . By inserting (1.7.37) in (1.7.36) one obtains:

$$\bar{\mathcal{H}}_1 = \frac{\omega_{\mathcal{H}}^2}{2t_c} \sum_{\kappa} \sum_{i>j} \varepsilon_{\delta\epsilon\kappa} \cdot \tau_i \cdot \tau_j \cdot k^\delta(\tau_i) k^\epsilon(\tau_j) \cdot \hat{B}_\kappa \quad (1.7.38)$$

where the sum over κ accounts for all operators \hat{B}_κ that contribute to $\bar{\mathcal{H}}_1$ and the somewhat lengthy expression of (1.7.38) can be rewritten as:

$$\begin{aligned} \bar{\mathcal{H}}_1 &= \omega_{\mathcal{H}}^2 \cdot \sum_{\kappa} \bar{k}_1^\kappa \cdot |\hat{B}_\kappa\rangle \\ \text{with: } \bar{k}_1^\kappa &= \frac{1}{2t_c} \sum_{i>j} \varepsilon_{\delta\epsilon\kappa} \cdot k^\delta(\tau_i) \tau_i \cdot k^\epsilon(\tau_j) \tau_j. \end{aligned} \quad (1.7.39)$$

In order to calculate \bar{k}_1^κ efficiently one can define two vectors, \mathbf{v}_δ and \mathbf{v}_ϵ , in which the trajectory of \hat{B}_δ and \hat{B}_ϵ is stored, respectively:

$$\begin{aligned} \mathbf{v}_\delta &= [v_{1\delta} \ \dots \ v_{i\delta}] = [k^\delta(\tau_1)\tau_1 \ \dots \ k^\delta(\tau_i)\tau_i] \\ \mathbf{v}_\epsilon &= [v_{1\epsilon} \ \dots \ v_{i\epsilon}] = [k^\epsilon(\tau_1)\tau_1 \ \dots \ k^\epsilon(\tau_i)\tau_i]. \end{aligned} \quad (1.7.40)$$

From the dyadic product (discussed in Section 1.3.2) one obtains a square matrix \mathcal{M} in which all required elements for the calculation of \bar{k}_1^κ are present:

$$\mathcal{M}_{\delta\epsilon} = \mathbf{v}_\delta^T \mathbf{v}_\epsilon = \begin{bmatrix} v_{1\delta}v_{1\epsilon} & \dots & v_{1\delta}v_{j\epsilon} \\ \vdots & \ddots & \vdots \\ v_{i\delta}v_{1\epsilon} & \dots & v_{i\delta}v_{j\epsilon} \end{bmatrix}. \quad (1.7.41)$$

For the elements below the diagonal it is true that $i>j$ which is required to contribute to $\bar{\mathcal{H}}_1$. These values are connected to the commutator $[\hat{B}_\delta, \hat{B}_\epsilon] = \varepsilon_{\delta\epsilon\kappa} \cdot \hat{B}_\kappa$ with $\varepsilon_{\delta\epsilon\kappa} = +1$. The elements above the

diagonal, on the other hand, are connected to the commutator $[\hat{B}_\epsilon, \hat{B}_\delta] = \varepsilon_{\epsilon\delta\kappa} \cdot \hat{B}_\kappa$ with $\varepsilon_{\epsilon\delta\kappa} = -1$ and also contribute to $\bar{\mathcal{H}}_1$ if $j > i$. Hence, the first order average Hamiltonian $\bar{\mathcal{H}}_1$ and its coefficients \bar{k}_1^κ can be calculated numerically from:

$$\bar{\mathcal{H}}_1 = \omega_{\mathcal{H}}^2 \cdot \sum_{\kappa} \bar{k}_1^\kappa \cdot |\hat{B}_\kappa\rangle \quad (1.7.42)$$

with: $\bar{k}_1^\kappa = \frac{1}{2t_c} \left(\varepsilon_{\delta\epsilon\kappa} \sum \text{Trilow}\{\mathcal{M}_{\delta\epsilon}\} + \varepsilon_{\epsilon\delta\kappa} \sum \text{Triup}\{\mathcal{M}_{\delta\epsilon}\} \right)$

where $\text{Trilow}\{\}$ and $\text{Triup}\{\}$ are functions that select the lower and upper triangle of the matrix $\mathcal{M}_{\delta\epsilon}$ corresponding to the values below and above the diagonal, respectively.

1.8 Relaxation

Relaxation is a process that describes the return of a coherence or population, created during an experiment, to its equilibrium state. This process is caused by fluctuating fields that stem from anisotropic interactions in combination with molecular motion. Commonly, one distinguishes between longitudinal and transverse relaxation times, T_1 and T_2 , respectively, which were first introduced in combination with the so-called *Bloch equations*^[14] and further discussed by Bloembergen, Purcell and Pound.^[59] For an ensemble of isolated spins- $\frac{1}{2}$ the effect of relaxation is given by:

$$\frac{d\hat{\rho}_z}{dt} = -R_1 \cdot [\hat{\rho}_z(t) - \hat{\rho}_0] \quad \text{and:} \quad \frac{d\hat{\rho}_{xy}}{dt} = -R_2 \cdot \hat{\rho}_{xy}(t) \quad (1.8.1)$$

where $\hat{\rho}_0$ is the equilibrium state operator (discussed in Section 1.8.1) and R_1 and R_2 are the relaxation rates given by the inverse of T_1 and T_2 , respectively. Solving the differential equations in (1.8.1) reveals that single quantum coherences ($\hat{\rho}_{xy}$) decay exponentially while populations ($\hat{\rho}_z$) exponentially converge towards the equilibrium state $\hat{\rho}_0$. An exponential decay of the time domain signal given by R_2 leads to a Lorentzian peak in the spectrum and its full width at half maximum is given by $\frac{1}{\pi T_2}$ which is commonly referred to as the natural linewidth.

1.8.1 Thermal Equilibrium State

The equilibrium state operator $\hat{\rho}_0$ is determined by the underlying Hamiltonian $\hat{\mathcal{H}}$ with respect to the system's thermal energy ($k_B T$). From statistical thermodynamics one can derive the population of the eigenstates to be given by:

$$\hat{\rho}_0 = \frac{1}{Z} \exp \left\{ -\frac{\hbar \hat{\mathcal{H}}}{k_B T} \right\} \quad (1.8.2)$$

$$\text{with:} \quad Z = \text{Tr} \left\{ \exp \left\{ -\frac{\hbar \hat{\mathcal{H}}}{k_B T} \right\} \right\} \quad (1.8.3)$$

which corresponds to a Boltzmann distribution in the Hamiltonian's eigenbasis.^[17] Expressing the equilibrium state operator by the first two orders of a power series reveals that the equilibrium state operator $\hat{\rho}_0$ is approximately proportional to the Hamiltonian²⁷ while the unity matrix $\mathbb{1}$ is commonly omitted.²⁸

1.8.2 Random Field Relaxation

In order to describe the effect of a fluctuating magnetic field on a spin system, a random external field $B_r(t)$ is assumed which depends on the molecule's size – its origin at firsthand is of no relevance. Furthermore, it is *assumed* to be independent of the considered spin's state and its magnitude is isotropically distributed on the spatial coordinates x, y and z. Such a simplification does only allow a qualitative treatment, still, it can be used to illustrate common relaxation mechanisms. The field's fluctuation is supposed to be fast for small and slow for large molecules which resembles their molecular motion. A correlation time τ_c is obtained from the auto-correlation function $G(\tau)$ which contains a measure of how fast the fluctuating field changes on average within a time step τ .²⁹ Assuming a spherical molecule the

^[59] N. Bloembergen, E. M. Purcell and R. V. Pound. *Physical Review* **1948**, 73, 679–712.

²⁷ The second term of the power series is actually given as $(-\hbar \hat{\mathcal{H}}/Z k_B T)$, nonetheless, since scaling is arbitrary the prefactors are normally omitted and the equilibrium state operator is approximated by: $\hat{\rho}_0 \approx \hat{\mathcal{H}}$.

²⁸ The unity matrix corresponds to the isotropically distributed spins with no effective magnetization which are, therefore, not directly observed by NMR. Still, this does not mean these spins are absent – relaxation will make use of this reservoir to create populations and coupling evolution can induce a coherent motion originating from the coupled spins in $\mathbb{1}$.

²⁹ The correlation function is actually calculated from the spatial second rank tensors $A_2^m(t)$ whose time-dependence is determined by molecular motion (discussed in Section 1.3.2). The tensor originates from an anisotropic interaction and its auto-correlation function is given as: $G_m(\tau) = \overline{A_2^m(t) A_2^{m*}(t + \tau)}$ where $A_2^{m*} = A_2^{-m}$. For a spherical molecule it is assumed that $G_m(\tau) = |A_2^m(0)|^2 \exp\{-\frac{1}{\tau_c} |\tau|\}$.

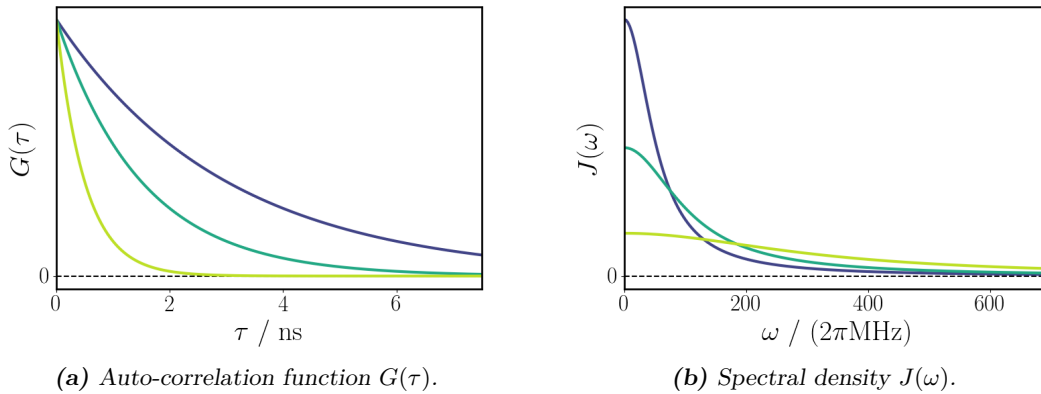


Figure 1.14: The auto-correlation function $G(\tau)$ and spectral density $J(\omega)$ are plotted for correlation times τ_c of 0.5 ns (green), 1.5 ns (blue) and 3 ns (Violet).

auto-correlation function $G(\tau)$ adopts the form of a simple exponential decay and its Fourier transform will lead to a spectral distribution that is called the *spectral density*. The auto-correlation $G(\tau)$ and its Fourier transform $J(\omega)$ are given as:

$$G(\tau) = \overline{B_r(t)^2} \exp\left\{-\frac{1}{\tau_c}|\tau|\right\} \quad \text{and:} \quad J(\omega) = \overline{2B_r(t)^2} \cdot \frac{\tau_c}{1 + \omega^2\tau_c^2} \quad (1.8.4)$$

where $\overline{B_r(t)^2}$ is the squared mean value of the random field and in $J(\omega)$ the factor of 2 stems from the Fourier transform.³⁰ Both functions are plotted in Figure 1.14 for a correlation time of 0.5 ns (green), 1.5 ns (blue) and 3 ns (violet).

For an ensemble of isolated spins- $\frac{1}{2}$ there are only two transitions between the Hamiltonian's two eigenstates which are induced at the Larmor frequency ω_0 and the longitudinal and transverse relaxation rates are given as:

$$R_1 = \gamma^2 \overline{B_r(t)^2} J(\omega_0) \quad (1.8.5)$$

$$R_2 = \underbrace{\gamma^2 \overline{B_r(t)^2} J(0)}_{\text{secular}} + \underbrace{\frac{1}{2} R_1}_{\text{non-secular}} \quad (1.8.6)$$

where the secular contribution in Equation (1.8.6) is determined by the spectral density $J(0)$ which does not correspond to a transition probability but rather a field distribution that leads to *homogeneous broadening*. The factor of $\frac{1}{2}$ for the non-secular term is usually ascribed to the fact that a random field along one axis commutes with a state aligned to the same axis.^[16]

1.8.3 Dipolar Relaxation in a Two Spin System

For an ensemble of coupled spin- $\frac{1}{2}$ the dipolar coupling (Section 1.3.7) is commonly the largest anisotropic interaction and, therefore, provides the largest contribution to the system's relaxation mechanisms. Assuming a dipolar (weakly) coupled two spin system, \hat{I} and \hat{S} , there are four Zeeman eigenstates ($|\alpha\alpha\rangle$, $|\alpha\beta\rangle$, $|\beta\alpha\rangle$, $|\beta\beta\rangle$) from which one can derive 12 transitions.³¹ These transitions can be induced at the respective frequencies and the rate constants for zero-quantum (W_0), single-quantum (W_1) and double

³⁰ Usually, a *normalized* spectral density is defined which is independent of the field's magnitude $\overline{B_r(t)^2}$. In literature the definition for $J(\omega)$ is not always consistent and the factor of 2 from the Fourier series is sometimes excluded. In the following, we shall include the factor of 2. The integral over the normalized spectral density is independent of the correlation time τ_c and with a factor of 2 given as: $\int_0^\infty d\omega \frac{2}{1+\omega^2} = \pi$.

³¹ These involve two zero and two double quantum transitions while for each spin four single quantum transitions exist.

quantum transitions (W_2) are given as:^[16,59–61]

$$W_0 = \frac{1}{20} b^2 \cdot J(|\omega_0^I - \omega_0^S|) \quad (1.8.7)$$

$$W_1^{I/S} = \frac{3}{40} b^2 \cdot J(\omega_0^{I/S}) \quad (1.8.8)$$

$$W_2 = \frac{3}{10} b^2 \cdot J(\omega_0^I + \omega_0^S) \quad (1.8.9)$$

where b summarizes multiple prefactors of the dipolar coupling and is given in Equation (1.3.29). While transverse relaxation in all cases leads to a simple exponential decay, it is examined by Solomon^[60] that this situation is not always met for longitudinal relaxation. This is described by the so-called *Solomon equations*:

$$\frac{d\hat{\rho}_z^{I/S}}{dt} = -R_{\text{auto}}^{I/S} \cdot [\hat{\rho}_z^{I/S}(t) - \hat{\rho}_0^{I/S}] - \sigma_{IS} \cdot [\hat{\rho}_z^{S/I}(t) - \hat{\rho}_0^{S/I}] \quad (1.8.10)$$

$$\frac{d\hat{\rho}_{xy}^{I/S}}{dt} = -R_2^{I/S} \cdot \hat{\rho}_{xy}^{I/S}(t) \quad (1.8.11)$$

where the longitudinal relaxation is given by the auto- (R_{auto}) and cross-relaxation rate (σ_{IS}) which depends on the state of the considered spin and its coupling partner, respectively. Considering the transitions that are involved in the process of relaxation the rates in Equation (1.8.10) and (1.8.11) can be expressed as³²:

$$R_{\text{auto}}^{I/S} = W_2 + W_0 + 2 \cdot W_1^{I/S} \quad (1.8.12)$$

$$\sigma_{IS} = W_2 - W_0. \quad (1.8.13)$$

From the auto- and cross-relaxation rates the longitudinal relaxation (R_1) can be derived for the entity of a *homonuclear* two-spin system. This is shown by Solomon^[60] as well as a derivation for the transverse relaxation rate (R_2) – these rates are given as:

$$R_1 = R_{\text{auto}} + \sigma_{IS} \quad (1.8.14)$$

$$= \frac{3}{20} b^2 \cdot [J(\omega_0) + 4 \cdot J(2\omega_0)] \quad (1.8.15)$$

$$R_2 = \frac{3}{40} b^2 \cdot [3 \cdot J(0) + 5 \cdot J(\omega_0) + 2 \cdot J(2\omega_0)]. \quad (1.8.16)$$

In Figure 1.15 (a) both relaxation times (transverse and longitudinal) are plotted as a function of the correlation time τ_c where a minimum of T_1 is found at approximately $\tau_c \approx \frac{1}{\omega_0}$.

The effect of cross-relaxation (σ_{IS}) is commonly called the *Nuclear Overhauser Effect* (NOE)^[62] which can be exploited by saturating the coupling partner^[63] or in 2D experiments^[64]. Considering a heteronuclear spin system, consisting of a proton (\hat{I}) and a carbon (\hat{S}), the NOE leads to an enhancement ϵ of the carbon magnetization if the proton is continuously saturated. Solving the Solomon equation by assuming a carbon steady-state one can derive the enhancement for carbon which is given by:

$$\epsilon_{\text{steady}} = \frac{\gamma_I}{\gamma_S} \frac{\sigma_{IS}}{R_{\text{auto}}^S}. \quad (1.8.17)$$

^[60] I. Solomon. *Physical Review* **1955**, *99*, 559–565.

^[61] A. Gupta et al. *Concepts in Magnetic Resonance Part A: Bridging Education and Research* **2015**, *44*, 74–113.

^[62] A. W. Overhauser. *Physical Review* **1953**, *92*, 411–415.

^[63] F. A. Anet and A. J. Bourn. *Journal of the American Chemical Society* **1965**, *87*, 5250–5251.

^[64] J. Jeener et al. *The Journal of Chemical Physics* **1979**, *71*, 4546–4553.

³² For the transverse relaxation rates one actually needs to consider the transitions between the eigenstates of the \hat{I}_x operator which are $|++\rangle$, $|+-\rangle$, $|-+\rangle$, $|--\rangle$.

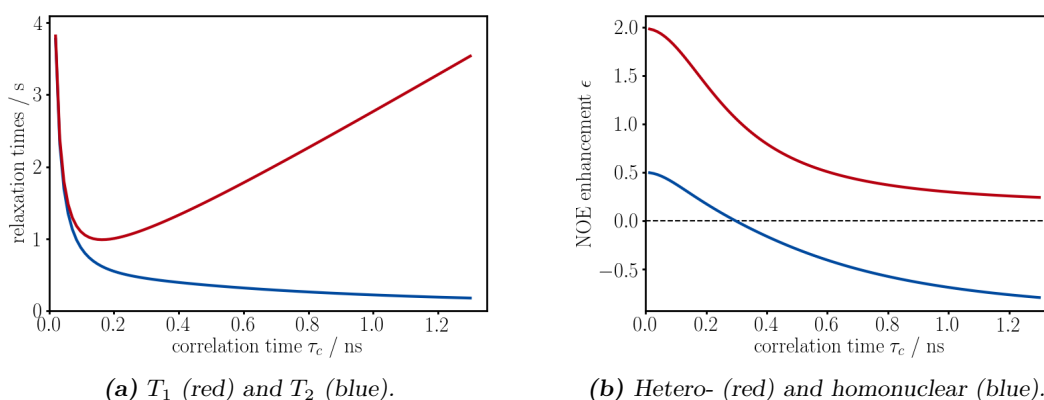


Figure 1.15: In (a) the dipolar relaxation rates T_1 (red) and T_2 (blue) are plotted against the correlation time τ_c at 14.07 Tesla for a spin system of two protons at a distance of $r = 2 \text{ \AA}$. In (b) the steady-state NOE enhancement ϵ at 14.07 Tesla is shown for a CH group (red) with $r = 1.08 \text{ \AA}$ and two protons (blue) with $r = 2 \text{ \AA}$.

The enhancement that one can achieve by the so-called *steady-state* NOE is plotted in Figure 1.15 (b) for two protons (blue) and a heteronuclear spin system (red) consisting of a proton and carbon spin.

1.8.4 Cross Correlated Relaxation

So far relaxation mechanisms were based on a single anisotropic interaction and in many cases it is assumed that other contributions simply add up. However, it was found by Pervushin et al.^[65] that if the time-dependence of two anisotropic tensors is correlated³³ their field might cancel and relaxation times are enhanced. Such a case is met in the amide nitrogen and proton spin pair where the time-dependent field, created from the anisotropic components of the dipolar coupling and the chemical shift, is increased or diminished according to the state of the coupled spin. Transition rates for transverse proton magnetization (denoted I) and the respective nitrogen spin state (α , β) are expressed in a rather condensed way:^[65]

$$\begin{aligned}
 W_1^{I,\alpha} &= W_{\text{dipolar}} + W_{\text{CSA}} - \frac{1}{60} \cdot b \cdot \delta_I \cdot [4 \cdot J(0) + 3 \cdot J(\omega_0^I)] \\
 W_1^{I,\beta} &= W_{\text{dipolar}} + W_{\text{CSA}} + \underbrace{\frac{1}{60} \cdot b \cdot \delta_I \cdot [4 \cdot J(0) + 3 \cdot J(\omega_0^I)]}_{\text{cross correlated}}
 \end{aligned}
 \tag{1.8.18}$$

where W_{dipolar} and W_{CSA} are the non-correlated terms and it is assumed that the principal symmetry axis of the chemical shielding tensor (Equation 1.3.14) is oriented parallel with the NH vector. The constant δ_I describes the chemical shielding anisotropy (CSA) and can be expressed as:

$$\delta_I = \gamma_I B_0 \Delta\sigma_I \quad \text{with:} \quad \Delta\sigma = \sigma_{\parallel} - \sigma_{\perp}
 \tag{1.8.19}$$

where σ_{\parallel} and σ_{\perp} are the axial and perpendicular principal components of the axially symmetric chemical shift tensor. The NH spin pair is an extraordinary example for cross correlated relaxation since the effect is given for both transverse magnetization of proton and nitrogen – a spectrum of a non-decoupled HSQC is shown in Figure 1.16. The pulse sequence of the so-called *transverse optimized spectroscopy* (TROSY) is designed in a subtle way that only the sharpest component of the four peaks is retained (upper right signal). Especially for large molecules (i.e. long correlation times τ_c) cross correlated relaxation can be strongly pronounced since the spectral density towards low frequencies increases drastically and, hence, so is the difference between the two cross correlated terms in Equation (1.8.18).

^[65] K. Pervushin et al. *Proceedings of the National Academy of Sciences* **1997**, *94*, 12366–12371.

³³ The time-dependence of intramolecular interactions is based on the same random motion considering a rigid molecule.

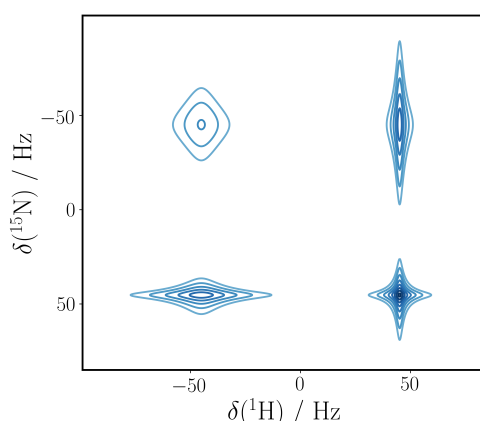


Figure 1.16: A non-decoupled ^{15}N -HSQC for an amide group exhibiting cross correlated relaxation is simulated in python using the super operator formalism^[66]. The relaxation matrix was calculated for a correlation time of $\tau_c = 4.4$ ns using spinach.^[67] The sharpest component of the multiplet is commonly referred to as TROSY-peak (lower right) while the broadest is called the anti-TROSY peak (upper left).

Chapter 2

Coherence Transfer Elements

2.1 Introduction

The existence of *coherence* implies that non-averaged *superposition states* evolve in a *correlated* way for all members of the spin ensemble (as discussed in Section 1.2.1). Such a correlated time evolution lays the basis for numerous applications and opened up the field of multi-dimensional NMR. The fact that coherence can be *transferred* via couplings was first exploited in an experiment proposed by Jeener in 1971^[68] and later realized by Ernst^[69,70] – a homonuclear experiment that is today known as COSY. While in the COSY experiment a single 90° pulse causes *mixing* between *directly* coupled spins, it is well known that *planar* or *isotropic mixing* can be obtained from a cascade of pulses which has led to various TOCSY experiments.^[5,71–77] The conception of coherence transfer was further extended to heteronuclear systems and the so-called INEPT^[78,79] and other heteronuclear two-dimensional experiments^[80–87] evolved of which the HSQC^[82], HMQC^[83,84] and HMBC^[87,88] became part of today's standard NMR-toolbox in numerous variations.

^[68] J. Jeener and G. Alewaeters. *Progress in Nuclear Magnetic Resonance Spectroscopy* **2016**, 94-95, 75–80.

^[69] R. R. Ernst. *Chimia* **1975**, 179.

^[70] W. P. Aue, E. Bartholdi and R. R. Ernst. *The Journal of Chemical Physics* **1976**, 64, 2229–2246.

^[71] S. R. Hartmann and E. L. Hahn. *Physical Review* **1962**, 128, 2042–2053.

^[72] R. D. Bertrand et al. *Journal of the American Chemical Society* **1978**, 100, 5227–5229.

^[73] M. Ernst et al. *Molecular Physics* **1991**, 74, 219–252.

^[74] T. Carlomagno, B. Luy and S. J. Glaser. *Journal of Magnetic Resonance* **1997**, 126, 110–119.

^[75] R. Konrat, I. Burghardt and G. Bodenhausen. *Journal of the American Chemical Society* **1991**, 113, 9135–9140.

^[76] A. Allerhand. *The Journal of Chemical Physics* **1966**, 44, 1.

^[77] D. G. Davis and A. Bax. *Journal of the American Chemical Society* **1985**, 107, 2820–2821.

^[78] G. A. Morris and R. Freeman. *Journal of the American Chemical Society* **1979**, 101, 760–762.

^[79] D. P. Burum and R. R. Ernst. *Journal of Magnetic Resonance* **1980**, 39, 163–168.

^[80] A. A. Maudsley and R. R. Ernst. *Chemical Physics Letters* **1977**, 50, 368–372.

^[81] A. A. Maudsley, L. Moller and R. R. Ernst. *Journal of Magnetic Resonance* **1977**, 28, 463–469.

^[82] G. Bodenhausen and D. J. Ruben. *Chemical Physics Letters* **1980**, 69, 185–189.

^[83] L. Müller. *Journal of the American Chemical Society* **1979**, 101, 4481–4484.

^[84] A. Bax, R. H. Griffey and B. L. Hawkins. *Journal of Magnetic Resonance* **1983**, 55, 301–315.

^[85] H. Kessler et al. *Journal of Magnetic Resonance* **1984**, 57, 331–336.

^[86] H. Kessler, W. Bermel and C. Griesinger. *Journal of the American Chemical Society* **1985**, 107, 1083–1084.

^[87] A. Bax and M. F. Summers. *Journal of the American Chemical Society* **1986**, 108, 2093–2094.

^[88] A. Bax and D. Marion. *Journal of Magnetic Resonance* **1988**, 78, 186–191.

In the present chapter a special focus is put on mixing sequences that are made of pulse-delay-elements and a coherent treatment in the toggling frame with average Hamiltonian theory shall be given (described in Section 1.6 and 1.7). In contrast to common “windowless” multi-pulse sequences³⁴, they exhibit a much greater variability – basically, the complete repertoire of common pulse shapes can be used within the sequences. In turn, the sequence adopts the pulses’ properties and planar or isotropic mixing is obtained at variable bandwidths (e.g. broadband or band-selective) or in systems that require a considerable compensation of B_1 -field inhomogeneity.

In this context, the recently proposed relayed CLIP COSY^[90,91] is further discussed and we shall see that a ^{13}C , ^{13}C -TOCSY at a so far unrivaled bandwidth of ~ 50 kHz is obtained on a 1.0 GHz spectrometer using effective *planar mixing* (Section 2.2).³⁵ The exemplarily application in a modified 3D (H)CC(CO)NH experiment^[93,94], which is typically used to investigate protein side-chains, shall demonstrate that planar mixing provides potential solutions to obtain broadband TOCSY even for highest available field strengths.

Furthermore, various pulse-delay sequences are proposed that all result in *isotropic mixing* (Section 2.3). Since the design of considered sequences is similar to the perfect echo (resulting in planar mixing), it is likewise possible to make use of sophisticated pulse shapes and corresponding properties (e.g. broadband pulses for the application to fluorine compounds^[92]). While isotropic mixing from proposed sequences is less efficient compared to conventional multi-pulse sequences,^[95–99] still, they are highly suitable for spin state preservation at considerably lower energy dissipation and high quality. It turns out that such properties are especially valuable for fast experiments where polarization can be preserved through-out the entire experiment and time-optimal sensitivity using Ernst angle excitation at high repetition rates is obtained.^[100] The use of *isotropic mixing* shall be illustrated in a newly designed fast experiment used for diffusion-ordered spectroscopy (DOSY). Additionally, J -modulation is suppressed by isotropic mixing leading to clean in-phase spectra and in analogy to related DOSY experiments^[101,102] likewise an exchange compensated fast DOSY is possible.

For both types of sequences, resulting either in planar or isotropic mixing, the use of pulse shapes has turned out to be a valuable feature and it is, hence, indispensable to hold a detailed analysis on the effect of *homo- and heteronuclear J-coupling* evolution during applied shaped pulses. Therefore, an extensive investigation shall be given in Section 2.4 using the toggling frame in combination with average Hamiltonian theory^[4,28,45,46] and a basic set of known pulse shapes is examined. While average Hamiltonian theory is well-established in literature, still, the interference of strong coupling with simultaneous pulsing might, at first sight, seem like a tedious task. However, it turns out that within the discussed limits of convergence (Section 1.7.3) the proposed algorithm (Section 2.4.2) can be rigidly applied – a time-dependence of the coupling Hamiltonian induced by the Zeeman interaction can be treated as any other. With few exceptions^[103,104], available pulse shapes are not optimized for coupled spins and arbitrary coupling behavior is regularly encountered. For this reason, a basic pulse shape optimization is

^[90] M. R. Koos et al. *Angewandte Chemie - International Edition* **2016**, *55*, 7655–7659.

^[91] T. Gyöngyösi et al. *ChemPlusChem* **2018**, *83*, 53–60.

^[93] S. Grzesiek, J. Anglister and A. Bax. *Journal of Magnetic Resonance* **1993**, *B101*, 114–119.

^[94] H. Kovacs and A. Gossert. *Journal of Biomolecular NMR* **2014**, *58*, 101–112.

^[95] A. Bax and D. G. Davis. *Journal of Magnetic Resonance* **1985**, *65*, 355–360.

^[96] A. J. Shaka, C. J. Lee and A. Pines. *Journal of Magnetic Resonance* **1988**, *77*, 274–293.

^[97] S. P. Rucker and A. J. Shaka. *Molecular Physics* **1989**, *68*, 509–517.

^[98] M. Kadkhodaie et al. *Journal of Magnetic Resonance* **1991**, *91*, 437–443.

^[99] I. C. Felli et al. *Journal of Biomolecular NMR* **2009**, *43*, 187–196.

^[100] R. R. Ernst and W. A. Anderson. *Review of Scientific Instruments* **1966**, *37*, 93–102.

^[101] A. M. Torres, G. Zheng and W. S. Price. *Magnetic Resonance in Chemistry* **2010**, *48*, 129–133.

^[102] J. A. Aguilar et al. *Journal of Magnetic Resonance* **2014**, *238*, 16–19.

^[103] S. Ehni and B. Luy. *Journal of Magnetic Resonance* **2013**, *232*, 7–17.

^[104] S. Ehni and B. Luy. *Journal of Magnetic Resonance* **2014**, *247*, 111–117.

³⁴ The here used expression “windowless” originates from the field of solid state NMR where in multi-pulse sequences pulse power is reduced at cost of inter-pulse delays in order to minimize the total dissipated energy from RF pulsing.^[89]

³⁵ With state-of-the-art shaped pulses^[92] and a standard RF amplitude of 10 kHz it would be possible to cover bandwidths of 60 kHz, which is more than sufficient for a ^{13}C , ^{13}C -TOCSY on today’s highest available field strengths of 1.2 GHz.

undertaken in order to provide a tailored shaped pulse, called isotropic mixing pulse (IMP), for proposed mixing sequences – in the toggling frame it can be shown that *homonuclear* couplings are able to evolve during nearly the full length of the considered shaped pulse.

In the same context, the strong coupling Hamiltonian of a homonuclear two spin system in the double rotating frame shall be analyzed in detail, revealing an interesting similarity to the well-known Berry-^[42] or Bloch-Siegert shift^[41] that originate from a time-dependent RF perturbation. A step-by-step examination of all apparent second order effects from strong coupling is done and a comparison to the basic calculation via the Hamiltonians eigenvalues and functions is given.

At the end of the present chapter, an HSQC-type experiment is introduced that is based on a modified INEPT-like coherence transfer step. It allows the creation of ordered quantum states that evolve according to only a single $^1J_{C,H}$ -coupling independent of the considered spin system (i.e. CH, CH₂ or CH₃) and can be used for the *sign-sensitive* measurement of $^1J_{C,H}$ - and $^2J_{H,H}$ -couplings. Further, a spin state selective back-transfer from carbon to acquired protons in combination with a subsequent TOCSY allows the straight-forward sign-sensitive extraction of heteronuclear $^nJ_{C,H}$ couplings in an E.COSY^[105–107] like manner.

^[105] C. Griesinger, O. W. Sørensen and R. R. Ernst. *Journal of the American Chemical Society* **1985**, *107*, 6394–6396.

^[106] C. Griesinger, O. W. Sørensen and R. R. Ernst. *The Journal of Chemical Physics* **1986**, *85*, 6837–6852.

^[107] C. Griesinger, O. W. Sørensen and R. R. Ernst. *Journal of Magnetic Resonance* **1987**, *75*, 474–492.

2.2 Planar Mixing from Perfect Echo

The large variety of NMR experiments is based on the fact that coherent spin states commonly exhibit a remarkable half life which allows to perform sophisticated spin dynamics and extract an extensive amount of information. Here, the Hahn echo^[108] constitutes one of the most fundamental building blocks which is applied in nearly any pulse sequence of solid and liquid state NMR. It allows to refocus various interactions as e.g. chemical shifts and heteronuclear couplings – however, homonuclear couplings are invariant under a non-selective inversion and cannot be refocused by the Hahn echo. For this reason, a certain fraction of undesired dispersive anti-phase often has to be tolerated in various experiments if larger homonuclear couplings are present. An elegant modification, on the other hand, was proposed by Takegoshi et al.^[6] where *homonuclear J-couplings* can be refocused within the so-called *perfect echo* (PE). It was first used as relaxation filter in the field of *in vivo* NMR^[109] and shortly after for coherence transfer in COSY^[110]- and TOCSY-type experiments^[111]. Ever since, the perfect echo building block progressively gained in popularity and has already been applied to suppress homonuclear couplings in DOSY experiments^[101,102], for solvent suppression^[112], pure shift NMR^[113,114], and for the measurement of heteronuclear couplings^[115] and transverse relaxation rates^[116]. A summarizing review on the perfect echo was published just recently.^[117] Still, so far only in few cases the perfect echo is used for what it is – a planar mixing sequences.^[90,91,110,111]

2.2.1 Planar Mixing

The remarkable property of the perfect echo (Figure 1.7) to allow homonuclear *J*-refocusing for weakly coupled spin systems is based on the fact that *planar mixing* (PM) is induced. Most adequately, and in coherence with remaining chapters, this can be explained from the combined use of a so-called toggling frame (Section 1.6) and average Hamiltonian theory (Section 1.7). As revealed in the toggling frame of the perfect echo³⁶ the weak coupling Hamiltonian ($\hat{\mathcal{H}}_{zz} = \sum_{k>j} 2\pi J_{k,j} \cdot \hat{I}_{kz} \hat{I}_{jz}$) is transformed to a time-dependent Hamiltonian $\hat{\mathcal{H}}_{T,zz}$ whose predominant components are:

$$\begin{aligned} \hat{\mathcal{H}}_{T,zz}^{xx'}(\tau) &= \hat{k}_{zz}^{xx'}(\tau) \cdot \sum_{k>j} 2\pi J_{k,j} \cdot \hat{I}_{kx} \hat{I}_{jx} \\ \text{and: } \hat{\mathcal{H}}_{T,zz}^{yy'}(\tau) &= \hat{k}_{zz}^{yy'}(\tau) \cdot \sum_{k>j} 2\pi J_{k,j} \cdot \hat{I}_{ky} \hat{I}_{jy} \end{aligned} \quad (2.2.1)$$

where $\hat{k}_{zz}^{xx'}(\tau)$ and $\hat{k}_{zz}^{yy'}(\tau)$ are the time-dependent coefficients and $J_{k,j}$ is the size of the coupling between spin \hat{I}_k and \hat{I}_j . For a two spin system, both components commute and, to good approximation, the effective Hamiltonian can be described by the zeroth order average Hamiltonian $\bar{\mathcal{H}}_{0,zz}^{\text{PE}}$ which corresponds to planar mixing $\hat{\mathcal{H}}^{\text{PM}}$ of half the effective *J*-coupling:

$$\begin{aligned} \bar{\mathcal{H}}_{0,zz}^{\text{PE}} &\approx \hat{\mathcal{H}}_{T,zz}^{xx'} + \hat{\mathcal{H}}_{T,zz}^{yy'} \\ &\approx \frac{1}{2} \hat{\mathcal{H}}^{\text{PM}} = \pi J_{1,2} \cdot (\hat{I}_{1x} \hat{I}_{2x} + \hat{I}_{1y} \hat{I}_{2y}). \end{aligned} \quad (2.2.2)$$

^[108] E. L. Hahn. *Physical Review* **1950**, *80*, 580–594.

^[109] P. C. M. VAN Zijl, C. T. W. Moonen and M. VON Kienlin. *Journal of Magnetic Resonance* **1990**, *89*, 28–40.

^[110] T. Schulte-Herbrüggen et al. *Molecular Physics* **1991**, *72*, 847–871.

^[111] Z. Mádi et al. *Chemical Physics Letters* **1997**, *268*, 300–305.

^[112] D. Sinnaeve. *Journal of Magnetic Resonance* **2014**, *245*, 24–30.

^[113] A. Verma, S. Bhattacharya and B. Baishya. *RSC Advances* **2018**, *8*, 19990–19999.

^[114] J. Ilgen, L. Kaltschnee and C. M. Thiele. *Magnetic Resonance in Chemistry* **2018**, *56*, 918–933.

^[115] L. Kaltschnee et al. *Chemical Communications* **2014**, *50*, 15702–15705.

^[116] J. A. Aguilar et al. *Chemical Communications* **2012**, *48*, 811–813.

^[117] T. Parella. *Magnetic Resonance in Chemistry* **2019**, *57*, 13–29.

³⁶ The transformation to the toggling frame of the perfect echo is elaborately discussed in Section 1.6.3 and 1.6.4.

For larger spin systems the two components in Equation (2.2.1) no longer commute and planar mixing is obtained *only* for intervals t_c that fulfill the inequality $\|\hat{\mathcal{H}}_{\Gamma,zz}\| \cdot t_c \ll 2\pi$. In general, a planar mixing Hamiltonian $\hat{\mathcal{H}}_{\alpha}^{\text{PM}}$ is of the form:

$$\hat{\mathcal{H}}_{\alpha}^{\text{PM}} = \sum_{k>j} 2\pi J_{k,j} \cdot (\hat{I}_{k\beta} \hat{I}_{j\beta} + \hat{I}_{k\gamma} \hat{I}_{j\gamma})$$

where $\{\alpha, \beta, \gamma\}$ corresponds to a permutation of $\{x, y, z\}$. At this point it shall be mentioned that for a coupled k -spin system where all spins are found in *equivalent* states ($\hat{I}_{k\alpha}$), planar mixing ($\hat{\mathcal{H}}_{\alpha}^{\text{PM}}$) is capable to effectively suppress the evolution of homonuclear J -couplings:

$$\sum_k \hat{I}_{k\alpha} \xrightarrow{\hat{\mathcal{H}}_{\text{PM},\alpha} t} \sum_k \hat{I}_{k\alpha} \quad (2.2.3)$$

where the subscript α denotes the axes $\{x, y, z\}$ that is *orthogonal* to both bilinear operators in $\hat{\mathcal{H}}_{\alpha}^{\text{PM}}$.³⁷ It is, therefore, crucial to note that even if the zeroth order average Hamiltonian $\bar{\mathcal{H}}_{0,zz}^{\text{PE}}$ of the perfect echo results in effective planar mixing, an apparent J -refocusing is obtained only for a *single* axes (α) and, additionally, *only* if coupled spins are in *equivalent* states. If, on the other hand, the symmetry is broken and spin states are different (e.g. in amplitude) an *observable* transfer between spins will occur. This can be easily seen if planar mixing is applied to only one out of two weakly coupled spins, \hat{I}_1 and \hat{I}_2 . Due to commutation of $\hat{\mathcal{H}}_{\Gamma,zz}^{xx'}$ and $\hat{\mathcal{H}}_{\Gamma,zz}^{yy'}$ in a two spin system the effect of planar mixing $\hat{\mathcal{H}}_{\alpha}^{\text{PM}}$ on the population \hat{I}_{1z} can be described by successive application of Equation (1.4.10). An in-phase to in-phase transfer ($\hat{I}_{1z} \rightarrow \hat{I}_{2z}$) is obtained:

$$\begin{aligned} \hat{I}_{1z} &\xrightarrow{\pi J(2\hat{I}_{1x}\hat{I}_{2x})t} \cos(\pi Jt) \hat{I}_{1z} - \sin(\pi Jt) 2\hat{I}_{1y}\hat{I}_{2x} \\ &\xrightarrow{\pi J(2\hat{I}_{1y}\hat{I}_{2y})t} \cos^2(\pi Jt) \hat{I}_{1z} - \cos(\pi Jt) \sin(\pi Jt) 2\hat{I}_{1y}\hat{I}_{2x} \\ &\quad + \sin(\pi Jt) \cos(\pi Jt) 2\hat{I}_{1x}\hat{I}_{2y} + \sin^2(\pi Jt) \hat{I}_{2z}. \end{aligned} \quad (2.2.4)$$

Note, in addition to the desired in-phase transfer, also multi quantum terms ($2\hat{I}_{1y}\hat{I}_{2x}$ and $2\hat{I}_{1x}\hat{I}_{2y}$) arise which generally need to be suppressed by so-called z-filters.^[118–121] The transfer from planar mixing is notably different from typical TOCSY sequences that induce isotropic mixing (IM).^[95–99] In Figure 2.1 simulated transfer functions for both methods are compared which are based on a uniformly J -coupled chain-like spin system. In comparison to isotropic mixing, where transfer is subject to a diffusive decay throughout the spin system (Figure 2.1 (a)), in planar mixing a transfer of so-called *spin waves*^[111] is encountered (Figure 2.1 (b)). Apparently, the coherence of these spin waves is preserved for a considerably longer time, which, in principle, allows tailored transfer resulting in correlations with possibly increased intensities. While short mixing times (corresponding to $t < 1/J$ in Figure 2.1) are certainly more useful for practical applications it is still remarkable that for longer mixing times the considered spin waves are even reflected at the end of the spin chain. Further transfer functions for various spin systems are derived numerically and analytically in literature.^[52,122–125]

^[118] M. Rance. *Journal of Magnetic Resonance* **1987**, *74*, 557–564.

^[119] M. J. Thrippleton and J. Keeler. *Angewandte Chemie - International Edition* **2003**, *42*, 3938–3941.

^[120] P. W. Howe. *Journal of Magnetic Resonance* **2006**, *179*, 217–222.

^[121] J. J. Koivisto. *Chemical Communications* **2013**, *49*, 96–98.

^[122] O. Schedletsky, B. Luy and S. J. Glaser. *Journal of Applied Physics* **1998**, *130*, 27–32.

^[123] B. Luy and S. J. Glaser. *Journal of Magnetic Resonance* **2001**, *153*, 210–214.

^[124] B. Luy and S. J. Glaser. *Journal of Magnetic Resonance* **2003**, *164*, 304–309.

^[125] L. Müller and R. R. Ernst. *Molecular Physics* **1979**, *38*, 963–992.

³⁷ An equivalent but more general property shall be described for isotropic mixing in the following Section 2.3.

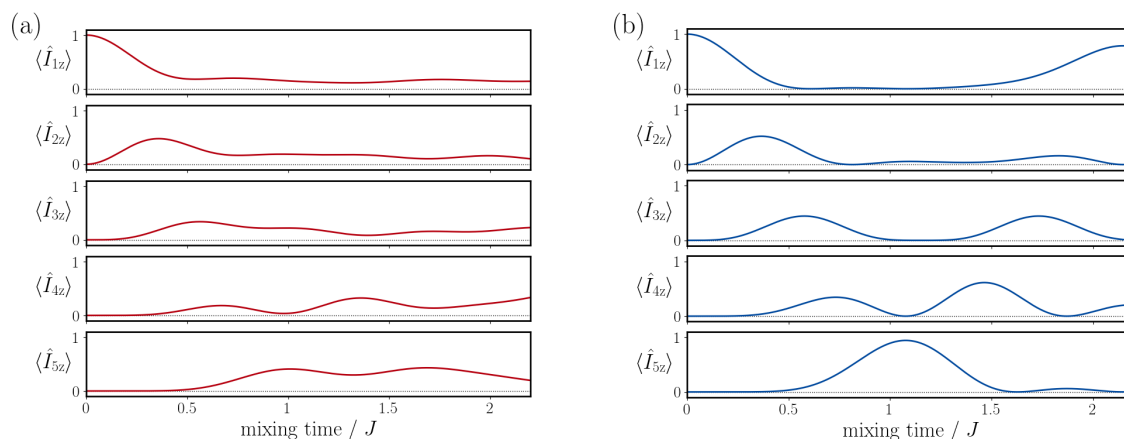


Figure 2.1: The effect of an isotropic (a) and a planar mixing Hamiltonian (b) of comparable strength is illustrated using numerical simulations for a spin chain consisting of 5 spins with uniform J -coupling.

2.2.2 Relayed CLIP-COSY

One experiment in which the perfect echo is not used for J -refocusing, but for coherence transfer, is the so-called clean in-phase COSY (CLIP-COSY). The pulse sequence is shown in Figure 2.2 where the perfect echo is flanked by two z-filters in order to remove MQ-coherences created before and during the transfer step (see Equation 2.2.4).^[118–121] In contrast to conventional DQF-COSY^[126,127] the mixing process for the CLIP-COSY is independent of t_1 and, hence, cross-peak intensities do not depend on the resolution of the indirect dimension. Therefore, in-phase signals are obtained and linebroadening (e.g. due to passive couplings or short acquisition times) do not result in signal cancellation – a considerable speed up is obtained. Further, it is possible to apply multiple, consecutive perfect echoes that cause a relayed transfer to indirectly coupled spins as originally proposed by Eich et al.^[128] In this way, a spin system can be tracked down step-by-step in a straight-forward manner which is especially efficient for chain-like spin systems (e.g. the proton network in sugars). In this respect, it is crucial to note that, also for relayed steps, transfer by the perfect echo occurs only in between *directly* coupled spins. This is in clear contrast to relayed transfer obtained from TOCSY experiments (i.e. using a range of mixing times) where an overshoot to indirectly coupled spins cannot be prevented.

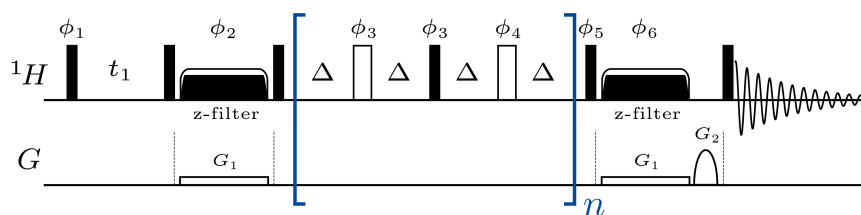


Figure 2.2: The CLIP-COSY pulse sequence is illustrated where relayed transfer is achieved if the mixing step is applied multiple times ($n > 1$). Before and after mixing a z-filter^[119] is applied which is composed of a frequency swept chirp pulse during a weak gradient field (G_1) – in addition a spoil gradient (G_2) is used. All phases are x if not annotated differently where $\phi_1 = 4(x)4(-x)$, $\phi_2 = 2(x,y)2(y,x)$, $\phi_3 = y, -y, -y, y$, $\phi_4 = -y, x, -y, x$, $\phi_5 = 2(x)2(-x)$, $\phi_6 = 2(-x, -y)2(-y, -x)$ and $\phi_{\text{rec}} = (x, -x, -x, x, -x, x, x, -x)$. Frequency discrimination was achieved by States-TPPI.^[129]

^[126] U. Piantini, O. W. Sørensen and R. R. Ernst. *Journal of the American Chemical Society* **1982**, *104*, 6800–6801.

^[127] M. Rance et al. *Biochemical and Biophysical Research Communications* **1983**, *117*, 479–485.

^[128] G. Eich, G. Bodenhausen and R. R. Ernst. *Journal of the American Chemical Society* **1982**, *104*, 3731–3732.

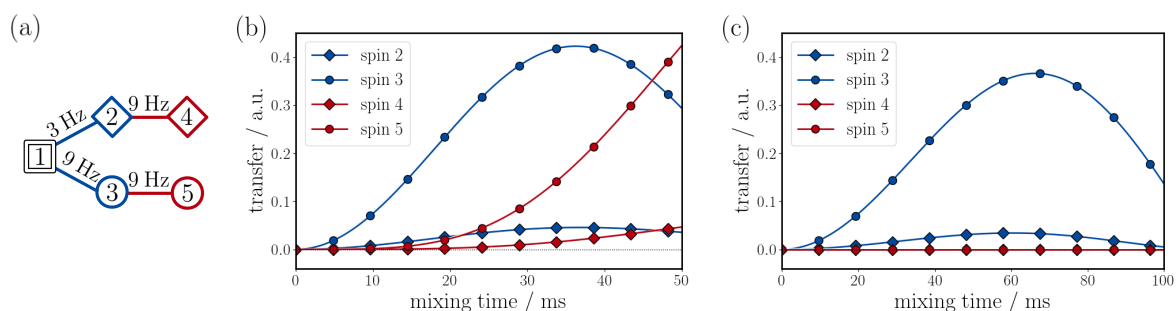


Figure 2.3: For the spin system in (a) relayed transfer is compared for TOCSY (b) and CLIP-COSY (c). Colors and markers are used coherently in (a-c) and couplings are set as stated in (a). Note, mixing times in both simulations differ by a factor of 2.

An example is given in Figure 2.3 where numerical simulations for the illustrated spin system are undertaken for isotropic mixing (TOCSY) and the perfect echo. The desired coherence transfer to only next neighboring spins ($n = 1$) is colored in blue and corresponding simulations for TOCSY and the perfect echo are given in Figure 2.3 (b) and (c), respectively. Clearly, coherence transfer from isotropic mixing leads to misleading results and already for short mixing times of ~ 25 ms the cross-peak to spin 5 overshoots the desired (non-relayed) correlation to spin 2 – a step-by-step elucidation of successive spin spheres is, hence, not possible. On the other hand, the simulations for the perfect echo indicate zero transfer to indirectly coupled spins. Hence, each of the n echoes transfers coherence only to the next spins in row and an unambiguous, step-by-step assignment can be achieved^[91] – an experimental verification for α -D-glucose shall be given.

A particular simplification by relayed transfer is encountered for chain-like spin systems where, starting from one end, the assignment can be done by walking through the chain. Such a situation is given e.g. for hexoses where each carbon is typically attached to a single proton and a linear spin network is given. While most protons in glucose are situated in a similar electronic environment (i.e. similar resonance frequency), the anomeric protons are further deshielded and, therefore, they exhibit a considerably larger chemical shift. Hence, for a stepwise assignment, the isolated signal of anomeric protons has shown to be a suitable starting point using relayed CLIP-COSY. In Figure 2.4 various CLIP-COSY spectra are shown for α -D-glucose and a straight-forward assignment can be made as indicated. For each additional echo (n) a new signal of the next spin in row appears until the whole chain is assigned and a TOCSY-like experiment is obtained. Note, in some cases signal dispersion might not be sufficient (e.g. $6'\alpha$ is not resolved due to overlap with 5α) and an equivalent assignment strategy with higher resolution can be achieved using an HSQC-CLIP-COSY.^[91,130,131] In this way, the considerably higher signal dispersion of carbon is exploited to prevent overlap.³⁸ While the stepwise transfer obtained from perfect echo is a valuable assignment tool, it is further noteworthy that, for larger values of n , TOCSY-like conditions can be obtained as encountered in Figure 2.4 (b). In the following section, it shall, hence, be the aim to examine the potential of planar mixing-based TOCSY sequences (PM-TOCSY) with special focus on biomolecular samples.

^[130] K. Kövér, O. Prakash and V. Hruby. *Journal of Magnetic Resonance* **1993**, A103, 92–96.

^[131] K. E. Kövér, V. J. Hruby and D. Uhrin. *Journal of Magnetic Resonance* **1997**, 129, 125–129.

³⁸ A similar combination of the perfect echo with an HSQC-type experiment shall be used in Section 2.6 where the stepwise transfer is used for the determination of long-range heteronuclear couplings.

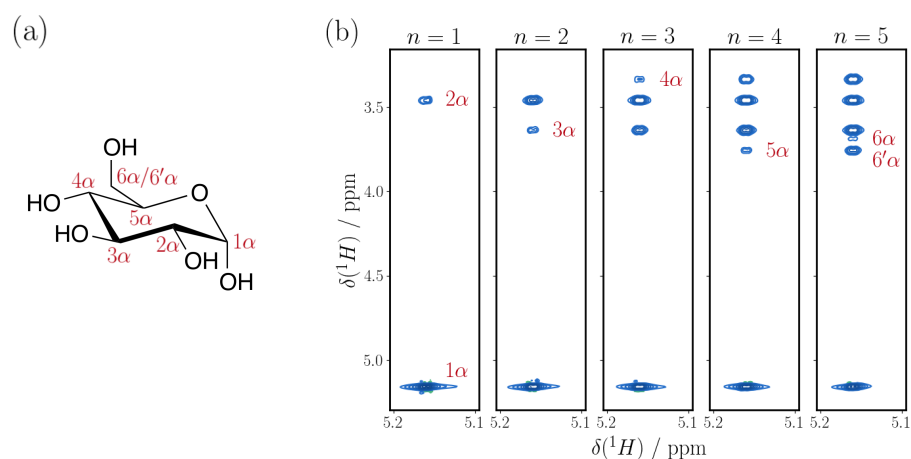


Figure 2.4: Stepwise transfer for α -D-glucose (a) is found for relayed CLIP-COSY spectra (b) where n is increased from 1 to 5 (left to right). All spectra were recorded on a 600 MHz Avance III spectrometer equipped with a cryogenically cooled TCI probe. 4096×256 complex points were acquired with 1 transient, a spectral width of 5 ppm and a relaxation recovery delay of $d1 = 0.5$ s.

2.2.3 $^{13}\text{C}, ^{13}\text{C}$ -PM-TOCSY

In biomolecular NMR numerous experiments have been developed to assign the backbone of proteins. For the assignment of side chains, it was shown in the early 90's that in uniformly ^{13}C -labeled proteins a $^{13}\text{C}, ^{13}\text{C}$ -TOCSY^[132] offers a straight-forward way to correlate and assign side-chain to respective backbone resonances. Large $^1J_{\text{C,C}}$ couplings enable a very efficient transfer and little overlap is expected in the highly dispersed carbon-dimension. However, the bandwidth of so far available isotropic mixing sequences used in $^{13}\text{C}, ^{13}\text{C}$ -TOCSY^[96,98,133], is technically limited by the applied RF amplitude and, therefore, common experiments fail at high magnetic fields where larger bandwidths are required. Kovacs and Gossert^[94,134] demonstrated that cryogenically cooled probes^[135] are able to stand a ^{13}C -spin lock at high power (i.e. an RF amplitude of up to 17.9 kHz) and a $^{13}\text{C}, ^{13}\text{C}$ -TOCSY, correlating the whole carbon range from CO to $\text{C}_{\text{aliph.}}$, is achieved at 700 MHz (corresponding to a ^{13}C -bandwidth of ~ 36 kHz). Still, the approach can, clearly, *not* be extended to larger bandwidths using high resolution probeheads and in the advent of higher magnetic fields³⁹, suitable solutions for broadband TOCSY-type experiments are required.

Here, another approach shall be presented that is based on the combined use of perfect echo and broadband shaped pulses – TOCSY-type correlations are obtained from planar mixing (PM) at bandwidths large enough to cover the *full* carbon band even on 1.2 GHz spectrometers. Since the proposed transfer is induced by pulse-delay sequences, individual pulses can be efficiently compensated with respect to chemical shift offsets and B_1 -inhomogeneity. Hence, with state-of-the-art broadband shaped pulses,^[92] a $^{13}\text{C}, ^{13}\text{C}$ -PM-TOCSY at a bandwidth of 60 kHz is achievable even for reduced RF amplitudes of 10 kHz. In the following, the proposed PM-TOCSY experiment shall be discussed in detail and *in silico* verification is given. Further, the sequence was tested on a high field spectrometer of 1.0 GHz⁴⁰ and spectra for an amino acid mixture, an intrinsically disordered and a globular protein are shown. The results shall be compared to the state-of-the-art broadband isotropic mixing sequence, FLOPSY, which fails given the high magnetic field and according large bandwidths.

^[132] S. W. Fesik et al. *Journal of the American Chemical Society* **1990**, *112*, 886–888.

^[133] A. E. Bennett, J. D. Gross and G. Wagner. *Journal of Magnetic Resonance* **2003**, *165*, 59–79.

^[134] D. Ban et al. *Journal of Magnetic Resonance* **2012**, *221*, 1–4.

^[135] H. Kovacs, D. Moskau and M. Spraul. *Progress in Nuclear Magnetic Resonance Spectroscopy* **2005**, *46*, 131–155.

³⁹ Up to date, the largest available field strength is 1.2 GHz corresponding to 28 Tesla which was first installed at the University of Florence.

⁴⁰ Measured at CRMN - Very High Field NMR Center in Lyon with Davy Sinnaeve and Burkhard Luy.

Pulse Sequence

The pulse sequence of the ^{13}C , ^{13}C -PM-TOCSY is illustrated in Figure 2.5 (a) where planar mixing is obtained from pulse schemes illustrated in Figure 2.5 (b) to (e). In analogy to the CLIP-COSY (Figure 2.2), z-filters are used after chemical shift encoding (t_1) and transfer from planar mixing.^[119] All pulses in the sequence are replaced by broadband shaped pulses^[92,103,136] in order to cover the full ^{13}C -bandwidth at high fields.⁴¹ While excitation pulses (E) and respective time-reversed counterparts (E^{tr}) are sufficient for the pulse sequence shown in Figure 2.5 (a), in the planar mixing sequence universal rotations of 90° ($UR90$) are required.⁴² This is based on the fact that excitation pulses are optimized to transfer a *single* axes which would *not* lead to the desired effect within the perfect echo. For the 180° shaped pulses, several variations are thinkable that all induce planar mixing. In general, a lower number of pulses is beneficial since more time can be used for mixing that *predominantly* occurs during delays Δ . On the other hand, consecutive pulses can compensate pulse imperfections and the choice on proposed planar mixing sequences, hence, also depends on the quality of the pulse shapes at hand. The most straight-forward sequence is illustrated in Figure 2.5 (b) where only broadband refocusing pulses (R) are used. For consecutive echoes it is, however, possible to use a single refocusing pulse, as is shown in Figure 2.5 (c), which leads to a power- and time-optimized version. Such a sequence can, thus, be used e.g. for biomolecular samples where typically reduced transverse relaxation times are encountered. In this respect, it is crucial to note that in literature it was demonstrated that an inversion requires roughly half the time compared to a refocusing pulse of equal quality.^[136] On this ground, two inversions (I) can be used to replace two refocusing pulses of successive echoes (Figure 2.5 (d)) which can be equally time-efficient as the sequence proposed in Figure 2.5 (c). If no refocusing pulse with desired properties is available, it is thinkable to use two inversion pulses also in the first and last echo of the mixing sequence (Figure 2.5 (e)). With respect to the selection of pulse shapes in the perfect echo, the reader is, again, referred to Section 2.4 where coupling evolution during shaped pulses is investigated – it turns out that also the right choice of pulse shapes can lead to more efficient transfer. This is based on the fact that some broadband shaped pulses efficiently suppress the homonuclear weak coupling Hamiltonian (e.g. Section 2.4.11 and 2.4.13) while others can contribute to planar mixing since couplings are allowed to partially evolve during the pulse (e.g. Section 2.4.12, 2.4.18 and 2.4.17). In contrast to multi pulse sequences for isotropic mixing (e.g. FLOPSY^[98]), in the above described planar mixing schemes only a fraction of the time is actually used for irradiation and, even for equivalent RF amplitudes, the average energy dissipation is considerably lower in the proposed PM-TOCSY.⁴³ This, in principle, allows to extend the bandwidth even further by increasing RF amplitudes for applied pulses. It shall also be mentioned that an enhancement of carbon magnetization, e.g. from heteronuclear NOE, INEPT- or CP-based transfer, is thinkable in the given ^{13}C , ^{13}C -PM-TOCSY.^[62,63,72,78,79] In the following section, numerical simulations shall at first be used to verify that *broadband* transfer is obtained by PM-TOCSY combined with shaped pulses and a comparison to broadband isotropic mixing (FLOPSY) is given.

^[136] K. Kobzar et al. *Journal of Magnetic Resonance* **2012**, *225*, 142–160.

⁴¹ Considering a 1.0 GHz spectrometer the required ^{13}C -bandwidth is 200 ppm corresponding to ≈ 50 kHz.

⁴² A description of common pulse classes and respective nomenclature is given in Section 2.4.1.

⁴³ Using an RF amplitude of 10 kHz for shaped pulses of length $\tau_P = 1$ ms and a delay $\Delta = 1$ ms, the introduced energy corresponds to the continuous irradiation with an RF amplitude of $\sqrt{(10 \text{ kHz})^2/2} = 7.07$ kHz.

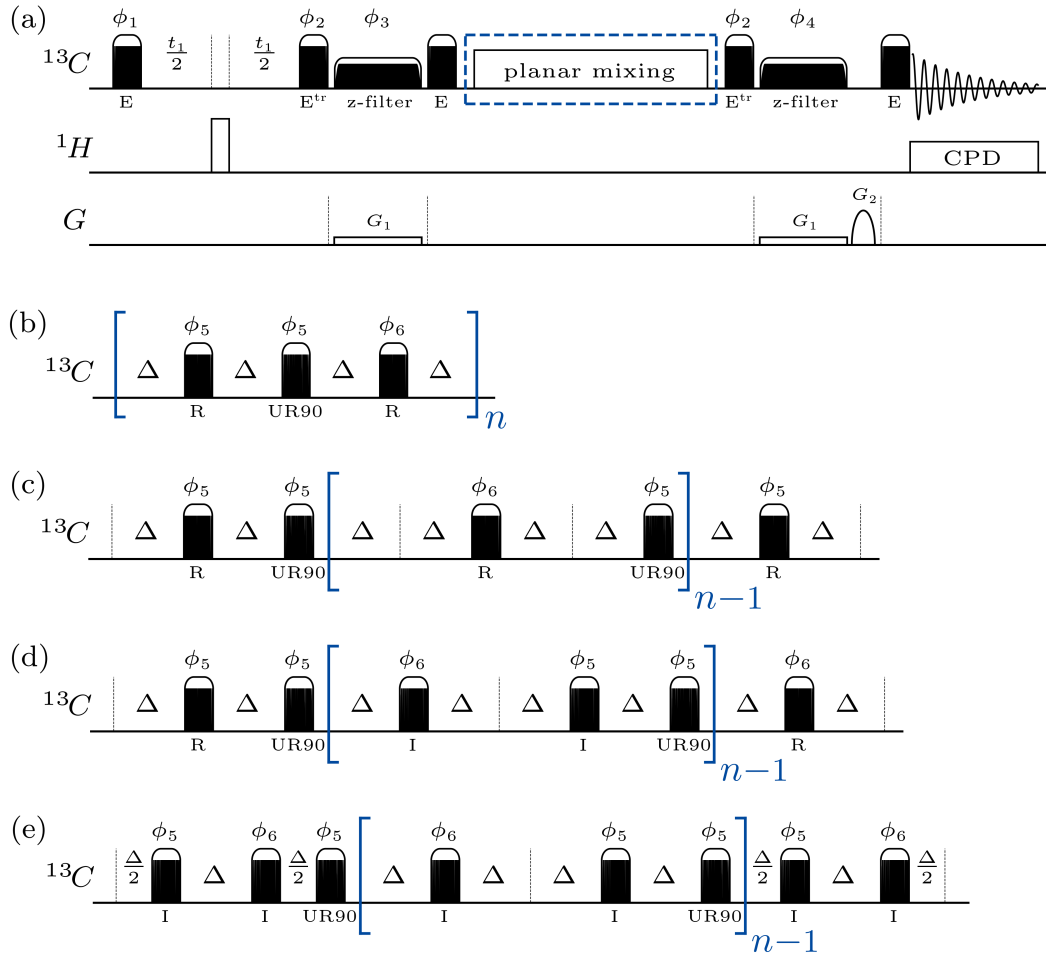


Figure 2.5: The pulse sequence for $^{13}\text{C},^{13}\text{C}$ -PM-TOCSY is illustrated in (a) with proton decoupling and various planar mixing schemes for different sets of shaped pulses are given in (b), (c) and (d). Broadband shaped pulses on carbon correspond to BEBOP (E), time-reversed BEBOP (E^{tr}), BURBOP-180 (R), BURBOP-90 (UR90) and BIBOP (I) as indicated.^[103,136] A z-filter^[119] is applied before and after planar mixing which is composed of a frequency swept chirp pulse during a weak gradient field (G_1) and a spoil gradient (G_2) is used additionally. All phases are x unless annotated otherwise and $\phi_1 = x, -x$, $\phi_2 = -x$, $\phi_3 = x$, $\phi_4 = -x$, $\phi_5 = y$, $\phi_6 = -y$ and $\phi_{\text{rec}} = x, -x$. The phases ϕ_5 and ϕ_6 undergo a MLEV-supercycle with $\phi_{\text{sc}} = x, x, -x, -x, -x, x, x, -x, -x, -x, x, x, -x, -x, x$.

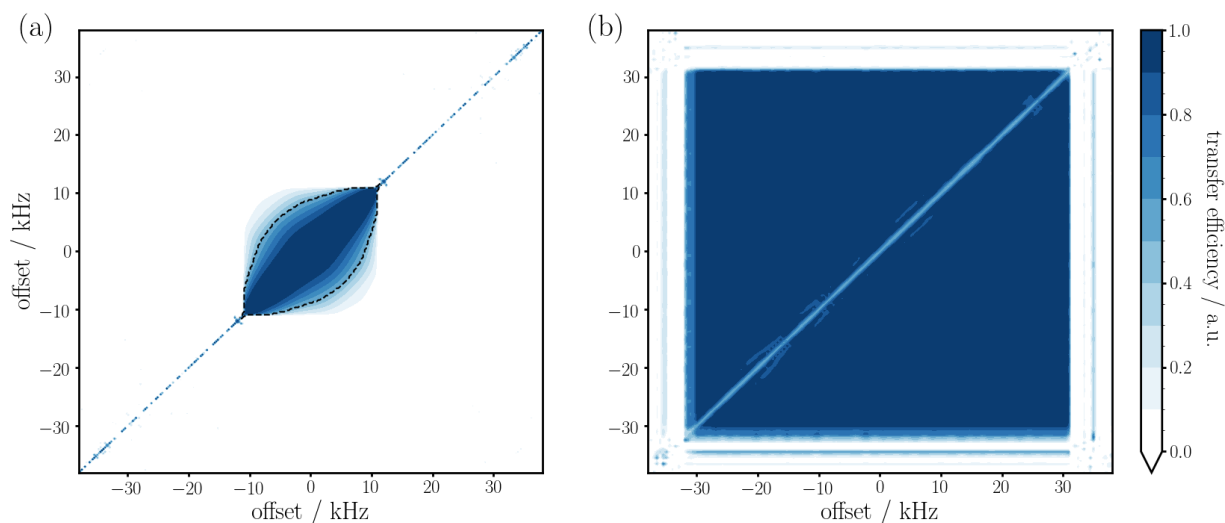


Figure 2.6: Effective coherence transfer in a two-spin system is numerically simulated for FLOPSY (a) and PM-TOCSY with 4 echoes (b) – the mixing sequence in Figure 2.5 (b) is used with UR pulses.^[92] Various chemical shift offsets (151 points linearly distributed on 76 kHz) are calculated for both spins and offset contour maps are obtained. For both experiments, equivalent parameters were used which corresponds to an RF amplitude of 10 kHz and optimal mixing times of $1/(2J)$ (FLOPSY) and $1/J$ (PM-TOCSY). The dashed line in (a) indicates a transfer efficiency of 0.5.

Numerical Simulations

The effective coherence transfer for FLOPSY and PM-TOCSY is simulated for various chemical shift offsets using the spin density formalism (Section 1.2). These simulations result in offset contour maps that indicate the spectral areas in which coherence transfer is achieved – they can be considered virtual 2D spectra where potential cross-peaks appear only in blue areas in Figure 2.6. In white areas, on the other hand, the effective J -coupling is zero and *no* transfer can be achieved by the sequence. For FLOPSY and PM-TOCSY, equally, an RF amplitude of 10 kHz was chosen, which, for FLOPSY, results in coherence transfer within the spectral areas illustrated in Figure 2.6 (a). Clearly, the effective transfer is far from uniform and it strongly depends on the chemical shifts of involved spins. The dashed line indicates a transfer efficiency of 0.5 and a bandwidth of up to ~ 20 kHz is covered in favorable cases. For the PM-TOCSY, on the other hand, a bandwidth of 60 kHz is obtained which conveniently covers the band needed for a ^{13}C , ^{13}C -TOCSY at today's largest-available field strength of 1.2 GHz. The transfer efficiency is uniformly distributed within the entire bandwidth and a square-shaped contour map is obtained as shown in Figure 2.6 (b). As already mentioned in Section 1.6.3 it shall, again, be noted that transfer from isotropic mixing in the considered two-spin system is faster compared to *planar mixing from perfect echo* and the optimal mixing times used in the simulations are $1/(2J)$ and $1/J$ for FLOPSY and PM-TOCSY, respectively.⁴⁴ It is, however, crucial to note that the illustrated contour maps in Figure 2.6 could likewise be interpreted as scaling factors that reduce the *effective* J -coupling.^[137] Hence, for FLOPSY the required mixing times are strongly offset-dependent and rapidly drop towards the off-diagonal edges. Considering areas outside the dashed line in Figure 2.6 (a), the effective J -coupling is reduced by a factor of 2 or more and coherence transfer from planar mixing can be considered faster.

^[137] A. Bax, G. Clore and A. M. Gronenborn. *Journal of Magnetic Resonance* **1990**, 88, 425–431.

⁴⁴ Due to the mixing time of $1/J$, there is no apparent transfer on the diagonal for the PM-TOCSY in Figure 2.6 (b) – a mixing time of $1/J$ for an isotropically coupled *two-spin* system causes exactly one oscillation resulting in the initial state again and no *effective* transfer is observed.

Experimental

For an experimental proof the proposed PM-TOCSY (Figure 2.5) was implemented on a high field spectrometer of 1.0 GHz and tested on various uniformly ^{13}C , ^{15}N -labeled samples: an amino acid mixture (Sigma Aldrich), an intrinsically disordered protein ($\sim 480 \mu\text{M}$ TauF4 fragment consisting of residues 208-324,⁴⁵ 50 mM Na_2HPO_4 , 30 mM NaCl , 2.5 mM EDTA in 95%:5% $\text{H}_2\text{O}:\text{D}_2\text{O}$ with $\text{pH} = 6.7$)^[138] and a globular protein, human ubiquitin.⁴⁶ A comparable experiment using broadband isotropic mixing (FLOPSY^[98]) instead of planar mixing was likewise acquired for the amino acid mixture.

The conventional FLOPSY-spectrum of the amino acid mixture is illustrated in Figure 2.7 (a) and, in accordance to above shown simulations, reliable correlations are obtained only on a limited band of 20 kHz corresponding to the spectral range of 60-140 ppm with its center at 100 ppm. Hence, a TOCSY-type spectrum is obtained only *within* aromatic side-chains and few signals close to the diagonal. In order to avoid probe damage, the RF amplitude was set to the maximum allowed value by the manufacturer, 10 kHz, and an increase in B_1 field as proposed by Kovacs and Gossert was not risked. Further, it is worth mentioning that also artifact signals are observed that indicate COSY-type transfer from aliphatic carbons to carbonyls. The considered signals invariably exhibit dispersive anti-phase lineshapes and are highlighted by a dashed box in Figure 2.7 – their origin cannot be ascribed to isotropic mixing and comparable artifacts are not encountered in the PM-TOCSY. The spectrum of amino acids obtained by PM-TOCSY, on the other hand, is shown in Figure 2.7 (b) and correlations are observed within the full ^{13}C -band of 45 kHz. All signals exhibit the desired in-phase lineshape and for the considered sample numerous TOCSY-type correlations throughout the spin systems are found. In Figure 2.7 (b), a straight-forward evidence is given e.g. by the cross peak correlating the two carbonyls at both ends of glutamate (177.36 ppm and 184.08 ppm) or cross peaks that imply transfer from aromatic side-chains to carbonyls (highlighted by dashed boxes). These correlations can be considered a proof of principle and even on high field spectrometers of 1.0 GHz effective transfer throughout an entire spin system is achieved by the PM-TOCSY sequence.

Due to the fact that amino acids exhibit long transverse relaxation times, the duration of planar or isotropic mixing is noncritical. Clearly, application-oriented protein samples, typically, might not benefit from such relaxation properties and, therefore, they constitute a more challenging task for the proposed sequence. PM-TOCSY spectra of an intrinsically disordered (tauF4) and a globular protein (human ubiquitin), likewise acquired on a 1.0 GHz spectrometer, are illustrated in Figure 2.8 (a) and (b), respectively. In both spectra the *entire* ^{13}C -bandwidth of 45 kHz is covered by planar mixing and in-phase correlations from aliphatic side-chains to carbonyls are, thus, observable. For the tauF4 fragment one can additionally observe that coherence transfer from the aromatic side-chain to carbonyls and *vice versa* was achieved by planar mixing (dashed box). In the ubiquitin spectrum, these correlations are not observable which might be due to the lower signal to noise (i.e. carbon detection with initial carbon polarization recorded in 2 h 25 min) and less favorable relaxation times compared to the intrinsically disordered protein (IDP). It is further worth mentioning that, in general, relaxation rates in aromatic side-chains are increased due to a comparably large chemical shift anisotropy (CSA) which can be ascribed to *ring currents*.^[139] Since chemical shifts are linear with respect to the outer magnetic field (Section 1.3.3), it is expected that aromatic relaxation rates are likewise increased at higher magnetic fields. However, based on the fact that experimental proof for broadband planar mixing is given, the PM sequence is subsequently introduced in a more elaborate experiment with proton detection that is based on an (H)CC(CO)NH-TOCSY, commonly used for the assignment of protein side-chains.

^[138] N. Sibille et al. *Proteins: Structure, Function and Bioinformatics* **2012**, *80*, 454–462.

^[139] J. A. Pople. *The Journal of Chemical Physics* **1956**, *24*, 1111–1111.

⁴⁵ The amino acid sequence of the measured TauF4 fragment with a single mutation C291S (here, at position 84):

10	20	30	40	50	60
SRSRTPSLPT	PPTREPKKVA	VVRTPPKSPS	SAKSRLQTAP	VPMPDLKNVK	SKIGSTENLK
70	80	90	100	110	
HQPGGGKVQI	INKKLDLSNV	QSKSGSKDNI	KHVPGGGSVQ	IVYKPVDSLK	VTSKCGS

⁴⁶ I would like to thank Dr. Isabelle Landrieu to have made available these valuable protein samples in Lyon.

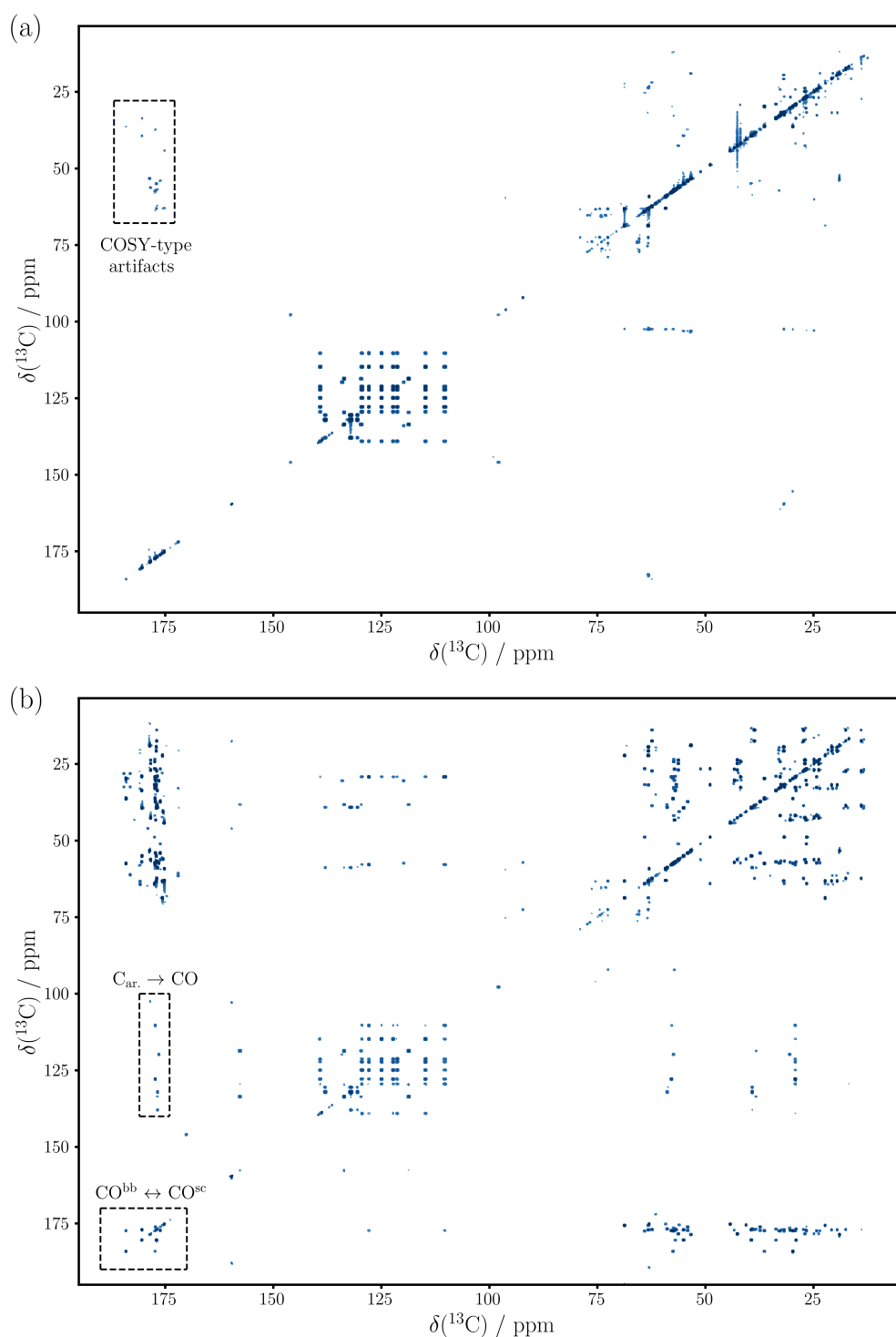


Figure 2.7: FLOPSY^[98] (a) and PM-TOCSY (b) of amino acid mixture recorded at 1 GHz. For comparable results, the sequence in Figure 2.5 (a) was equipped with respective mixing scheme, FLOPSY and PM, using an RF amplitude of 10 kHz. For both spectra 2 transients of 4096×1024 complex points were acquired in roughly 1 h 20 min with $d1 = 1.0$ s. For FLOPSY a mixing time of 25 ms was chosen while for PM the scheme using only inversion pulses (Figure 2.5 (e)) was applied with $n = 6$ and $\Delta = 1.0$ ms. COSY-type artifact signals with dispersive anti-phase lineshapes, encountered for FLOPSY, are highlighted in (a).

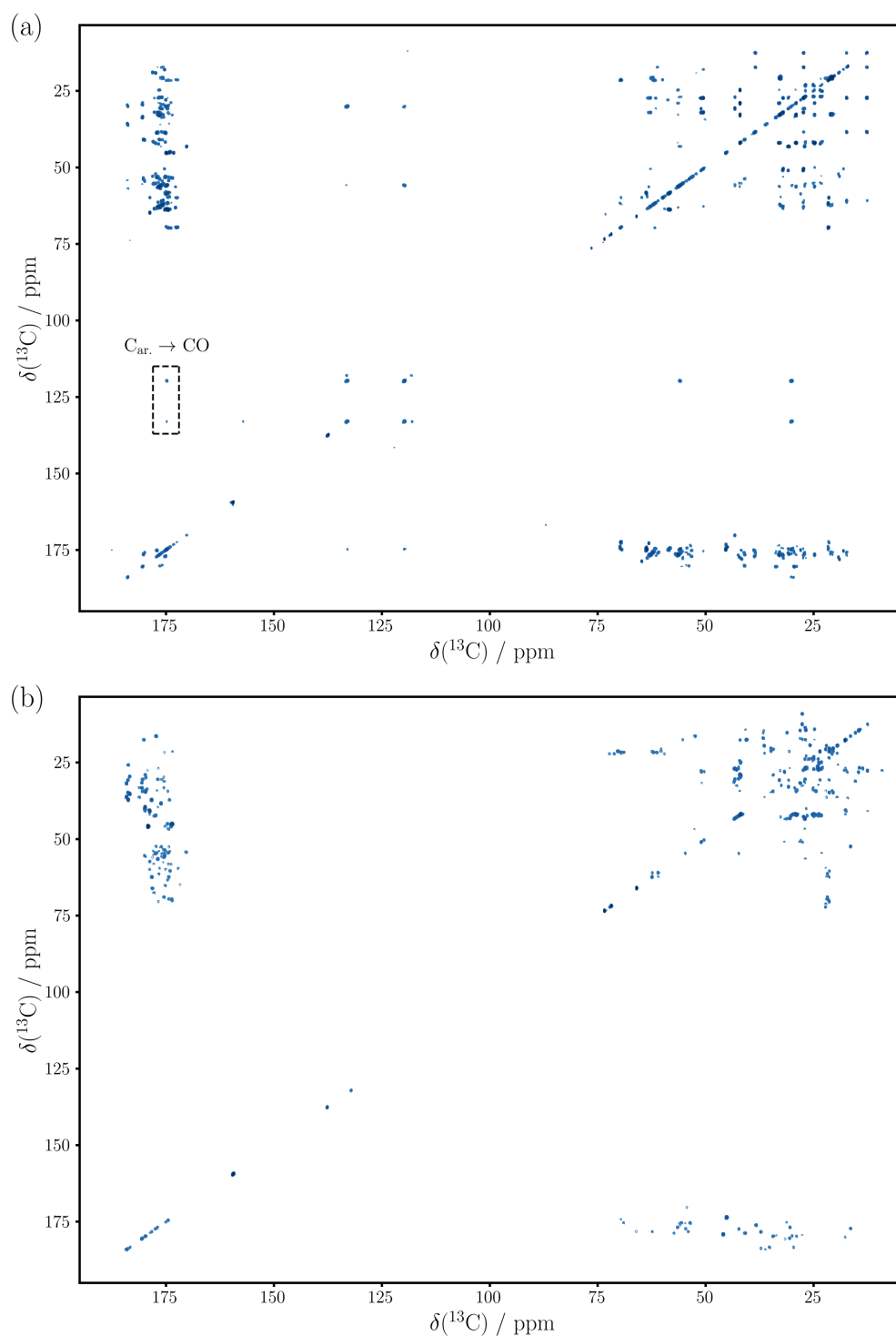


Figure 2.8: PM-TOCSY spectra of TauF4 fragment and human ubiquitin were acquired at a 1 GHz spectrometer with 32 transients of 4096×512 complex points for TauF4 (≈ 10 h 55 min) and 8 transients of 4096×457 complex points for ubiquitin (≈ 2 h 25 min). The mixing scheme using only inversion pulses (Figure 2.5 (e)) was applied with $\Delta = 1.0$ ms and $n = 5$ for TauF4 ($n = 6$ for ubiquitin).

2.2.4 Planar Mixing in a 3D (H)CC(CO)NH Experiment

In the conventional (H)CC(CO)NH experiment isotropic mixing is applied to achieve coherence transfer from side-chain carbons to C_α where subsequent INEPT-like steps cause transfer via carbonyls to the amide proton for acquisition.^[93,94,140–142] Based on comparably large $^1J_{C,C}$ -couplings an efficient transfer can be achieved within the carbon backbone. Using cryogenically cooled probes, Kovacs and Gossert modified the (H)CC(CO)NH experiment and introduced high-power isotropic mixing (i.e. at an RF amplitude of up to 17.9 kHz) which is able to cover a bandwidth of roughly 36 kHz. By this means it is possible to obtain fast and efficient coherence transfer from the side-chain *directly* to carbonyls omitting the separate $C_\alpha \rightarrow CO$ transfer step – so far, this was achieved on spectrometers of up to 700 MHz. At today's largest available fields of 1.2 GHz, on the other hand, the bandwidth to achieve mixing of *just* aliphatic and aromatic carbons (as intended in the conventional (H)CC(CO)NH) is already at 42 kHz (140 ppm). Even daring high-power isotropic mixing (~ 36 kHz) is, hence, not sufficient to cover the required $C_{\text{arom.}}-C_{\text{ali.}}$ -band and a direct transfer to carbonyls, as proposed by Kovacs and Gossert, is even less thinkable. As demonstrated in the previous Section 2.2.3, the planar mixing-based approach, on the other hand, is able to cover large bands in combination with broadband shaped pulses. Planar mixing from perfect echo, hence, represents a potential solution which could be used to substitute isotropic mixing in the (H)CC(CO)NH experiment at today's high magnetic fields.

In the following, an optimized planar mixing sequence shall be used in a modified (H)CC(CO)NH experiment which is tested on human ubiquitin (0.5 mM in 93%:7% $H_2O:D_2O$, pH = 4.7, 30 mM NaOAc, 50 mM NaCl, Silantes). It shall be shown that aromatic correlations are achievable – although not for all residues of ubiquitin. Due to the absence of a 1.0 GHz spectrometer at KIT (and only limited measurement time at 1.0 GHz in Lyon) the (H)CC(CO)NH experiment was recorded at a field of 600 MHz where the requirements with respect to bandwidth are less severe. Still, considering the spectra in Figure 2.7 and 2.8 it is conceivable that the applied planar mixing is transferable to higher fields. Due to numerous delays without irradiation during PM, the average energy dissipation of the perfect echo is considerably lower and it is even thinkable to use the identical shaped pulses applied at 600 MHz with increased RF amplitude also at higher fields.⁴⁷

Pulse Sequence

The (H)CC(CO)NH pulse sequence (Figure 2.9) consists of a first transfer from initial proton magnetization to aliphatic carbons ($C_{\text{ali.}}$) whose chemical shifts are subsequently acquired in the first indirect dimension (t_1) – simultaneously the proton anti-phase coherence is refocused. A band-selective pulse on CO is used to suppress homonuclear couplings and in order to avoid Bloch-Siegert shifts the shaped pulse is applied a second time as explained in literature.^[43] Afterwards, planar mixing using broadband shaped pulses causes in-phase to in-phase coherence transfer from side-chain carbons *directly* to carbonyls (CO). From CO a transfer to nitrogen is conducted where the second indirect dimension (t_2) is acquired – it also comprises the removal of anti-phase coherence in a semi-CT way. The direct dimension is finally acquired using amide protons after a phase sensitive back-transfer with coherence transfer pathway selection from echo/anti-echo gradients. In contrast to the conventional (H)CC(CO)NH experiment, where side-chain coherence is transferred to C_α by isotropic mixing and subsequently to CO by an INEPT-like step, *broad-band* planar mixing allows direct transfer to CO, which, to some extent, can compensate longer mixing times required by PM. It is further thinkable to omit both z-filters before and after mixing (each with a duration of $\tau_{zf} \geq 10$ ms) in order to obtain time-optimized transfer. Since during the z-filters, desired coherences are stored in longitudinal states, commonly, the T_1 relaxation loss is affordable.

^[140] G. T. Montelione et al. *Journal of the American Chemical Society* **1992**, *114*, 10974–10975.

^[141] B. Lyons and G. Montelione. *Journal of Magnetic Resonance* **1993**, *B101*, 206–209.

^[142] R. Clowes et al. *Journal of Biomolecular NMR* **1993**, *3*, 349–354.

⁴⁷ With an RF amplitude of 10 kHz the applied shaped pulses cover a bandwidth of 37.5 kHz. Hence, increasing the RF amplitude by factor of 1.2 the pulses cover a bandwidth of ≈ 45 kHz which corresponds to ≈ 200 ppm on ^{13}C at 900 MHz. Additionally, the reduced pulse length (i.e. factor 1.2) also reduces loss from transverse relaxation.

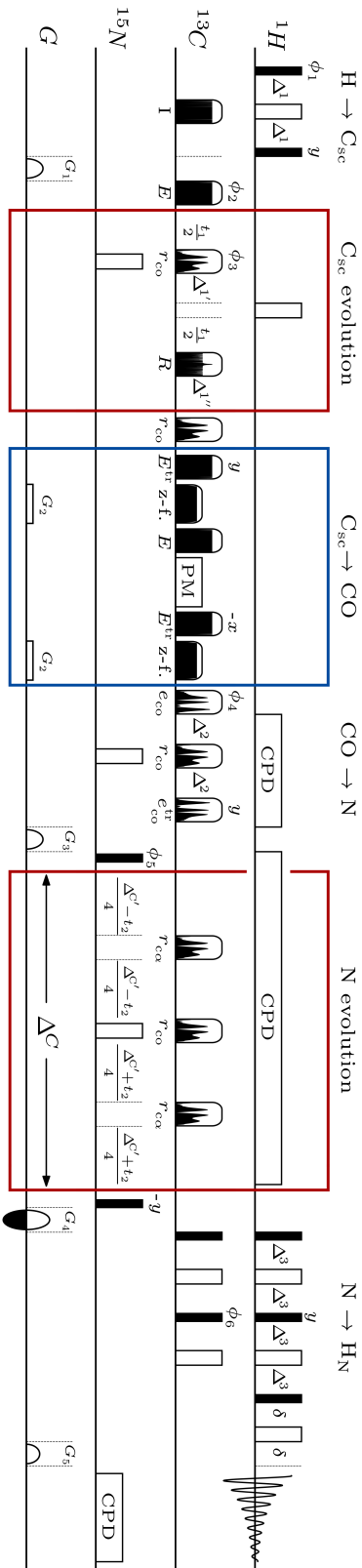


Figure 2.9: The pulse sequence for broadband planar mixing-based 3D (H)CC(CO)NH experiment^[93,94] is illustrated. On carbon broadband shaped pulses are BEBOP (E, inversion), BEBOP (E, excitation), time-reversed BEBOP (E^{tr}) and BURBOP-180 (R, refocusing), while band-selective pulses are Q3-SURBOP (e) and Q5-SURBOP (e and e^{tr}) applied on the band as indicated by the subscript.^[103,136,143] The blue box highlights broadband planar mixing where the scheme in Figure 2.5 (c) is used to achieve coherence transfer from side-chain carbons (C_{sc}) to carbonyls (CO). A z-filter is applied before and after mixing which is composed of a frequency swept chirp pulse (~ 10 ms) during a weak gradient field (G_2).^[119] The incrementation for both indirect dimensions are highlighted by red boxes – both time slots are likewise used to refocus anti-to in-phase coherences (using Δ^1 and Δ^C). Transfer delays are set according to $\Delta^1 = 1/(4 \cdot {}^1J_{CH})$, $\Delta^2 = 1/(4 \cdot {}^1J_{CO,N})$, $\Delta^C = 1/(2 \cdot {}^1J_{CO,N})$ and $\Delta^3 = 1/(4 \cdot {}^1J_{HN,N})$ where primes indicate modifications due to shaped pulses. Note, the band-selective pulses for carbonyl decoupling (r_{CO}) are applied twice to avoid Bloch-Siegert shifts on side-chain carbons. WALTZ and GARP composite pulse decoupling is used on proton and nitrogen, respectively.^[144,145] Pulse phases are x if not indicated differently with $\phi_1 = 8(x)$, $8(-x)$; $\phi_2 = 2(x)$, $2(-x)$; $\phi_3 = x$, y ; $\phi_4 = 4(x)$, $4(-x)$; $\phi_5 = x$, $-x$ and $\phi_{rec} = x$, $-x-x$, x , $-x$, x , $-x$, x , $-x$, x , x , $-x$, x , $-x$, x , $-x$, x , $-x$, x . While for the carbon dimension (t_1) frequency discrimination is achieved by States-TPPI, for nitrogen (t_2) a sensitivity improved phase sensitive back transfer is used where ϕ_6 is phase inverted with the echo/anti-echo gradient cycle of G_4 .^[120,146,147] Gradients $G_1 = 50\%$ and $G_3 = -30\%$ are used to suppress unwanted coherences while coherence pathway selection is obtained from $G_4 = 80\%$ and $G_5 = 8.1\%$ (of maximum gradient strength).

Experimental

For the proposed 3D (H)CC(CO)NH experiment a planar mixing sequence is used which was optimized to obtain time-efficient transfer for the globular protein, human ubiquitin. In this context it is noteworthy that in perfect echo-based PM, effective mixing occurs predominantly during delays and, hence, a favorable sequence with a low number of pulses is chosen (illustrated in Figure 2.5 (c)). Further, in the applied planar mixing sequence the X-BURBOP-180 shaped pulse of the BUBU sandwich (Section 2.4.17) can be used which, simultaneously, allows the evolution of homonuclear weak coupling during $\sim 27\%$ of the pulse length. Hence, the shaped pulse can contribute to PM and the effective mixing time is increased – correspondingly the delays can be shortened resulting in a reduced loss from transverse relaxation. For the spectrum of ubiquitin in Figure 2.10 a total mixing time of $\tau_m = 38.75$ ms with $n = 5$ echoes and $\Delta = 1.4$ ms was chosen whereof approximately 30 ms can contribute to effective planar mixing.⁴⁸ Due to the fact that a 3D intensity distribution is cumbersome to visualize (especially for TOCSY-type experiments where numerous correlations are expected) only the 2D $^1\text{H}, ^{13}\text{C}$ -plane was recorded which is shown in Figure 2.10 – one could imagine the third ^{15}N -dimension being collapsed onto the paper plane. In the illustrated spectrum it is apparent that broadband planar mixing covers the full ^{13}C -band and numerous side-chain correlations of aliphatic residues can be observed. These are based on TOCSY-like transfer from side-chain carbons to the residue’s carbonyl that is used as intermediate for a subsequent transfer to the amide nitrogen and proton. While for certain aromatic side-chains, correlations can be observed in Figure 2.10, again, this is not achieved for all aromatic residues. One reason could also be, that an unfavorable spin topology in aromatic side-chains does not allow an efficient transfer at high yield. Assuming CSA-relaxation, it shall be mentioned that cross-correlated relaxation (Section 1.8) can be exploited which leads to an aromatic TROSY where the component with favorable relaxation properties is isolated from the fast decaying signal.^[148] Further, transverse relaxation occurs during numerous transfer steps within the (H)CC(CO)NH sequence as well as during the mixing time τ_m . It would, thus, be beneficial to minimize τ_m e.g. by the application of broadband shaped pulses that significantly contribute to PM or using pulse shapes that exhibit short pulse lengths. For intrinsically disordered proteins, on the other hand, transverse relaxation times are typically longer. Already in the carbon detected $^{13}\text{C}, ^{13}\text{C}$ -PM-TOCSY and at 1.0 GHz, where CSA-relaxation is typically more significant, a transfer from aromatic carbons to carbonyls was observed (Figure 2.8 (a)). It can be expected that also the (H)CC(CO)NH would benefit from the favorable relaxation properties – for intrinsically disordered proteins, however, the successful application of the proposed experiment remains to be proven.

^[148] K. Pervushin et al. *Journal of the American Chemical Society* **1998**, *120*, 6394–6400.

⁴⁸ Planar mixing in the (H)CC(CO)NH experiment is based on the sequence shown in Figure 2.5 (c) where a BURBOP-180 of $1000 \mu\text{s}$ and a BURBOP-90 of $750 \mu\text{s}$ is used. For 5 echoes the total time of RF irradiation is, hence, calculated from $\tau_{\text{RF}} = 5 \cdot (750 \mu\text{s} + 1000 \mu\text{s}) + 2 \cdot 1000 \mu\text{s} = 10.75$ ms. On the other hand, with a delay $\Delta = 1400 \mu\text{s}$ effective planar mixing takes place during $\tau_{\text{eff}} = 5 \cdot 4 \cdot 1400 \mu\text{s} + 0.27 \cdot 7 \cdot 1000 \mu\text{s} \approx 30$ ms where also coupling evolution during the BURBOP-180 is considered.

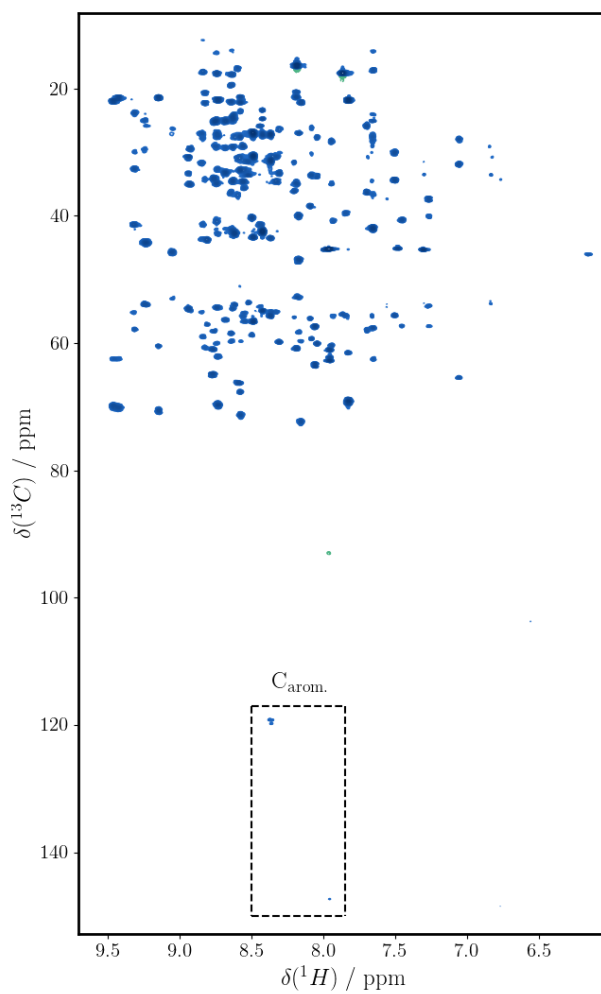


Figure 2.10: The $^1\text{H},^{13}\text{C}$ -plane of the 3D (H)CC(CO)NH experiment was acquired for human ubiquitin on a 600 MHz spectrometer with 32 transients of 1024×300 complex points corresponding to an acquisition time of 7 h. For planar mixing $n = 5$ echoes were chosen and the delay was set to $\Delta = 1.4$ ms. Based on the fact that amide protons are acquired the sample has to be dissolved in $\text{H}_2\text{O}/\text{D}_2\text{O}$ ($\sim 90\%/10\%$).

2.2.5 Conclusion

The perfect echo has proven to be a versatile tool that has found various applications in pulse sequence development of which many exploit the capability for J -refocusing during a certain time interval. As explained above J -refocusing is *actually* based on the fact that perfect echo is able to induce planar mixing which can further be used for *coherence transfer* between coupled spins. Since the number of perfect echoes (n) directly limits the number of transfer steps, it was demonstrated that a relayed CLIP-COSY enables a straight-forward step-by-step assignment with well-resolved in-phase signals.^[91] In analogy to J -refocusing, the repetitive application of the perfect echo leads to an effective planar mixing Hamiltonian which can be used in combination with corresponding shaped pulses to result in *broadband* PM-TOCSY. In comparison to so far available isotropic mixing sequences (e.g. FLOPSY) a three-fold wider band can be covered using equivalent RF amplitudes. In the advent of higher magnetic fields it is evident that broadband experiments are needed to cover the required bandwidths and the discussed PM-TOCSY constitutes a potential solution.

In this context the proposed ^{13}C , ^{13}C -PM-TOCSY was tested on a 1.0 GHz spectrometer and, as shown for various samples, the full ^{13}C -band can be covered. Since coherence under planar mixing travels in so-called spin waves, it is less diffusive compared to IM and it is even thinkable that under favorable conditions a tailored transfer might exceed efficiency from IM. Further, it should be mentioned that a faster transfer from planar mixing is obtained if large chemical shift differences are involved (see Figure 2.6). In proteins a larger offset is commonly given only for certain transfer steps (e.g. between $\text{C}\alpha$ and CO or for carboxylic and aromatic side-chains) while many others are within the aliphatic chain. Therefore, planar mixing from perfect echo typically occupies more time compared to isotropic mixing and a somewhat larger loss due to transverse relaxation is expected. Especially in aromatic side-chains where effective CSA-relaxation occurs, it is concluded that some correlation might not be observable. Likewise, the (H)CC(CO)NH, comprising numerous transfer steps throughout the protein backbone, accounts for a non-negligible loss in signal intensity and might not constitute the most suitable frame. At high fields, not only CSA-relaxation of aromatic carbons increases quadratic with respect to the field strength, also carbonyls exhibit a distinct chemical shift anisotropy which is considered the predominant relaxation mechanism.^[149,150]

Instead of the (H)CC(CO)NH, being based on numerous transfer steps, it is conceivable that a shorter HCCH-TOCSY-type experiment is favorable.^[132,137,151,152] In this respect, a promising prospect is offered by the conception of the selective acquisition of $\text{H}\alpha$, $\text{C}\alpha$ -correlations which is elaborately discussed in Section 3.4 and 3.6. In the frame of so-called SHACA experiments, a shorter PM-transfer from side-chain carbons to $\text{C}\alpha$ would suffice and the considered (H)CC α H α -PM-TOCSY could offer a sensitive and broadband solution for complete investigations on protein side-chains at high magnetic fields.

Further, it shall be mentioned that the discussed broadband PM-TOCSY does not only find application in the field of biomolecular NMR, but could also be used in any field of NMR where nuclei with large signal dispersion are investigated (e.g. ^{19}F) or the experimental setup requires a large compensation of B_1 fields. In the following section a related topic shall be discussed where *isotropic mixing* is obtained from a pulse-delay sequence similar to the perfect echo.

^[149] P. Allard and T. Härd. *Journal of Magnetic Resonance* **1997**, *126*, 48–57.

^[150] W. Bermel et al. *Concepts in Magnetic Resonance Part A* **2008**, *32A*, 183–200.

^[151] E. T. Olejniczak, R. X. Xu and S. W. Fesik. *Journal of Biomolecular NMR* **1992**, *2*, 655–659.

^[152] A. Majumdar et al. *Journal of Biomolecular NMR* **1993**, *3*, 387–397.

2.3 Isotropic Mixing from Isotropic Perfect Echo

Isotropic mixing (IM) lays the foundation of the well-known TOCSY experiment and was first proposed and used for homonuclear coherence transfer in solution state NMR by Braunschweiler and Ernst.^[5] It is based on a scalar coupling Hamiltonian ($\hat{\mathcal{H}}_J$) that is *not* truncated by chemical shift offsets of involved spins⁴⁹ – it is frequently referred to as an *isotropic* Hamiltonian. In general, for two weakly coupled spins (sometimes denoted AX spin system) the scalar coupling Hamiltonian is subject to an evolution in spin space that is induced by the chemical shifts and a secular approximation, therefore, causes averaging over zero-quantum operators⁵⁰ – an in-phase to in-phase coherence transfer is not given. The full isotropic Hamiltonian can, however, be regained if a pulse sequence achieves the effective suppression of chemical shifts and the spin system is then said to be in the strong coupling regime and isotropic mixing occurs. While IM is, in principle, obtained by any pulse sequence that effectuates spin lock,^[5] a notably elegant approach was later added by Bax and Davis.^[77,95,153] They discovered that *heteronuclear* decoupling sequences, typically, achieve the suppression of linear terms in the spin Hamiltonian of spins on which the sequence is applied. Since the Zeeman interaction is also described by a linear operator it is suppressed by composite pulse decoupling (e.g. MLEV^[154]) and, hence, *heteronuclear* decoupling sequences further cause isotropic mixing of irradiated *homonuclear* spins.

In the present section a basic analysis on the isotropic coupling Hamiltonian $\hat{\mathcal{H}}_J$ shall be given that allows a general comprehension of its effects and how it can be used in pulse sequence development. Moreover, different *isotropic perfect echo* (IPE) sequences are proposed that result in *heteronuclear isotropic Hartmann Hahn transfer* (HIHHA) at low average power.^[155–158] The zeroth order average corresponds to an isotropic Hamiltonian with reduced effective J -coupling and, hence, it shall likewise be referred to as isotropic mixing – an application in a DOSY experiment is shown. Based on the fact that IM is able to preserve spin states, the proposed DOSY sequences can be combined with Ernst angle excitation which results in a fast experiment at optimal signal-to-noise per square-root time.^[100]

2.3.1 Isotropic Mixing

Isotropic mixing in solution state NMR is based on *scalar* couplings⁵¹ and due to the spherical shape of the isotropic Hamiltonian ($\hat{\mathcal{H}}_J$)^[161] it is invariant under any rotation that acts on any involved spin. Rotations on individual spins (e.g. chemical shift), on the other hand, are able to modify the interaction in spin space, as shown in Section 2.5. In contrast to the planar coupling Hamiltonian, being composed of *two* orthogonal bilinear operators, the isotropic Hamiltonian $\hat{\mathcal{H}}_J$ is given as:

$$\hat{\mathcal{H}}_J = 2\pi \sum_{k>j} J_{k,j} \cdot (\hat{I}_{kz}\hat{I}_{jz} + \hat{I}_{ky}\hat{I}_{jy} + \hat{I}_{kx}\hat{I}_{jx})$$

where k and j denote the interacting spins and $J_{k,j}$ are the respective coupling strengths. Since J is typically given in units of Hertz, the Hamiltonian $\hat{\mathcal{H}}_J$ has to be multiplied by the factor of 2π in order to result in angular frequency units. Due to the fact that all bilinear terms commute with each other, the effect of an isotropic coupling Hamiltonian $\hat{\mathcal{H}}_{\text{IM}}$ on transversal coherence can be described using

^[153] J. S. Waugh. *Journal of Magnetic Resonance* **1986**, 68, 189–192.

^[154] M. H. Levitt, R. Freeman and T. Frenkiel. *Journal of Magnetic Resonance* **1982**, 50, 157–160.

^[155] P. Caravatti, L. Braunschweiler and R. R. Ernst. *Chemical Physics Letters* **1983**, 100, 305–310.

^[156] D. P. Weitekamp, J. R. Garbow and A. Pines. *The Journal of Chemical Physics* **1982**, 77, 2870–2883.

^[157] D. P. Burum and W. K. Rhim. *The Journal of Chemical Physics* **1979**, 71, 944–956.

^[158] J. Klages et al. *Journal of Magnetic Resonance* **2007**, 189, 217–227.

^[161] A. Garon, R. Zeier and S. J. Glaser. *Physical Review* **2015**, A91, 042122.

⁴⁹ Note, there is still the high field truncation of any spin tensor component T_l^m with $m \neq 0$ induced by the Zeeman interaction (Section 1.3.2), as well as, motional averaging e.g. due to fluctuations of bond angles (Section 1.3.2).^[36,37]

⁵⁰ A further truncation of the isotropic Hamiltonian is elaborately described in Section 2.5.

⁵¹ Mixing via dipolar couplings is likewise possible and is commonly referred to as *dipolar mixing*.^[159,160]

Equation (1.4.10) and we obtain:⁵²

$$\begin{aligned}
 \hat{I}_{1x} & \xrightarrow{\pi J(2\hat{I}_{1x}\hat{I}_{2x})t} \hat{I}_{1x} \\
 & \xrightarrow{\pi J(2\hat{I}_{1y}\hat{I}_{2y})t} \cos(\pi Jt) \hat{I}_{1x} - \sin(\pi Jt) 2\hat{I}_{1z}\hat{I}_{2y} \\
 & \xrightarrow{\pi J(2\hat{I}_{1z}\hat{I}_{2z})t} \cos^2(\pi Jt) \hat{I}_{1x} - \cos(\pi Jt) \sin(\pi Jt) 2\hat{I}_{1z}\hat{I}_{2y} \\
 & \quad + \sin(\pi Jt) \cos(\pi Jt) 2\hat{I}_{1y}\hat{I}_{2z} + \sin^2(\pi Jt) \hat{I}_{2x}.
 \end{aligned} \tag{2.3.1}$$

Such a simplified solution can, however, only be applied if *no* additional Zeeman interaction $\hat{\mathcal{H}}_Z$ is considered. This is based on the fact that the motion induced by the Zeeman term imposes a time-dependence on the isotropic Hamiltonian in spin space and it can no longer be considered *inhomogeneous* (see Section 1.1.1). It is further interesting to note that for the considered *two-spin* system a distinct similarity to planar mixing (Section 2.2) is given which is due to commutation of state and Hamilton operator ($[\hat{I}_{1x}, 2\hat{I}_{1x}\hat{I}_{2x}] = 0$) in the first line of Equation (2.3.1) – the term $2\hat{I}_{1x}\hat{I}_{2x}$ is, hence, without consequences. For systems consisting of more than two spins, however, cross-terms of multiple spins come in to play (again, the Hamiltonian is no longer inhomogeneous) and the transfer from planar and isotropic mixing exhibits a fundamentally different behavior as shown in Figure 2.1. In early NMR literature it was already discovered that no J -modulation occurs under spin lock^[76,162] and with $[\hat{\mathcal{H}}_{\text{IM}}, \sum_k \hat{I}_{k\alpha}] = 0$, one can further state:

$$\sum_k \hat{I}_{k\alpha} \xrightarrow{\hat{\mathcal{H}}_J t} \sum_k \hat{I}_{k\alpha} \tag{2.3.2}$$

where, in contrast to planar mixing, α denotes an *arbitrary* axes. Hence, isotropic mixing does not only suppress the apparent J coupling evolution, it *additionally* preserves *all* axes of the sum over all state operators ($\sum_k \hat{I}_{k\alpha}$). As mentioned already for PM, spin preservation fails if symmetry is broken i.e. the states of involved spins differ (e.g. in amplitude) – an *observable* transfer between considered spins would occur as shown in Equation (2.3.1). The preservation of spin states can be used e.g. to retain a spin polarization reservoir for rapid experimental repetitions with low flip angle excitation. In the following a low-energy isotropic mixing sequence is introduced that shall be applied in a DOSY experiment – spin polarization is preserved and reduced measurement time can be obtained from fast experimental repetition rates.

Ernst Angle Excitation

The theory of low flip angle excitation is based on the principle that stored polarization can directly be used in a subsequent experiment. Therefore, a reduction of the recovery delay is possible which results in a shorter experimental duration. The theoretical background, neglecting offset effects, shall be discussed shortly using a similar nomenclature found in literature.^[17,100,163] The length of the pulse sequence is assumed to be zero and any loss of polarization shall be accounted for by a factor (f_z).⁵³

Preserved polarization after the pulse sequence and, hence, directly before acquisition shall be denoted $M_z(0_+)$. It can be calculated from the initial polarization $M_z(0_-)$, the factor f_z and the excitation flip

^[162] E. J. Wells and H. S. Gutowsky. *The Journal of Chemical Physics* **1965**, *43*, 3414–3415.

^[163] M. R. Koos and B. Luy. *Journal of Magnetic Resonance* **2019**, *300*, 61–75.

⁵² A general and more compact form of Equation (2.3.1) can be derived from Braunschweiler^[5]:

$$\hat{I}_\alpha \xrightarrow{\hat{\mathcal{H}}_J t} \frac{1}{2} \hat{I}_{1\alpha} \cdot [1 + \cos(2\pi Jt)] + \frac{1}{2} \hat{I}_{2\alpha} \cdot [1 - \cos(2\pi Jt)] + (\hat{I}_{1\beta} \hat{I}_{2\gamma} + \hat{I}_{1\gamma} \hat{I}_{2\beta}) \cdot \sin(2\pi Jt)$$

where $\{\alpha, \beta, \gamma\}$ corresponds to a cyclic permutation of $\{x, y, z\}$.

⁵³ It shall be mentioned that in principle there is also a factor f_{xy} for loss in transverse coherence. However, it linearly scales the acquired signal and, hence, has no influence on the flip angle or the inter-scan delay.

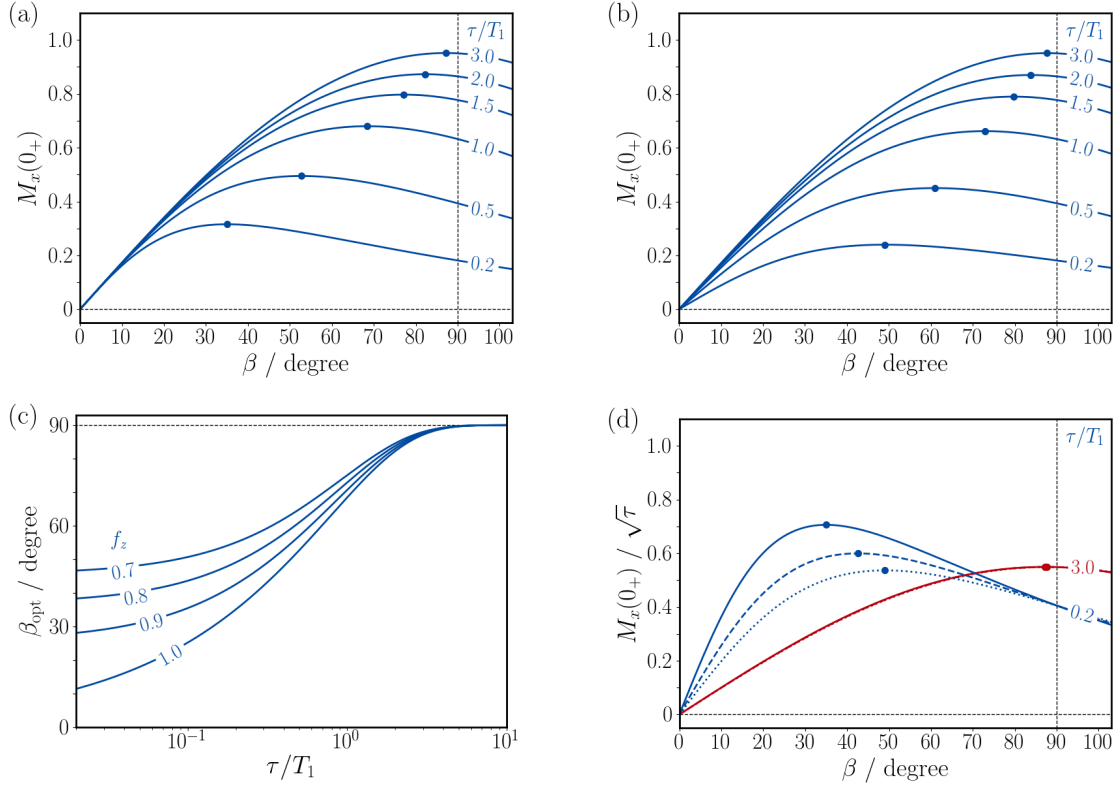


Figure 2.11: The steady-state intensity $M_x(0_+)$ with $f_z = 1$ (a) and $f_z = 0.8$ (b) is shown for various values of τ/T as indicated on lines. The maxima are highlighted by dots and corresponding flip angles β_{opt} are plotted against τ/T in (c) for various values of f_z as indicated on lines. In (d) the time-optimal sensitivity $M_x(0_+)/\sqrt{\tau}$ is plotted in blue ($\tau/T = 0.2$) and red ($\tau/T = 3.0$) with solid ($f_z = 1.0$), dashed ($f_z = 0.9$) and dotted lines ($f_z = 0.8$).

angle β with:

$$M_z(0_+) = M_z(0_-) \cdot f_z \cdot \cos \beta. \quad (2.3.3)$$

Further one can calculate the polarization $M_z(\tau)$ during the recovery delay τ from the equilibrium M_0 and $M_z(0_+)$ with:

$$M_z(\tau) = M_0 - [M_0 - M_z(0_+)] E_1 \quad (2.3.4)$$

where $E_1 = e^{-\tau/T_1}$ describes the polarization build-up with T_1 being the longitudinal relaxation time. If a steady state is assumed after a sufficiently large number of experimental repetitions one can state that $M_z(\tau) = M_z(0_-)$ which leads to:

$$M_z(0_-) = M_0 \frac{1 - E_1}{1 - E_1 \cdot f_z \cdot \cos \beta} \quad (2.3.5)$$

$$\text{and: } M_x(0_-) = M_0 \frac{1 - E_1}{1 - E_1 \cdot f_z \cdot \cos \beta} \cdot \sin \beta. \quad (2.3.6)$$

From Equation (2.3.6) one can calculate the intensity of the acquired signal $M_x(0_-)$ which depends on the flip angle β , the factor f_z and E_1 being determined by the ratio τ/T_1 . The signal intensities $M_x(0_-)$ assuming no loss in polarization ($f_z = 1$) is illustrated in Figure 2.11 (a) where maxima are highlighted by dots. It becomes clear that for short recovery delays ($\tau/T = 0.2$) the maximum signal intensity in a steady state is achieved by low flip angles. If a certain amount of polarization is lost

during the sequence it shall be noted that the maximum signal intensity is found for slightly higher flip angles as shown in Figure 2.11 (b) where $f_z = 0.8$. The optimal flip angle β_{opt} can be determined by the derivative of Equation (2.3.6) and it is calculated from $\beta_{\text{opt}} = \arccos(f_z E_1)$. In Figure 2.11 (c) the optimal flip angles are illustrated for different values of f_z . Due to the fact that an n -times shorter experiment can be recorded n -times during a certain duration, a higher signal intensity can be obtained for fast experiments. It is further worth noting that noise increases by \sqrt{n} and with this respect it is the signal per square-root time ($M_x(0_+)/\sqrt{\tau}$) that determines time-optimal sensitivity. As illustrated in Figure 2.11 (d) the factor f_z has a stronger influence for fast repetition rates (blue) while for long recovery delays (red) it is negligible and nearly congruent lines are found.

2.3.2 Isotropic Perfect Echo

Isotropic mixing from continuous irradiation is associated to a considerable energy dissipation and, in order to avoid hardware damage or sample heating, it has to be applied with special care – this especially holds if used in fast experiments. For this reason two *isotropic perfect echoes* (IPE) are proposed that result in low-energy isotropic mixing⁵⁴ as can be seen from a transformation of the weak coupling Hamiltonian. In analogy to planar mixing from perfect echo (Section 1.6.3), again, the toggling frame (Section 1.6) and average Hamiltonian theory (Section 1.7) is used for an elaborate discussion and it shall, further, be shown that the IPE-sequences allow spin state preservation at low energy dissipation on time scales that are well suitable for DOSY.

The IPE-sequences are illustrated in Figure 2.12 and 2.13 which are both composed of two basic cycles (BC) that result in isotropic mixing. While the former is based on simple Hahn echoes, in the latter double echoes are used and, therefore, the sequences shall be referred to as IPE-1 and IPE-2, respectively. Clearly, energy consumption during IPE-1 is reduced, however, IPE-2 promises higher quality echoes already for fewer basic cycles. For both sequences the basic cycles are each composed of three (double) echoes being split by two 90° pulses and it is worth mentioning that, if all 180° pulses are removed, a distinct similarity to the WAHUA sequence is given.⁵⁵ For both sequences the time-evolution of a weak coupling and a Zeeman Hamiltonian in the toggling frame shall be analyzed – both Hamiltonians are illustrated in Figure 2.12 and 2.13 for IPE-1 and IPE-2, respectively.

If the weak coupling ($\hat{\mathcal{H}}_{R,zz}$) or the Zeeman Hamiltonian in the *rotating frame* ($\hat{\mathcal{H}}_{R,z}$) of a two spin system is transformed to the toggling frame of a IPE-sequence, various bilinear and linear terms arise. These are of the form $\hat{\mathcal{H}}_{T,zz}^{\gamma\gamma'}$ and $\hat{\mathcal{H}}_{T,z}^{\gamma''}$, respectively, where the superscript denotes the Hamiltonian in the toggling frame and $\{\gamma, \gamma', \gamma''\}$ correspond to arbitrary Cartesian axes of $\{x, y, z\}$. While the zeroth order average Hamiltonian of $\hat{\mathcal{H}}_{T,z}^{\gamma''}$ during two basic cycles is always zero (last three rows), for $\hat{\mathcal{H}}_{T,zz}^{\gamma\gamma'}$ an effective Hamiltonian is accumulated mainly from three non-zero components (first three rows). These are:

$$\begin{aligned}\hat{\mathcal{H}}_{T,zz}^{xx'}(\tau) &= \hat{k}_{zz}^{xx'}(\tau) \cdot \sum_{k>j} 2\pi J_{k,j} \cdot \hat{I}_{kx} \hat{I}_{jx}, \\ \hat{\mathcal{H}}_{T,zz}^{yy'}(\tau) &= \hat{k}_{zz}^{yy'}(\tau) \cdot \sum_{k>j} 2\pi J_{k,j} \cdot \hat{I}_{ky} \hat{I}_{jy} \\ \text{and: } \hat{\mathcal{H}}_{T,zz}^{zz'}(\tau) &= \hat{k}_{zz}^{zz'}(\tau) \cdot \sum_{k>j} 2\pi J_{k,j} \cdot \hat{I}_{kz} \hat{I}_{jz}\end{aligned}\tag{2.3.7}$$

where $\hat{k}_{zz}^{xx'}(\tau)$, $\hat{k}_{zz}^{yy'}(\tau)$ and $\hat{k}_{zz}^{zz'}(\tau)$ are the time-dependent coefficients and $J_{k,j}$ is the size of the coupling

⁵⁴ It is noteworthy that hard pulses are used during the proposed sequences and, hence, the *maximum* power is larger compared to common IM-sequences. Due to numerous delays in IPE, however, the *average* power is reduced and so is the required energy with respect to a particular mixing time.

⁵⁵ Note, WAHUA-like modifications are likewise used in solid state NMR to achieve transfer from isotropic mixing via *heteronuclear dipolar* coupling while suppressing *homonuclear dipolar* couplings.^[155–157]

between spin \hat{I}_k and \hat{I}_j . To first approximation, the zeroth order average Hamiltonian $\bar{\mathcal{H}}_{T,zz}^{\text{IM}}$ is determined by the terms $\hat{\mathcal{H}}_{T,zz}^{x'x'}$, $\hat{\mathcal{H}}_{T,zz}^{y'y'}$ and $\hat{\mathcal{H}}_{T,zz}^{z'z'}$ and, hence, the IPE-sequences result in effective isotropic mixing with threefold reduced coupling strength:

$$\begin{aligned}\bar{\mathcal{H}}_{T,zz}^{\text{IM}} &\approx \hat{\mathcal{H}}_{T,zz}^{x'x'} + \hat{\mathcal{H}}_{T,zz}^{y'y'} + \hat{\mathcal{H}}_{T,zz}^{z'z'} \\ &\approx \frac{1}{3}\hat{\mathcal{H}}_J = \frac{2}{3}\pi \sum_{k>j} J_{k,j} \cdot (\hat{I}_{kz}\hat{I}_{jz} + \hat{I}_{ky}\hat{I}_{jy} + \hat{I}_{kx}\hat{I}_{jx}).\end{aligned}\tag{2.3.8}$$

In order to eliminate odd-ordered higher terms in the average Hamiltonian (Section 1.7.3) both sequences are designed in a way that a purely symmetric Hamiltonian in the toggling frame $\hat{\mathcal{H}}_{T,zz}^{\gamma\gamma'}$ is obtained after 4 and 2 basic cycles for IPE-1 and IPE-2, respectively. Further, the expansion to an extended number of basic cycles is performed starting from the center of the sequence. This way, it is made sure that the second part always corresponds to a time- and phase-inverted version of the first part of the sequence and symmetry properties are retained. With given *phase sequences*⁵⁶ for IPE-1 and IPE-2 different objectives are pursued. First, and most importantly, the coupling and Zeeman Hamiltonian in the toggling frame *always* stays symmetric (for IPE-1 after 4 basic cycles). Second, in the IPE-1 sequence coupling evolution during 180° pulses is uniformly distributed on all three components after 8 basic cycles – for IPE-2 this holds already for 2 basic cycles. Third, in both sequences the suppression of $\hat{\mathcal{H}}_{T,zz}^{x'y'}$ and $\hat{\mathcal{H}}_{T,zz}^{y'x'}$, as well as $\hat{\mathcal{H}}_{T,zz}^{y'z'}$ and $\hat{\mathcal{H}}_{T,zz}^{z'y'}$ in the zeroth order average Hamiltonian is obtained after 8 and 16 basic cycles, respectively. In order to compensate linear phases induced by the 90° pulses, in each basic cycle the first and last delay is extended where $\Delta' = \Delta + \frac{2}{\pi}\tau_{90^\circ}$ and $\Delta'' = \Delta + \frac{4}{\pi}\tau_{90^\circ}$ with τ_{90° being the 90° pulse length. Being well aware of possible threefold symmetry properties of elaborate WAHUA-cycles for the suppression of second order terms in the average Hamiltonian, still, the given sequence is chosen. The choice is based on the fact that for the proposed IPE no additional 90° pulses are required and, assuming non-perfect pulses, no undesired terms are introduced to the zeroth order average Hamiltonian. Furthermore, phase sequences are shorter, hence, more flexible and experimental data revealed better performance than with the threefold symmetry discussed in literature.^[28] Note, for the reason of clarity pulse widths in Figure 2.12 and 2.13 are largely exaggerated and during hard pulses coupling evolution is of minor importance – this, however, might not apply if shaped pulses are used.

⁵⁶ Note, the term supercycle shall be avoided, since, in given IPE sequences, entire basic cycles are not subject to phase cycling. Rather, the pulses within successive basic cycles follow a certain sequence of phases.

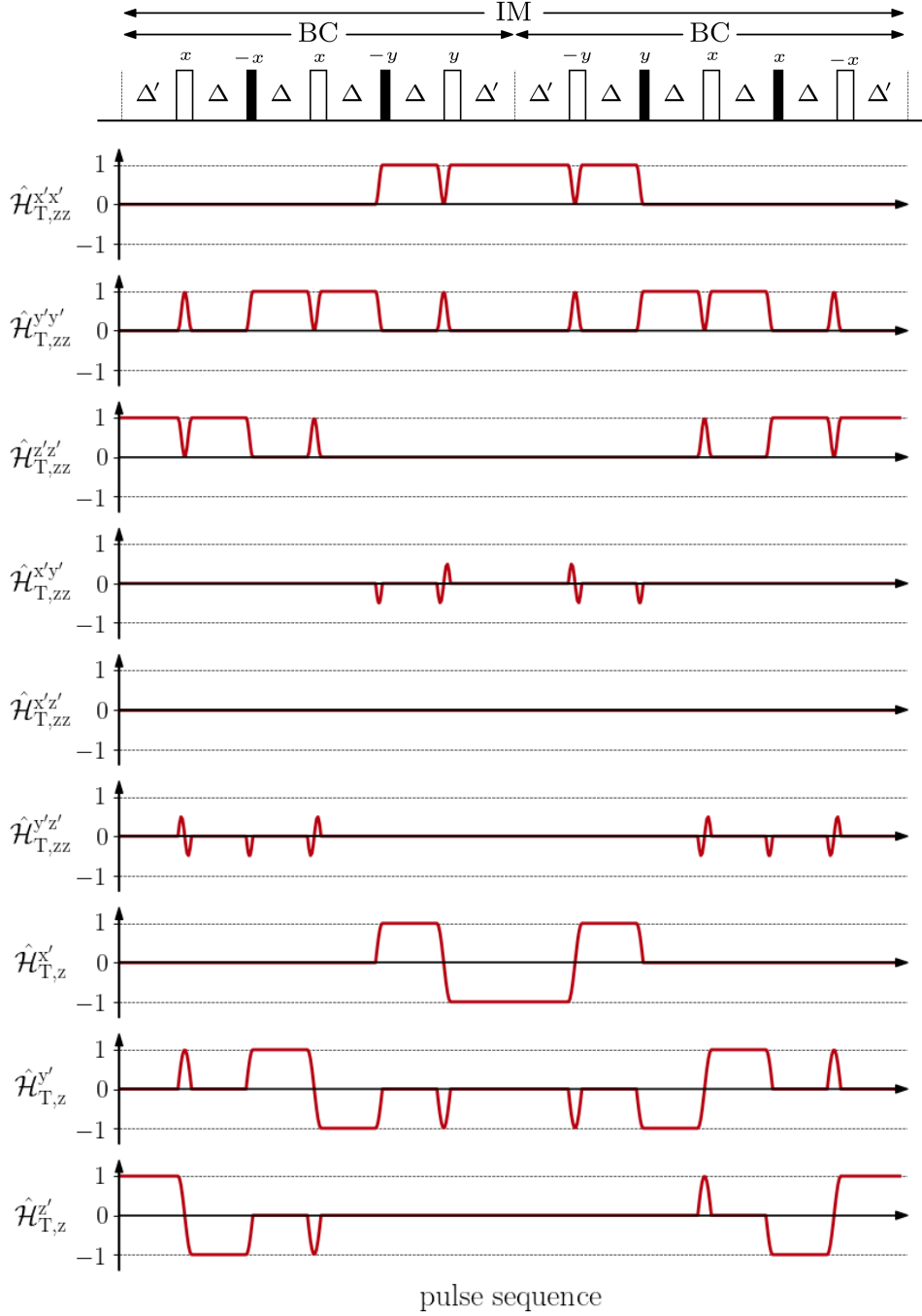


Figure 2.12: The time-dependent Hamiltonian of a weakly coupled two-spin system in the toggling frame of IPE-1 is illustrated. Bilinear terms (first 6 rows) originate from weak coupling, while linear terms (last 3 rows) are based on the Zeeman Hamiltonian. Omitted terms are congruent to the ones shown and, hence, only 9 out of 16 basis operators are given. In order to compensate linear phases induced by 90° pulses, the first and last delay in each basic cycle is extended to $\Delta' = \Delta + \frac{2}{\pi}\tau_{90^\circ}$ with τ_{90° being the 90° pulse length – for phase-compensated shaped pulses $\Delta' = \Delta$. For IPE-1, a complete symmetric toggling Hamiltonian is obtained after 4 basic cycles (BC) and, including coupling evolution during 180° pulses, uniform isotropic mixing is obtained after 8 basic cycles. The second half of the sequence is created by time- and phase-inversion of the first half, where phase sequences for 90° and 180° pulses are given as: $\phi_{90^\circ}^{\text{ps}} = \{-x, -y, y, x\} \{-x, y, -y, x\} \{x, -y, y, -x\} \{x, y, -y, -x\}$, $\phi_{180^\circ}^{\text{ps}} = \{x, x, y, -y, x, -x\} \{-y, -y, x, x, -y, -y\} \{-x, x, y, -y, x, x\} \{-y, -y, x, x, -y, -y\}$

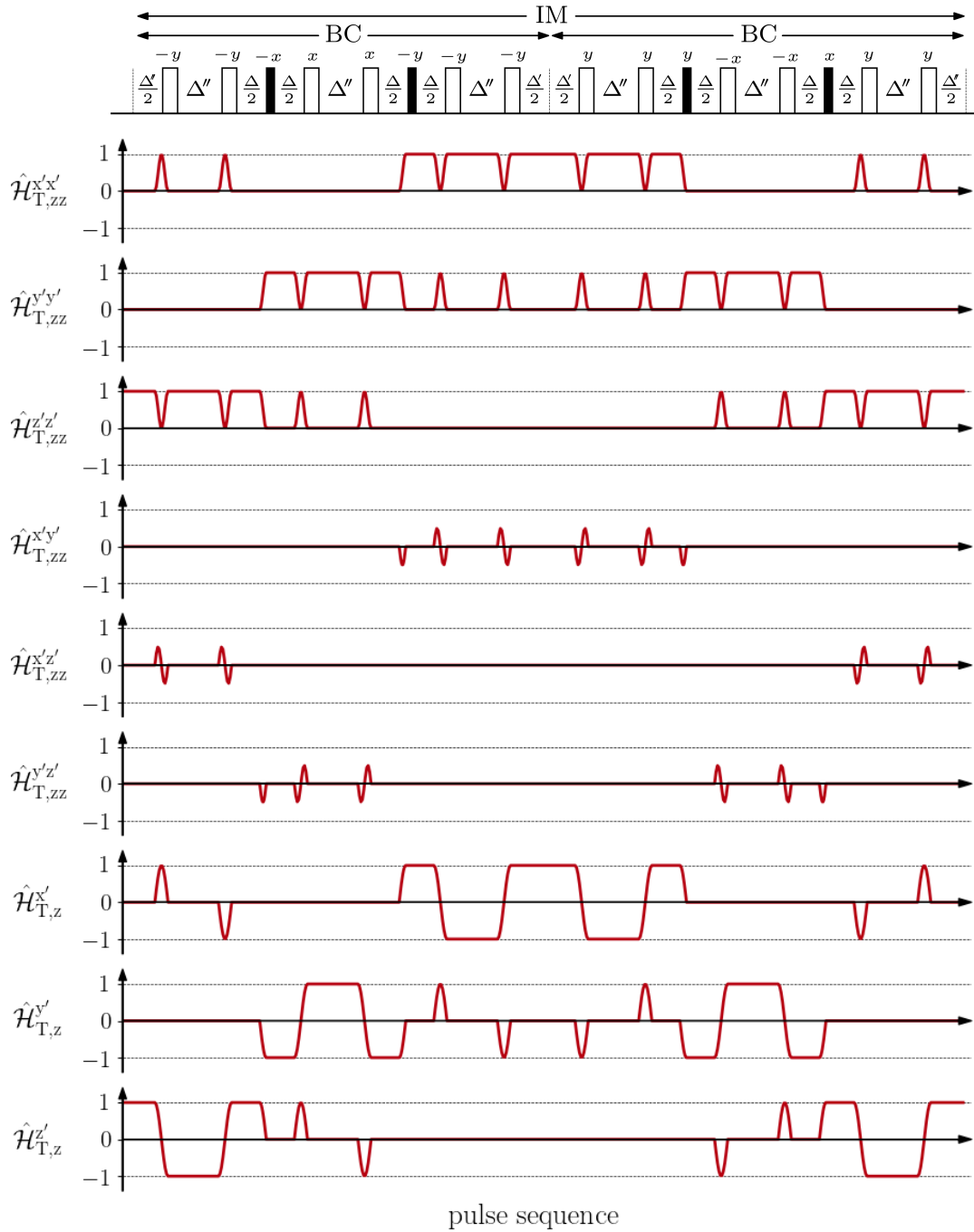


Figure 2.13: The time-dependent Hamiltonian of a weakly coupled two-spin system in the toggling frame of IPE-2 is illustrated. Bilinear terms (first 6 rows) originate from weak coupling, while linear terms (last 3 rows) are based on the Zeeman Hamiltonian. Omitted terms are congruent to the ones shown and, hence, only 9 out of 16 basis operators are given. In order to compensate linear phases induced by 90° pulses, certain delays in each basic cycle are extended to $\Delta' = \Delta + \frac{4}{\pi}\tau_{90^\circ}$ with τ_{90° being the 90° pulse length – for phase-compensated shaped pulses $\Delta' = \Delta$. For IPE-2, a complete symmetric toggling Hamiltonian is obtained after 2 basic cycles (BC) and, including coupling evolution during 180° pulses, uniform isotropic mixing is obtained after 2 basic cycles. The second half of the sequence is created by time- and phase-inversion of the first half, where phase sequences for 90° and 180° pulses are given as: $\phi_{90^\circ}^{\text{ps}} = \{-x, -y, y, x\} \{-x, y, -y, x\} \{x, -y, y, -x\} \{x, y, -y, -x\}$, $\phi_{180^\circ}^{\text{ps}} = \{-y, -y, x, x, -y, -y\} \{y, y, -x, -x, y, y\}$

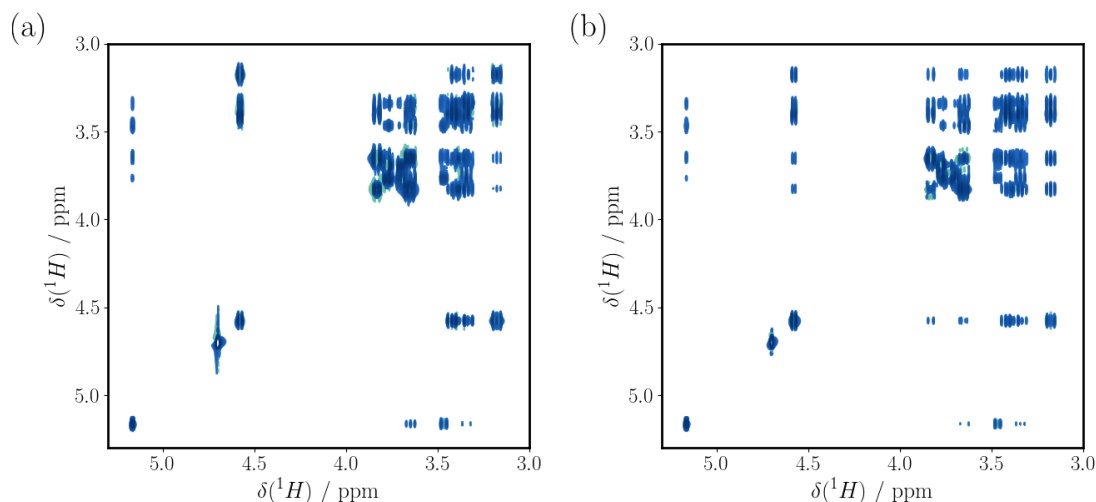


Figure 2.14: DIPSIs-2 (a) and hard pulse IPE-1 (b) in a conventional TOCSY of Glucose. While for DIPSIs the mixing time is set to $\tau_m \approx 55$ ms, for IPE-1, eight basic cycles are used with a delay $\Delta = 3.125$ ms resulting in a total mixing time of $\tau_m \approx 150$ ms.

Experimental

In order to provide experimental proof that isotropic mixing is obtained from IPE-sequences, conventional TOCSY experiments were recorded for Glucose. The spectra using DIPSIs and IPE-1 are plotted with identical contour levels in Figure 2.14 (a) and (b), respectively. In both cases comparable acquisition parameters were used. In this respect, it shall again be mentioned that the coupling strength of isotropic mixing from IPE is reduced by a factor of 3 and, hence, an extended mixing time has to be used for comparable results. Indeed, both spectra are very similar and due to longer mixing times, an increased relaxation loss from IPE-1 is expected. Despite the relaxation penalty, one should keep in mind that, as shown for PM in the previous Section 2.2, also the IPE-sequences can be used in combination with state-of-the-art shaped pulses and e.g. broadband *isotropic* mixing can be obtained. For spin state preservation by isotropic mixing, on the other hand, the transfer speed is of no importance and an apparent transfer is not desired. For this reason, a further *in silico* and experimental examination on spin state preservation from proposed sequences is conducted.

Spin State Preservation from IPE-Sequences: Numerical Simulations

In contrast to planar mixing where only a single axis of the states' sum can be preserved (this is commonly referred to as J -refocusing), the approach using isotropic mixing is more general and all axes can be retained. Numerical simulations based on the spin density formalism (Section 1.2) are used to examine the effect of the IPE-1 and IPE-2 sequence on a weakly coupled two-spin system. In-phase coherence $F_\alpha = \sum_k \hat{I}_{k\alpha}$ is chosen as initial state with $\alpha = \{x, y, z\}$ and, again, in-phase coherence is observed after isotropic mixing. The results are shown for IPE-1 and IPE-2, each applied with two basic cycles, in Figure 2.15 and 2.16, respectively.¹ Clearly, both sequences are able to preserve the initial state F_α and, as already indicated by the simulations of the Hamiltonian in the toggling frame (Figure 2.12 and 2.13), a better quality is obtained from IPE-2 if only two basic cycles are considered. However, it is shown in the Appendix 5.2.1 that imperfections observed for IPE-1 are suppressed for additional basic cycles or if shaped pulses (e.g. IMP, Section 2.4.16) are used. An experimental verification is given below.

¹ Note, the initial state is preserved at a considerably high level close to one and transfer to operators other than the ones shown can, hence, be largely excluded.

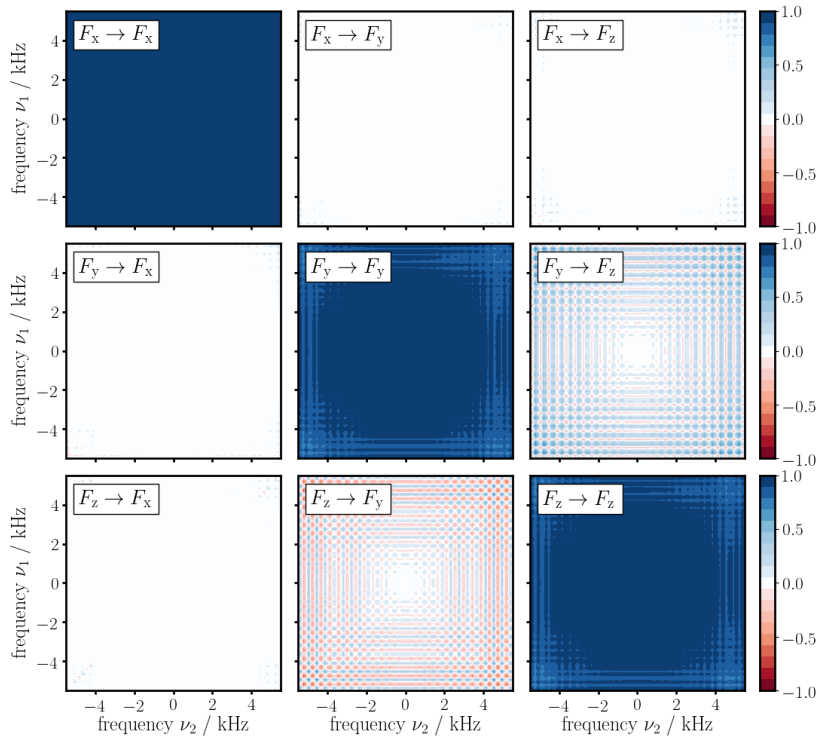


Figure 2.15: The preservation of spin states ($F_\alpha = \sum_k \hat{I}_{k\alpha}$ with $\alpha = \{x, y, z\}$) by IPE-1 with two basic cycles is examined for a two-spin system using numerical simulations.

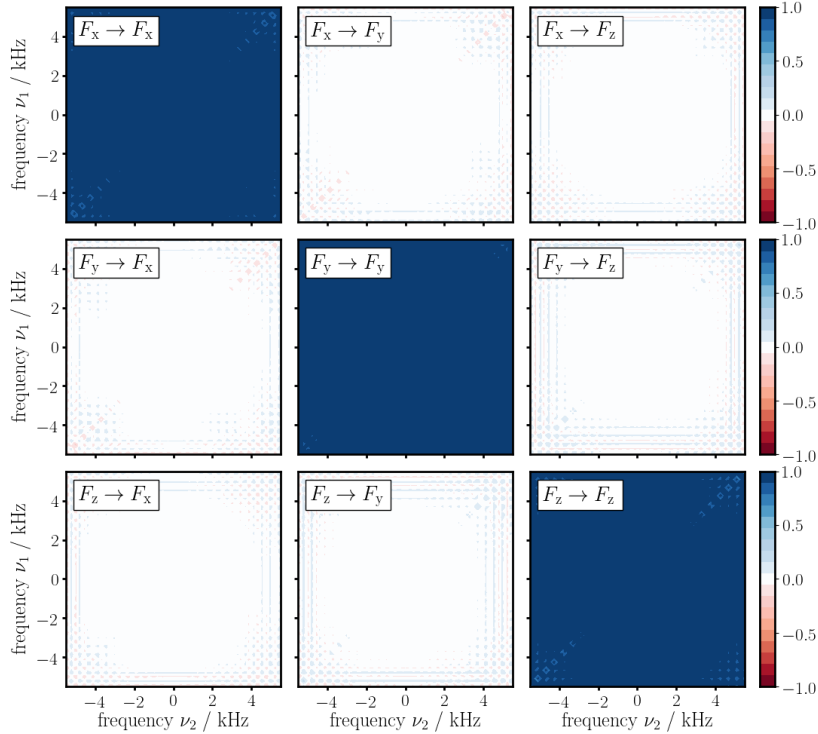


Figure 2.16: The preservation of spin states ($F_\alpha = \sum_k \hat{I}_{k\alpha}$ with $\alpha = \{x, y, z\}$) by IPE-2 with two basic cycles is examined for a two-spin system using numerical simulations.

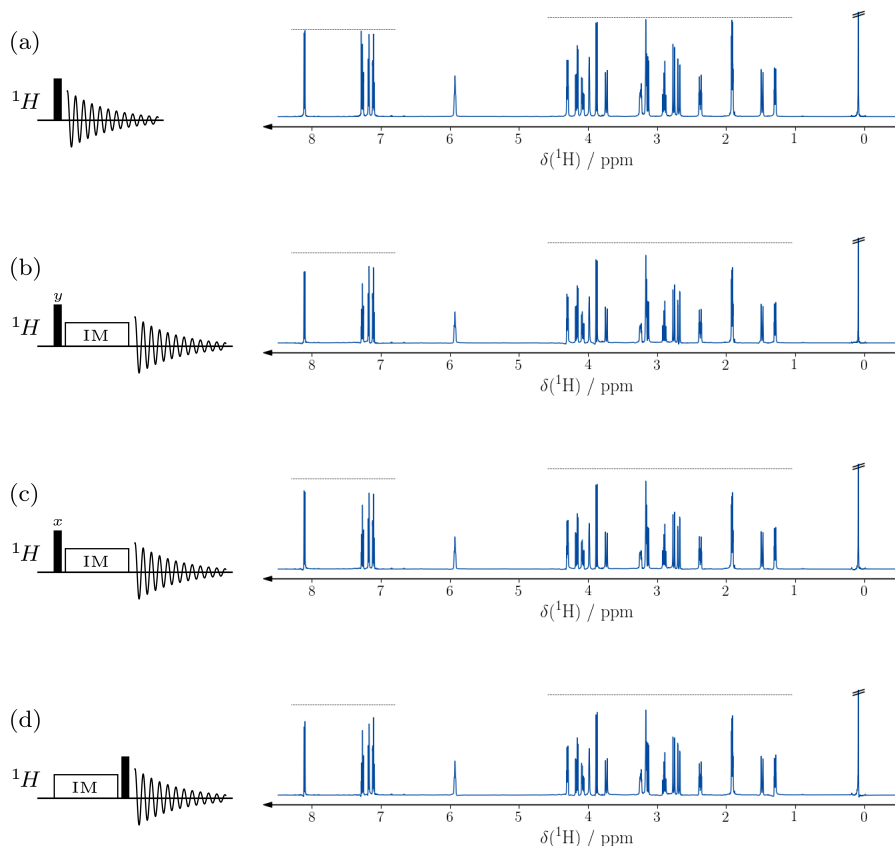


Figure 2.17: A conventional proton 1D (a) is compared to spectra where IPE-1 is applied to \hat{F}_x (b), \hat{F}_y (c) and \hat{F}_z (d). While pulse sequences are illustrated on the left, resulting spectra of strychnine in CDCl_3 are shown on the right. For IPE-1, eight basic cycles and a 1 ms IMP (Section 2.4.16) were used with $\Delta = 1.5$ ms corresponding to a total mixing time of ≈ 96 ms.

Spin State Preservation from IPE-Sequences: Experimental Verification

In analogy to numerical simulations shown in the previous section, pulse sequences were designed to examine spin state preservation. These are based on a preparation of an initial spin state (\hat{F}_x , \hat{F}_y and \hat{F}_z) before mixing by IPE-1. Experiments and resulting spectra of strychnine are shown in Figure 2.17 and a comparison to a conventional proton 1D is given. As expected, for *all* preserved axes (x, y, z) very similar spectra are obtained that do not exhibit dispersive anti-phase from homonuclear coupling during IM – it is evident that J -refocusing is achieved. Clearly, a certain loss due to relaxation is expected as indicated by horizontal dashed lines² and minor phase errors ($< 5^\circ$) from pulse imperfections might be encountered.

Further, the experiments illustrated in Figure 2.17 are tested with variable mixing times for IPE-1 and IPE-2. Additionally, a comparison to isotropic mixing from continuous irradiation, DIPSI, is given. For DIPSI the RF amplitude was reduced in order to achieve longer mixing times and, hence, a narrower bandwidth is covered. The results are shown in Figure 2.18, where a sum over all signals of the non-anomeric coupling network of α - and β -D-Glucose is normalized with respect to the conventional proton 1D and plotted against the mixing time – relaxation loss during sequences is included. For the given example, IPE-sequences using 4 (blue) and 8 basic cycles (red) perform better or equal to DIPSI (black). Considering longer mixing times or large coupling networks, it should, however, be noted that

² Non-coupled spins spend 2/3 of the mixing time in the transverse plane and 1/3 in a longitudinal state (\hat{I}_z and $-\hat{I}_z$). Hence, it is expected that the relaxation loss during mixing can be calculated accordingly.

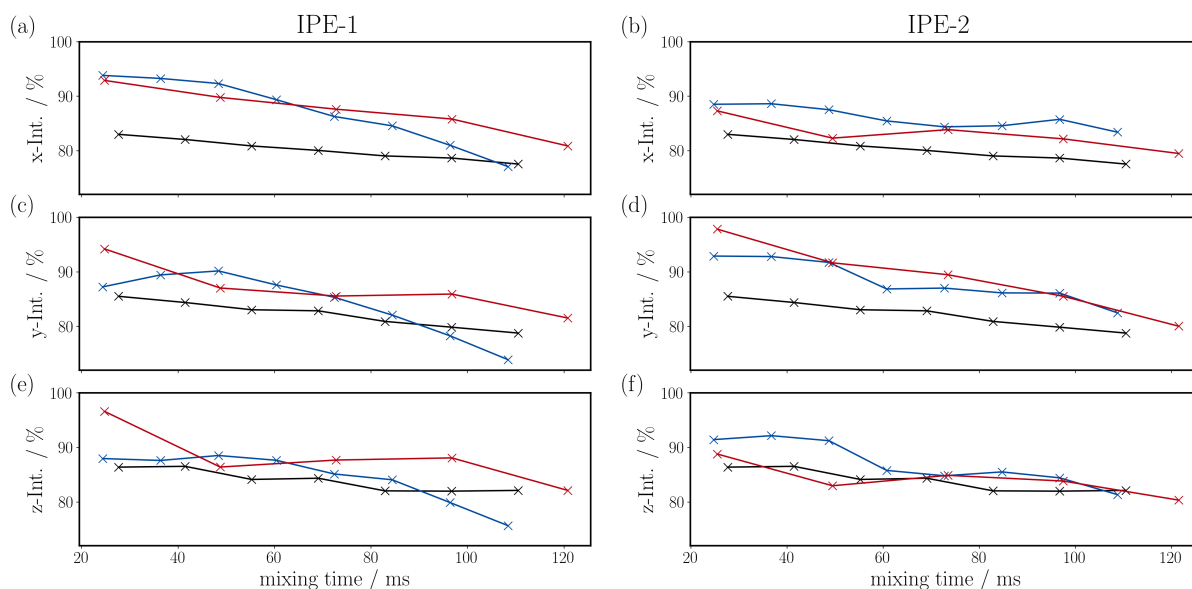


Figure 2.18: Spin state preservation from IPE-1 (left column) and IPE-2 (right column) is shown for 4 (blue) and 8 basic cycles (red) and compared to DIPSI (black). The values are calculated from the sum over all signals of the non-anomeric coupling network of α - and β -D-Glucose and normalized with respect to conventional proton 1D – a certain decay from relaxation is, hence, expected. Spin states were prepared in \hat{F}_x ((a) and (b)), \hat{F}_y ((c) and (d)) and \hat{F}_z ((e) and (f)). For better visibility experimental points are connected by lines which should not be confused with interpolation.

the assumption of zeroth order Hamiltonian might break down and extended mixing sequences with additional basic cycles should be used (see Section 1.7.3).⁵⁷ DIPSI, in this respect, seems to be superior for longer mixing times and larger spin systems where typically an increased number of couplings is found – further, it benefits from the presence of strong coupling. IPE-sequences, on the other hand, exhibit a considerably lower average power and for the illustrated cases in Figure 2.18 the introduced energy is reduced by a factor of 3.5 to up to 54 (depending mainly on the value of Δ).⁵⁸ This, in turn, allows the convenient application of IPE in fast experiments, where typically recycle delays are considerably shorter compared to conventional experiments and only a controlled measure of energy should be introduced in order to avoid hardware damage or sample heating. In the following Section 2.3.3 different fast DOSY experiments shall be proposed, that are based on the above introduced IPE-sequences.

⁵⁷ Note, the values shown in Figure 2.18 (e) and (f) correspond to the factor f_z used in Equation (2.3.6) and Figure 2.11.

⁵⁸ Considering RF amplitudes of 10 kHz for DIPSI and 25 kHz for hard pulses in IPE (in both cases IM is achieved on a similar bandwidth of 10 kHz), one can conclude that the maximum power for IPE is increased by a factor of 6.25. The highest average power in Figure 2.18 is given for IPE-2 with $\Delta = 0.5$ ms and, hence, during 3.14 ms hard pulses are applied for 140 μ s – in turn this corresponds to a reduction in average power by a factor of 22.4. Hence, in total the introduced energy during the considered time of 3.14 ms is reduced by a factor of $22.4/6.25 \approx 3.5$. Equivalent calculations can be made for all other cases.

2.3.3 Fast DOSY Using the Isotropic Perfect Echo

Already in early NMR literature it was discovered that magnetic field inhomogeneity during Hahn echoes causes a signal attenuation due to self-diffusion.^[108,164,165] A quantification was first achieved by Stejskal and Tanner who used pulsed field gradients (PFG, Section 1.3.5) in a spin echo and provided a profound theoretical treatment for the determination of diffusion coefficients.^[7] An improved pulse sequence has been proposed shortly after – it is based on a stimulated echo (STE) where magnetization during the diffusion delay is stored in a longitudinal state.^[166] This way, homonuclear coupling evolution is largely suppressed and transverse relaxation loss is reduced, which is particularly beneficial for samples where $T_1 \gg T_2$. Further, the effects of eddy currents in metal parts of the probe induced by large gradient amplitudes can be avoided by means of a longitudinal-eddy-current delay^[167] or bipolar gradients.^[168] Another obstacle is formed by small temperature gradients during the experiment which in turn causes convection. Especially for low-viscous solvents an increased migration within the sample is encountered that can easily be mistaken for faster self diffusion.⁵⁹ By means of a second echo with inversed pulsed field gradients, it is, however, possible to compensate the convection bias of a constant laminar flow.^[170,171] All along, diffusion-ordered spectroscopy (DOSY)^[8] has evolved to become a widely used method that allows the non-invasive extraction of molecular properties (e.g. size and shape) – numerous applications and modifications are summarized in different reviews.^[172,173]

In the present section, the conception of spin state preservation from isotropic mixing shall be introduced to DOSY, which allows faster experimental repetitions and, thus, reduced overall measurement time at high sensitivity. In contrast to fast DOSY using a spin echo,^[174] J -coupling evolution shall be suppressed from mixing and spectra are obtained at high resolution – an exchange compensated version is also conceivable.^[102] Compared to a conventional DOSY sequence with convection compensation, the measurement time can be reduced by more than one order of magnitude and well-resolved spectra are obtained in less than half a minute.

Introduction

The most basic DOSY sequence is illustrated in Figure 2.19 where two pulsed field gradients are applied during a spin echo as originally used in literature.^[7] Further, the evolution of transverse magnetization during the experiment is illustrated at significant time points i.e. before and after each pulsed field gradient. The first gradient causes magnetization with uniform phase (Figure 2.19 (b)) to acquire a phase that depends on its z -coordinate (Figure 2.19 (c)) – the process is commonly referred to as *gradient encoding*. During a specified period (Δ_D), diffusion subsequently causes molecules to migrate within the sample (Figure 2.19 (d)) and *decoding* from a second pulsed field gradient does not allow complete refocusing (Figure 2.19 (e)). The consequence is signal attenuation that depends on the PFG's duration (δ) and strength (g), as well as on the period's length (Δ_D) during which diffusion is observed.

^[164] H. Y. Carr and E. M. Purcell. *Physical Review* **1954**, *94*, 630–638.

^[165] A. G. Anderson et al. *Journal of Applied Physics* **1955**, *26*, 1324–1338.

^[166] J. E. Tanner. *The Journal of Chemical Physics* **1970**, *52*, 2523–2526.

^[167] S. J. Gibbs and C. S. Johnson. *Journal of Magnetic Resonance* **1991**, *93*, 395–402.

^[168] D. H. Wu, A. Chen and C. S. Johnson. *Journal of Magnetic Resonance* **1995**, *A115*, 260–264.

^[170] A. Jerschow and N. Müller. *Journal of Magnetic Resonance* **1997**, *125*, 372–375.

^[171] A. Jerschow and N. Müller. *Journal of Magnetic Resonance* **1998**, *132*, 13–18.

^[172] C. Johnson. *Progress in Nuclear Magnetic Resonance Spectroscopy* **1999**, *34*, 203–256.

^[173] G. Pagès et al. *The Analyst* **2017**, *142*, 3771–3796.

^[174] X. Guo et al. *Macromolecular Chemistry and Physics* **2019**, *220*, 1900155.

⁵⁹ In electrophoretic NMR, it is also possible to determine the *translation* of charged particles by field inhomogeneities.^[169] Considering a unidirectional flow, the signal acquires a phase that is directly proportional to its migration in the sample. Within a spatially closed system, however, convection causes a signal attenuation as likewise expected for self diffusion.

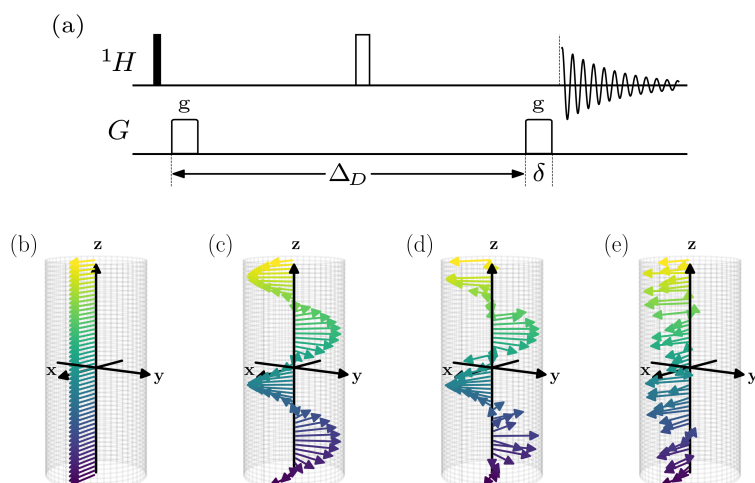


Figure 2.19: A basic SE-DOSY sequence is illustrated in (a) where Δ_D is the diffusion delay and the gradients are determined by the length δ and strength g . Transverse magnetization before (b) and after the encoding gradient (c), as well as before (d) and after decoding gradient (e) is shown below.

The signal attenuation can be quantified by means of the theory provided by Stejskal and Tanner^[7] which leads to the so-called Stejskal-Tanner equation. It allows the determination of diffusion coefficients and in the given case, it results in a Gaussian decay of the form:

$$\mathbf{I}(g) = \mathbf{I}(0) \exp \left\{ -D\gamma^2\delta^2 \left(\Delta_D - \frac{\delta}{3} \right) \cdot g^2 \right\} \quad (2.3.9)$$

where \mathbf{I} is the signal's intensity according to the gradient strength (g) and γ is the gyromagnetic ratio.⁶⁰ Equivalent equations for more elaborate experiments are deduced in literature.^[175,176] Repeating the experiment of Figure 2.19 (a) multiple times with increasing gradient strength, it is possible to sample the signal attenuation from diffusion and the diffusion coefficient D can be extracted using Equation 2.3.9. Molecular properties can be derived from the coefficient D which is described by the Stokes-Einstein equation:

$$D = \frac{kT}{6\pi\eta r_H} \quad (2.3.10)$$

where kT corresponds to the thermal energy and the denominator determines the so-called friction factor of a spherical molecule with η being the solvent's viscosity and r_H being the hydrodynamic radius.

Pulse Sequence

DOSY sequences that are based on a stimulated echo are able to sufficiently prevent homonuclear coupling evolution during the experiment and absorptive, in-phase spectra at high resolution are obtained. On the other hand, the STE suffers from the fact, that only half the signal can be transferred to a longitudinal state. The other part has to be dephased by a spoiler gradient in order to avoid artifacts and sensitivity is reduced significantly. In convection compensated versions the STE has to be applied even twice and only a fourth of the signal can be observed. Using spin state preservation by isotropic mixing, on the other hand, it is possible to avoid the effect of homonuclear couplings and the full signal is available – optimal sensitivity can be obtained in combination with Ernst angle excitation.

^[176] D. Sinnaeve. *Concepts in Magnetic Resonance Part A* **2012**, 40A, 39–65.

⁶⁰ It should further be mentioned that, in principle, also the coherence order (Section 1.2.1) has to be considered. Commonly, single quantum coherence is measured in DOSY and, hence, the fact is usually neglected.^[175]

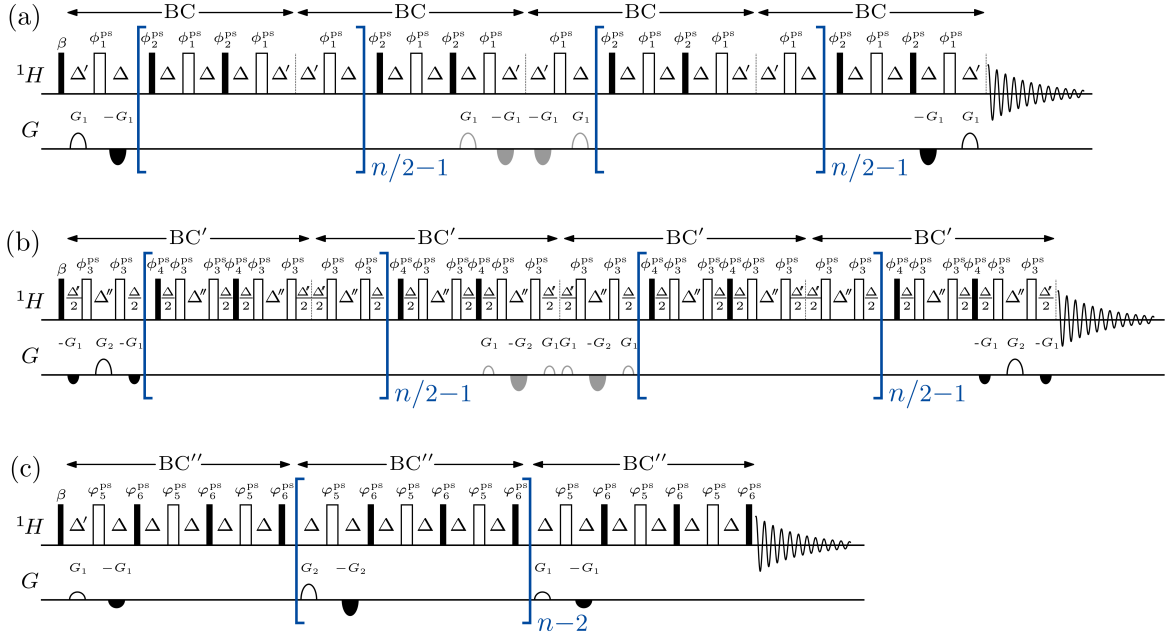


Figure 2.20: Convection compensated DOSY pulse sequences using IPE-1 in (a) and IPE-2 in (b) are illustrated in addition to an exchange compensated version in (c). In order to account for linear phases induced by 90° pulses, certain delays are extended to $\Delta' = \Delta + \frac{2}{\pi}\tau_{90^\circ}$ and $\Delta'' = \Delta + \frac{4}{\pi}\tau_{90^\circ}$ with τ_{90° being the 90° pulse length. Gradient strengths are $G_2 = 2 \cdot G_1$ and n is an even number of basic cycles (BC). Phase sequences for $\varphi_1^{\text{ps}}/\varphi_2^{\text{ps}}$ and $\varphi_3^{\text{ps}}/\varphi_4^{\text{ps}}$ are set according to Figure 2.12 and 2.13. In (c), the following phase sequences are used:

$$\begin{aligned} \varphi_5^{\text{ps}} &= \{x, -y, -y, y, -y, -y\} \{-x, x, x, y, x, x\} \{x, -x, -x, -y, -x, -x\} \{-x, y, y, -y, y, y\} \\ &\quad \{-x, x, x, y, x, x\} \{-x, y, y, -y, y, y\} \{x, -y, -y, y, -y, -y\} \{x, -x, -x, -y, -x, -x\} \\ \varphi_6^{\text{ps}} &= \{y, -x, -y, -y, -x, y\} \{x, -y, -x, -x, -y, x\} \{-x, y, x, x, y, -x\} \{-y, x, y, y, x, -y\} \\ &\quad \{x, -y, -x, -x, -y, x\} \{-y, x, y, y, x, -y\} \{y, -x, -y, -y, -x, y\} \{-x, y, x, x, y, -x\} \end{aligned}$$

In proposed fast DOSY sequences (Figure 2.20), after β -excitation, pulsed field gradients are applied during isotropic mixing – two convection and an exchange compensated DOSY are obtained.⁶¹ For an arbitrary excitation angle β in combination with a pulsed field gradient, spin magnetization within the sample is able to adopt *any* state on a Bloch sphere. It is, however, crucial to note that within a *single* molecule, all spins experience the same external Hamiltonian (i.e. β -pulse and PFG) and, hence, one can assume they are in *identical* states. Under given conditions, it is, thus, possible to use isotropic mixing in order to preserve *all* spin components along *arbitrary* axes as shown in Equation (2.3.2). Simultaneously, isotropic mixing provides J -refocusing and absorptive, in-phase spectra at high resolution are obtained. In contrast to isotropic mixing from continuous irradiation, it is further possible with IPE to include gradients within mixing periods and homonuclear couplings are *fully* refocused. The lowest amount of energy is introduced if IPE-1 is applied (Figure 2.20 (a)), while higher quality for fewer basic cycles is expected from IPE-2 (Figure 2.20 (b)). In (c) a modified isotropic mixing sequence for exchange compensated DOSY is illustrated where every third spin echo a pair of gradients is applied.⁶² This way, diffusion is repeatedly measured during a single basic cycle and it is expected, that chemical exchange processes occurring on a time-scale longer than one basic cycle are compensated. Experimental verification of a fast DOSY obtained from isotropic mixing using IPE-1 shall be given below.

⁶¹ From the two upper most sequences in Figure 2.20 a standard version without convection compensation can be obtained by omitting gradients in the center and inverting gradients at the end of the sequence.

⁶² In contrast to the exchange compensated DOSY proposed in literature, gradients should not be applied in each spin echo. Diffusion would cause a saturation of the spin reservoir which, in turn, would lead to an artificial signal attenuation and, hence, to biased results. In the given sequence, z-axis of the rotating and the toggling frame are aligned (same or opposite direction) whenever PFGs are applied and gradient en- and decoding is achieved.

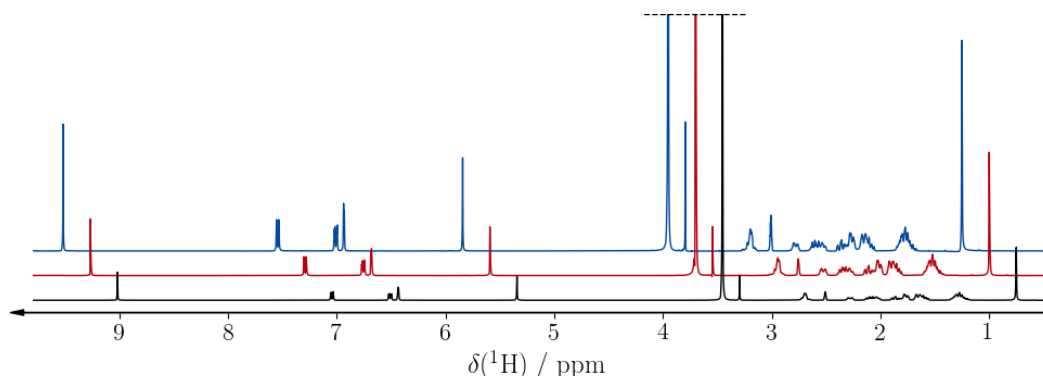


Figure 2.21: DOSY 1D spectra are shown using double STE (black), STE (red) and IPE-1 (blue) for ethinylestradiol in DMSO at 300 K. In total 8 transients are acquired with 4 dummy scans, a recovery delay of $\tau_r = 4.7$ s (including acquisition time), $\Delta_D \approx 60$ ms and no en- or decoding gradients. For IPE-1 four basic cycles are used with $\beta = 90^\circ$ and $\Delta = 3$ ms.

Experimental

The proposed DOSY experiment using IPE-1 is recorded as a 1D for a mixture of flavone and catechin in deuterated DMSO and compared to conventional DOSY sequences being based on single STE or double STE (DSTE, for convection compensation). As demonstrated in Figure 2.21, all spectra exhibit absorptive in-phase signals and the effect of homonuclear coupling during all sequences is successfully suppressed. In order to prevent artifacts in the conventional DOSY, for each STE half the magnetization has to be saturated from spoiler gradients and sensitivity is considerably decreased. Therefore, in low-viscous solvents or small molecules where $T_1 \approx T_2$, the proposed DOSY inherently benefits from stronger signals that are increased by a factor of up to 2 or 4 compared to STE or DSTE, respectively (Figure 2.21). As mentioned in Section 2.3.2, in larger spin networks a certain loss in signal intensity might also be encountered using IPE-1 and, in certain cases, the application of DIPSI could be favorable.

In order to obtain reliable results for the determination of diffusion coefficients by fast DOSY, it is crucial for the system to be in a steady state. This way, it is made sure that signal attenuation during the experiment can solely be ascribed to self diffusion. It is verified from 1D experiments, that a steady state is typically reached after 4 to 8 dummy scans.⁶³

In Figure 2.22 the conventional 2D DSTE-DOSY is compared to the proposed DOSY sequence in which IPE-1 is applied. As landmark, the DSTE-DOSY is used and clean, reliable results are obtained (Figure 2.22 (b)), if the spectrum is measured in 8 min 50 s using standard acquisition parameters. However, if the experimental time is drastically reduced to 28 s, the conventional DSTE-DOSY fails – peaks are shifted or missing (Figure 2.22 (c)). It should also be noted that the experiment suffers from low sensitivity and due to the short measurement time, signal intensity is further reduced by a factor of ≈ 16 . The proposed fast DOSY experiment, on the other hand, delivers reliable results in only 28 s at *high* sensitivity as illustrated in Figure 2.22 (d). All peaks of flavone and catechin are close to the corresponding dotted lines which indicate the overall diffusion coefficient for respective molecules. With this regard, it is interesting to note one small difference compared to the landmark DSTE-DOSY (Figure 2.22 (b)). As stated in literature^[102], hydroxyl protons in catechin undergo chemical exchange with the small water impurity in DMSO and respective hydroxyl protons exhibit an accelerated signal attenuation in DOSY experiments. Despite the fact, that in total only four bipolar gradient pairs are applied in the convection compensated version (Figure 2.20 (a)), apparently, exchange processes are to some extent compensated. The given effect is completely reproducible and it seems conceivable that it is based on coherence transfer between exchangeable and non-exchangeable spins. In principle, coherence transfer during the DOSY sequence would lead to an averaged signal attenuation of coupled spins and, hence, to identical diffusion

⁶³ A 1D DOSY with n dummy scans can be compared to an equivalent 1D using a large number of dummy scans (> 16). If both spectra are identical, the steady state is reached and n dummy scans should be used.

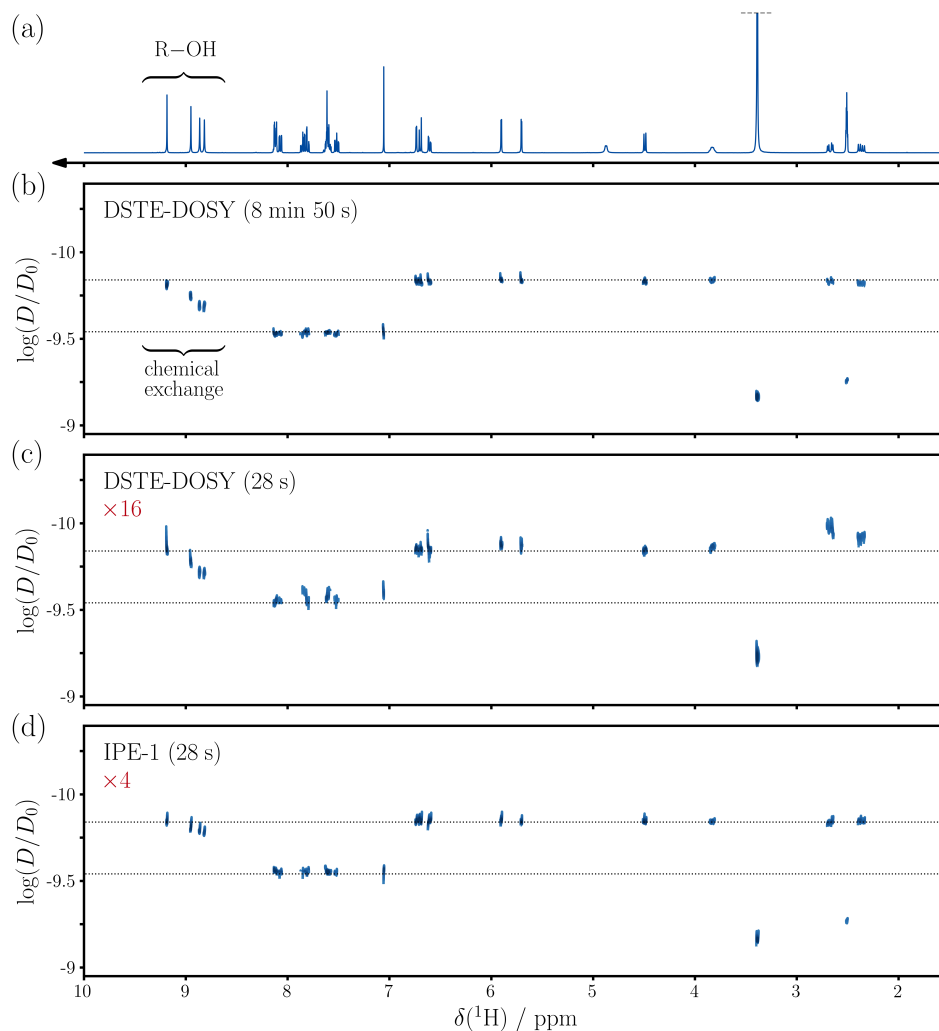


Figure 2.22: A proton 1D (a), 2D DSTE-DOSY with conventional (b) and short measurement time (c) as well as a fast DOSY using IPE-1 (d) is illustrated for a mixture of flavone and catechin in DMSO at 300 K. All DOSY spectra are acquired with 8 dummy scans, $\Delta_D \approx 176.7$ ms, a gradient length of $\delta = 1.5$ ms and a variable gradient strength from 2-80% (corresponding to 0.96-38.52 Gcm^{-1}). For conventional DSTE-DOSY in (b), 8 transients are acquired with $\tau_r \approx 3.7$ s (including acquisition time) resulting in a total measurement time of 8 min 50 s. In (c) and (d), only a single transient is recorded and recovery delay is reduced to $\tau_r \approx 1$ s leading to a total time of 28 s. Contour levels are scaled by a factor of 16 (b) and 4 (c). For IPE-1 eight basic cycles are used with $\Delta = 4$ ms and $\beta \approx 54^\circ$. Upper and lower horizontal dotted lines indicate the coefficient D for catechin and flavone, respectively. While signal intensities in (b) are ~ 4 times higher than in (d), also noise is increased by a factor of $\sqrt{8}$. Hence, despite much longer measurement time the signal-to-noise in (b) is only a factor of $\sqrt{2}$ higher than in (d). Note, the log-function's argument is made dimensionless by using D_0 .

coefficients – smaller outliers could be drawn back in line. Since considered hydroxyl protons exhibit negligible J -couplings to surrounding spins, TOCSY-type transfer can be excluded. It, hence, seems *likely* that NOE transfer takes place as soon as fast and slowly attenuated signals are inverted by a 180° pulse.⁶⁴ Further, it shall be mentioned that hardware related duty cycles occasionally represent a limiting factor for fast experiments. For the given fast DOSY spectrum (Figure 2.22 (d), acquired in 28 s), however, the gradient duty cycle was at only $\sim 77\%$ ⁶⁵ and compared to DIPSI the average power is reduced by a factor of ~ 48 – sample heating was not observed.

2.3.4 Conclusion

In contrast to planar mixing, that in literature is primarily used for J -refocusing^[117], isotropic mixing is so far mainly used for coherence transfer. Due to the fact that not only a single, but *all* axes for equivalent spin states can be preserved (see Equation 2.3.2), the potential use of isotropic mixing, other than coherence transfer, seems not yet to be exhausted. In the present section, different pulse-delay sequences, related to the perfect echo, were introduced from which isotropic mixing is obtained at low energy dissipation. It was demonstrated that the so-called IPE-sequences are highly suitable to be applied for spin state preservation and an application in DOSY was shown. Conventional DOSY sequences are mostly based on stimulated echoes, which reject half the signal, and sensitivity is decreased by a factor of 2 (or 4 if convection is compensated). Using isotropic mixing in a newly developed fast DOSY experiment allows to preserve spin magnetization for maximum sensitivity and a DOSY spectrum was acquired in only 28 s. Another obstacle in diffusion-ordered spectroscopy is formed by chemical exchange, e.g. with the solvent that typically exhibits faster diffusion, and a separate signal attenuation of the compound is induced. So far available exchange compensated DOSY sequences are based on subdivided diffusion delays at high repetition rates forcing a considerable strain on the gradients' duty cycle. Gradient strengths, therefore, have to be reduced drastically and long overall diffusion delays of 450 ms are not exceptional^[102] – a considerable loss due to transverse relaxation is expected. In the proposed fast DOSY sequence, on the other hand, a partial compensation of chemical exchange processes can be observed. The effect is ascribed to coherence transfer (i.e. from IM or NOE) induced during the sequence which distributes signal attenuation from chemical exchange within the spin system. To some extent diffusion coefficients are, hence, assimilated. The introduced bias for smaller outliers has shown to be negligible and compound identification in DOSY is facilitated if signals of individual compounds are brought in line.

Furthermore, the application of proposed isotropic mixing sequences is thinkable in many other experiments and a short outlook shall be ventured. Obvious examples constitute other DOSY-type sequences, that are so far based on the STE approach and suffer from a two- or fourfold reduced sensitivity (e.g. the ultrafast DOSY^[177]). Likewise a fast ^{19}F -DOSY is thinkable, if broadband shaped pulses are applied in the IPE. But also beyond DOSY, spin state preservation could be applicable, e.g. in the field of MRI where stimulated echoes are likewise applied.^[178–180] Due to *essential* RF energy limits in MRI, that are required to avoid “sample heating”, isotropic mixing at low energy dissipation could be of supplemental value. Furthermore, in recently proposed ASAP-experiments^[181–183], where isotropic mixing is used during the recovery delay in order to transfer polarization from a spin reservoir to detected nuclei, a mixing sequence with reduced average power might be beneficial to prevent hardware damage.

^[177] Y. Shrot and L. Frydman. *Journal of Magnetic Resonance* **2008**, *195*, 226–231.

^[178] D. Burstein. *Concepts in Magnetic Resonance* **1996**, *8*, 269–278.

^[179] J. Frahm et al. *Journal of Magnetic Resonance* **1985**, *64*, 81–93.

^[180] W. Sattin, T. H. Mareci and K. N. Scott. *Journal of Magnetic Resonance* **1985**, *65*, 298–307.

^[181] Ě. Kupče and R. Freeman. *Magnetic Resonance in Chemistry* **2007**, *45*, 2–4.

^[182] D. Schulze-Sünninghausen, J. Becker and B. Luy. *Journal of the American Chemical Society* **2014**, *136*, 1242–1245.

^[183] D. Schulze-Sünninghausen et al. *Journal of Magnetic Resonance* **2017**, *281*, 151–161.

⁶⁴ This holds considering a small molecule with positive NOE enhancement factor, see Section 1.8.3.

⁶⁵ On Bruker spectrometers, the recommended maximum gradient strength per duty cycle is calculated from:

$V = 1/\tau_r \sum_i (x_i/10)^2 \cdot \delta_i$ where x_i is the considered gradient strength (in %), δ_i its duration (in ms) and for V a value of 1000 should not be exceeded. Any value for $\tau_r > 1$ s is set to 1 s in the calculation. Assuming $\tau_r = 1$ s, $x_i = 80\%$ and $n \cdot \delta_i = 12$ ms it follows that $V = 768$.

2.4 Pulse Shapes in the Toggling Frame

The design of pulse shapes started when the so-called composite pulse was discovered by Levitt^[184] and in order to satisfy the needs of various applications ever since plenty of pulse shapes have been developed – broadband pulses^[92,103,136,184–193], pulses with compensation of RF inhomogeneity^[92,103,184,187,191,193], band-selective pulses^[143,194–197] – to name just a few. One of the most powerful approach for the design of pulse shapes is offered by the GRAPE algorithm^[198] which is based on optimal control theory and has lead to an impressive advance towards the physical limits of shaped pulses.^[136,189,190] Pulse shapes modulated in phase and/or amplitude can be tailored for different kinds of experimental challenges including coupled spin systems.^[92,103] Recently, a new optimization routine was published by Coote et al.^[199,200] that is based on a transformation to the toggling frame in which the propagation of the pulse becomes time-independent.⁶⁶ Also adiabatic pulses can cover a large bandwidth as shown e.g. by the CHORUS sequence.^[201]

However, the high performance of shaped pulses has its price – compared to a hard pulse shaped pulses are roughly two orders of magnitude longer and special care has to be taken when placed in a pulse sequence. The most prevailing issue arises from the evolution of large couplings (e.g. in a heteronuclear spin system) during the much longer shaped pulse. With this regard, different attempts were made where e.g. the coupling is directly included in the process of optimization,^[103,104] or certain pulse shapes are approximated by a simplified scheme.^[202] Also, the property of adiabatic pulses to result in frequency swept and, hence, time shifted inversions is exploited in a way that the coupling evolution matches the correlation between ¹³C-offset and the ¹J_{C,H}-coupling strength.^[203,204]

In the following another approach shall be presented that is based on numerical simulations of the toggling frame which was first introduced in the field of solid state NMR by Waugh, Huber and Haeberlen already in the late 1960's.^[4] Pulse shapes with highly complex structure can be analyzed even for homonuclear spin systems and a condensed result can be obtained from the application of average Hamiltonian theory (Section 1.7.3) or the matrix logarithm (Section 1.7.1).^[12,53] Yet, it is not limited to shaped pulses and can also be used to illustrate the effect of coupling evolution for any multi pulse sequence. Below, a selection of pulse shapes is reviewed with the help of the toggling frame and classified according to common practice.

^[184] M. H. Levitt and R. Freeman. *Journal of Magnetic Resonance* **1979**, *33*, 473–476.

^[185] A. J. Shaka. *Chemical Physics Letters* **1985**, *120*, 201–205.

^[186] J. Baum, R. Tycko and A. Pines. *Physical Review* **1985**, *A32*, 3435–3447.

^[187] Ě. Kupče and R. Freeman. *Journal of Magnetic Resonance* **1995**, *A117*, 246–256.

^[188] M. A. Smith, H. Hu and A. J. Shaka. *Journal of Magnetic Resonance* **2001**, *151*, 269–283.

^[189] K. Kobzar et al. *Journal of Magnetic Resonance* **2004**, *170*, 236–243.

^[190] K. Kobzar et al. *Journal of Magnetic Resonance* **2008**, *194*, 58–66.

^[191] T. E. Skinner et al. *Journal of Magnetic Resonance* **2006**, *179*, 241–249.

^[192] T. E. Skinner et al. *Journal of Magnetic Resonance* **2012**, *216*, 78–87.

^[193] D. L. Goodwin, M. R. M. Koos and B. Luy. *Physical Review Research* **2020**, *2*, 33157.

^[143] L. Emsley and G. Bodenhausen. *Journal of Magnetic Resonance* **1992**, *97*, 135–148.

^[194] L. Emsley and G. Bodenhausen. *Chemical Physics Letters* **1990**, *165*, 469–476.

^[195] H. Geen and R. Freeman. *Journal of Magnetic Resonance* **1991**, *93*, 93–141.

^[196] Ě. Kupče and R. Freeman. *Journal of Magnetic Resonance* **1993**, *A102*, 122–126.

^[197] Ě. Kupče, J. Boyd and I. D. Campbell. *Journal of Magnetic Resonance* **1995**, *B106*, 300–303.

^[198] N. Khaneja et al. *Journal of Magnetic Resonance* **2005**, *172*, 296–305.

^[199] P. Coote et al. *Journal of Magnetic Resonance* **2017**, *281*, 94–103.

^[200] P. W. Coote et al. *Nature Communications* **2018**, *9*, 3014.

^[201] J. E. Power et al. *Chemical Communications* **2016**, *52*, 2916–2919.

^[202] E. Lescop, T. Kern and B. Brutscher. *Journal of Magnetic Resonance* **2010**, *203*, 190–198.

^[203] R. D. Boyer, R. Johnson and K. Krishnamurthy. *Journal of Magnetic Resonance* **2003**, *165*, 253–259.

^[204] Ě. Kupče and R. Freeman. *Journal of Magnetic Resonance* **2007**, *187*, 258–265.

⁶⁶ The toggling frame discussed by Coote et al. is fundamentally different from the one discussed in the dissertation at hand. While in the former the only thing left is the Hamiltonian of the pulse, in the latter the pulse is removed completely.

2.4.1 Introduction: Pulse Shape Classification

It is helpful to classify pulse shapes by the effective rotations they induce in order to determine the right shape for a certain experimental issue. Following the nomenclature of Levitt^[205] for 180° pulses there are two classes, A and B, that are illustrated in Figure 2.23. For class A there is only a single rotation axis of the considered space (e.g. offset frequency or B_1 -fields) and these pulse shapes are commonly called *universal rotations* or *refocusing pulses*.^[195] Pulse shapes of class B, on the other hand, transfer only \hat{I}_z to $-\hat{I}_z$ or vice versa and are, therefore, referred to as *point-to-point* or *inversion pulses*. It is evident from Figure 2.23 (b) that such an inversion can be obtained from all 180° rotation axes within the transverse plane. Due to these less strict constraints, it could be shown that a pulse of class B requires roughly half the time with respect to a comparable universal rotation.^[136] The formal propagators for class A and B are given as:

$$\begin{aligned} \text{class A: } U_P &= U_{180x}, \\ \text{class B: } U_P &= U_\varphi U_{180x} U_\varphi^\dagger \end{aligned} \quad (2.4.1)$$

where U_P is the effective propagator of the pulse shape which for class A is considered a 180° rotation around x and U_φ is a variable z rotation.

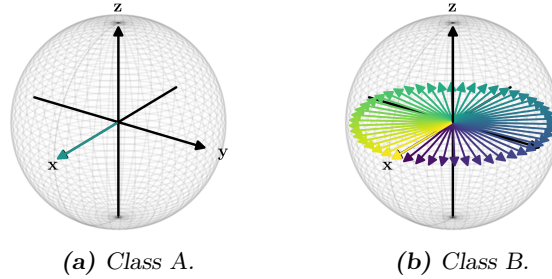


Figure 2.23: Classification of 180° pulses by normalized effective rotation axes.^[205]

A similar classification can be made for 90° pulses which are shown in Figure 2.24. The most obvious are class A and B1 which are in close analogy to the classes A and B of 180° pulses. It is crucial to mention that for illustrative reasons the rotation axes in Figure 2.24 are normalized and the vectors' lengths do not correspond to the induced rotation angle. Commonly, 90° pulses of the class B2 are referred to as *point-to-point* or *excitation pulses* which, in general, are optimized for a transfer from \hat{I}_z to a specific state in the transverse plane (e.g. \hat{I}_y). For such a transfer several rotation axes in a tilted plane are thinkable as shown in Figure 2.24 (c). Again, it is crucial that normalized vectors are shown and while the rotations in the yz-plane require an angle of 180° to result in a transfer from \hat{I}_z to \hat{I}_y rotations around x and $-x$ necessitate an angle of -90° and 90° , respectively. A time-reversed pulse shape of class B2 with inverted phase is commonly used for a back transfer (e.g. from \hat{I}_y to \hat{I}_z) which with respect to the toggling frame shall be further discussed at the end of Section 2.4.2. The class B3 corresponds to pulse shapes that excite to an arbitrary state in the transverse plane and are sometimes called *saturation pulses*. In Figure 2.24 (d) only a fraction of all possible rotation axes are shown – in principle, all axes with matching rotation angle in between the two illustrated cones can transfer from \hat{I}_z to the transverse plane $\hat{I}_{x/y}$. The four classes of 90° pulses can be expressed in terms of their propagators:

$$\begin{aligned} \text{class A: } U_P &= U_{90x}, \\ \text{class B1: } U_P &= U_\varphi U_{90x} U_\varphi^\dagger \\ \text{class B2: } U_P \hat{I}_z U_P^\dagger &= \hat{I}_y \\ \text{class B3: } U_P \hat{I}_z U_P^\dagger &= U_\varphi \hat{I}_y U_\varphi^\dagger \end{aligned} \quad (2.4.2)$$

where U_φ is an arbitrary z rotation and for B2 a transfer from \hat{I}_z to \hat{I}_y is assumed.

^[205] M. H. Levitt. *Progress in Nuclear Magnetic Resonance Spectroscopy* **1986**, 18, 61–122.

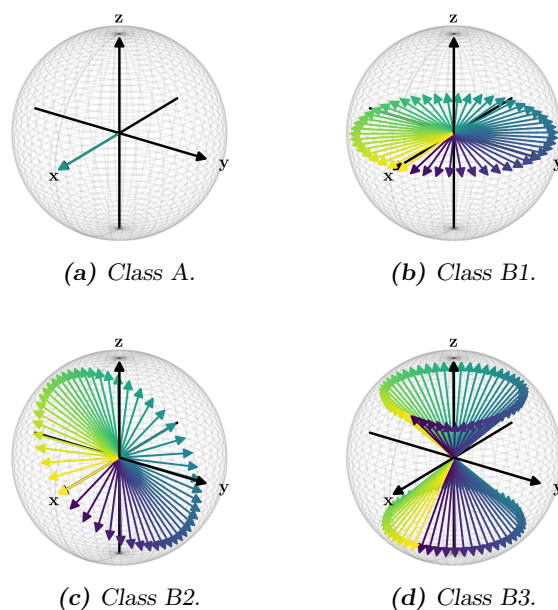


Figure 2.24: Classification of 90° pulses by normalized effective rotation axes.^[205]

In the following the rotation axes of a considered pulse shape shall not be illustrated in a sphere but rather in a graph where the Cartesian components of the rotation axes are plotted against the offset. With this regard, it is easier to illustrate how the rotation axes depend on the offset frequency.

2.4.2 Introduction: Toggling Frame of Shaped Pulses

With few exceptions^[103] it is common that the optimization of pulse shapes is performed for a single spin and couplings to surrounding spins are neglected. In principle, for a shaped pulse leading to a constant phase, coupling evolution is self-compensated⁶⁷ if applied exclusively on one spin.^[103] If during the shaped pulse additional pulses are applied to the coupled spin the phase created from coupling does no more evolve linearly and the predicted outcome will deviate. Still, couplings can be neglected if the length of the shaped pulse is much smaller than the inverse coupling strength $t_P \ll |\frac{1}{J}|$. Considering large couplings (e.g. heteronuclear one-bond $^1J_{XH}$ or homonuclear fluorine couplings $^nJ_{FF}$), very long pulses (e.g. highly selective pulses) or even both, this assumption, however, will surely break down. For this reason it is highly important to know about the shapes' properties and what influence is exerted by coupling evolution.

A very helpful tool to investigate the influence of coupling evolution during a shaped pulse is based on the numerical simulation of its toggling frame. The frame transformation can be chosen in a way that all linear terms of the Hamiltonian are transferred to the Heisenberg picture. Hence, the evolution of states is given only by bilinear terms of the considered coupling and the resulting time-dependent Hamiltonian can be subject to average Hamiltonian theory. The underlying theory for the toggling frame and average Hamiltonian theory is discussed in Sections 1.6 and 1.7, respectively. Different examples are discussed considering the perfect echo sequence in Section 1.6.3 and strong coupling in Section 2.5.

⁶⁷ Such a shaped pulse creates a constant phase from various offsets independent on whether the offset originates from chemical shielding or a *secular* coupling. It is crucial to note, that for point-to-point pulses this is only true for the optimized transfer while the effective coupling on other initial states might have an influence.

Theoretical Background

In order to investigate the coupling evolution during a shaped pulse we shall consider a coupled two spin system. The general Hamiltonian $\hat{\mathcal{H}}(\tau)$ with the piecewise time-independent shaped pulse $\hat{\mathcal{H}}_P(\tau)$ is given as:

$$\hat{\mathcal{H}}(\tau) = \hat{\mathcal{H}}_Z + \hat{\mathcal{H}}_P(\tau) + \hat{\mathcal{H}}_J \quad (2.4.3)$$

where $\hat{\mathcal{H}}_Z$ is the Zeeman term and $\hat{\mathcal{H}}_J$ corresponds to the scalar coupling Hamiltonian under examination⁶⁸ with $\hat{\mathcal{H}}_J = \sum_{k>j} 2\omega_J \cdot (\hat{I}_{kx}\hat{I}_{jx} + \hat{I}_{ky}\hat{I}_{jy} + \hat{I}_{kz}\hat{I}_{jz})$. The Hamiltonian of the shaped pulse $\hat{\mathcal{H}}_P(\tau)$ can be expressed by its n consecutive steps of length τ_n :

$$\hat{\mathcal{H}}_P(\tau) = \begin{cases} \hat{\mathcal{H}}_{P_1} = \sum_k \omega_k \hat{I}_{k\gamma} & \text{for } \tau_1 \\ \hat{\mathcal{H}}_{P_2} = \sum_k \omega'_k \hat{I}_{k\gamma'} & \text{for } \tau_2 \\ \dots \\ \hat{\mathcal{H}}_{P_n} = \sum_k \omega''_k \hat{I}_{k\gamma''} & \text{for } \tau_n \end{cases} \quad (2.4.4)$$

where $\gamma = x,y$ and k is the index for the spin on which the shaped pulse is applied. The effective propagator of the shaped pulse can, hence, be written by the n propagators of all individual steps:

$$U_{\mathcal{H}} = (U_n \dots U_1) \quad (2.4.5)$$

$$\text{with: } U_n = \exp \left\{ -i \left(\underbrace{\hat{\mathcal{H}}_Z + \hat{\mathcal{H}}_{P_n}}_{\text{linear}} + \underbrace{\hat{\mathcal{H}}_J}_{\text{bilinear}} \right) \tau_n \right\}. \quad (2.4.6)$$

If τ_n is very short compared to the inverse strength of the Hamiltonian and $\|\hat{\mathcal{H}}_n\|\tau_n \ll 2\pi$ the propagator U_n can be expressed by a Suzuki-Trotter approximation⁶⁹ (Equation 1.7.28):

$$U_n \approx (U_{L_n} U_J)^m \quad (2.4.7)$$

where all linear and bilinear terms of Equation (2.4.6) are condensed in U_L and U_J , respectively. On today's spectrometers τ_n is in the range of $0.5 \mu s$ and for common coupling strengths Equation (2.4.7) leads to a valid description of U_n even for $m = 1$ (see Section 1.7.3 for more details). Introducing Equation (2.4.7) in (2.4.5) the effective propagator of the shaped pulse $U_{\mathcal{H}}$ can be approximated by:

$$U_{\mathcal{H}} \approx (U_{L_n} U_J \dots U_{L_1} U_J). \quad (2.4.8)$$

As discussed in Section 1.6.4, the propagators of linear and bilinear operators (U_L and U_J) shall be separated by introducing the unity matrix $\mathbb{1}$ at consecutive steps:

$$\begin{aligned} U_{\mathcal{H}} &\approx (U_{L_n} U_J \dots U_{L_2} U_J U_{L_1} U_J) \\ &= U_{L_n} U_J U_{L_{n-1}} \dots U_{L_2} U_{L_1} \underbrace{U_{L_1}^\dagger U_J U_{L_1}}_{U_{J_1}} \underbrace{U_J}_{U_{J_0}} \\ &= U_{L_n} U_J U_{L_{n-1}} \dots \underbrace{(U_{L_2} U_{L_1})}_{\mathbb{1}} \underbrace{(U_{L_1}^\dagger U_{L_2}^\dagger) U_J (U_{L_2} U_{L_1})}_{U_{J_2}} \underbrace{U_{L_1}^\dagger U_J U_{L_1}}_{U_{J_1}} \underbrace{U_J}_{U_{J_0}} \\ &= \underbrace{(U_{L_n} \dots U_{L_1})}_{\text{linear}} \underbrace{(U_{L_1}^\dagger \dots U_{L_{n-1}}^\dagger) U_J (U_{L_{n-1}} \dots U_{L_1})}_{U_{J_{n-1}}} \dots \underbrace{U_{L_1}^\dagger U_J U_{L_1}}_{U_{J_1}} \underbrace{U_J}_{U_{J_0}}. \end{aligned} \quad (2.4.9)$$

From Equation (2.4.9) it is evident that the linear term $(U_{L_n} \dots U_{L_1})$ corresponds to the effective rotation induced by the shaped pulse *and* the Zeeman interaction *exclusively*. The term $(U_{J_{n-1}} \dots U_{J_0})$, on the

⁶⁸ In liquid state NMR the scalar coupling is the most prevailing, however, any other coupling could likewise be examined.

⁶⁹ The approximation is discussed in Section 1.7.3 and used for the description of strong coupling in Section 2.5.

other hand, describes the coupling evolution modulated by the linear operators U_L . Using the identity $U^\dagger \exp\{-i\hat{\mathcal{H}}t\}U = \exp\{-iU^\dagger\hat{\mathcal{H}}U t\}$ (Appendix 5.1.5) it is evident that $(U_{J_{n-1}} \dots U_{J_0})$ corresponds to the propagation of the coupling Hamiltonian in the toggling frame of the shaped pulse and the Zeeman interaction – the underlying Hamiltonian can be expressed as:

$$\hat{\mathcal{H}}_{T,J}(\tau) = \begin{cases} \hat{\mathcal{H}}_{T_0,J} = \hat{\mathcal{H}}_J & \text{for } \tau_1 \\ \hat{\mathcal{H}}_{T_1,J} = U_{L_1}^\dagger \hat{\mathcal{H}}_J U_{L_1} & \text{for } \tau_2 \\ \dots & \\ \hat{\mathcal{H}}_{T_{n-1},J} = (U_{L_1}^\dagger \dots U_{L_{n-1}}^\dagger) \hat{\mathcal{H}}_J (U_{L_{n-1}} \dots U_{L_1}) & \text{for } \tau_n \end{cases} \quad (2.4.10)$$

where the subscript T indicates the toggling frame. Clearly, the Hamiltonian $\hat{\mathcal{H}}_{T,J}(\tau)$ describes the effect of coupling evolution during the shaped pulse and if $\hat{\mathcal{H}}_J = 0$ the effective propagator $U_{\mathcal{H}}$ in Equation (2.4.9) is given only by the linear term $(U_{L_n} \dots U_{L_1})$. Using average Hamiltonian theory (Section 1.7) the time-independent zeroth order average Hamiltonian $\bar{\mathcal{H}}_{0,J}$ can be approximated from the piecewise Hamiltonian $\hat{\mathcal{H}}_{T,J}(\tau)$ and Equation (2.4.9) can be expressed as:

$$U_{\mathcal{H}} \approx U_L \bar{U}_{0,J} \quad (2.4.11)$$

where $\bar{U}_{0,J}$ is the effective propagator determined by the average Hamiltonian $\bar{\mathcal{H}}_{0,J}$. By this means, a very compact result for the quantification of coupling evolution during shaped pulses is obtained. For the interpretation of subsequent results it is important to note that in Equation (2.4.11) the propagator U_L is to the left of $\bar{U}_{0,J}$. Hence, for the propagation of an initial state $\hat{\rho}_{\text{init}}$ it is first $\bar{U}_{0,J}$ that is applied and only afterwards the actual pulse is applied:

$$\begin{aligned} \hat{\rho}(t) &= U_{\mathcal{H}} \hat{\rho}_{\text{init}} U_{\mathcal{H}}^\dagger \\ &= U_L \bar{U}_{0,J} \hat{\rho}_{\text{init}} \bar{U}_{0,J}^\dagger U_L^\dagger. \end{aligned} \quad (2.4.12)$$

From this follows that if the average coupling propagator $\bar{U}_{0,J}$ commutes with the initial state $\hat{\rho}_{\text{init}}$ then the average coupling propagator $\bar{U}_{0,J}$ is without consequences. Examples where this circumstance is of relevance shall be found in Section 2.4.7, 2.4.9 and 2.4.14. It is likewise possible to calculate an average coupling propagator that depends on the final instead of the initial state which shall be discussed in the following section using the example of time-reversed pulses.

Time-reversed Pulse

As stated before, pulses of class B2 are often followed by their time-reversed version with inversed phase in order to achieve a reversion of the optimized transfer. In this context, we shall note that a shaped pulse with γ -phase and n steps is given as:

$$\begin{aligned} &U_{L,\gamma}(\nu) = [U_{L_n,\gamma}(\nu) \dots U_{L_1,\gamma}(\nu)] \\ \text{phase- and time-reversed:} &U'_{L,-\gamma}(\nu) = [U_{L_1,-\gamma}(\nu) \dots U_{L_n,-\gamma}(\nu)] \\ \text{and one can state:} &U_{L,-\gamma}^\dagger(\nu) = [U_{L_n,-\gamma}(\nu) \dots U_{L_1,-\gamma}(\nu)]^\dagger \\ &= [U_{L_1,-\gamma}^\dagger(\nu) \dots U_{L_n,-\gamma}^\dagger(\nu)] \\ &= [U_{L_1,\gamma}(-\nu) \dots U_{L_n,\gamma}(-\nu)] \end{aligned} \quad (2.4.13)$$

where the last line corresponds to the phase- and time-reversed version with inversed frequency offset ν . It is noteworthy that the adjoint causes a change in sign in the exponential which can be “compensated” by an inversion of the phase and offset profile if no coupling is active.^[206] These findings shall be used in

^[206] B. Luy et al. *Journal of Magnetic Resonance* **2005**, 176, 179–186.

the following. In contrast to Equation (2.4.9) it is likewise possible to separate linear (U_L) and bilinear terms (U_J) in a way that all linear terms end up on the right side and one obtains:

$$\begin{aligned} U_{\mathcal{H}} &\approx (U_J U_{L_n} \dots U_J U_{L_1}) \\ &= U_J \underbrace{U_{L_n} U_J U_{L_n}^\dagger}_{U'_{J_n}} \dots \underbrace{(U_{L_n} \dots U_{L_2}) U_J (U_{L_2}^\dagger \dots U_{L_n}^\dagger)}_{U'_{J_2}} \underbrace{(U_{L_n} \dots U_{L_1})}_{\text{linear}}. \end{aligned} \quad (2.4.14)$$

Using Equation (2.4.14) to calculate the effect of coupling evolution during a phase- and time-reversed shaped pulse, $U'_{L,-\gamma}(\nu)$ given in Equation (2.4.13), results in:

$$\begin{aligned} U_{\mathcal{H}} &\approx [U_J U_{L_1,-\gamma}(\nu) \dots U_J U_{L_n,-\gamma}(\nu)] \\ &= \underbrace{U_J}_{U'_{J_0}} \underbrace{U_{L_1,-\gamma}(\nu) U_J U_{L_1,-\gamma}^\dagger(\nu)}_{U'_{J_1}(\nu)} \dots \underbrace{[U_{L_1,-\gamma}(\nu) \dots U_{L_{n-1},-\gamma}(\nu)] U_J [U_{L_{n-1},-\gamma}^\dagger(\nu) \dots U_{L_1,-\gamma}^\dagger(\nu)]}_{U'_{J_{n-1}}(\nu)} \underbrace{[U_{L_1,-\gamma}(\nu) \dots U_{L_n,-\gamma}(\nu)]}_{\text{linear}} \\ &= \underbrace{U_J}_{U'_{J_0}} \underbrace{U_{L_1,\gamma}^\dagger(-\nu) U_J U_{L_1,\gamma}(-\nu)}_{U'_{J_1}(-\nu)} \dots \underbrace{[U_{L_1,\gamma}^\dagger(-\nu) \dots U_{L_{n-1},\gamma}^\dagger(-\nu)] U_J [U_{L_{n-1},\gamma}(-\nu) \dots U_{L_1,\gamma}(-\nu)]}_{U'_{J_{n-1}}(-\nu)} \underbrace{[U_{L_1,-\gamma}(\nu) \dots U_{L_n,-\gamma}(\nu)]}_{\text{linear}} \\ &\approx \bar{U}_{0,J}(-\nu) U'_{L,-\gamma}(\nu) \end{aligned} \quad (2.4.15)$$

where the last two lines of Equation (2.4.13) were used. It is crucial to note that ($U_{J_0} \dots U_{J_{n-1}}$) can be approximated by the same *zeroth order* average coupling propagator $\bar{U}_{0,J}$ as obtained from Equation (2.4.9), however, with inversed frequency offset. The linear terms still correspond to the time-reversed shaped pulse $U'_{L,-\gamma}(\nu)$ and in contrast to Equation (2.4.11) they are now to the right of $\bar{U}_{0,J}$. Hence, propagating an initial state $\hat{\rho}_{\text{init}}$ using Equation (2.4.15) it is first the shaped pulse $U'_{L,-\gamma}(\nu)$ that is applied:

$$\hat{\rho}(t) = \bar{U}_{0,J}(-\nu) \underbrace{U'_{L,-\gamma}(\nu) \hat{\rho}_{\text{init}} U'_{L,-\gamma}(\nu)}_{\hat{\rho}_{\text{final}}} \bar{U}_{0,J}^\dagger(-\nu). \quad (2.4.16)$$

and only afterwards the effective coupling propagator $\bar{U}_{0,J}(-\nu)$ is applied to the final state $\hat{\rho}_{\text{final}}$. When compared to the findings in the preceding section this is a very interesting result. From this we can follow that during a phase- and time-reversed shaped pulse the coupling evolves very similar to the non-reversed version. However, the effective coupling propagator is not applied to the initial but on the final state and with inversed frequency offset. Two examples shall be given for the E-BURP-2 and a BEBOP pulse shape in Section 2.4.9 and 2.4.14, respectively.

Numerically Simulated Results

The Hamiltonians $\hat{\mathcal{H}}_{T,J}(\tau)$ and $\bar{\mathcal{H}}_{0,J}$ shall be illustrated by a linear combination of bilinear basis operators in the toggling frame (\hat{B}_γ) as discussed in Section 1.6.2 and 1.7.4. Hence, both $\hat{\mathcal{H}}_{T,J}(\tau)$ and $\bar{\mathcal{H}}_{0,J}$ are determined by their coefficients $k_J^\gamma(\tau)$ and $\bar{k}_{0,J}^\gamma$, respectively. Decomposed into its basis operators \hat{B}_γ the time-dependent Hamiltonian $\hat{\mathcal{H}}_{T,J}(\tau)$ can be expressed as:

$$\begin{aligned} \hat{\mathcal{H}}_{T,J}(\tau) &= \omega_J \cdot \sum_{\gamma} k_J^\gamma(\tau) \cdot \hat{B}_\gamma \\ \text{with: } k_J^\gamma(\tau) &= \frac{1}{\omega_J} \cdot \text{Tr} \left\{ \hat{B}_\gamma^\dagger \hat{\mathcal{H}}_{T,J}(\tau) \right\} \end{aligned} \quad (2.4.17)$$

where ω_J is the coupling strength determined for normalized bilinear operators.⁷⁰ In the present case where $\hat{\mathcal{H}}_{T,J}(\tau)$ is given by the scalar coupling it is $\omega_J = \pi J$. Likewise the zeroth order average Hamiltonian $\bar{\mathcal{H}}_0$ can be written as:

$$\bar{\mathcal{H}}_0 = \omega_J \cdot \sum_{\gamma} \bar{k}_{0,J}^{\gamma} \cdot \hat{B}_{\gamma} \quad (2.4.18)$$

with: $\bar{k}_{0,J}^{\gamma} = \frac{1}{t_c} \sum_i k_J^{\gamma}(\tau_i) \cdot \tau_i$

where $\bar{k}_{0,J}^{\gamma}$ can be considered the zeroth order average coefficient for the respective basis operator \hat{B}_{γ} and the pulse length is $t_c = \sum \tau_i$.

In order to interpret the simulations of coupling in the toggling frame it is important to answer one question: what is the significance of the coefficients $k_J^{\gamma}(\tau)$ and $\bar{k}_{0,J}^{\gamma}$? In mathematical terms, the answer is already given in Equation (2.4.17) and (2.4.18) where both coefficients act as scaling factors for respective basis operators in the toggling frame (\hat{B}_{γ}). Both coefficients are, in principle, independent of the coupling strength ω_J and for the *scalar coupling* Hamiltonian $\hat{\mathcal{H}}_J$ they range from -1 to 1 . Hence, considering a coefficient $k_J^{\gamma}(\tau)$ with a value of 1 signifies that for a given time point the respective operator is at full strength ω_J . Likewise an average coefficient $\bar{k}_{0,J}^{\gamma}$ with a value of 1 either signifies that the respective operator *in the toggling frame* is at full strength ω_J or active during 100% of the shaped pulse. Despite the fact that in the following all bilinear operators *in the toggling frame* are illustrated separately, the average Hamiltonian $\bar{\mathcal{H}}_0$ is given by the *sum* over all operators (Equation 2.4.18). In this context, it is important to note that bilinear operators can only be propagated *individually* if considered terms commute with all other non-zero operators. In more complex systems the interpretation of obtained results, hence, has to be conducted with special care on this matter.

2.4.3 Introduction: Investigation on Common Pulse Shapes

The theory discussed in the preceding section shall be used in numerical simulations to examine a selection of common pulse shapes within basic pulse sequence elements (described below). The investigation reveals that the evolution of coupling depends strongly on the pulse shape and the sequence in which it is applied. Parameters of shaped pulses are chosen in a way that pulses with similar purpose are comparable – for band-selective pulses the pulse length was set to $\tau_P = 1$ ms and broadband pulses were applied with RF = 10 kHz. For each pulse shape the Cartesian components of the effective rotation axes are illustrated for an isolated spin where it is crucial to note that these rotation axes correspond to the linear propagators ($U_{L_n} \dots U_{L_1}$) given in the preceding section. Additionally, an offset profile is simulated where the shaped pulse is applied to a spin density $\rho_z = \hat{I}_z$ of an isolated spin without coupling. In combination these various simulations can be used to conceive the total effect of shaped pulses (Equation 2.4.9) even if the coupling is non-negligible and different pulse shapes can be compared.

For the simulation of the coupling Hamiltonian in the toggling frame $\hat{\mathcal{H}}_{T,J}(\tau)$ four cases shall be distinguished which are, again, illustrated in Figure 2.25. Each case assumes a different spin system and/or pulse sequence element in which the shaped pulse $\hat{\mathcal{H}}_P(\tau)$ is applied:

- (a) Case 1: shaped pulse exclusively on spin \hat{S} which is weakly coupled to spin \hat{I} .

$$\hat{\mathcal{H}}_1 = 2\pi \cdot \nu_S \hat{S}_z + \hat{\mathcal{H}}_{P,\hat{S}}(\tau) + \pi J \cdot 2\hat{I}_z \hat{S}_z$$

From $\hat{\mathcal{H}}_1$ the coupling Hamiltonian in the toggling frame $\hat{\mathcal{H}}_{T,J}(\tau)$ is calculated (Section 2.4.2) and its coefficients $k_J^{\gamma}(\tau)$ are plotted against time for $\nu_S = 0$ Hz. Additionally, the average Hamiltonian $\bar{\mathcal{H}}_0(\nu_S)$ is simulated for various offsets ν_S and its coefficients $\bar{k}_{0,J}^{\gamma}(\nu_S)$ are plotted

⁷⁰ It shall, again, be noted that some interactions consist of multiple bilinear terms that each might be scaled differently (e.g. dipolar coupling). In such a case the range of the coefficients also depends on the definition of ω_J .

in red against ν_S . In order to verify the approximation from zeroth order average Hamiltonian the effective propagator of $\hat{\mathcal{H}}_{T,J}(\tau)$ is simulated numerically. The matrix logarithm of the effective propagator leads to coefficients comparable to $\bar{k}_{0,J}^\gamma$ which are plotted on top (blue dashed line). Even for a very large coupling ($J = 300$ Hz) in all cases two congruent lines are obtained which affirms the zeroth order average Hamiltonian (discussion in Section 1.7.3).

- (b) Case 2: shaped pulse in heteronuclear echo on spin \hat{S} with centered delta pulse on spin \hat{I} .

$$\hat{\mathcal{H}}_2 = 2\pi \cdot \nu_S \hat{S}_z + \hat{\mathcal{H}}_{P,\hat{S}}(\tau) + \pi J \cdot 2\hat{I}_z \hat{S}_z$$

The simulations of Case 1 are repeated for Case 2 while spin \hat{I} is inverted by a centered 180° delta pulse. Such a sequence corresponds to a heteronuclear “double-echo” and Case 2 shall only be considered for 180° pulse shapes. The verification of the zeroth order average Hamiltonian by numerical simulations comprising the matrix logarithm is, again, in all cases fulfilled and plotted on top in blue dashed lines.

- (c) Case 3: shaped pulse sandwich with matched pulses on spin \hat{I} and \hat{S} simultaneously.

$$\hat{\mathcal{H}}_{2'} = 2\pi \cdot (\nu_1 \hat{I}_z + \nu_S \hat{S}_z) + \hat{\mathcal{H}}_{P,\hat{I}}(\tau) + \hat{\mathcal{H}}_{P,\hat{S}}(\tau) + \pi J \cdot 2\hat{I}_z \hat{S}_z$$

Two matched shaped pulses (created in a single optimization) are simultaneous applied to a weakly coupled heteronuclear spin system, \hat{I} and \hat{S} , as first introduced in literature.^[103] These simulations are based on the fast calculation described in Section 1.6.2. The verification of the zeroth order average Hamiltonian $\bar{\mathcal{H}}_0(\nu_1, \nu_S)$ is undertaken for a single slice with $\nu_1 = 0$ and $J = 300$ Hz and for considered pulse parameters a good agreement is obtained for all pulses examined throughout the text (data not shown).

- (d) Case 4: one shaped pulse applied to two coupled homonuclear spins, \hat{I}_1 and \hat{I}_2 .

$$\hat{\mathcal{H}}_3 = 2\pi \cdot (\nu_1 \hat{I}_{1z} + \nu_2 \hat{I}_{2z}) + \hat{\mathcal{H}}_{P,\hat{I}}(\tau) + \pi J \cdot (2\hat{I}_{1x} \hat{I}_{2x} + 2\hat{I}_{1y} \hat{I}_{2y} + 2\hat{I}_{1z} \hat{I}_{2z})$$

The difference in the respective offsets, ν_1 and ν_2 , can cause secularization of the strong coupling Hamiltonian as described in Section 2.5. Therefore, the average Hamiltonian $\bar{\mathcal{H}}_0(\nu_1, \nu_2)$ is calculated for various offsets, ν_1 and ν_2 , and its coefficients $\bar{k}_{0,J}^\gamma(\nu_1, \nu_2)$ are illustrated as a contour plot. These simulations are based on the fast calculation described in Section 1.6.2. An equivalent verification of the zeroth order average Hamiltonian $\bar{\mathcal{H}}_0(\nu_1, \nu_2)$ as for Case 3 is undertaken and for considered pulse parameters a good agreement is obtained for all pulses (data not shown).

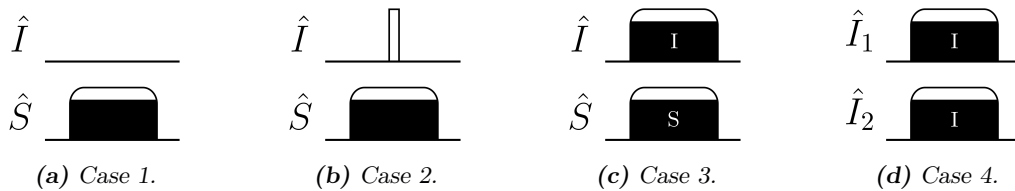


Figure 2.25: Four cases used for the investigation of coupling evolution during a shaped pulse. In (a-c) a heteronuclear in (d) a homonuclear two spin system is assumed. Narrow open and filled wide block correspond to 180° delta and shaped pulse, respectively.

2.4.4 Selective 180° Pulse: Q3 (A)

The amplitude-modulated Q3 pulse shape was introduced by Emsley and Bodenhausen^[143] and is shown in Figure 2.26 (a). It is based on a Gaussian pulse cascade optimized for a band-selective 180° universal rotation (A) – the rotation axes for an x-pulse are shown in Figure 2.26 (b). The band on which the selective rotation acts is indicated by vertical dashed lines while far-off the considered band the effective rotation is only given by the Zeeman interaction (i.e. offset ν). For a pulse length of $\tau_P = 1$ ms corresponding to a maximum RF ampl 3300.8 Hz the selected bandwidth is ± 1.3 kHz and after an additional transition width of 1.9 kHz the pulse's effect is negligible as shown in Figure 2.26 (c). The

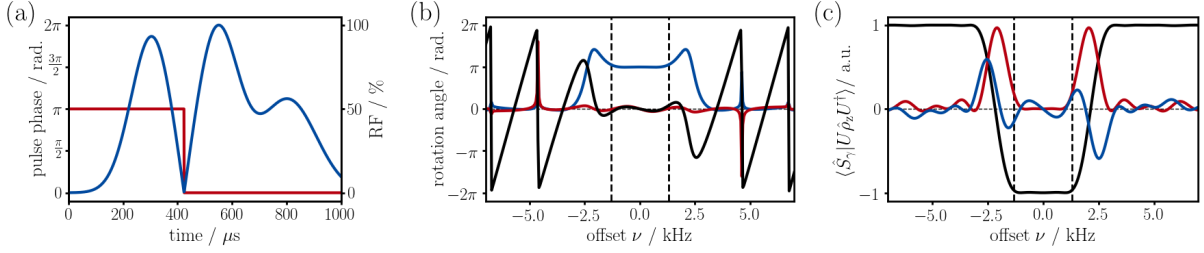


Figure 2.26: The Q3 pulse shape is shown in (a) as phase- (red) and amplitude-profile (blue). Effective rotation axes in (b) and expectation value $\langle \hat{S}_\gamma | U \hat{\rho}_z U^\dagger \rangle$ of the shaped pulse applied to $\hat{\rho}_z = \hat{S}_z$ in (c) are plotted for Cartesian operators \hat{S}_x (blue), \hat{S}_y (red) and \hat{S}_z (black).

time-dependent Hamiltonian in the toggling frame $\hat{\mathcal{H}}_{T,J}(\tau)$ for Case 1 and $\nu_S = 0$ Hz is shown in Figure 2.27 (a) to (c). Since the pulse is amplitude-modulated, the coefficient $k_T^{zx}(\tau)$ is zero considering an x-pulse. For a pulse resulting in states of constant phase no coupling evolution is expected^[103] which is also found within the selected band in Figure 2.27 (d) to (f). If placed in an echo (Case 2) the \hat{I}_z component of $\hat{\mathcal{H}}_{T,J}(\tau)$ is inverted at half the pulse length which also has an influence on the average Hamiltonian $\bar{\mathcal{H}}_{0,J}(\nu_S)$ shown in Figure 2.28. As stated by Lescop et al.^[202] the Q3 exhibits no (or only little) coupling evolution in such an echo – for $\nu_S = 0$ Hz the coupling is active during 10% of the pulse length. However, moving away from the band's center the coupling can no longer be neglected (up to 35%) which is shown in Figure 2.28 (d) to (f). In order to avoid coupling evolution one could place the shaped pulse in an echo where the delta pulse on \hat{I} is left or right aligned and the coupling evolution would then be given by Figure 2.27. However, this might require to compensate chemical shift evolution on spin \hat{I} at another time in the pulse sequence. If the shaped pulse is applied to a band in which two

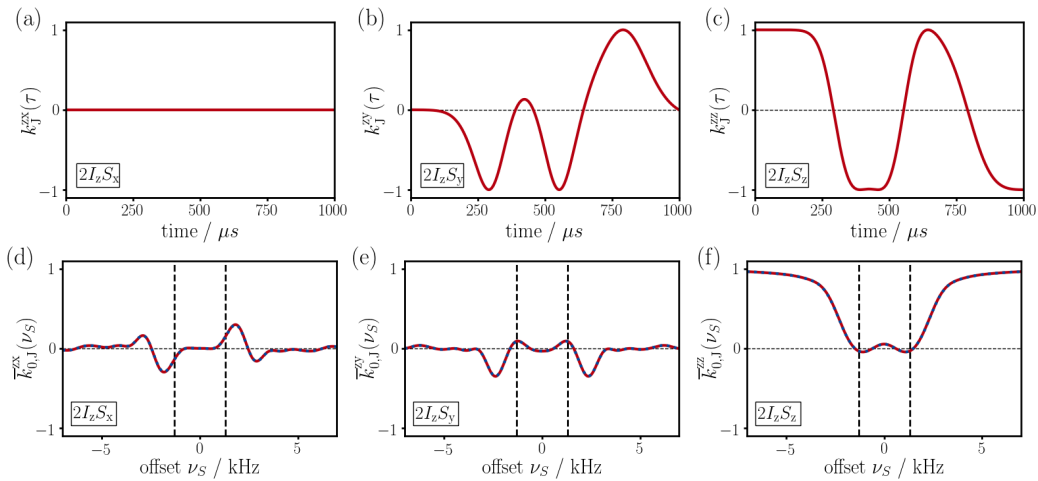


Figure 2.27: Case 1 (Section 2.4.3) – Hamiltonian in toggling frame $\hat{\mathcal{H}}_{T,J}(\tau)$ with $\nu_S = 0$ Hz in (a-c) and the average Hamiltonian $\bar{\mathcal{H}}_{0,J}(\nu_S)$ in (d-f) are plotted in red for non-zero operators. Shape: Q3 (UR 180°); $RF_{max} = 3301$ Hz; $\tau_P = 1$ ms; $BW \approx \pm 1.3$ kHz; transition ≈ 1.9 kHz.

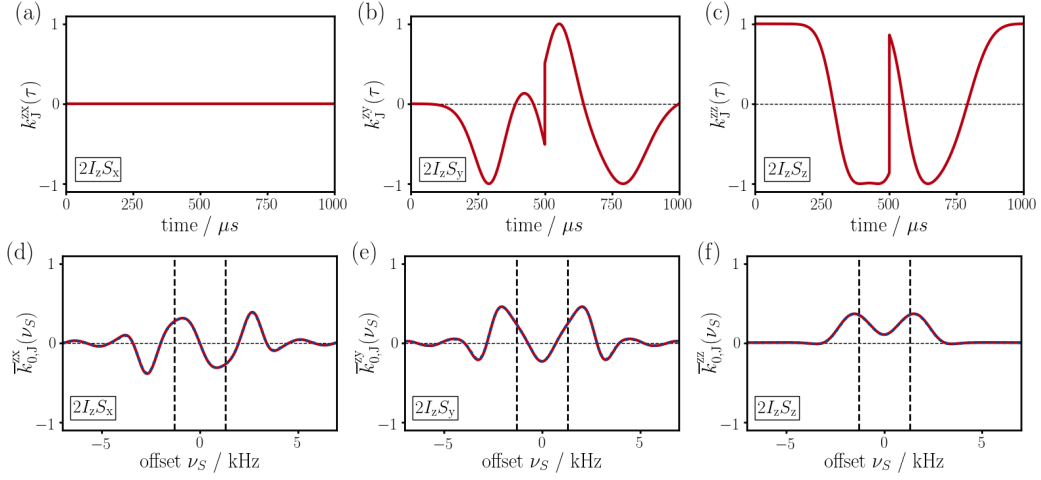


Figure 2.28: Case 2 (Section 2.4.3) – Hamiltonian in toggling frame $\hat{\mathcal{H}}_{T,j}(\tau)$ with $\nu_S = 0$ Hz in (a-c) and the average Hamiltonian $\bar{\mathcal{H}}_{0,j}(\nu_S)$ in (d-f) are plotted in red for non-zero operators. Shape: Q3 (UR 180°); $RF_{\max} = 3301$ Hz; $\tau_P = 1$ ms; $BW \approx \pm 1.3$ kHz; transition ≈ 1.9 kHz.

spins, \hat{I}_1 and \hat{I}_2 , are located (Case 4) the coupling during the shaped pulse depends on both offsets, ν_1 and ν_2 , as illustrated in Figure 2.29. Compared to other band-selective 180° universal rotations (r-SNOB 2.4.6 and RE-BURP 2.4.5) it is apparent that bilinear terms within the optimized area (dashed lines) are non-uniformly distributed. The weak coupling term ($2I_{1z}I_{2z}$) decreases towards the off-diagonal edges and so-called anti-phase terms ($2I_{1z}I_{2x/y}$ and $2I_{1x/y}I_{2z}$) are non-zero. Also, the zero-quantum terms that arise from strong coupling ($2I_{1x/y}I_{2x/y}$) exhibit an enlarged diagonal compared to the diagonal far-off the selected band – strong coupling artifacts are expected for a wider band.

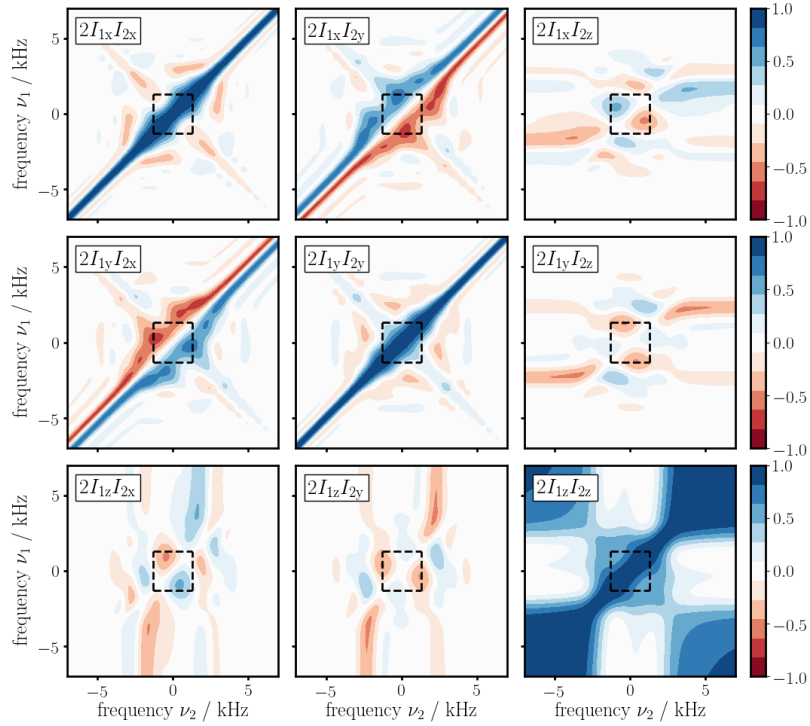


Figure 2.29: Case 4 (Section 2.4.3) – average Hamiltonian $\bar{\mathcal{H}}_{0,j}(\nu_1, \nu_2)$ for homonuclear system. Shape: Q3 (UR 180°); $RF_{\max} = 3301$ Hz; $\tau_P = 1$ ms; $BW \approx \pm 1.3$ kHz; transition ≈ 1.9 kHz.

2.4.5 Selective 180° Pulse: RE-BURP (A)

The RE-BURP pulse shape was optimized by Geen and Freeman^[195] and is shown in Figure 2.30 (a). The amplitude-modulated shape reminds of a sinc function with the by far largest amplitude in the center. It corresponds to a band-selective 180° universal rotation (A) and since it is time-symmetric the effective rotation axes for an x-pulse are in the xz-plane⁷¹ as shown in Figure 2.30 (b). For a pulse length of $\tau_P = 1$ ms corresponding to a maximum RF amplitude of 6264.9 Hz the selected bandwidth is ± 2.0 kHz (indicated by vertical dashed lines). The transition width is estimated as 2.0 kHz and the pulse's effect is negligible for an offset larger ± 4.0 kHz as shown in Figure 2.30 (c). The time-dependent Hamiltonian

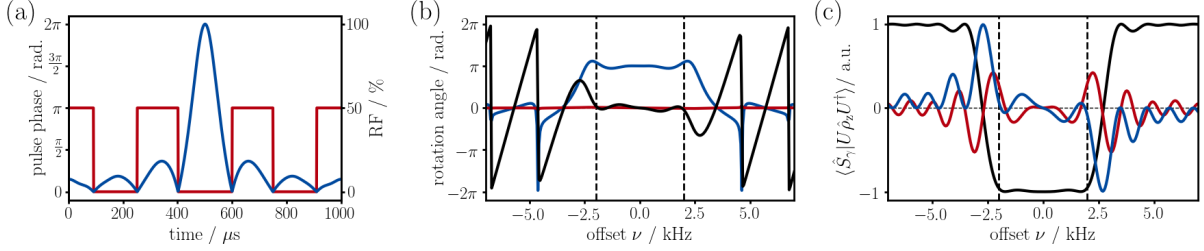


Figure 2.30: The RE-BURP pulse shape is shown in (a) as phase- (red) and amplitude-profile (blue). Effective rotation axes in (b) and expectation value $\langle \hat{S}_\gamma | U \hat{\rho}_z U^\dagger \rangle$ of the shaped pulse applied to $\hat{\rho}_z = \hat{S}_z$ in (c) are plotted for Cartesian operators \hat{S}_x (blue), \hat{S}_y (red) and \hat{S}_z (black).

in the toggling frame $\hat{\mathcal{H}}_{T,J}(\tau)$ for Case 1 and $\nu_S = 0$ Hz is shown in Figure 2.31 (a) to (c). It is obvious from (c) that coupling evolution is reversed in the center of the pulse shape comparable to an echo (Section 2.4.15) and the coupling is suppressed as shown for the average coupling Hamiltonian $\bar{\mathcal{H}}_{0,J}(\nu_S)$ in Figure 2.31 (d) to (f). If placed in a heteronuclear echo (Case 2) the I_z component of $\hat{\mathcal{H}}_{T,J}(\tau)$ is inverted at half the pulse length and coupling evolution is to be considered during 95% of the pulse length (Figure 2.32). Certainly, this is a desirable property if the shaped pulse is applied in a coherence

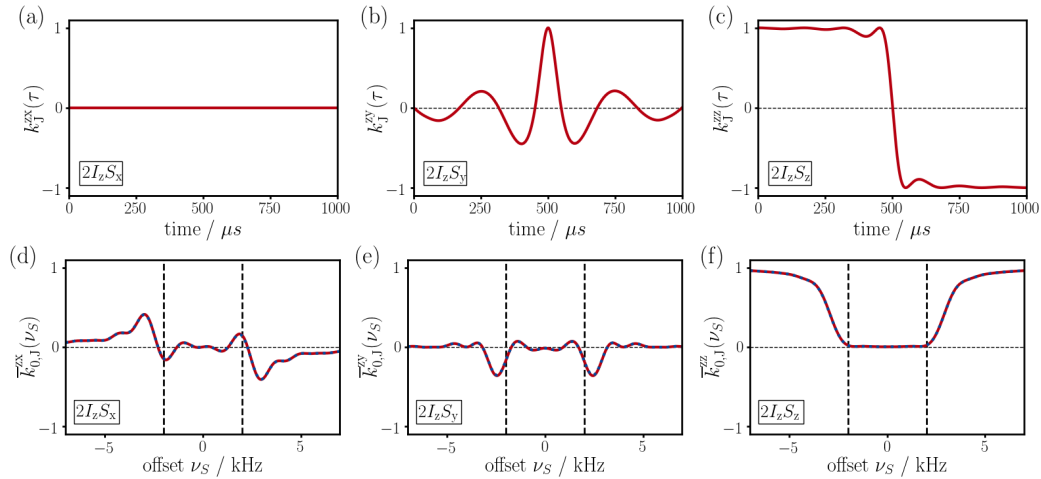


Figure 2.31: Case 1 (Section 2.4.3) – Hamiltonian in toggling frame $\hat{\mathcal{H}}_{T,J}(\tau)$ with $\nu_S = 0$ Hz in (a-c) and the average Hamiltonian $\bar{\mathcal{H}}_{0,J}(\nu_S)$ in (d-f) are plotted in red for non-zero operators. Shape: RE-BURP (UR 180°); $RF_{\max} = 6265$ Hz; $\tau_P = 1$ ms; $BW \approx \pm 2.0$ kHz; transition ≈ 2.0 kHz.

⁷¹ From the discussion in Section 1.7.3 we know that the average Hamiltonian $\bar{\mathcal{H}}$ of a time-symmetric Hamiltonian is given only by even terms $\bar{\mathcal{H}}_{\text{even}}$ of the Magnus series. Any contribution to $\bar{\mathcal{H}}_{\text{even}}$ (except zeroth order) is given by even numbered nested commutators that contain the Hamiltonian $\hat{\mathcal{H}}(t)$ at different time points with $\hat{\mathcal{H}}(t) = 2\pi [\nu_P(t)\hat{I}_x + \nu_z\hat{I}_z]$. Based on its linear property the sum in the commutator can be rewritten to a sum of commutators. Due to the cyclic commutation any commutator of the general form $[A, [B, C]]$ with $A, B, C = \hat{I}_x, \hat{I}_z$ (commutator in second order terms) is either 0 or equal to \hat{I}_x or \hat{I}_z (neglecting prefactors). Hence, $\bar{\mathcal{H}}_{\text{even}}$ is given only by terms of \hat{I}_x and \hat{I}_z .

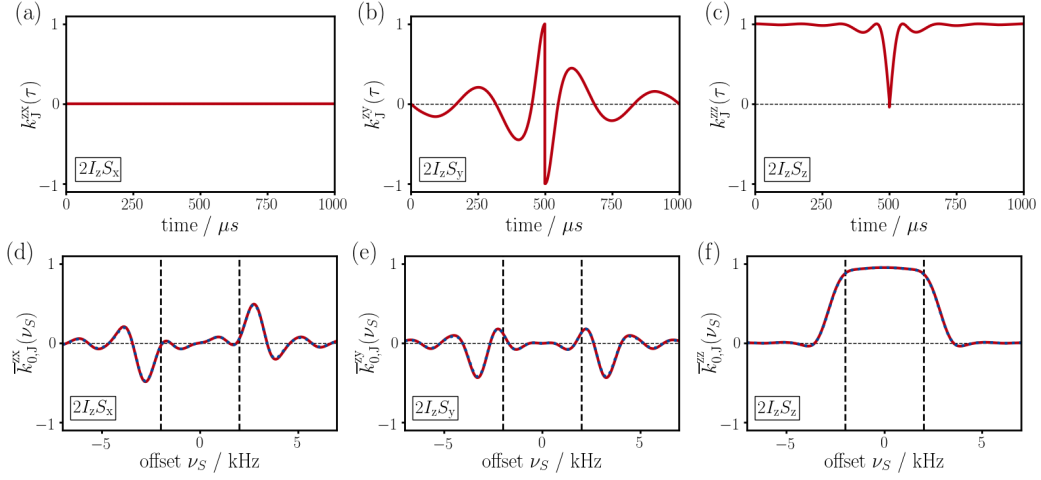


Figure 2.32: Case 2 (Section 2.4.3) – Hamiltonian in toggling frame $\hat{H}_{T,J}(\tau)$ with $\nu_S = 0$ Hz in (a-c) and the average Hamiltonian $\bar{H}_{0,J}(\nu_S)$ in (d-f) are plotted in red for non-zero operators. Shape: RE-BURP (UR 180°); $RF_{\max} = 6265$ Hz; $\tau_P = 1$ ms; $BW \approx \pm 2.0$ kHz; transition ≈ 2.0 kHz.

transfer element.^[12] It is worth noting that the offset profile of $2I_z S_z$ is quite uniform and at the edges of considered band it is still at roughly 90%. A remarkable property of the RE-BURP pulse shape is also found for the application to a homonuclear two spin system (Case 4) – within the considered band the pulse shape can, again, be approximated by an echo. In Figure 2.33 the weak coupling term ($2I_{1z}I_{2z}$) is uniformly active and the anti-phase terms ($2I_{1z}I_{2x/y}$ and $2I_{1x/y}I_{2z}$) are likewise uniformly zero. The zero-quantum terms ($2I_{1x/y}I_{2x/y}$), arising from strong coupling, are non zero for similar offsets, ν_1 and ν_2 , and, as expected, the diagonal is slightly broadened (Appendix 5.2.2). Also, for certain areas of the anti-phase terms a broad transition width is noticed.

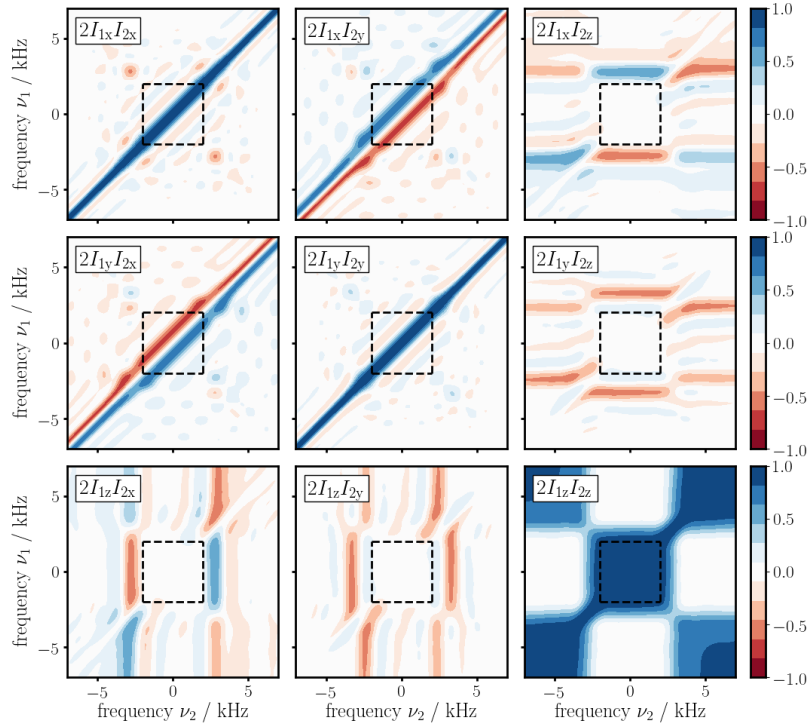


Figure 2.33: Case 4 (Section 2.4.3) – average Hamiltonian $\bar{H}_{0,J}(\nu_1, \nu_2)$ for homonuclear system. Shape: RE-BURP (UR 180°); $RF_{\max} = 6265$ Hz; $\tau_P = 1$ ms; $BW \approx \pm 2.0$ kHz; transition ≈ 2.0 kHz.

2.4.6 Selective 180° Pulse: r-SNOB (A)

The amplitude-modulated r-SNOB pulse shape was proposed by Kupče et al.^[197] and is shown in Figure 2.34 (a). It induces a band-selective 180° universal rotation (A) – the rotation axes for an x-pulse are shown in Figure 2.34 (b). The pulse was optimized with respect to selectivity and for a pulse length of $\tau_P = 1$ ms corresponding to a maximum RF amplitude of 2339.8 Hz the selected bandwidth is only ± 0.6 kHz (vertical dashed lines). Hence, for a given bandwidth the r-SNOB is roughly two times shorter than the Q3 (2.4.4) and even three times shorter than the RE-BURP (2.4.5). The transition width is estimated as 1.4 kHz and the pulse's effect is negligible for an offset larger ± 2.0 kHz as shown in Figure 2.34 (c).

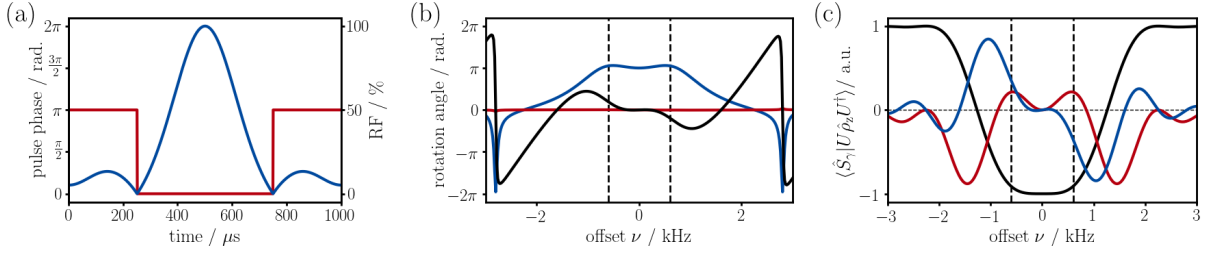


Figure 2.34: The r-SNOB pulse shape is shown in (a) as phase- (red) and amplitude-profile (blue). Effective rotation axes in (b) and expectation value $\langle \hat{S}_\gamma | U \hat{\rho}_z U^\dagger \rangle$ of the shaped pulse applied to $\hat{\rho}_z = \hat{S}_z$ in (c) are plotted for Cartesian operators \hat{S}_x (blue), \hat{S}_y (red) and \hat{S}_z (black).

For Case 1 and $\nu_S = 0$ Hz the Hamiltonian in the toggling frame $\hat{H}_{T,J}(\tau)$ is shown in Figure 2.35 (a) to (c) and a certain similarity to the RE-BURP pulse (2.4.5) is evident. Again, for a pulse resulting in a state of constant phase no coupling evolution is expected.^[103] However, due to imperfections for the terms $2I_z S_x$ and $2I_z S_y$ coupling evolves during up to 9% and 25% of the pulse length, respectively, as is shown in Figure 2.35 (d) to (f). For Case 2 in a heteronuclear echo the pulse shape behaves, again, similar to the RE-BURP pulse shape. The time-dependent Hamiltonian in the toggling $\hat{H}_{T,J}(\tau)$ is inverted at half the pulse length (Figure 2.36 (a) to (c)) and the weak coupling term ($2I_z S_z$) is active during 84% (edges) and 90% (center) of the pulse length (Figure 2.36 (d) to (f)). Hence, with respect to the above mentioned properties the quality of the RE-BURP is somewhat better compared to the r-SNOB. However, considering the same selected bandwidth the r-SNOB is also roughly three times shorter. With this regard, also the coupling evolution during the r-SNOB is less significant compared to RE-BURP.

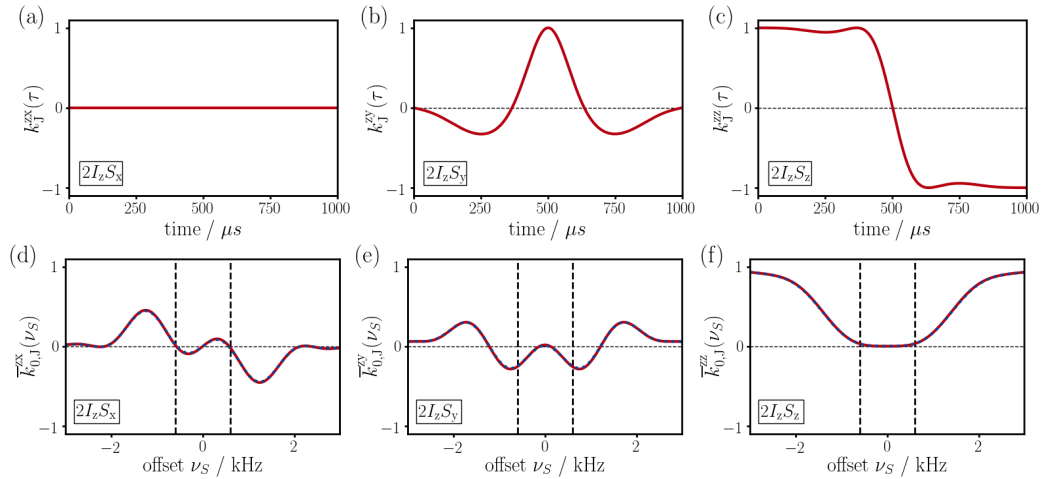


Figure 2.35: Case 1 (Section 2.4.3) – Hamiltonian in toggling frame $\hat{H}_{T,J}(\tau)$ with $\nu_S = 0$ Hz in (a-c) and the average Hamiltonian $\bar{H}_{0,J}(\nu_S)$ in (d-f) are plotted in red for non-zero operators. Shape: r-SNOB (UR 180°); $RF_{\max} = 2340$ Hz; $\tau_P = 1$ ms; $BW \approx \pm 0.6$ kHz; transition ≈ 1.4 kHz.

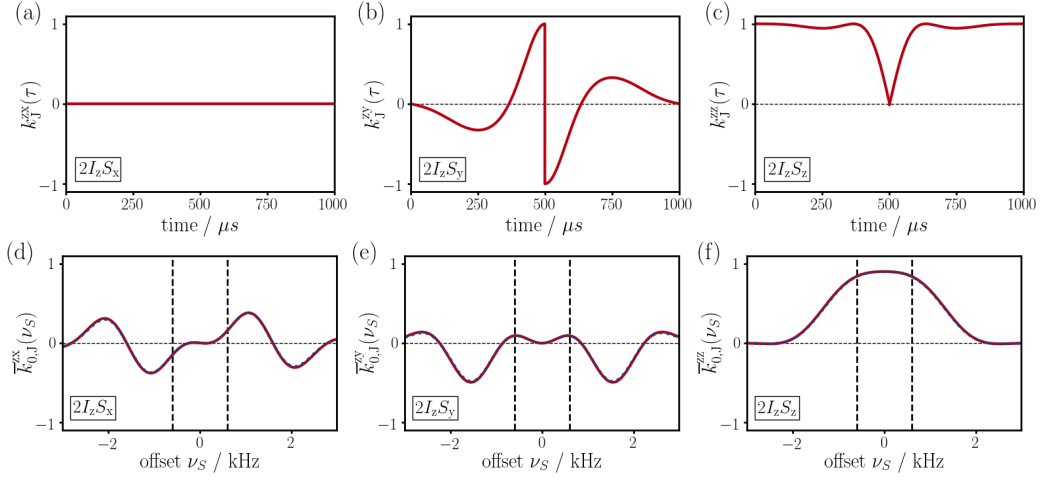


Figure 2.36: Case 2 (Section 2.4.3) – Hamiltonian in toggling frame $\hat{\mathcal{H}}_{T,j}(\tau)$ with $\nu_S = 0$ Hz in (a-c) and the average Hamiltonian $\bar{\mathcal{H}}_{0,j}(\nu_S)$ in (d-f) are plotted in red for non-zero operators. Shape: r-SNOB (UR 180°); $RF_{\max} = 2340$ Hz; $\tau_P = 1$ ms; $BW \approx \pm 0.6$ kHz; transition ≈ 1.4 kHz.

Applied to a homonuclear two spin system (Case 4) the coupling evolution during the r-SNOB pulse shape is illustrated in Figure 2.37. Again, it is similar to the RE-BURP and mainly the effect of strong coupling ($2I_{1x/y}I_{2x/y}$) is more dominant within dashed lines. Compared to an area that is not perturbed by the pulse it is evident that the increase in strong coupling can be addressed to the narrower bandwidth that the r-SNOB covers. Anti-phase ($2I_{1z}I_{2x/y}$ and $2I_{1x/y}I_{2z}$) and weak coupling terms ($2I_{1z}I_{2z}$) are equal to more or less 0 and 1, respectively, and the transition width is increased for certain areas.

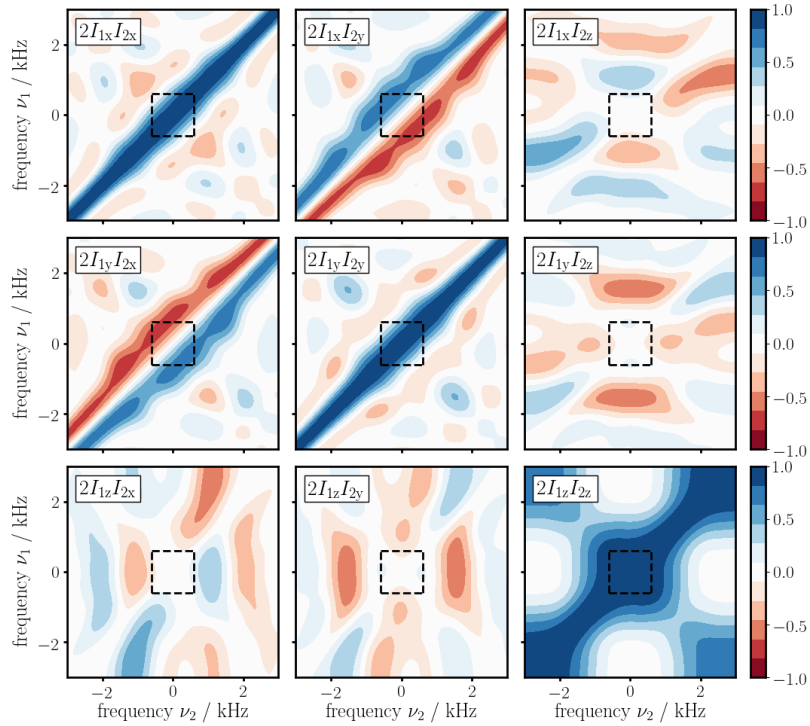


Figure 2.37: Case 4 (Section 2.4.3) – average Hamiltonian $\bar{\mathcal{H}}_{0,j}(\nu_1, \nu_2)$ for homonuclear system. Shape: r-SNOB (UR 180°); $RF_{\max} = 2340$ Hz; $\tau_P = 1$ ms; $BW \approx \pm 0.6$ kHz; transition ≈ 1.4 kHz.

2.4.7 Selective 180° Pulse: I-BURP-2 (B)

The I-BURP-2 is an amplitude-modulated pulse shape that belongs to the BURP family^[195] and is shown in Figure 2.38 (a). It corresponds to a band-selective 180° inversion pulse (B) whose rotation axes are distributed in the transverse plane as illustrated in Figure 2.38 (b). Hence, if applied to transverse coherences phase distortions are expected unless the pulse is applied twice consecutively. For a pulse length of $\tau_P = 1$ ms corresponding to a maximum RF amplitude of 4968.3 Hz the selected bandwidth is ± 2.0 kHz (vertical dashed lines). The transition width is estimated as 1.5 kHz and the pulse's effect is negligible for an offset larger ± 3.5 kHz as shown in Figure 2.38 (c). These are, hence, smaller values compared to its big brother, the RE-BURP (Section 2.4.5), whose transition width is roughly 2.0 kHz. Considering Case 1 the Hamiltonian in the toggling frame $\hat{\mathcal{H}}_{T,J}(\tau)$ for $\nu_S = 0$ Hz is illustrated in

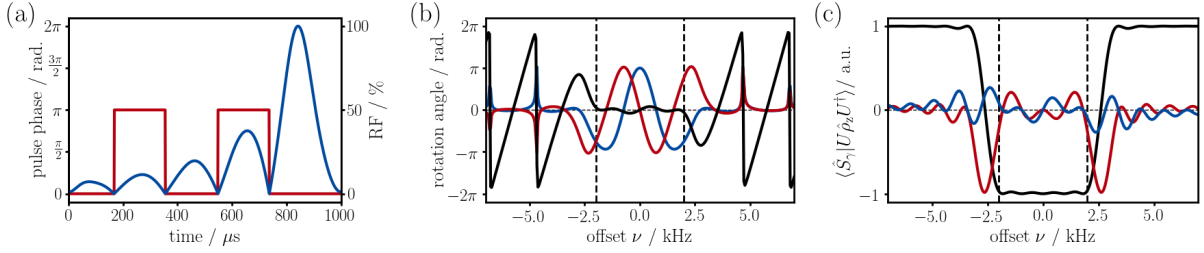


Figure 2.38: The I-BURP-2 pulse shape is shown in (a) as phase- (red) and amplitude-profile (blue). Effective rotation axes in (b) and expectation value $\langle \hat{S}_\gamma | U \hat{\rho}_z U^\dagger \rangle$ of the shaped pulse applied to $\hat{\rho}_z = \hat{S}_z$ in (c) are plotted for Cartesian operators \hat{S}_x (blue), \hat{S}_y (red) and \hat{S}_z (black).

Figure 2.39 (a) to (c). It is crucial to note that in Figure 2.39 (c) the weak coupling term ($2I_z S_z$) is active during a long part of the pulse. This is based on the fact that the largest effect of the pulse is found at the end of the shape. In contrast to pulse shapes discussed in preceding sections the I-BURP-2 is no refocusing pulse. Hence, the average coupling Hamiltonian $\bar{\mathcal{H}}_{0,J}(\nu_S)$ is not required to be suppressed entirely which is shown in Figure 2.39 (d) to (f). For Case 1, weak coupling can be considered active during 48% (edges) and 68% (center) of the pulse length (Figure 2.39 (f)) which is, ironically, longer than for Case 2 where the I-BURP-2 is applied in a double-echo. Here, the time-dependent Hamiltonian in the toggling frame $\hat{\mathcal{H}}_{T,J}(\tau)$ is inverted at half the pulse length (Figure 2.40 (a) to (c) and the effective weak coupling is active only during 45% (edges) and 31% (center) of the pulse length (Figure 2.40 (f)). Note, if the I-BURP-2 is applied as inversion pulse on an initial state of S_z the term $2I_z S_z$ has no effect due

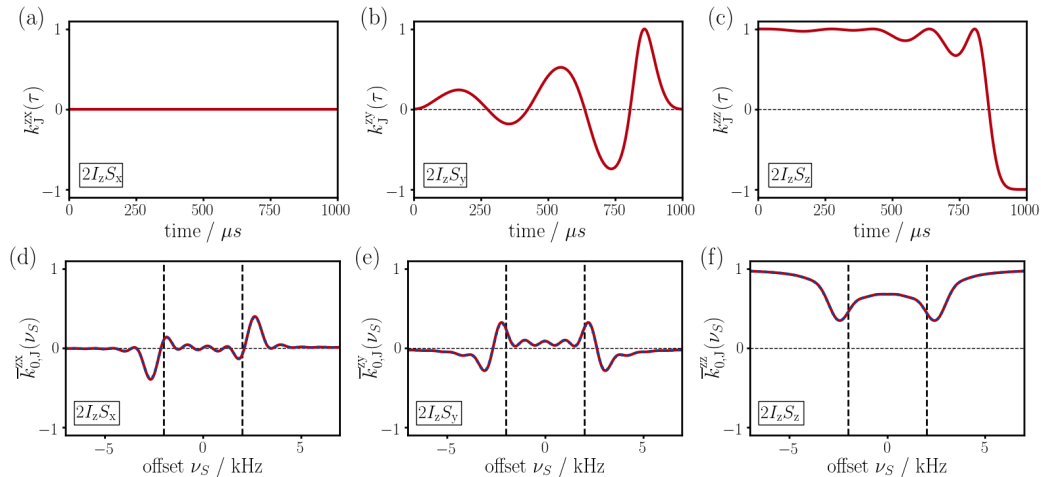


Figure 2.39: Case 1 (Section 2.4.3) – Hamiltonian in toggling frame $\hat{\mathcal{H}}_{T,J}(\tau)$ with $\nu_S = 0$ Hz in (a-c) and the average Hamiltonian $\bar{\mathcal{H}}_{0,J}(\nu_S)$ in (d-f) are plotted in red for non-zero operators. Shape: I-BURP-2 (inversion); $RF_{\max} = 4968$ Hz; $\tau_P = 1$ ms; $BW \approx \pm 2.0$ kHz; transition ≈ 1.5 kHz.

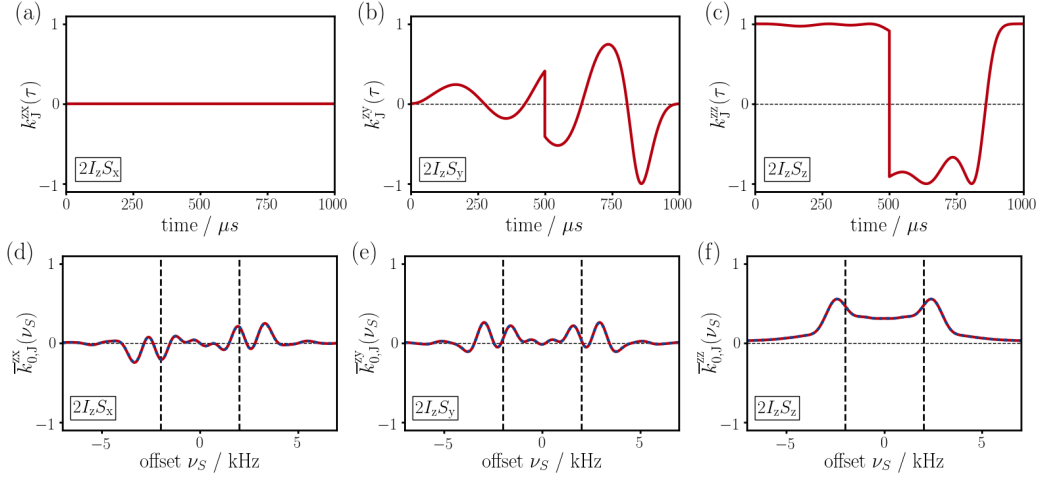


Figure 2.40: Case 2 (Section 2.4.3) – Hamiltonian in toggling frame $\hat{\mathcal{H}}_{T,j}(\tau)$ with $\nu_S = 0$ Hz in (a-c) and the average Hamiltonian $\bar{\mathcal{H}}_{0,j}(\nu_S)$ in (d-f) are plotted in red for non-zero operators. Shape: I-BURP-2 (inversion); $RF_{\max} = 4968$ Hz; $\tau_P = 1$ ms; $BW \approx \pm 2.0$ kHz; transition ≈ 1.5 kHz.

to commutation (Equation 2.4.11) – for transverse coherence on either spin \hat{I} or \hat{S} , on the other hand, these terms no longer commute. In Figure 2.41 the average coupling Hamiltonian $\bar{\mathcal{H}}_{0,j}(\nu_1, \nu_2)$ during the I-BURP-2 is shown if applied to a homonuclear two spin system (Case 4). Compared to preceding pulse shapes the I-BURP-2 exhibits a surprisingly narrow diagonal for zero-quantum terms ($2I_{1x/y}I_{2x/y}$). This is, again, due to the fact that the major rotation occurs at the end of the shape and the evolution of zero quantum terms in $\hat{\mathcal{H}}_{T,j}(\tau)$ is not refocused during a longer period – it is somewhat similar to increasing the delay in a CPMG sequence (see CPMG in toggling frame in Appendix 5.2.2). The weak coupling term ($2I_{1z}I_{2z}$) is relatively uniform at ≈ 1 while minor effects or artifacts could emanate from anti-phase terms ($2I_{1y}I_{2z}$ and $2I_{1z}I_{2y}$).

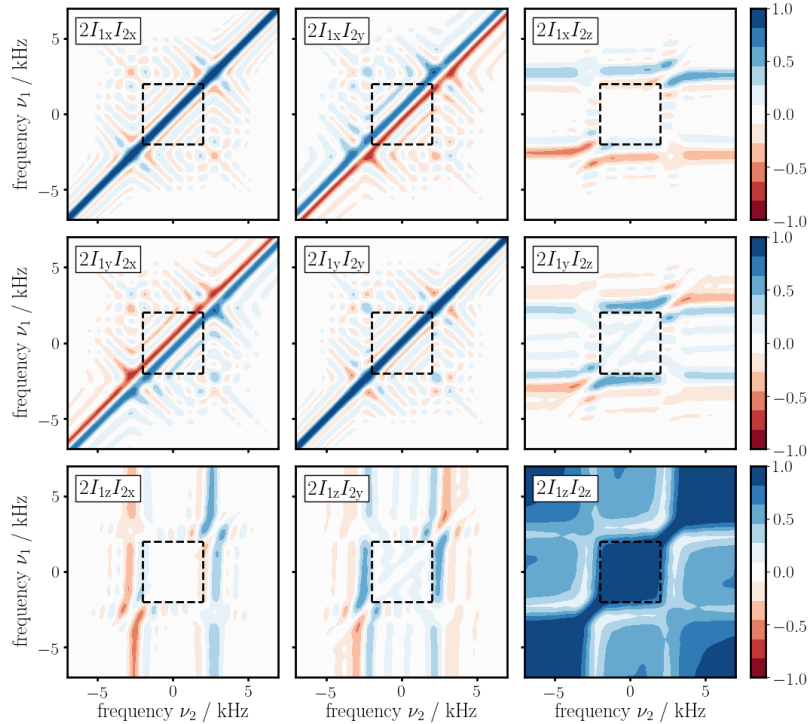


Figure 2.41: Case 4 (Section 2.4.3) – average Hamiltonian $\bar{\mathcal{H}}_{0,j}(\nu_1, \nu_2)$ for homonuclear system. Shape: I-BURP-2 (inversion); $RF_{\max} = 4968$ Hz; $\tau_P = 1$ ms; $BW \approx \pm 2.0$ kHz; transition ≈ 1.5 kHz.

2.4.8 Selective 90° Pulse: Q5 (A)

The Q5 pulse shape, shown in Figure 2.42 (a), is based on a Gaussian pulse cascade and is, hence, familiar to the Q3 (Section 2.4.4).^[143] Like all selective pulses discussed in this chapter the Q5 is amplitude-modulated and it was optimized for a band-selective 90° universal rotation (A). The rotation axes for an x-pulse are shown in Figure 2.42 (b), where the effective rotation far-off the considered band is only given by the Zeeman interaction (i.e. offset ν). For a pulse length of $\tau_P = 1$ ms corresponding to an RF amplitude of 4586.31 Hz the selected bandwidth is ± 2.6 kHz which is twice as broad as the Q3 refocusing pulse (± 1.3 kHz). After an additional transition width of 1.2 kHz (Q3: 1.9 kHz) the pulse's effect is negligible at ± 3.8 kHz (Q3: ± 3.2 kHz) as shown in Figure 2.42 (c). For the Q5 the effective rotation was

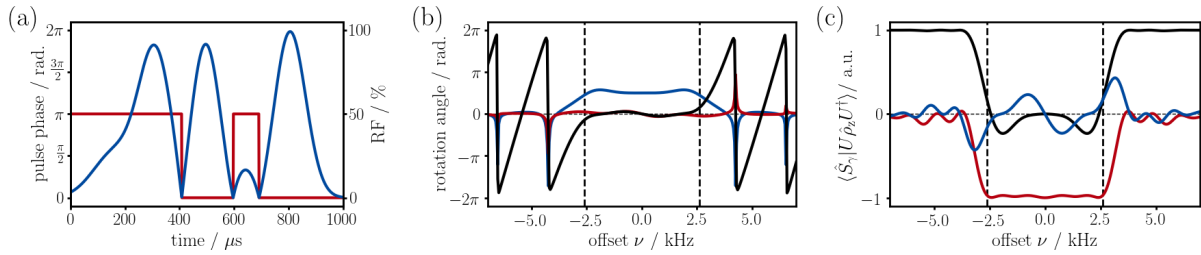


Figure 2.42: The Q5 pulse shape is shown in (a) as phase- (red) and amplitude-profile (blue). Effective rotation axes in (b) and expectation value $\langle \hat{S}_\gamma | U \hat{\rho}_z U^\dagger \rangle$ of the shaped pulse applied to $\hat{\rho}_z = \hat{S}_z$ in (c) are plotted for Cartesian operators \hat{S}_x (blue), \hat{S}_y (red) and \hat{S}_z (black).

optimized to result in a 90° universal rotation and, hence, in Case 1 a heteronuclear coupling does not evolve during the shaped pulse. The simulations of the time-dependent Hamiltonian in the toggling frame $\hat{\mathcal{H}}_{T,J}(\tau)$ are shown in Figure 2.43 (a) to (c) which indicate a rather complex trajectory that includes multiple inversions. Still, the average Hamiltonian $\bar{\mathcal{H}}_{0,J}(\nu_S)$ in Figure 2.43 (d) to (f) can confirm that over the selected band more or less no coupling evolution is found – as expected for a pulse of class A. This is, clearly, an advantage over some of the following selective excitation pulse shapes, e.g. the e-SNOB (B3, Section 2.4.10) or likewise the E-BURP-2 (B2, Section 2.4.9) and BEBOP (B2, Section 2.4.14) where the coupling evolution has to be considered depending on the initial or final state on which the pulse is applied.

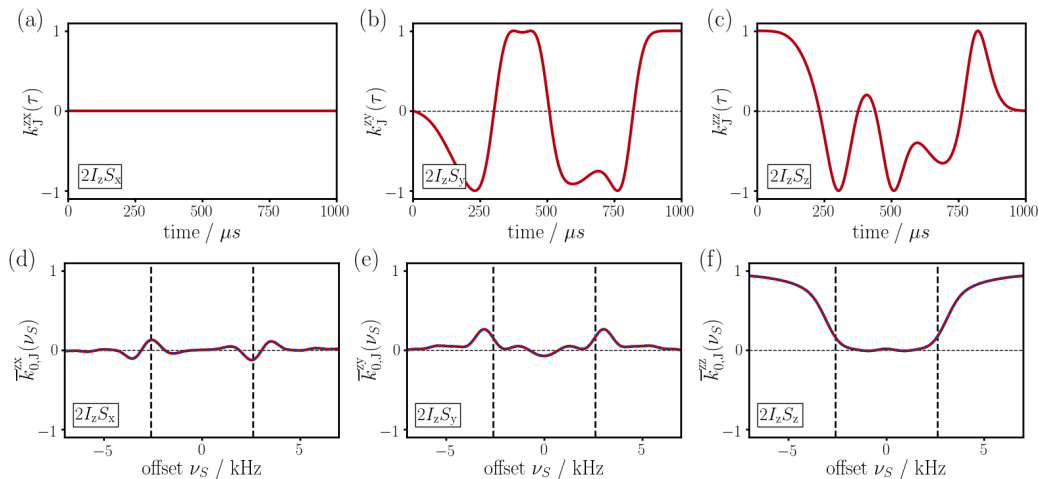


Figure 2.43: Case 2 (Section 2.4.3) – Hamiltonian in toggling frame $\hat{\mathcal{H}}_{T,J}(\tau)$ with $\nu_S = 0$ Hz in (a-c) and the average Hamiltonian $\bar{\mathcal{H}}_{0,J}(\nu_S)$ in (d-f) are plotted in red for non-zero operators. Shape: Q5 (UR 90°); $RF_{\max} = 4586$ Hz; $\tau_P = 1$ ms; $BW \approx \pm 2.6$ kHz; transition ≈ 1.2 kHz.

If applied to a homonuclear spin system (Case 4) it is conceivable that above mentioned multiple inversions during the Q5 shaped pulse can operate comparable to a CPMG sequence. This would lead to a repetitive refocusing of the offset and, in turn, to a broadening of the strong coupling regime. Indeed, in the simulations of the average Hamiltonian $\bar{\mathcal{H}}_{0,j}(\nu_1, \nu_2)$ shown in Figure 2.44 the zero-quantum operators ($2I_{1x/y}I_{2x/y}$) exhibit a broadened diagonal what can be considered a consequence of multiple inversions during the shaped pulse. Additionally, some of the anti-phase terms ($2I_{1z}I_{2x/y}$ and $2I_{1x/y}I_{2z}$) are notably non-zero and the weak coupling term ($2I_{1z}I_{2z}$) is far from being uniform. The effect of homonuclear coupling evolution during the Q5 shaped pulse, hence, strongly depends on the offset of considered spins, ν_1 and ν_2 , and artifacts could arise also from anti-phase terms. In presence of large couplings or if the application requires a narrow band and, hence, a very long pulse other pulse shapes might be preferable – e.g. the E-BURP-2 in the following Section 2.4.9 if no pulse of class A is required.

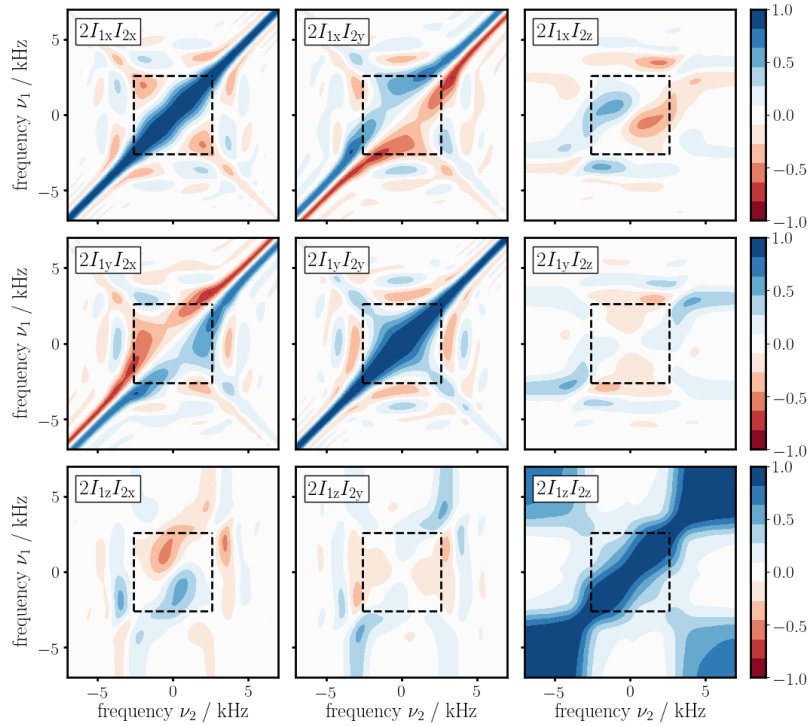


Figure 2.44: Case 4 (Section 2.4.3) – average Hamiltonian $\bar{\mathcal{H}}_{0,j}(\nu_1, \nu_2)$ for homonuclear system. Shape: Q5 (UR 90°); $RF_{max} = 4586$ Hz; $\tau_P = 1$ ms; $BW \approx \pm 2.6$ kHz; transition ≈ 1.2 kHz.

2.4.9 Selective 90° Pulse: E-BURP-2 (B2)

The E-BURP-2 is another amplitude-modulated pulse shape from the BURP family^[195] and is shown in Figure 2.45 (a). In contrast to the RE-BURP (Section 2.4.5) and the I-BURP-2 (Section 2.4.7) the E-BURP-2 leads to a band-selective 90° excitation that was optimized for a point-to-point transfer (B2) – its rotation axes are distributed on a tilted plane and the Cartesian components are illustrated in Figure 2.45 (b). For a pulse length of $\tau_P = 1$ ms corresponding to an RF amplitude of 4096.4 Hz the selected bandwidth is ± 2.0 kHz (indicated by vertical dashed lines). The transition width is estimated as 1.3 kHz and the pulse's effect is negligible for an offset larger ± 3.3 kHz as shown in Figure 2.45 (c). These are, hence, smaller values compared to the RE-BURP (transition: 2.0 kHz) and similar values compared to the I-BURP-2 (transition: 1.5 kHz).^[195] Another similarity to the I-BURP-2 is found when

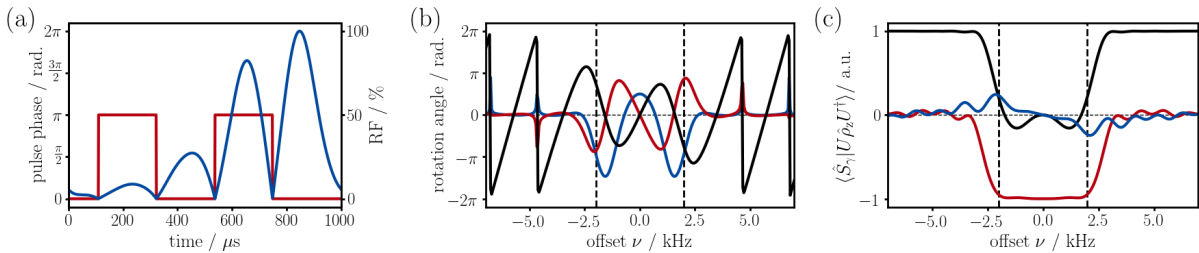


Figure 2.45: The E-BURP-2 pulse shape is shown in (a) as phase- (red) and amplitude-profile (blue). Effective rotation axes in (b) and expectation value $\langle \hat{S}_\gamma | U \hat{\rho}_z U^\dagger \rangle$ of the shaped pulse applied to $\hat{\rho}_z = \hat{S}_z$ in (c) are plotted for Cartesian operators \hat{S}_x (blue), \hat{S}_y (red) and \hat{S}_z (black).

the scalar coupling Hamiltonian in the toggling frame $\hat{\mathcal{H}}_{T,J}(\tau)$ for Case 1 is considered. The largest effect of the E-BURP-2 is found at the end and, therefore, the weak coupling term ($2I_z S_z$) is active during a long time in the beginning as shown in Figure 2.46 (c). As expected for an amplitude-modulated x-pulse the term $2I_z S_x$ is zero while the term $2I_z S_y$ is modulated (Figure 2.46 (a) to (b)). Due to the modulations the term $2I_z S_y$ averages to zero and within the selected bandwidth the zeroth order average coupling Hamiltonian $\bar{\mathcal{H}}_{0,J}(\nu_S)$ during the shaped pulse is, hence, dominated by the weak coupling term (Figure 2.46 (d) to (f)). The E-BURP-2 is optimized for an excitation starting from an initial population (e.g. \hat{S}_z or $\hat{I}_z \hat{S}_z$). With this regard, the average coupling propagator $\bar{U}_{0,J}$ of the E-BURP-2 shaped pulse, which is dominated by $2I_z S_z$, commutes with the initial state (\hat{S}_z or $\hat{I}_z \hat{S}_z$) and the coupling is without consequences (see Equation 2.4.11). As stated before, this does not apply for transverse coherence on either spin \hat{I} or \hat{S} .

Commonly (e.g. in a heteronuclear correlation experiment) the E-BURP-2 is followed by its time-reversed version with inverted phase in order to transfer the excited coherence back to a population (likewise e.g. \hat{S}_z or $\hat{I}_z \hat{S}_z$). Hence, it would be interesting to know about the effective coupling during the time-reversed E-BURP-2, too. From the discussion in Section 2.4.2 it turns out that for the time-reversed version an average coupling propagator $\bar{U}_{0,J}(-\nu_S)$ can be obtained that, with *reversed* offset profile, is *identical* to the one obtained for the non-reversed E-BURP-2 (Figure 2.46 (d) to (f)) – it is, however, applied to the final state created from the shaped pulse. Since the average coupling propagator is dominated by the weak coupling term and the final state is in most cases also a population (e.g. \hat{S}_z or $\hat{I}_z \hat{S}_z$) there is again no effect from coupling due to commutation with $[\bar{U}_{0,J}(-\nu_S), \hat{\rho}_{\text{final}}] \approx 0$. Still, for the sake of completeness, the simulations of the average coupling Hamiltonian $\bar{\mathcal{H}}_{0,J}(\nu_S)$ during the time-reversed E-BURP-2 are shown in Figure 2.46 (g) to (i) which are supposed to act on the *initial* state.

A further analogy to the I-BURP-2 is found for the examination of a homonuclear two spin system (Case 4). The simulations of the average Hamiltonian $\bar{\mathcal{H}}_{0,J}(\nu_1, \nu_2)$ in Figure 2.47 reveal that the strong coupling diagonal is barely broadened and zero-quantum terms ($2I_{1x/y} I_{2x/y}$) are more or less comparable to the unperturbed area. This could be based on the fact that the actual rotation happens at the very end of the pulse shape as was discussed already for the I-BURP-2. Compared to the Q5 pulse shape, clearly, the effect of a scalar coupling during the E-BURP-2 shaped pulse seems to be more predictable – anti-phase terms ($2I_{1z} I_{2x/y}$ and $2I_{1x/y} I_{2z}$) are close to zero and weak coupling is in larger parts ≈ 1 .

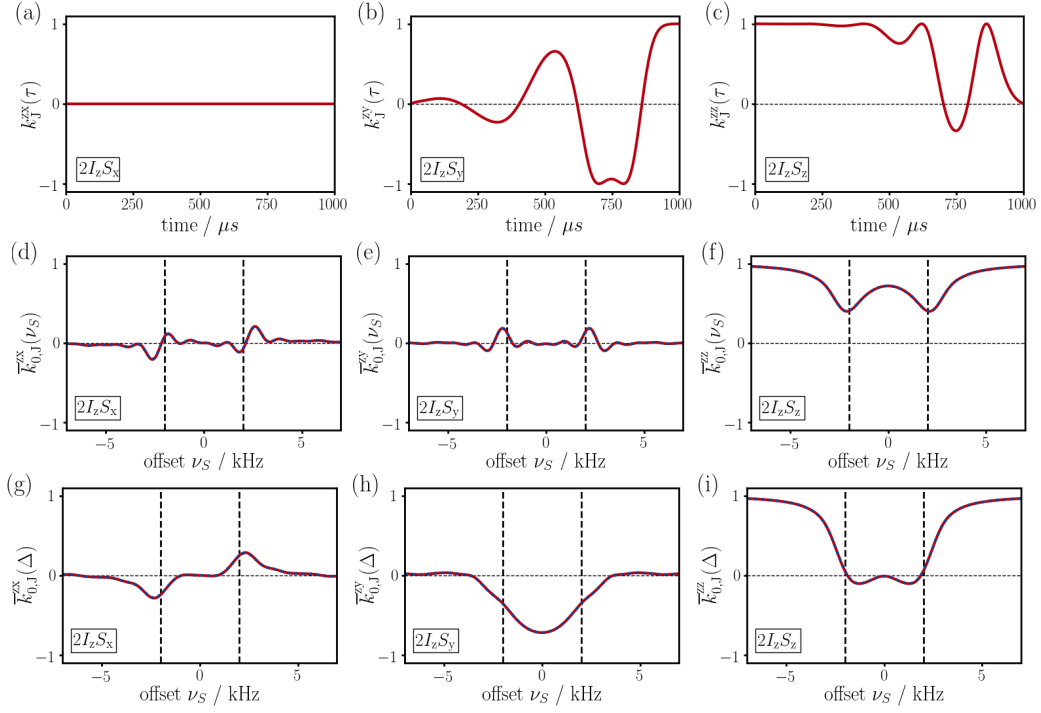


Figure 2.46: Case 1 (Section 2.4.3) – Hamiltonian in toggling frame $\hat{H}_{T,J}(\tau)$ with $\nu_S = 0$ Hz in (a-c) and the average Hamiltonian $\bar{H}_{0,j}(\nu_S)$ in (d-f) are plotted in red for non-zero operators. In (g-i) the results for a time-reversed E-BURP-2 are shown (for application to initial state). Shape: E-BURP-2 (excitation, B2); $RF_{\max} = 4096$ Hz; $\tau_P = 1$ ms; $BW \approx \pm 2.0$ kHz; transition ≈ 1.3 kHz.

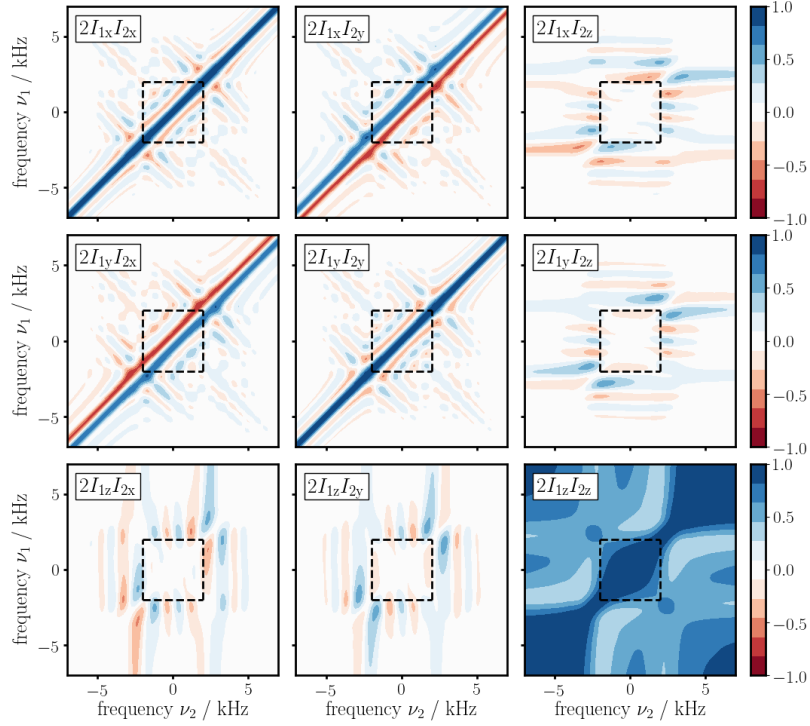


Figure 2.47: Case 4 (Section 2.4.3) – average Hamiltonian $\bar{H}_{0,j}(\nu_1, \nu_2)$ for homonuclear system. Shape: E-BURP-2 (excitation, B2); $RF_{\max} = 4096$ Hz; $\tau_P = 1$ ms; $BW \approx \pm 2.0$ kHz; transition ≈ 1.3 kHz.

2.4.10 Selective 90° Pulse: e-SNOB (B3)

The e-SNOB is related to the previously discussed r-SNOB (Section 2.4.6) and is likewise a time-optimized pulse shape that is shown in Figure 2.48 (a).^[197] The pulse shape corresponds to a band-selective 90° excitation pulse (B3) whose rotation axes are shown in Figure 2.48 (b). It becomes evident that the Zeeman interaction (i.e. offset) is not entirely suppressed and the z-component is illustrated by a “zick-zack” line – this shall be of further relevance in the following discussion about the evolution of heteronuclear scalar coupling (Case 1). For a pulse length of $\tau_P = 1$ ms with an RF amplitude of 561.4 Hz the selected bandwidth is only at roughly ± 0.2 kHz which is indicated by vertical dashed lines in Figure 2.48 (c). Such a selectivity is exceptional compared to other selective excitation pulses. However, it comes with a rather large transition width that is estimated as 1.8 kHz and the pulse’s effect is negligible for an offset larger ± 2.0 kHz. The toggling frame Hamiltonian of heteronuclear scalar coupling $\hat{\mathcal{H}}_{T,J}(\tau)$ is of rather

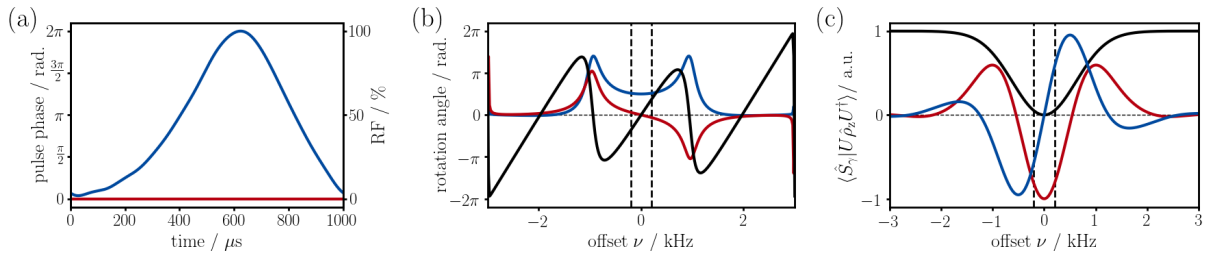


Figure 2.48: The e-SNOB pulse shape is shown in (a) as phase- (red) and amplitude-profile (blue). Effective rotation axes in (b) and expectation value $\langle \hat{S}_\gamma | U \hat{\rho}_z U^\dagger \rangle$ of the shaped pulse applied to $\hat{\rho}_z = \hat{S}_z$ in (c) are plotted for Cartesian operators \hat{S}_x (blue), \hat{S}_y (red) and \hat{S}_z (black).

simple form and is illustrated in Figure 2.49 (a) to (c) for $\nu_S = 0$ Hz (Case 1). In the first part of the pulse shape the amplitude is rather low with little effect and, hence, it is the term $2I_z S_z$ that is active. Only in the course of the shaped pulse the coupling Hamiltonian is tilted and the operator $2I_z S_y$ gains in relevance. Since the e-SNOB is amplitude-modulated the term $2I_z S_x$ is zero for $\nu_S = 0$ Hz. For other offset frequencies, however, the transformation to the toggling frame changes and also the $2I_z S_x$ part has to be taken into account (Figure 2.49 (d) to (f)). In contrast to pulse shapes of class A (Q3, Section 2.4.4) and B2 (E-BURP-2, Section 2.4.9) the e-SNOB is class B3 and, therefore, does not produce a state of constant phase over the selected band.^[103] With this regard, a heteronuclear coupling can be considered an additional *offset* that depends on the state of the coupled spin. As much as a heteronuclear coupling is suppressed for a pulse creating constant phase it likewise evolves if the resulting phase is not constant. Both, the heteronuclear scalar coupling and the offset, evolve in a correlated way during the shaped pulse which can be observed for B1 and B3 pulses.

Considering a homonuclear spin system (Case 4) the coupling evolution during the e-SNOB is shown in Figure 2.50. Due to its very narrow bandwidth zero-quantum operators ($2I_{1x/y} I_{2x/y}$) are approximately ≈ 1 within the range in dashed lines. Likewise the weak coupling operator ($2I_{1z} I_{2z}$) is uniformly at ≈ 1 while anti-phase operators ($2I_{1x/y} I_{2z}$ and $2I_{1z} I_{2x/y}$) are more or less at zero in the center and exhibit some non-zero areas in the range of transition.

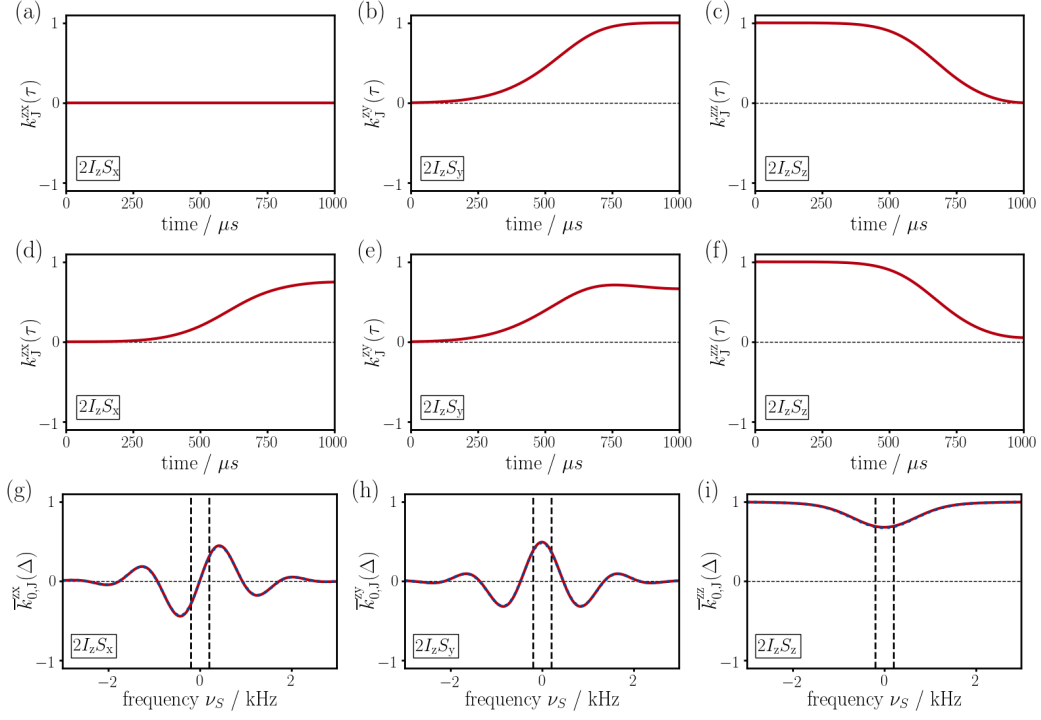


Figure 2.49: Case 1 (Section 2.4.3) – Hamiltonian in the toggling frame $\hat{H}_{T,J}(\tau)$ with $\nu_S = 0$ Hz in (a-c), with $\nu_S = 200$ Hz in (d-f) and the average Hamiltonian $\bar{H}_{0,J}(\nu_S)$ in (g-i) for non-zero operators. Shape: e-SNOB (excitation, B3); $RF_{max} = 561$ Hz; $\tau_P = 1$ ms; $BW \approx \pm 0.2$ kHz; transition ≈ 1.8 kHz.

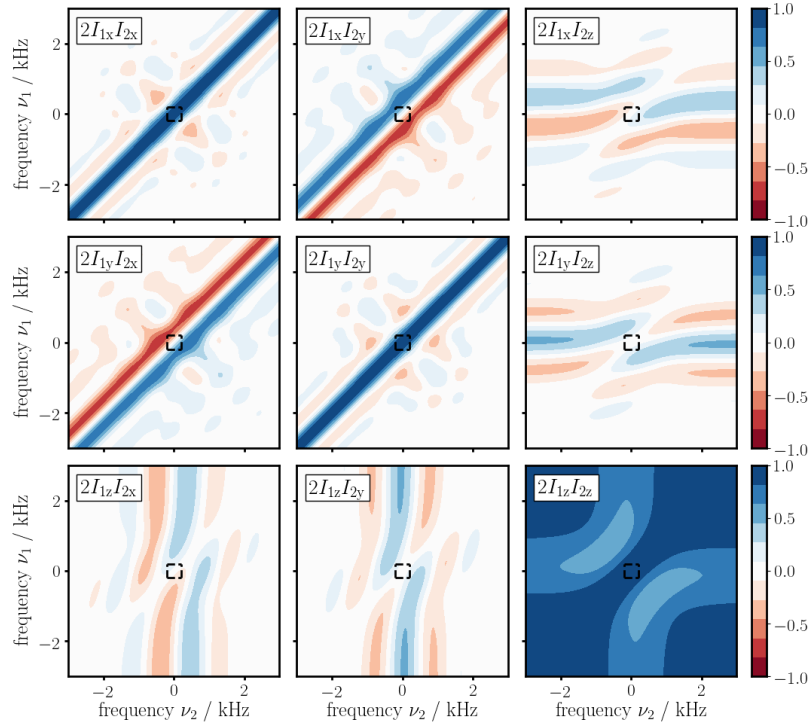


Figure 2.50: Case 4 (Section 2.4.3) – average Hamiltonian $\bar{H}_{0,J}(\nu_1, \nu_2)$ for homonuclear system. Shape: e-SNOB (excitation, B3); $RF_{max} = 561$ Hz; $\tau_P = 1$ ms; $BW \approx \pm 0.2$ kHz; transition ≈ 1.8 kHz.

2.4.11 Broadband 180° Pulse: BURBOP-180 (A)

The BURBOP pulse shape discussed in the present section is one of many BURBOP pulses^[136,192] and was designed with the GRAPE algorithm^[198] by Reinsperger.^[92] The pulse is purely phase-modulated (shown in Figure 2.51 (a)) and it appears magical that a seemingly random phase produces such an exceptional outcome. From the pulse shape a broadband 180° refocusing pulse (A) is obtained whose rotation axes are aligned along a single axis as illustrated in Figure 2.51 (b). For an RF amplitude of 10 kHz corresponding to a pulse length of 2 ms an effective refocusing pulse over a bandwidth of 60 kHz is obtained which is indicated by vertical dashed lines in Figure 2.51 (c). The respective broadband 90° universal rotation is discussed in Section 2.4.13. The time-dependent Hamiltonian in the toggling

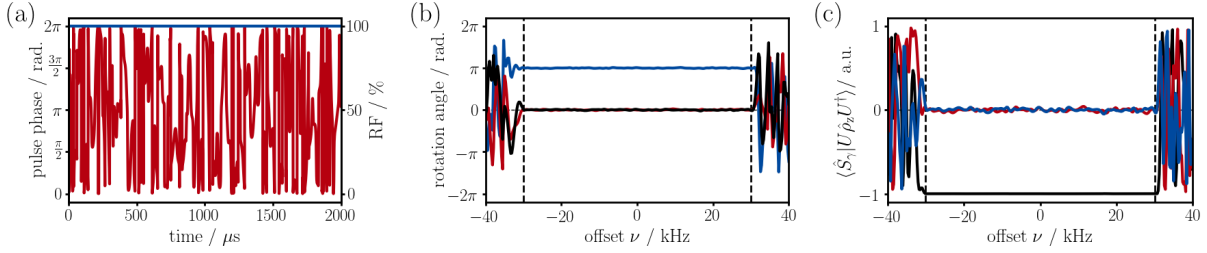


Figure 2.51: The BURBOP-180 pulse shape is shown in (a) as phase- (red) and amplitude-profile (blue). Effective rotation axes in (b) and expectation value $\langle \hat{S}_\gamma | U \hat{\rho}_z U^\dagger \rangle$ of the shaped pulse applied to $\hat{\rho}_z = \hat{S}_z$ in (c) are plotted for Cartesian operators \hat{S}_x (blue), \hat{S}_y (red) and \hat{S}_z (black).

frame $\hat{H}_{T,j}(\tau)$ is illustrated for Case 1 and $\nu_S = 0$ Hz in Figure 2.52 (a) to (c) which seems as random as the shape's phase. Still, as stated before, the heteronuclear scalar coupling is suppressed for pulse shapes of class A and within the considered bandwidth completely flat lines are obtained for the average Hamiltonian $\bar{\mathcal{H}}_{0,j}(\nu_S)$ as shown in Figure 2.52 (d) to (f). If spin \hat{I} is inverted in the middle of the shaped pulse the coupling does no longer evolve correlated to the offset and an effective evolution of heteronuclear scalar coupling might be obtained in the course of the shaped pulse. This is shown in Figure 2.53 from which is clear that coupling evolves non-uniformly throughout the considered band. The shown values correspond to coupling evolution in the range of roughly -31% to $+36\%$ of the pulse length. As proposed for Q3 (Section 2.4.4) coupling evolution can be avoided if the BURBOP pulse is not centered with the pulse on spin \hat{I} . If instead the pulses are right or left aligned the coupling evolution would, again, be given by Figure 2.52 (d) to (f). This, on the other hand, might require to compensate the chemical shift of spin \hat{I} at a later time. If the BURBOP is applied to two spins, \hat{I}_1

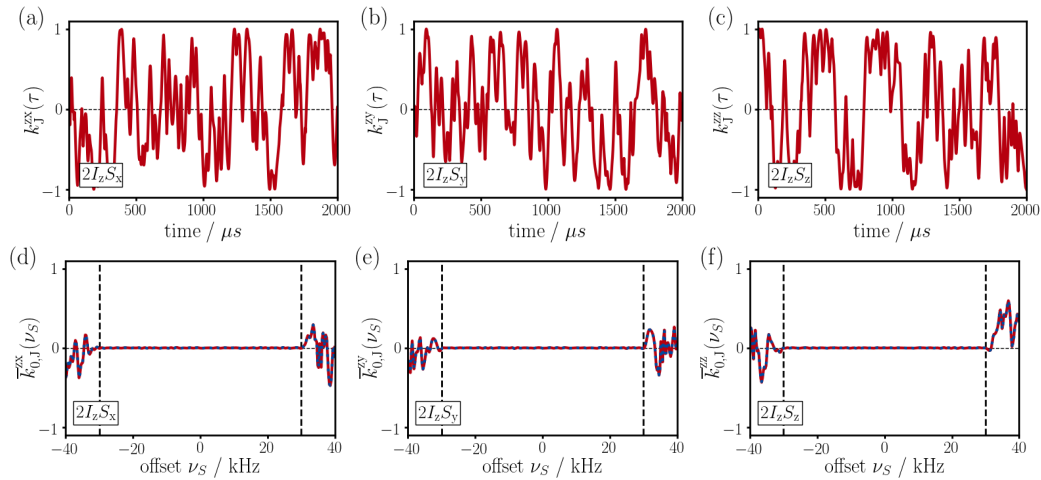


Figure 2.52: Case 1 (Section 2.4.3) – Hamiltonian in toggling frame $\hat{H}_{T,j}(\tau)$ with $\nu_S = 0$ Hz in (a-c) and the average Hamiltonian $\bar{\mathcal{H}}_{0,j}(\nu_S)$ in (d-f) are plotted in red for non-zero operators. Shape: BURBOP (UR 180°); $RF_{max} = 10$ kHz; $\tau_P = 2$ ms; $BW \approx 60$ kHz.

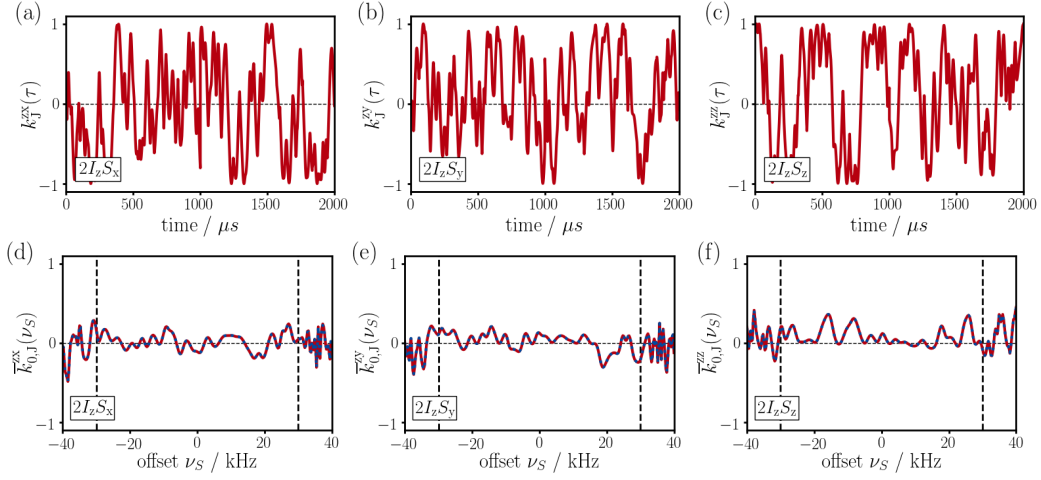


Figure 2.53: Case 2 (Section 2.4.3) – Hamiltonian in toggling frame $\hat{\mathcal{H}}_{T,j}(\tau)$ with $\nu_S = 0$ Hz in (a-c) and the average Hamiltonian $\bar{\mathcal{H}}_{0,j}(\nu_S)$ in (d-f) are plotted in red for non-zero operators. Shape: BURBOP (UR 180°); $RF_{\max} = 10$ kHz; $\tau_P = 2$ ms; $BW \approx 60$ kHz.

and \hat{I}_2 , simultaneously (Case 4) the coupling evolution depends on both offsets, ν_1 and ν_2 , as illustrated in Figure 2.54. Except for the diagonal all bilinear operators are close to zero and only for some rather random spots coupling evolution is expected. From these results it is clear that, at least for given pulse length (τ_P) and RF amplitude, no effective isotropic mixing (i.e. in terms of a spin lock) is obtained in off-diagonal areas. Hence, if applied in a CPMG sequence, the covered bandwidth orthogonal to the diagonal is not given by the bandwidth of the shaped pulse, as implied by Marchione and Diaz^[207], but from the pulse-repetition rate.

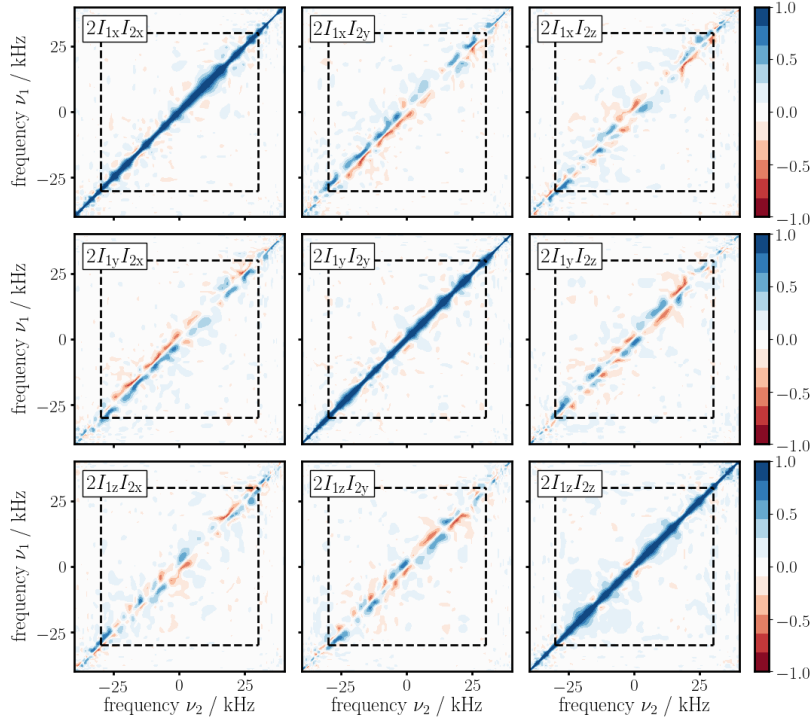


Figure 2.54: Case 4 (Section 2.4.3) – average Hamiltonian $\bar{\mathcal{H}}_{0,j}(\nu_1, \nu_2)$ for homonuclear system. Shape: BURBOP (UR 180°); $RF_{\max} = 10$ kHz; $\tau_P = 2$ ms; $BW \approx 60$ kHz.

^[207] A. A. Marchione and E. L. Diaz. *Journal of Magnetic Resonance* **2018**, 286, 143–147.

2.4.12 Broadband 180° Pulse: Chirped Pulse (B)

Another important class of broad band pulse shapes is given by so-called *adiabatic* or *chirped pulses*⁷² where the magnetization follows the effective field of the frequency swept pulse and the offset.^[186] Such a frequency sweep is achieved by a quadratic phase-modulation as is shown in Figure 2.55 (a) for a common smoothed chirped pulse from the Bruker library (“Crp60,0.5,20.1”). The resulting rotation corresponds to a 180° inversion pulse (B) whose axes are shown in Figure 2.55 (b). With an applied RF amplitude of 10 kHz and a pulse length of 488.6 μs a bandwidth of 40 kHz is covered as shown in the offset profile in Figure 2.55 (c). It should be noted that an exceptional feature of adiabatic pulses is the intrinsic resilience against RF amplitude inhomogeneity and that the frequency sweep range can simply be extended for longer pulse lengths. For Case 1 the coupling Hamiltonian in the toggling frame $\hat{\mathcal{H}}_{T,J}(\tau)$ for $\nu_S = 0$ Hz is

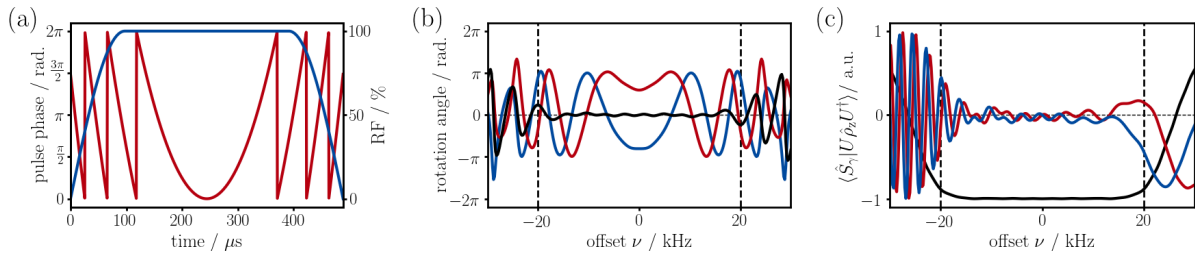


Figure 2.55: The shape of an adiabatic chirp is shown in (a) as phase- (red) and amplitude-profile (blue). Effective rotation axes in (b) and expectation value $\langle \hat{S}_\gamma | U \hat{\rho}_z U^\dagger \rangle$ of the shaped pulse applied to $\hat{\rho}_z = \hat{S}_z$ in (c) are plotted for Cartesian operators \hat{S}_x (blue), \hat{S}_y (red) and \hat{S}_z (black).

shown in Figure 2.56 (a) to (c) and the effective heteronuclear coupling during the chirped pulse is linear with respect to the offset frequency (Figure 2.56 (f)) ranging from -52% to $+60\%$. Approximating the frequency swept pulse as time shifted inversions correlated to the offset, surely, this is an expected result which already is involved in the methods called CRISIS^[203] and SCRAPER^[204]. As discussed before, these methods are based on the correlation between ^{13}C offset (i.e. also the ^{13}C multiplicity) and ^{13}C - ^1H coupling strength. If applied in an echo, as described by Case 2, the maximum effective coupling is found in the center (75%) which declines towards the edges on the left (32%) and right (36%) as illustrated in Figure 2.57. For Case 4, considering two homonuclear spins on which the chirped pulse is applied,

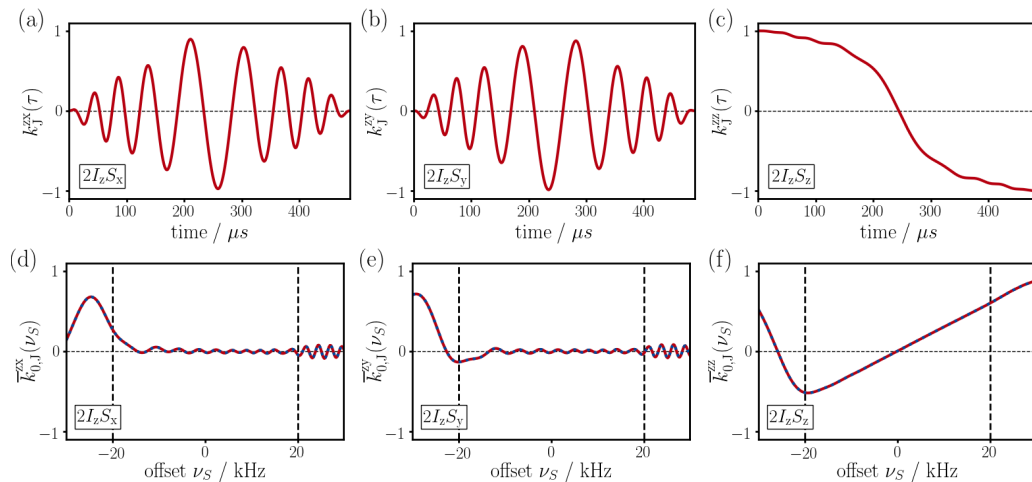


Figure 2.56: Case 1 (Section 2.4.3) – Hamiltonian in toggling frame $\hat{\mathcal{H}}_{T,J}(\tau)$ with $\nu_S = 0$ Hz in (a-c) and the average Hamiltonian $\bar{\mathcal{H}}_{0,J}(\nu_S)$ in (d-f) are plotted in red for non-zero operators. Shape: Adiabatic Chirp (inversion); $\text{RF}_{\text{max}} = 10$ kHz; $\tau_P = 488.6$ μs ; $\text{BW} \approx 40$ kHz.

⁷² The expression “chirp” refers to the continuous change of the pulse’s frequency.

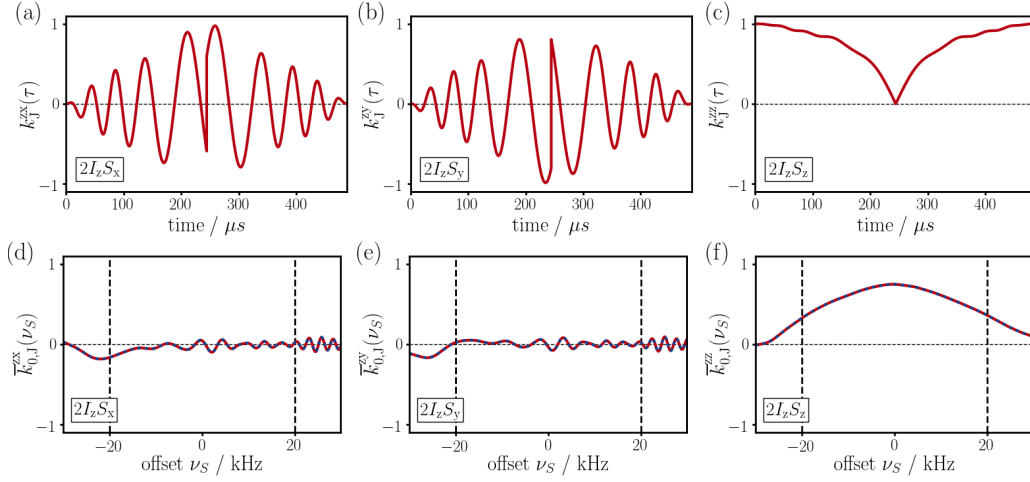


Figure 2.57: Case 2 (Section 2.4.3) – Hamiltonian in toggling frame $\hat{H}_{T,J}(\tau)$ with $\nu_S = 0$ Hz in (a-c) and the average Hamiltonian $\bar{H}_{0,J}(\nu_S)$ in (d-f) are plotted in red for non-zero operators. Shape: Adiabatic Chirp (inversion); $RF_{max} = 10$ kHz; $\tau_P = 488.6$ μ s; $BW \approx 40$ kHz.

the average Hamiltonian $\bar{H}_{0,J}(\nu_1, \nu_2)$ is shown in Figure 2.58. While anti-phase operators ($2I_{1x/y}I_{2z}$ and $2I_{1z}I_{2x/y}$) are uniformly ≈ 0 the weak coupling term ($2I_{1z}I_{2z}$) is non-uniformly present on a broad range along the diagonal and decays towards the off-diagonal edges. Commonly, an intuitive prediction is easier for a uniform distribution and, therefore, these are preferable. Also, zero-quantum operators ($2I_{1x/y}I_{2x/y}$) are close to an expected behaviour (see CPMG in toggling frame in Appendix 5.2.2) and only a slight asymmetry towards the off-diagonal is noticed.

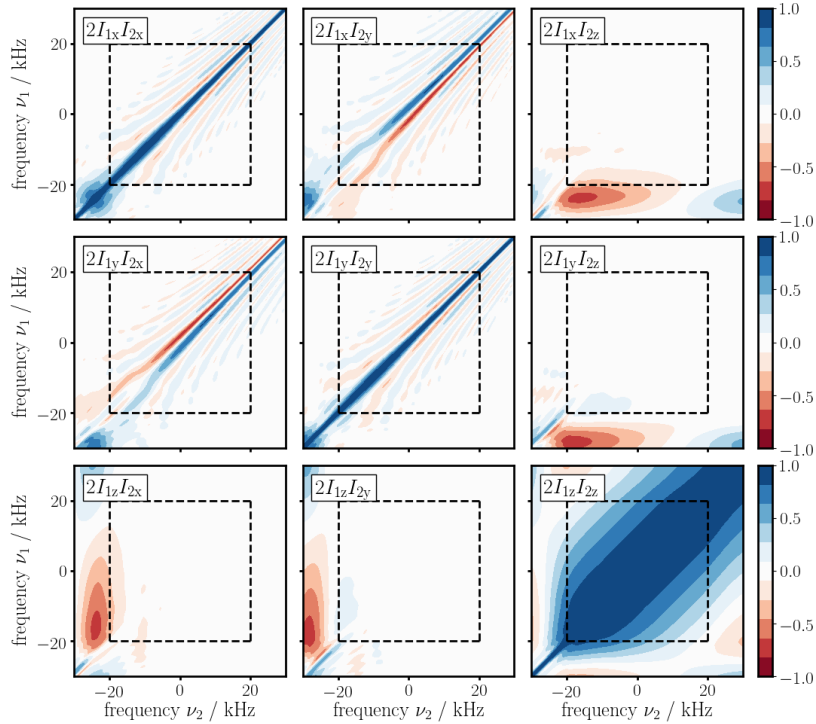


Figure 2.58: Case 4 (Section 2.4.3) – average Hamiltonian $\bar{H}_{0,J}(\nu_1, \nu_2)$ for homonuclear system. Shape: Adiabatic Chirp (inversion); $RF_{max} = 10$ kHz; $\tau_P = 488.6$ μ s; $BW \approx 40$ kHz.

2.4.13 Broadband 90° Pulse: BURBOP-90 (A)

The BURBOP pulse shape discussed in the present section is the 90° counterpart to the 180° BURBOP (Section 2.4.11) optimized by Reinsperger.^[92] Also, the 90° BURBOP pulse shape is purely phase-modulated (shown in Figure 2.59 (a)) and it is likewise astonishing that from the incomprehensible pulse shape a broadband 90° universal rotation (A) is obtained. The rotation axes (inducing a $\frac{\pi}{2}$ rotation) are aligned along a single axis for the entire bandwidth as illustrated in Figure 2.59 (b). For an RF amplitude of 10 kHz corresponding to a pulse length of 1.2 ms an effective 90° universal rotation over a bandwidth of 60 kHz is obtained (indicated by vertical dashed lines in following figures). The shaped pulse with x-phase applied to a state $\hat{\rho}_z = \hat{I}_z$ leads to nearly perfect excitation as illustrated in Figure 2.59 (c). As

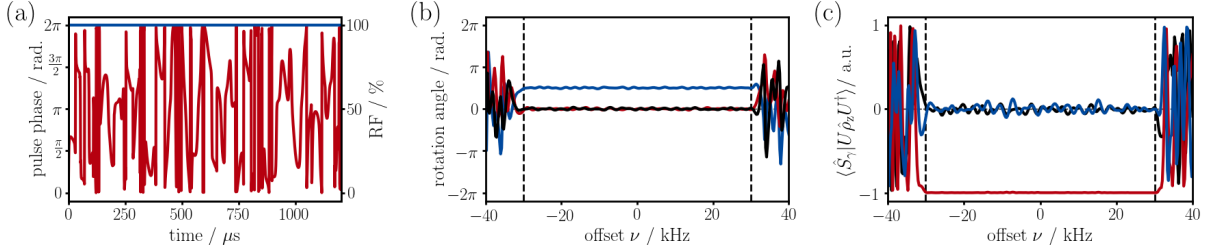


Figure 2.59: The BURBOP-90 pulse shape is shown in (a) as phase- (red) and amplitude-profile (blue). Effective rotation axes in (b) and expectation value $\langle \hat{S}_\gamma | U \hat{\rho}_z U^\dagger \rangle$ of the shaped pulse applied to $\hat{\rho}_z = \hat{S}_z$ in (c) are plotted for Cartesian operators \hat{S}_x (blue), \hat{S}_y (red) and \hat{S}_z (black).

stated before, a heteronuclear coupling during a shaped pulse of class A or B2 (if used for excitation) does not lead to coupling evolution (Section 2.4.2 and 2.4.10) which is based on the fact that offset is refocused no matter its origin. Hence, for Case 1 the resulting simulations of the toggling frame Hamiltonian $\hat{\mathcal{H}}_{T,J}(\tau)$ for $\nu_S = 0$ Hz and its time average Hamiltonian $\bar{\mathcal{H}}_{0,J}(\nu_S)$ are little surprising ≈ 0 which is illustrated in Figure 2.60. If a homonuclear coupling between spin \hat{I}_1 and \hat{I}_2 during the shaped pulse is considered (Case 4) the difference in the respective offsets, ν_1 and ν_2 , can cause secularization of the coupling Hamiltonian (described in Section 2.5) and both offsets have to be taken into account. For the BURBOP-90 similar results to the BURBOP-180 are found as shown in Figure 2.61 – except for the diagonal all bilinear operators are close to zero. Only for some rather randomly distributed spots coupling evolution is shown which could lead to minor artifacts like transfer or phase distortions.

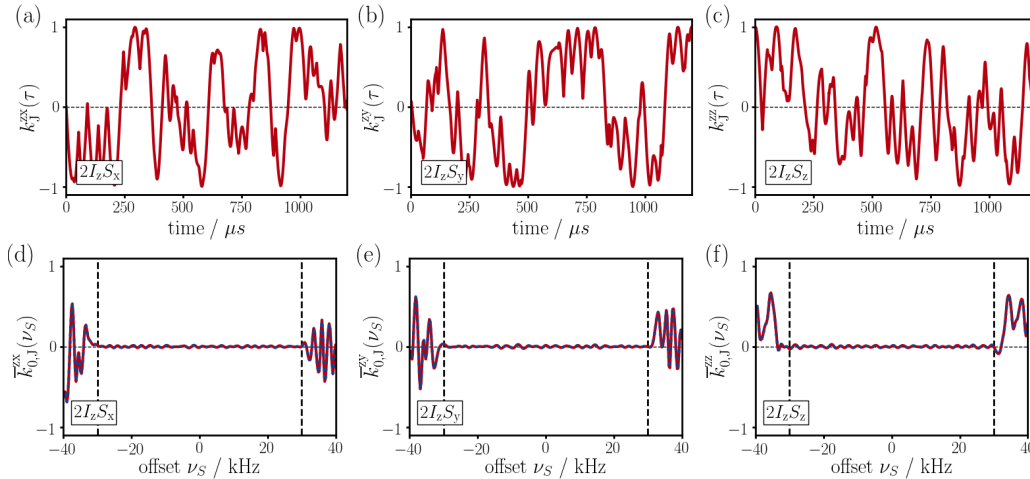


Figure 2.60: Case 1 (Section 2.4.3) – Hamiltonian in toggling frame $\hat{\mathcal{H}}_{T,J}(\tau)$ with $\nu_S = 0$ Hz in (a-c) and the average Hamiltonian $\bar{\mathcal{H}}_{0,J}(\nu_S)$ in (d-f) are plotted in red for non-zero operators. Shape: BURBOP (UR 90°); $RF_{\max} = 10$ kHz; $\tau_P = 1.2$ ms; $BW \approx 60$ kHz.

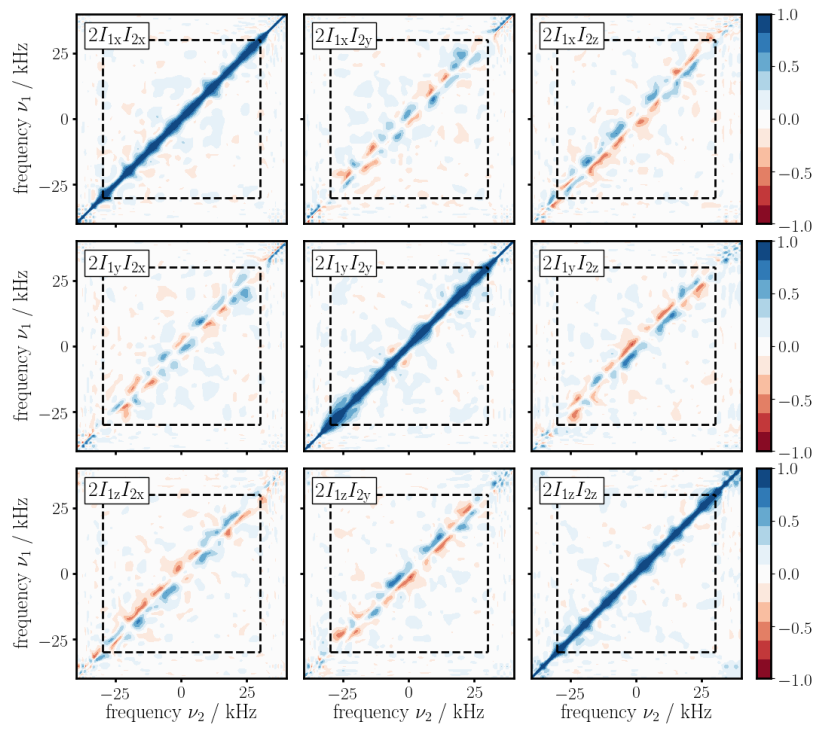


Figure 2.61: Case 4 (Section 2.4.3) – average Hamiltonian $\bar{H}_{0,j}(\nu_1, \nu_2)$ for homonuclear system. Shape: BURBOP (UR 90°); $RF_{\max} = 10$ kHz; $\tau_P = 1.2$ ms; $BW \approx 60$ kHz.

2.4.14 Broadband 90° Pulse: BEBOP (B2)

The BEBOP is another phase-modulated pulse shape designed by Skinner et al.^[191] and is shown in Figure 2.62 (a). In contrast to the BURBOP-90 (Section 2.4.13) the BEBOP corresponds to a broadband 90° excitation pulse that was optimized for a point-to-point transfer (B2) – its rotation axes are distributed on a tilted plane (Figure 2.24 (c)) and the Cartesian components are illustrated in Figure 2.62 (b). For an RF amplitude of 10 kHz corresponding to a pulse length of 1.0 ms an effective transfer from a state $\hat{\rho}_z = \hat{I}_z$ to \hat{I}_x is obtained over a bandwidth of 50 kHz as illustrated in Figure 2.62 (c). Again, a seemingly random phase leads to a well-defined outcome. The considered BEBOP comprises another extraordinary feature – due to its enormous compensation of RF inhomogeneity it can be considered a ”calibration-free“ pulse that offers the desired transfer for an RF amplitude range of 10 to 20 kHz. The

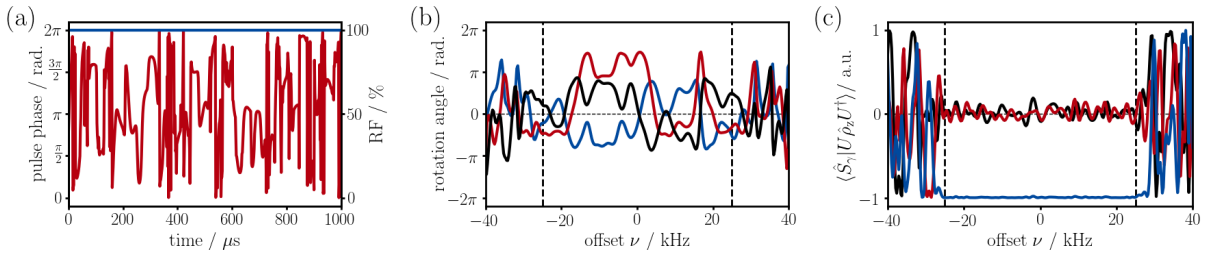


Figure 2.62: The BEBOP pulse shape is shown in (a) as phase- (red) and amplitude-profile (blue). Effective rotation axes in (b) and expectation value $\langle \hat{S}_\gamma | U \hat{\rho}_z U^\dagger \rangle$ of the shaped pulse applied to $\hat{\rho}_z = \hat{S}_z$ in (c) are plotted for Cartesian operators \hat{S}_x (blue), \hat{S}_y (red) and \hat{S}_z (black).

simulation of the heteronuclear coupling Hamiltonian in toggling frame $\hat{\mathcal{H}}_{T,j}(\tau)$ for Case 1 leads again to seemingly random oscillations as shown for $\nu_S = 0$ Hz in Figure 2.63 (a) to (c). However, the calculation of the average Hamiltonian $\bar{\mathcal{H}}_{0,j}(\nu_S)$ reveals that during the BEBOP all anti-phase terms are ≈ 0 and the only remaining effective bilinear operator is given by the weak coupling term ($2I_z S_z$). Since the BEBOP pulse shape is optimized for a transfer starting from an initial population (e.g. \hat{S}_z or $2I_z S_z$) the effective propagator of the coupling (dominated by the operator $2I_z S_z$) is without consequences. This is based on the fact that, following Equation (2.4.9), the effective coupling propagator is directly applied to the initial state and $[S_z, 2I_z S_z] = 0$ and $[2I_z S_z, 2I_z S_z] = 0$. As discussed already for the E-BURP-2 (Section 2.4.9) this is also true for a time-reversed version of the BEBOP that is commonly used in heteronuclear correlation experiments for the back-transfer from the transverse plane to a population. It is, however, crucial to note that coupling evolution has to be considered for an initial state (or final state for time-reversed version) of e.g. $2I_x S_z$.

Compared to other pulses optimized by optimal control theory (e.g. BURBOP-180 in Section 2.4.11 or BURBOP-90 in Section 2.4.13) the BEBOP exhibits similar results considering a homonuclear two spin system (Case 4). The average Hamiltonian $\bar{\mathcal{H}}_{0,j}(\nu_1, \nu_2)$ is shown in Figure 2.64 and except for the diagonal all bilinear operators are, again, close to zero. Only for some rather randomly distributed spots coupling evolution is shown which could lead to minor transfer or phase distortions.

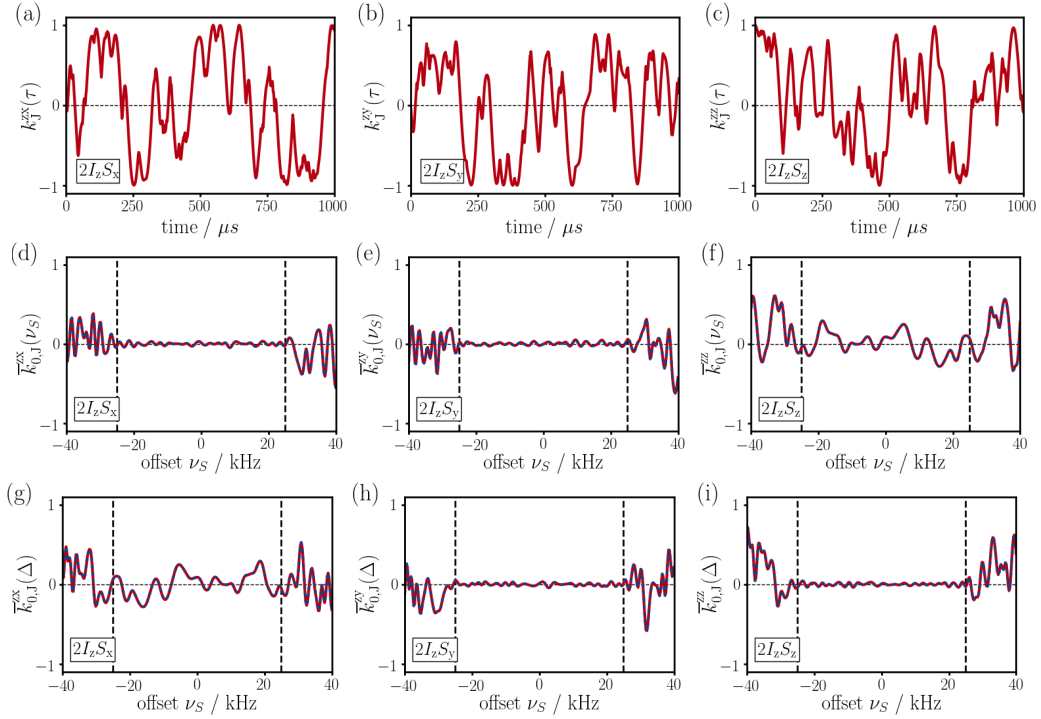


Figure 2.63: Case 1 (Section 2.4.3) – Hamiltonian in toggling frame $\hat{H}_{T,J}(\tau)$ with $\nu_S = 0$ Hz in (a-c) and the average Hamiltonian $\bar{H}_{0,J}(\nu_S)$ in (d-f) are plotted in red for non-zero operators. In (g-i) the results for a time-reversed BEBOP are shown (for application to initial state). Shape: BEBOP (excitation, B2); $RF_{\max} = 10$ kHz; $\tau_P = 1.0$ ms; $BW \approx 50$ kHz.

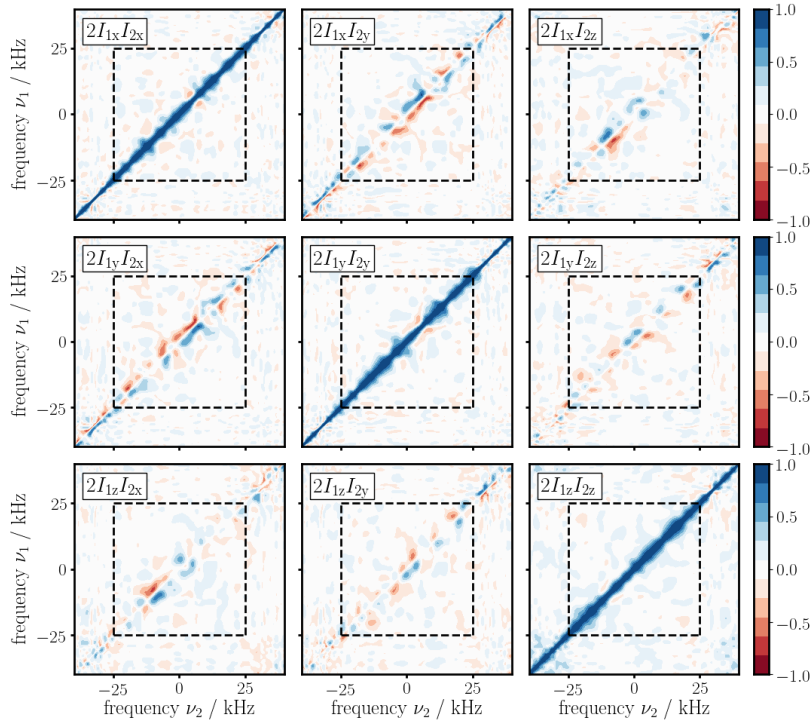


Figure 2.64: Case 4 (Section 2.4.3) – average Hamiltonian $\bar{H}_{0,J}(\nu_1, \nu_2)$ for homonuclear system. Shape: BEBOP (excitation, B2); $RF_{\max} = 10$ kHz; $\tau_P = 1.0$ ms; $BW \approx 50$ kHz.

2.4.15 Hard 180° Pulse: Echo

One of the most basic elements, which can be found in practically any elaborate sequence, is the so-called spin echo.^[108] If applied multiple consecutive times (e.g. in CPMG sequences^[164,208]) it is commonly subject to supercycles in order to compensate for pulse imperfections and offset effects.^[154,209] However, there are cases where supercycles can not be performed rigorously as e.g. is the case for the isotropic mixing sequence in Section 2.3. With this regard, imperfections of the spin echo shall be illustrated and compared to the pulse shape (IMP) discussed in the following section. As illustrated in Figure 2.65 (a) the considered spin echo consists of a 180° pulse that is flanked by two delays of each 500 μs . For the hard pulse an RF amplitude of 10 kHz is assumed and a bandwidth of 7 kHz is marked by dashed lines in Figure 2.65 (b) and (c) where the effective rotation axes and the offset profile ($\hat{\rho}_{\text{init}} = \hat{S}_z$) are shown, respectively. The bandwidth of 7 kHz roughly corresponds to the required band for a proton spectrum at a field strength of 14.1 T and it conforms with the optimized bandwidth for the IMP pulse shape. Clearly, large undesired oscillations are encountered in Figure 2.65 due to offset effects and a complete refocusing is not being obtained. If, in addition, a scalar coupling is considered during the spin

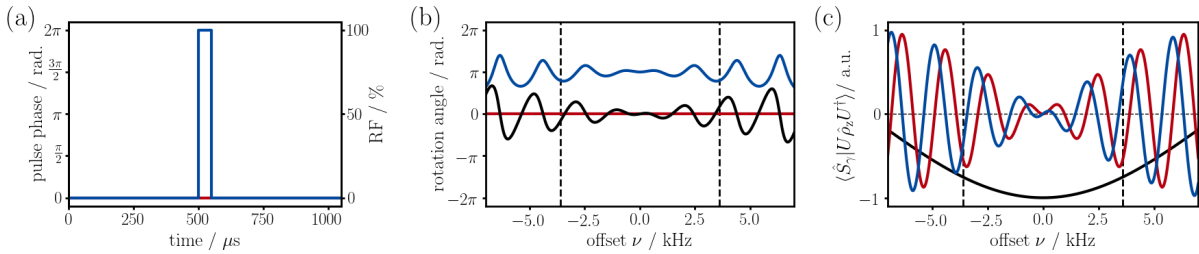


Figure 2.65: The echo sequence is shown in (a) as phase- (red) and amplitude-profile (blue). Effective rotation axes in (b) and expectation value $\langle \hat{S}_\gamma | U \hat{\rho}_z U^\dagger \rangle$ of the shaped pulse applied to $\hat{\rho}_z = \hat{S}_z$ in (c) are plotted for Cartesian operators \hat{S}_x (blue), \hat{S}_y (red) and \hat{S}_z (black).

echo the offset effects are further increased. For Case 1, the time-dependent coupling Hamiltonian in toggling frame $\hat{\mathcal{H}}_{T,J}(\tau)$ with $\nu_S = 0$ Hz is illustrated in Figure 2.66 (a) to (c) and, as expected, for the on-resonant case the scalar coupling is refocused. However, the average coupling Hamiltonian $\bar{\mathcal{H}}_{0,J}(\nu_S)$ in the toggling frame reveals in Figure 2.66 (d) to (f) that likewise offset dependent oscillations are encountered. Within the considered bandwidth a maximum value of $k_{0,J}^{ZY} = 0.3$ is found which indicates that the respective term is active during 30% of the spin echo length. In Figure 2.66 (g) to (i) similar findings are illustrated for Case 2 where a heteronuclear echo is assumed and only if on-resonant the expected result of an effective weak coupling Hamiltonian is obtained. For the homonuclear Case 4 a strongly coupled spin system is assumed and even more coupling terms have to be considered. The zeroth order average Hamiltonian $\bar{\mathcal{H}}_{0,J}(\nu_1, \nu_2)$ is shown in Figure 2.67. While the weak coupling ($2I_{1z}I_{2z}$) and zero-quantum components ($2I_{1x/y}I_{2x/y}$) exhibit a rather uniform profile, oscillations comparable to the ones in 2.66 are found for all anti-phase terms ($2I_{1z}I_{2x/y}$ and $2I_{1x/y}I_{2z}$). It is obvious that such irregular and offset dependent profiles of the effective coupling during the spin echo opens up new coherence pathways which might cause artifacts – especially if in between consecutive echoes additional 90° pulses are applied (as is the case for the isotropic mixing sequence in Section 2.3). With this regard, the IMP pulse shape of the following section might be preferable where such offset effects are drastically reduced.

^[208] S. Meiboom and D. Gill. *Review of Scientific Instruments* **1958**, 29, 688–691.

^[209] J. W. Jacobs, J. W. Van Os and W. S. Veeman. *Journal of Magnetic Resonance* **1983**, 51, 56–66.

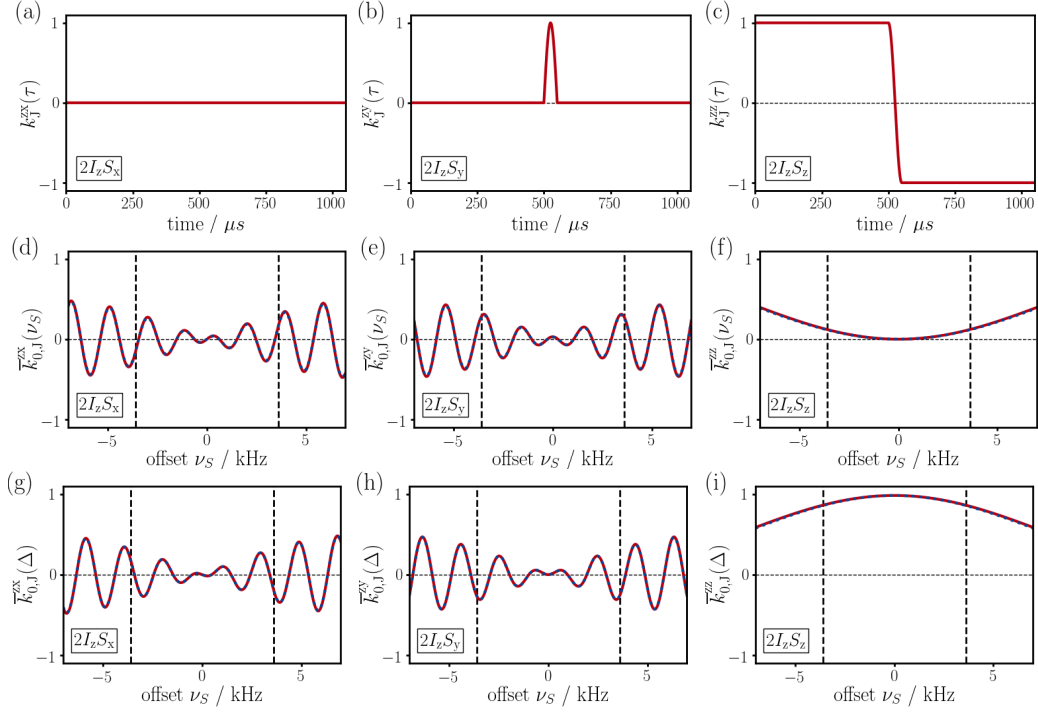


Figure 2.66: For Case 1 (Section 2.4.3) the time-dependent Hamiltonian in toggling frame $\hat{\mathcal{H}}_{T,j}(\tau)$ with $\nu_S = 0$ Hz is plotted in (a-c). The average Hamiltonian $\bar{\mathcal{H}}_{0,j}(\nu_S)$ is plotted for non-zero operators $2\hat{I}_z\hat{S}_\gamma$ in (d-f) for Case 1 and in (g-i) for Case 2. Shape: Echo; $RF_{\max} = 10$ kHz; $\tau_{\text{Echo}} \approx 1.0$ ms.

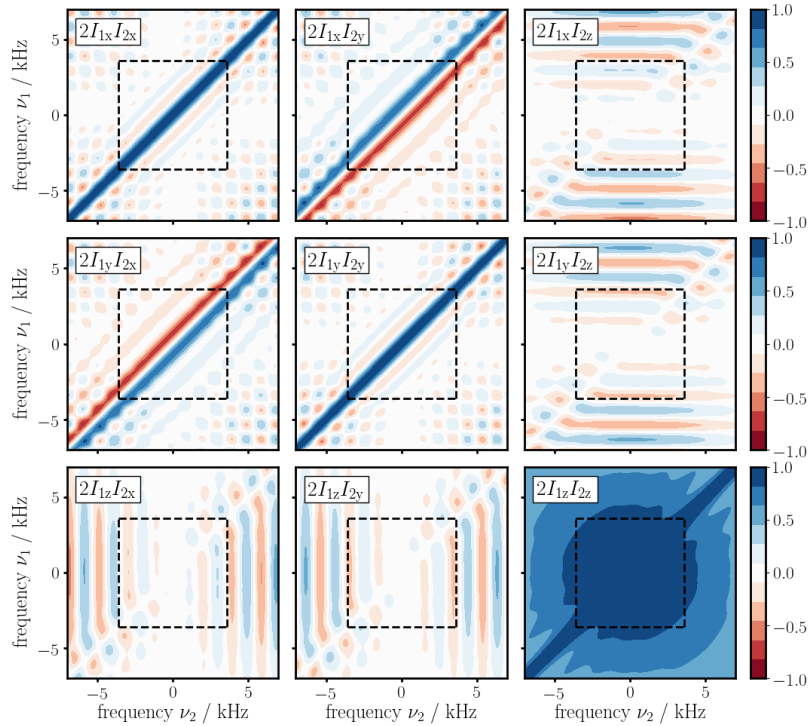


Figure 2.67: Case 4 (Section 2.4.3) – average Hamiltonian $\bar{\mathcal{H}}_{0,j}(\nu_1, \nu_2)$ for homonuclear system. Shape: Echo; $RF_{\max} = 10$ kHz; $\tau_{\text{Echo}} \approx 1.0$ ms.

2.4.16 Shaped 180° Pulse: IMP (A)

The *isotropic mixing pulse* (IMP) is a pulse shape that was optimized in the course of the present dissertation for the application in the low-power isotropic mixing sequence (Section 2.3) which is created from *echo – 90°-pulse – echo* elements. The optimization was realized using the GRAPE algorithm^[198] and implemented with the help of various libraries^[210–212] in python⁷³. As starting point for the optimization an modified RE-BURP pulse was used in order to obtain similar coupling properties in the toggling frame. Indeed a *local* minimum was targeted – the resulting amplitude-modulated pulse shape of the IMP is shown in Figure 2.68 (a) which clearly exhibits the desired appearance similar to the RE-BURP. However, in contrast to RE-BURP, the IMP is not supposed to be a selective pulse and outside the optimized bandwidth arbitrary rotations are accepted. Thus, these loosened constraints enable a much higher quality within the considered bandwidth (quality factor $\langle U_{\text{opt}} | U_{\text{IMP}} \rangle = 0.9999942$) as illustrated in Figure 2.68 (b) and (c) and the IMP is, hence, suitable for a repetitive application without offset effects. For an RF = 10 kHz a universal rotation (A) over a bandwidth of 7 kHz is obtained which roughly corresponds to the required band of a proton spectrum at a field strength of 14.1 T. It is important to note that with respect to other pulse shapes neither the bandwidth nor the obtained quality of the IMP is extraordinary. However, only when examined in the toggling frame the IMP reveals its asset. In the

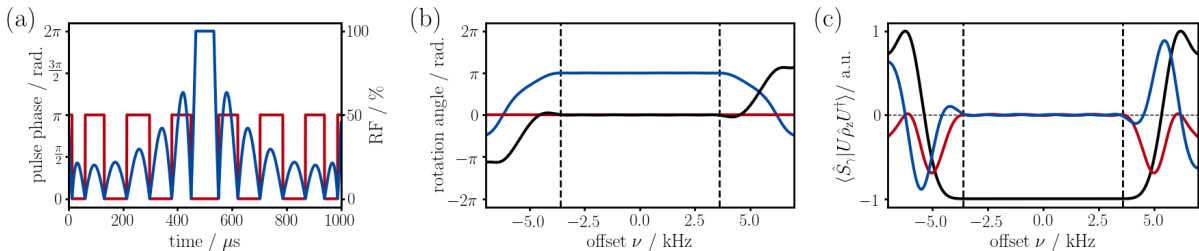


Figure 2.68: The IMP pulse shape is shown in (a) as phase- (red) and amplitude-profile (blue). Effective rotation axes in (b) and expectation value $\langle \hat{S}_\gamma | U_{\text{IMP}} \hat{\rho}_z U_{\text{IMP}}^\dagger \rangle$ of the shaped pulse applied to $\hat{\rho}_z = \hat{S}_z$ in (c) are plotted for Cartesian operators \hat{S}_x (blue), \hat{S}_y (red) and \hat{S}_z (black).

toggling frame for Case 1 the scalar coupling Hamiltonian $\hat{H}_{T,J}(\tau)$ is illustrated in Figure 2.69 (a) to (c) from which the average Hamiltonian $\bar{H}_{0,J}(\nu_S)$ can be obtained if calculated for multiple offsets ν_S . In contrast to the hard pulse spin echo discussed in the previous section the effective coupling during the IMP is negligible within the optimized bandwidth as shown in Figure 2.69d-f). If, on the other hand, in a heteronuclear echo the coupling partner is inverted at half the pulse length (Case 2) an effective *weak coupling* Hamiltonian can be considered during the longest part of the pulse (90% in the center and 80% at the edges). Hence, the coupling is neither suppressed nor strongly modified by the shaped pulse which is, surely, desired for the application in the isotropic mixing sequence discussed in Section 2.3. For Case 4, assuming two *homonuclear* spins on which the IMP is applied simultaneously, the average Hamiltonian $\bar{H}_{0,J}(\nu_1, \nu_2)$ is shown in Figure 2.70. Compared to the simulations of the hard pulse spin echo (Figure 2.67) similarities and certain differences are determined. On the one hand, the weak coupling ($2I_{1z}I_{2z}$) and zero-quantum terms ($2I_{1x/y}I_{2x/y}$) of the effective coupling Hamiltonian are, in the considered bandwidth, more or less congruent with the simulations of the hard pulse spin echo. On the other hand, a distinct deviation is found for anti-phase operators ($2I_{1x/y}I_{2z}$ and $2I_{1z}I_{2x/y}$) and for the IMP no offset-dependent oscillations are encountered in Figure 2.70 – the anti-phase terms are close to ≈ 0 within the optimized bandwidth. Clearly, the application of the IMP pulse shape implies less artifacts due to transfer or phase distortions compared to a hard pulse spin echo and both are, again, compared when applied in the considered isotropic mixing sequence in Section 2.3.

[210] C. R. Harris et al. *Nature* **2020**, 585, 357–362.

[211] P. Virtanen et al. *Nature Methods* **2020**, 17, 261–272.

[212] J. D. Hunter. *Computing in Science and Engineering* **2007**, 9, 90–95.

⁷³ Python Software Foundation. Python Language Reference, version 3.6. Available at <http://www.python.org>.

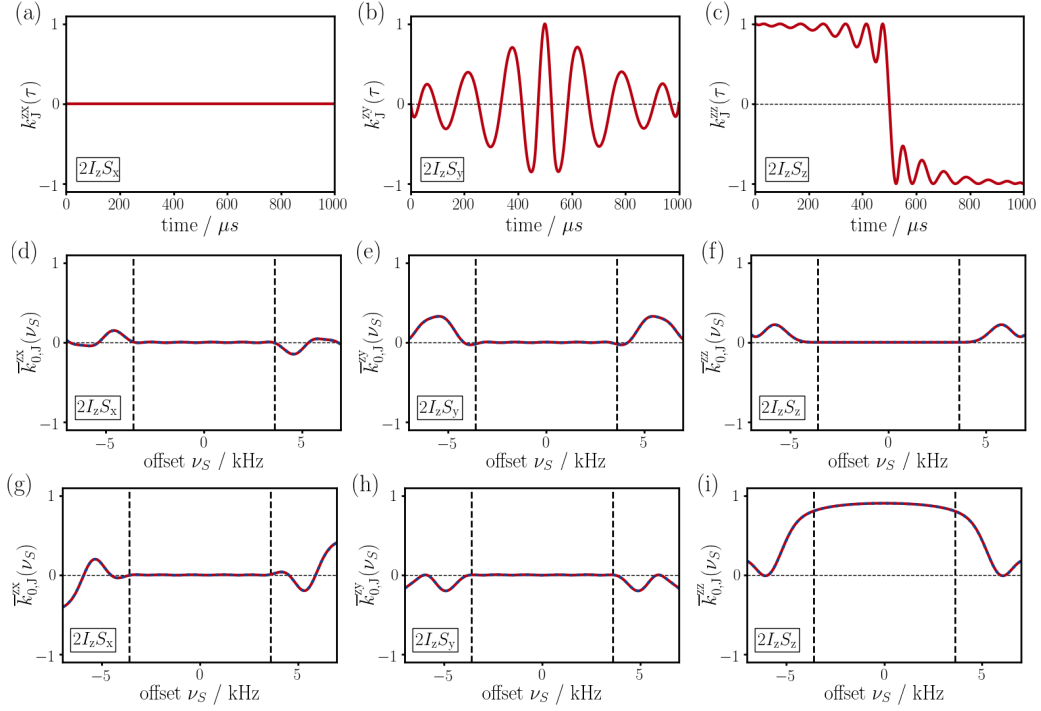


Figure 2.69: For Case 1 (Section 2.4.3) the time-dependent Hamiltonian in toggling frame $\hat{\mathcal{H}}_{T,j}(\tau)$ with $\nu_S = 0$ Hz is plotted in (a-c). The average Hamiltonian $\bar{\mathcal{H}}_{0,j}(\nu_S)$ is plotted against the offset ν_S for non-zero operators $2\hat{I}_z\hat{S}_\gamma$ in (d-f) for Case 1 and in (g-i) for Case 2. Shape: IMP (UR 180°); $RF_{\max} = 10$ kHz; $\tau_P = 1.0$ ms; $BW \approx 7$ kHz.

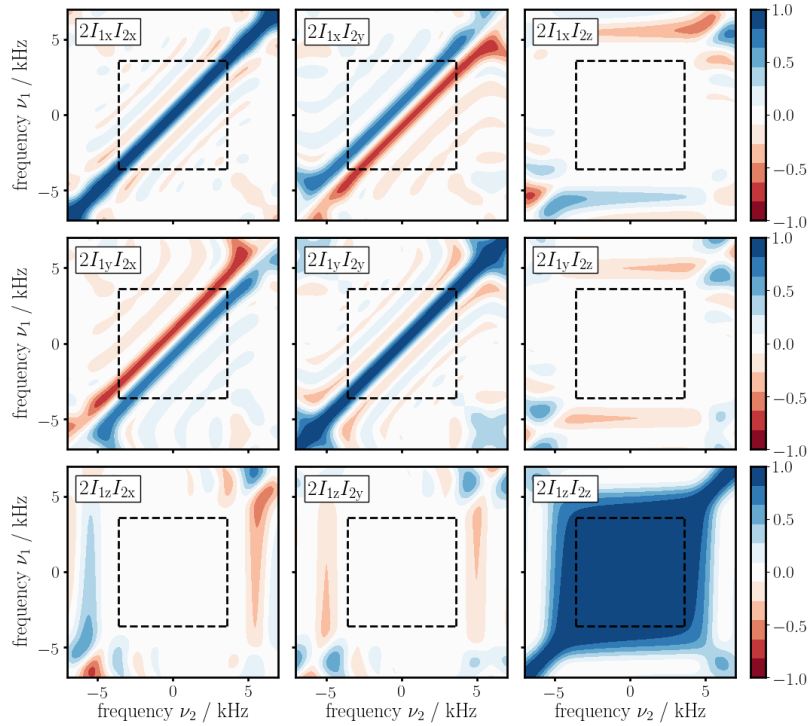


Figure 2.70: Case 4 (Section 2.4.3) – average Hamiltonian $\bar{\mathcal{H}}_{0,j}(\nu_1, \nu_2)$ for homonuclear system. Shape: IMP (UR 180°); $RF_{\max} = 10$ kHz; $\tau_P = 1.0$ ms; $BW \approx 7$ kHz.

2.4.17 Broadband 180° Pulse Sandwich: BUBU (A)

For so-called pulse sandwiches, a pair of matched pulse shapes is applied simultaneously on the proton and the X-channel. In the present case, these two pulses correspond to two phase- and amplitude-modulated BURBOP shapes that are shown in Figure 2.71 (a) and (d). Both induce a universal 180°-rotation (A) for respective nuclei and rotation axes are aligned to a single axis (Figure 2.71 (b) and (e)). The pulse parameters for the ^1H -shape (X-shape) are set to an RF amplitude of 20 kHz (10 kHz) corresponding to a pulse length of 1.0 ms (1.0 ms) and an effective rotation over a bandwidth of 7 kHz (37.5 kHz) is obtained. It shall be mentioned that the maximum RF amplitude for proton is twice as large as for previous non-selective pulses under investigation and results might not be directly comparable. A concurrent optimization of both pulse shapes allows that a coupling between considered nuclei can be taken into account and, by this means, a distinct result is obtained also for the *simultaneous* application of shaped pulses. For the considered BURBOP-BURBOP (BUBU) sandwich the optimization was targeted on the evolution of heteronuclear coupling during 80% of the pulse length which is examined in the following.

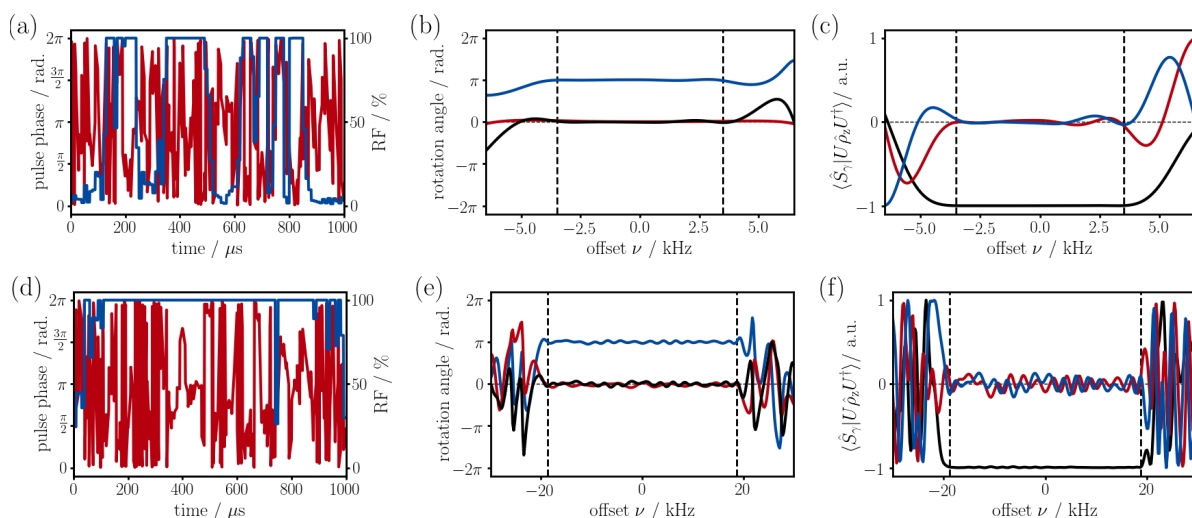


Figure 2.71: The BUBU pulse shape sandwich is shown as phase- (red) and amplitude-profile (blue) in (a) for proton and (d) for heteronuclei. For the ^1H -shaped pulse, effective rotation axes in (b) and expectation value $\langle \hat{S}_\gamma | U \hat{\rho}_z U^\dagger \rangle$ in (c) are plotted for Cartesian operators \hat{S}_x (blue), \hat{S}_y (red) and \hat{S}_z (black). For the X-shaped pulse the results are shown in (e) and (f), respectively.

An investigation in the toggling frame is undertaken where both pulse shapes are *together* applied to a heteronuclear spin system (Case 3) as intended by the optimization and further when applied *individually* to homonuclear spin systems (Case 4).

The results for Case 3 are shown in Figure 2.72 where during the concurrent shaped pulses the effect of heteronuclear coupling is examined. As desired, all operators other than the weak coupling term ($2I_z S_z$) are more or less zero with only few imperfections and one can estimate that little artifacts are introduced by the pulse sandwich from undesired coherence transfer due to a heteronuclear coupling. The intended evolution of weak coupling, on the other hand, is active during the shaped pulses. The values for the $2I_{1z}I_{2z}$ -term ranges from 37% to 53% with an average of 46% of the pulse length and is, hence, slightly lower as the targeted 80%.

It is further interesting to see the effect of a potential *homonuclear* coupling during the shaped pulses. In this context, it is important to note that bilinear operators in the toggling frame can only be propagated *individually* if considered terms commute with *all* other non-zero operators. Hence, the interpretation of simulations in a more complex spin system with homo- and heteronuclear couplings has to be conducted with special care. The results are shown in Figure 2.73 for the ^1H -shape and in Figure 2.74 for the X-shape. For the ^1H -shape it is remarkable that the findings are similar to the echo-like IMP (Section 2.4.16)

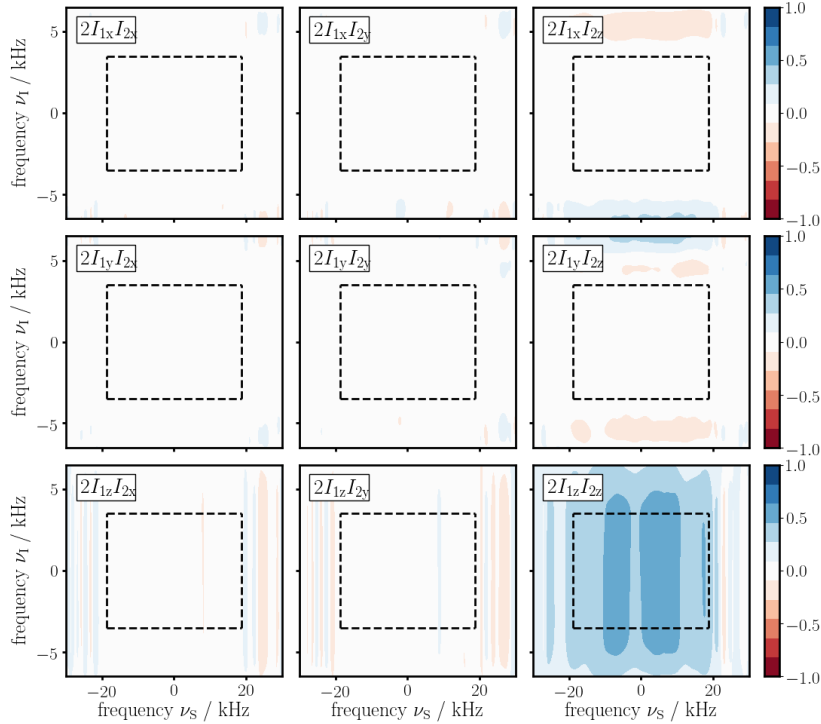


Figure 2.72: Case 3 (Section 2.4.3) – average Hamiltonian $\bar{\mathcal{H}}_{0,J}(\nu_I, \nu_S)$ for heteronuclear system.
¹H-shape: BURBOP (UR 180°); $RF_{max} = 20$ kHz; $\tau_P = 1.0$ ms; $BW \approx 7$ kHz.
X-shape: BURBOP (UR 180°); $RF_{max} = 10$ kHz; $\tau_P = 1.0$ ms; $BW \approx 37.5$ kHz.

or an echo itself (Section 2.4.15) and the weak coupling operator ($2I_{1z}I_{2z}$) is completely active while anti-phase operators ($2I_{1x/y}I_{2z}$ and $2I_{1z}I_{2x/y}$) are more or less zero in the indicated area. Likewise, zero-quantum terms ($2I_{1x/y}I_{2x/y}$) behave similar as found for the IMP or a homonuclear echo, yet, with oscillations that are somewhat broadened.

The results for the X-shape are shown in Figure 2.74 and exhibit a likewise remarkable feature compared to the other examined BURBOP which was optimized for a single spin (Section 2.4.11). For the single-spin BURBOP most operators reveal a non-continuous diagonal while off-diagonal areas show rather randomly distributed spots. For the BUBU-X-shape, on the other hand, the evolution of homonuclear X,X-coupling during the shaped pulse leads to a different outcome. While anti-phase operators ($2S_{1x/y}S_{2z}$ and $2S_{1z}S_{2x/y}$) also show positive and negative spots around the diagonal, a more or less continuous diagonal is found for zero-quantum terms ($2S_{1x/y}S_{2x/y}$). The most outstanding component, however, is given by the weak coupling operator ($2S_{1z}S_{2z}$) which, next to a broadened diagonal, further exhibits a more or less uniformly, *non-zero* value also in off-diagonal areas. This implies that the weak coupling is not suppressed by the pulse and, in average, evolves during $\approx 27\%$ of the pulse length. Hence, both the ¹H- and the X-shape might have a benefit if used individually in mixing sequences where coupling evolution is desired.

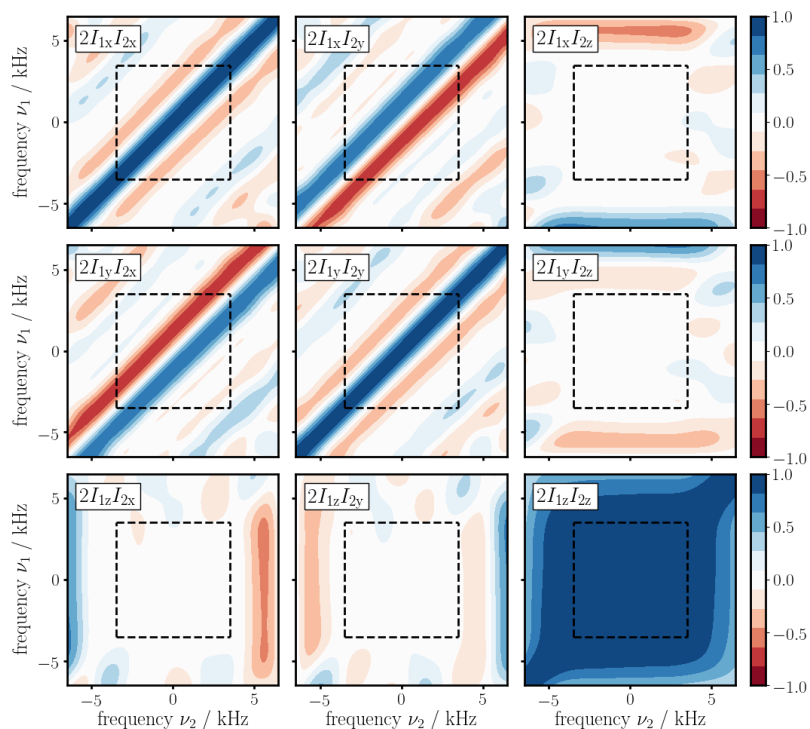


Figure 2.73: Case 4 (Section 2.4.3) – homonuclear average Hamiltonian $\bar{\mathcal{H}}_{0,J}(\nu_1, \nu_2)$ for ${}^1\text{H}$ -shape. ${}^1\text{H}$ -shape: BURBOP (UR 180°); $RF_{\max} = 20$ kHz; $\tau_P = 1.0$ ms; $BW \approx 7$ kHz.

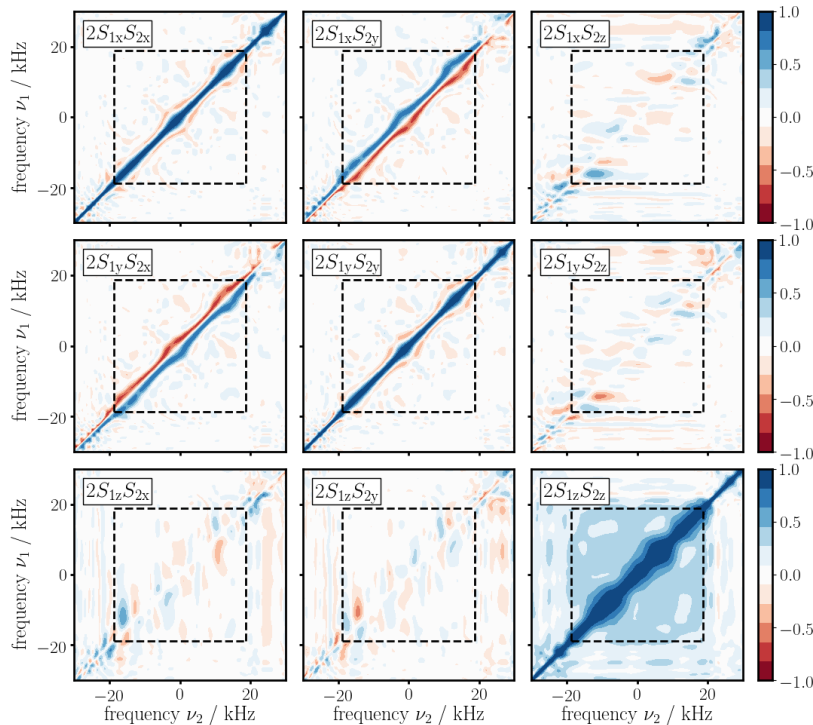


Figure 2.74: Case 4 (Section 2.4.3) – homonuclear average Hamiltonian $\bar{\mathcal{H}}_{0,J}(\nu_1, \nu_2)$ for X-shape. X-shape: BURBOP (UR 180°); $RF_{\max} = 10$ kHz; $\tau_P = 1.0$ ms; $BW \approx 37.5$ kHz.

2.4.18 Broadband 180° Pulse Sandwich: BUBI (A, B)

The BUBI-pair is another pulse sandwich in which two matched shapes are applied simultaneously on the proton- and an X-channel and was originally designed for the application in INEPT-like coherence transfer.^[103] Both are phase- and amplitude-modulated (Figure 2.75 (a) and (d)) but while on protons a universal 180°-rotation is induced by a BURBOP (A) on the X-nuclei an inversion is effected by a BIBOP (B) – the rotation axes are shown in Figure 2.75 (b) and (e), respectively. The pulse parameters for the ¹H-shape (X-shape) are set to an RF amplitude of 20 kHz (10 kHz) corresponding to a pulse length of 600 μ s (600 μ s) and an effective rotation over a bandwidth of 10 kHz (37.5 kHz) is obtained. It shall be mentioned that the maximum RF amplitude for proton is, as for all pulse sandwiches, twice as large as for other non-selective pulses under investigation and results might not be directly comparable. The concurrently optimized BUBI pulse shapes aim at the suppression of any bilinear operator originating from a heteronuclear ¹J-coupling during the pulse shape and, hence, achieve a lower artifact level as for a non-*J*-compensated pair of simultaneously applied shaped pulses.

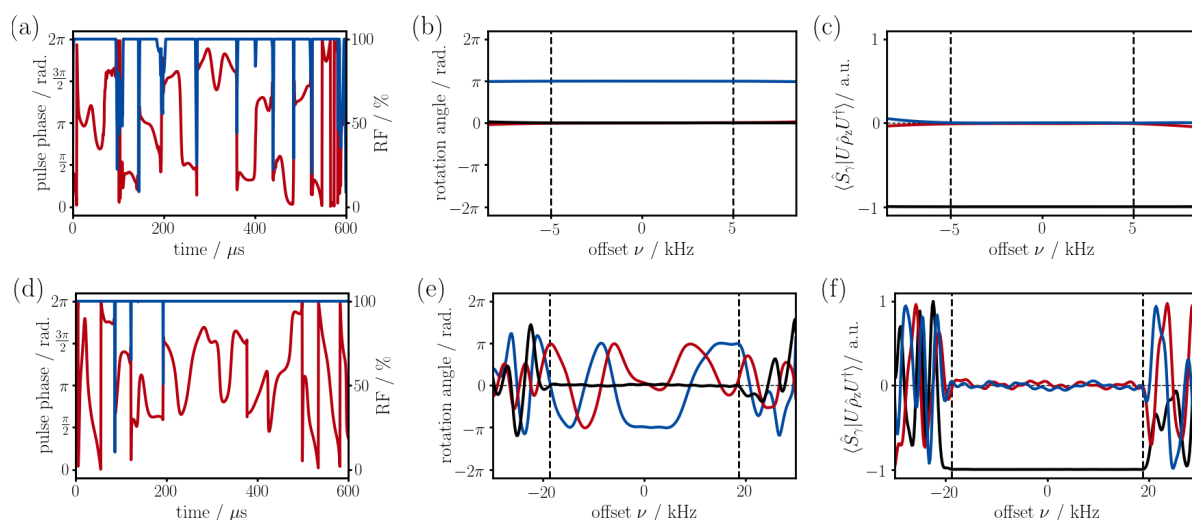


Figure 2.75: The BUBI pulse shape sandwich is shown as phase- (red) and amplitude-profile (blue) in (a) for proton and (d) for heteronuclei. For the ¹H-shaped pulse, effective rotation axes in (b) and expectation value $\langle \hat{S}_\gamma | U \hat{\rho}_z U^\dagger \rangle$ in (c) are plotted for Cartesian operators \hat{S}_x (blue), \hat{S}_y (red) and \hat{S}_z (black). For the X-shaped pulse the results are shown in (e) and (f), respectively.

Simulations in the toggling frame are undertaken where both pulse shapes are *concurrently* applied to a heteronuclear spin system (Case 3) as intended by the optimization and further when applied *individually* to homonuclear spin systems (Case 4). The results for Case 3 are shown in Figure 2.76 and, indeed, for all coupling operators in the toggling frame basically empty plots are obtained. Hence, heteronuclear coupling is successfully suppressed during the BUBI-pulse pair and no artifacts from undesired *heteronuclear* coherence transfer is expected. However, the situation changes if homonuclear couplings are considered as illustrated for the ¹H- and X-shape in Figure 2.77 and 2.78, respectively. If the proton pulse is individually applied to a homonuclear two spin system, the diagonal lines of strong coupling operators ($2I_{1x}I_{2x}$, $2I_{1y}I_{2y}$ and $2I_{1z}I_{2z}$) are remarkably broadened. Furthermore, all other examined bilinear operators exhibit a non-uniform distribution within the considered area (dashed box). Also for the X-shape, a somewhat broadened diagonal is encountered for the weak coupling ($2S_{1z}S_{2z}$) and zero-quantum terms ($2S_{1x/y}S_{2x/y}$) and, further, off-diagonal areas as well as anti-phase operators ($2S_{1x/y}S_{2z}$ and $2S_{1z}S_{2x/y}$) exhibit a seemingly random distribution of positive and negative spots. Hence, the presence of homonuclear couplings between protons or X-nuclei could lead to undesired artifacts from coherence transfer during the pulse. However, the BUBI pulse length is only 600 μ s and for smaller couplings the *effective* coherence transfer might not be as severe as expected. In fact, weak coupling evolution can be desired if used repetitively e.g. in a planar mixing sequence (Section 2.2).

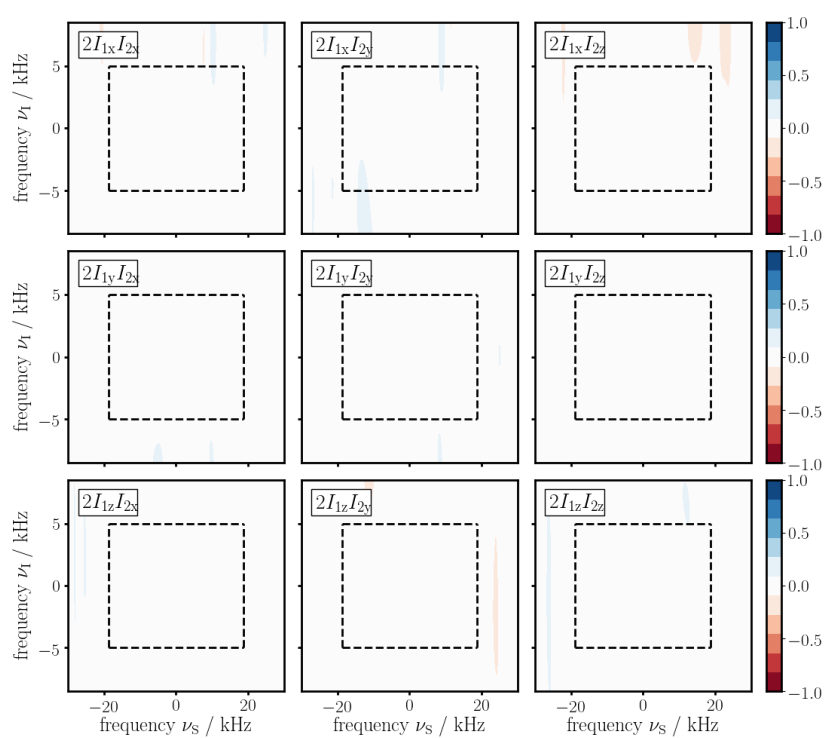


Figure 2.76: Case 3 (Section 2.4.3) – average Hamiltonian $\bar{\mathcal{H}}_{0,J}(\nu_1, \nu_S)$ for heteronuclear system.

¹H-shape: BURBOP (UR 180°); $RF_{\max} = 20$ kHz; $\tau_P = 600$ μ s; $BW \approx 10$ kHz.

X-shape: BIBOP (inversion); $RF_{\max} = 10$ kHz; $\tau_P = 600$ μ s; $BW \approx 37.5$ kHz.

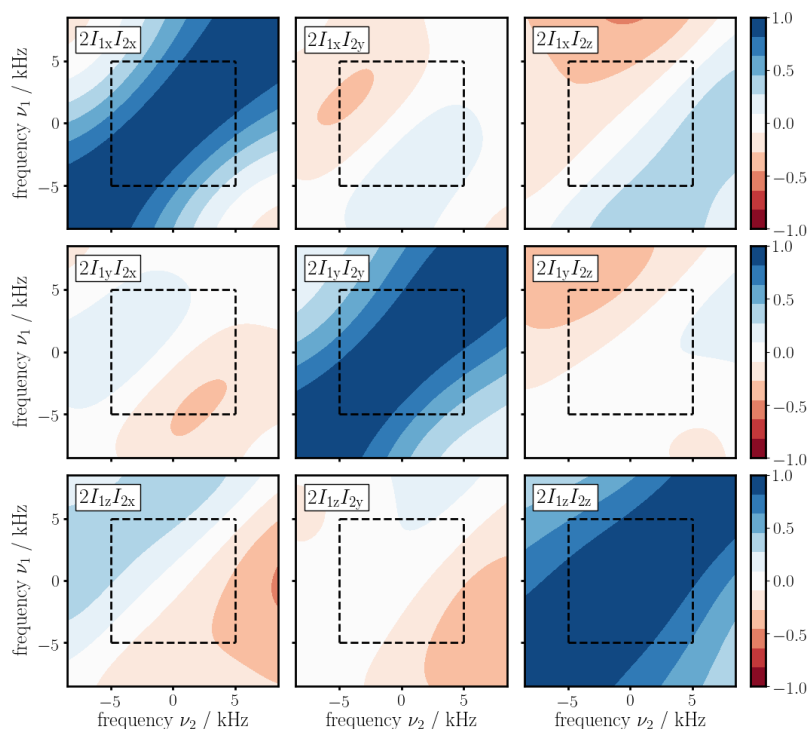


Figure 2.77: Case 4 (Section 2.4.3) – homonuclear average Hamiltonian $\bar{\mathcal{H}}_{0,J}(\nu_1, \nu_2)$ for ${}^1\text{H}$ -shape. ${}^1\text{H}$ -shape: BURBOP (UR 180°); $RF_{\max} = 20$ kHz; $\tau_P = 600$ μs ; $BW \approx 10$ kHz.

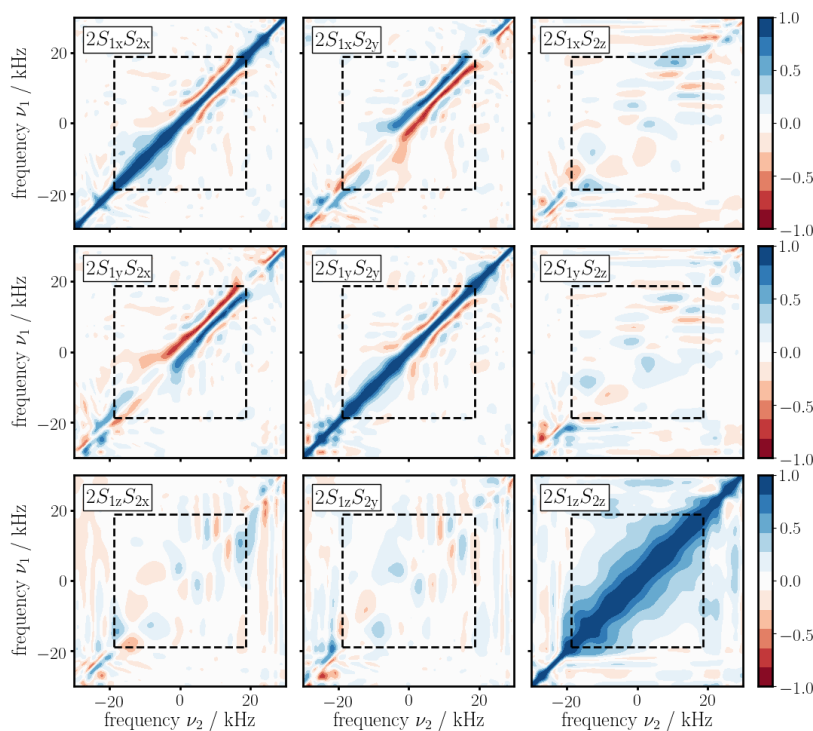


Figure 2.78: Case 4 (Section 2.4.3) – homonuclear average Hamiltonian $\bar{\mathcal{H}}_{0,J}(\nu_1, \nu_2)$ for X-shape. X-shape: BIBOP (inversion); $RF_{\max} = 10$ kHz; $\tau_P = 600$ μs ; $BW \approx 37.5$ kHz.

2.4.19 Broadband 90° Pulse Sandwich: BE^{tr}BE (B2)

The BE^{tr}BE pulse pair is a pulse sandwich that was optimized in combination with the BUBI pulses (Section 2.4.18) and is likewise intended to be used in INEPT-like coherence transfer elements.^[103] Again, two phase- and amplitude-modulated shaped pulses (Figure 2.79 (a) and (d)) are applied simultaneously on the proton- and an X-channel and, in order to avoid undesired coherence transfer, the heteronuclear ¹J-coupling is supposed to be suppressed during the shaped pulses. On protons, de-excitation is obtained from a *time-reversed* BEBOP (B2) while X-nuclei are excited from a *non-reversed* BEBOP (B2) and the rotation axes are shown in Figure 2.79 (b) and (e), respectively. Note, the inversed effect can be obtained from time-reversion with (BE^{tr}BE)^{tr} ≡ BEBE^{tr}. The pulse parameters for the ¹H-shape (X-shape) are set to an RF amplitude of 20 kHz (10 kHz) corresponding to a pulse length of 550 μs (550 μs) and an effective rotation over a bandwidth of 10 kHz (37.5 kHz) is obtained. It shall be mentioned that the maximum RF amplitude for proton is, as for all pulse sandwiches, twice as large as for other non-selective pulses under investigation and results might not be directly comparable.

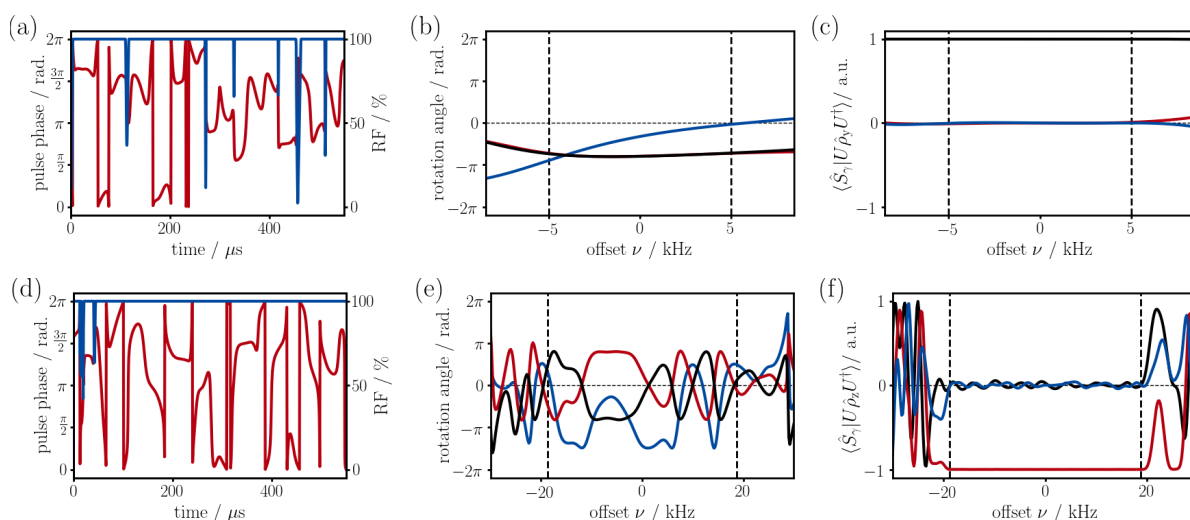


Figure 2.79: The BE^{tr}BE pulse shape sandwich is shown as phase- (red) and amplitude-profile (blue) in (a) for proton and (d) for heteronuclei. For the ¹H-shaped pulse, effective rotation axes in (b) and expectation value $\langle \hat{S}_\gamma | U \hat{\rho}_y U^\dagger \rangle$ in (c) are plotted for Cartesian operators \hat{S}_x (blue), \hat{S}_y (red) and \hat{S}_z (black). For the shaped pulse dedicated to coupled heteronuclei the results (using the expectation value $\langle \hat{S}_\gamma | U \hat{\rho}_z U^\dagger \rangle$) are shown in (e) and (f), respectively.

In analogy to previous pulse sandwiches, simulations in the toggling frame are undertaken where both pulse shapes are *concurrently* applied to a heteronuclear spin system (Case 3) as intended by the optimization and further when applied *individually* to homonuclear spin systems (Case 4).

The results for Case 3 are shown for the BE^{tr}BE- and BEBE^{tr}-sandwich in Figure 2.80 and 2.81, respectively. In both cases, all coupling operators in the toggling frame are basically zero and, hence, heteronuclear coupling is successfully suppressed during both BEBE-pulse pairs – no artifacts from undesired *heteronuclear* coherence transfer is expected.

On the other hand, the toggling frame simulations for Case 4 (considering individual pulse shapes of the BE^{tr}BE-sandwich applied to a homonuclear spin system) reveal that homonuclear coupling evolution during the pulse shapes could lead to undesired coherence transfer. The results are shown for the ¹H-BEBOP^{tr} and X-BEBOP in Figure 2.80 and 2.81, respectively. For the ¹H-pulse, the diagonal lines of strong coupling operators ($2I_{1x}I_{2x}$, $2I_{1y}I_{2y}$ and $2I_{1z}I_{2z}$) are remarkably broadened while other examined bilinear operators are non-zero within the considered area. Likewise for the X-shape, a broadened diagonal is encountered for the weak coupling ($2S_{1z}S_{2z}$) and zero-quantum terms ($2S_{1x/y}S_{2x/y}$) and, further, off-diagonal areas and anti-phase operators exhibit numerous positive and negative spots. Still, it is crucial to note that the BEBE pulse length is only 550 μs and for smaller homonuclear couplings the *effective* coherence transfer might not be as severe as expected.

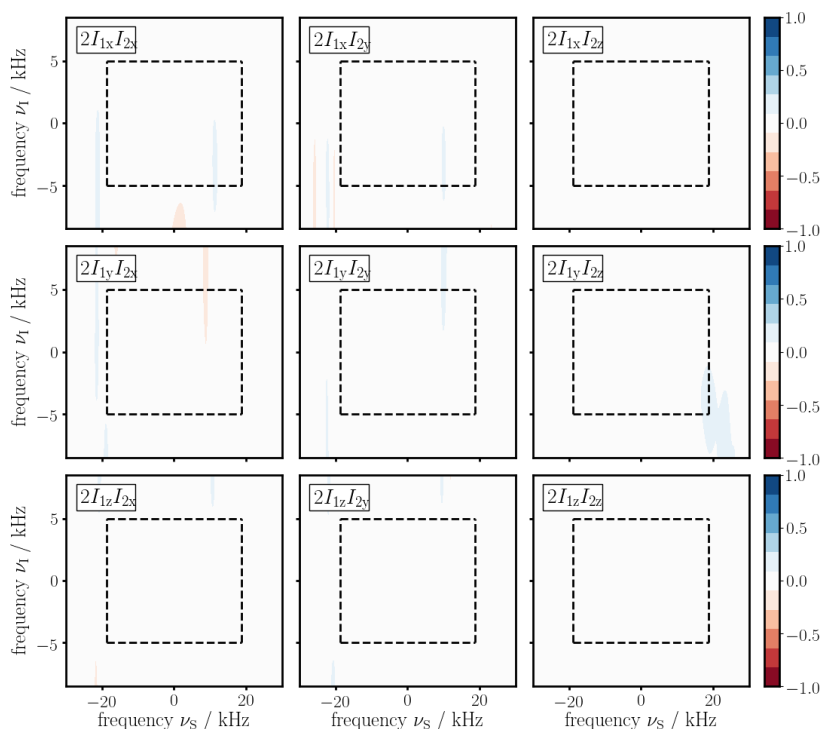


Figure 2.80: Case 3 (Section 2.4.3) – average Hamiltonian $\bar{\mathcal{H}}_{0,J}(\nu_1, \nu_S)$ for heteronuclear system.
 1 H-shape: BEBOP^{tr} (time-reversed excitation); $RF_{\max} = 20$ kHz; $\tau_P = 550$ μ s; $BW \approx 10$ kHz.
X-shape: BEBOP (excitation); $RF_{\max} = 10$ kHz; $\tau_P = 550$ μ s; $BW \approx 37.5$ kHz.

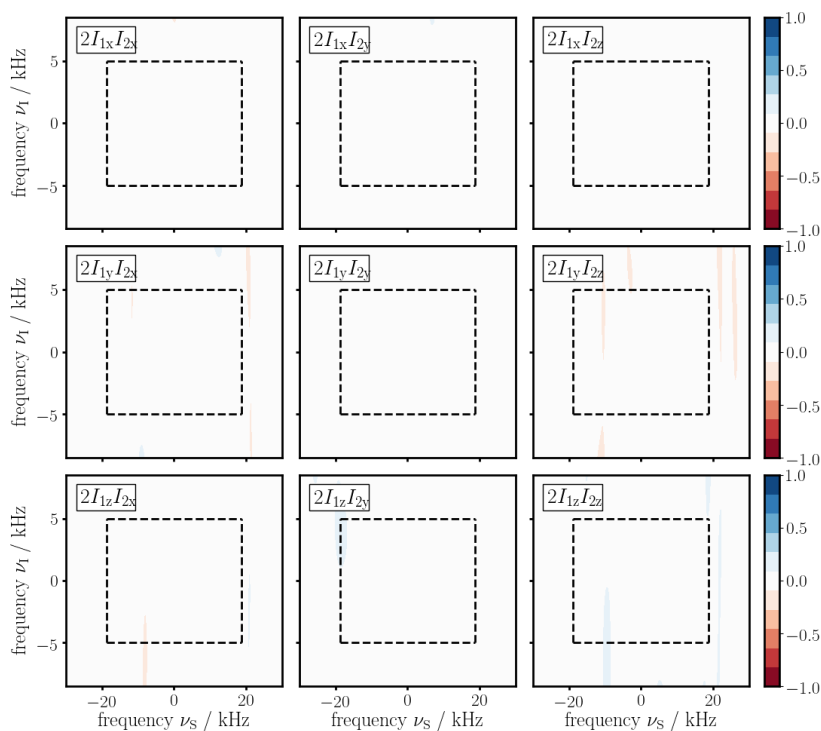


Figure 2.81: Case 3 (Section 2.4.3) – average Hamiltonian $\bar{\mathcal{H}}_{0,J}(\nu_1, \nu_S)$ for heteronuclear system.
 1 H-shape: BEBOP (time-reversed excitation); $RF_{\max} = 20$ kHz; $\tau_P = 550$ μ s; $BW \approx 10$ kHz.
X-shape: BEBOP^{tr} (excitation); $RF_{\max} = 10$ kHz; $\tau_P = 550$ μ s; $BW \approx 37.5$ kHz.

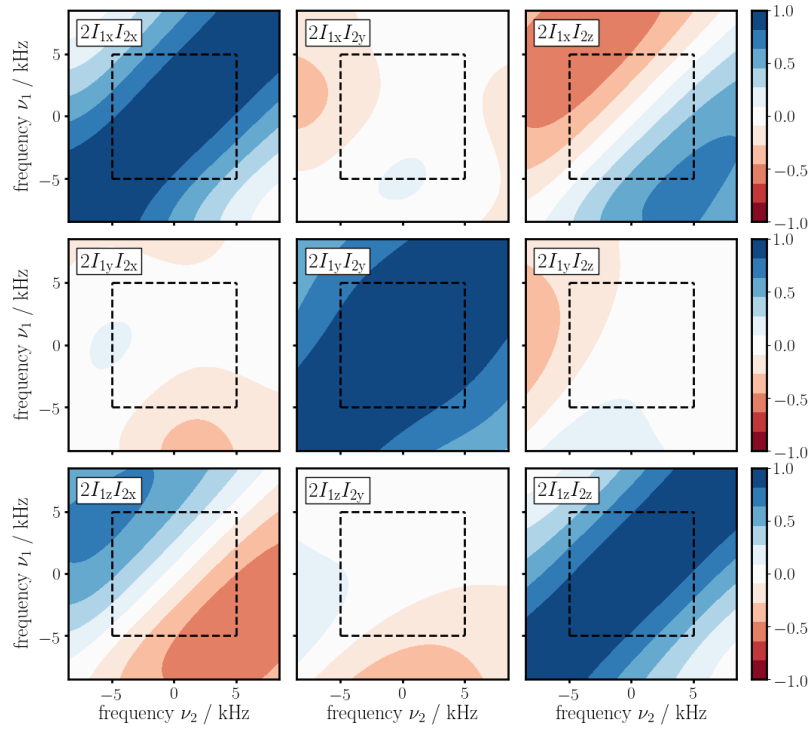


Figure 2.82: Case 4 (Section 2.4.3) – homonuclear average Hamiltonian $\bar{\mathcal{H}}_{0,J}(\nu_1, \nu_2)$ for ${}^1\text{H}$ -shape. ${}^1\text{H}$ -shape: BEBOP^{tr} (time-reversed excitation); $RF_{\max} = 20$ kHz; $\tau_P = 550$ μs ; $BW \approx 10$ kHz.

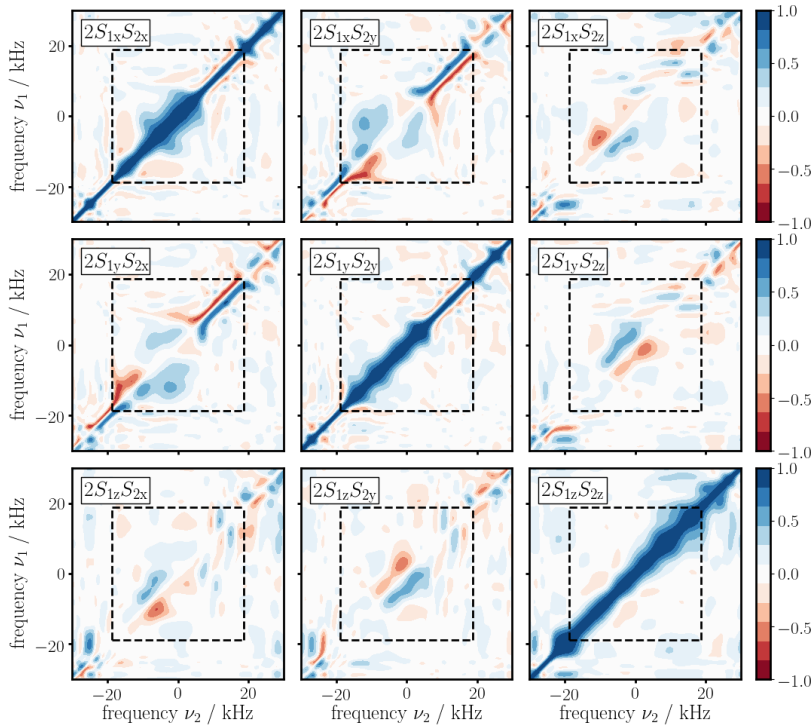


Figure 2.83: Case 4 (Section 2.4.3) – homonuclear average Hamiltonian $\bar{\mathcal{H}}_{0,J}(\nu_1, \nu_2)$ for X-shape. X-shape: BEBOP (excitation); $RF_{\max} = 10$ kHz; $\tau_P = 550$ μs ; $BW \approx 37.5$ kHz.

2.5 A Different Perspective on Strong Coupling

In the present section a detailed discussion on so-called *second order effects* of strong coupling shall be given. The transformation to an interaction frame reveals the time-dependence of the strong coupling Hamiltonian which induces a geometric phase similar to the Berry phase (discussed in Section 1.5.3).^[42] Likewise it can be shown that the time-dependence leads to the secular approximation when average Hamiltonian theory is applied.

As discussed in Section 1.3.3 and 1.3.6 the Hamiltonian $\hat{\mathcal{H}}_{\text{strong}}$ of a strongly coupled two-spin system, denoted \hat{I}_1 and \hat{I}_2 , can be described by:

$$\hat{\mathcal{H}}_{\text{strong}} = \hat{\mathcal{H}}_Z + \hat{\mathcal{H}}_J \quad (2.5.1)$$

$$\text{where: } \hat{\mathcal{H}}_Z = 2\pi(\nu_1 \hat{I}_{1z} + \nu_2 \hat{I}_{2z})$$

$$\text{and: } \hat{\mathcal{H}}_J = \pi J(2\hat{I}_{1x}\hat{I}_{2x} + 2\hat{I}_{1y}\hat{I}_{2y} + 2\hat{I}_{1z}\hat{I}_{2z})$$

where ν_1 and ν_2 are the Zeeman interaction frequencies in the rotating frame for spins 1 and 2, respectively, and J is the coupling constant. It is crucial to note that writing $\hat{\mathcal{H}}_J$ in terms of normalized bilinear operators reveals that $\hat{\mathcal{H}}_J$ induces a rotation (described by Equation 1.4.10) with a frequency of $\frac{1}{2}J$ only. The spectrum of such a strongly coupled two-spin system with $\nu_1 = 10$ Hz, $\nu_2 = -10$ Hz and $J_{12} = 10$ Hz is simulated and shown in Figure 2.84. Due to the phenomenological intensity distribution in the spectrum it is often referred to as *roof effect*.

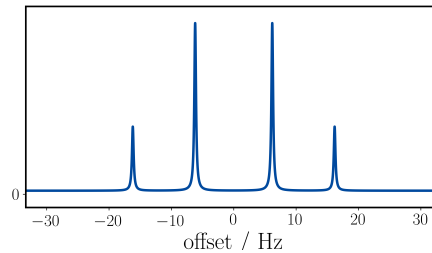


Figure 2.84: Spectrum of a strongly coupled two-spin system, \hat{I}_1 and \hat{I}_2 .

By using Zeeman product basis operators for the observation the overall spectrum can be decomposed into its underlying components which are shown in Figure 2.85 - the sum of all spectra would result again in Figure 2.84. It is important to note that the Zeeman product basis is no longer an eigenbasis of the considered strong coupling Hamiltonian $\hat{\mathcal{H}}_{\text{strong}}$. In order to deal with a strongly coupled spin system it was so far common to determine the energy eigenvalues and eigenfunctions of the considered Hamiltonian⁷⁴ and it turns out that the eigenfunctions are given by a linear combination of the Zeeman product basis. The spectrum of the considered spin system can be determined from the transition frequencies that are calculated from the difference of respective energy eigenvalues. Hence, in the *Hamiltonian's eigenbasis* the evolution of a single spin density element ρ_{mn} is still given by:

$$\rho_{mn}(t) = \exp\{-i(E_m - E_n)t\} \rho_{mn}(0) \quad (2.5.2)$$

where E_m and E_n are the eigenvalues of corresponding eigenfunctions $|m\rangle$ and $|n\rangle$, respectively.^[13,17,213] The intensities of respective transitions, on the other hand, are calculated as derived in Equation (1.2.3)

^[213] M. J. Thrippleton, R. A. E. Edden and J. Keeler. *Journal of Magnetic Resonance* **2005**, *174*, 97–109.

⁷⁴ The energy eigenvalues E can be determined by the linear system of equations: $(\hat{\mathcal{H}} - E\mathbb{1}) \cdot |m\rangle = 0$ where the non-trivial solution is given for $\det(\hat{\mathcal{H}} - E\mathbb{1}) = 0$. The eigenfunctions $|m\rangle$ can be calculated subsequently by introducing the calculated eigenvalues E in the linear system of equations.

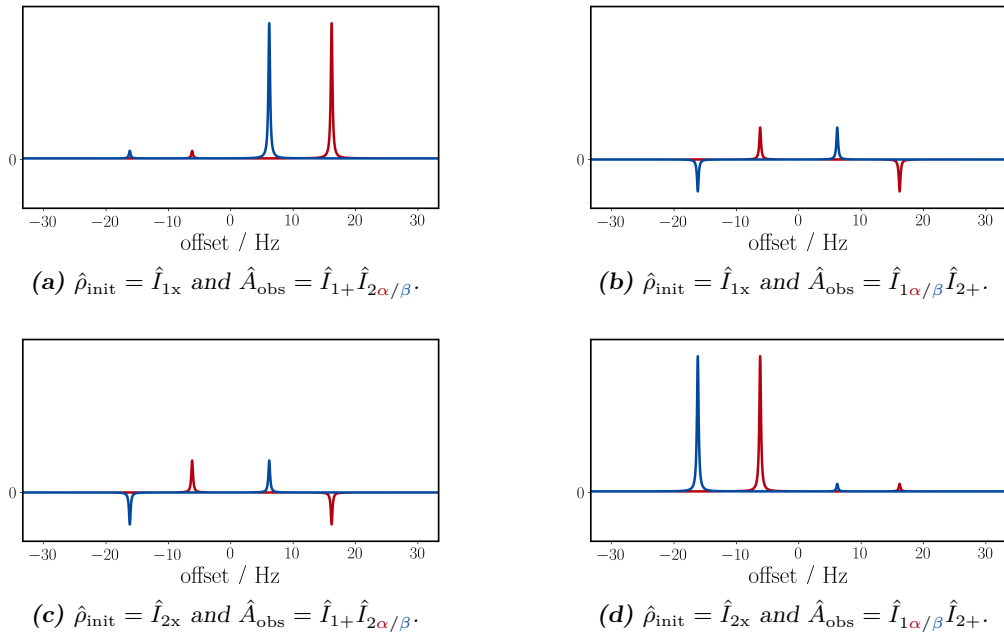


Figure 2.85: The spectrum of a strongly coupled two-spin system, \hat{I}_1 and \hat{I}_2 , is observed using the Zeeman product basis operators (\hat{A}_{obs}) given below each spectrum (a-d).

from the expectation value of the observable operator \hat{A} :

$$\langle \hat{A} \rangle = \text{Tr}\{\hat{\rho}\hat{A}\} = \sum_m \sum_n \rho_{mn} \langle m | \hat{A} | n \rangle. \quad (2.5.3)$$

In the following another approach shall be pursued that is based on the transformation to an interaction frame in which the coupling Hamiltonian becomes time-dependent. A further comparison to the classical calculation known from standard text books is subsequently given.

2.5.1 Strong Coupling in the Double Rotating Frame

The secular approximation for homonuclear couplings is commonly deduced from spherical spin tensors as discussed in Section 1.3.2. Likewise the transformation to an interaction frame can be undertaken for Cartesian operators which, in the following, is done using the theory discussed in Section 1.6.2 and 1.6.4. We shall note at this point that the propagator U_{strong} of the considered Hamiltonian \hat{H}_{strong} can be expressed in terms of a Suzuki-Trotter approximation (Equation 2.5.4) which is discussed in more detail in Section 1.7.3. We choose n to be a large number and we transform the propagator U_{strong} to an interaction frame by introducing the unity matrix $\mathbb{1}$ (Section 1.6.4) at consecutive time steps in Equation (2.5.5). We obtain:

$$U_{\text{strong}} = \exp\{-i(\hat{H}_Z + \hat{H}_J)t\} \approx (U_Z U_J)^n \quad (2.5.4)$$

$$= U_Z U_J U_Z \dots U_Z \underbrace{U_Z^\dagger U_J U_Z}_{U_{J_1}} \underbrace{U_Z^\dagger U_J U_Z}_{U_{J_0}} U_J \quad (2.5.5)$$

$$= (U_Z)^n \underbrace{(U_Z^\dagger)^{n-1} U_J (U_Z)^{n-1}}_{U_{J_{n-1}}} \dots \underbrace{(U_Z^\dagger)^2 U_J (U_Z)^2}_{U_{J_2}} \underbrace{U_Z^\dagger U_J U_Z}_{U_{J_1}} \underbrace{U_J}_{U_{J_0}} \quad (2.5.6)$$

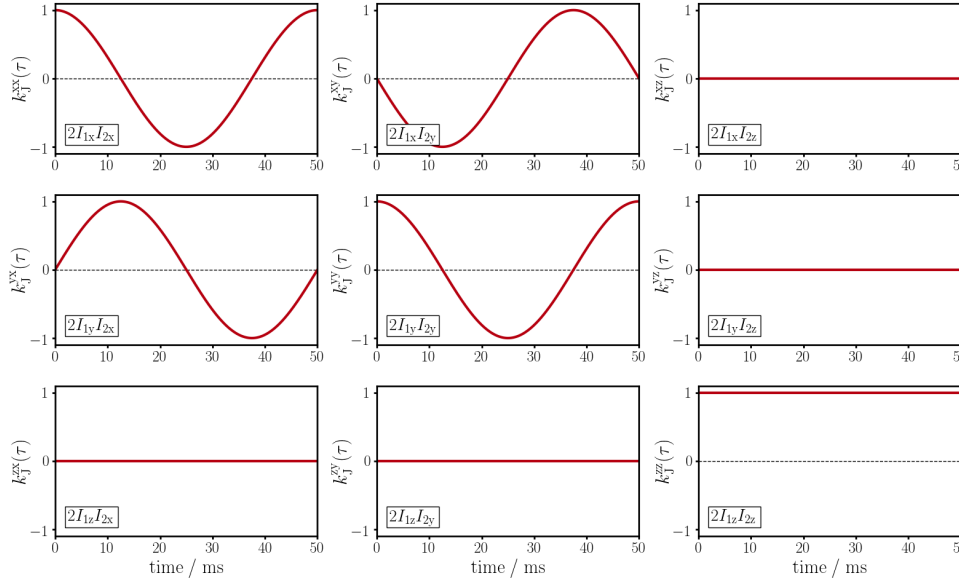


Figure 2.86: The evolution of the strong coupling Hamiltonian $\hat{\mathcal{H}}_{D,J}(\tau)$ during a delay is shown in the double rotating frame. A two-spin system is assumed with $\Delta = |\nu_2 - \nu_1| = 20$ Hz and a delay of length $t_c = 50$ ms.

and we realize that the consecutive coupling propagators ($U_{J_{n-1}} \dots U_{J_0}$) approximate the propagation of a time-dependent Hamiltonian $\hat{\mathcal{H}}_{D,J}(\tau)$ in the *interaction frame*. In analogy to Section 1.6.3, the Hamiltonian $\hat{\mathcal{H}}_{D,J}(\tau)$ is decomposed into its normalized bilinear components $2\hat{I}_{1\gamma}\hat{I}_{2\gamma'}$ (with $\gamma, \gamma' = x, y, z$ being the axes of the interaction frame) which are scaled by the time-dependent coefficients $k_J^{\gamma\gamma'}(\tau)$. These are illustrated in Figure 2.86 for a two-spin system where the evolution of the transformed Hamiltonian $\hat{\mathcal{H}}_{D,J}(\tau)$ is followed by numerical simulations during a delay of length $t_c = 50$ ms. While the zero quantum terms ($2\hat{I}_{1x}\hat{I}_{2x} + 2\hat{I}_{1y}\hat{I}_{2y}$) of $\hat{\mathcal{H}}_{D,J}(\tau)$ evolve under the Zeeman interaction $\hat{\mathcal{H}}_Z$ the longitudinal term ($2\hat{I}_{1z}\hat{I}_{2z}$) is invariant. The illustrated oscillation has a frequency which is given by the offset $\Delta = |\nu_2 - \nu_1|$ and the interaction frame can be considered a *double rotating frame* which rotates at the Larmor frequency of spin 1 and spin 2, *simultaneously*. Imagining such a double rotating frame confronts us with a problem that commonly in NMR can silently be ignored: a frame transformation imposes a motion on the observable operators. Despite the fact that in NMR one of the most basic concepts is the rotating frame the observables are, in general, time-independent. We owe this convenience our spectrometers that directly put us in the rotating frame as is discussed in Section 1.5.3. Note, also in heteronuclear experiments the spectrometer fulfills its part where, in principle, one is likewise in a double rotating frame (though with a much larger frequency difference). It is, however, possible to think of a theoretical scenario where the time-dependence of the observable in the double rotating frame is no longer of relevance. With this regard, it is important to note that the expectation value of an operator \hat{A} in the double rotating frame can be deduced from Equation (2.5.6) to be given as:

$$\begin{aligned} \langle \hat{A} \rangle &= \text{Tr} \left\{ \hat{A} (U_Z)^n (U_{J_{n-1}} \dots U_{J_0}) \hat{\rho} (U_{J_0}^\dagger \dots U_{J_{n-1}}^\dagger) (U_Z^\dagger)^n \right\} \\ &= \text{Tr} \left\{ \underbrace{(U_Z^\dagger)^n \hat{A} (U_Z)^n}_{\text{Heisenberg}} \underbrace{(U_{J_{n-1}} \dots U_{J_0}) \hat{\rho} (U_{J_0}^\dagger \dots U_{J_{n-1}}^\dagger)}_{\text{Schrödinger}} \right\}. \end{aligned} \quad (2.5.7)$$

Clearly, in the Heisenberg picture the observable \hat{A} is rotated by $(U_Z)^n$ at a frequency that is different for spin 1 and 2 – the double rotating frame is on-resonant with both spins while $\nu_1 \neq \nu_2$. Still, the illusion of being in a “conventional” rotating frame can be preserved if spin 1 and 2 are observed separately. In the case that the observable \hat{A} commutes with the rotation U_Z the transformation to the double

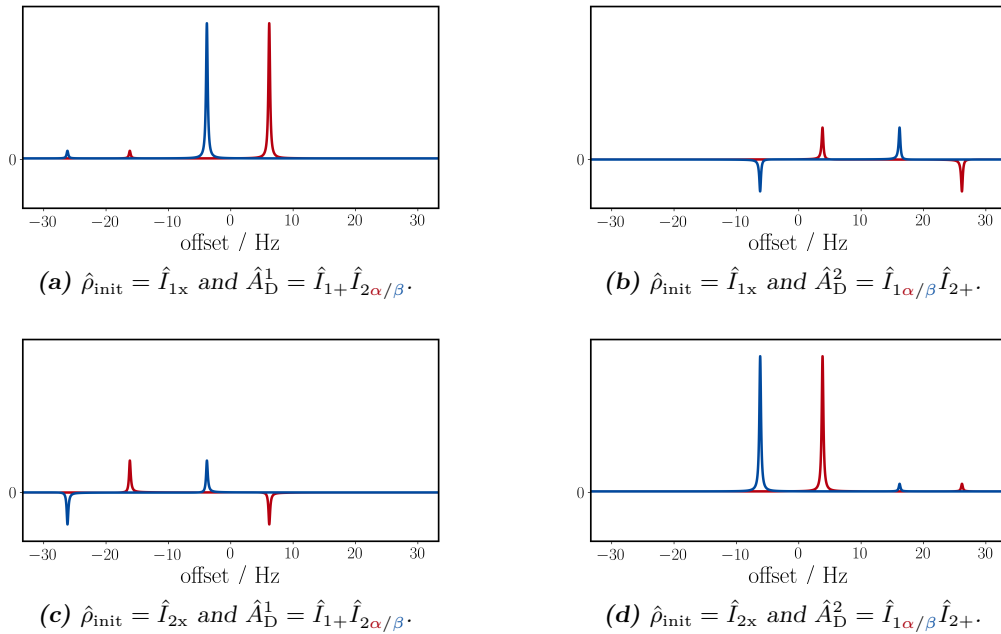


Figure 2.87: Spectra of a strongly coupled two-spin system, \hat{I}_1 and \hat{I}_2 , simulated from the transformed Hamiltonian $\hat{\mathcal{H}}_{D,J}(\tau)$ (Equation 2.5.6) using the observables $\hat{A}_D^{1/2}$.

rotating frame will have no effect on the observable's expectation value.⁷⁵ Given these circumstances it is legitimate to state that certain observables \hat{A} (in the Heisenberg picture of Equation 2.5.7) are time-independent in the double rotating frame.

An example shall be given where the time-domain signal of a strongly coupled two-spin system described by the Hamiltonian in Equation (2.5.1) with $\nu_1 = 10$ Hz, $\nu_2 = -10$ Hz and $J_{12} = 10$ Hz is simulated. Zeeman product operators are used for the observation which are given by $\hat{A}^1 = \hat{I}_{1+}\hat{I}_{2\alpha/\beta}$ and $\hat{A}^2 = \hat{I}_{1\alpha/\beta}\hat{I}_{2+}$ for spin \hat{I}_1 and \hat{I}_2 , respectively. As discussed above, both observables commute with respective rotations on the coupled spin: $[\hat{A}^{1/2}, U_Z^{2/1}] = 0$ and the observables in the rotating ($\hat{A}^{1/2}$) and double rotating frame ($\hat{A}_D^{1/2}$) are identical. Still, the subscript (D) shall be kept in the following to indicate an observation in the interaction frame. The time-domain signal is *directly* calculated from the propagators in the double rotating frame given in Equation (2.5.6) and the expectation value of Equation (2.5.7) can now be simplified to:

$$\langle \hat{A} \rangle = \text{Tr} \left\{ \hat{A}_D^{1/2} (U_{J_{n-1}} \dots U_{J_0}) \hat{\rho} (U_{J_0}^\dagger \dots U_{J_{n-1}}^\dagger) \right\}. \quad (2.5.8)$$

Clearly, the resulting spectra in Figure 2.87 are comparable to the simulations in the rotating frame shown in Figure 2.85. They only differ by a frequency shift that is caused from the fact that the double rotating frame is on-resonant with both spins. It is remarkable that in the considered double rotating frame the only present interaction is the time-dependent coupling Hamiltonian $\hat{\mathcal{H}}_{D,J}(\tau)$, illustrated in Figure 2.86, from which the spectra are generated. A further discussion on the effect of such time-dependence is given in the subsequent section.

⁷⁵ If $[\hat{A}, U] = 0$ the expectation value simplifies to: $\langle \hat{A} \rangle = \text{Tr}\{U^\dagger \hat{A} U \hat{\rho}\} = \text{Tr}\{U^\dagger U \hat{A} \hat{\rho}\} = \text{Tr}\{\hat{A} \hat{\rho}\}$.

2.5.2 Geometric Phase Induced by Strong Coupling

The effect of a time-dependent periodic Hamiltonian was discussed with respect to the Berry phase in Section 1.5.3 and it was shown that a geometric phase is acquired. In contrast to the Berry phase, the strong coupling Hamiltonian is based on *bilinear* terms of which only the zero-quantum terms ($2\hat{I}_{1x}\hat{I}_{2x} + 2\hat{I}_{1y}\hat{I}_{2y}$ and $2\hat{I}_{1y}\hat{I}_{2x} - 2\hat{I}_{1x}\hat{I}_{2y}$) are time-dependent (Figure 2.86) while the secular part of the Hamiltonian ($2\hat{I}_{1z}\hat{I}_{2z}$) is time-independent. Since the secular part commutes with any zero-quantum term involved (see Table 1.1) they can be treated separately one after the other. If first the time-dependent zero quantum part is considered it turns out that it induces a geometric phase comparable to the Berry phase while the effect of the weak coupling part afterwards simply results in a spectral shift that depends on the state of the coupled spin. A detailed discussion shall be given.

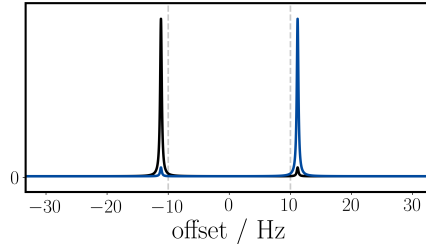


Figure 2.88: Spectrum of a zero-quantum coupled two-spin system, \hat{I}_1 and \hat{I}_2 , with $J_{12} = 10$ Hz, $\nu_1 = 10$ Hz and $\nu_2 = -10$ Hz. Observables are $\hat{A} = \hat{I}_{1+}$ (blue) and $\hat{A} = \hat{I}_{2+}$ (black).

In the double rotating frame the zero-quantum part evolves under the z-rotation U_Z and is, hence, periodic as is the off-resonant perturbation that causes the Berry phase. For the above considered two-spin system the time-dependent zero-quantum terms lead to the spectrum shown in Figure 2.88 and it is notable that all peaks are shifted away from the resonance frequencies, ν_1 and ν_2 , indicated by dashed lines. In addition, each spin exhibits a minor peak at the frequency of the coupled spin. In order to elucidate the origin of these effects numerical simulations are undertaken that are comparable to the ones representing the Berry phase in Section 1.5.3. These are shown in Figure 2.89 where a detailed comparison of both time-dependent perturbations is illustrated for different frames.

In Figure 2.89 (a) an initial state $\hat{\rho}_{\text{init}} = \hat{I}_x$ is subject to a periodic perturbation of a pulse along y and since the illustrated frame is on-resonant with the perturbative field (indicated by red dashed line) the Hamiltonian of the pulse becomes time-independent. The offset of the perturbation (with a frequency ν_P) with respect to the considered signal of spin \hat{I} is assumed to be $\Delta = \nu_1 - \nu_P = 10$ Hz and the Rabi frequency is $\nu_{\text{RF}} = 5$ Hz. The trajectory of $\hat{\rho}_{\text{init}}$ (from purple to yellow) is shown in the upper sphere while the corresponding spectrum is shown below. Clearly, the perturbation transfers parts of the transverse coherence into an unobservable state \hat{I}_z which results in a trajectory on a tilted plane. This tilt causes that a *fraction* of the amplitude of the observable signal is cosine-modulated which can be easily realized when imagining the projection of the trajectory onto the transverse plane. The Fourier transform is a linear transformation and the *non-* and *cosine-*modulated signal can be treated separately. For the non-modulated signal quadrature detection can be achieved and a single large peak is obtained at $\nu \approx 10$ Hz in the spectrum of Figure 2.89 (a). For the cosine-modulated signal, on the other hand, the sign of the frequency is indeterminable. From the *convolution theorem*^[17] it is known that a cosine-modulated amplitude causes a splitting (of twice the modulation frequency) whereof one peak appears at the negative frequency $\nu \approx -10$ Hz in Figure 2.89 (a) while the other is overlapped by the large peak. Since only a fraction of the amplitude is cosine-modulated the peak at $\nu \approx -10$ Hz is much smaller compared to its counterpart. In addition to the minor peak, it is notable that the time-dependent perturbation likewise causes a shift of the signals away from the center frequency at which is irradiated. This circumstance was already discussed in Section 1.5.3 and can be ascribed to the acquisition of a *purely* geometric phase. It can best be illustrated by going to the frame that rotates *exactly* at the Larmor frequency of the considered signal (gray dashed line) as shown in Figure 2.89 (d). Such a frame transformation causes a z-rotation of the illustrated sphere where the tangential velocity at the “equator” is higher compared to

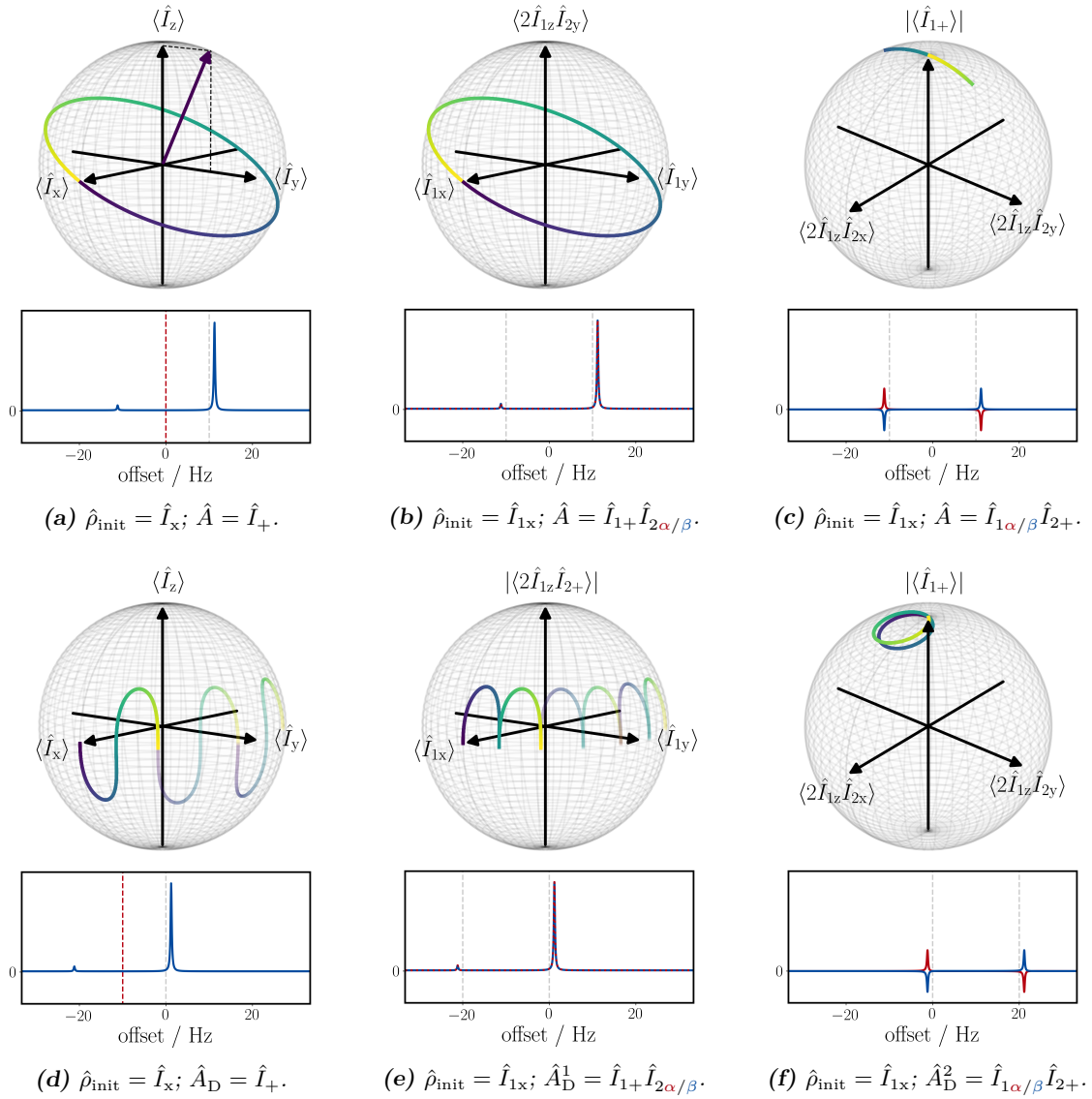


Figure 2.89: A comparison of the geometric phase induced by off-resonant irradiation (a,d) and the ZQ-terms originating from strong coupling (b,c,e,f) is shown. In the upper row the observation takes place in the rotating frame (a-c) while in the lower row the Zeeman interaction is completely removed by the transformation to the on-resonant (d) and double rotating frame (e,f).

the “poles”. With this regard, it is crucial to note that the signal’s trajectory in the transverse plane is *exactly* vertical and evidently both, frame and signal, rotate around the z-axis at the *same* frequency. However, each time the trajectory leaves the transverse plane the tangential velocity of the frame decreases and the signal moves faster than the sphere i.e. our frame. Hence, in Figure 2.89 (d) a wave like trajectory is observed that exhibits “horizontal velocity” (i.e. an acquisition of a phase) only outside the transverse plane – an effect which in the end causes an apparent shift away from the perturbative field.

It is surprising that the time-dependent zero-quantum Hamiltonian discussed above causes a very similar evolution. For the above considered two-spin system, \hat{I}_1 and \hat{I}_2 , an initial state $\hat{\rho}_{\text{init}} = \hat{I}_{1x}$ evolves likewise on a tilted plane as shown in Figure 2.89 (b). Note, for all illustrated coordinate systems, *all* operators involved in the transfer process are ascribed to one out of the three Cartesian axis. In contrast to the perturbation by the pulse, the bilinear terms of the zero-quantum Hamiltonian cause a coherence transfer

to a *likewise* unobservable anti-phase state ($2\hat{I}_{1z}\hat{I}_{2y}$) whose expectation value is, hence, illustrated along z. The spectrum below is plotted for the coupled spin (\hat{I}_2) being in the state $\hat{I}_{2\alpha}$ (red) and $\hat{I}_{2\beta}$ (blue) and, so far, both spectra are identical. The Larmor frequencies $\nu_1 = 10$ Hz and $\nu_2 = -10$ Hz are indicated by gray dashed lines. It is noteworthy that $J = 10$ Hz is twice the frequency compared to the perturbation by the pulse ($\nu_{\text{RF}} = 5$ Hz) which is based on the fact that the transfer to the unobservable state ($2\hat{I}_{1z}\hat{I}_{2y}$) occurs at a frequency of $\frac{1}{2}J$ only. In the frame illustrated in Figure 2.89 (b) the anti-phase $2\hat{I}_{1z}\hat{I}_{2y}$ does not evolve under the Zeeman interaction, however, its amplitude is sine-modulated due to the coherence transfer. The time-dependent transfer to $2\hat{I}_{1z}\hat{I}_{2y}$ is likewise shown in Figure 2.89 (c) where axes of the transverse plane are given by the expectation value of the anti-phase coherences $2\hat{I}_{1z}\hat{I}_{2x}$ and $2\hat{I}_{1z}\hat{I}_{2y}$. The z-axis, on the other hand, corresponds to the absolute value of transverse coherence on spin \hat{I}_1 . The term $2\hat{I}_{1z}\hat{I}_{2y}$ ($= 2\hat{I}_{1\alpha}\hat{I}_{2y} - 2\hat{I}_{1\beta}\hat{I}_{2y}$) is, in principle, unobservable, however, its single components, $2\hat{I}_{1\alpha}\hat{I}_{2y}$ and $2\hat{I}_{1\beta}\hat{I}_{2y}$, can be observed and both are shown in the spectrum of Figure 2.89 (c) in red and blue, respectively. It is crucial to note that the apparent *anti-phase* spectrum of both components originates from the sine-modulation and is not a direct consequence of the unobservable *anti-phase* coherence $2\hat{I}_{1z}\hat{I}_{2y}$. Again, a frame transformation is helpful to reveal that a geometric phase is acquired and likewise the signals are shifted away from their Larmor frequencies. However, this time the frame transformation leads to the *double rotating frame* that resonates at the Larmor frequency of spin \hat{I}_1 and \hat{I}_2 simultaneously as discussed in the previous section.⁷⁶ The evolution in the double rotating frame is shown in Figure 2.89 (e) and (f) where in both cases the “horizontal velocity” (i.e. the phase) depends on the trajectory on the sphere’s surface. It is noteworthy that in the considered frame of Figure 2.89 (e) the anti-phase coherence $2\hat{I}_{1z}\hat{I}_{2y}$ evolves under the Zeeman interaction⁷⁷ and the z-axis of Figure 2.89 (b) is replaced by its absolute value that comprises also the term $2\hat{I}_{1z}\hat{I}_{2x}$.

While the lengthy examination of the time-dependent perturbation by zero-quantum terms had to be done in detail, the effect of the commuting weak coupling Hamiltonian ($2\hat{I}_{1z}\hat{I}_{2z}$) can be treated rather fast – it simply causes a shift that is based on the spin state of the coupled spin. In the spectra of Figure 2.89 (b) and (c) the spin states $\hat{I}_{2\alpha}$ and $\hat{I}_{2\beta}$ are indicated by the colors, red and blue, respectively. Shifting the red and blue spectra by $\frac{1}{2}J$ to the right and left, respectively, produces exactly the spectra shown in Figure 2.85. It is noteworthy that despite the shifted frequencies (which is due to the acquired geometric phase) the splitting caused by the $2\hat{I}_{1z}\hat{I}_{2z}$ term is still given by the coupling constant J . With this regard, all the non-intuitive effects that the spectrum in Figure 2.84 exhibits can be examined simply by a subtle choice of frame transformations.

Comparison to Classical Calculation

The above findings shall be compared to the well-established treatment of strongly coupled spin systems known from standard text books. For the analysis of such spin system the eigenvalue problem of the Hamiltonian $\hat{\mathcal{H}}_{\text{strong}}$ has to be solved. Considering a two-spin system with the respective Hamiltonian:

$$\hat{\mathcal{H}}_{\text{strong}} = 2\pi(\nu_1\hat{I}_{1z} + \nu_2\hat{I}_{2z}) + \pi J(2\hat{I}_{1x}\hat{I}_{2x} + 2\hat{I}_{1y}\hat{I}_{2y} + 2\hat{I}_{1z}\hat{I}_{2z}) \quad (2.5.9)$$

the Zeeman basis is no longer an eigenbasis. However, it turns out that the eigenfunctions of $\hat{\mathcal{H}}_{\text{strong}}$ can be calculated from a linear combination of the Zeeman basis which are shown in Table 2.1 along with the corresponding eigenvalues. The angle θ is determined by the individual components of the Hamiltonian $\hat{\mathcal{H}}_{\text{strong}}$ and is given as:

$$\tan \theta = \frac{J}{(\nu_1 - \nu_2)} \quad (2.5.10)$$

and it is interesting to note, that θ corresponds to the tilt of the trajectory’s plane illustrated in Figure 2.89 (b). From respective eigenvalues one can further derive the resonance frequencies of allowed

⁷⁶ Keeping in mind the discussion of the previous section it is clear that certain observables can still be considered time-independent which facilitates the observation.

⁷⁷ Only in the rotating frame that is in the center of both signals the anti-phase coherence does not evolve under the Zeeman Hamiltonian as illustrated in Figure 2.89 (b) and (c).

Table 2.1: Eigenfunctions and eigenvalues of strongly coupled two-spin system.

eigenfunctions (new basis)	eigenfunctions (Zeeman basis)	eigenvalues
1⟩	$ \alpha\alpha\rangle$	$+\frac{1}{2}(\nu_1 + \nu_2) + \frac{1}{4}J$
2⟩	$\cos\frac{1}{2}\theta \alpha\beta\rangle + \sin\frac{1}{2}\theta \beta\alpha\rangle$	$+\frac{1}{2}\sqrt{J^2 + (\nu_1 - \nu_2)^2} - \frac{1}{4}J$
3⟩	$\cos\frac{1}{2}\theta \beta\alpha\rangle - \sin\frac{1}{2}\theta \alpha\beta\rangle$	$-\frac{1}{2}\sqrt{J^2 + (\nu_1 - \nu_2)^2} - \frac{1}{4}J$
4⟩	$ \beta\beta\rangle$	$-\frac{1}{2}(\nu_1 + \nu_2) + \frac{1}{4}J$

Table 2.2: Transition frequencies and intensities in spectrum of strongly coupled two-spin system.

transition	resonance frequencies	intensities
1⟩ → 3⟩	$-\frac{1}{2}(\nu_1 + \nu_2) - \frac{1}{2}\sqrt{J^2 + (\nu_1 - \nu_2)^2} - \frac{1}{2}J$	$\frac{1}{2}(1 - \sin\theta)$
2⟩ → 4⟩	$-\frac{1}{2}(\nu_1 + \nu_2) - \frac{1}{2}\sqrt{J^2 + (\nu_1 - \nu_2)^2} + \frac{1}{2}J$	$\frac{1}{2}(1 + \sin\theta)$
1⟩ → 2⟩	$-\frac{1}{2}(\nu_1 + \nu_2) + \frac{1}{2}\sqrt{J^2 + (\nu_1 - \nu_2)^2} - \frac{1}{2}J$	$\frac{1}{2}(1 + \sin\theta)$
3⟩ → 4⟩	$-\frac{1}{2}(\nu_1 + \nu_2) + \frac{1}{2}\sqrt{J^2 + (\nu_1 - \nu_2)^2} + \frac{1}{2}J$	$\frac{1}{2}(1 - \sin\theta)$

center
Berry-shift
zz-shift

transitions that are given in Table 2.2 and a clear analogy to above mentioned analysis is found. All transition frequencies are composed of three terms that can be ascribed to effects discussed in the previous section. The *first* term determines the frequency in the center between the signals of spin \hat{I}_1 and \hat{I}_2 and is, hence, equal for all transitions. The *second* term originates from the zero-quantum Hamiltonian ($2\hat{I}_{1x}\hat{I}_{2x} + 2\hat{I}_{1y}\hat{I}_{2y}$ and $2\hat{I}_{1y}\hat{I}_{2x} - 2\hat{I}_{1x}\hat{I}_{2y}$) that is time-dependent in the double rotating frame and whose effect is illustrated explicitly in Figure 2.89. Its size can be calculated in analogy to the shift from an off-resonant perturbative field, where in the frame *on-resonant* with the perturbation the Berry-shift (ν_{Berry}) is calculated from the length of the Hamiltonian's eigenvector illustrated in Figure 2.89 (a). For an off-resonant perturbative field it is, hence, given as:

$$\nu_{\text{Berry}} = \sqrt{\nu_{\text{RF}}^2 + \Delta^2} \quad (2.5.11)$$

where ν_{RF} is the Rabi frequency of the perturbation and Δ is the offset. An equal expression is found also for the Berry-shift originating from strong coupling which is comparably determined by the strength of the coupling (J) and the frequency difference ($\nu_1 - \nu_2$) as described in Table 2.2. Note, such a calculation is only practicable in the *rotating frame* illustrated in Figure 2.89 (b). In this context, it is crucial to further note the factor $\frac{1}{2}$ outside the square root which, in the calculation, scales both the J -coupling and the frequency difference used. The *third* term, determining the resonance frequencies for a strongly coupled two-spin system, is given by $\pm\frac{1}{2}J$ and originates from the weak coupling Hamiltonian ($2\hat{I}_{1z}\hat{I}_{2z}$) that commutes with the zero-quantum part of $\hat{\mathcal{H}}_{\text{strong}}$.

Moreover, in Table 2.2 it becomes evident that the peak intensities depend directly on the tilt of the trajectory's plane illustrated in Figure 2.89 (b). Note, the additional, small peak from cosine-modulation of the in-phase coherence illustrated in Figure 2.89 (b) does always coincide with other major peaks (see Figure 2.85 (a) and (d)) and has, hence, no influence on the relative peak intensities. The arising anti-phase operators (Figure 2.89 (c)), on the other hand, cause a de- and increase of respective signals and are, thus, responsible for the so-called *roofing* – this can most easily be seen from Figure 2.85 (b) and (c). As expected, both ways lead to the same results and while the calculation via the Hamiltonian's eigenvectors offers a straight-forward and direct access to essential parameters of the spectrum of a strongly coupled two-spin system the approach via the double rotating frame involves a more intuitive picture.

2.5.3 Average Hamiltonian of Strong Coupling

An interesting discussion on the symmetry properties of a time-dependent Hamiltonian in a spin echo experiment and whether an exact solution is obtained by the zeroth order average Hamiltonian (discussed in Section 1.7.3) is given by Kumar & Ernst.^[214] Following their argumentation a time-dependent Hamiltonian can be decomposed into a symmetric and antisymmetric part and an average Hamiltonian is obtained only if these two parts commute. For a spin echo of strongly coupled spins they do not commute and an (exact zeroth order) average Hamiltonian can not be obtained.^[17]

However, we shall anyway try to approximate the average effect of free evolution under strong coupling for variable frequency offsets $\Delta = |\nu_2 - \nu_1|$ where each value of Δ requires a double rotating frame on its own. For each frame a different time-dependent Hamiltonian $\hat{\mathcal{H}}_{D,J}^{\Delta}(\tau)$ is obtained whose zero quantum parts oscillate at the frequency Δ as illustrated in Figure 2.86 (for $\Delta = 6$ Hz). For each offset (Δ) the zeroth order average Hamiltonian $\bar{\mathcal{H}}_{0,J}(\Delta)$ can now be calculated from the time average of the time-dependent Hamiltonian $\hat{\mathcal{H}}_{D,J}^{\Delta}(\tau)$. Since the time-dependence of $\hat{\mathcal{H}}_{D,J}^{\Delta}(\tau)$ is determined by its coefficients $k_J^{\gamma\gamma'}(\tau)$ the time average can be calculated as described in Equation (1.7.35) from the average coefficients:

$$\bar{k}_{0,J}^{\gamma\gamma'} = \frac{1}{t_c} \sum_i k_J^{\gamma\gamma'}(\tau_i) \cdot \tau_i \quad (2.5.12)$$

where $t_c = \sum_i \tau_i$ and $\bar{k}_{0,J}^{\gamma\gamma'}$ are the coefficients for the zeroth order average Hamiltonian $\bar{\mathcal{H}}_{0,J}(\Delta)$. In Figure 2.90 these average coefficients are plotted in red against the offset (Δ) and compared to analog coefficients obtained from numerical simulations (Section 1.7.1) plotted as blue dashed line. Based on the discussion of the preceding Section 1.7.3 we find for a delay of $t_c = 50$ ms and a coupling strength of $J = 10$ Hz that the condition for convergence of the Magnus series ($\|\hat{\mathcal{H}}_J\|t_c = \pi J \cdot t_c = \frac{\pi}{2} < 2\pi$) is fulfilled. However, considering the fact that only the zeroth order average Hamiltonian is used, the blue dashed line is surprisingly well approximated. For larger offset frequencies the zero quantum parts ($2\hat{I}_{1x}\hat{I}_{2x} + 2\hat{I}_{1y}\hat{I}_{2y}$) of the strong coupling Hamiltonian vanish. Hence, if the oscillation in Figure 2.86 is fast enough the secular approximation can be applied and the spin system is said to be *weakly coupled*.^[17] As is well-known from the literature, for large frequency offsets (Δ) the strong coupling Hamiltonian is truncated and:

$$\hat{\mathcal{H}}_{\text{strong}} \xrightarrow{\text{larger } \Delta} \hat{\mathcal{H}}_{\text{weak}},$$

where:

$$\hat{\mathcal{H}}_{\text{weak}} = 2\pi(\nu_1\hat{I}_{1z} + \nu_2\hat{I}_{2z}) + 2\pi J \cdot \hat{I}_{1z}\hat{I}_{2z}.$$

These simulations are repeated for a spin echo in the Appendix 5.2.2 where, equally, a good approximation is obtained by the zeroth order average Hamiltonian. Since in the spin echo a 180° pulse reverses the oscillation of the zero quantum components the strong coupling regime is, as expected, further extended to larger frequency offsets.

^[214] A. Kumar and R. R. Ernst. *Journal of Magnetic Resonance* **1976**, *24*, 425–447.

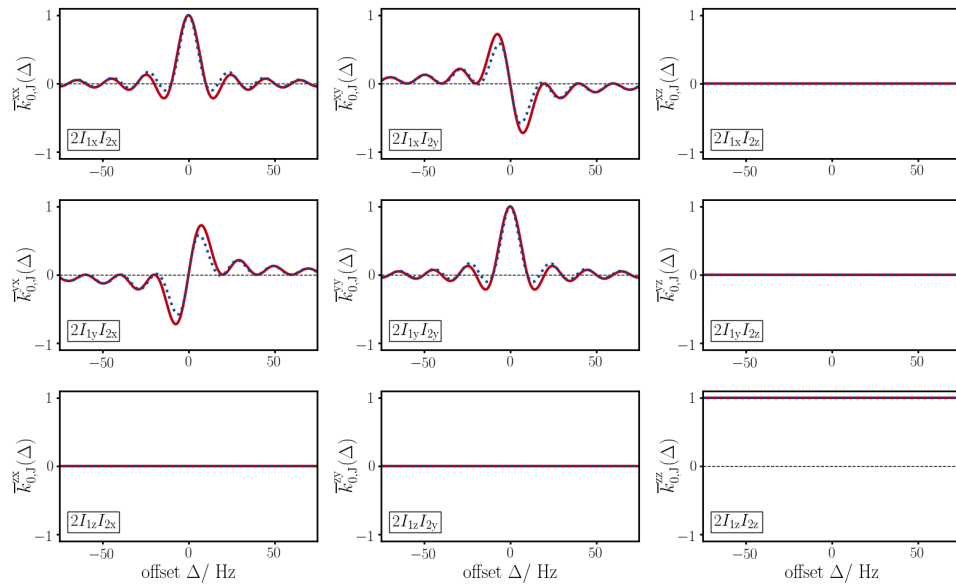


Figure 2.90: The zeroth order average Hamiltonian $\bar{\mathcal{H}}_{0,J}(\Delta)$ during a delay in the double rotating frame is plotted in red against the offset Δ . Comparable numerical simulations which are based on the logarithm of the effective propagator are plotted in blue dashed lines.

2.6 Heteronuclear Ordered Multi-Quantum Correlations

2.6.1 Introduction

Heteronuclear correlations are one of the most fundamental concepts in NMR spectroscopy and deliver valuable insight into the molecular system of investigation. In the field of small molecules, heteronuclear experiments typically build on correlations to the magnetically active ^{13}C -isotope which exhibits a natural abundance of $\sim 1.1\%$. While carbon 1D experiments typically suffer from low sensitivity, the application of inverse detection greatly enhances signal intensity,⁷⁸ which further favors the application of common HSQC-^[82], HMQC-^[83,84] and HMBC-type experiments.^[87,88]

For chemists, scalar couplings represent a useful probe that reveal structural, dynamical and electronic characteristics. In this context, the Karplus curve for vicinal $^3J_{\text{HH}}$ couplings certainly constitutes the most popular relation used to determine the dihedral angle^[36,37] while geminal $^2J_{\text{HH}}$ couplings, moreover, are affected by neighboring π -orbitals and indicate on the hybridization of methylene carbons. The heteronuclear $^1J_{\text{CH}}$ -coupling, on the other hand, has proven sensitive to the s-character of involved bonds and long-range $^nJ_{\text{CH}}$ -couplings further depend on bond lengths, valence and dihedral angles – a Karplus-like relation can be approximated also for $^3J_{\text{CH}}$ -couplings.^[216–219] The information content of coupling constants has also been proven essential in the field of *residual dipolar couplings* (RDC), where a complete averaging of dipolar couplings is prevented by aligning the investigated molecule in a *non-isotropic* medium (e.g. a stretched gel). These dipolar couplings strongly depend on the orientation of considered internuclear vectors in relation to the outer magnetic field and can, hence, be used to elucidate conformation and configuration by means of a molecular alignment tensor or e.g. tensorial orientational restraints used in molecular dynamic simulations.^[220,221]

For the sign-sensitive measurement of homo- and heteronuclear couplings numerous experiments have been proposed. Large heteronuclear 1J -couplings are frequently measured in the direct dimension using the CLIP/CLAP-HSQC^[222] where highly resolved signals are obtained at low costs in measurement time. A simplification of multiplets from passive couplings can be obtained from homonuclear decoupling in an interferogram-type acquisition^[115,223,224] that has to be applied with a certain care if strong couplings are present. Another approach is likewise based on the acquisition of separate in-phase and anti-phase spectra (IPAP)^[225–227] – double- and zero-quantum correlations are obtained in the indirect dimension and, in the presence of a large passive coupling, the coupling between involved spins can be extracted sign-sensitive (discussed below).^[228–230] Sampling the couplings of interest in the indirect dimension, moreover, exhibits the advantage that the application of homonuclear decoupling is facilitated. Due to the dilute presence of carbon spins, homonuclear decoupling is achieved by means of a single BIRD-filter centered during t_1 -incrementation and only geminal proton-proton couplings in methylene groups remain active. The technique is extensively used in a suite of JRES-HSQC experiments that allow the extraction

^[216] H. Günther. *NMR Spectroscopy - Basic Principles, Concepts, and Applications in Chemistry*. Wiley-VCH, 2013.

^[217] B. Mulloy, T. A. Frenkiel and D. B. Davies. *Carbohydrate Research* **1988**, *184*, 39–46.

^[218] W. Thomas. *Progress in Nuclear Magnetic Resonance Spectroscopy* **1997**, *30*, 183–207.

^[219] T. Parella and J. F. Espinosa. *Progress in Nuclear Magnetic Resonance Spectroscopy* **2013**, *73*, 17–55.

^[220] G. Kummerlöwe and B. Luy. *Trends in Analytical Chemistry* **2009**, *28*, 483–493.

^[221] P. Tzvetkova et al. *Chemical Science* **2019**, *10*, 8774–8791.

^[222] A. Enthart et al. *Journal of Magnetic Resonance* **2008**, *192*, 314–322.

^[223] T. Reinsperger and B. Luy. *Journal of Magnetic Resonance* **2014**, *239*, 110–120.

^[224] I. Timári et al. *Journal of Magnetic Resonance* **2014**, *239*, 130–138.

^[225] M. Ottiger, F. Delaglio and A. Bax. *Journal of Magnetic Resonance* **1998**, *131*, 373–378.

^[226] P. Andersson, A. Annala and G. Otting. *Journal of Magnetic Resonance* **1998**, *133*, 364–367.

^[227] P. Andersson, J. Weigelt and G. Otting. *Journal of Biomolecular NMR* **1998**, *12*, 435–441.

^[228] A. Rexroth et al. *Journal of the American Chemical Society* **1995**, *117*, 10389–10390.

^[229] T. Carlomagno et al. *Journal of Magnetic Resonance* **1998**, *135*, 216–226.

^[230] E. Miclet et al. *Journal of the American Chemical Society* **2004**, *126*, 10560–10570.

⁷⁸ While sensitivity is reduced by a factor of ~ 2 when going from 1D to 2D^[215], inversed detection exploits the fourfold larger gyromagnetic ratio of protons. The signal-to-noise ratio is proportional to: $S/N \propto \gamma_{\text{exc}}\gamma_{\text{obs}}^{3/2} \cdot [1 - \exp\{-\tau_r/T_1^{\text{exc}}\}]$.

of magnitude values for ${}^1J_{\text{CH}}$ - and ${}^2J_{\text{HH}}$ -coupling constants – doublet J -splittings in the indirect dimension are obtained for CH-, CH₂- and CH₃-groups.^[231–234] Based on the large value of ${}^1J_{\text{CH}}$ -couplings, in weakly orienting media it is further possible to determine also the sign of ${}^1D_{\text{CH}}$ residual dipolar couplings. On the other hand, the magnitude of proton-proton scalar couplings and respective RDCs are typically of comparable size, which hinders an unambiguous sign determination solely from proton- J -resolved spectroscopy e.g. (G)SERF.^[235–238] The issue can be circumvented if accompanied by an additional spectrum as shown in two perfectly adapted experiments using the PSYCHEDELIC scheme.^[239] A basic, but elegant, approach further constitutes the P.E.HSQC that allows the extraction of ${}^1J_{\text{CH}}$ - and ${}^2J_{\text{HH}}$ -couplings in a single experiment and information on the sign of ${}^2J_{\text{HH}}$ - or ${}^2D_{\text{HH}}$ -couplings can be determined from E.COSY-type patterns.^[105,106,240]

In the present section two HSQC-type experiments shall be proposed that provide a straight-forward measurement of ${}^1J_{\text{CH}}$ - and ${}^2J_{\text{HH}}$ -coupling constants, the latter sign-sensitive, from the indirect dimension (Section 2.6.2) as well as of ${}^nJ_{\text{CH}}$ -couplings in E.COSY-type patterns (Section 2.6.3). Both sequences are based on a novel pulse sequence element that allows broadband heteronuclear decoupling for *selected* ${}^1J_{\text{CH}}$ -couplings. This is achieved by the excitation of *ordered multi-quantum states* and doublet ${}^1J_{\text{CH}}$ -splittings are obtained for CH-, CH₂- and CH₃-groups. A detailed analysis using numerical simulations and a selection of experimental examples are given.

2.6.2 JRES-HOMQC

In the proposed experiment the measurement of ${}^1J_{\text{CH}}$ - and ${}^2J_{\text{HH}}$ -coupling constants relies on the observation of *heteronuclear ordered multi-quantum correlations* (HOMQC) that directly depend on the considered spin system (CH, CH₂ or CH₃). During the pulse sequence, the excited quantum states of CH- and CH₃-groups acquire phases given solely by a single ${}^1J_{\text{CH}}$ -coupling to the attached proton which is detected subsequently in the direct dimension. For CH₂-groups, on the other hand, the excited transitions are further determined by double-quantum (DQ) and zero-quantum (ZQ) evolution and an additional splitting from the geminal ${}^2J_{\text{HH}}$ -coupling is observed. Numerical simulations for a CH₂-group with non-equivalent protons are shown in Figure 2.91 in order to exemplify the sign-sensitive coupling extraction using the DQ/ZQ approach. Signals in the in-phase spectrum (IP) in Figure 2.91 (a) are split due to the ${}^1J_{\text{CH}}$ and ${}^2J_{\text{HH}}$ in the indirect dimension while the large heteronuclear ${}^1J_{\text{CH}}$ -coupling can be suppressed from composite pulse decoupling (CPD) in the direct dimension. In the anti-phase spectrum (AP) in Figure 2.91 (b) double-quantum correlations have switched signs and isolated DQ- and ZQ-components can be obtained from the subtraction or summation, respectively. The splitting of DQ correlations is given by ${}^1J_{\text{CH}} + {}^2J_{\text{HH}}$, while ZQ evolve according to ${}^1J_{\text{CH}} - {}^2J_{\text{HH}}$ and the sign of ${}^2J_{\text{HH}}$ can be determined as long as ${}^1J_{\text{CH}} \gg {}^2J_{\text{HH}}$. Note, in the illustrated case ${}^2J_{\text{HH}}$ is positive and a larger splitting is observed for DQ-correlations.

[231] L. Castañar et al. *The Journal of Organic Chemistry* **2016**, *81*, 11126–11131.

[232] N. Marcó et al. *Journal of Magnetic Resonance* **2017**, *282*, 18–26.

[233] N. Marcó et al. *Journal of Magnetic Resonance* **2017**, *276*, 37–42.

[234] N. Marcó, R. R. Gil and T. Parella. *Magnetic Resonance in Chemistry* **2017**, *55*, 540–545.

[235] T. Fäcke and S. Berger. *Journal of Magnetic Resonance* **1995**, *A113*, 114–116.

[236] N. Giraud et al. *Angewandte Chemie - International Edition* **2010**, *49*, 3481–3484.

[237] D. Pitoux et al. *Chemistry - A European Journal* **2015**, *21*, 9044–9047.

[238] J. E. Herbert Pucheta et al. *Chemical Communications* **2015**, *51*, 7939–7942.

[239] D. Sinnaeve et al. *Angewandte Chemie - International Edition* **2020**, *132*, 5354–5358.

[240] P. Tzvetkova, S. Simova and B. Luy. *Journal of Magnetic Resonance* **2007**, *186*, 193–200.

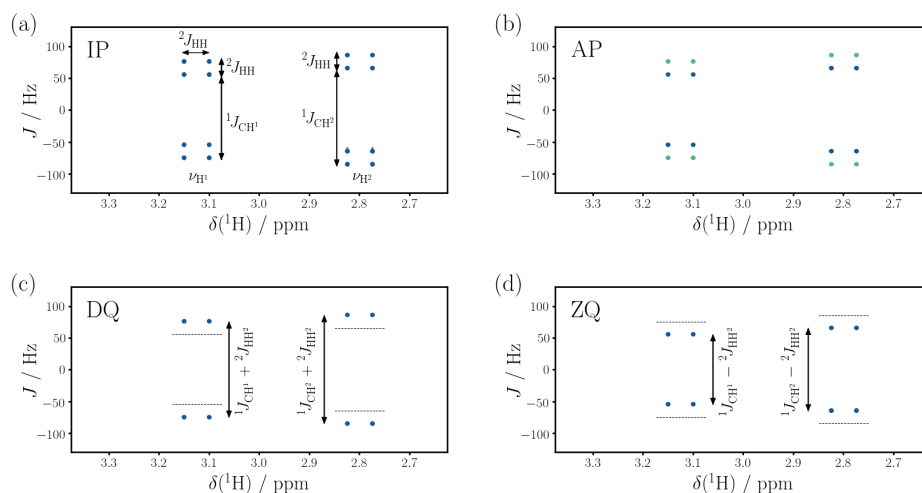


Figure 2.91: Numerical simulations of in-phase (a) and anti-phase coupling patterns (b) are illustrated for a CH_2 -group with non-equivalent protons. Double- (c) and zero-quantum correlations (d) are obtained from (IP-AP) and (IP+AP), respectively. Couplings are $^2J_{\text{HH}} = 20$ Hz, $^1J_{\text{CH}^1} = 130$ Hz and $^1J_{\text{CH}^2} = 150$ Hz.

Pulse Sequence

The pulse sequence of the proposed HOMQC experiment is based on a conventional HSQC using gradients for coherence pathways selection as illustrated in Figure 2.96. Proton polarization is excited and transferred via an INEPT-step to carbon single-quantum coherence. A subsequent κ -scaled evolution period allows to acquire carbon chemical shifts in cases where signal overlap is encountered. This is typically used to retain spectral width at a minimum, while high resolution is still obtained at short experimental times. The novel pulse sequence element is highlighted by a blue box and shall be thoroughly examined using the product operator formalism (Section 1.4) at certain points in time (A-D). It shall be demonstrated that the observed coherences evolve only according to a single $^1J_{\text{CH}}$ -coupling while additional heteronuclear couplings in the CH_2 and CH_3 spin system are suppressed. This is based on the fact that MQ states are created which commute with the heteronuclear coupling Hamiltonian with $[2\hat{I}_z\hat{S}_z, 2\hat{I}_\alpha\hat{S}_\beta] = 0$ and α, β corresponding to x or y. Further, it is shown that multiplicity editing (ME) can be obtained from a simple shift of pulse phases acting on MQ states.

The creation of MQ coherences (A \rightarrow B) is achieved by a heteronuclear echo which is followed by a 90° pulse on proton – analogous elements for MQ-excitation are proposed in literature.^[241] The evolution through-out the MQ-element is given individually for CH, CH_2 and CH_3 -groups starting at point A and only coherences originating from spin \hat{I}_1 (prior to INEPT) shall be considered. For the reason of clarity, it is assumed that $\kappa = 0$ and $\Delta = 1/(4^1J_{\text{CH}^1})$ with $J_{\text{CH}^1} = J_{\text{CH}^2} = J_{\text{CH}^3}$. At point A, carbon anti-phase coherence is present for all moieties and the MQ-excitation yields:

$$\text{CH} : -2\hat{I}_{1z}\hat{S}_y \text{ (A}_1\text{)} \xrightarrow{\Delta-180_{\text{CH}}^\circ-\Delta} -\hat{S}_x \xrightarrow{90_{\text{H}}^\circ} -\hat{S}_x \text{ (B}_1\text{)}$$

$$\text{CH}_2 : -2\hat{I}_{1z}\hat{S}_y \text{ (A}_2\text{)} \xrightarrow{\Delta-180_{\text{CH}}^\circ-\Delta} -2\hat{S}_y\hat{I}_{2z} \xrightarrow{90_{\text{H}}^\circ} 2\hat{S}_y\hat{I}_{2y} \text{ (B}_2\text{)}$$

$$\text{CH}_3 : -2\hat{I}_{1z}\hat{S}_y \text{ (A}_3\text{)} \xrightarrow{\Delta-180_{\text{CH}}^\circ-\Delta} 4\hat{S}_x\hat{I}_{2z}\hat{I}_{3z} \xrightarrow{90_{\text{H}}^\circ} 4\hat{S}_x\hat{I}_{2y}\hat{I}_{3y} \text{ (B}_3\text{)}$$

It is crucial to note that during the heteronuclear echo the anti-phase contribution from spin \hat{I}_1 is completely removed, while anti-phase to all other remaining protons is created. A subsequent 90° proton pulse transfers anti-phase coherences to single-quantum (CH), double- and zero-quantum (CH_2), or

^[241] O. Sørensen, M. H. Levitt and R. Ernst. *Journal of Magnetic Resonance* **1983**, 55, 104–113.

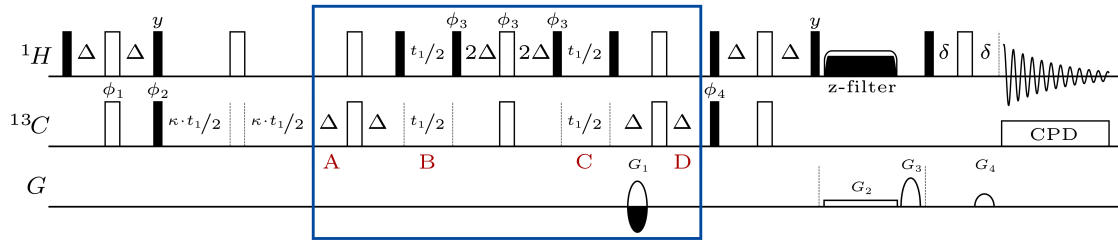


Figure 2.92: The pulse sequence of the JRES-HOMQC experiment is illustrated where MQ-evolution period is marked by the blue box. Narrow black and open wide bars correspond to 90° and 180° pulses, respectively, and phases are x unless annotated otherwise. The chemical shift evolution period is scaled by the factor κ and transfer delays are set according to $\Delta = 1/(4^1J_{CH})$. The following phase cycles are used: $\phi_2 = x, -x$; $\phi_4 = x, x, -x, -x$; $\phi_5 = -y$; $\phi_{rec} = x, -x, -x, x$. The receiver phase ϕ_{rec} , ϕ_1 and ϕ_2 undergo time proportional phase incrementation (TPPI) and are inverted for successive t_1 -increments. Note, in-phase spectra with ($\phi_3 = 270^\circ$) and without ME ($\phi_3 = 270^\circ$), as well as anti-phase spectra with ($\phi_3 = 45^\circ$) and without ME ($\phi_3 = 135^\circ$) are obtained by a phase shift of ϕ_3 . For ^{13}C coherence selection gradients are given by the ratio $G_1/G_4 = 80\%/20.1\%$ using EA for frequency discrimination. A z-filter is used to remove dispersive anti-phase contributions that originate from homonuclear coupling evolution where a weak gradient pulse (G_2) and a spoiler gradient (G_3) are used.^[119]

single- and triple-quantum coherences (CH_3) – spin \hat{I}_1 , however, is not involved at point B₁, B₂ and B₃. Hence, the only heteronuclear coupling that evolves during t_1 -incrementation (B→C) is given by the $^1J_{\text{CH}}$ -coupling between spin \hat{S} and \hat{I}_1 while heteronuclear coupling Hamiltonians to other protons commute with given MQ states. Chemical shift as well as homonuclear proton-proton couplings to remote spins are suppressed by a centered BIRD^{d,X}-filter.⁷⁹ Neglecting the geminal $^2J_{\text{HH}}$ -coupling for a start, the t_1 -evolution period results in:

$$\text{CH} : \text{B}_1 \xrightarrow{t_1/2\text{-BIRD}^{\text{d,X}}-t_1/2} + \cos(\pi^1J_{\text{CH}}t_1) \cdot \hat{S}_x + \sin(\pi^1J_{\text{CH}}t_1) \cdot 2\hat{I}_{1z}\hat{S}_y \quad (\text{C}_1)$$

$$\text{CH}_2 : \text{B}_2 \xrightarrow{t_1/2\text{-BIRD}^{\text{d,X}}-t_1/2} - \cos(\pi^1J_{\text{CH}}t_1) \cdot 2\hat{S}_y\hat{I}_{2y} + \sin(\pi^1J_{\text{CH}}t_1) \cdot 4\hat{I}_{1z}\hat{S}_x\hat{I}_{2y} \quad (\text{C}_2)$$

$$\text{CH}_3 : \text{B}_3 \xrightarrow{t_1/2\text{-BIRD}^{\text{d,X}}-t_1/2} - \cos(\pi^1J_{\text{CH}}t_1) \cdot 4\hat{S}_x\hat{I}_{2y}\hat{I}_{3y} - \sin(\pi^1J_{\text{CH}}t_1) \cdot 8\hat{I}_{1z}\hat{S}_y\hat{I}_{2y}\hat{I}_{3y} \quad (\text{C}_3)$$

A symmetric element for MQ-de-excitation is subsequently used (C→D) and *identical* spin states are again obtained for all moieties at points D₁, D₂ and D₃.

$$\text{CH} : \text{C}_1 \xrightarrow{90^\circ_{\text{H}}-\Delta-180^\circ_{\text{CH}}-\Delta} \cos(\pi^1J_{\text{CH}}t_1) \cdot 2\hat{I}_{1z}\hat{S}_y - \sin(\pi^1J_{\text{CH}}t_1) \cdot 2\hat{I}_{1y}\hat{S}_y \quad (\text{D}_1)$$

$$\text{CH}_2 : \text{C}_2 \xrightarrow{90^\circ_{\text{H}}-\Delta-180^\circ_{\text{CH}}-\Delta} \cos(\pi^1J_{\text{CH}}t_1) \cdot 2\hat{I}_{1z}\hat{S}_y - \sin(\pi^1J_{\text{CH}}t_1) \cdot 2\hat{I}_{1y}\hat{S}_y \quad (\text{D}_2)$$

$$\text{CH}_3 : \text{C}_3 \xrightarrow{90^\circ_{\text{H}}-\Delta-180^\circ_{\text{CH}}-\Delta} \cos(\pi^1J_{\text{CH}}t_1) \cdot 2\hat{I}_{1z}\hat{S}_y - \sin(\pi^1J_{\text{CH}}t_1) \cdot 2\hat{I}_{1y}\hat{S}_y \quad (\text{D}_3)$$

Interestingly, coupling evolution *due to* spin \hat{I}_1 during the proposed element effectively appears as an x -rotation *solely* on spin \hat{I}_1 . Subsequently, the cosine-modulated carbon anti-phase component at point D ($2\hat{I}_{1z}\hat{S}_y$) is back-transferred in analogy to a conventional HSQC and dispersive anti-phase contributions due to homonuclear couplings can be removed by a z-filter. Considering geminal couplings in methylene groups, which cannot be suppressed by a BIRD-filter, the final states are additionally modulated by the

⁷⁹ For BIRD-filters the nomenclature is used as proposed in literature where heteronuclei and attached protons are denoted X and d, respectively, while all other protons are referred to as remote protons (r).^[242]

homonuclear proton coupling during t_1 -incrementation. One obtains:

$$\begin{aligned} \text{CH}_2 : \mathbf{B}_2 \xrightarrow{t_1/2 - \text{BIRD}^{\text{d,x}} - t_1/2} & -\cos(\pi^1 J_{\text{CH}} t_1) \left(\cos(\pi^2 J_{\text{HH}} t_1) \cdot 2\hat{S}_y \hat{I}_{2y} - \sin(\pi^2 J_{\text{HH}} t_1) \cdot 4\hat{I}_{1z} \hat{S}_y \hat{I}_{2x} \right) \\ & + \sin(\pi^1 J_{\text{CH}} t_1) \left(\cos(\pi^2 J_{\text{HH}} t_1) \cdot 4\hat{I}_{1z} \hat{S}_x \hat{I}_{2y} - \sin(\pi^2 J_{\text{HH}} t_1) \cdot 2\hat{S}_x \hat{I}_{2x} \right) \quad (\mathbf{C}'_2) \end{aligned}$$

and further after MQ-de-excitation it follows:

$$\begin{aligned} \text{CH}_2 : \mathbf{C}'_2 \xrightarrow{90^\circ_{\text{H}} - \Delta - 180^\circ_{\text{CH}} - \Delta} & + \cos(\pi^1 J_{\text{CH}} t_1) \left(\cos(\pi^2 J_{\text{HH}} t_1) \cdot 2\hat{I}_{1z} \hat{S}_y - \sin(\pi^2 J_{\text{HH}} t_1) \cdot 4\hat{I}_{1y} \hat{S}_y \hat{I}_{2x} \right) \\ & - \sin(\pi^1 J_{\text{CH}} t_1) \left(\cos(\pi^2 J_{\text{HH}} t_1) \cdot 2\hat{I}_{1y} \hat{S}_y + \sin(\pi^2 J_{\text{HH}} t_1) \cdot 4\hat{I}_{1z} \hat{S}_y \hat{I}_{2x} \right) \quad (\mathbf{D}'_2) \end{aligned}$$

where, again, only the carbon anti-phase ($2\hat{I}_{1z}\hat{S}_y$), that is now doubly cosine-modulated, survives the back-transfer. Moreover, an interesting feature of the examined sequence is obtained by adding certain phase shifts to all proton pulses of the applied BIRD-filter (ϕ_3 in Figure 2.92). The regular in-phase spectrum is obtained for $\phi_3 = 180^\circ$ ($-x$) and by shifting the phase to $\phi_3 = 270^\circ$ ($-y$) multiplicity editing (ME) is obtained and all CH_2 groups are negative, which greatly facilitates spectral assignments. A phase of $\phi_3 = 45^\circ$, on the other hand, allows the transfer of the doubly sine-modulated term for CH_2 groups (in \mathbf{C}'_2). Hence, one obtains the anti-phase spectrum with negative DQ-correlations (as shown in Figure 2.91 (b)), however, with dispersive phase compared to CH/CH_3 . Yet, the dispersive phase can simply be changed by filtering CH/CH_3 and CH_2 from ME with $\phi_3 = 135^\circ$. It should also be mentioned that signals of methyl-groups in the anti-phase spectra are partially suppressed and, hence, AP-spectra do not fully contribute to CH_3 -sensitivity if recombined with IP-spectra. The loss in signal-to-noise for *only* CH_3 -groups, however, can typically be well tolerated. In the following section, four spectra of camphor with a chosen set of ϕ_3 -phases shall be examined and selected correlations are obtained from recombination. Among the four spectra two exhibit in-phase signals with ($\phi_3 = 270^\circ$) and without ME ($\phi_3 = 180^\circ$) as well as two anti-phase spectra where likewise opposite signs for methylene signals are obtained ($\phi_3 = 45^\circ$ and $\phi_3 = 135^\circ$).

Experimental

The four acquired basic spectra of camphor are illustrated in Figure 2.93 (a) to (d). The in-phase spectrum with only positive signals is termed IP_{pos} (in (a) with $\phi_3 = 180^\circ$), while IP_{ed} denotes the multiplicity edited version (in (b) with $\phi_3 = 270^\circ$). The double anti-phase spectra with opposite signs for methylene signals are denoted AP_1 (in (c) with $\phi_3 = 45^\circ$) and AP_2 (in (d) with $\phi_3 = 135^\circ$).

The spectra for CH and CH_3 groups are subsequently obtained from recombining ($\text{IP}_{\text{pos}} + \text{IP}_{\text{ed}}$) and ($\text{AP}_1 + \text{AP}_2$) as shown in Figure 2.93 (e) and (g), while CH_2 spectra result from ($\text{IP}_{\text{pos}} - \text{IP}_{\text{ed}}$) and $+90^\circ$ phase shifted ($\text{AP}_1 - \text{AP}_2$), which is illustrated in (f) and (h). In order to increase sensitivity, both CH/CH_3 -spectra of Figure 2.93 (e) and (g) can be added in a second step and the final CH/CH_3 spectrum is obtained from ($\text{IP}_{\text{pos}} + \text{IP}_{\text{ed}}$) + ($\text{AP}_1 + \text{AP}_2$) as shown in Figure 2.94 (a). Also the filtered IP- and AP-spectra for CH_2 -groups, illustrated in Figure 2.93 (f) and (h), can be recombined and DQ- and ZQ-spectra are obtained as illustrated in Figure 2.94 (c) and (e). In order to circumvent spectral overlap, all steps are repeated for equivalent camphor spectra with $\kappa = 0.2$ and final results are shown in the right column of Figure 2.94 in (b), (d) and (f). Note, all calculations are again annotated above respective spectra.

After recombination, simple doublets are obtained in all created spectra (Figure 2.94), which allows a straight-forward extraction of couplings at high resolution. The $^1J_{\text{CH}}$ -coupling in methine and methyle groups is directly given by the splitting in Figure 2.94 (a) while splittings for DQ- and ZQ-coherences further contain the value of geminal $^2J_{\text{HH}}$ -couplings. Double quantum coherences oscillate at the sum of both couplings and the splitting is given by $J_\Sigma = ^1J_{\text{CH}} + ^2J_{\text{HH}}$. Zero quantum coherences, on the other hand, are split by the difference with $J_\Delta = ^1J_{\text{CH}} - ^2J_{\text{HH}}$. The individual couplings can thus be extracted from simple calculations with $^1J_{\text{CH}} = \frac{1}{2}(J_\Sigma + J_\Delta)$ and $^2J_{\text{HH}} = \frac{1}{2}(J_\Sigma - J_\Delta)$. In the DQ- and ZQ-spectra

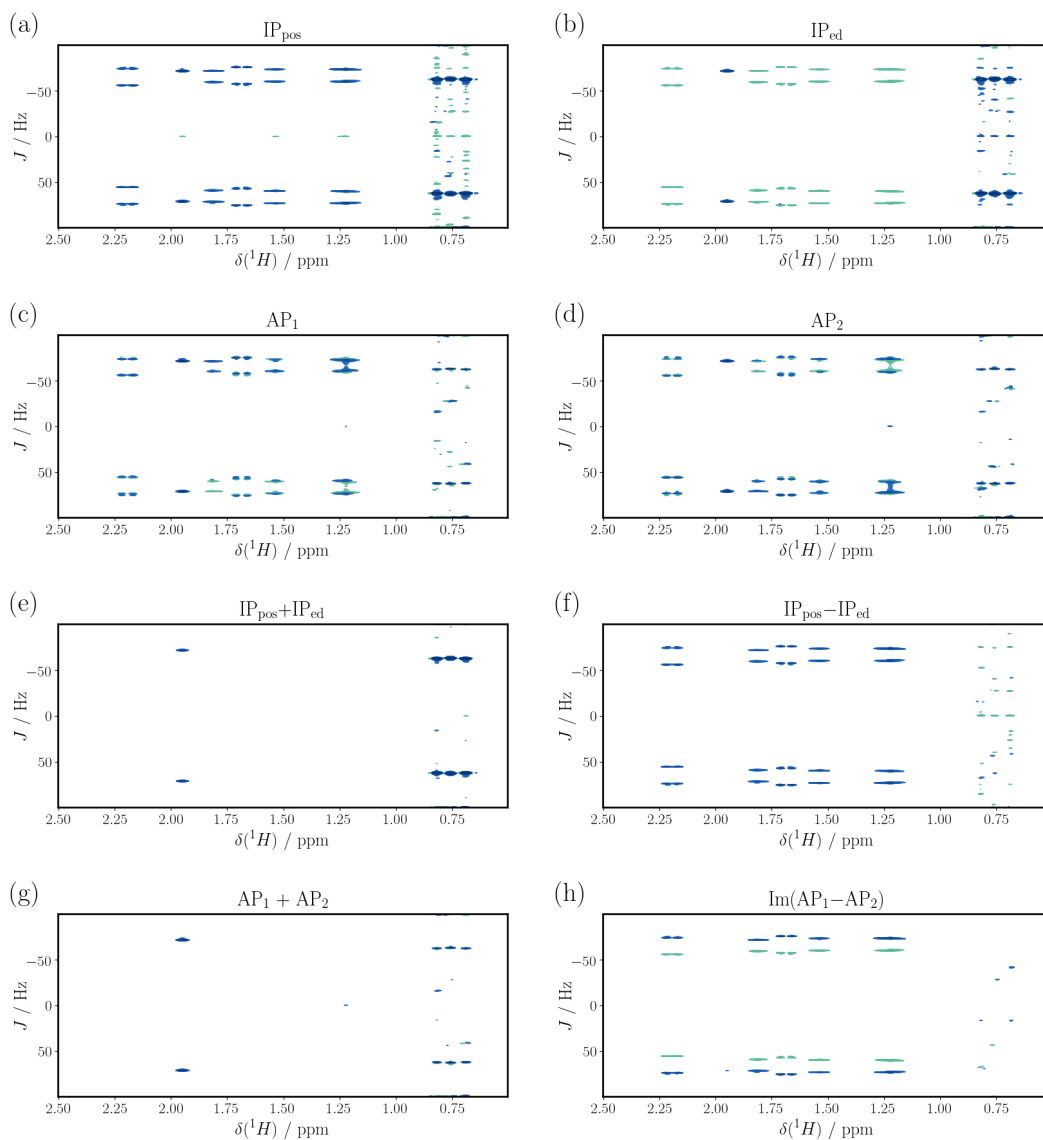


Figure 2.93: A set of JRES-HOMQC spectra of camphor are shown with $\phi_3 = 180^\circ$ (a), $\phi_3 = 270^\circ$ (b), $\phi_3 = 45^\circ$ (c) and $\phi_3 = 135^\circ$ (d) and $\kappa = 0$. All spectra were acquired with 2 transients and a spectral width of 12 ppm and 512 complex points in the direct dimension. In the indirect dimension a spectral width of 200 Hz and 256 complex points (corresponding to a digital resolution of ~ 0.78 Hz) were acquired on a 400 MHz spectrometer in 31 min 15 s per spectrum. Transfer delays are set according to $\Delta = 1/(4^1 J_{CH})$ with $J_{CH} = 130$ Hz. Recombination of initial spectra (a) to (d) results in filtered spectra that only contain CH/CH₃ ((e) and (g)) or in-phase (f) and double anti-phase CH₂-signals (h). Calculations are done as indicated above respective spectra.

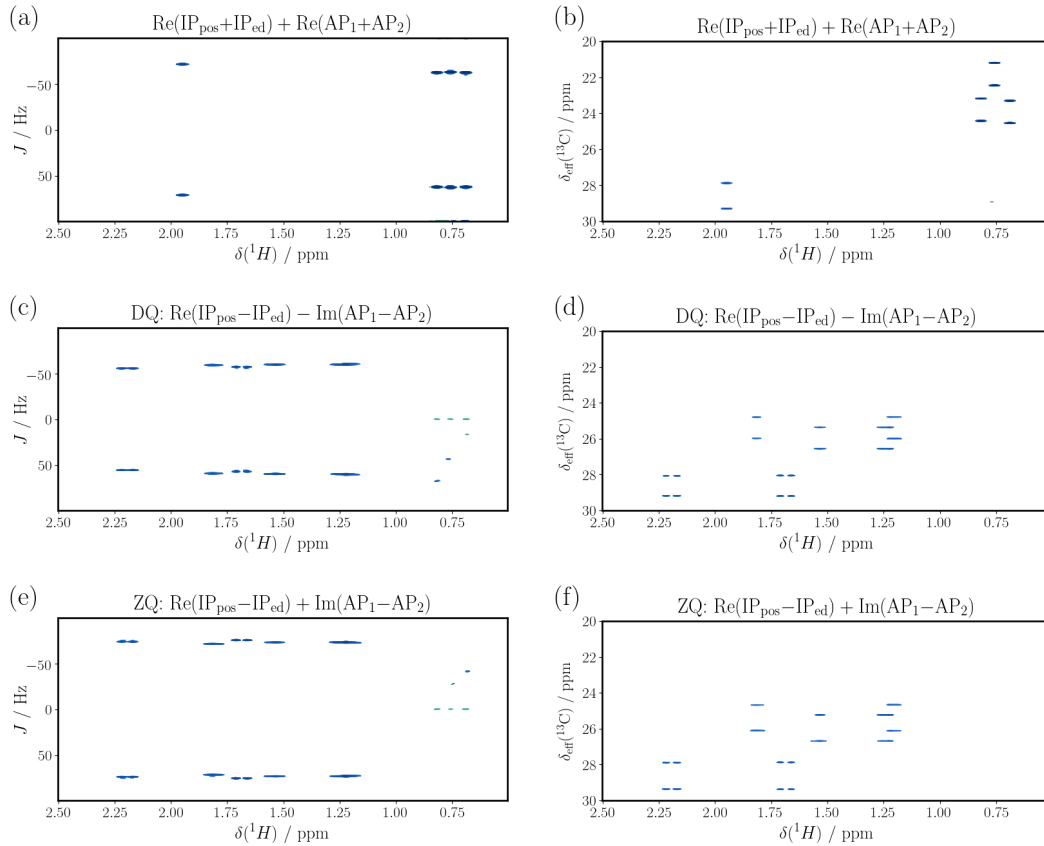


Figure 2.94: The final JRES-HOMQC spectra of camphor after recombination using spectra of Figure 2.93 are shown with $\kappa = 0$ (left column) and $\kappa = 0.2$ (right column) with $\delta_C = 25$ ppm. Signals for CH- and CH₃-groups are shown in the first row while once more filtered CH₂-DQ- and CH₂-ZQ-correlations are illustrated in the middle and last row, respectively. The value for $\delta_{\text{eff}}(^{13}\text{C})$ can be calculated from $\delta_{\text{eff}}(^{13}\text{C}) = \delta_c + \kappa \cdot [\delta(^{13}\text{C}) - \delta_c]$ where δ_c is the carrier-offset. The shown spectra originate in Figure 2.94 where also the acquisition parameters can be found.

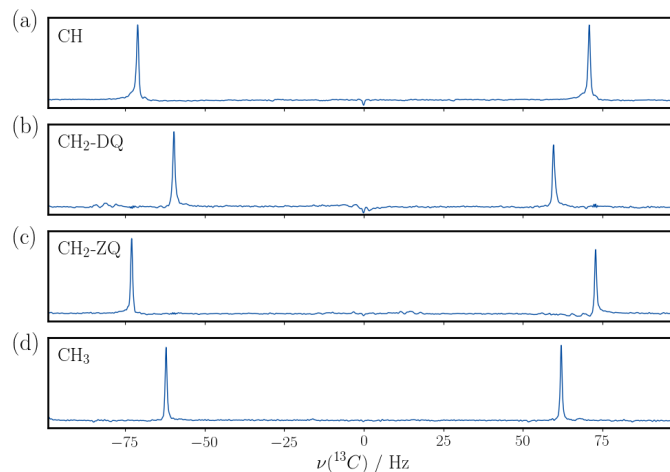


Figure 2.95: Extracted 1D columns from the final JRES-HOMQC spectra of camphor after recombination (Figure 2.94) are shown for CH- (a), CH₂-DQ- (b), CH₂-ZQ- (c), and CH₃-signals (d). The shown spectra originate in Figure 2.94 where also the acquisition parameters can be found.

of camphor (Figure 2.94 (c) and (e)) it can be observed at a single glance that for all methylene groups $J_{\Sigma} > J_{\Delta}$, which further implies that geminal ${}^2J_{\text{HH}}$ -couplings are all *negative*. In the acquired spectra of camphor, coupling extraction can be achieved at nearly highest resolution and homonuclear decoupled signals at a linewidth of down to 0.7 Hz (CH), 0.55 Hz (CH₂) and 0.55 Hz (CH₃) are achieved in the indirect dimension (data not shown).⁸⁰ This is close to the linewidth of 0.46 Hz for chloroform and four- to sixfold better than *apparent* CH₃-singlets (2-3 Hz) obtained in a proton 1D. It shall also be mentioned that a low artifact level is observed as can be seen from column-wise 1D extractions for all moieties illustrated in Figure 2.95. A certain increase of the artifact level is expected for delay mis-set as shown in the Appendix 5.2.3, which is most notably the case for CH₃-groups. However, illustrated artifacts are almost exclusively negative which allows easy identification and, hence, they do not further disturb the process of coupling extraction.

A general origin of artifacts in the proposed experiment can be ascribed to the fact that during MQ-evolution CH-, CH₂- and CH₃-groups are on different coherence transfer paths which all have to remain open in order to avoid signal suppression. However, a subsequent filtering of CH/CH₃- and CH₂-signals (which is based on coherence order selection) will cause that artifacts with *undesired* coherence order are transferred to another spectrum – e.g. DQ-artifacts for CH₃-groups show up in a presumably empty region of DQ-spectra that are only used to extract couplings for CH₂.

For methylene signals, further artifacts are observed if $\kappa \neq 0$ (data not shown) as well as COSY-type artifacts originating from coherence transfer between *non*-geminal protons as illustrated in Appendix 5.2.3. It is notable that the modulation in the indirect dimension of COSY-type cross- and respective diagonal-peaks are identical which indicates transfer after t_1 -incrementation.⁸¹ Presumably, the conventional HSQC backtransfer is not appropriate for the given experiment and further adaptations are planned in future investigations.

2.6.3 HOMQC-TOCSY

The proposed JRES-HOMQC experiment of the previous Section 2.6.2 shall be adapted in a way, that signals exhibit an E.COSY-type pattern in order to allow a sign-sensitive measurement of ${}^nJ_{\text{CH}}$ -couplings in the direct dimension. This can be achieved by a spin state selective carbon-proton backtransfer without CPD during acquisition and *reduced multiplets* are obtained that are split by the ${}^1J_{\text{CH}}$ -coupling in both dimensions. The peaks shall be referred to according the spin state (α/β) of the coupled proton in the *indirect* dimension ($\omega_1^{\alpha/\beta}$) and the spin state of the carbon in the *direct* dimension ($\omega_2^{\alpha/\beta}$). The considered multiplet consists of only the $\omega_1^{\beta}\omega_2^{\alpha}$ - (upper left corner) and the $\omega_1^{\alpha}\omega_2^{\beta}$ -peak (lower right corner) and the well-known E.COSY tilt is obtained. A subsequent TOCSY-type mixing on the proton channel causes coherence transfer to neighboring proton spins and the splitting in the direct dimension is then given by the ${}^nJ_{\text{CH}}$ -coupling as originally proposed in literature.^[130,244] The tilt of the reduced multiplet further determines the relative sign of the considered long-range coupling. An extended discussion on the measurement of long-range ${}^nJ_{\text{CH}}$ -couplings can be found in literature.^[245,246]

Pulse Sequence

The pulse sequence of the proposed HOMQC-TOCSY is illustrated in Figure 2.96 and in contrast to the JRES-HMOQC (Figure 2.92) certain modifications are made. First, the conventional HSQC-type backtransfer is replaced by a spin state selective transfer which shall be thoroughly examined below using Cartesian operators. Second, CPD is omitted during acquisition in order to allow proton-carbon coupling

^[244] L. Lerner and A. Bax. *Journal of Magnetic Resonance* **1986**, 69, 375–380.

^[245] B. L. Marquez, W. H. Gerwick and R. Thomas Williamson. *Magnetic Resonance in Chemistry* **2001**, 39, 499–530.

^[246] T. Parella and J. F. Espinosa. *Progress in Nuclear Magnetic Resonance Spectroscopy* **2013**, 73, 17–55.

⁸⁰ Data was acquired with a digital resolution of 0.39 Hz and the deconvolution function in Bruker Topspin Software was used to determine the given Lorentzian linewidths.

⁸¹ COSY-type artifacts induced by the centered BIRD-filter could likely be suppressed from a frequency-swept adiabatic pulse in combination with a weak gradient field that are applied on both sides of the BIRD-inversion. By this means signals would acquire an offset-dependent gradient phase that is only rephased if *no* transfer occurs. An analogous principle for the suppression of cross peaks is also used in the well-known PSYCHE sequence.^[243]

where the factors $c_{J\Delta} = 1/\sqrt{2}$ and $c_{J\Delta}^2 = 1/2$. Since the term $2\hat{I}_{1y}\hat{S}_z$ shall be dephased by a subsequent gradient, it is no further of relevance and is, hence, omitted in later steps. The pulses on proton and carbon (C→D) have the following effect:

$$\text{CH} : \mathbf{C}_1 \xrightarrow{90^\circ_{\text{H},y}/90^\circ_{\text{C},x}} -1 c_{\omega t_1} c_{J t_1} \cdot 2\hat{I}_{1z}\hat{S}_z - s_{J\Delta} s_{\omega t_1} s_{J t_1} \cdot \hat{I}_{1z} \quad (\mathbf{D}_1)$$

$$\text{CH}_2 : \mathbf{C}_2 \xrightarrow{90^\circ_{\text{H},y}/90^\circ_{\text{C},x}} -c_{J\Delta} c_{\omega t_1} c_{J t_1} \cdot 2\hat{I}_{1z}\hat{S}_z - s_{J\Delta} s_{\omega t_1} s_{J t_1} \cdot \hat{I}_{1z} \quad (\mathbf{D}_2)$$

$$\text{CH}_3 : \mathbf{C}_3 \xrightarrow{90^\circ_{\text{H},y}/90^\circ_{\text{C},x}} -c_{J\Delta}^2 c_{\omega t_1} c_{J t_1} \cdot 2\hat{I}_{1z}\hat{S}_z - s_{J\Delta} s_{\omega t_1} s_{J t_1} \cdot \hat{I}_{1z} \quad (\mathbf{D}_3)$$

The obtained Cartesian operators all correspond to populations and, hence, they are not dephased by the subsequent z-filter which is used for the suppression of dispersive anti-phase. Prior to the z-filter proton-proton coherence transfer is obtained from isotropic mixing or the perfect echo (D→E):

$$\text{CH} : \mathbf{D}_1 \xrightarrow{\text{PE} / \text{IM}} -1 c_{\omega t_1} c_{J t_1} \cdot 2\hat{I}_{\gamma z}\hat{S}_z - s_{J\Delta} s_{\omega t_1} s_{J t_1} \cdot \hat{I}_{\gamma z} \quad (\mathbf{E}_1)$$

$$\text{CH}_2 : \mathbf{D}_2 \xrightarrow{\text{PE} / \text{IM}} -c_{J\Delta} c_{\omega t_1} c_{J t_1} \cdot 2\hat{I}_{\gamma z}\hat{S}_z - s_{J\Delta} s_{\omega t_1} s_{J t_1} \cdot \hat{I}_{\gamma z} \quad (\mathbf{E}_2)$$

$$\text{CH}_3 : \mathbf{D}_3 \xrightarrow{\text{PE} / \text{IM}} -c_{J\Delta}^2 c_{\omega t_1} c_{J t_1} \cdot 2\hat{I}_{\gamma z}\hat{S}_z - s_{J\Delta} s_{\omega t_1} s_{J t_1} \cdot \hat{I}_{\gamma z} \quad (\mathbf{E}_3)$$

where γ denotes a remote proton spin within the spin system and whose long-range ${}^n J_{\text{CH}}$ -coupling shall be extracted. Note, for the reason of simplicity the transfer efficiency is assumed to be at 100%. A final proton pulse excites the considered operators (\mathbf{D}_1 to \mathbf{D}_3 and \mathbf{E}_1 to \mathbf{E}_3) and they are subsequently acquired without heteronuclear decoupling. Considering only coupling evolution in the indirect dimension the resulting in-phase and anti-phase operators will have a spectrum as simulated in Figure 2.97. The in-phase operator, being sine-modulated during t_1 , exhibits anti-phase with respect to the ${}^1 J_{\text{CH}}$ -coupling in the indirect dimension (Figure 2.97 (a)). The anti-phase operator is cosine-modulated during t_1 which leads to signals of equal sign in the indirect dimension. On the other hand, an anti-phase signal is measured in the direct dimension for anti-phase operators (Figure 2.97 (b)) and a combination of both operators results in a reduced multiplet with E.COSY-type tilt (Figure 2.97 (c)). Note, it is further possible to change the phase of the proton pulse before the z-filter to $\phi_5 = x$ and both $\omega_1^\beta \omega_2^\alpha$ - and $\omega_1^\alpha \omega_2^\beta$ -peak are obtained with equal sign as shown in Figure 2.97 (d). By this means, it is possible to select only one out of two peaks and condensed spectra are obtained that are comparable to a conventional HSQC-TOCSY.

The modulation by a carbon frequency (ω_S), on the other hand, results in spectra illustrated in Figure 2.98. Cosine- and sine-modulation by ω_S likewise causes in-phase and anti-phase signal at a frequency ω_S and $-\omega_S$ as shown in Figure 2.97(a) and (b), respectively. A combination of both will lead to the correct frequency (Figure 2.97 (c)). A subsequent coherence transfer to a remote proton is illustrated in Figure 2.97 (d) where a negative ${}^n J_{\text{CH}}$ -coupling is assumed. It is crucial to note that the tilt of the reduced multiplet has changed which also indicates that the ${}^1 J_{\text{CH}}$ and ${}^n J_{\text{CH}}$ are of opposite signs. It is assumed that the ${}^1 J_{\text{CH}}$ -coupling is *always* positive and, hence, ${}^n J_{\text{CH}}$ is negative. Note, for a negative ${}^1 J_{\text{CH}}$ -coupling the $\omega_1^\beta \omega_2^\alpha$ - and $\omega_1^\alpha \omega_2^\beta$ -peak in Figure 2.97 (c) would change sign – a negative $\omega_1^\beta \omega_2^\alpha$ - and a positive $\omega_1^\alpha \omega_2^\beta$ -peak would be obtained.

As proposed in the previous Section 2.6.2 also in the HOMQC-TOCSY multiplicity editing can be achieved by shifting the phases of all proton BIRD-pulses by 90° . This could also be used for filtering CH/CH₃- and CH₂-groups which greatly simplifies the spectral appearance. Moreover, the extraction of DQ- and ZQ-correlations is *in principle* possible which is, however, not the aim of the proposed HOMQC-TOCSY and with this respect, simpler and faster results are obtained from the JRES-HOMQC. In the HOMQC-TOCSY, measurements of the ${}^n J_{\text{CH}}$ -coupling are done in the *direct* dimension and, hence, high resolution in the *indirect* dimension is not required. Only the ${}^1 J_{\text{CH}}$ -coupling has to be resolved in the indirect dimension which can be achieved with lower resolution in a much shorter time.

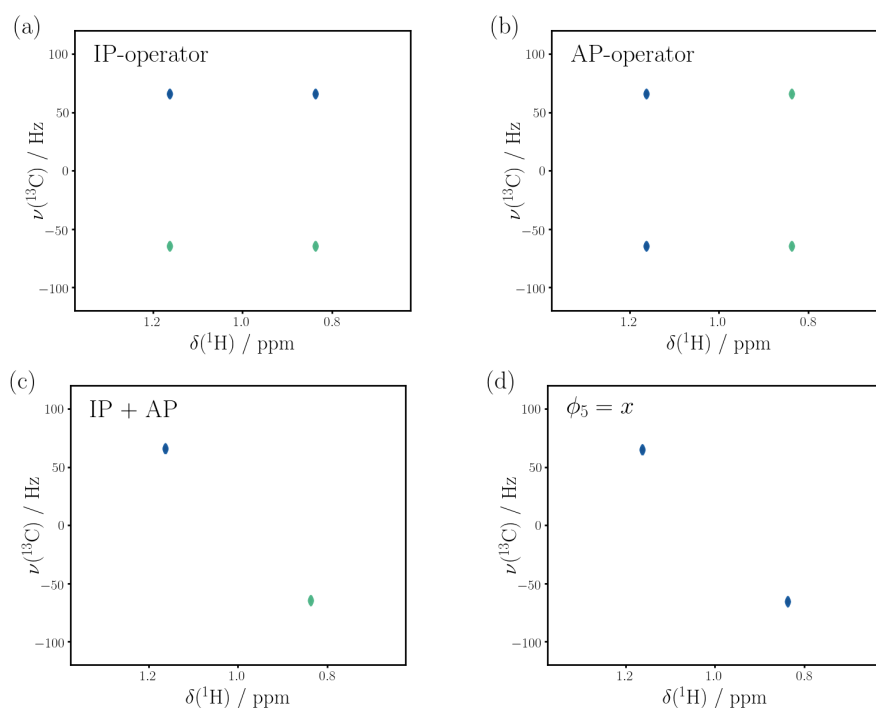


Figure 2.97: Numerical simulations of the signal components in the HOMQC-TOCSY are shown for the in-phase (a) and the anti-phase operator (b). Summation over both operators result in a reduced multiplet with blue, positive $\omega_1^\beta \omega_2^\alpha$ - and green, negative $\omega_1^\alpha \omega_2^\beta$ -peak (c). By changing $\phi_5 = x$ both peaks are positive (d).

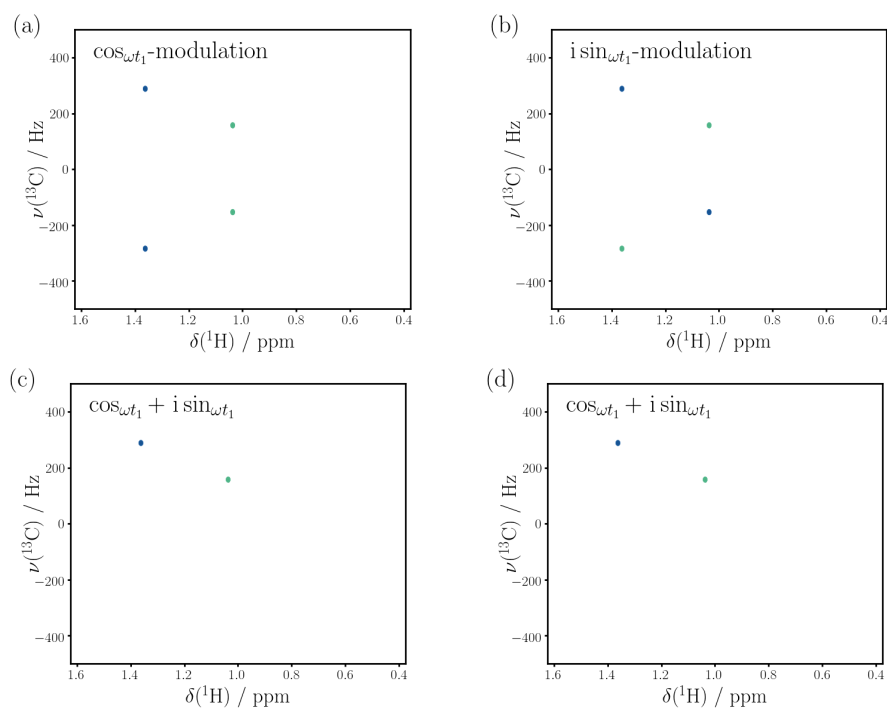


Figure 2.98: Numerical simulations show the effect of signal modulation by ω_S and how frequency discrimination is obtained by the states method (a), (b) and (c). Transfer to a remote proton with negative ${}^nJ_{CH}$ -coupling is shown in (d).

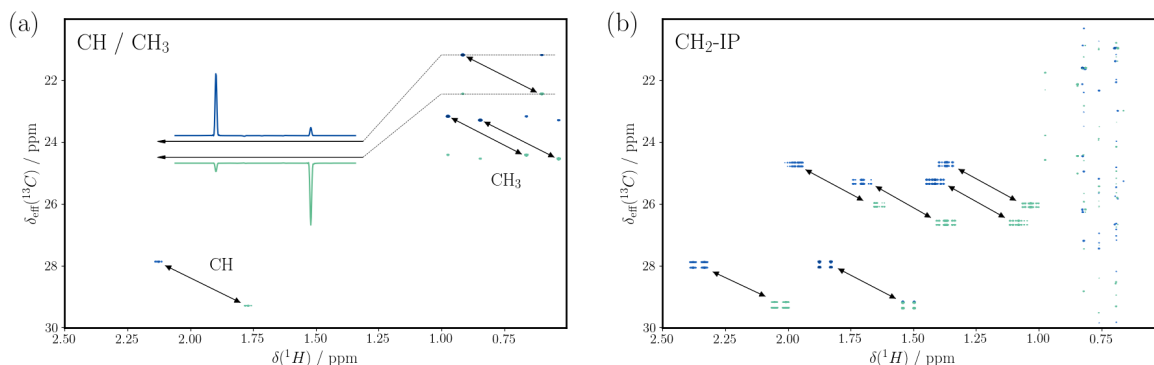


Figure 2.99: HOMQC-TOCSY spectra of camphor are shown where filtering of CH/CH₃ (a) and CH₂-groups (b) is achieved from recombination of two sub-spectra with $\phi_2 = 180^\circ$ and $\phi_2 = 270^\circ$. Associated peaks are connected by an arrow and 1D extractions are shown for methyl-groups in order to illustrate the size of $\omega_1^\beta \omega_2^\alpha$ - and $\omega_1^\alpha \omega_2^\beta$ -peaks. All spectra were acquired with 4 transients and a spectral width of 12 ppm and 2048 complex points in the direct dimension. In the indirect dimension a spectral width of 10 ppm and 256 complex points (corresponding to a resolution of ~ 3.9 Hz) were acquired on a 400 MHz spectrometer. Transfer delays are set according to $\Delta = 1/(4^1 J_{CH})$ with $J_{CH} = 130$ Hz and for a proof of principle proton-proton coherence transfer is, at first, omitted. The value for $\delta_{\text{eff}}(^{13}\text{C})$ can be calculated from $\delta_{\text{eff}}(^{13}\text{C}) = \delta_c + \kappa \cdot [\delta(^{13}\text{C}) - \delta_c]$ where δ_c is the carrier-offset.

Experimental

The HOMQC-TOCSY sequence is tested on two standard test samples, camphor and vincamine both dissolved in chloroform. As a first proof of principle, filtered camphor spectra are shown without proton-proton coherence transfer for CH/CH₃- and CH₂-groups in Figure 2.99 (a) and (b), respectively. For all signals, reduced multiplets with positive $\omega_1^\beta \omega_2^\alpha$ - and negative $\omega_1^\alpha \omega_2^\beta$ -peak are obtained ($\phi_5 = y$), which simplifies the identification of associated peaks. In case of signal cancellation from spectral overlap it is also possible to acquire spectra where only positive peaks are obtained ($\phi_5 = x$, data not shown), which further allows filtering of the $\omega_1^\beta \omega_2^\alpha$ - and $\omega_1^\alpha \omega_2^\beta$ -peak. As shown by 1D extractions in Figure 2.99 (a), to a small extent residual peaks of multiplets are still present which, however, are considerably lower than desired signals. Moreover, so-called t_1 -noise is encountered for strong signals stemming from residual ¹²C-bound proton magnetization (Figure 2.99 (b)), which might require a further optimization of the applied gradient suppression in future investigations. Note, exemplary data is acquired with high resolution in the indirect dimension, which, however, is not required for the given experiment – coupling extraction is done in the direct dimension and only the ¹J_{CH}-coupling has to be resolved.

The extraction of long-range ⁿJ_{CH}-couplings using the HOMQC-TOCSY pulse sequence is exemplarily shown in Figure 2.100 for an ethyl-group in vincamine. Coherence transfer from the methyl-group to each of the non-equivalent protons in the CH₂-group is obtained using DIPSI and indicated by arrows. The signal of considered methyl-protons, being ¹³C-bound, are split by the ¹J_{CH}-coupling in both dimensions. Protons of the CH₂-group, on the other hand, are also coupled to the ¹³C of the methyl-group but via a ²J_{CH}-coupling. Due to the fact that the applied coherence transfer on the proton channel does not change the carbon spin state, also the relative sign of the ²J_{CH}-coupling (with respect to ¹J_{CH}) can be determined. As illustrated in Figure 2.100 the ²J_{CH}-coupling is negative for both protons and can be measured at high accuracy – a value of ²J_{CH} = -4.3 Hz and ²J'_{CH} = -4.6 Hz is found. Since couplings are extracted in the direct dimension, high resolution is obtained at only little extra measurement time.

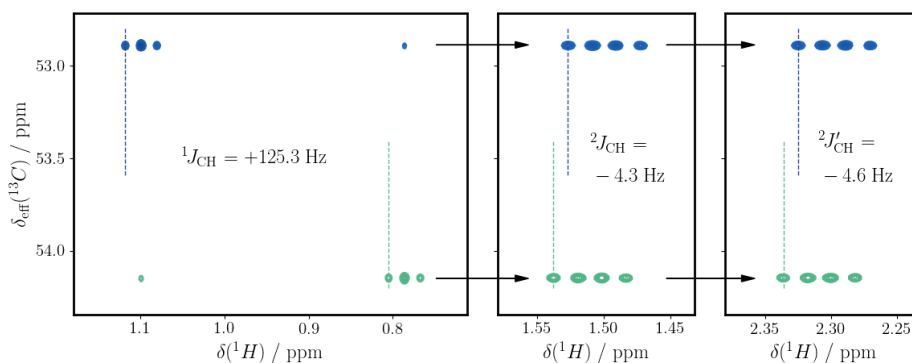


Figure 2.100: Clippings of the HOMQC-TOCSY spectra of vincamine are shown for an ethyl-group with magnetically non-equivalent CH_2 -group. DIPSI is used for coherence transfer. The spectrum was acquired with 4 transients and a spectral width of 12 ppm and 2048 complex points in the direct dimension. In the indirect dimension a spectral width of 10 ppm and 256 complex points (corresponding to a resolution of ~ 3.9 Hz) were acquired on a 400 MHz spectrometer. Transfer delays are set according to $\Delta = 1/(4^1J_{\text{CH}})$ with $J_{\text{CH}} = 130$ Hz. The value for $\delta_{\text{eff}}(^{13}\text{C})$ can be calculated from $\delta_{\text{eff}}(^{13}\text{C}) = \delta_c + \kappa \cdot [\delta(^{13}\text{C}) - \delta_c]$ where δ_c is the carrier-offset.

2.6.4 Conclusion

In the present section a novel element for ^{13}C -HSQC-type pulse sequences was thoroughly examined and applied in two experiments that allow the sign-sensitive measurement of various homo- and heteronuclear couplings. The new element is based on the creation of ordered multi-quantum states that evolve only according to a single heteronuclear $^1J_{\text{CH}}$ -coupling independent of the spin system (CH, CH_2 or CH_3). The Hamiltonians of residual couplings commute with respective multi-quantum spin states and selective heteronuclear decoupling is achieved broadband. Further, the novel element allows signal editing by a simple shift of pulse phases and filtering of CH/ CH_3 , CH_2 , or DQ- and ZQ-coherence can be obtained which greatly facilitates the interpretation of acquired spectra – i.e. the spectral content can be reduced to the most essential information.

Two applications of the proposed element were shown of which one is the so-called JRES-HOMQC experiment that can be used for the measurement of $^1J_{\text{CH}}$ - and $^2J_{\text{HH}}$ -couplings. It was demonstrated for camphor that a linewidth of down to 0.55 Hz in the indirect dimension was achieved, which is close to the value of the solvent, chloroform with 0.46 Hz and coupling extraction is possible at high accuracy. Moreover, sensitivity could be increased from the application of real-time homonuclear decoupling as discussed in Section 3.1. The other experiment is the so-called HOMQC-TOCSY that is based on a modified backtransfer and can be used for the sign-sensitive determination of $^1J_{\text{CH}}$ - and long-range $^nJ_{\text{CH}}$ -couplings in the direct dimension. From signal-filtering (by measuring the $\omega_1^\alpha \omega_2^\beta$ -peak with positive and negative sign), one can avoid overcrowded spectra and only the least amount of necessary information is given. Due to the fact that various MQ-coherences are created during the proposed element, the suppression of artifacts is not a trivial task and further investigations seem useful in order to find their origin and means of suppression.

Chapter 3

Homonuclear Decoupling

3.1 Introduction

The application of homonuclear decoupling has found widespread use in different fields of high resolution liquid-state NMR. Especially, in large spin networks broad multiplets are encountered and the disentangling of individual signals represents a prerequisite for the unambiguous interpretation of spectral resonances. The collapse of multiplets obtained from homonuclear decoupling inevitably leads to an increase in resolution and the overlap in crowded spectra can be avoided to very large extent. By this means the only information left in the spectrum is the chemical shift⁸² and the field is often referred to as *pure shift* NMR. Various pure shift methods are available and essential differences shall be presented in the following outline – comprehensive and more detailed descriptions are given in the literature.^[251,252]

3.1.1 *J*-Resolved Experiments

The very first homonuclear decoupled proton spectra are based on so-called 2D *J*-resolved experiments where in the indirect dimension the scalar coupling is sampled.^[253] A subsequent skew projection causes a collapse of the indirect dimension where subsets of 2D signals collide in a single resonance.^[254] Since the 2D *J*-resolved spectrum exhibits phase-twist lineshape (i.e. negative intensities are present from dispersive contributions) different procedures were undertaken to avoid cancellation. These comprise the use of absolute value spectra^[254], different processing algorithms to obtain a *pseudo echo*^[255,256] or the use of a computer algorithm that removes dispersive contributions.^[257] Later on, more elaborate solutions followed where the phase-twist lineshape in 2D *J*-resolved spectra is avoided by abandoning frequency discrimination in the indirect dimension (achieved with a z-filter^[119]) and a subsequent pattern-recognition performed by a computer algorithm.^[258,259] A simple but efficient method was proposed by Pell and Keeler^[260] where the coupling evolution is reversed in analogy to the acquisition of an *echo* / *anti-echo* spectrum. Yet, the method is no longer *broadband* – it requires a band selection in which the *passive* spins (i.e. non-recorded coupling partners) are situated in order to refocus the coupling.

^[251] K. Zangger. *Progress in Nuclear Magnetic Resonance Spectroscopy* **2015**, 86-87, 1–20.

^[252] L. Castañar and T. Parella. *Magnetic Resonance in Chemistry* **2015**, 53, 399–426.

^[253] W. P. Aue, J. Karhan and R. R. Ernst. *The Journal of Chemical Physics* **1976**, 64, 4226–4227.

^[254] K. Nagayama et al. *Journal of Magnetic Resonance* **1978**, 31, 133–148.

^[255] A. Bax, R. Freeman and G. A. Morris. *Journal of Magnetic Resonance* **1981**, 43, 333–338.

^[256] A. Martinez et al. *Magnetic Resonance in Chemistry* **2012**, 50, 28–32.

^[257] A. J. Shaka, J. Keeler and R. Freeman. *Journal of Magnetic Resonance* **1984**, 56, 294–313.

^[258] S. Simova, H. Sengstschmid and R. Freeman. *Journal of Magnetic Resonance* **1997**, 124, 104–121.

^[259] B. Luy. *Journal of Magnetic Resonance* **2009**, 201, 18–24.

^[260] A. J. Pell and J. Keeler. *Journal of Magnetic Resonance* **2007**, 189, 293–299.

⁸² Without doubt valuable insight on structure and confirmation can be obtained from scalar couplings and it is a justified question whether such information should be abandoned. However, there is no contradiction in stating that homonuclear decoupling greatly facilitates even the measurement of homonuclear couplings as shown by various experiments^[248–250] of which the so-called PSYCHEDELIC by Sinnaeve et al. probably constitutes the most extraordinary example.

Many more J -resolved variations for the acquisition of pure shift spectra were elaborated where an inversion is induced by a large coupling to a heteronucleus (called BIRD-filter),^[242,261] that aim at the suppression of strong coupling artifacts^[213,261] or induce a “time reversal” from low flip angle pulses.^[262] Such low flip angle pulses are likewise applied in the z-COSY experiment from whose diagonal a pure shift projection can be obtained.^[263,264] Other approaches make use of a *constant time* acquisition during which the coupling modulation is time-independent while the chemical shift evolves according to a shifted inversion pulse.^[10] Furthermore, a J -resolved dimension can also be used in a pseudo 3D experiment whose projection then offers a homonuclear decoupled 2D spectrum.^[265–267] While all of these methods lead to *broadband* homonuclear decoupling they come with an inherent time penalty – an *additional* J -resolved dimension has to be acquired.

3.1.2 Time-Shared Acquisition

In the early days of NMR it was already proven that the perturbation of a radiofrequency field has an influence on the nuclear spin coupling.^[268,269] In *heteronuclear* experiments multi pulse sequences (e.g. MLEV^[209], WALTZ^[144] or GARP^[145]) are routinely applied during acquisition on the channel of the heteronucleus in order to remove heteronuclear couplings. For *homonuclear* decoupling a similar approach exists which is considerably more complicated – a single channel has to be used for acquisition and decoupling in a *time-shared* way.⁸³ It was first proposed by Jesson et al.^[271] that during the acquisition of an FID a part of the dwell time can be used to apply a perturbative field acting on a narrow band in order to saturate *passive* spins selectively. Fast switching between the receiver and decoupler is, hence, necessary in order to acquire and perturb alternately. Hammarström and Otting discovered that a band-selective shaped pulse sliced into numerous pieces can be used for perturbation during acquisition.^[272,273] This way, the decoupling profile approximates an ideal rectangular function that is given by the selective pulse. In analogy to a DANTE sequence,^[58] excitation sidebands are encountered at frequencies of the inverse dwell time. Instead of selective pulses, Kupče and Wagner applied adiabatic pulses in order to obtain a wider (but still selective) band.^[274] By doing so, homonuclear decoupling during the acquisition of amide protons was used to suppress the 3J -coupling to vicinal $H\alpha$.

In contrast to homonuclear decoupling obtained from J -resolved experiments, the time-shared acquisition is limited to *band-selective* decoupling which, however, is achieved in a *very* time efficient way. Since the decoupler occupies a fraction of the acquisition time there is a little loss in sensitivity – in general, the loss can be compensated by the collapse of multiplets. Still, in order to keep the loss in sensitivity small (in the range of few percent^[274]) the lowest possible RF field should be used for decoupling so that long duty cycles are avoided. Too low RF fields, on the other hand, cause decoupling sidebands since spin inversions have to occur much faster than the coupling frequency⁸⁴ and a certain compromise has to be found. However, it should be noted that a perturbative field is repeatedly applied during acquisition and

^[261] J. R. Garbow, D. P. Weitekamp and A. Pines. *Chemical Physics Letters* **1982**, *93*, 504–509.

^[262] O. W. Sørensen, C. Griesinger and R. R. Ernst. *Journal of the American Chemical Society* **1985**, *107*, 7778–7779.

^[263] H. Oschkinat et al. *Journal of Magnetic Resonance* **1986**, *69*, 559–566.

^[264] A. J. Pell, R. A. E. Edden and J. Keeler. *Magnetic Resonance in Chemistry* **2007**, *45*, 296–316.

^[265] K. Furihata, M. Tashiro and H. Seto. *Magnetic Resonance in Chemistry* **2010**, *48*, 179–183.

^[266] B. Görling, S. Bräse and B. Luy. *Magnetic Resonance in Chemistry* **2012**, *50*, S58–S62.

^[267] P. Sakhaii, B. Haase and W. Bermel. *Journal of Magnetic Resonance* **2013**, *228*, 125–129.

^[268] A. L. Bloom and J. N. Shoolery. *Physical Review* **1955**, *97*, 1261–1265.

^[269] W. A. Anderson and R. Freeman. *The Journal of Chemical Physics* **1962**, *37*, 85–103.

^[144] A. J. Shaka et al. *Journal of Magnetic Resonance* **1983**, *52*, 335–338.

^[145] A. J. Shaka, P. B. Barker and R. Freeman. *Journal of Magnetic Resonance* **1985**, *64*, 547–552.

^[271] J. P. Jesson, P. Meakin and G. Kneissel. *Journal of the American Chemical Society* **1973**, *95*, 618–620.

^[272] A. Hammarström and G. Otting. *Journal of the American Chemical Society* **1994**, *116*, 8847–8848.

^[273] J. Weigelt et al. *Journal of Magnetic Resonance* **1996**, *B110*, 219–224.

^[274] Ě. Kupče and G. Wagner. *Journal of Magnetic Resonance* **1995**, *B109*, 329–333.

⁸³ The expression “time-shared” in this context should not be confused with the field of “time-shared NMR” where various NMR experiments are entangled in a way that they share the indirect dimension. Subspectra are acquired with sign-modulation and disentanglement can be obtained from summation or subtraction.^[270]

⁸⁴ This is related to the discussion about convergence of the zeroth order average Hamiltonian in Section 1.7.3.

Bloch-Siegert shifts are commonly encountered. Hence, the acquired resonances do no longer correspond to the actual chemical shifts as discussed in Section 1.5.3. Additionally, the suppression of strong resonances (e.g. water in biological samples) has to be conducted with particular care. In contrast to other pure shift methods that are applied during acquisition (discussed in Section 3.1.4) time-shared homonuclear decoupling does not allow the repetitive application of spoiler gradients which could reduce artifacts from incomplete suppression of such strong resonances by an order of magnitude.^[275]

3.1.3 Pseudo-2D Chunked Acquisition

With the groundbreaking paper by Zangger and Sterk^[276] immediately two concepts were introduced to the field of homonuclear decoupling. First, *band-selective* pulses are applied during a z-gradient and a *spatial selectivity* is obtained throughout the pulse sequence. The height of the slice depends on the strength of the gradient and the band that the selective pulses cover. Each resonance in the acquired spectrum originates no longer from the entire sample but only from a *spatially selected* slice – clearly, this causes a severe loss in sensitivity which can partially be compensated from fast pulsing or using multiple-frequency pulses.^[277–280] Second, the FID is acquired in multiple *chunks* which can be concatenated to a single FID as schematically illustrated in Figure 3.1 (commonly $n=16-32$). The length of individual chunks (τ_c) is chosen in a way that during the chunk homonuclear couplings evolve only marginally (a further discussion is found in Section 3.1.5). This way minor artifacts have to be condoned, however, compared to broadband homonuclear decoupling obtained from *J*-resolved experiments a speed-up of one to two orders of magnitude is possible.^[251] In order to obtain an FID where chemical shifts evolve continuously while homonuclear couplings are refocused Zangger and Sterk used a combination of hard and selective pulses similar to the one proposed by Brüschweiler et al.^[281] During all *band-selective* pulses gradients of well-chosen strength are applied and *broadband* homonuclear decoupling is achieved. The application of spatial selective decoupling is shown in various homonuclear experiments in literature^[282–284] and the conception of a chunked FID found widespread echo leading to numerous methods for homonuclear decoupling. These methods (including the approach proposed by Zangger and Sterk) are all based on *selective elements* that refocus the homonuclear coupling to *passive spins* (i.e. spins that are

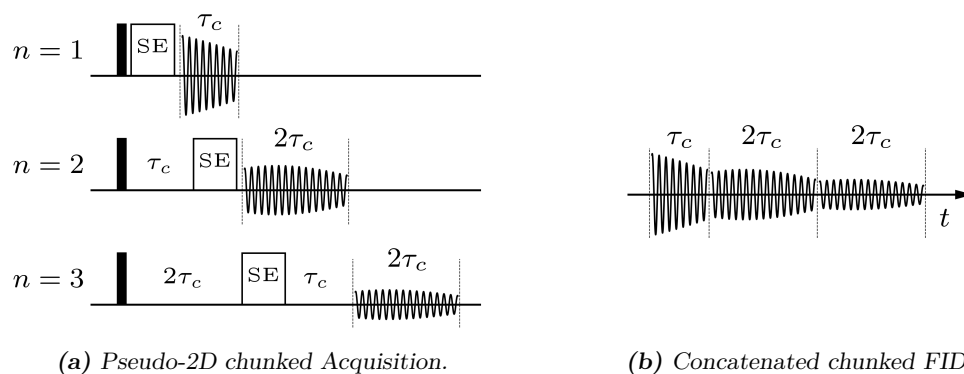


Figure 3.1: In (a) the pseudo-2D acquisition of a chunked FID is illustrated. The open block (“SE”) corresponds to a selective element that reverses coupling evolution. Chunk lengths are $\tau_c \ll \frac{1}{\Sigma J}$ (typically ≈ 10 ms). In (b) the reconstruction of the FID is illustrated.

^[275] P. Király et al. *Journal of Biomolecular NMR* **2015**, *62*, 43–52.

^[276] K. Zangger and H. Sterk. *Journal of Magnetic Resonance* **1997**, *124*, 486–489.

^[277] P. Sakhaei et al. *Journal of Magnetic Resonance* **2013**, *233*, 92–95.

^[278] G. E. Wagner et al. *Chemical Communications* **2013**, *49*, 3155–3157.

^[279] L. Castañar et al. *Chemistry - A European Journal* **2013**, *19*, 15472–15475.

^[280] M. Foroozandeh, P. Giraudeau and D. Jeannerat. *Magnetic Resonance in Chemistry* **2013**, *51*, 808–814.

^[281] R. Brüschweiler et al. *Journal of Magnetic Resonance* **1988**, *78*, 178–185.

^[282] M. Nilsson and G. A. Morris. *Chemical Communications* **2007**, 933–935.

^[283] G. A. Morris et al. *Journal of the American Chemical Society* **2010**, *132*, 12770–12772.

^[284] J. A. Aguilar et al. *Angewandte Chemie - International Edition* **2010**, *49*, 3901–3903.

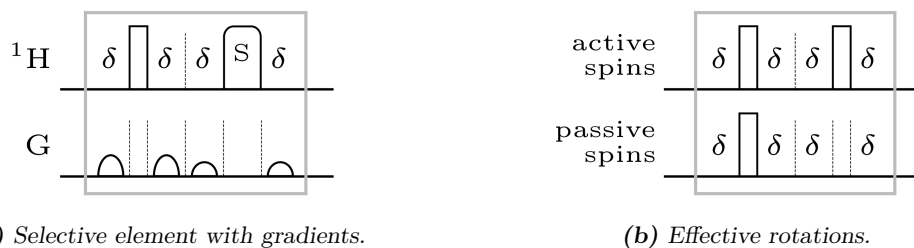


Figure 3.2: A selective element used for homonuclear decoupling in a chunked acquisition is illustrated schematically in grey boxes. A typical pulse sequence is shown in (a) where rectangular open box corresponds to a broadband inversion while the selective inversion is denoted by “S”. Gradients of variable strength are used for coherence pathway selection. In (b) the effective rotations of the radiofrequency pulses are illustrated. It is obvious that scalar couplings to *passive* spins are reversed while chemical shifts of *active* spins are not.

not being observed in the considered signal but induce a splitting) while chemical shifts of *active spins* (i.e. the desired signal to be observed) are *effectively* not reversed. As illustrated in Figure 3.2 (a), such selective elements are typically composed of a *broadband inversion* of both active and passive spins (i.e. hard 180° pulse) and a subsequent *selective inversion* of the *active* spins. In general, spoiler gradients are used to suppress undesired coherence pathways from pulse imperfections. While the combined use of a hard and selective pulse inverts passive spins, active spins are inverted twice and, hence, are *effectively* not inverted (Figure 3.2 (b)).

Clearly, a band-selective pulse fulfills the required properties for a selective inversion (“S” in Figure 3.2 (a)) of active spins. A particular elaborated version of this approach is combined with the perfect echo (see Section 2.2) in order to obtain homonuclear decoupling for the simultaneous acquisition of both amide protons and the $H\alpha$ region.^[114] Furthermore, a selection of *statistically distributed* active spins can be undertaken by the use of a ^{13}C -BIRD-filter^[242,261] in order to obtain *broadband* homonuclear decoupling.^[285] Since in non-labeled samples the natural abundance of the ^{13}C isotope is only at $\sim 1.1\%$ the approach works quite well, however, it is connected to a loss of $\sim 98.9\%$ of the signal. Yet, if applied in certain heteronuclear experiments (e.g. ^1H , ^{13}C -HSQC) there is no additional loss in sensitivity and in literature the BIRD-approach is used extensively for the determination of heteronuclear couplings.^[115,223,224,286] It was shown by Reinsperger and Luy that pure shift signals can be obtained even for a CH_2 group where both protons are bound to the same ^{13}C .^[223] The so-called PSYCHE^[243,287] constitutes another mind-boggling approach that is based on two low flip angle pulses and is, hence, comparable to the time-reversal experiment^[262] or the z-COSY.^[263,264] In all these experiments the two low flip angle pulses provide a *statistical* inversion for a small part of the spin ensemble which so is decoupled from all other spins. In contrast to pre-existing methods, the PSYCHE approach uses two frequency-swept pulses with low flip angle applied during a weak gradient. By this means a subtle coherence pathway selection is undertaken in order to suppress coherence transfer (i.e. cross peaks in terms of the z-COSY). Compared to the chunking techniques discussed so far, PSYCHE offers broadband homonuclear decoupling with an increase in sensitivity of roughly one to two orders of magnitude.^[243] In literature the PSYCHE approach has found widespread application in e.g. TOCSY^[288], DOSY^[289], the field of metabolomics^[290] or for the selective measurement of homonuclear couplings.^[250,291]

In conclusion, the pseudo-2D acquisition of a chunked FID offers a large variety of valuable experiments. Still, an *additional* dimension is required which drastically inflates measurement time. Despite the fact

^[285] J. A. Aguilar, M. Nilsson and G. A. Morris. *Angewandte Chemie - International Edition* **2011**, *50*, 9716–9717.

^[286] I. Timári et al. *Chemistry - A European Journal* **2015**, *21*, 3472–3479.

^[287] M. Foroozandeh, G. A. Morris and M. Nilsson. *Chemistry - A European Journal* **2018**, *24*, 13988–14000.

^[288] M. Foroozandeh et al. *Journal of the American Chemical Society* **2014**, *136*, 11867–11869.

^[289] M. Foroozandeh et al. *Angewandte Chemie - International Edition* **2016**, *55*, 15579–15582.

^[290] J. M. Lopez, R. Cabrera and H. Maruenda. *Scientific Reports* **2019**, *9*, 1–8.

^[291] M. Foroozandeh et al. *Chemical Communications* **2015**, *51*, 15410–15413.

that there are possibilities to enhance sensitivity from subtle processing^[292] or to reduce the number of points in the pseudo dimension^[293,294] an application to low concentrated samples (e.g. in the field of biomolecular NMR) is rather impractical. However, a solution to the sensitivity issue is offered by a similar concept that is based on the acquisition of a chunked FID in a *single shot*. Commonly, it is referred to as *real-time pure shift NMR* and nearly no additional measurement time is required – it shall be discussed in more detail in the following section.

3.1.4 Real-Time Chunked Acquisition

The real-time acquisition of all chunks in a single shot was first proposed by Lupulescu et al.^[295] where, in contrast to the pseudo-2D version (Section 3.1.3), the coupling is *repeatedly* reversed *during* the acquisition (Figure 3.3). In order to refocus homonuclear couplings while chemical shifts of active spins evolve, the acquisition is interrupted and, again, a selective element (“SE”) is applied. Like for the pseudo-2D approach (Figure 3.2) the selective elements are composed of a hard pulse and a selective inversion which, in practice, is realized by either a BIRD-filter, a band-selective or spatial-selective pulse. Only PSYCHE^[243,287] fails within the real-time approach since each application of the PSYCHE-element discards large parts of the signal and it is, hence, not intended for a repetitive use. Again, chunk lengths are chosen in a way that the coupling evolves only a little bit ($\tau_c \ll \frac{1}{\Sigma J}$) which shall be further discussed in Section 3.1.5. Comparable to the time-shared acquisition nearly no additional measurement time is required and even an increase in sensitivity can be obtained from the collapse of multiplets. It should be noted that, due to transverse relaxation, interruptions in between chunks are limited in time – artifacts and an artificial linebroadening can be introduced from a stepwise decrease of chunk intensity (see discussion in Section 3.1.5).

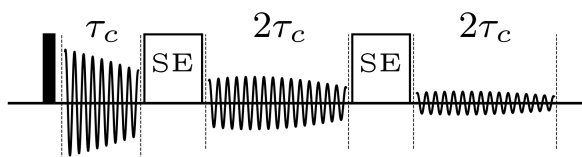


Figure 3.3: Real-time pure shift acquisition. The open block (“SE”) corresponds to a selective element that reverses coupling evolution while chemical shift evolves continuously. Commonly, 8-16 chunks are acquired with a length $\tau_c \ll \frac{1}{\Sigma J}$ (typically ≈ 10 ms).

In the seminal paper by Lupulescu et al.^[295] a ^{13}C -BIRD-filter was used to proof that broadband homonuclear decoupling is obtained from a single scan. Later, the method was introduced into various heteronuclear experiments where broadband homonuclear decoupling is obtained without additional loss in sensitivity. By this means a homonuclear decoupled ^1H , ^{13}C - and ^1H , ^{15}N -HSQC^[296] was elaborated and the approach was further used for the characterization of low concentrated metabolites^[297], enantiodifferentiation^[298] or the measurement of heteronuclear couplings.^[299] Since the BIRD-filter is based on statistical inversions, *broadband* homonuclear decoupling works only if a low abundant isotope is present but fails for uniformly isotope labeled samples. Broadband homonuclear decoupling is likewise obtained from spatial selectivity as proposed by Zangger and Sterk (ZS) – its *real-time* approach was successfully incorporated in a ZS-TOCSY^[300] and ZS-DOSY.^[301] Especially in DOSY experiments

^[292] P. Sakhaii, B. Haase and W. Bermel. *Journal of Magnetic Resonance* **2009**, *199*, 192–198.

^[293] I. E. Ndukwe et al. *ChemPhysChem* **2017**, *18*, 2081–2087.

^[294] A. Shchukina et al. *Chemical Communications* **2019**, *55*, 9563–9566.

^[295] A. Lupulescu, G. L. Olsen and L. Frydman. *Journal of Magnetic Resonance* **2012**, *218*, 141–146.

^[296] L. Paudel et al. *Angewandte Chemie - International Edition* **2013**, *52*, 11616–11619.

^[297] Y. Liu et al. *Tetrahedron Letters* **2014**, *55*, 5450–5453.

^[298] M. Pérez-Trujillo et al. *Chemical Communications* **2014**, *50*, 10214–10217.

^[299] I. Timári et al. *RSC Advances* **2016**, *6*, 87848–87855.

^[300] N. H. Meyer and K. Zangger. *Angewandte Chemie - International Edition* **2013**, *52*, 7143–7146.

^[301] S. Glanzer and K. Zangger. *Chemistry - A European Journal* **2014**, *20*, 11171–11175.

overlapping signals cause the Laplace transform to deliver unreliable results and disentanglement by homonuclear decoupling can greatly improve spectral quality. Furthermore, the real-time ZS-approach was applied in a $^1\text{H},^{13}\text{C}$ -HSQC where the assignment of methyl groups in sidechains of an intrinsically disordered protein (IDP) and the subsequent determination of chemical shift perturbations from intermolecular interactions was rendered possible.^[302] However, *broadband* homonuclear decoupling from spatial selectivity drastically reduces sensitivity. Only in the case that $\text{H}\alpha$ and H-methyl regions are recorded *separately* in two different spectra the loss in sensitivity can be reduced to roughly 80%. Moreover, homonuclear decoupling is obtained from band-selective pulses applied within the real-time chunked acquisition scheme and a certain similarity to time-shared homonuclear decoupling (Section 3.1.2) might be apparent. Though, it is important to note that in the time-shared approach only a *selected* band of *passive* spins is decoupled while in the real-time chunked acquisition the band of *active* spins is decoupled from *all* others. Homonuclear decoupling from band-selective pulses is either referred to as HOBS^[303] or BASHD^[304], yet, they signify the same concept. While in the former publication^[303] homonuclear decoupling is tested on a cyclic peptide (cyclosporine) in the latter^[304] it is used for the measurements of residual dipolar couplings (RDC) from protein alignment in a liquid crystalline phase. It is reported that BASHD fails in the removal of homonuclear RDCs to aromatic sidechains and certain signals are still broadened due to unresolved dipolar couplings.⁸⁵

In the present dissertation two novel concepts shall be introduced that, amongst others, tackle most of the above mentioned problems. Both approaches do not suffer from the loss in sensitivity that is inherited by many other pure shift methods. Hence, they are well suited even for the application to low concentrated biomolecular samples. The first approach (Section 3.2) is meant for the pure shift acquisition of amide protons ($^1\text{H}_N$) in uniformly isotope labeled samples. It is based on a ^{13}C -BIRD filter that refocuses *all* couplings of amide protons to ^{13}C and ^{13}C -bound protons. In contrast to so far existing methods a saturation of the water spin reservoir is not required and the acquired amide protons, being in exchange with water, no longer diminish or even disappear – far from it! Being “in touch” with the water reservoir reduces the effective longitudinal relaxation time and signal-to-noise per time unit is enhanced considerably. Also, the suppression of long-range proton-carbon couplings does no longer require power intensive composite pulse decoupling and long acquisition times for high resolution experiments are accessible. In the second approach (Section 3.3) a BIRD-filter in combination with an X-band-selective pulse (X being the heteronucleus) is used for homonuclear decoupling in uniformly X-labeled samples.^[12] The BIRD-filter acts as a transfer which passes the band-selectivity from heteronuclei to the acquired protons and the extended heteronuclear signal dispersion can be exploited for the design of tailored homonuclear decoupling. Additionally, the suppression of long-range proton-carbon couplings is achieved in a chunk-like way and an acquisition time limit from high power CPD is vastly extended. Even though the sequence provides decoupling only for a selected band, many experiments already inherit such a selection of spins e.g. in biomolecular NMR where commonly NMR experiments are based on very distinct and elaborated coherence transfers. With this regard, the considered pure shift approach was incorporated in a selective- $\text{H}\alpha\text{C}\alpha$ -HSQC (Section 3.4) which allows the characterization of biomolecules under physiological conditions at high resolution and sensitivity.^[11]

^[302] N. H. Meyer and K. Zangger. *Chemical Communications* **2014**, 50, 1488–1490.

^[303] L. Castañar et al. *Chemistry - A European Journal* **2013**, 19, 17283–17286.

^[304] J. Ying, J. Roche and A. Bax. *Journal of Magnetic Resonance* **2014**, 241, 97–102.

⁸⁵ These are couplings to spins that are situated in the same band as amide protons. The novel approach discussed in Section 3.2 would provide a solution for the suppression of most undesired long-range RDCs (except $^1\text{H}_N$ - $^1\text{H}_N$ couplings).

3.1.5 Selective Averaging in Real-Time Pure Shift Acquisition

As mentioned in previous sections (3.1.3 and 3.1.4), homonuclear decoupling from a chunked acquisition is based on the assumption that during each chunk the coupling evolves only marginally. This is achieved if the chunk length τ_c is much shorter than the inverse multiplet width ($\tau_c \ll \frac{1}{\Sigma J}$) which can be explained by the combined use of the toggling frame and average Hamiltonian theory. For Figure 3.4 a two-spin system is assumed and the weak coupling Hamiltonian in the toggling frame (further details are discussed in Section 1.6) together with the resulting FID and its spectrum are illustrated for different scenarios. First, if no J -coupling is present (Figure 3.4a,d,g) also the coupling Hamiltonian in the toggling frame is constantly at zero and for the considered *active* spins a singulett is obtained. Second, for a standard acquisition the toggling frame is equal to the rotating frame and, hence, there is no modulation of the coupling Hamiltonian. A weak J -coupling, hence, leads to a cosine-modulation of the signals amplitude which, in turn, causes a splitting of resonances (Figure 3.4b,e,h). Third, the scalar coupling can be suppressed from a real-time chunked acquisition (Figure 3.4c,f,i) where a *perfect* selective element is assumed (i.e. all passive spins are inverted *instantly*) – clearly, the result approximates the case where no J -coupling is present (Figure 3.4a,d,g). Since the time-dependent weak coupling Hamiltonian in the toggling frame is still *inhomogeneous*⁸⁶ an *exact* zeroth order average Hamiltonian $\bar{\mathcal{H}}_0$ can be obtained. Following the discussion in Section 1.7.2 the zeroth order $\bar{\mathcal{H}}_0$ can be calculated from the time integral. As expected, only in the middle of each chunk the effective coupling ($\bar{\mathcal{H}}_0$) is truly zero (indicated by vertical gray dashed lines in Figure 3.4 (c)) which is where the coupling is said to be refocused.

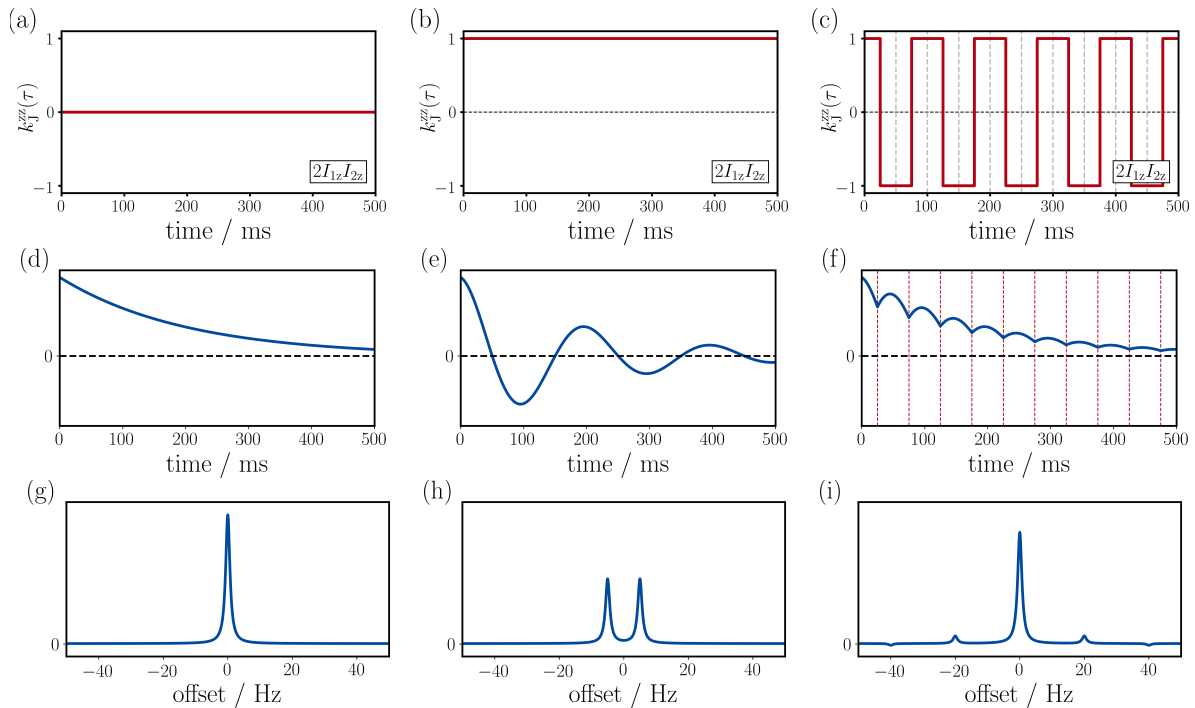


Figure 3.4: Selective averaging in homonuclear decoupling. The weak coupling Hamiltonian in the toggling frame (i.e. its coefficient k_J^{zz}) is examined during acquisition (a-c) and the respective FID (d-f) and spectrum (g-i) is illustrated. While in the first column (a,d,g) no scalar coupling is assumed in the second (b,e,h) and third column (c,f,i) the coupling constant is $J = 10$ Hz and standard acquisition (b,e,h) is compared to real-time homonuclear decoupling (c,f,i). Homonuclear decoupling modulates the weak coupling Hamiltonian in the toggling frame (c) and the zeroth order average Hamiltonian is approximated by ≈ 0 . By this means the case for $J = 0$ Hz shown in (a,d,g) is approached. In order to enhance artifacts a relatively long chunk length of $\tau_c = 25$ ms was chosen.

⁸⁶ A Hamiltonian is *inhomogeneous*^[9] if it *commutes* with itself at *any* two time points (discussed in Section 1.7.2).

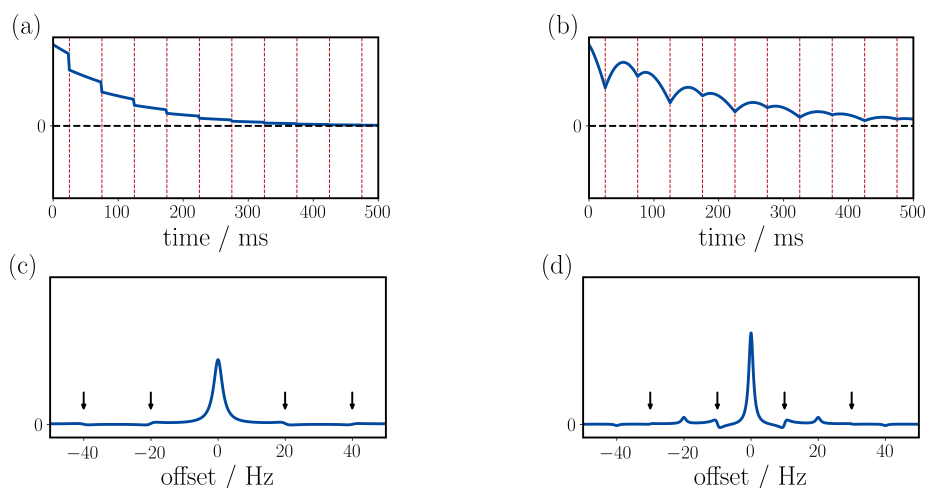


Figure 3.5: Chunk artifacts from transverse relaxation (a,c) and the presence of a dispersive anti-phase coherence at the start of the acquisition (b,d) are illustrated. In order to enhance artifacts from relaxation a factor of $f = 2$ with $\tau_{\text{break}} = 2\tau_c$ was considered in (a,c).

The largest effects due to coupling evolution are, hence, observed directly before and after the selective element is applied (indicated by vertical red dashed lines in Figure 3.4 (f)). These dips appear at regular intervals of twice the chunk length ($2\tau_c$) and the resulting artifacts are encountered in the spectrum at frequencies of $\nu_{\text{art.}} = \frac{n}{2\tau_c}$. Hence, an increase in τ_c causes the artifacts to shift frequencies in the spectrum and summation over multiple transients (of various τ_c) results in reduced artifacts.^[305] In analogy to bi-level composite pulse decoupling^[306], it is likewise possible to change only the length of the first chunk which shifts the dips in the FID of Figure 3.4 (f). By this means the phases of artifacts in the spectrum are modulated and can, hence, be suppressed again from summation over multiple transients.^[307] It is crucial to note that transverse relaxation during a *non-perfect* selective element causes an *artificial* decay of the FID – a downside that is not met in the pseudo-2D acquisition of chunks.⁸⁷ The increase in linewidth can be expressed as a factor f which is calculated from the ratio:

$$f = \frac{2\tau_c + \tau_{\text{break}}}{2\tau_c} \quad (3.1.1)$$

where τ_{break} is the length of the break in between chunks.^[304] Since τ_{break} is given by the selective element it is determined by experimental circumstances and, commonly, it can not be shortened. Even though the linewidth could be reduced for longer chunk lengths τ_c this could also lead to stronger artifacts from coupling evolution and a certain compromise for τ_c has to be found. Additionally, the drops in chunk intensity introduce artifacts again at frequencies of $\nu_{\text{art.}} = \frac{n}{2\tau_c}$. These are shown in Figure 3.5a,c) where an extraordinary long interruption of $\tau_{\text{break}} = 2\tau_c = 50$ ms is considered in order to enhance *dispersive* artifacts from transverse relaxation. It is worth noting that the presence of a homonuclear anti-phase term at the start of the acquisition induces similar dispersive artifacts (see Figure 3.5b,d). However, these can be easily identified since they appear at different frequencies of $\nu_{\text{art.}} = \frac{2n+1}{4\tau_c}$. Similar but in-phase artifacts are introduced from a non-refocused coupling that evolves during the acquisition break which is illustrated in the subsequent Section 3.3 in Figure 3.21. For the reason of consistency in both Figure 3.4 and 3.5 the spectra are plotted with the same intensity scale.

^[305] J. Mauhart et al. *Journal of Magnetic Resonance* **2015**, 259, 207–215.

^[306] Ě. Kupĉe et al. *Journal of Magnetic Resonance* **1996**, A122, 81–84.

^[307] P. Moutzouri et al. *Chemical Communications* **2017**, 53, 10188–10191.

⁸⁷ It is, however, possible to modify the real-time acquisition in way that chunks are recorded “semi-real-time”. By this means chunks are acquired alternately in the two different scans and the relaxation gap in between chunks can, hence, be eliminated from the combination of both saw-tooth transients.^[308]

3.2 Real-Time Pure Shift Acquisition of Amide Protons

In general, biomolecular samples are composed of numerous repeating units that exhibit a substantial similarity and in order to prevent overlap a fundamental requirement is high resolution. With this regard, great improvement has been achieved by the development of stronger magnetic fields and experiments of high dimensionality available at moderate measurement time using *non-uniform sampling*.^[309–312] Yet, an orthogonal approach, constitutes pure shift NMR where the collapse of, sometimes unresolved, multiplets can cause an increase in both resolution and sensitivity. In practice only certain pure shift methods are applicable to biomolecules – the time-shared (Section 3.1.2) and real-time pure shift acquisition (Section 3.1.4). In both methods homonuclear decoupling is obtained on the fly and nearly no additional measurement time is required. While best resolution and sensitivity is obtained from the time-shared approach, Bloch-Siegert shifts have to be tolerated and solvent suppression is roughly an order of magnitude worse compared to the real-time pure shift acquisition (considering a room-temperature probe).^[275]

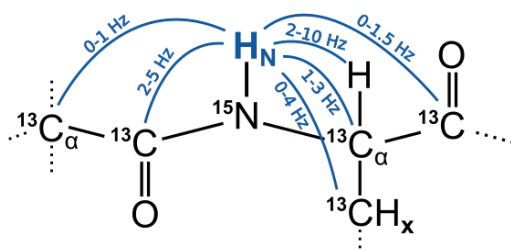


Figure 3.6: Typical spin network of an amide proton in a uniformly ^{13}C , ^{15}N -labeled protein is illustrated including a rough estimate for the size of the coupling constant.

In this section another real-time pure shift method shall be introduced which is designed for the acquisition of amide protons in uniformly ^{13}C , ^{15}N -labeled biomolecules. The method no longer requires the saturation of water and amide protons being in slow exchange with the solvent are *not* suppressed – instead they profit from the polarization stored in water (commonly referred to as “reservoir”) and relaxation recovery delays can be decreased. Also, the suppression of long-range heteronuclear couplings is included at *no additional* power consumption and considerably longer acquisition times and, hence, higher resolution is accessible. As illustrated in Figure 3.6, these long-range couplings are commonly small in size but large in number and, hence, multiplets are most likely unresolved – none the less they contribute to linebroadening (in average ~ 3.7 Hz). In principle, the discussed pure shift acquisition is compatible with any ^1H , ^{15}N -HSQC- or ^1H , ^{15}N -TROSY-type experiment and in the following it shall be analyzed in a FHSQC^[313] and BEST-TROSY^[314,315]. Due to its favorable relaxation properties the BEST-TROSY is slightly advantageous over the FHSQC (see Section 1.8 for *cross correlated relaxation*). On the one hand, the FHSQC and BEST-TROSY are tested on human ubiquitin, a globular protein of 8.5 kDa, at pH=4.6 and T=303 K where proton exchange with water is typically suppressed^[316,317] and, practically, no advantage can be derived from the retained water spin reservoir. Still, it appears helpful to estimate the effect of homonuclear decoupling and what benefits can be gained from the collapse of unresolved homo- and heteronuclear couplings – in ubiquitin the average linewidth is reduced from 16.0 Hz to 7.3 Hz. A detailed discussion on accessible resolution and sensitivity from the proposed pure shift acquisition is given in Section 3.2.3.

[309] J. C. Barna and E. D. Laue. *Journal of Magnetic Resonance* **1987**, *75*, 384–389.

[310] V. Y. Orekhov, I. Ibraghimov and M. Billeter. *Journal of Biomolecular NMR* **2003**, *27*, 165–173.

[311] D. Rovnyak et al. *Journal of Magnetic Resonance* **2004**, *170*, 15–21.

[312] S. Hiller et al. *Journal of the American Chemical Society* **2007**, *129*, 10823–10828.

[313] S. Mori et al. *Journal of Magnetic Resonance* **1995**, *B108*, 94–98.

[314] P. Schanda, H. Van Melckebeke and B. Brutscher. *Journal of the American Chemical Society* **2006**, *128*, 9042–9043.

[315] J. Farjon et al. *Journal of the American Chemical Society* **2009**, *131*, 8571–8577.

[316] R. S. Molday, S. W. Englander and R. G. Kallen. *Biochemistry* **1972**, *11*, 150–158.

[317] Y. Bai et al. *Proteins: Structure, Function, and Genetics* **1993**, *17*, 75–86.

On the other hand, the BEST-TROSY is tested on the *disordered* transactivation domain of the tumor suppressor p53 protein (p53TAD¹⁻⁶⁰) that lacks in tertiary structure (measured at pH=6.5 and T=313 K). Due to the flexibility of intrinsically disordered proteins (IDP), chemical shifts are distributed closer to random coil values and overlap is a frequent issue.^[318] For the same reason, transverse relaxation times are comparably high and, in principle, higher resolution can be obtained than for globular proteins. These are both properties that make IDPs a perfect target for the application of real-time homonuclear decoupling. Yet, the lack of tertiary structure causes the amide protons to be further exposed to water and, hence, to solvent exchange – further considerations are given in Section 3.2.4. In the following a more detailed discussion on the here proposed pulse sequence shall be given where major focus is put on solvent exchange and the potential for high resolution.

3.2.1 Pulse Sequence

The real-time pure shift acquisition as proposed by Lupulescu et al.^[295] is based on a chunked FID described in Section 3.1.4. In between chunks a J -refocusing selective element is applied that has no net effect on active spins while passive spins are inverted and, hence, the J -coupling is refocused. Here, an acquisition sequence for amide protons in uniformly ^{13}C , ^{15}N -labeled biomolecules shall be proposed where suppression of homo- and long-range heteronuclear couplings is achieved by a combination of a ^{13}C -BIRD^{r,X} filter⁸⁸ and a hard 180° pulse as illustrated in Figure 3.7.^[242,261] If applied in an HSQC, composite pulse decoupling (CPD) can be applied to decouple the large $^1J_{\text{NHN}}$ -coupling to nitrogen while no ^{15}N -CPD is required in TROSY and limitations due to power consumption are lifted. Pulsed field gradients are applied in order to suppress radiation damping and undesired coherence transfer from pulse imperfections and delay misset. The functionality of the considered pure shift acquisition can best be described using Figure 3.8 (a) where the pulse sequence is illustrated schematically and only effective rotations are shown. The ^{13}C -BIRD-filter necessitates a discrimination between *directly* ^{13}C -bound protons ($^1H^d$) and *remote* non- ^{13}C -bound protons ($^1H^r$) and both are treated separately. In Figure 3.8 (b) an exemplary protein is illustrated where different groups of spins are highlighted in red ($^1H^d$) and blue ($^1H^r$). Amide protons *not* being bound to ^{13}C are inverted by the ^{13}C -BIRD^{r,X}-filter as well as by the hard 180° pulse and in total they are not effected by the selective element (see $^1H^r$ channel in Figure 3.8 (a)). The surrounding protons (passive spins), on the other hand, are all

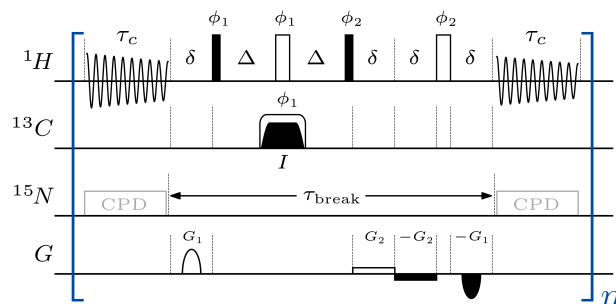


Figure 3.7: The pulse sequence for the real-time pure shift acquisition of amide protons in uniformly ^{13}C , ^{15}N -labeled biomolecules is illustrated. The FID is n times interrupted for the length of $\tau_{\text{break}} = 9.2$ ms during which the coupling to passive spins is refocused. Typical chunk lengths τ_c are in the range of 12 – 20 ms. Filled black and open white bars correspond to 90° and 180° pulses, respectively, with phases $\phi_1 = x, -x$ and $\phi_2 = -x, x$ that undergo a super-cycle $\phi_{sc} = x, -x, -x, x, -x, x, x, -x$. A BIP pulse^[188] (I) is used in the ^{13}C -BIRD^{r,X}-filter and $\Delta = 1/(2^1J_{\text{CH}})$. Gradients of length 0.3 ms are applied during $\delta = 0.5$ ms either for coherence pathway selection (G_1 determined as described in Appendix 5.3.1) or for the suppression of radiation damping ($G_2 = 0.1\%$ of maximum gradient strength).

^[318] D. Neri, G. Wider and K. Wüthrich. *Proceedings of the National Academy of Sciences* **1992**, 89, 4397–4401.

⁸⁸ For BIRD filters the nomenclature of Uhrín et al.^[242] is used where superscripts indicate the inverted groups of spins. (d: directly X-bound protons; r: remote non-X-bound protons; X: heteronucleus)

as *radiation damping*.^[319,320] Especially for high-Q probes,⁸⁹ which have shown to be particularly valuable in the field of biomolecular NMR, radiation damping is very pronounced and strong water chunking artifacts are encountered whenever water is flipped during acquisition. Such an effect is illustrated in Figure 3.9 (a) where every second chunk is dominated by the strong water signal and tremendous artifacts are caused in the spectrum (Figure 3.9 (c)). For the pure shift acquisition of amide protons, so far, water had to be saturated (either by gradients or presaturation) in order to suppress these artifacts and it was impossible to retain the water spin reservoir.

On the contrary, strong chunking artifacts due to radiation damping can be avoided if water is *not* flipped from chunk to chunk. This is achieved by the pure shift acquisition using a ^{13}C -BIRD^{r,X}-filter proposed in Figure 3.7 where during the acquisition water is kept in the state of $+\hat{I}_z$. By this means a feedback loop with the resonant circuit does not lead to an increasing water signal. Clearly, the effect of radiation damping during the chunked FID is suppressed which is illustrated in Figure 3.9 (b) – water artifacts in the spectrum (Figure 3.9 (d)) are reduced by more than two orders of magnitude (compared to Figure 3.9 (c)). Note, the intensity of the water signal can be drastically reduced from subtraction of two successive transients, however, due to the unreproducible nature of radiation damping^[321] artifacts are still predominant if water is flipped during acquisition (see Figure 3.9e and g).⁹⁰ Also for the ^{13}C -BIRD-based pure shift acquisition the water signal is notably reduced from two scans (Figure 3.9f and h) and artifacts are still lower by a factor of ~ 40 compared to Figure 3.9 (g). Clearly, from these results it is evident that for the pure shift acquisition of exchanging amide protons (which necessitate the preservation of the water spin reservoir) an acceptable level of solvent suppression can only be achieved if water is *not* flipped in between chunks.

The quality of water suppression in the standard FHSQC shall be compared to the FHSQC equipped with the available real-time pure shift methods. For the standard FHSQC spectrum of ubiquitin a 1D projection of absolute values along the indirect dimension is shown in Figure 3.10 (a) and the water signal (at ~ 4.7 ppm) is suppressed to great extent. As described above the water suppression for pure shift acquisition sequences is far more challenging since pulses are repetitively applied during acquisition. Therefore, a certain increase in “artificial” noise from water chunking artifacts has to be faced in areas closer to the water resonance which is illustrated in Figure 3.10 (b) to (d) and further quantized in the Appendix (Figure 5.8). While all pure shift methods exhibit a comparable artifact level⁹¹ it is crucial to note that, in contrast to the application of a ^{15}N -BIRD-filter or band selective pulses (Figure 3.10 (c) and (d)), water is *not* saturated in Figure 3.10 (b) where a ^{13}C -BIRD^{r,X}-filter is used. Hence, in the here proposed real-time pure shift acquisition of amide protons the chunking artifact level from manifold stronger water signal is reduced to a minimum while the water spin reservoir is preserved and fast experiments are achievable. In order to obtain best water suppression an optimization of the gradient strength is *obligatory* and described in Appendix 5.3.1.

^[319] N. Bloembergen and R. V. Pound. *Physical Review* **1954**, *95*, 8–12.

^[320] A. Vlassenbroek, J. Jeener and P. Broekaert. *The Journal of Chemical Physics* **1995**, *103*, 5886–5897.

^[321] Y. Y. Lin et al. *Science* **2000**, *290*, 118–121.

⁸⁹ The Q factor of a probe is determined by the AC resistance of the resonant circuit (coil, capacitor and sample) and higher Q factors, in principle, signify higher sensitivity. Also recoupling with the coil is enhanced and high-Q probes are more susceptible to radiation damping.

⁹⁰ Radiation damping is a non-linear effect where small changes might lead to large deviations. Its strength depends on the signal intensity at a given frequency, where it induces its own B_1 field in the RF-coil. Therefore, it is possible to reduce the effect by the application of a weak field gradient that reduces maximum signal intensities by line-broadening.

⁹¹ The use of band-selective pulses seems to be have slightly better water suppression.

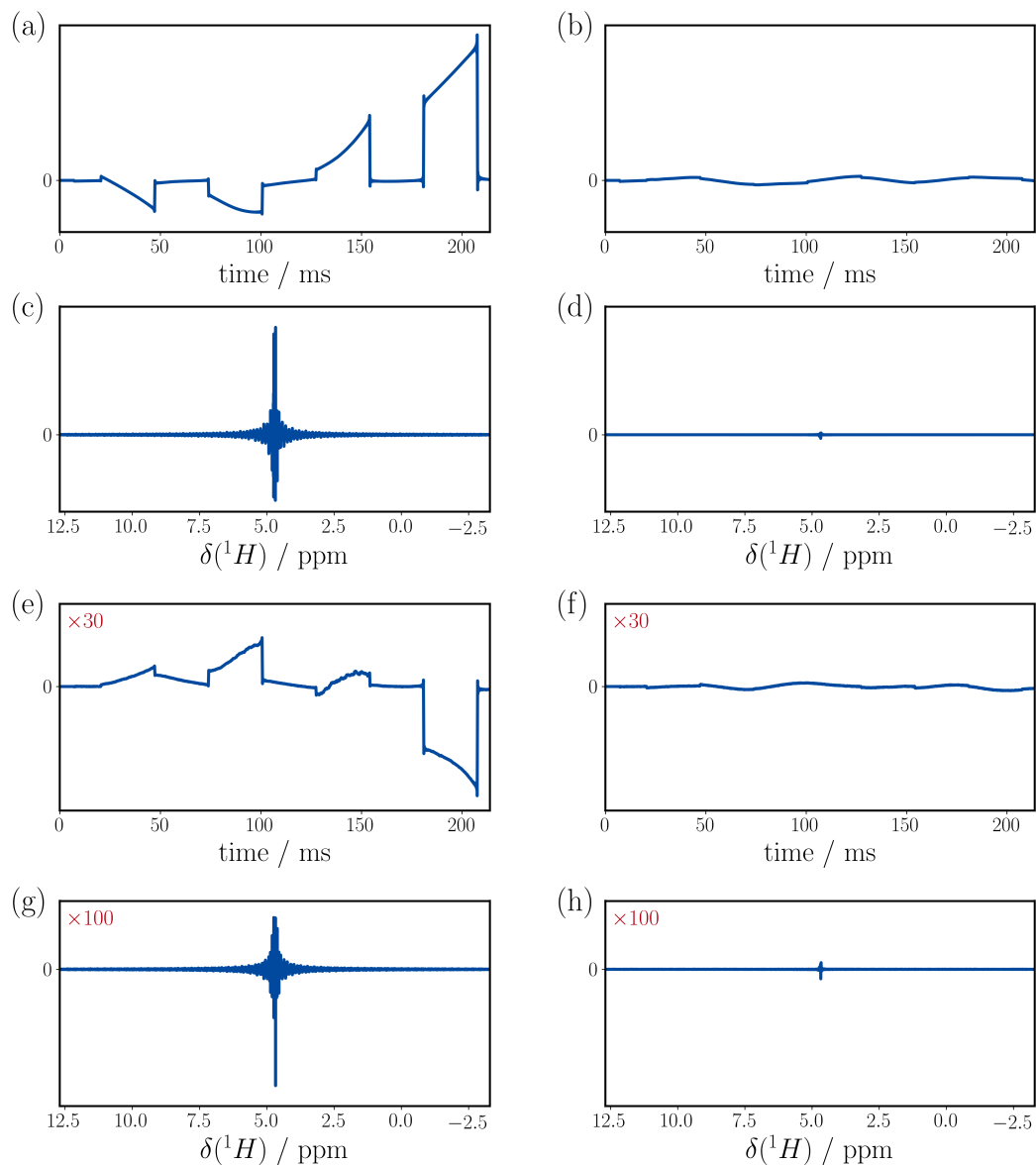


Figure 3.9: The effect of radiation damping on transverse magnetization during acquisition of pure shift FHSQC is compared for the use of a ^{15}N -BIRD-filter (left column) and a ^{13}C -BIRD-filter (right column). While in the upper part (a-d) one transient is acquired, in the lower part (e-h) the water signal is reduced by subtraction from two transients and in (e-h) axes are scaled as indicated in red. In the FID of (a+e) every second chunk a strong water resonance is encountered and water artifacts dominate the spectrum (c+g). Uncontrolled transverse magnetization due to radiation damping can be largely circumvented by the use of a ^{13}C -BIRD-filter (b+f) and in (d+h) water artifacts are reduced by more than two orders of magnitude compared to (c+g). In both cases only the first FID was acquired with 16 dummy scans using a high-Q TCI probe.

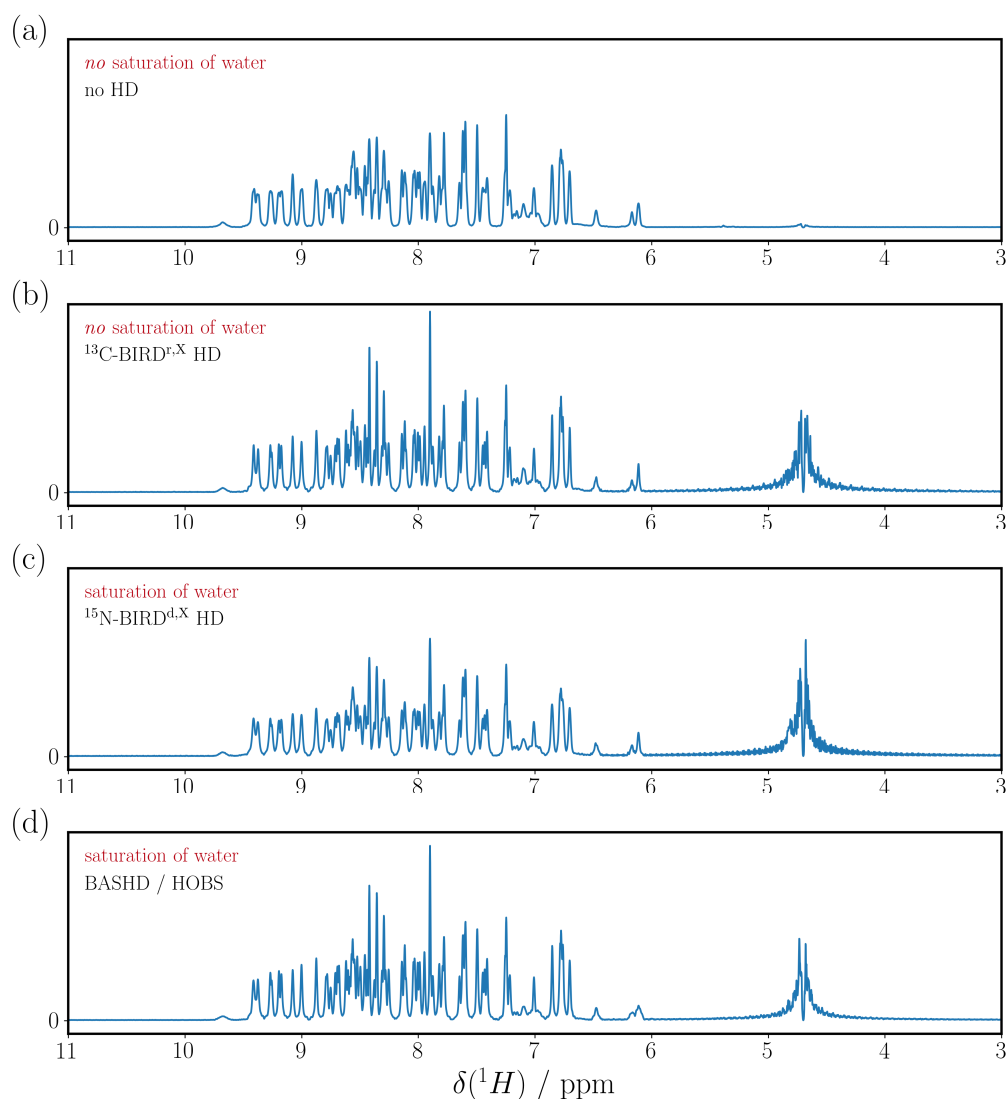


Figure 3.10: The quality of water suppression is compared for different real-time pure shift methods using a high-Q TCI probe. The methods were incorporated in an FHSQC and 1D projections along the indirect dimension of ubiquitin spectra are illustrated for the standard acquisition (a), pure shift acquisition using ^{13}C -BIRD r,X -filter (b), ^{15}N -BIRD d,X -filter (c) and band-selective pulses (d). While (c) and (d) require the saturation of water during the pulse sequence, in (a) and (b) the water spin reservoir is retained. Still, quality of water suppression for all homonuclear decoupled spectra is comparable (b-d). Note, signal intensity is lower for the use of a ^{15}N -BIRD-filter (c) due to the longer τ_{break} .

3.2.3 Application to Globular Proteins

In the present section the ^{13}C -BIRD-based pure shift acquisition shall be examined in detail using a uniformly ^{13}C , ^{15}N -labeled globular protein, ubiquitin. The sequence is incorporated in an FHSQC and BEST-TROSY in order to investigate on the gain in resolution and it is shown that overlapping signals are resolved. A theoretical discussion on the obtainable linewidth compared to other pure shift methods is given and what influence can be ascribed to long-range heteronuclear couplings. Furthermore, the influence of the considered pure shift acquisition on sensitivity is elaborated.

An overview spectrum for BEST-TROSY with and without pure shift acquisition is given in Figure 3.11.

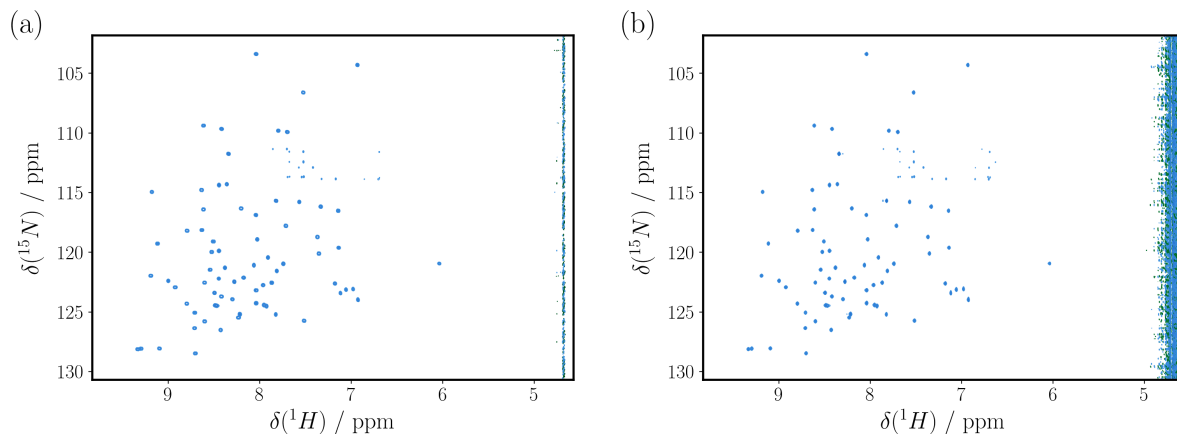


Figure 3.11: Comparison of standard (a) and ^{13}C -BIRD real-time pure shift acquisition (b) in BEST-TROSY spectra of ubiquitin in aqueous solution ($500\ \mu\text{M}$, 93% H_2O , 7% D_2O). Recorded on a 600 MHz spectrometer equipped with TCI probe and 256×3072 complex points, which corresponds to an acquisition time of 110 ms (indirect) and 321 ms (direct dimension).

Increase in Resolution

Although the application of homonuclear decoupling to biomolecules has repeatedly been shown in literature^[11,274,275,296,302,304], still, a certain skepticism has remained in some parts of the NMR community. Clearly, enhanced resolution can only be expected if the natural linewidth is considerably lower than the underlying multiplet width and larger globular biomolecules with fast transverse relaxation are rightly excluded. Yet, the potential of pure shift NMR can very easily be misjudged if the origin of broad spectral lines is falsely ascribed to the sample's relaxation properties. It might turn out that, on a closer look and sufficiently long acquisition time, the lineshape of a considered signal deviates from a Lorentzian function and the signal's width is actually determined by numerous, small and unresolved homo- and heteronuclear couplings.

A selected area of FHSQC and BEST-TROSY spectra of uniformly ^{13}C , ^{15}N -labeled ubiquitin is illustrated in Figure 3.12. In Figure 3.12 (a) and (b) standard acquisition was used and, indeed, the considered peaks exhibit broad lines with a notably flattened top which indicates broadening from homo- and heteronuclear couplings. In pure shift spectra these couplings are collapsed to a single line and in Figure 3.12 (c) and (d) signals adopt a Lorentzian-like shape. This way, a substantial increase in resolution is obtained and two overlapping signals (Q31 and R72) can be resolved distinctly.

It is interesting to see that also in the two pure shift spectra (Figure 3.12c and d) a different resolution is encountered which has several reasons. While in HSQC-type experiments higher sensitivity is expected for small- to medium-sized biomolecules, the resolution in the direct dimension is limited due to power intensive ^{15}N -CPD. For the HSQC spectra shown in Figure 3.12 (a) and (c) a remarkably long acquisition time of 214 ms was *carefully* chosen. On the other hand, no such power limitation is given for BEST-TROSY and an even longer acquisition time of 321 ms can be securely carried out. Note, the suppression of long-range heteronuclear couplings to surrounding ^{13}C was so far achieved by *additional*

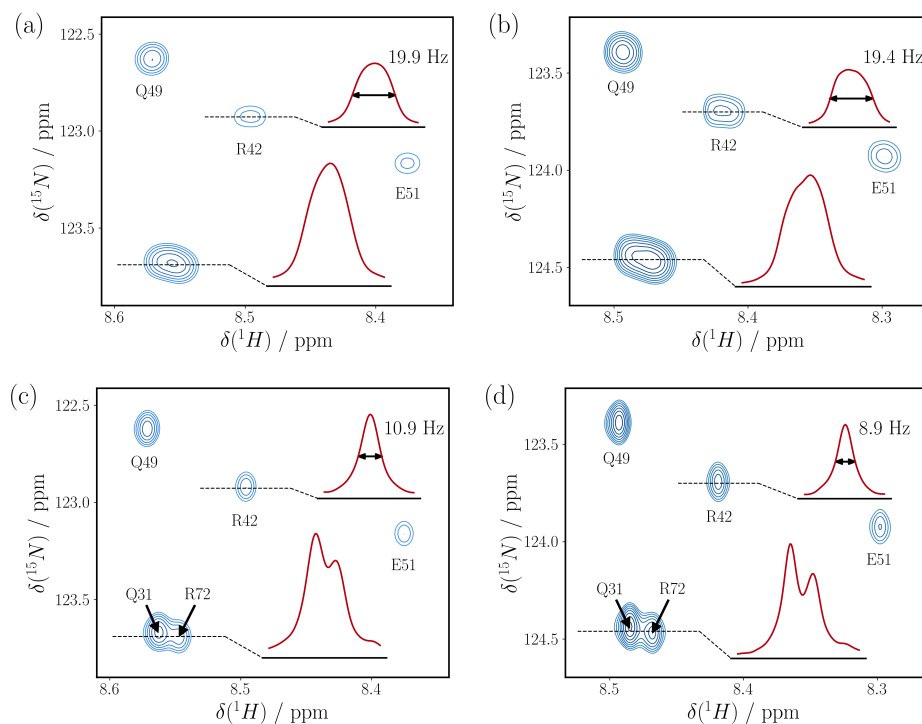


Figure 3.12: Clipped spectra of ubiquitin were acquired at 600 MHz using a FHSQC (a+c) and BEST-TROSY (b+d) with standard (a+b) and ^{13}C -BIRD r,X pure shift acquisition (c+d). While in the FHSQC $n = 6$ chunks were acquired in 214 ms ($\tau_c = 17.8$ ms), for the TROSY a longer acquisition time of 321 ms was feasible with (next higher loop counter) $n = 8$ chunks ($\tau_c = 20$ ms). Both experiments were recorded with an interscan delay of $\tau_r = 1.0$ s and 256 complex points in the indirect ^{15}N -dimension corresponding to an acquisition time of 120 ms. The assignments are based on literature^[322,323] and overlapping signals (Q31 and R72) can be resolved in (c) and (d). In order to increase signal-to-noise (at the price of resolution) a quadratic sine was used for apodization.

^{13}C -CPD which further worsened the power issue. Keeping in mind that the RF-channels for ^{13}C and ^{15}N commonly share the same coil it is evident that *simultaneous* application of ^{13}C - and ^{15}N -CPD imposes a severe limit on the acquisition time (≤ 80 ms^[304]) and the full pure shift potential cannot be tapped. On the other hand, the ^{13}C -BIRD-based pure shift acquisition inherently refocuses long-range heteronuclear couplings from chunk to chunk *without* extra power consumption and from extended acquisition times the potential resolution is achievable.

Furthermore, the BEST-TROSY exhibits a slight advantage due to the favorable relaxation properties. Although the effect of cross-correlated relaxation (Section 1.8) is more strongly pronounced for large molecules, for ubiquitin, already at 600 MHz narrower lines are encountered for the TROSY-lines. A comparison⁹² of the FHSQC and BEST-TROSY reveals that already for ubiquitin an average decrease in linewidth of ~ 1.3 Hz is obtained for the pure shift BEST-TROSY. Using standard acquisition, on the other hand, the reduction in linewidth is barely notable since the signal's width is dominated by homo- and heteronuclear couplings.

In Figure 3.13 a statistical evaluation is given where the signal width of individual residues for standard and pure shift acquisition are plotted against each other. In these correlation plots the gain in resolution can be estimated at first sight and average values are plotted as red dashed lines. For the FHSQC (Figure 3.13 (a)) resolution could be increased by a factor of up to ~ 2.7 leading to a linewidth of down to 4.0 Hz and the average signal width is reduced from 16.3 Hz to 8.8 Hz. For BEST-TROSY (Figure 3.13 (b)) an even higher increase in resolution is obtained. A linewidth of down to 2.8 Hz is

⁹² The considered FHSQC and BEST-TROSY spectra, recorded with *comparable* acquisition parameters, are illustrated in the Appendix 5.3.2.

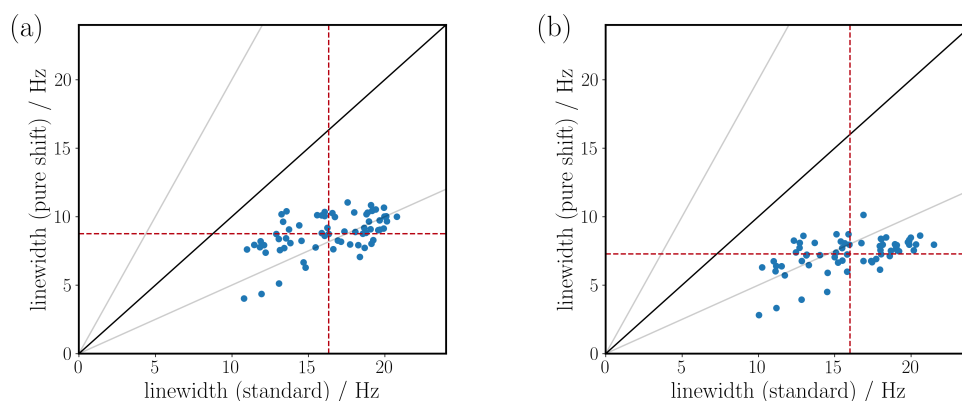


Figure 3.13: The linewidths of amide protons in ubiquitin using a standard and pure shift acquisition are compared in a correlation plot for the FHSQC (a) and BEST-TROSY (b) – no apodization is used. Average values are indicated by red dashed lines which are 16.3 Hz (standard) and 8.8 Hz (pure shift) in (a) and 16.0 Hz (standard) and 7.3 Hz (pure shift) in (b).

observed which corresponds to an increase in resolution of a factor of ~ 3.6 and the average linewidth was reduced from 16.0 Hz to 7.3 Hz. Hence, in both cases the average resolution is roughly doubled and the width of *all* signals could be reduced. Note, in contrast to Figure 3.12, where standard quadratic sine apodization is used for enhanced signal-to-noise, no apodization was applied in Figure 3.13 in order to obtain an unbiased examination of the achievable linewidth (signal width is increased by ~ 1 Hz from quadratic sine apodization) – in the following, such a difference in processing shall be used consistently. The linewidths of all correlation plots were determined automatically with user-supervision using a self-written python program.

Although the increase in resolution is considerable, the obtained linewidth does *not* correspond to the lowest possible, the natural linewidth. As more thoroughly discussed in Section 3.1.5, the acquisition of a chunked FID induces an artificial decay of the transverse signal which causes an additional broadening of the signal. It originates from transverse relaxation during the selective J -refocusing elements and, hence, it depends also on the length of the acquisition break (τ_{break}). In comparison to the real-time pure shift acquisition using band-selective pulses ($\tau_{\text{break}} \approx 4$ ms) or a ^{15}N -BIRD filter ($\tau_{\text{break}} \approx 13.2$ ms) J -refocusing from a ^{13}C -BIRD filter requires a total acquisition break of $\tau_{\text{break}} \approx 9.2$ ms. Following Equation (3.1.1) for considered chunk lengths (τ_c) of 12 to 20 ms the linewidth is increased by 10-16% for band-selective pulses, by 23-38% for the ^{13}C -BIRD filter and by 33-55% for the ^{15}N -BIRD filter. The lowest linewidth would, hence, be obtained from the use of band-selective pulses – *if* technical limitations due to ^{13}C - and ^{15}N -CPD power consumption are neglected.⁹³ It shall be mentioned that a chunk length of $\tau_c = 20$ ms is comparatively long and considerable artifacts are expected which, however, can be suppressed as shown in the Appendix 5.3.3.

It is noteworthy that even higher resolution is provided by time-shared homonuclear decoupling since no breaks longer than a fraction of the dwell time are required. However, as explicated in Section 3.1.2, the time-shared acquisition is inherently connected to Bloch-Siegert shifts and the application of field gradients for enhanced water suppression is not feasible. Furthermore, long-range heteronuclear couplings cannot be suppressed in chunks and additional ^{13}C -CPD is required for highest possible resolution in uniformly ^{13}C , ^{15}N -labeled samples – their influence on resolution shall be discussed in the following.

The effect of long-range heteronuclear couplings for the acquisition of amide protons is shown in Figure 3.14 where homonuclear decoupling (using ^{13}C -BIRD^r filter) is compared to homo- *and* heteronuclear

⁹³ Yet, one could circumvent the use of additional ^{13}C -CPD in comparable methods^[296,304] if a single ^{13}C -inversion pulse is applied simultaneously to the ^{15}N -BIRD filter or the band-selective pulse. By this means small long-range heteronuclear couplings are chunk-wise suppressed at less power than required for ^{13}C -CPD and long acquisition times for higher resolution could be achievable. Still, the additional use of a broadband ^{13}C -inversion pulse cannot retain the water spin reservoir and its application is rather restricted to samples where amide protons are not in solvent exchange.

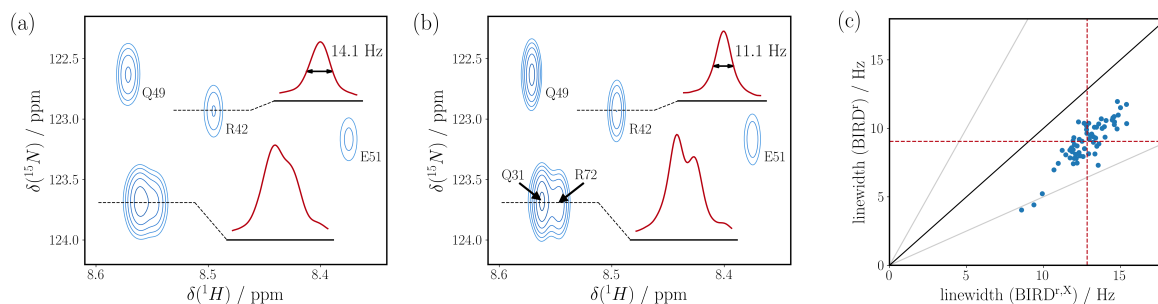


Figure 3.14: The impact of proton carbon long-range couplings on the linewidth is examined in an FHSQC by the use of a ^{13}C -BIRD^f- (a) and ^{13}C -BIRD^{f,X}-filter (b) – quadratic sine apodization is applied. In the direct dimension, 2048 complex points were acquired in 214 ms (with $\tau_c = 17.8$ ms) while in the indirect dimension 64 complex points were acquired in 30 ms. The linewidths of peaks in spectra (a) and (b) are illustrated in a correlation plot (c). No apodization is applied in (c) and average values are indicated by red dashed lines where a value of 12.8 Hz (BIRD^f) and 9.1 Hz (BIRD^{f,X}) is found. Note, the break in between chunks (τ_{break}) is slightly larger for the BIRD^f-filter (with $\tau_{\text{break}} = 9.46$ ms instead of 9.14 ms) which, however, has only a minor effect on the linewidth ($< 1\%$).

decoupling (using a ^{13}C -BIRD^{f,X} filter) in an FHSQC. As indicated by the superscript, the ^{13}C -BIRD^f filter only inverts remote protons and, in contrast to the ^{13}C -BIRD^{f,X}, long-range heteronuclear couplings are not refocused in between chunks. Hence, broader lines are encountered due to the considered heteronuclear couplings and in Figure 3.14 (a) much lower resolution is obtained compared to Figure 3.14 (b) – overlapping signals (Q31 and R72) are hardly resolved. Also, the statistical evaluation in the correlation plot of Figure 3.14 (c) confirms that the average linewidth of ~ 9.1 Hz increases to ~ 12.8 Hz if long-range heteronuclear couplings are *not* suppressed.⁹⁴ Despite the fact that long-range heteronuclear couplings are commonly small in size in the closer environment of amide protons a large number of ^{13}C nuclei is encountered (illustrated in Figure 3.6). In sum and average a reduction in linewidth of ~ 3.7 Hz can, hence, be obtained if these heteronuclear long-range couplings are suppressed. In turn, this corresponds to a simultaneous increase in sensitivity of 17% (with quadratic sine apodization). A general discussion on the obtained sensitivity from pure shift FHSQC and BEST-TROSY is given in the following section for the case of ubiquitin.

Impact on Sensitivity

Next to resolution, sensitivity is the most limiting factor in biomolecular NMR and it is, therefore, common to use so-called *fast experiments* where the available magnetization is managed efficiently. One example is the previously mentioned FHSQC^[313] where the solvent magnetization is to be stored throughout the experiment. Another is the so-called BEST approach^[314] where the entire magnetization of unobserved spins is retained.⁹⁵ In both cases the stored magnetization is, prior to the next scan, transferred to amide protons and the interscan delay can be reduced significantly leading to an increase in signal-to-noise per unit time. In general, for the buildup of magnetization different effects have to be distinguished. First, and most obviously, longitudinal relaxation causes a magnetization buildup of practically any spin in an outer magnetic field. Second, proton exchange with the solvent can cause a transfer of water magnetization to amide protons as was originally examined for the FHSQC.^[313] Third, a magnetization transfer can be obtained via *spin diffusion* from surrounding, carbon-bound protons (only BEST). The process is based on cross relaxation and, therefore, its significance increases for larger,

⁹⁴ In Figure 3.14 (b) the determined average value for the linewidth (9.1 Hz) is marginally smaller compared to the spectrum illustrated in Figure 3.12 (c) where a value of 8.8 Hz is examined. Since the former spectrum is acquired with lower resolution in the indirect dimension (64 complex points) certain deviations are expected which could lead to smaller changes also in the linewidths determined by the semi-automatic python program.

⁹⁵ In BEST sequences this is achieved by the consistent use of band-selective pulses acting only on amide protons (observed spins) while other spins remain in the equilibrium state and act as reservoir.

slow-tumbling molecules (Section 1.8). Forth, a transfer of magnetization can also be induced by the application of planar or isotropic mixing where actively a contact between acquired spins and the reservoir is created.^[182,183,324] For amide protons, the second and third buildup process have both shown to lead to a considerable decrease of the effective longitudinal relaxation time which allows the acquisition of scans at much higher rates.^[313–315,325]

The situation is, however, more complicated if a pure shift acquisition for high resolution in the direct dimension is used. Pulses are applied during acquisition and the use of pure shift commonly indicates a *different* experimental focus – the informative value of a direct comparison to sensitivity-trimmed experiments is, therefore, questionable.⁹⁶ Still, in terms of sensitivity certain aspects have to be reconsidered. First, and most importantly, high resolution *requires* long acquisition times and, in turn, longer experimental time. Second, for the application of CPD during a long acquisition also a longer interscan delay is *advisable* to prevent hardware damage. Third, repetitive pulsing might interfere with the magnetization buildup from longitudinal relaxation of amide protons during acquisition (further analyzed below). Forth, if solvent suppression is achieved without the saturation of the water reservoir, exchange of amide protons can still lead to magnetization buildup. If, on the other hand, amide protons are practically *not* in exchange with water no enhancement in sensitivity is to be expected.⁹⁷ Fifth, and only important with respect to the BEST approach, all carbon-bound protons are flipped repeatedly in order to obtain homonuclear decoupling. Since these protons constitute one part of the spin reservoir the BEST approach is certainly not fully exploitable. Still, one could speculate that for an even number of *J*-refocusing elements it might be possible to retain the effect partially during the relaxation recovery delay – a more detailed discussion on the BEST approach in combination with pure shift is beyond the scope of the present dissertation and no further investigation shall be given.

In the present section a rough estimate for the achievable sensitivity from *high resolution* pure shift experiments shall be elaborated using ubiquitin and the here proposed ¹³C-BIRD-based real-time acquisition. Despite the fact that the water reservoir is not saturated, in the present case an effective magnetization transfer is not expected. This is based on the fact that, under given conditions, amide protons of ubiquitin are considered not to be in solvent exchange.^[316,317] Still, an increase in sensitivity can be obtained from collapsing multiplets.

In order to investigate on the achievable sensitivity obtained from the ¹³C-BIRD-based pure shift acquisition, the above considered FHSQC and BEST-TROSY spectra (of Figure 3.12) shall be further examined. This way, the maximal intensity of every peak was extracted by a self-written python program and plotted in correlation plots. These plots are shown in Figure 3.15 (a) and (b) for FHSQC and BEST-TROSY, respectively, and a considerable increase in sensitivity is found for most of the residues. The gain is based on the collapse of multiplets and average values (illustrated by red dashed lines) are increased by 23% (FHSQC) and 25% (BEST-TROSY) – in both cases a rather usual relaxation recovery delay of $\tau_r = 1.0$ s was set. In case that one of the above mentioned processes (e.g. solvent exchange) leads to efficient transfer to amide protons a reduced recovery delay would be possible. It is, however, expected that repetitive pulsing during the pure shift acquisition interferes with the magnetization buildup from longitudinal relaxation. With this regard, the acquisition time (of length ~ 200 -300 ms) might not or only partially contribute to magnetization recovery and, thus, lead to a certain penalty with respect to sensitivity compared to standard acquisition. In order to elucidate the recovery process during the interscan delay (τ_r) multiple FHSQC spectra with and without pure shift acquisition were acquired for ubiquitin (i.e. no solvent exchange expected) in which the recovery delay τ_r was varied in the range of 0.8 s to 1.5 s. From these spectra the maximum peak intensities were extracted (in analogy to Figure 3.15)

^[324] J. Becker and B. Luy. *Magnetic Resonance in Chemistry* **2015**, *53*, 878–885.

^[325] Z. Solyom et al. *Journal of Biomolecular NMR* **2013**, *55*, 311–321.

⁹⁶ In contrast to the experiments presented in this section, commonly, resolution in the direct dimension is not in the main focus of BEST-type sequences. In order to obtain highest possible sensitivity per time unit an acquisition of only ~ 70 -80 ms is typically chosen in combination with a short relaxation recovery delay of ~ 0.2 s. Given these conditions the potential of pure shift is, clearly, far from being reached and in order to obtain high resolution, acquisition parameters have to be adapted appropriately.

⁹⁷ The absence of solvent exchange also implies that there is no consequence from the saturation of water.

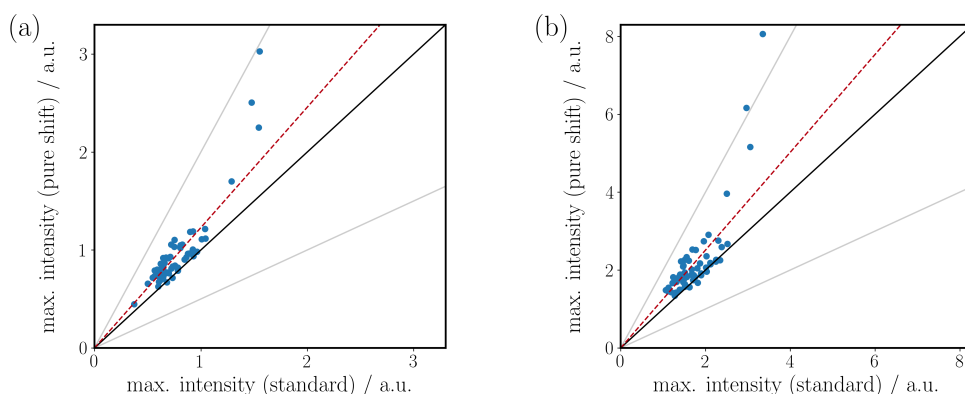


Figure 3.15: The maximum intensities of amide protons in ubiquitin using a standard and pure shift acquisition are compared in a correlation plot for the FHSQC (a) and BEST-TROSY (b) – a quadratic sine apodization is used. Average values are indicated by red dashed lines which for the pure shift FHSQC (a) corresponds to an increase in sensitivity of 23% while for the pure shift BEST-TROSY (b) an increase of 25% is obtained ($\tau_r = 1.0$ s).

and their average values fitted to a mono-exponential recovery function of the following form:

$$f(I_0, R_1, A, \tau_r) = I_0 \cdot (1 - A \cdot \exp\{-R_1 \cdot \tau_r\}) \quad (3.2.1)$$

where I_0 is the average value (of maximal intensities) obtained for $\tau_r \rightarrow \infty$, R_1 is the average longitudinal relaxation rate and A is a scaling factor. While for standard acquisition the parameter A can be calculated from the relaxation rate (R_1) and the acquisition time ($\tau_{\text{acq.}}$) with $A = \exp\{-R_1 \cdot \tau_{\text{acq.}}\}$, for the pure shift data A is determined by the fit. The parameter space was further decreased by a simultaneous fit of both data sets using the same average relaxation rate R_1 . In Figure 3.16 standard (blue) and pure shift data (red) is plotted together with the resulting exponential recovery fit (Equation 3.2.1) against the recovery delay τ_r . According to the fit the value of I_0 can be increased by 32% if the ^{13}C -BIRD-based pure shift acquisition is applied (indicated by blue and red dashed lines). Furthermore, it was deduced from the fitted value of A that $\sim 20\%$ of the magnetization could be restored during standard acquisition, while a considerably lower value of $\sim 8\%$ is found using pure shift. However, for a recovery delay of $\tau_r = 0.25$ s the pure shift penalty is already compensated from the collapse of multiplets and higher sensitivity is expected. Clearly, the given fit can be considered only a *rough* estimate and a wider range of experimental data points would improve its explanatory power. Yet, the reduction of τ_r to shorter values is not feasible without jeopardizing the probe (^{15}N -CPD was active during 214 ms acquisition) and longer values come at the delicate cost of experimental time. Conclusively one can still derive that from repetitive pulsing during acquisition no critical relaxation penalty is expected and, for ubiquitin, the increase in sensitivity from collapsing multiplets predominates for $\tau_r > 0.25$ s. Furthermore, it should be noted that, in some cases, artificial noise introduced from incomplete water suppression can deplete the gain in signal-to-noise – which is a general issue of homonuclear decoupling in aqueous solutions.^[275] It is, therefore, *crucial* to optimize water suppression as described in the Appendix 5.3.1. In general, for the ^{13}C -BIRD-based pure shift acquisition similar noise levels are encountered compared to other real-time methods (see Figure 3.10) and a further quantification is illustrated in Figure 5.8.

Although a closer investigation on the recovery process for BEST-TROSY is not given it shall be stated that, in my hands, I find a delay of $\tau_r \geq 0.5$ s had to be used for *ubiquitin*⁹⁸ in order to obtain an *average* intensity that is slightly lower (6%) compared to standard BEST-TROSY without pure shift acquisition (shown in Appendix 5.3.4).

⁹⁸ A shorter delay of $\tau_r \geq 0.2$ s can be used if amide protons are in slow exchange as shown below in Section 3.2.4.

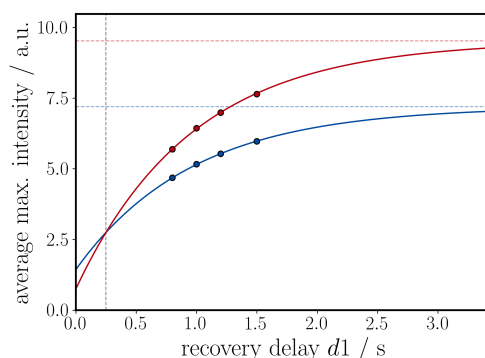


Figure 3.16: Average maximal intensities are fitted to a mono-exponential recovery function using an FHSQC with standard (blue) and ^{13}C -BIRD-based pure shift acquisition (red) for ubiquitin. For all experiments 2048 complex points were acquired in 214 ms with $n = 6$ chunks and $\tau_c = 17.8$ ms. While horizontal dashed lines mark the values for I_0 with (red) and without pure shift (blue) the vertical line (gray) indicates the crossing of both recovery functions. An average relaxation rate of $R_1 \approx 1 \text{ s}^{-1}$ is determined for ubiquitin.

3.2.4 Application to Intrinsically Disordered Proteins

With respect to various properties intrinsically disordered proteins behave much different to globular proteins and certain aspects of previous discussions have to be re-considered. Due to the high flexibility of IDPs, molecular motion occurs on a shorter timescale and longer transverse relaxation rates are expected (Section 1.8). Furthermore, the unstructured nature causes the protein to adopt a variety of conformations where individual residues are subject to a similar flux of electronic environments and chemical shifts are encountered closer to random coil values. While longer transverse relaxation times are beneficial for the use of real-time homonuclear decoupling, lower signal dispersion, on the other hand, represents an obstacle that can very well be overcome by pure shift experiments. However, the higher flexibility also causes the protein backbone to be further exposed to the solvent and enhanced proton exchange rates are uniformly encountered in IDPs.^[326–329] For the acquisition of amide protons, such solvent exchange can lead to linebroadening (if in slow exchange) or even cause the signal to be entirely swallowed by the large water resonance (if in fast exchange). In order to (partially) suppress exchange processes the pH, temperature or both^[317] are commonly lowered to a tolerable extent where no major structural change is expected.⁹⁹ Since IDPs are well exposed to water, amide protons are commonly still in slow exchange and an additional transverse signal decay is induced by the solvent exchange rate (in the slow regime). Although exchange prevents the optimal achievable linewidth it brings the amide protons in contact with the water spin reservoir which allows an effective transfer for a fast recovery of amide proton magnetization.^[313] In such a case, obviously, water must *not* be saturated which otherwise would lead to severe signal loss.

The application of a ^{13}C -BIRD-based pure shift acquisition in BEST-TROSY is further tested on the disordered transactivation domain of tumor suppression p53 protein (p53TAD^{1–60}). The full spectra using standard and pure shift acquisition are shown in Figure 3.17 where, under comparable conditions, real-time decoupling leads to considerably narrower lines and various overlapping peaks are resolved. It is noteworthy that the linewidth is reduced to a point where a good shim of a few Hertz becomes decisive. Furthermore, a relaxation recovery delay of only $\tau_r = 0.2 \text{ s}$ was used while intensities are still comparable

^[326] H. Roder, G. Wagner and K. Wuethrich. *Biochemistry* **1985**, *24*, 7407–7411.

^[327] A. D. Robertson and R. L. Baldwin. *Biochemistry* **1991**, *30*, 9907–9914.

^[328] Y. Pérez et al. *Journal of Molecular Biology* **2009**, *391*, 136–148.

^[329] M. G. Murralli et al. *Journal of Biomolecular NMR* **2018**, *70*, 167–175.

⁹⁹ In Section 3.4 an approach for the examination of IDPs shall be introduced which is practically independent of pH and temperature. By this means the IDP can be investigated under near-physiological conditions.

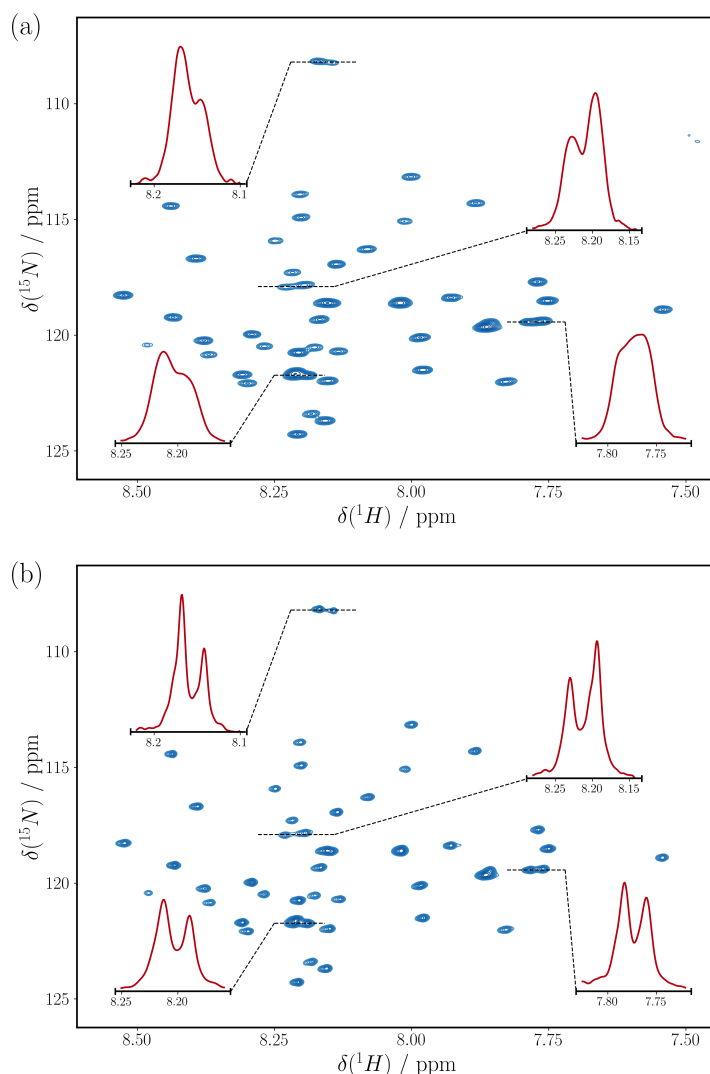


Figure 3.17: BEST-TROSY spectra of p53TAD are compared for standard (a) and ^{13}C -BIRD real-time pure shift acquisition (b) recorded at 700 MHz using a liquid nitrogen cooled prodigy probe. In both cases 2048×128 complex points are acquired corresponding to acquisition times of 244 ms and 64 ms, respectively, and a relaxation recovery delay of $\tau_r = 0.2$ s is used. For the pure shift acquisition a chunk length of $\tau_c = 15.2$ ms is chosen which relates to $n = 8$ chunks.

to the standard BEST-TROSY. A statistical analysis with respect to resolution is undertaken by means of a correlation plot where the signal width of respective peaks are extracted for the standard and pure shift acquisition and plotted against each other. The result is illustrated in Figure 3.18 (a) where average values are indicated by red dashed lines and resolution is on average doubled (increase by 101%). A comparable plot with respect to sensitivity is illustrated in Figure 3.18 (b) where the maximal intensities of signals acquired with standard and pure shift acquisition are correlated. Despite the fact that a short recovery delay of $\tau_r = 0.2$ s is used, on average an increase in sensitivity of $\sim 11\%$ can be found.

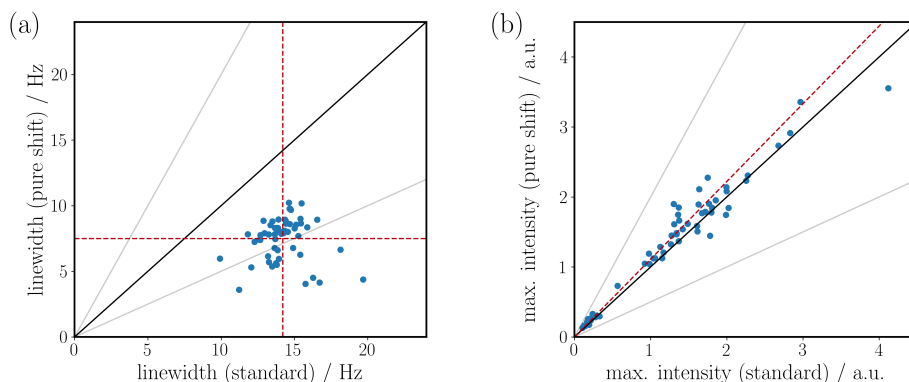


Figure 3.18: Signal widths (a) and maximum intensities (b) of amide protons in p53TAD using a standard and pure shift acquisition are compared in a correlation plot for a BEST-TROSY (with $\tau_r = 0.2$ s) – in (a) no and in (b) a quadratic sine apodization is used. Average values are indicated by red dashed lines which in (a) are 14.2 Hz (standard) and 7.5 Hz (pure shift) and in (b) an average increase in signal intensity by $\sim 11\%$ is obtained.

3.2.5 Conclusion

It could be shown that the presented ^{13}C -BIRD-based real-time acquisition of amide protons provides access to pure shift experiments where homo- and small heteronuclear couplings are suppressed at low power. Long acquisition times of 200 ms and more are achieved and for both, ubiquitin and p53TAD, resolution is doubled with only little or even no sensitivity penalty compared to common fast experiments. Despite the fact that repetitive pulsing during acquisition hinders the recovery of amide proton magnetization it was elaborated that for ubiquitin the average increase in sensitivity from collapsing multiplets outweighs the relaxation penalty already after an interscan delay of $\tau_r \geq 0.25$ s. Furthermore, the saturation of the water reservoir can be avoided and a faster recovery of amide protons is expected if they are in solvent exchange. If sample conditions are chosen in a way that amide protons are practically not in solvent exchange the preservation of the water reservoir is without consequence and the choice of band-selective pulses for J -refocusing might be preferential in terms of resolution. In such a case it is proposed that the suppression of long-range heteronuclear couplings is achieved by a broadband ^{13}C pulse applied simultaneously to the band-selective pulse and limitations to the acquisition time due to ^{13}C -CPD can be avoided. Still, the suppression of homonuclear residual dipolar couplings to aromatic protons is, in contrast to the ^{13}C -BIRD-based pure shift acquisition, not achieved from band-selective pulses.^[304]

3.3 BIRD-Based Real-Time Pure Shift Acquisition of Uniformly Isotope-Labeled Samples

In the present section a novel selective element for the real-time pure shift acquisition of uniformly isotope-labeled samples shall be introduced. It is based on a special BIRD filter which provides a band-selective refocusing via X-nuclei (BASEREX) and is best suitable for the application in heteronuclear correlation experiments. The pulse sequence shall be discussed in detail using numerical simulations and exemplary spectra are shown for uniformly ^{13}C -labeled glucose and a uniformly $^{13}\text{C},^{15}\text{N}$ -labeled amino acid mixture. In the following Section 3.4 the acquisition sequence shall further be used in a selective-HaCa-HSQC where pure shift correlations are obtained in both dimensions.^[11]

3.3.1 Pulse Sequence

In general, BIRD filters induce a spin inversion (π -rotation) from a bilinear operator that originates from a rather large $^1J_{\text{XH}}$ -coupling and decoupling is achieved if only few, *active* protons are bound to the low-abundant X-nuclei. In uniformly X-labeled samples, on the other hand, the $^1J_{\text{XH}}$ -coupling evolves for any proton-X-pair and the BIRD filter leads to a non-selective inversion – decoupling is not achieved. In the following approach the BIRD filter is made X-band-selective and only protons bound to selected X-nuclei experience a bilinear rotation due to the $^1J_{\text{XH}}$ -coupling. Hence, the BIRD filter transfers the band-selectivity of the X-nuclei to attached protons and the large signal dispersion of X can be exploited as shown experimentally in the course of the present section. By this means real-time decoupling is obtained *only* for a selected X-band – yet, in the field of biomolecular NMR, where the use of uniformly labeled samples is by far no curiosity, many experiments are anyway based on very distinct and elaborated coherence transfers and, in general, an inherent selection of spins is already established.

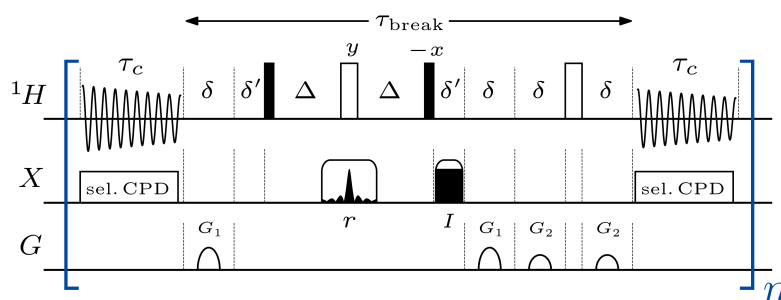


Figure 3.19: The pulse sequence for the real-time pure shift acquisition using band-selective refocusing on X-nuclei (BASEREX) is illustrated. The FID is n -times interrupted for the length of $\tau_{\text{break}} \approx 9.4$ ms during which the coupling to passive spins is refocused. Typical chunk lengths τ_c are in the range of 10 – 15 ms. Filled black and open white bars correspond to 90° and 180° pulses, respectively, with phases being x if not annotated differently. A band-selective RE-BURP^[195] refocusing pulse (r) of length τ_r and a broadband BIP^[188] or BIBOP^[189,190] inversion pulse (I) are used in the X-band-selective BIRD^d filter – the inversion pulse length is compensated by the delay δ' . For longer acquisition times, composite pulse decoupling (WALTZ16^[144]) is applied only on the narrow band that is covered by the refocusing pulse (r) resulting in a ~ 16 times lower CPD-power. The BIRD delay is set according to the $^1J_{\text{CH}}$ coupling with $\Delta = 1/(2^1J_{\text{CH}}) - 0.95 \cdot \tau_r$ and gradients of length 0.3 ms are applied during $\delta = 0.5$ ms with a relative strength of $G_1 \approx 5\%$ and $G_2 \approx 3\%$.

In Figure 3.19 the X-band-selective BIRD^d filter is used in a pure shift acquisition for uniformly X-labeled samples where the FID is interrupted n -times and multiple chunks are acquired in real-time as discussed in Section 3.1 and literature.^[295,296] In between chunks homo- and long-range heteronuclear couplings to passive spins are refocused by the X-selective BIRD filter while, in theory, active spins experience no effective rotation – a condensed illustration is again given in Figure 3.20 and further discussed below. Such an effect is achieved by the use of an X-band-selective pulse within the proposed BIRD filter

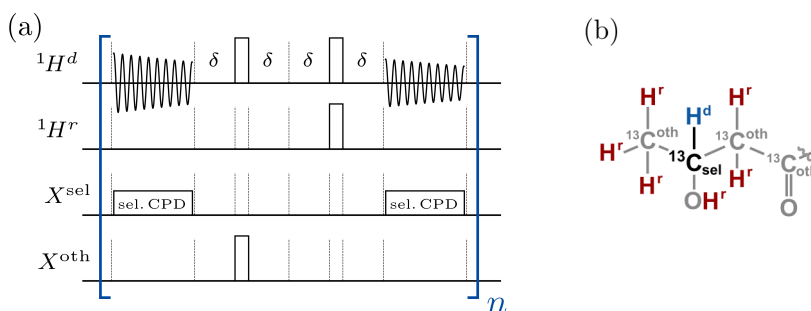


Figure 3.20: Effective rotations of the BASEREX acquisition (Figure 3.19) are illustrated in (a). X-nuclei that are inverted by the band-selective pulse and their directly attached protons are denoted X^{sel} and ${}^1\text{H}^d$, respectively. Heteronuclei outside the band are referred to as X^{oth} and the X^{oth} -bound remote protons are ${}^1\text{H}^r$. In (b) the considered groups of X-nuclei (X^{sel} in black and X^{oth} in gray) and attached protons (${}^1\text{H}^d$ in blue and ${}^1\text{H}^r$ in red) are illustrated in an exemplary uniformly ${}^{13}\text{C}$ -labeled molecule where X corresponds to ${}^{13}\text{C}$.

and *only* for the selected proton-X-pair the large ${}^1J_{\text{XH}}$ -coupling can evolve. By this means, only *active* protons bound to *selected* X-nuclei are subject to the bilinear rotation from the coupling and, hence, can be decoupled from surrounding *passive* protons that are bound to *non-selected* X-nuclei outside the considered band. The choice of a suitable band-selective pulse within the BIRD filter turns out to be crucial for optimal results. In Figure 3.19 the RE-BURP pulse is used which has the formidable property to allow coupling evolution during $\sim 95\%$ of the full pulse length (investigated in Section 2.4.5) and the BIRD delay (Δ) can be set *precisely* to the required value (with $\Delta = 1/(2{}^1J_{\text{CH}}) - 0.95 \cdot \tau_r$). Furthermore, the application of the RE-BURP pulse does not lead to a significant increase of the acquisition break (τ_{break}) and the artificial decay due to transverse relaxation during τ_{break} is barely enhanced even if the RE-BURP occupies the full BIRD delay (line broadening from real-time chunked acquisition is further discussed in Section 3.1.5). On the other hand, a selective pulse that allows only little coupling evolution (e.g. the Q3 discussed in Section 2.4.4) can be advantageous for a very narrow X-band which in turn might require pulse lengths longer than 2Δ . As for other real-time acquisition sequences, the chunk length τ_c depends on the multiplet width of active spins and, commonly, lays in the range of 10-20 ms.¹⁰⁰ Since active spins are situated *only* in the band covered by the selective pulse, the suppression of ${}^1J_{\text{XH}}$ -couplings is achieved from X-CPD at much lower power. Therefore, high resolution in biomolecular samples comprising long acquisition times of more than 200 ms are securely possible.

A schematic illustration of the acquisition sequence is shown in Figure 3.20 (a) where the applied elements for spin inversion are represented by simplified 180° pulses to allow for a condensed explanation. Since effective rotations of the band-selective pulse *and* the BIRD filter depends strongly on the considered spin a certain discrimination of spin groups has to be done. Selected X-nuclei within the band of the considered selective pulse shall further be denoted X^{sel} while all others are referred to as X^{oth} . In analogy to standard BIRD filters, protons directly bound to *selected* X-nuclei (X^{sel}) are labeled ${}^1\text{H}^d$ while all others are named ${}^1\text{H}^r$. The different spin groups are assigned to separated (fictitious) channels in Figure 3.20 (a) and shall again be illustrated in an exemplary molecule in Figure 3.20 (b). The acquired protons (${}^1\text{H}^d$) are inverted twice and chemical shift evolution is refocused – effectively, the acquisition break is without consequence (neglecting relaxation). Passive, remote protons, on the other hand, are flipped only once and the homonuclear ${}^1\text{H}^d$ - ${}^1\text{H}^r$ -couplings can be suppressed in a chunk-like manner. Note, also X-nuclei outside the selected band (X^{oth}) are inverted once and, therefore, long-range heteronuclear ${}^1\text{H}^d$ - X^{oth} -couplings can likewise be suppressed in the chunked acquisition. The only remaining coupling of acquired protons (${}^1\text{H}^d$) in the considered system is given by the ${}^1J_{\text{XH}}$ -coupling to selected X-nuclei (X^{sel}) which can simply be suppressed by the application of composite pulse decoupling at low power acting only on the narrow band of the selective pulse. For optimal results it is noteworthy

¹⁰⁰ As mentioned in the previous section longer chunk lengths decreases artificial linebroadening (Section 3.1.5) and the resulting stronger artifacts can be suppressed using methods discussed in literature.^[305,307]

that lower power increases the pulse length and, hence, the cycle length of composite pulse decoupling – in this respect a shorter CPD-cycle turned out superior (e.g. WALTZ compared to GARP).

The effect of the above proposed real-time chunked acquisition (Figure 3.19) is illustrated using numerical simulations of various hydrocarbon compounds (^{13}C corresponding to the X-nuclei) and further compared to other BIRD filters applied in pure shift sequences. The spectra for standard, *non*-selective $\text{BIRD}^{\text{d,X}}$ and BIRD^{d} are shown in Figure 3.21 (a) and spin systems at ^{13}C natural abundance and with uniformly ^{13}C -labeling are assumed for the *in silico* investigation. As shown in the left and middle column, homonuclear decoupling is achieved from standard BIRD-based pure shift acquisitions for molecules at ^{13}C natural abundance. Yet, the standard $\text{BIRD}^{\text{d,X}}$ filter exhibits stronger artifacts in all cases which is based on the fact that the large $^1J_{\text{XH}}$ -coupling is not refocused during a period of 2δ and the respective BIRD^{d} filter turns out to be superior. Note that geminal couplings between protons being bound to the same carbon (middle column) can not be suppressed from BIRD filters and signals are still split into doublets. For the real-time pure shift acquisition of *uniformly* isotope-labeled samples, however, both standard BIRD filters fail as illustrated in the right column. As discussed above, a potential solution is provided by X-band-selective BIRD filters where only selected ^{13}C -nuclei (indicated by red dashed boxes) are inverted and for attached protons homonuclear decoupling can be achieved. Corresponding spectra from numerical simulations are shown in Figure 3.21 (b) where X-selective $\text{BIRD}^{\text{d,X}}$ and BIRD^{d} filters are compared for uniformly ^{13}C -labeled samples. The illustrated spectra consist only of signals of protons being attached to selected carbons and homonuclear couplings are chunk-wise suppressed. Again, the X-selective $\text{BIRD}^{\text{d,X}}$ exhibits stronger artifacts compared to the equivalent BIRD^{d} filter which is due to the evolution of the large $^1J_{\text{XH}}$ -coupling during 2δ . Furthermore, signals in the upper row of Figure 3.21 (b) are all split by a small coupling of ~ 3 Hz which corresponds to the long-range $^2J_{\text{CH}}$ -coupling to the neighboring carbon.¹⁰¹ On the other hand, using the X-selective BIRD^{d} filter not only homonuclear but also long-range heteronuclear couplings are suppressed in the chunked acquisition and sharper lines are obtained as shall be verified experimentally in the following. Note, heteronuclear couplings can also contribute to chunking artifacts and, hence, chunk lengths (τ_c) have to be adapted appropriately. As for standard BIRD filters, protons being bound to the same carbon are still split into doublets due to the geminal $^2J_{\text{HH}}$ -coupling. In the right column of Figure 3.21 (b) a strongly coupled CH_2 -group is assumed and second order effects result in the expected distribution of signal intensities (roofing). Comparable results for the real-time pure shift acquisition using an X-selective BIRD^{d} and $\text{BIRD}^{\text{d,X}}$ are also found experimentally and further investigations are discussed in the following.

¹⁰¹ In order to enable long acquisition times, the 1^{13}C -CPD bandwidth is reduced to roughly the band covered by the selective pulse and long-range heteronuclear couplings are not suppressed from CPD.

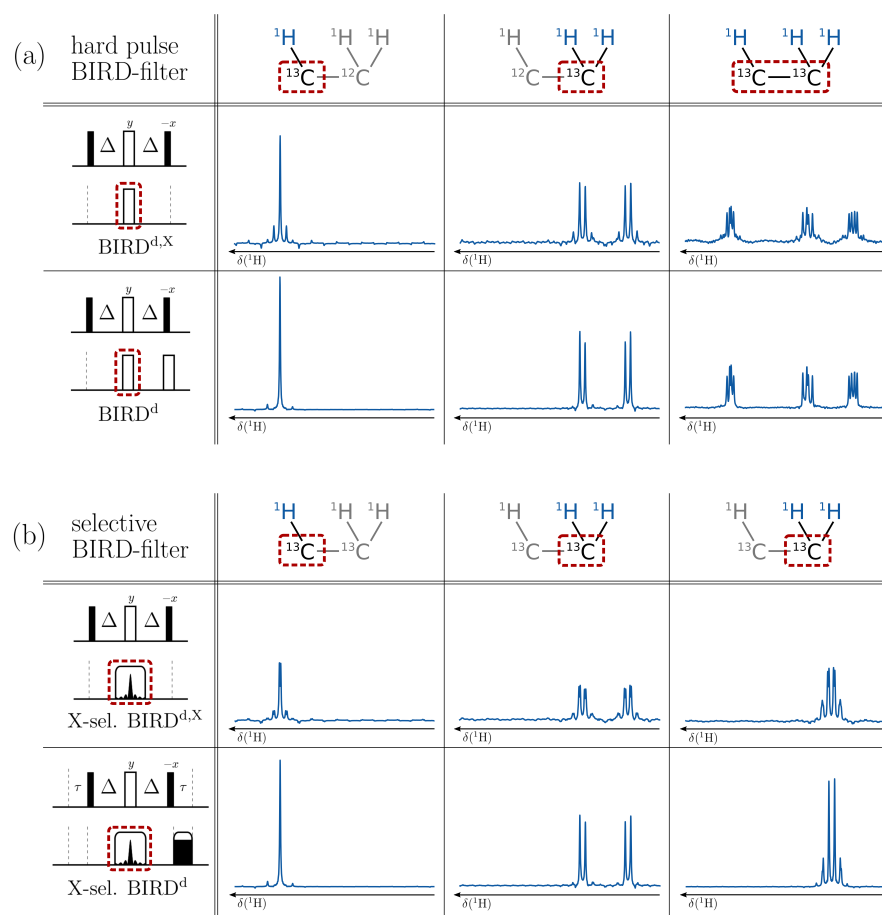


Figure 3.21: The real-time pure shift acquisition using standard (a) and X-selective BIRD-filters (b) are investigated using numerical simulations of various hydrocarbon spin systems. Red dashed boxes indicate the ^{13}C nuclei on which the ^{13}C -pulse acts. In (a) standard BIRD-filters achieve broadband homonuclear decoupling for ^{13}C at low abundance (left and middle column) while it fails for uniformly ^{13}C -labeled compounds (right column). Note, the $\text{BIRD}^{\text{d},\text{X}}$ filter allows the large $^1J_{\text{CH}}$ coupling to evolve during 2δ leading to large in-phase artifacts (with $\delta = 1$ ms which is twice the experimental value to further emphasize the effect). In (b) band-selective pulses act on selected ^{13}C nuclei and homonuclear decoupling is achieved also for uniformly ^{13}C -labeled samples. In contrast to (a) the use of a BIRD^{d} filter in (b) does not only prevent the evolution of the large $^1J_{\text{CH}}$ coupling, it further suppresses numerous long-range $^1H^{\text{d}}\text{-X}^{\text{oth}}$ couplings. A strongly coupled CH_2 group is considered in the right most column. A chunk length of $\tau_c = 18.1$ ms was used and couplings were set according to: $^1J_{\text{CH}} = 145$ Hz, $^1J_{\text{CC}} = 40$ Hz, $^2J_{\text{HH}} = -11$ Hz, $^2J_{\text{CH}} = -3$ Hz and $^3J_{\text{HH}} = 5$ and 8 Hz.

3.3.2 Experimental

As noted above the real-time pure shift acquisition using an X-band-selective BIRD filter is tailored for the application in heteronuclear correlation experiments. Following results, comprising mainly 1D spectra, should, hence, be considered rather a proof of principle and further, application-oriented examples are given in the following Section 3.4. Figure 3.22 illustrates the standard and pure shift 1D spectra of the anomeric centers of uniformly ^{13}C -labeled α - and β -Glucose which are well-separated from other resonances and a straight-forward experimental setup for a first proof is, hence, possible. The effect of a BIRD delay mis-set is examined and all proton signals outside the considered X-band are saturated from field gradients before acquisition in order to suppress signals of passive spins. A bandwidth of ~ 800 Hz is selected on ^{13}C by a RE-BURP corresponding to a pulse length of 5 ms and the BIRD delay was calculated from various $^1J_{\text{CH}}$ -values of: 125 Hz, 145 Hz, 160 Hz, 170 Hz, 180 Hz and 200 Hz. As shown in Figure 3.22 (b), the quality of pure shift spectra exhibits a clear dependency on the $^1J_{\text{CH}}$ -value used for the calculation of Δ (increasing values of $^1J_{\text{CH}}$ from left to right) where black spectra are shifted for better visibility. Obviously, best results are obtained for values closest to the actual coupling size which is 161 Hz and 170 for α - (5.17 ppm) and β -Glucose (4.58 ppm), respectively. On the other hand, a delay mis-set not only causes a reduction in intensity but also broader lines and the illustrated spectra further pronounce the importance of a detailed examination of coupling evolution during shaped pulses. From the data shown in Figure 3.22 (b) it is evident that pure shift spectra can be obtained from the proposed selective element and in the following a more complex sample shall be investigated.

As a first step towards the application to biomolecules, e.g. proteins, a uniformly ^{13}C , ^{15}N -labeled amino acid mixture in D_2O was used in order to elucidate the nature of X-band-selectivity and, further, the effect of X-selective $\text{BIRD}^{\text{d,X}}$ and BIRD^{d} filters. In Figure 3.23 two narrow bands are selected in a spectral area where mainly $\text{C}\alpha$ -resonances are situated and resulting 1D spectra using standard and different chunked acquisitions are compared. Selected areas are indicated by boxes in the CT-HSQC (Figure 3.23 (e)) where hashed borders correspond to the transition width of the X-band-selective pulse. Compared to

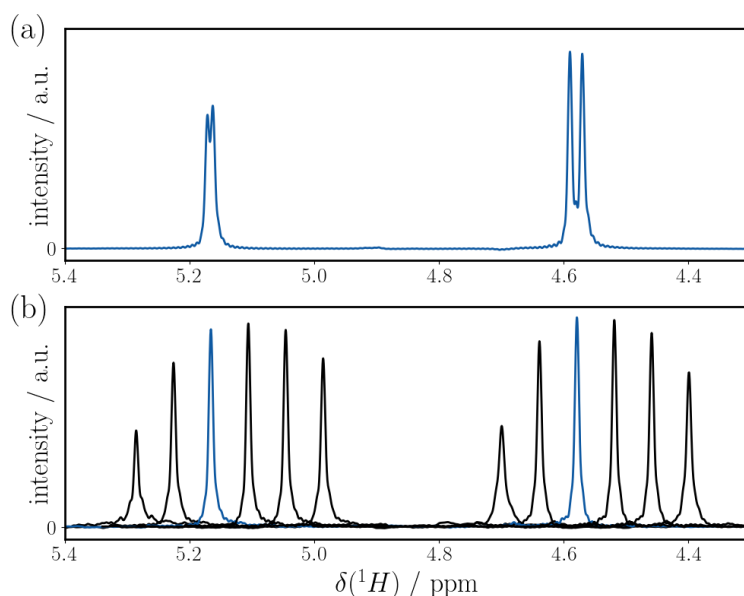


Figure 3.22: Standard (a) and BASEREX acquisition for homo- and heteronuclear decoupling (b) is tested on the anomeric centers of α - and β -Glucose in D_2O . Chunk length in (b) is set to $\tau_c = 12.2$ ms and BIRD delays (with $\Delta = 1/(2^1J_{\text{CH}}) - \tau_r$) are varied with $^1J_{\text{CH}}$ from left to right according to: 125 Hz, 145 Hz, 160 Hz, 170 Hz, 180 Hz and 200 Hz. The 1D spectrum in blue corresponds to $^1J_{\text{CH}} = 160$ Hz while 1Ds for other $^1J_{\text{CH}}$ -values are plotted in black and shifted for better visibility. For α - (5.17 ppm) and β -Glucose (4.58 ppm) the $^1J_{\text{CH}}$ coupling was determined to be 161 Hz and 170 Hz, respectively.

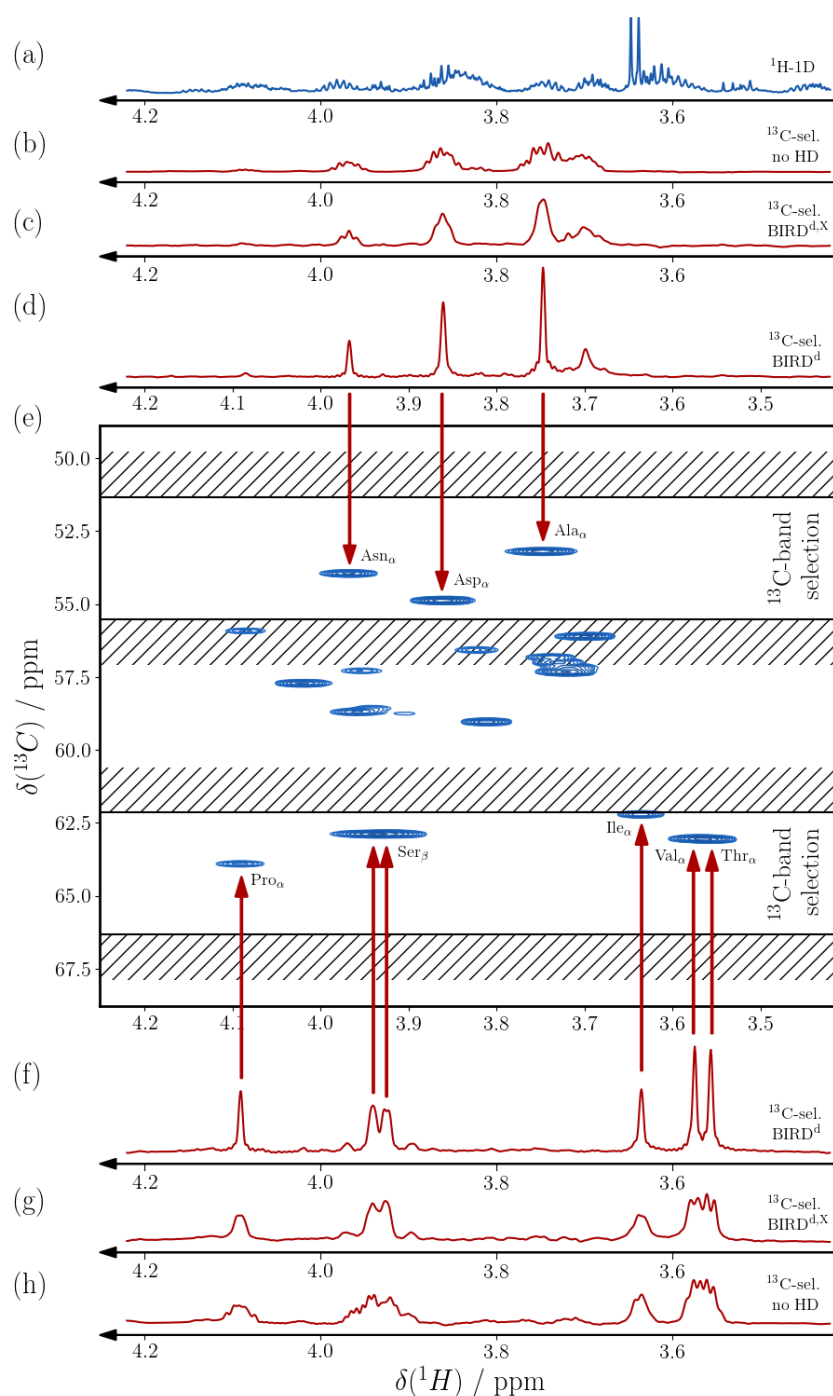


Figure 3.23: The BASEREX acquisition is tested on uniformly ^{13}C , ^{15}N -labeled amino acid mixture dissolved in D_2O . A standard proton 1D (a) is illustrated in black together with various 1Ds in red (b-d and f-h) which originate from two ^{13}C -band-selections – the selected bands are indicated in a standard CT-HSQC of the $\text{H}\alpha$, $\text{C}\alpha$ -region (e). For ^{13}C -band-selected 1Ds, standard (no HD) and real-time decoupled acquisition using $\text{BIRD}^{\text{d,X}}$ and BIRD^{d} are compared as indicated on the right (a similar comparison is illustrated for numerical simulations in Figure 3.21). While for the standard 1D (a) 8192 complex points were acquired corresponding to a resolution of 0.88 Hz in ^{13}C -band-selected 1Ds 2048 complex points were recorded with a resolution of 3.51 Hz. The chunk length was set to $\tau_c = 11.8$ ms and a RE-BURP pulse of 6 ms length was applied within the BIRD filter. All 1Ds were processed using line broadening of 0.9 Hz and linear prediction.

the proton-1D in Figure 3.23 (a) the spectra of selected bands are considerably simplified where few signals within the hashed transition areas persist partially. While spectra from standard acquisition (Figure 3.23 (b) and (h)) still exhibit broad multiplets, these can be suppressed to some extent in the real-time decoupled spectra using an X-selective BIRD^{d,X} filter (Figure 3.23 (c) and (g)). Still, as already examined from numerical simulations (Figure 3.21 (b)), complete pure shift spectra are obtained only if *additionally* long-range heteronuclear couplings are suppressed. This is achieved by the pure shift acquisition being based on a X-selective BIRD^d filter and a complete collapse of multiplets is obtained resulting in a remarkable increase in resolution and sensitivity (Figure 3.23 (d) and (f)). The overlapping H α signals of valine and threonine are nicely resolved which for any other shown case are hardly separable. Only for serine the geminal $^2J_{\text{HH}}$ coupling of the two β -protons can not be suppressed and a further influence from strong coupling is expected (as simulated in Figure 3.21 (b)).

3.3.3 Conclusion

The proposed real-time chunked acquisition using an X-band-selective BIRD^d filter has proven to be an effective approach for the suppression of homo- and furthermore long-range heteronuclear couplings. While, so far, the utilization of standard BIRD filters was limited to samples at low abundance of the heteronucleus, the X-band-selective BIRD is tailored for the application to uniformly isotope-labeled samples. Up to now, the only promising real-time pure shift approaches for isotope-enriched samples were based on spatially selective (Zangger and Sterk^[276,302]) or proton-band-selective pulses (termed HOBS^[303] or BASHD^[304]). While the former results in *broadband* homonuclear decoupling, it inherently comes with a severe loss in sensitivity and only the latter would lead to a comparable result as obtained from the X-band-selective BIRD. Although heteronuclear dispersion typically promises enhanced selectivity compared to proton-band-selective pulses, in principle, both approaches offer orthogonal ways and the method of choice strongly depends on the considered sample. Still, the chunked acquisition using X-selective BIRD inherently decouples long-range heteronuclear couplings, which exert a severe influence on resolution and sensitivity as demonstrated in Figure 3.23 (c) and (g). This way, low power CPD can be used acting only the considered X-band¹⁰² and long acquisition times for high resolution are securely accessible without the risk of damaging the probe. Furthermore, the present development confirms that the elucidation of coupling evolution during shaped pulses is a crucial step for the design of optimized pulse sequences (Section 2.4). In the following section, the proposed pure shift acquisition shall be used in a selective-H α ,C α -HSQC that incorporates C α -band-selective homonuclear decoupling and the combination of both decoupling schemes offers pure shift correlations for highest resolution in both dimensions.

¹⁰² As already stated in the previous section, the suppression of long-range heteronuclear couplings could also for HOBS or BASHD be implemented in a chunk-like way circumventing power intensive CPD.^[304] Such decoupling could be achieved by an additional broadband pulse on the X-channel during the acquisition break refocusing heteronuclear couplings.

biomolecules are much narrower compared to globular proteins, it is crucial to realize that the major effect on the signal width can be ascribed to numerous homo- and heteronuclear couplings as illustrated for an exemplary ^{13}C , ^{15}N -labeled protein in Figure 3.24. In the here proposed selective $\text{H}\alpha$, $\text{C}\alpha$ -HSQC the considered couplings are collapsed in both dimensions without limiting the acquisition time and a remarkable increase in both resolution and sensitivity is obtained. The approach is generally applicable also for experiments with higher dimensionality and further allows the detection of low concentrated substrates or minor conformations at near-physiological conditions and high resolution.

3.4.1 Pulse Sequence

For the detection of $\text{H}\alpha$, $\text{C}\alpha$ -correlations in uniformly ^{13}C -labeled samples, homonuclear decoupling has to be applied in the indirect dimension in order to suppress dispersive anti-phase components originating from large homonuclear $^1J_{\text{C},\text{C}}$ couplings. This is usually achieved by a so-called constant time (CT) period, which is set to an n -fold multiple of half the coupling period ($\delta_{\text{CT}} = n/2 \cdot ^1J_{\text{C},\text{C}}$) and chemical shift evolution within the period is varied according to t_1 -incrementation by shifting a 180° pulse.^[10] By this means each increment suffers from equal relaxation loss during the CT-period (δ_{CT}) and resolution is bought at the cost of sensitivity.¹⁰³ Furthermore, the accurate determination of δ_{CT} is crucial to avoid signal loss and for a single coupling a straight-forward calculation leads to multiple solutions. However, if numerous homonuclear carbon couplings of various size are active (see Figure 3.24) the CT-period has to be given by an n -fold multiple of *each* coupling which typically leads to a poor compromise between resolution and sensitivity. A partial remedy is given by the application of additional band-selective pulses with which larger couplings to carbonyls are typically suppressed – still, due to numerous long-range couplings the issue prevails for high resolution (i.e. long acquisition times).

In the SHACA-HSQC pulse sequence homo- and heteronuclear decoupling is obtained from ^{13}C -band-selective pulses resulting in pure shift $\text{H}\alpha$, $\text{C}\alpha$ -correlations in *both* dimensions without above mentioned tradeoffs. The responsible decoupling blocks are highlighted by blue and red boxes in Figure 3.25 (a). Suppression of couplings in the indirect dimension is achieved by an element similar to the one proposed in early literature^[281] and nearly all $\text{C}\alpha$ couplings shown in Figure 3.24 can be removed. The element is based on a combination of broadband and band-selective refocusing pulses and a schematic illustration is given in Figure 3.25 (b). While the first set of simultaneously applied 180° pulses affects all considered channels, the second band-selective pulse acts only on the $\text{C}\alpha$ -band and suppression of most couplings is achieved. The only remaining couplings are found for carbon pairs both resonating within the considered band – these are the small $^3J_{\text{C}\alpha\text{C}\alpha}$ and further the $^1J_{\text{C}\alpha\text{C}\beta}$ coupling in serine-residues where similar chemical shifts are encountered for $\text{C}\alpha$ and $\text{C}\beta$ (a CT approach for serine-residues is discussed in the following Section 3.6). While the broadband pulse on carbon has to induce a universal rotation (e.g. BURBOP^[136,192]) for the suppression of nitrogen couplings (i.e. $^1J_{\text{C}\alpha\text{N}}$ and $^2J_{\text{C}\alpha\text{N}}$) an inversion pulse is sufficient (e.g. BIP^[188] or BIBOP^[103,189,190]).

In the *direct* dimension, homo- and heteronuclear decoupling can readily be achieved by the BASEREX acquisition scheme (Section 3.3) which benefits from the typically larger signal dispersion of carbon. In contrast to other pure shift methods, BASEREX includes the suppression of long-range heteronuclear couplings and power intensive CPD can be avoided which, in turn, allows for long acquisition times and, hence, high resolution. While the *pure shift* $\text{H}\alpha$ -detection from ^1H -band-selective pulses (HOBS / BASHD) certainly affects the nearby large water signal leading to large artifacts, in BASEREX, radiation damping can be avoided by weak gradient fields during acquisition breaks. The most convenient advantage though is that BASEREX can be considered congruent to the pulse sequence block during t_1 -incrementation – decoupling in *both* dimensions is achieved by the *same* ^{13}C -band-selective shaped pulse and pure shift correlations are obtained for *all* selected signals.

It is further worth to note that a slightly modified back transfer is used in Figure 3.25 (a) which is supposed to avoid saturation of $\text{H}\alpha$ -signals close to the water resonance. It is constructed in a way that $\text{C}\alpha$ -magnetization is likewise back-transferred for $\text{H}\alpha$ -detection and $\text{H}\alpha$ -resonances being suppressed by

¹⁰³ It is noteworthy that the time-domain signal in the indirect dimension, hence, does not exhibit an exponential decay which favors the application of linear prediction – resolution is further increased and the loss in sensitivity can be compensated to some extent.

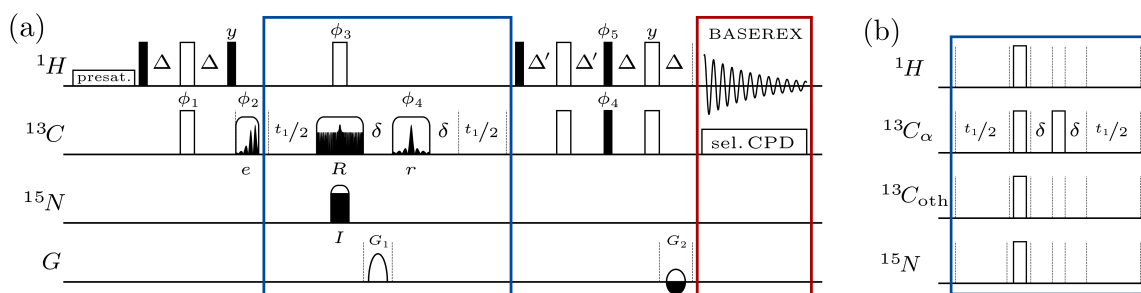


Figure 3.25: The pulse sequence for the selective $H\alpha, C\alpha$ -HSQC is shown in (a) where pure shift correlations are obtained from the elements highlighted by the blue and red box (BASEREX). In (b) effective rotations of the blue box are again illustrated schematically. Narrow black and open wide bars correspond to 90° and 180° pulses, respectively, and phases are x if not annotated differently. Band-selective excitation and refocusing is achieved by an E-BURP (e) and RE-BURP (r), respectively, while a BURBOP is used for broadband refocusing (R) and a BIBOP or BIP for broadband inversion (I). Delays were set according to the $^1J_{C,H}$ coupling where $\Delta = 1/(4^1J_{C,H})$ and $\Delta' = 1/(4^1J_{C,H})$ for CH -groups and $\Delta' = 1/(8^1J_{C,H})$ for CH_2 -groups. The following phase cycles are used: $\phi_1 = x$; $\phi_2 = x, -x$; $\phi_3 = 2(x)2(-x)$; $\phi_4 = 4(x)4(-x)$; $\phi_5 = -y$; $\phi_{rec} = 2(x, -x)2(-x, x)$. For ^{13}C coherence selection gradients are given by the ratio $G_1/G_2 = 80\%/20.1\%$ and ϕ_5 is phase inverted with the Echo/Antiecho cycle (G_2) while ϕ_1 and ϕ_2 undergo TPPI.

presaturation, still, appear in the spectrum. Fortunately, in highly flexible proteins like IDPs, enhanced $C\alpha$ -magnetization is expected from heteronuclear NOE transfer (if attached $H\alpha$ -proton is saturated) and the actual signal intensity originating from $C\alpha$ -magnetization might outperform first expectations (the steady-state NOE can be estimated from Section 1.8.3). After carbon chemical shift evolution, in-phase coherence starting on $C\alpha$ evolves to anti-phase during the echo ($2\Delta'$) while coherence starting on proton is transferred to a multi quantum state and the $^1J_{C\alpha H\alpha}$ coupling does not evolve during $2\Delta'$. Despite the here proposed compensation for saturated $H\alpha$ resonances another and even better solution could be achieved if the sample was prepared in pure D_2O and a (likely preferential) sensitivity enhanced back-transfer could be used.

Further modifications of the pure shift SHACA-HSQC are proposed subsequently where a sensitivity improved version of the SHACA-HSQC is used to detect H_{Methyl}, C_{Methyl} -correlations (Section 3.5) and a CT-SHACA-HSQC is introduced for the in-phase detection of serines (Section 3.6).

3.4.2 Experimental

In the present section the potential of the proposed SHACA-HSQC sequence shall be examined using various uniformly $^{13}C, ^{15}N$ -labeled biomolecular samples: a mixture of amino acids (in D_2O , Sigma-Aldrich), a globular protein ubiquitin (1.5 mM in 90%:10% $H_2O:D_2O$, 25 mM KH_2PO_4 , pH= 4.6, His-tagged) and two intrinsically disordered proteins, p53TAD¹⁻⁶⁰ (1 mM in 90%:10% $H_2O:D_2O$, 150 mM NaCl, pH= 6.5) and α -synuclein (50 μM and 200 μM in PBS and 95%:5% $H_2O:D_2O$, pH= 7.2). The spectra were measured at 303 K on a 600 MHz Bruker Avance III spectrometer equipped with a cryogenically cooled TCI probe and on a 700 MHz Bruker Avance III spectrometer using a liquid-nitrogen cooled Prodigy TCI probe.¹⁰⁴

In order to estimate the gain in resolution and sensitivity obtained from the decoupling blocks applied in the SHACA-HSQC (red and blue boxes in Figure 3.25) these blocks were activated successively in an experimental row and compared to a state-of-the-art CT-HSQC. Exemplary spectra are illustrated in Figure 3.26 for the proline-rich p53TAD where in conventional 1H_N -detected experiments relevant proline signals are absent. While most prolines for the conventional CT-HSQC in Figure 3.26 (a) are unresolved,

¹⁰⁴ Experimental data for the SHACA-HSQC recorded at a field strength corresponding to 700.05 MHz was acquired by Andrea Bodor.^[11]

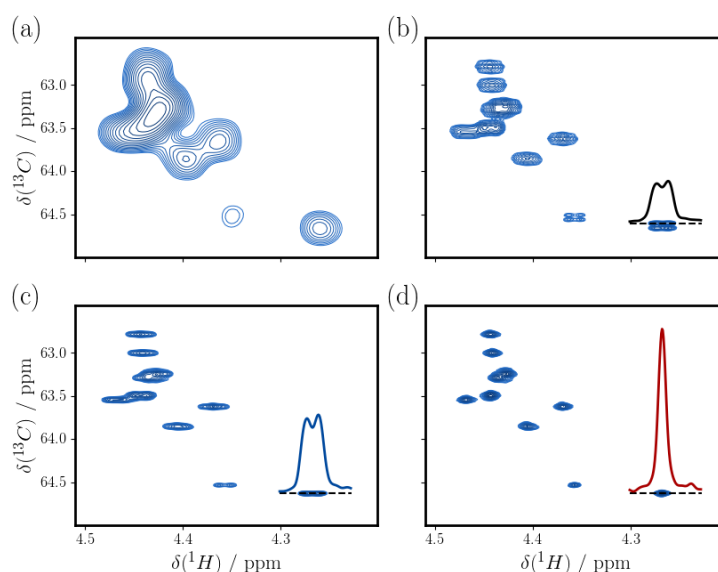


Figure 3.26: Conventional CT-HSQC (a) is compared to selective $H\alpha, C\alpha$ -HSQC with 1H - and ^{13}C -decoupling (b), with 1H -, ^{13}C - and ^{15}N -decoupling in the indirect dimension (c) and full decoupling using BASEREX (d) – the proline region of $p53TAD^{1-60}$ is shown.

$C\alpha$ -band-selective decoupling in the indirect dimension lifts the acquisition time limit from CT and already in Figure 3.26 (b), where no ^{15}N -decoupling is applied, spectral overlap is greatly decreased. Further improvements in resolution and sensitivity are obtained if ^{15}N -decoupling and the pure shift acquisition, BASEREX, are applied as illustrated in Figure 3.26 (c) and (d), respectively. For the fully decoupled SHACA-HSQC a remarkable increase is observed and all of the 9 prolines illustrated in the considered spectral area can be well-resolved.

A similar investigation is undertaken for all above-mentioned samples where for each case three amino acids with neighboring CH- (isoleucine), CH_2 - (proline) and CH_3 -group (alanine) are examined. In all cases the collapse of the ^{15}N -splitting in the indirect dimension should roughly double signal intensities¹⁰⁵ while the effect of BASEREX depends on the considered spin system. From the resulting SHACA-HSQC spectra different 1D slices are extracted for each sample and illustrated in Figure 3.27 where for the respective experiments the same color code is used as in Figure 3.26. For amino acids (first column) the neighboring group in the side-chain appears to have the strongest influence on the appearance of the signal while in the other considered samples, signals are further broadened due to relaxation and additional small couplings. For all cases the intensity is increased from decoupling in the indirect dimension whereas BASEREX might not always be beneficial for globular proteins. Due to the large number of $H\alpha$ -couplings a shorter chunk length has to be chosen which increases the artificial decay from transverse relaxation during the acquisition breaks (Section 3.1.5). It would, however, be possible to partially increase the chunk length and remove resulting artifacts by methods discussed in literature.^[305,307] For amino acids and α -synuclein sensitivity is increased by a factor of more than 5 while for p53 still an increase in the range of 2.5 to 3 is achieved. One can state that if underlying multiplets are resolved the natural linewidth is obviously smaller than the signal width and an increase in sensitivity is expected from coupling suppression. Yet, it should be considered that broadened lines can also originate from numerous small couplings and the collapse of unresolved multiplets might be just as beneficial (see second column in Figure 3.27).

A further challenging sample on which the potential of the SHACA-HSQC shall be tested is the intrinsically disordered protein α -synuclein which contains multiple similar blocks of amino acids and,

¹⁰⁵ For amino acids a single ^{15}N -coupling and, hence, a doublet is expected while in a protein backbone two ^{15}N -couplings are present. It turns out, that in the protein backbone the doublet of doublets mostly emerges to a phenomenological overlapping triplet – sometimes doublet – from whose collapse likewise twice the signal intensity is more or less expected.

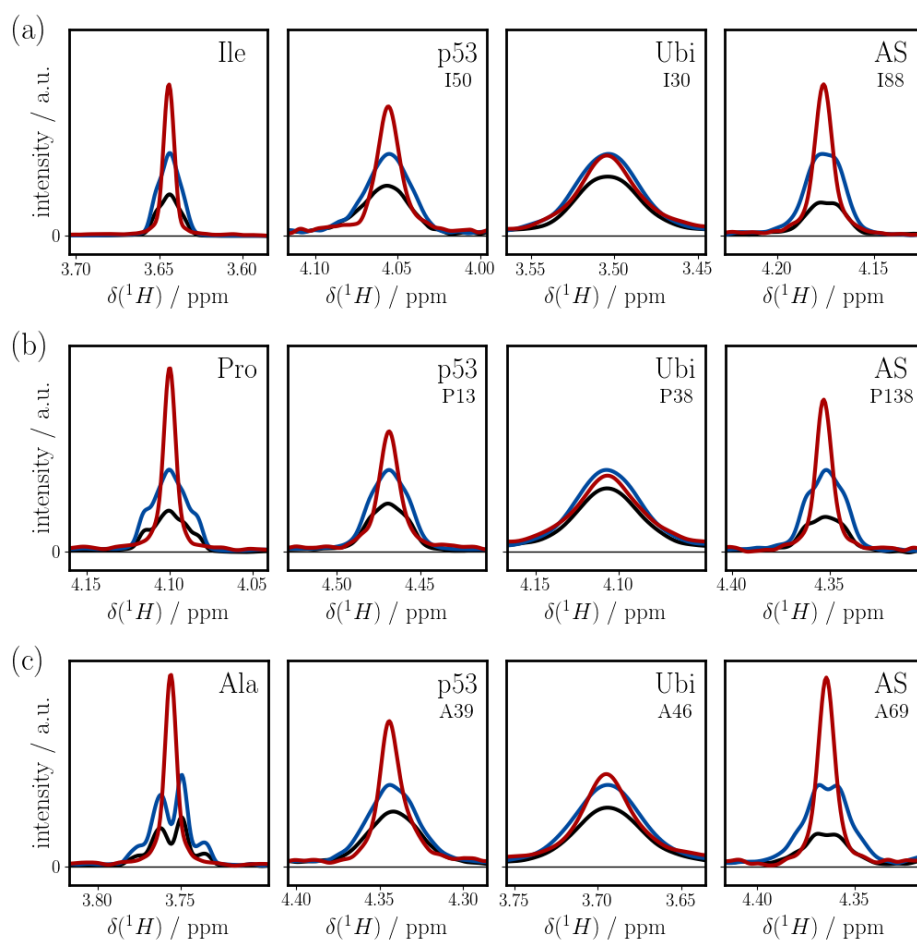


Figure 3.27: A selection of 1D rows are extracted from selective $H\alpha, C\alpha$ -HSQCs where 1H - and ^{13}C -decoupling (black), 1H -, ^{13}C - and ^{15}N -decoupling (blue) and full decoupling using BASEREX (red) is compared. The illustrated $H\alpha$ -resonances are 3J -coupled to a CH - (isoleucine), a CH_2 - (proline) and a CH_3 -group (alanine) in (a), (b) and (c), respectively, and specific indication is given in the top right corner. All spectra are normalized according to the blue signal. Acquisition time and chunk lengths (τ_c) for BASEREX were set to 285 ms and 10.2 ms (for amino acids), 285 ms and 10.2 ms (for p53TAD¹⁻⁶⁰), 143 ms and 8.9 ms (for His-tagged ubiquitin) and 243 ms and 10.1 ms (for α -synuclein).

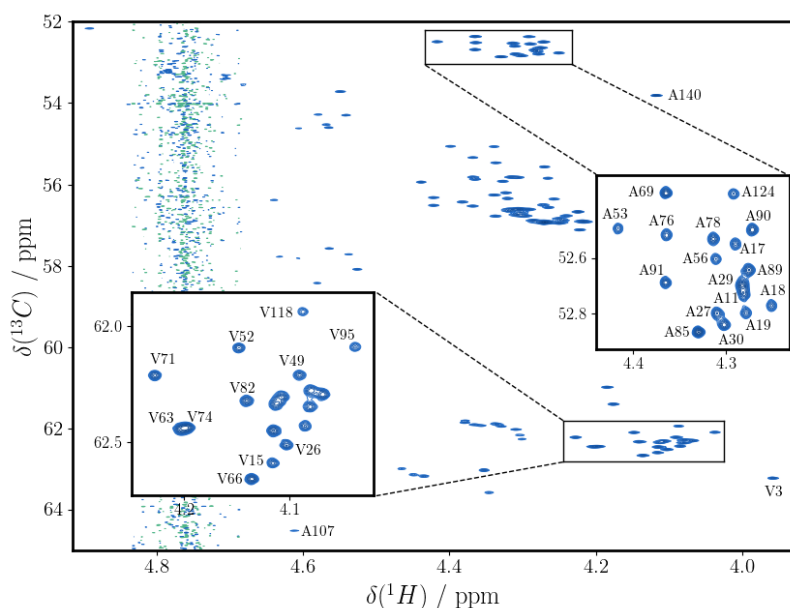


Figure 3.28: A selective $H\alpha,C\alpha$ -HSQC using BASEREX was acquired at a field strength corresponding to 700 MHz with 2048×512 complex points and 4 scans in 1 h 25 min for α -synuclein ($200 \mu\text{M}$ in $90\%H_2O:10\%D_2O$). Most signals are resolved as illustrated in the magnified alanine and valine region. The acquisition time was set to 243 ms and a chunk length of 10.1 ms was used.

accordingly, low signal dispersion is encountered. The pure shift SHACA-HSQC was recorded using a $200 \mu\text{M}$ concentrated sample with 2048×512 complex points in 1 h 25 min and the result is shown in Figure 3.28. Zoomed inset spectra highlight areas where mainly the numerous valines and alanines are agglomerated and most signals can distinctly be resolved.

Table 3.1: Comparing resolution for $^1H,^{15}N$ -HSQC, CON and SHACA-HSQC.

experiment	direct dimension			indirect dimension		
	nucleus	SD (Hz)	SW (Hz)	nucleus	SD (Hz)	SW (Hz)
$^1H,^{15}N$ -HSQC	1H_N	700	4.5–13	^{15}N (w P)	1680	7–15
CON ^[150]	^{13}CO	1050	7–10	^{15}N (w/o P)	2450	4.5–13
SHACA-HSQC	$^1H_\alpha$	700	7–9	$^{13}C_\alpha$	2800	6–8

Assuming that resonances in the conventional $^1H,^{15}N$ -HSQC, CON and SHACA-HSQC are dispersed within the area and with a signal width as indicated in Table 3.1, the resolution obtained from the SHACA-HSQC is higher compared to the $^1H,^{15}N$ -HSQC and more or less equal to the CON experiment. The investigation of IDPs under physiological conditions is commonly not possible for the $^1H,^{15}N$ -HSQC due to fast solvent exchange and missing prolines, hence, the detection of non-exchangeable nuclei as in the SHACA-HSQC or CON is clearly preferential. However, carbon detection in the CON experiment suffers from lower sensitivity and for the SHACA-HSQC a roughly 7-fold increase in signal-to-noise per \sqrt{t} is found. That in turn implies that CON measurement time has to be chosen 49 times longer in order to obtain an equal ratio of signal-to-noise.

The remarkable sensitivity that can be achieved from the SHACA-HSQC is further illustrated in Figure 3.29 (a) where a selection of *non*-proline signals of α -synuclein exhibit a small, neighboring peak shifted by ~ 100 ppb. These peaks originate from the low-concentrated protein fraction in which the amide proton is exchanged by a deuterium and $C\alpha$ -resonances are changed due to an isotope shift as was

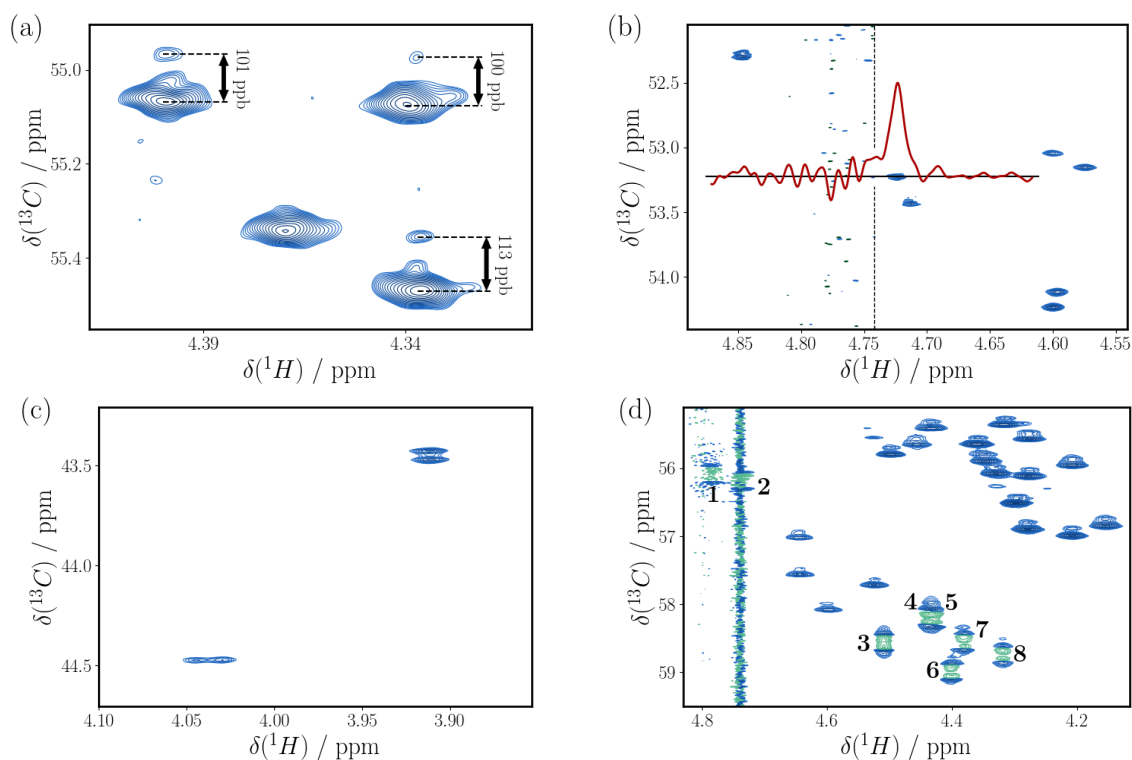


Figure 3.29: A zoomed view on signals of α -synuclein ($50 \mu\text{M}$ in $95\%H_2O:5\%D_2O$, acquired in 42 min) is shown in (a) where small side-peaks correspond to isotope-shifted resonances due to deuteration of neighboring amide. In (b) the quality of water suppression and nearby signals of p53TAD are illustrated where the vertical dashed line indicates the frequency of applied presaturation. In (c) an adapted SHACA-HSQC for the acquisition of glycines in p53TAD with $\Delta' = 1/(8^1J_{C,H})$ is shown. The signal of the N-terminal glycine is a doublet in the indirect dimension since NH_2 is outside the band of the applied ^{15}N -inversion pulses and so the $^1J_{CN}$ -coupling ($= 8.3 \text{ Hz}$) evolves. In (d) 8 serine residues of p53TAD are numbered which exhibit dispersive anti-phase lineshapes in the indirect dimension which is due to the fact that neighboring side chain carbons resonate in the band of the selective pulse and the $^1J_{C,C}$ coupling can evolve.

reported recently.^[346] One can estimate that the solvent ratio of H₂O:D₂O determines the concentration of the deuterated protein fraction which is as low as $\sim 2.5 \mu\text{M}$ for the spectra in Figure 3.29 (a) recorded in only 42 min. It is noteworthy that the proton-deuteron exchange rate varies for different residues and if in fast exchange, the peak does not show up.

The high concentration of H₂O requires a powerful solvent suppression also because H α resonances can be found close to the water frequency. As illustrated in Figure 3.29 (b) a sound quality of water suppression can be achieved by the SHACA-HSQC where H α signals of p53TAD, being partially saturated by the weak perturbative field for solvent suppression, still benefit from heteronuclear NOE. Despite the proximity to the water resonance, signals in Figure 3.29 (b) unequivocally stand out from nearby water artifacts. Glycine is the only amino acid that consists of a CH₂-group at the α -position and for the detection of glycines the SHACA-HSQC sequence has to be adapted appropriately. Since two large $^1J_{\text{C}\alpha\text{H}\alpha}$ -couplings are present, the delay for the back-transfer has to be set to $\Delta' = 1/(8^1J_{\text{C}\alpha\text{H}\alpha})$. Further, C α -resonances for glycine residues are typically at somewhat lower ppm values and the band-selective pulse has to be shifted accordingly. An exemplary spectrum is shown in Figure 3.29 (c) where a doublet in the direct dimension is expected for CH₂-groups even if BASEREX is applied. Note, the upper signal is further split in the indirect dimension which is based on the fact that it is an N-terminal glycine and the ¹⁵N-resonance of the NH₂-group is outside the band of the applied ¹⁵N decoupling pulse.

As mentioned above, in the considered version of the SHACA-HSQC (Figure 3.25), serines exhibit dispersive anti-phase lineshapes which arise from the $^1J_{\text{C}\alpha\text{C}\beta}$ coupling that is not suppressed by the band-selective pulse. Such serine signals are illustrated in Figure 3.29 (d) for p53TAD where, again, resonances close to water are not saturated and further isotope-shifted peaks are visible for non-proline residues.

3.4.3 Conclusion

As has been examined, the SHACA-HSQC is a pulse sequence highly suitable for the investigation on intrinsically disordered proteins at near-physiological conditions. It does not suffer from signal loss due to exchanging protons and is, hence, very robust with respect to pH and temperature changes. Compared to carbon-detected experiments a considerably higher sensitivity is encountered which allows the measurement of low-concentrated samples ($\sim 2.5 \mu\text{M}$) in much less than an hour. In combination with BASEREX (Section 3.3) highly resolved H α ,C α -correlation spectra can be obtained and measurement time could be further reduced based on the compatibility with non-uniform sampling (40% for p53TAD in a 2D experiment, data not shown) – an extension to triple-resonance experiments is well-thinkable. Even for the application of BASEREX a low artifact level from water is found using presaturation and the novel back-transfer allows to detect signals close to water even if H α polarization is saturated. Since glycines are typically outside the optimal band of applied selective pulses, an additional glycine-adapted experiment might be required. Furthermore, serines exhibit a dispersive anti-phase lineshape in the described SHACA-HSQC which can be circumvented by a CT approach discussed in Section 3.6.

^[346] A. S. Maltsev, J. Ying and A. Bax. *Journal of Biomolecular NMR* **2012**, *54*, 181–191.

3.5 Selective Pure Shift $H_{\text{Methyl}}, C_{\text{Methyl}}$ -Correlations

In analogy to the previous section, where band-selective pulses were used to obtain $H\alpha, C\alpha$ -correlations, the SHACA-HSQC can likewise be used to obtain pure shift correlations of signals that are situated in any distinct ^{13}C -band. Another suitable example in this context is given for methyl groups that commonly resonate at considerably low ^{13}C -ppm values. In the following a sensitivity improved version of the SHACA-HSQC shall be used to acquire $H_{\text{Methyl}}, C_{\text{Methyl}}$ -correlations for a uniformly $^{13}\text{C}, ^{15}\text{N}$ -labeled amino acid mixture (Sigma-Aldrich) and human ubiquitin (0.5 mM, pH = 4.7, 30 mM NaOAc, 50 mM NaCl, Silantes) both dissolved in pure D_2O .

3.5.1 Pulse Sequence

The modified pulse sequence of the SHACA-HSQC is illustrated in Figure 3.30 where band-selective pulses are adjusted such that the centered ^{13}C -band of methyl-groups is largely covered. Again, the ^{13}C -band-selective pulses are utilized for homonuclear decoupling in both dimensions using BASEREX (Section 3.3). Further, the considered sequence comprises a *sensitivity improved* transfer from which both transverse ^{13}C -coherences, $2\hat{I}_z\hat{S}_x$ and $2\hat{I}_z\hat{S}_y$, can be transferred for proton acquisition as originally proposed in literature.^[146,147] Such a back-transfer consists of two echoes in which the two intended components evolve individually such that they both end up on two orthogonal, transverse proton coherences, \hat{I}_x and \hat{I}_y . Since both considered samples are dissolved in D_2O no presaturation is required and the sensitivity improved back-transfer does not lead to signal loss. Note, the SHACA-HSQC discussed in the previous section was used for samples dissolved in H_2O and in order to circumvent saturation of signals close to the water resonance a special back-transfer was designed.

With respect to signal-to-noise the sensitivity improved back-transfer leads to an enhancement factor of up to 2 compared to the standard HSQC using gradients for coherence transfer pathway (CTP) selection or a factor of $\sqrt{2}$ if the states-method is used for frequency discrimination.^[347] Note, in the course of processing spectra being phase-modulated in t_1 the noise is inherently increased by a factor of $\sqrt{2}$. Especially for HSQC-type experiments where only a *selection* of coherences is measured, it is further

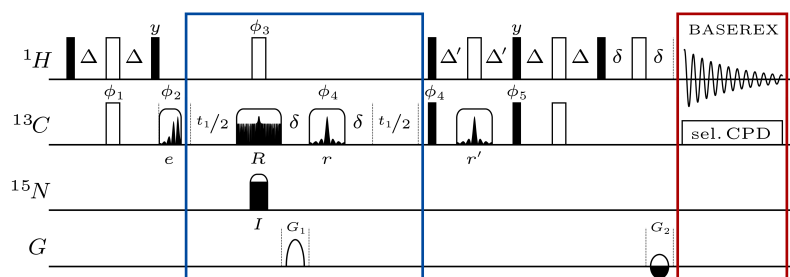


Figure 3.30: The pulse sequences of a sensitivity improved SHACA-HSQC is shown for samples in deuterated solvents and presaturation can be omitted. Narrow black and open wide bars correspond to 90° and 180° pulses, respectively, and phases are x if not annotated differently. Band-selective excitation and refocusing is achieved by an E-BURP (e) and RE-BURP (r and r'), respectively, while a BURBOP is used for broadband refocusing (R) and a BIBOP or BIP for broadband inversion (I). Delays were set according to the $^1J_{\text{C,H}}$ coupling where $\Delta = 1/(4^1J_{\text{C,H}})$ and $\Delta' = 1/(4^1J_{\text{C,H}})$ for CH-groups, $\Delta' = 1/(8^1J_{\text{C,H}})$ for CH_2 -groups (best compromise for all multiplicities) and $\Delta' = 1/(12^1J_{\text{C,H}})$ for CH_3 -groups. The following phase cycles are used: $\phi_1 = x$; $\phi_2 = x, -x$; $\phi_3 = 2(x)2(-x)$; $\phi_4 = 4(x)4(-x)$; $\phi_5 = -y$; $\phi_{\text{rec}} = 2(x, -x)2(-x, x)$. For ^{13}C coherence selection gradients are given by the ratio $G_1/G_2 = 80\%/20.1\%$ and ϕ_5 is phase inverted with the Echo/Antiecho cycle (G_2) while ϕ_1 and ϕ_2 undergo TPPI. In order to suppress homonuclear $^1J_{\text{C,C}}$ couplings during back transfer a selective RE-BURP pulse is used.

^[146] A. G. Palmer et al. *Journal of Magnetic Resonance* **1991**, 93, 151–170.

^[147] L. Kay, P. Keifer and T. Saarinen. *Journal of the American Chemical Society* **1992**, 114, 10663–10665.

^[347] J. Schleucher, M. Sattler and C. Griesinger. *Angewandte Chemie - International Edition* **1993**, 32, 1489–1491.

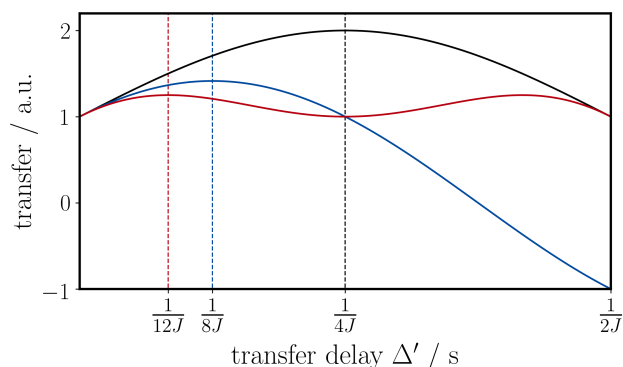


Figure 3.31: Transfer of sensitivity improved HSQC with respect to the delay Δ' is shown for CH (black), CH₂ (blue) and CH₃ groups (red) where the optimum is indicated by dashed, vertical lines.

worth mentioning that an increase in signal intensity by a factor of 2 is only achieved for CH-groups. This is based on the fact that multi quantum coherences of CH₂- or CH₃-groups still evolve under the large 1J -coupling to remaining, passive protons. Therefore, when it comes to sensitivity, the evolution of CH-, CH₂- and CH₃-groups during the back-transfer delay Δ' has to be examined individually. Starting on arbitrary anti-phase operators ($2\hat{I}_z\hat{S}_x + 2\hat{I}_z\hat{S}_y$) one can predict using theory discussed in Section 1.4 that the duration of delay Δ' impacts the amplitude of the acquired signal as follows:

$$\begin{aligned}
 \text{CH-group:} \quad & 2\hat{I}_z\hat{S}_x + 2\hat{I}_z\hat{S}_y \quad \rightarrow \dots \xrightarrow{\pi J(2\hat{I}_z\hat{S}_z)2\Delta'} \dots \rightarrow \hat{I}_x + \sin(\pi J \cdot 2\Delta') \hat{I}_y \\
 \text{CH}_2\text{-group:} \quad & 2\hat{I}_z\hat{S}_x + 2\hat{I}_z\hat{S}_y \quad \rightarrow \dots \xrightarrow{\pi J(2\hat{I}_z\hat{S}_z)2\Delta'} \dots \rightarrow \cos(\pi J \cdot 2\Delta') \hat{I}_x + \sin(\pi J \cdot 2\Delta') \hat{I}_y \\
 \text{CH}_3\text{-group:} \quad & 2\hat{I}_z\hat{S}_x + 2\hat{I}_z\hat{S}_y \quad \rightarrow \dots \xrightarrow{\pi J(2\hat{I}_z\hat{S}_z)2\Delta'} \dots \rightarrow \cos^2(\pi J \cdot 2\Delta') \hat{I}_x + \sin(\pi J \cdot 2\Delta') \hat{I}_y.
 \end{aligned}$$

If gradients are applied for CTP-selection the considered anti-phase operators are dephased *prior* to the back-transfer and in order to calculate the influence of Δ' on the signal's amplitude one can use the sum over the amplitudes of individual operators (\hat{I}_x and \hat{I}_y). In this context, the transfer efficiency of CH-, CH₂- and CH₃-groups is illustrated in Figure 3.31 where optimal values of Δ' are indicated by vertical dashed lines. As expected the signal intensity can be doubled for CH-groups, while the maximum improvement for CH₂- and CH₃-groups is given by a factor of $\sqrt{2}$ and 1.25, respectively (without considering relaxation).

It is worth to note that in the pulse sequence illustrated in Figure 3.30 a band-selective RE-BURP pulse (r') is used during the echo for heteronuclear coherence transfer. By this means, homonuclear $^1J_{C,C}$ -couplings during Δ' are suppressed which otherwise could lead to signal loss of more than 20%.¹⁰⁶ In order to still obtain the desired heteronuclear coherence transfer a thorough examination of heteronuclear coupling evolution during the shaped pulse is *essential* and the reader is referred to Section 2.4. With this respect the RE-BURP (Section 2.4.5) allows heteronuclear coupling evolution during nearly the full pulse length and Δ' can *not* be chosen shorter than roughly half the RE-BURP pulse length. Since the pulse length of any shaped pulse directly relates to the width of the selected ^{13}C -band, a narrower band and, hence, longer RE-BURP pulses would seriously interfere with the back-transfer. However, one could likewise use a Q3 pulse shape (Section 2.4.4) where much less of the pulse length has to be considered for heteronuclear coupling evolution and also narrower bands can be selected as is shown in the following.

¹⁰⁶ Considering two $^1J_{C,C}$ -couplings of size 35 Hz and 55 Hz, homonuclear coupling evolution during $2\Delta'$ would lead to a reduction in signal intensity of $\cos(\pi \cdot 2\Delta' \cdot 35 \text{ Hz}) \cdot \cos(\pi \cdot 2\Delta' \cdot 55 \text{ Hz}) \approx 0.77$ for a CH-group.

3.5.2 Experimental

The pulse sequence was first tested on a uniformly $^{13}\text{C}, ^{15}\text{N}$ -labeled amino acid mixture and, indeed, *all* methyl resonances are well-enough separated from their coupling partners. Hence, band-selective homonuclear decoupling can be applied without problems and from the considered experiment pure shift $H_{\text{Methyl}}, C_{\text{Methyl}}$ -correlations are obtained in both dimensions as illustrated in Figure 3.32 (a). A carbon linewidth below 3 Hz can be observed in the indirect dimension and, in contrast to standard CT-HSQC, the shape of the *FID* is determined by transverse relaxation starting with *maximum* intensity. A more challenging task is posed by a globular protein (e.g. ubiquitin) where a considerably higher signal dispersion of carbon resonances can be observed. In this respect, homonuclear decoupling from band-selection of *all* methyl groups might be hindered due to overlap with coupling partners and in such a case a narrower band has to be chosen. The spectra of ubiquitin from a standard sensitivity improved CT-HSQC and the SHACA-HSQC are compared in Figure 3.32 (b) and (c), respectively. Using the CT-HSQC, resolution is limited due to constant time decoupling and signal widths of more or less 18 Hz are encountered in the indirect dimension. For the SHACA-HSQC, on the other hand, high resolution comes at no cost in terms of sensitivity and linewidths of roughly 7 Hz are found. Note, while all methyl resonances can be acquired by the standard CT-HSQC, for band-selective homonuclear decoupling some signals overlap with neighbored methylene groups and, hence, should not be inverted by the band-selective shaped pulse. A potential solution is given in the following section where likewise a constant time version of the SHACA-HSQC is presented. It should further be considered that an opportune sample class is, again, represented by intrinsically disordered proteins where longer transverse relaxation times and lower signal dispersion is typically encountered. Hence, high resolution is required and band-selection of all methyl groups is likely possible as is the case for amino acids (Figure 3.32 (a)). Note, in Figure 3.32 (a) and (c) a Q3 pulse shape was used in the back transfer (r') in order to achieve the optimal delay $\Delta' = 1/(12^1J_{\text{C,H}})$ for CH_3 -groups. Conclusively, one can state that also the *sensitivity improved* SHACA-HSQC is a versatile tool for pure shift correlations especially for samples where presaturation is not required.

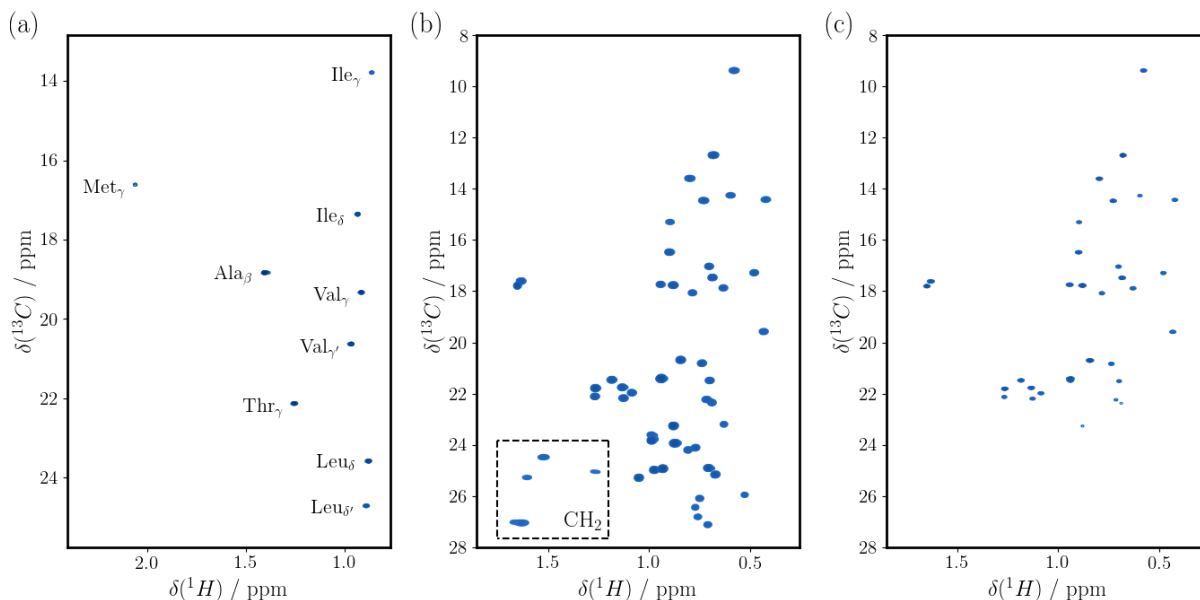


Figure 3.32: The SHACA-HSQC is applied on the methyl-regions of the amino acid mixture (a) and for human ubiquitin where a standard CT-HSQC (b) is compared to band-selective decoupling (c) at a field strength corresponding to 600 MHz. All spectra were acquired with 4 transients and a spectral width of 12 ppm and 2048 complex points in the direct dimension. In the indirect dimension a spectral width of 30 ppm and 1024 (a), 227 (b) and 768 (c) complex points were used. Note for (b), the constant time decoupling ($\frac{2}{7}$) limits the acquisition of additional points. In (a) and (c), a ^{13}C -band of 10 ppm and 14 ppm centered at 16.4 ppm and 12 ppm was selected, respectively.

3.6 Constant Time SHACA-HSQC

Band-selective homonuclear decoupling, as applied in the SHACA-HSQC (Section 3.4), constitutes a powerful tool for the development of novel pulse sequences. It is, however, limited if a considered group of signals is not well-enough separated from coupled spins as is commonly encountered for serine-residues using the SHACA-HSQC. In the present section a modified constant time decoupling shall be introduced to the SHACA-HSQC that allows homonuclear decoupling also for spin pairs where both are situated in the considered ^{13}C -band. A detailed discussion on the pulse sequence is given which shall further be compared to the standard CT-HSQC for the amino acid mixture (in D_2O , Sigma-Aldrich) and human ubiquitin (0.5 mM in pure D_2O , pH = 4.7, 30 mM NaOAc, 50 mM NaCl, Silantes). In contrast to standard constant time decoupling the acquisition period is not limited by long-range couplings and high resolution is accessible for samples with corresponding transverse relaxation times.

3.6.1 Pulse Sequence

Constant time homonuclear decoupling was first introduced by Bax et al.^[10] and later used on uniformly ^{13}C -labeled samples to suppress $^1J_{\text{C,C}}$ -couplings in the indirect dimension.^[348] For this purpose, the t_1 -incrementation is done within a constant time period (T_C) that is equal to a multiple of the inverse coupling strength ($\frac{1}{^1J_{\text{C,C}}}$). By doing so, the considered coupling is not refocused but evolves *identically* for all t_1 increments and, hence, does not lead to signal modulation in the indirect dimension. Clearly, the size of *all* homonuclear couplings has to be known in advance and mis-setting of T_C can cause severe signal loss. In uniformly ^{13}C -labeled samples numerous $^1J_{\text{C,C}}$ -couplings are present which exhibit a considerable range of J -values. Commonly, additional band-selective pulses are used to decouple well-separated carbonyls, thereby reducing the number of couplings. Still, the period T_C has to be set according to all *remaining* $^1J_{\text{C,C}}$ -couplings and the optimal value $T_C = \frac{n}{^1J_{\text{C,C}}}$ has to be compromised to some extent. In addition, a large number of long-range couplings is present and T_C is further limited to values where the contribution of these numerous, small couplings is, to first extent, negligible.^[348] In conventional experiments T_C is typically set to either 26.6 or 53.2 ms where signal loss due to long-range couplings can still be tolerated.¹⁰⁷ Moreover, transverse relaxation during T_C leads to signal decay that is *equal* for all t_1 increments – the FID in the indirect dimension does not exhibit a decay and might be completely zero if $T_C \gg T_2$. Constant time decoupling is, thus, inherently correlated to a certain loss in signal intensity and T_C has to be set according to transverse relaxation times – to some extent linear prediction can compensate the loss.

In the following a SHACA-HSQC with modified constant time period shall be introduced in which also long-range $^nJ_{\text{C,C}}$ -couplings are suppressed from band-selective pulses and coupling evolution is *only* given for spin pairs *both* resonating within the selected ^{13}C -band. In the SHACA-HSQC, typically, such a situation is encountered mainly for serines and T_C can be set *precisely* to the appropriate value with $^1J_{\text{C}\alpha,\text{C}\beta} = 37.5$ Hz. The pulse sequence is shown in Figure 3.33 where the constant time period is highlighted by the blue box. A sensitivity enhanced back-transfer, as discussed in the previous section, is used for samples dissolved in deuterated solvents. In analogy to standard SHACA-HSQC (Section 3.4), the sequence comprises a combination of hard and band-selective pulses which decouples signals within the ^{13}C -band from all others. After a delay of $\frac{T'_C}{2}$ a second band selective pulse is introduced which refocuses chemical shift evolution and likewise the considered $^1J_{\text{C}\alpha,\text{C}\beta}$ -coupling of serines. By in- and decrementing both delays, $\frac{t_1}{2}$ and $\frac{T'_C - t_1}{2}$, simultaneously, the overall period (T_C) during which the coupling evolves, stays constant and the acquired signal is not modulated by the $^1J_{\text{C}\alpha,\text{C}\beta}$ -coupling. Since two band-selective shaped pulses are applied during T_C the use of refocusing pulses is, in principle, no longer required – instead of two RE-BURPs one could likewise apply two I-BURPs that exhibit similar properties in terms of homonuclear coupling evolution but show a considerably narrower transition range (Section 2.4.7).

^[348] G. W. Vuister and A. Bax. *Journal of Magnetic Resonance* **1992**, 98, 428–435.

¹⁰⁷ Considering two long-range couplings with $^nJ_{\text{C,C}} = 2.5$ Hz and a constant time period of $T_C = 53.2$ ms in the indirect dimension, the signal intensity is, hence, reduced by a factor of $\cos^2(\pi J \cdot T_C) = 0.835$.

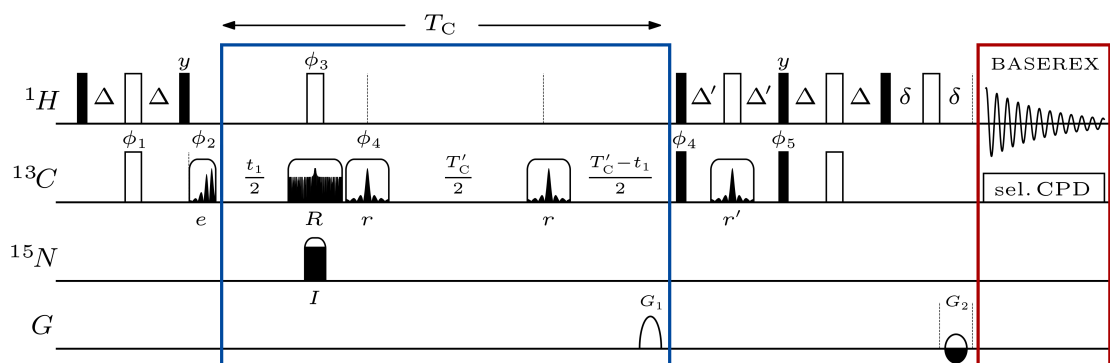


Figure 3.33: The pulse sequences of a sensitivity improved (a) and a constant time version (b) of the SHACA-HSQC is shown. In (a) and (b), narrow black and open wide bars correspond to 90° and 180° pulses, respectively, and phases are x if not annotated differently. Band-selective excitation and refocusing is achieved by a E-BURP (e) and RE-BURP (r and r'), respectively, while a BURBOP is used for broadband refocusing (R) and a BIBOP or BIP for broadband inversion (I). Note, a narrower transition width is obtained using two I-BURP inversion pulses during constant time decoupling (r). Delays were set according to the ${}^1J_{C,H}$ coupling where $\Delta = 1/(4{}^1J_{C,H})$ and $\Delta' = 1/(4{}^1J_{C,H})$ for CH-groups, $\Delta' = 1/(8{}^1J_{C,H})$ for CH_2 -groups (best compromise for all multiplicities) and $\Delta' = 1/(12{}^1J_{C,H})$ for CH_3 -groups. The following phase cycles are used: $\phi_1 = x$; $\phi_2 = x, -x$; $\phi_3 = 2(x)2(-x)$; $\phi_4 = 4(x)4(-x)$; $\phi_5 = -y$; $\phi_{rec} = 2(x, -x)2(-x, x)$. For ${}^{13}C$ coherence selection gradients are given by the ratio $G_1/G_2 = 80\%/20.1\%$ and ϕ_5 is phase inverted with the Echo/Antiecho cycle (G_2) while ϕ_1 and ϕ_2 undergo TPPI. In order to suppress homonuclear ${}^1J_{C,C}$ and long-range ${}^nJ_{C,H}$ couplings during transfer steps selective RE-BURP pulses are used. In (b) the constant time delay is set to $T_C = n/{}^1J_{C,C}$ and $T'_C = T_C - 2 \cdot f_c \cdot \tau_r$ where τ_r is the pulse length of the band-selective pulse r and f_c determines the coupling evolution during r according to Section 2.4.

3.6.2 Experimental

In order to estimate the effect of long-range homonuclear ${}^{13}C$ -couplings during the constant time period T_C without much interference from transverse relaxation, the CT-SHACA-HSQC was first tested on the mixture of uniformly ${}^{13}C, {}^{15}N$ -labeled amino acids. The results are illustrated in Figure 3.34 where a comparison of the standard SHACA-HSQC, the CT-SHACA-HSQC and a conventional sensitivity improved CT-HSQC is given. As expected for standard SHACA-HSQC, both serine signals (Ser $_\alpha$ and Ser $_\beta$) exhibit a dispersive anti-phase lineshape as shown in Figure 3.34 (a). Using the proposed CT-SHACA-HSQC also the ${}^1J_{C\alpha, C\beta}$ -coupling of serines can be removed from the spectrum and in-phase signals are found for all residues. Since the constant time period was set to $T_C = \frac{n}{{}^1J_{C\alpha, C\beta}}$ with $n = 11$ being an odd number, both serine signals are negative – an even number for n would, in turn, lead to only positive signals. It shall further be mentioned that serine signals are still broadened from ${}^3J_{H\alpha, H\beta}$ -couplings in the *direct* dimension since both, H $_\alpha$ and H $_\beta$, are inverted by the selective element used in BASEREX. The standard CT-HSQC spectrum is depicted in Figure 3.34 (c) using equivalent experimental parameters as employed for the CT-SHACA-HSQC – including the constant time period T_C . Since in the standard CT-HSQC long-range homonuclear ${}^nJ_{C,C}$ -couplings are not decoupled during T_C , the intensities of most illustrated signals are altered due to a *constant* evolution of non-suppressed couplings and it is very likely for peaks to disappear. Whether a signal is positive, negative or simply zero depends on the number and size of active long-range couplings during T_C and an intensity factor f can be calculated from:

$$f = \prod_i \cos(\pi J_i \cdot T_C) \quad (3.6.1)$$

where i is the number of long-range homonuclear couplings and J_i the corresponding coupling strength.

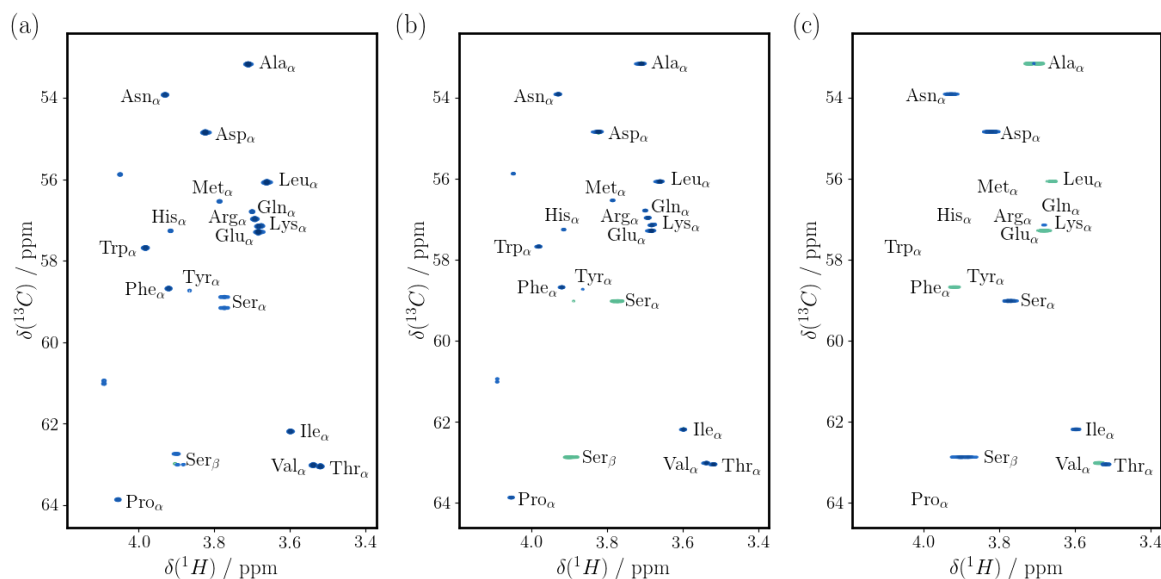


Figure 3.34: $H\alpha, C\alpha$ -correlations obtained from SHACA-HSQC (a), CT-SHACA-HSQC (b) and conventional CT-HSQC (c) are compared for uniformly $^{13}C, ^{15}N$ -labeled amino acids. All spectra were acquired with 4 transients and a spectral width of 12 ppm and 3072 complex points in the direct dimension. In the indirect dimension a spectral width of 26 ppm and 1132 (a), 1138 (b) and 1121 complex points (c) were acquired. Constant time period was set to an n -fold multiple of $^1J_{C\alpha, C\beta} = 37.5$ Hz with $T_C = 293.3$ ms. In (a) and (b), a ^{13}C -band of 10.6 ppm centered at 55.3 ppm was selected.

As illustrated in Figure 3.34 (c) it is basically impossible to find a suitable value T_C for all present couplings and, under given circumstances, the CT-SHACA-HSQC is clearly preferential. It shall further be mentioned that for typical biomolecular samples a constant time period of $T_C = \frac{11}{^1J_{C\alpha, C\beta}} = 293.3$ ms is unreasonably long and should only be considered for samples exhibiting much longer transverse relaxation times. Still, already for *much* shorter values of T_C severe signal loss can be encountered especially if additional inter-residue couplings are present e.g. in the side-chain of proteins (with $^3J_{C\alpha, C\alpha} \approx 1-2$ Hz). For this reason the sequence is further tested on human ubiquitin, a globular protein of ~ 9.0 kDa, and compared to a conventional CT-HSQC recorded with equivalent parameters. Clearly, transverse relaxation is much faster for larger proteins (Section 1.8) and the experimental setup has to be adapted accordingly. In order to obtain highest resolution the constant time period is set to $T_C = \frac{3}{^1J_{C\alpha, C\beta}} \approx 80$ ms where the coupling is matched to serines with $^1J_{C\alpha, C\beta} = 37.5$ Hz. Since the acquisition time in the indirect dimension is limited by the constant time period, a maximum FID resolution of approximately 13 Hz can be achieved with the given T_C . Using linear prediction the signal width can be further decreased and for the CT-SHACA-HSQC a linewidth of approximately 10 Hz can be obtained. The CT-SHACA-HSQC spectrum of ubiquitin is shown in Figure 3.35 and all peaks in the considered ^{13}C -band are present. As expected, $C\beta$ s of serines in ubiquitin are all within the covered ^{13}C -band and, hence, exhibit negative signals for odd values of n . Only certain threonine signals exhibit reduced intensities which is based on the fact that the corresponding $C\beta$ s resonate within the transition range of the applied band-selective pulse and a partial coupling evolution during T_C , hence, modulates the signal's amplitude. In the present case, a certain signal reduction of threonines could not be avoided despite the fact that two I-BURP shaped pulses with narrower transition range were used during the constant time period. However, it shall again be mentioned that also for the presented CT-SHACA-HSQC experiment, intrinsically disordered proteins constitute two highly suitable classes of biomolecular targets. Typically, signal dispersion is remarkably lower compared to globular proteins and, hence, it is very much likely to band-select all $H\alpha, C\alpha$ -correlations devoid of interference with coupled $C\beta$ resonances. Furthermore, low signal dispersion *requires* high resolution provided by CT-SHACA-HSQC and considerably longer transverse relaxation times allow for extended constant time periods T_C .

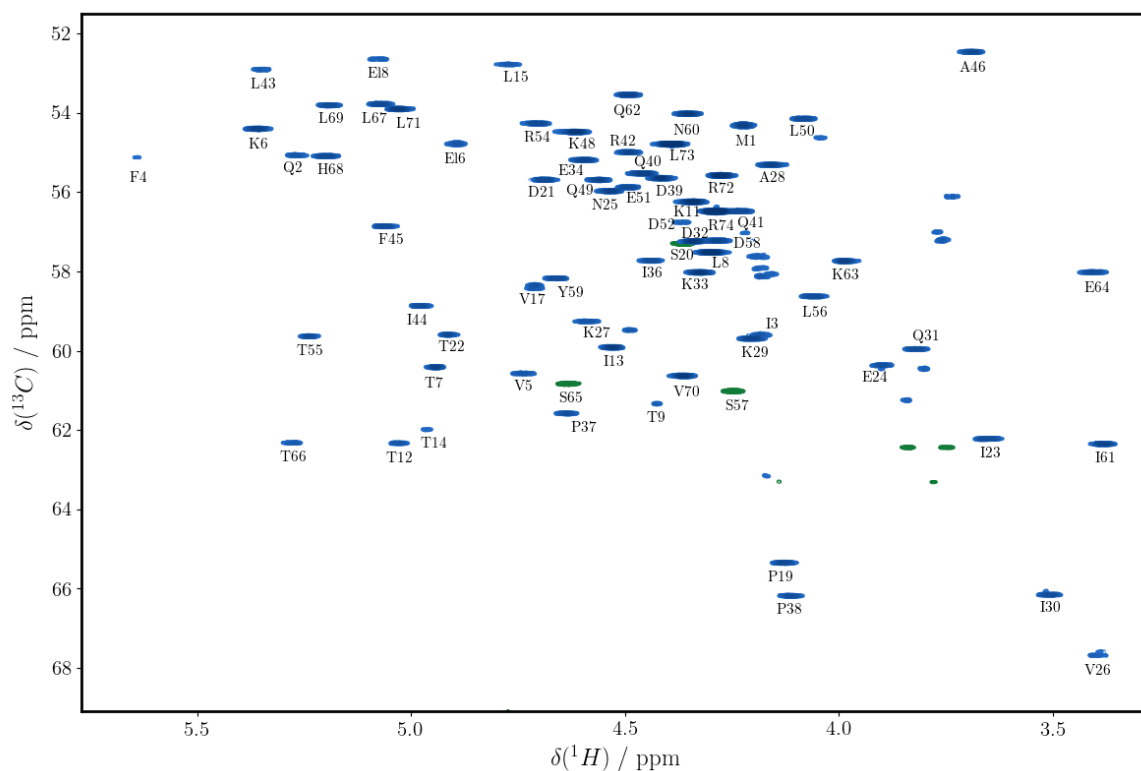


Figure 3.35: A CT-SHACA-HSQC spectrum of uniformly $^{13}\text{C},^{15}\text{N}$ -labeled ubiquitin is illustrated which was acquired at a field strength corresponding to 600 MHz using a cryogenically cooled TCI probe. In total, 8 transients were accumulated leading to an experiment time of 1 hour and 6 seconds. The constant time period T_C was set to an n -fold multiple of $^1J_{C\alpha,C\beta} = 37.5$ Hz with $n = 3$ and $T_C \approx 80$ ms leading to 200 complex points for a spectral width of 18 ppm in the indirect dimension. Note, all three serine signals are negative (green), since $C\beta$ s are situated within the ^{13}C -band that was set to a width of 14.5 ppm and centered at an offset of 57.4 ppm. In contrast to other spectra through-out the present chapter, no pure shift acquisition (i.e. BASEREX) was used. The assignment is based on literature.^[323]

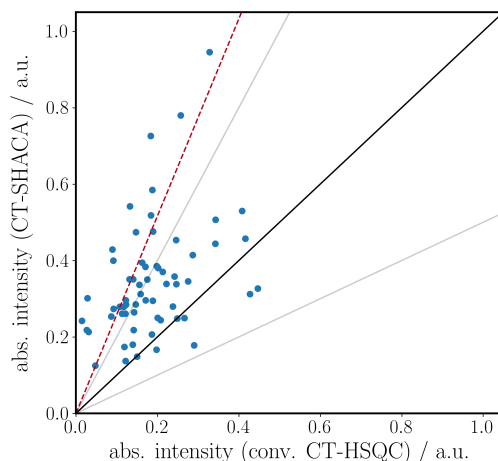


Figure 3.36: Signal intensities for ubiquitin are compared for CT-SHACA-HSQC and conventional CT-HSQC using a correlation plot. The average increase in intensity is indicated by the red dashed line which corresponds to a factor of approximately 2.58. As minimum and maximum a value of ≈ 0.61 and ≈ 16.9 are found, respectively. Intensities are determined from absolute value integration over a box of 20:12 Hz (width:height). For both the CT-SHACA-HSQC and conventional CT-HSQC, equivalent experimental parameters were used (see Figure 3.35) and in order to avoid signal overlap from folded peaks the spectral width was set to 30 ppm. For the reason of clarity, the two largest signals are cut off – both are considerably above the diagonal.

In comparison to the conventional CT-HSQC, the CT-SHACA-HSQC offers much higher sensitivity for most $\text{H}\alpha, \text{C}\alpha$ -correlations. The average increase in sensitivity¹⁰⁸ is given by a factor of approximately 2.58 which can be ascribed to the evolution of long-range homonuclear ^{13}C -couplings that are *not* suppressed in the conventional CT-HSQC. A more detailed analysis is offered by the correlation plot shown in Figure 3.36 where the integrals of individual signals¹⁰⁹ are compared. As illustrated, most signals exhibit a largely increased intensity for the CT-SHACA-HSQC and only few signals are below the diagonal. The signals with lower intensity can be traced back to be four threonines where the respective $\text{C}\beta$ is situated in the transition range of the band-selective pulse. For all other residues the loss in signal intensity depends strongly on the number and size of active homonuclear ^{13}C -couplings as can be calculated from Equation (3.6.1). Clearly, for longer acquisition times, as might be desired for small peptides and IDPs, the signal reduction of long-range homonuclear couplings might be enhanced even further. It is further interesting to note that the *by far* largest increase in signal intensity is obtained for the three proline residues which are basically zero in the conventional CT-HSQC. In intrinsically disordered proteins, prolines are typically present at high abundance and, hence, they constitute valuable information with respect to the protein's conformational stability^[335] – signal loss should be avoided at all cost. Note, the suitable real-time pure shift acquisition (BASEREX) is not used for ubiquitin in order to obtain results that are comparable to the conventional CT-HSQC. As mentioned in literature, if used to acquire $\text{H}\alpha, \text{C}\alpha$ -correlations for proteins of the size of ubiquitin, BASEREX would still lead to an increase in resolution, but possibly with slightly reduced sensitivity.^[12]

¹⁰⁸ The term refers to the increase of *individual* signals and should not be confused with the “increase in average intensity”.

¹⁰⁹ Note, negative intensities are encountered for signals whose coupling partner likewise resonates in the selected ^{13}C -band and for integration the absolute value is used.

3.6.3 Conclusion

Conclusively, the constant time version of the SHACA-HSQC offers a subtle way out if coupled spins both resonate within the selected ^{13}C -band. This is shown for serine residues that exhibit dispersive anti-phase signals in the standard SHACA-HSQC (Section 3.4) and coupling suppression is achieved from constant time acquisition in the indirect dimension. Note, signal loss can be encountered if one of the coupled spins resonates within the transition width of the selective pulse and the use of the I-BURP (Section 2.4.7) is recommended. Based on the fact that coupling partners are tolerated within the same selected band, it would, hence, be possible to increase the bandwidth of applied selective pulses and further include glycine residues in the CT-SHACA-HSQC experiment. Especially for intrinsically disordered proteins where, on the one hand, low signal dispersion facilitates the distinct $\text{C}\alpha$ -band-selection and, on the other hand, high resolution is desperately needed, the CT-SHACA-HSQC provides a valuable tool for pure shift $\text{H}\alpha, \text{C}\alpha$ -correlations.

Chapter 4

Summary

A principal aim of the dissertation at hand was to introduce novel conceptions, experimental methods and elements for pulse sequence development with particular focus on *coherence transfer* and *homonuclear decoupling*. Experimental results were regularly backed by numerical simulations and, if appropriate, discussions were embedded in the frame of *average Hamiltonian theory* (AHT) in order to provide a profound theoretical background.

In certain cases, technical advances – like the ongoing increase of static magnetic fields – require new experimental approaches and an adaption of existing methodology. For this reason, it was demonstrated that broadband *planar mixing* (PM), using the *perfect echo* with shaped pulses, is able to provide capable solutions at moderate RF amplitudes *also* for high magnetic fields, where large bandwidths are required and conventional mixing sequences break down (Section 2.2). A *full* ^{13}C , ^{13}C -PM-TOCSY was acquired on a spectrometer of 1.0 GHz proton Larmor frequency for a mixture of uniformly ^{13}C , ^{15}N -isotope labeled amino acids. Likewise, an application in a more elaborate 3D (H)CC(CO)NH experiment was presented, which can be used for the assignment of protein side-chains. For globular proteins, transfer in aromatic side-chains has appeared to be delicate and possible solutions have been discussed that remain to be tested in future investigations. Yet, the PM-approach is not limited to biomolecular NMR, but could be used for any homo- or heteronuclear coherence transfer involving nuclei with large signal dispersions (e.g. ^{19}F or ^{31}P) or if experimental setups require large compensation of B_1 -field inhomogeneity.

An extension of the conventional perfect echo has lead to the so-called *isotropic* perfect echo (IPE) – as thoroughly discussed using AHT, isotropic mixing was obtained at low average power (Section 2.3). An exemplary application to diffusion ordered spectroscopy (DOSY) was presented where the proposed low energy IPE is used to replace the conventionally applied stimulated echo. Isotropic mixing, exhibiting the remarkable property of *spin state preservation*, allows the suppression of J -modulation and *all* components of *transverse* magnetization are retained. As a consequence, for small- to medium-sized molecules, high resolution spectra were obtained with an up to fourfold increase in sensitivity compared to conventionally used DOSY with convection compensation. It could further be shown that also *longitudinal* magnetization is preserved during IPEs, which allows to transfer the concept of *Ernst angle excitation* to be applied in DOSY. By this means, *fast* DOSY experiments were obtained, that provide spectra at high resolution and sensitivity in less than half a minute – due to low average power of given IPE-sequences, no RF limits are met. Artifacts from chemical exchange are *less* pronounced than in conventional DOSY, which was ascribed to coherence transfer during the IPE sequence. Due to the fact, that also in the IPE hard pulses can be replaced by shaped pulses, a fast and broadband ^{19}F -DOSY is conceivable and intended in the near future.

In the given planar and isotropic mixing sequences, the use of shaped pulses constitutes a key aspect which has greatly enhanced versatility – however, little is known about the effect of couplings during the applied pulses. An *a posteriori* evaluation of effective *homo- and heteronuclear* coupling evolution during shaped pulses has, therefore, been undertaken (Section 2.4). For this, a set of selected pulse shapes was subject to a numerical examination using a self-derived extension of AHT including offset effects. The implemented python routines have provided a valuable measure for coupling effects, that

can quantitatively be used for pulse sequence development. It shall be mentioned, that already throughout the present dissertation, the pulse shape analyses have repeatedly been used (e.g. for PM-TOCSY, BASEREX or methyl-SHACA). It is supposed that the presented investigations provide a helpful guide for future experimenters, that allows to correctly embed shaped pulses in given experiments.

Developing the offset-dependent AHT analysis has also opened up the examination of other phenomena. In this context, the interaction of a strongly coupled two-spin system and how it can be treated in the frame of AHT has thoroughly been discussed: the *time-independent* Hamiltonian of a strongly coupled two-spin system was made *time-dependent* in a double-rotating frame and a closer look revealed, that all *second order effects* could be ascribed to a Berry-phase induced by the time-dependence of zero-quantum operators. The results, inevitably, are identical to the ones obtained from well-known calculations of standard textbooks, but are essential to acquire a deeper understanding of the nature of strong coupling.

At the end of Chapter 2, a novel element for ^{13}C -HSQC-type sequences was introduced and its application presented in two experiments, the JRES-HOMQC and HOMQC-TOCSY (Section 2.6). Due to the fact that so-called *ordered multi-quantum coherences*, which are created within the element, commute with selected parts of the heteronuclear coupling Hamiltonian, *all* multiplicities (CH, CH₂ and CH₃) exhibit only a doublet $^1J_{\text{CH}}$ -splitting in the *indirect*, carbon-evolved dimension. MQ-coherences for CH₂-groups additionally evolve according to the $^2J_{\text{HH}}$ -coupling, which was further used in the JRES-HOMQC to determine the *size and sign* of $^2J_{\text{HH}}$ from DQ- and ZQ-coherence selection. For investigated small molecules, remarkably sharp lines of down to 0.55 Hz were acquired in the indirect dimension (CHCl₃ at 0.46 Hz in 1H -1D), which allows coupling extractions at high accuracy. The HOMQC-TOCSY, on the other hand, was combined with a spin state selective backtransfer and used for sign-sensitive measurements of long-range $^nJ_{\text{CH}}$ -couplings in very reduced and simple E.COSY-type multiplets. Moreover, it was demonstrated that, within the novel element, multiplicity and DQ/ZQ-editing is achieved from a simple shift of pulse phases, and filtered spectra are obtained, that only comprise the desired, essential information. Yet, the proposed experiments still exhibit a certain artifact level and further modifications are intended.

In Chapter 3 of the present thesis, homonuclear decoupling (HD) as a very important tool for resolution enhancement in modern NMR spectroscopy has been extended to the effective use with uniformly ^{13}C , ^{15}N -labeled biomolecules. Most biomolecular NMR experiments rely on the detection of amide protons, which, being part of a large coupling network, are considerably broadened from underlying multiplets. For this reason, a ^{13}C -BIRD-based acquisition sequence was proposed, that allows *homo- and heteronuclear* decoupling. It was demonstrated for an intrinsically disordered (p53TAD) and globular protein (human ubiquitin) that resolution could be roughly doubled while high sensitivity was maintained. For ubiquitin, the average linewidth was reduced from ~ 16.3 Hz to ~ 8.8 Hz using a fast HSQC, whereof ~ 3.7 Hz are due to the suppression of long-range heteronuclear couplings. For a BEST-TROSY, comprising coherence selection with favorable relaxation properties, the average linewidth could be decreased even further from ~ 16.0 Hz to ~ 7.3 Hz. Similar results were obtained for p53TAD (from ~ 14.2 Hz to ~ 7.5 Hz) and an increased average signal intensity of $\sim 11\%$ was encountered for an interscan delay of $\tau_r = 0.2$ s. Due to the fact that radiation damping can largely be prevented, saturation of water was *not* required for solvent suppression and protons in moderate exchange with water can, hence, benefit from faster signal recovery. The encountered quality of solvent suppression was comparable to other HD methods that use gradients or weak RF-fields for saturating water.

It has further been shown that also the real-time pure shift acquisition of ^{13}C -bound protons provides high resolution using a ^{13}C -BIRD-filter in *combination* with a ^{13}C -band-selective pulse (Section 3.3).^[12] Consequently, the selection of BIRD-inverted protons is no longer given by the attached carbon-isotope, but from carbons on which the band-selective pulse is applied – the large signal dispersion of heteronuclei can, hence, be used for the suppression of homonuclear *proton-proton* couplings. The proposed acquisition sequence, termed BASEREX,^[12] was tested on uniformly ^{13}C -labeled D-glucose and ^{13}C , ^{15}N -labeled amino acids with a considerable increase in resolution and sensitivity. Based on the fact that also long-range *proton-carbon* couplings are suppressed by the chunked acquisition, ^{13}C -CPD could be applied with reduced bandwidth and long acquisition times exceeding 200 ms were accessible at no risk for the probe. The BASEREX acquisition scheme is intended for the application in HSQC-type experiments and was further used to obtain pure shift selective H α ,C α -correlations (SHACA).

The proposed SHACA-HSQC has been proven highly suitable for the investigation of intrinsically disordered proteins at near-physiological conditions (Section 3.4).^[11] Based on the high gyromagnetic ratio, it was demonstrated that non-exchangeable protons can be acquired at high sensitivity and even for low-concentrated samples ($\sim 2.5 \mu\text{M}$) $\text{H}\alpha, \text{C}\alpha$ -correlations were obtained in less than an hour. In combination with BASEREX, typically unresolved multiplets are collapsed in *both* dimensions of the 2D experiment and pure shift $\text{H}\alpha, \text{C}\alpha$ -correlations were acquired at high resolution and low water artifact level. Since glycine residues typically exhibit a distinct $\text{C}\alpha$ -chemical shift, band-selection for all residues might not always be possible. Also, decoupling of serine residues might be hindered due to similar chemical shifts of $\text{C}\alpha$ and $\text{C}\beta$. For this reason, the SHACA-HSQC was combined with a *constant time* (CT) period and decoupling was achieved for all nuclei within the selected $\text{C}\alpha$ -band as demonstrated for serine residues (Section 3.6). Due to the suppression of long-range heteronuclear couplings, high resolution was still accessible using CT and an extension of the $\text{C}\alpha$ -band to include glycine residues is likewise thinkable. Finally, a slightly modified SHACA-sequence was further used to detect *pure shift* $\text{H}_{\text{methyl}}, \text{C}_{\text{methyl}}$ -correlations for methyl-groups at likewise high resolution and sensitivity (Section 3.5).

In summary, four major achievements with potential impact on high resolution NMR spectroscopy have been the outcome of the present thesis. First, low average power planar and isotropic mixing sequences with up to an order of magnitude increase in accessible bandwidths have been presented and applied to TOCSY and DOSY-type correlation experiments. These coherence transfer blocks will certainly inspire a large variety of future experiments like fast-pulsing ASAP sequences and will enable spin-spin correlation on unprecedented chemical shift ranges e.g. the extremely large spectral widths of ^{19}F or ^{31}P nuclei. Second, novel HOMQC-type experiments were proposed that for the first time allow pure doublet evolution in the carbon dimension for all multiplicities. Coupling measurements become especially simple yet highly accurate. Third, the novel theoretical description of offset dependent average Hamiltonians will allow in the future a detailed but general description of pulse properties and fundamental processes like coupling evolution in the strong coupling limit. Fourth, specific homonuclear decoupling schemes for amide protons as well as carbon-bound protons in uniformly isotopically enriched samples will lead to significant gains in resolution of slow-relaxing biomacromolecules, thereby significantly increasing the range of potentially accessible target molecules.

Chapter 5

Appendix

5.1 Theory

5.1.1 Spin Rotation from Exponential Operator

In the present section it shall be shown that an exponential operator can induce a rotation in spin space and a general propagator U_A can be expressed in a power series where \hat{A} corresponds to one of the Cartesian operators \hat{I}_x , \hat{I}_y and \hat{I}_z and we note that $\hat{I}_x^2 = \hat{I}_y^2 = \hat{I}_z^2 = \frac{1}{4}\mathbb{1}$. The propagator U_A is given as:

$$\begin{aligned}
 U_A &= \exp \left\{ -i\theta\hat{A} \right\} \\
 &= \mathbb{1} + (-i\theta\hat{A}) + \frac{(-i\theta\hat{A})^2}{2!} + \frac{(-i\theta\hat{A})^3}{3!} + \frac{(-i\theta\hat{A})^4}{4!} + \frac{(-i\theta\hat{A})^5}{5!} + \dots \\
 &= \mathbb{1} + (-i\frac{\theta}{2})2\hat{A} + \frac{(-i\frac{\theta}{2})^2}{2!}(2\hat{A})^2 + \frac{(-i\frac{\theta}{2})^3}{3!}(2\hat{A})^3 + \frac{(-i\frac{\theta}{2})^4}{4!}(2\hat{A})^4 + \frac{(-i\frac{\theta}{2})^5}{5!}(2\hat{A})^5 + \dots \\
 &= \underbrace{\mathbb{1}}_{\cos} + \underbrace{(-i\frac{\theta}{2})2\hat{A}}_{\sin} + \underbrace{\frac{(-i\frac{\theta}{2})^2}{2!}\mathbb{1}}_{\cos} + \underbrace{\frac{(-i\frac{\theta}{2})^3}{3!}2\hat{A}}_{\sin} + \underbrace{\frac{(-i\frac{\theta}{2})^4}{4!}\mathbb{1}}_{\cos} + \underbrace{\frac{(-i\frac{\theta}{2})^5}{5!}2\hat{A}}_{\sin} + \dots \\
 &= \cos\left(\frac{\theta}{2}\right)\mathbb{1} - i\sin\left(\frac{\theta}{2}\right)2\hat{A}.
 \end{aligned}$$

Hence, the propagators U_x , U_y and U_z can be expressed in terms of rotation matrices:

$$\begin{aligned}
 U_x &= \exp \left\{ -i\theta\hat{I}_x \right\} = \cos\left(\frac{\theta}{2}\right)\mathbb{1} - i\sin\left(\frac{\theta}{2}\right)2\hat{I}_x = \begin{pmatrix} \cos\frac{\theta}{2} & -i\sin\frac{\theta}{2} \\ -i\sin\frac{\theta}{2} & \cos\frac{\theta}{2} \end{pmatrix} \\
 U_y &= \exp \left\{ -i\theta\hat{I}_y \right\} = \cos\left(\frac{\theta}{2}\right)\mathbb{1} - i\sin\left(\frac{\theta}{2}\right)2\hat{I}_y = \begin{pmatrix} \cos\frac{\theta}{2} & -\sin\frac{\theta}{2} \\ +\sin\frac{\theta}{2} & \cos\frac{\theta}{2} \end{pmatrix} \\
 U_z &= \exp \left\{ -i\theta\hat{I}_z \right\} = \cos\left(\frac{\theta}{2}\right)\mathbb{1} - i\sin\left(\frac{\theta}{2}\right)2\hat{I}_z = \begin{pmatrix} e^{-i\frac{\theta}{2}} & 0 \\ 0 & e^{+i\frac{\theta}{2}} \end{pmatrix}.
 \end{aligned}$$

5.1.2 Irreducible Tensor Components

The present section refers to Section 1.3.2 of the main text and different tensor notations are discussed. The result of the tensor decomposition in Cartesian and spherical coordinates shall be shown for the spatial tensor \mathcal{A} and the spin tensor \mathcal{T} , respectively. The decomposition of \mathcal{A} in Cartesian coordinates offers an intuitive illustration of the tensors' components in its principal axes (PAS) while the spherical spin components (T_l^m) of the tensor \mathcal{T} are helpful to conceive its evolution under a z-rotation.

Cartesian Tensor

A Cartesian rank 2 tensor \mathcal{A} (written in arbitrary axes. can be decomposed into three irreducible Cartesian tensors.

$$\mathcal{A} = \begin{pmatrix} A_{xx} & A_{xy} & A_{xz} \\ A_{yx} & A_{yy} & A_{yz} \\ A_{zx} & A_{zy} & A_{zz} \end{pmatrix} = \underbrace{a_{\text{iso}} \begin{pmatrix} 1 & 0 & 0 \\ 0 & 1 & 0 \\ 0 & 0 & 1 \end{pmatrix}}_{\mathcal{A}_0} + \underbrace{\begin{pmatrix} 0 & \alpha_{xy} & \alpha_{xz} \\ \alpha_{yx} & 0 & \alpha_{yz} \\ \alpha_{zx} & \alpha_{zy} & 0 \end{pmatrix}}_{\mathcal{A}_1} + \underbrace{\begin{pmatrix} \delta_{xx} & \delta_{xy} & \delta_{xz} \\ \delta_{yx} & \delta_{yy} & \delta_{yz} \\ \delta_{zx} & \delta_{zy} & \delta_{zz} \end{pmatrix}}_{\mathcal{A}_2} \quad (5.1.1)$$

whereof \mathcal{A}_0 is isotropic (rank 0), \mathcal{A}_1 is antisymmetric (rank 1) and \mathcal{A}_2 is a traceless symmetric tensor (rank 2). \mathcal{A}_0 , \mathcal{A}_1 and \mathcal{A}_2 consist of 1, 3 and 5 distinct coefficients, respectively, and these are given as:

$$a_{\text{iso}} = \frac{1}{3}(A_{xx} + A_{yy} + A_{zz}) \quad (5.1.2)$$

$$\alpha_{uv} = \frac{1}{2}(A_{uv} - A_{vu}) \quad (5.1.3)$$

$$\delta_{uv} = \frac{1}{2}(A_{uv} + A_{vu} - 2 \cdot a_{\text{iso}}) \quad (5.1.4)$$

from which is clear that \mathcal{A}_1 is antisymmetric since $\alpha_{uv} = -\alpha_{vu}$ and $\alpha_{uu} = 0$. Assuming the antisymmetric constituent is zero the tensor in its principal axes is diagonal and given as:

$$\mathcal{A}(\text{PAS}) = a_{\text{iso}} \begin{pmatrix} 1 & 0 & 0 \\ 0 & 1 & 0 \\ 0 & 0 & 1 \end{pmatrix} + \begin{pmatrix} \delta'_{xx} & 0 & 0 \\ 0 & \delta'_{yy} & 0 \\ 0 & 0 & \delta'_{zz} \end{pmatrix} \quad (5.1.5)$$

with $\delta'_{uu} = (A_{uu} - a_{\text{iso}})$. A discussion on the antisymmetric constituent of \mathcal{A} and its potential influences on spectroscopy is found in literature^[28] while its existence has already been verified.^[349]

Spherical Tensor

Recall that a tensor \mathcal{T} for an arbitrary spin-spin interaction is constructed by the dyadic product of two arbitrary spin vectors which in *Cartesian coordinates* are given as:

$$\mathcal{T} = \begin{pmatrix} \hat{I}_x \\ \hat{I}_y \\ \hat{I}_z \end{pmatrix} \begin{pmatrix} \hat{S}_x & \hat{S}_y & \hat{S}_z \end{pmatrix} = \begin{pmatrix} \hat{I}_x \hat{S}_x & \hat{I}_x \hat{S}_y & \hat{I}_x \hat{S}_z \\ \hat{I}_y \hat{S}_x & \hat{I}_y \hat{S}_y & \hat{I}_y \hat{S}_z \\ \hat{I}_z \hat{S}_x & \hat{I}_z \hat{S}_y & \hat{I}_z \hat{S}_z \end{pmatrix} \quad (5.1.6)$$

The tensor \mathcal{T} can be decomposed into its irreducible tensor components in *spherical coordinates* (T_l^m)

^[349] R. Paquin et al. *The Journal of Chemical Physics* **2010**, *133*, 034506.

which can be written in Cartesian operators as:^[26]

$$\begin{aligned}
T_0^0 &= -\frac{1}{\sqrt{3}}(\hat{I}_x\hat{S}_x + \hat{I}_y\hat{S}_y + \hat{I}_z\hat{S}_z) \\
T_1^0 &= \frac{i}{\sqrt{2}}(\hat{I}_x\hat{S}_y - \hat{I}_y\hat{S}_x) \\
T_1^{\pm 1} &= \frac{1}{2}[\hat{I}_z\hat{S}_x - \hat{I}_x\hat{S}_z \pm i(\hat{I}_z\hat{S}_y - \hat{I}_y\hat{S}_z)] \\
T_2^0 &= \frac{1}{\sqrt{6}}[3\hat{I}_z\hat{S}_z - (\hat{I}_x\hat{S}_x + \hat{I}_y\hat{S}_y + \hat{I}_z\hat{S}_z)] \\
T_2^{\pm 1} &= \mp\frac{1}{2}[\hat{I}_x\hat{S}_z + \hat{I}_z\hat{S}_x \pm i(\hat{I}_y\hat{S}_z + \hat{I}_z\hat{S}_y)] \\
T_2^{\pm 2} &= \frac{1}{2}[\hat{I}_x\hat{S}_x - \hat{I}_y\hat{S}_y \pm i(\hat{I}_x\hat{S}_y + \hat{I}_y\hat{S}_x)].
\end{aligned} \tag{5.1.7}$$

The spatial tensor \mathcal{A} can be decomposed in the same way and its spherical components (A_l^m) can be derived from Equation (5.1.7) with $A_{uv} = \hat{I}_u\hat{S}_v$. Likewise the tensor components in *spherical coordinates* (T_l^m) can be written in shift operators (only the symmetric parts shown):^[26]

$$\begin{aligned}
T_0^0 &= -\frac{1}{2\sqrt{3}}[2\hat{I}_z\hat{S}_z + (\hat{I}_+\hat{S}_- + \hat{I}_-\hat{S}_+)] \\
T_2^0 &= \frac{1}{2\sqrt{6}}[4\hat{I}_z\hat{S}_z - (\hat{I}_+\hat{S}_- + \hat{I}_-\hat{S}_+)] \\
T_2^{\pm 1} &= \mp\frac{1}{2}(\hat{I}_z\hat{S}_{\pm} + \hat{I}_{\pm}\hat{S}_z) \\
T_2^{\pm 2} &= \frac{1}{2}\hat{I}_{\pm}\hat{S}_{\pm}.
\end{aligned} \tag{5.1.8}$$

from which becomes clear that the adjoint of the tensor components is given as: $(T_l^m)^\dagger = (-1)T_l^{-m}$.

5.1.3 Basic Properties of the Trace

Some basic properties of the trace are shown, where \otimes denotes the Kronecker product:

$$\text{Tr}\{\hat{A}\} = \sum_m \langle m|\hat{A}|m\rangle \tag{5.1.9}$$

$$\text{Tr}\{A + B\} = \text{Tr}\{A\} + \text{Tr}\{B\} \tag{5.1.10}$$

$$\text{Tr}\{c \cdot A\} = c \cdot \text{Tr}\{A\} \tag{5.1.11}$$

$$\text{Tr}\{A \otimes B\} = \text{Tr}\{A\} \cdot \text{Tr}\{B\} \tag{5.1.12}$$

$$\text{Tr}\{ABC\} = \text{Tr}\{CAB\} = \text{Tr}\{BCA\} \tag{5.1.13}$$

5.1.4 Basic Properties of the Kronecker Product

A useful identity for the simultaneous application of the Kronecker and the Matrix product is given as:

$$(A \otimes B)(C \otimes D) = AC \otimes BD \quad (5.1.14)$$

from which follows that the Kronecker product of two Pauli matrices will lead to an expanded basis and product operators can be created. Note, a bilinear term can be obtained also from matrix multiplication of individual linear terms in the expanded basis. Using Equation (5.1.14) it can be shown:

$$\sigma_\gamma \otimes \sigma_\delta = \sigma_\gamma \mathbb{1} \otimes \mathbb{1} \sigma_\delta = (\sigma_\gamma \otimes \mathbb{1})(\mathbb{1} \otimes \sigma_\delta) = I_{1\gamma} I_{2\delta} \quad (5.1.15)$$

with $\gamma, \delta = (x, y, z)$. Following the above Equation (5.1.15) it can likewise be shown that:

$$I_{1\gamma} I_{2\delta} = (\sigma_\gamma \otimes \mathbb{1})(\mathbb{1} \otimes \sigma_\delta) = \sigma_\gamma \mathbb{1} \otimes \mathbb{1} \sigma_\delta = \mathbb{1} \sigma_\gamma \otimes \sigma_\delta \mathbb{1} = (\mathbb{1} \otimes \sigma_\delta)(\sigma_\gamma \otimes \mathbb{1}) = I_{2\delta} I_{1\gamma}. \quad (5.1.16)$$

5.1.5 Transformation of a Propagator

The transformation of the Hamiltonian in an exponential will lead to the same result as the transformation of the Hamiltonian's propagator:

$$\begin{aligned} \exp\{-i\theta (U^\dagger \hat{\mathcal{H}} U)\} &= \sum_n \frac{(-i\theta)^n}{n!} (U^\dagger \hat{\mathcal{H}} U)^n \\ &= \sum_n \frac{(-i\theta)^n}{n!} U^\dagger (\hat{\mathcal{H}})^n U \\ &= U^\dagger \left(\sum_n \frac{(-i\theta)^n}{n!} \hat{\mathcal{H}}^n \right) U \\ &= U^\dagger \exp\{-i\theta \hat{\mathcal{H}}\} U \end{aligned} \quad (5.1.17)$$

where in the second line the identity $UU^\dagger = \mathbb{1}$ is used.

5.1.6 In Detail: Transformation to the Toggling Frame

The calculation of the transformed Hamiltonian in the toggling frame from Section 1.6.1 will be derived in more detail and the same notation is used as in the main text. For the first step, the transformation from the rotating to the toggling frame is described by U_{T_1} and the spin state in the toggling frame $|\psi_{T_1}\rangle$ is given as:

$$\langle \psi_{T_1} | = \langle \psi_R | U_{T_1} \quad \text{and} \quad |\psi_{T_1}\rangle = U_{T_1}^\dagger |\psi_R\rangle. \quad (5.1.18)$$

The evolution of the spin state in the toggling frame can be derived in close analogy to Equation (1.5.15) and it should, again, be noted that $[U_{T_1}, \sum_k \omega_k \hat{I}_{k\gamma}] = 0$. We obtain the Hamiltonian for the first transformation:

$$\begin{aligned} \frac{\partial}{\partial t} |\psi_{T_1}\rangle &= \frac{\partial}{\partial t} (U_{T_1}^\dagger) |\psi_R\rangle + U_{T_1}^\dagger \frac{\partial}{\partial t} (|\psi_R\rangle) \\ &= U_{T_1}^\dagger (i\hat{\mathcal{H}}_{R,P_1}) |\psi_R\rangle - iU_{T_1}^\dagger [\hat{\mathcal{H}}_{R,P_1} + \hat{\mathcal{H}}_{R,C}] |\psi_R\rangle \\ &= -iU_{T_1}^\dagger \hat{\mathcal{H}}_{R,C} U_{T_1} |\psi_{T_1}\rangle \\ &= -i\hat{\mathcal{H}}_{T_1,C} |\psi_{T_1}\rangle. \end{aligned} \quad (5.1.19)$$

It is crucial to note that the coupling Hamiltonian $\hat{\mathcal{H}}_{T_1,C}$ is expressed in the toggling frame and given as:

$$\hat{\mathcal{H}}_{T_1,C} = U_{T_1}^\dagger \hat{\mathcal{H}}_{R,C} U_{T_1} \quad (5.1.20)$$

For the second time step, the transformation is described by U_{T_2} given in Equation (1.6.8) and the Hamiltonian of the pulse in the toggling frame can be derived using the Schrödinger equation:

$$\begin{aligned}
\frac{\partial}{\partial t}|\psi_{T_2}\rangle &= \frac{\partial}{\partial t}(U_{T_2}^\dagger)|\psi_{T_1}\rangle + U_{T_2}^\dagger \frac{\partial}{\partial t}(|\psi_{T_1}\rangle) \\
&= U_{T_2}^\dagger (iU_{T_1}^\dagger \hat{\mathcal{H}}_{R,P_2} U_{T_1})|\psi_{T_1}\rangle - iU_{T_2}^\dagger [U_{T_1}^\dagger \hat{\mathcal{H}}_{R,P_2} U_{T_1} + \hat{\mathcal{H}}_{T_1,C}]|\psi_{T_1}\rangle \\
&= -iU_{T_2}^\dagger \hat{\mathcal{H}}_{T_1,C} U_{T_2} |\psi_{T_2}\rangle \\
&= -i\hat{\mathcal{H}}_{T_2,C} |\psi_{T_2}\rangle.
\end{aligned} \tag{5.1.21}$$

where $\hat{\mathcal{H}}_{T_2,C}$ is the coupling Hamiltonian in the toggling frame and is given as:

$$\begin{aligned}
\hat{\mathcal{H}}_{T_2,C} &= U_{T_2}^\dagger \hat{\mathcal{H}}_{T_1,C} U_{T_2} \\
&= U_{T_2}^\dagger U_{T_1}^\dagger \hat{\mathcal{H}}_{R,C} U_{T_1} U_{T_2}
\end{aligned} \tag{5.1.22}$$

For the n -th step, the derivation can be applied in the very same way and shall, therefore, not be further discussed.

5.1.7 Suzuki-Trotter Approximation for Larger Values of θ

The present appendix affiliates to Section 1.7.3 and the convergence for the Suzuki-Trotter approximants, Equation (1.7.30) and (1.7.31), are shown in Figure 5.1 for large values of θ in red and blue, respectively. Despite the impression that large values of θ cause divergence for small numbers of n , both Suzuki-Trotter approximations converge if n is increased. Again, for full rotations ($n \cdot 2\pi$) the first (1.7.30) and second order (1.7.31) are identical. Since it is $\bar{\mathcal{H}}_0$ that is approximated, consequently, also the Magnus series with higher order terms converges for larger numbers of n .

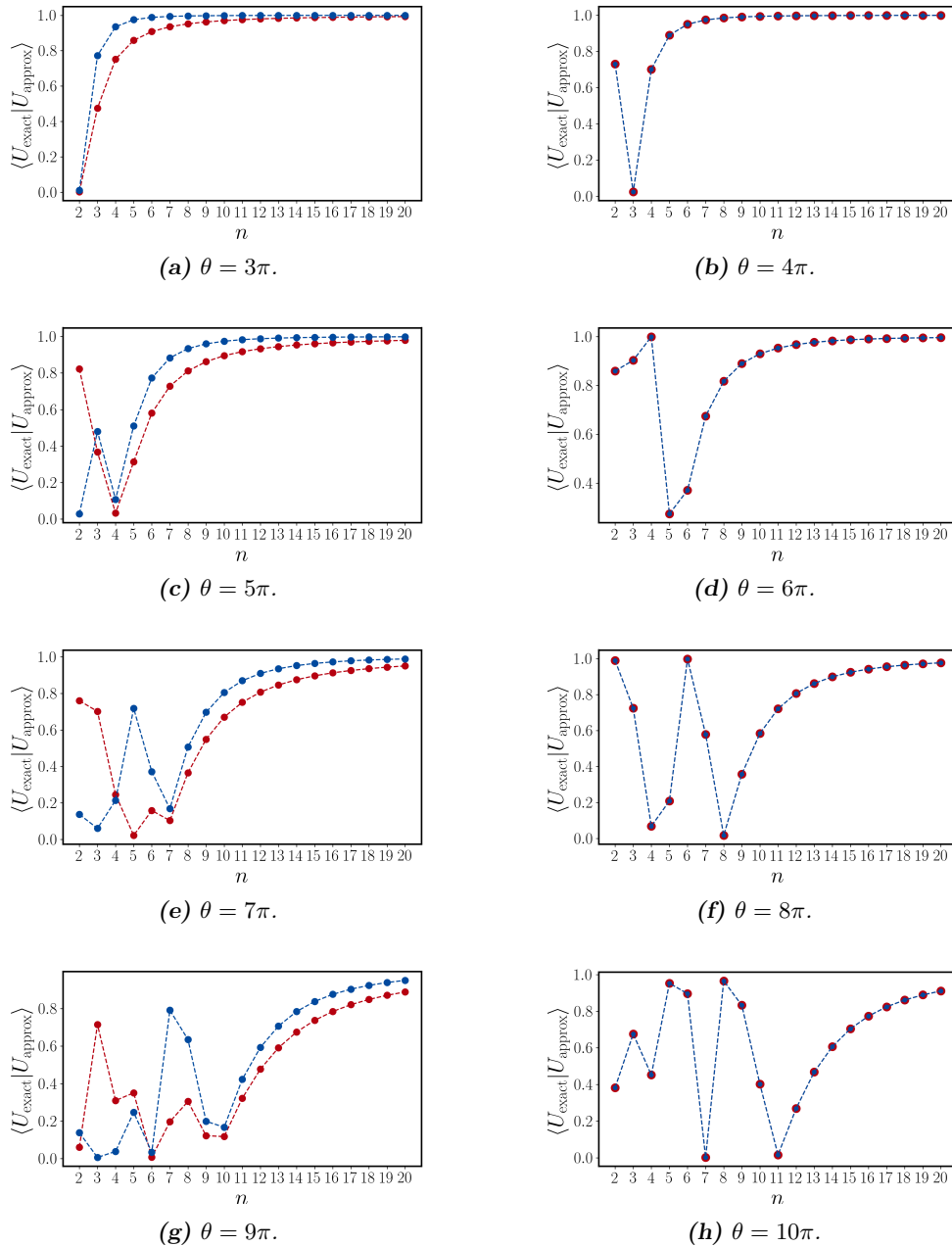


Figure 5.1: The dependency of the Suzuki-Trotter approximants on n considering large values for θ are shown where the first (1.7.30) and second order (1.7.31) are plotted in red and blue, respectively. The scalar product $\langle U_{\text{org}} | U_{\text{approx}} \rangle$ is plotted against n with $\theta = 3\pi$ in (a), $\theta = 4\pi$ in (b), $\theta = 5\pi$ in (c), $\theta = 6\pi$ in (d), $\theta = 7\pi$ in (e), $\theta = 8\pi$ in (f), $\theta = 9\pi$ in (g) and $\theta = 10\pi$ in (h).

5.2 Coherence Transfer Elements

5.2.1 Numerical Simulations of IPE-1

The present section affiliates to Section 2.3.2 where similar numerical simulations are undertaken. In-phase coherence $F_\alpha = \sum_k \hat{I}_{k\alpha}$ is chosen as initial state with $\alpha = \{x, y, z\}$ and, again, in-phase coherence is observed after isotropic mixing. For the applied mixing sequence, IPE-1, the IMP shape (Section 2.4.16) with two basic cycles and hard pulses with four basic cycles are used in Figures 5.2 and 5.3, respectively. From both measures, artifact levels are significantly reduced.

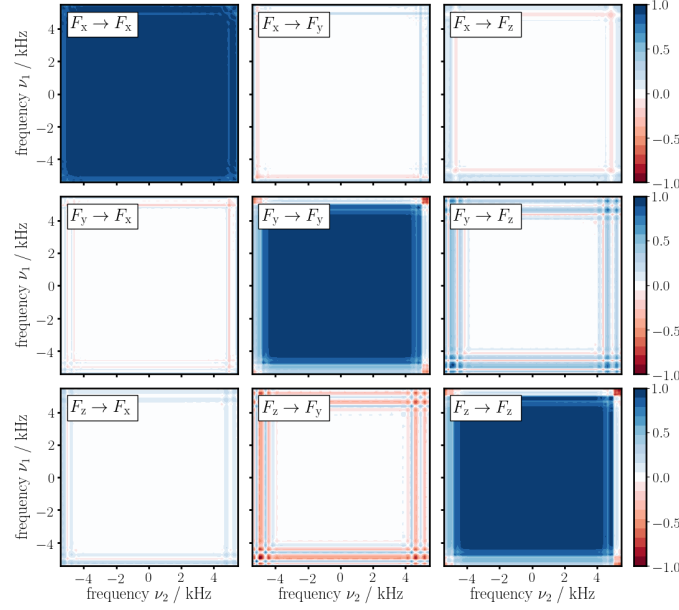


Figure 5.2: The preservation of spin states ($F_\alpha = \sum_k \hat{I}_{k\alpha}$ with $\alpha = \{x, y, z\}$) by IPE-1 with two basic cycles and the IMP shape is examined for a two-spin system using numerical simulations.

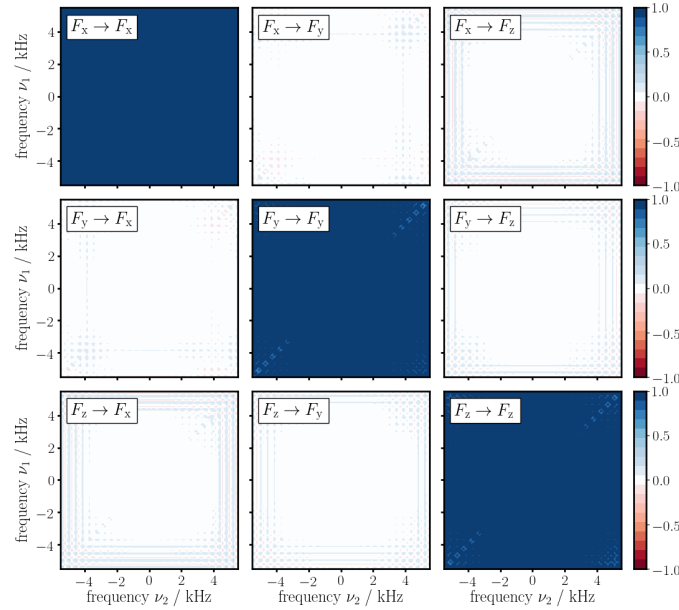


Figure 5.3: The preservation of spin states ($F_\alpha = \sum_k \hat{I}_{k\alpha}$ with $\alpha = \{x, y, z\}$) by IPE-1 with four basic cycles is examined for a two-spin system using numerical simulations.

5.2.2 Spin Echo in the Double Rotating Frame

The simulations in the double rotating frame for a strongly coupled two-spin system, \hat{I}_1 and \hat{I}_2 , are repeated for a spin echo experiment (under identical conditions as discussed in Section 2.5 – only in Figure 5.4 the value $\Delta = 10$ Hz is changed for illustrative reasons). The time evolution of the coupling Hamiltonian $\hat{\mathcal{H}}_{D,J}^{\Delta}(\tau)$ during a delay is shown in Figure 5.4 where the 180° pulse reverses the evolution of the zero quantum parts while the longitudinal part is unaffected. Calculating the zeroth order average Hamiltonian $\bar{\mathcal{H}}_{0,J}(\Delta)$ over the period t_c reveals that strong coupling is retained for larger offsets ($\Delta = |\nu_2 - \nu_1|$) compared to free evolution (Section 2.5) which is shown in Figure 5.5.

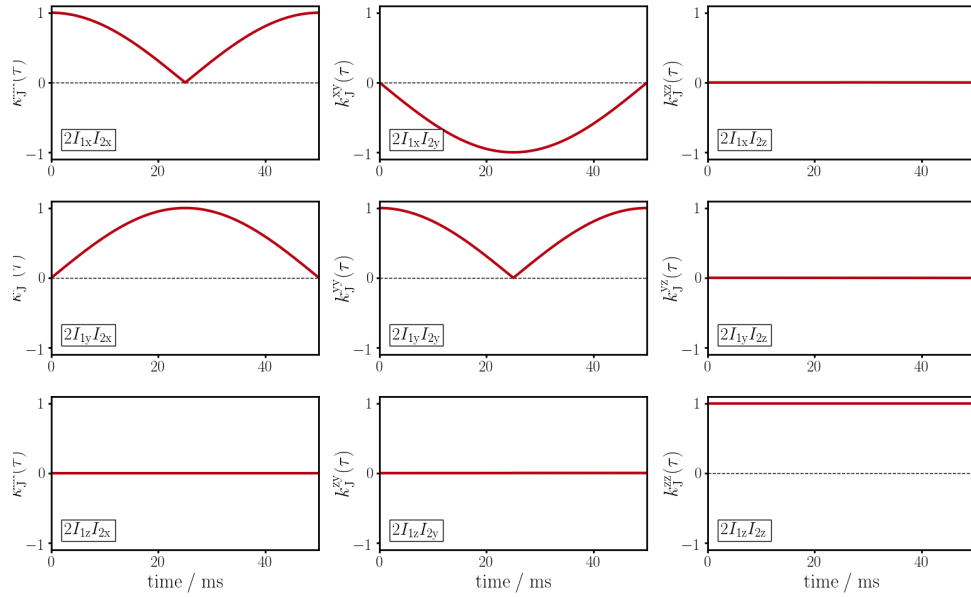


Figure 5.4: The evolution of the strong coupling Hamiltonian $\hat{\mathcal{H}}_{D,J}^{\Delta}(t)$ during a spin echo is shown in the double rotating frame. A two-spin system is assumed with $\Delta = |\nu_2 - \nu_1| = 10$ Hz and $t_c = 50$ ms.

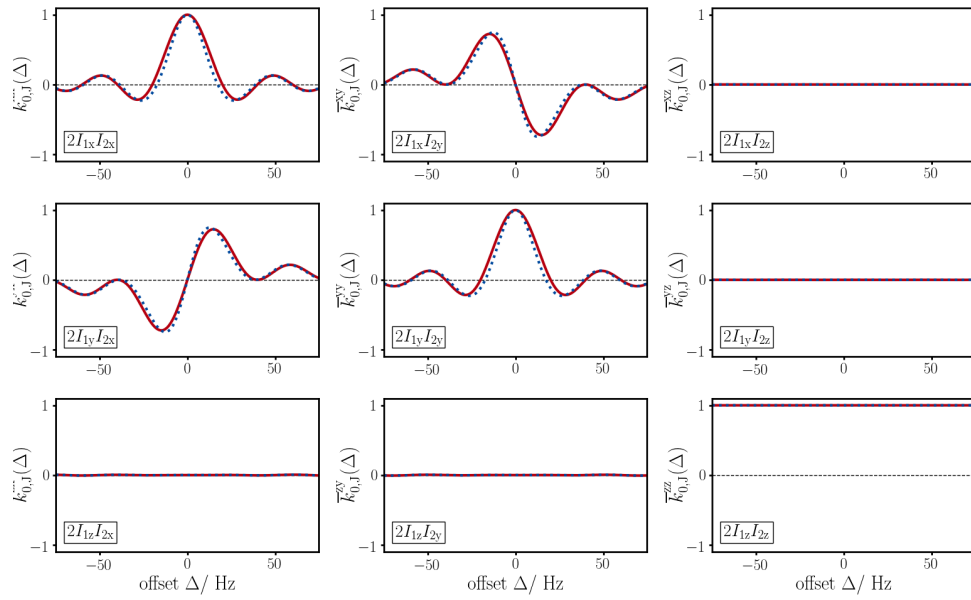


Figure 5.5: The zeroth order average Hamiltonian $\bar{H}_{D,j}(\Delta)$ during a spin echo in the double rotating frame is plotted in red against the offset Δ . Comparable numerical simulations which are based on the logarithm of the effective propagator are plotted in blue dashed lines.

5.2.3 Artifacts in the JRES-HOMQC

The present appendix affiliates to Section 2.6.2 and certain artifacts observed the JRES-HOMQC are shown. Presumably, the conventional HSQC backtransfer is not appropriate for the given experiment and should further be adapted in future investigations.

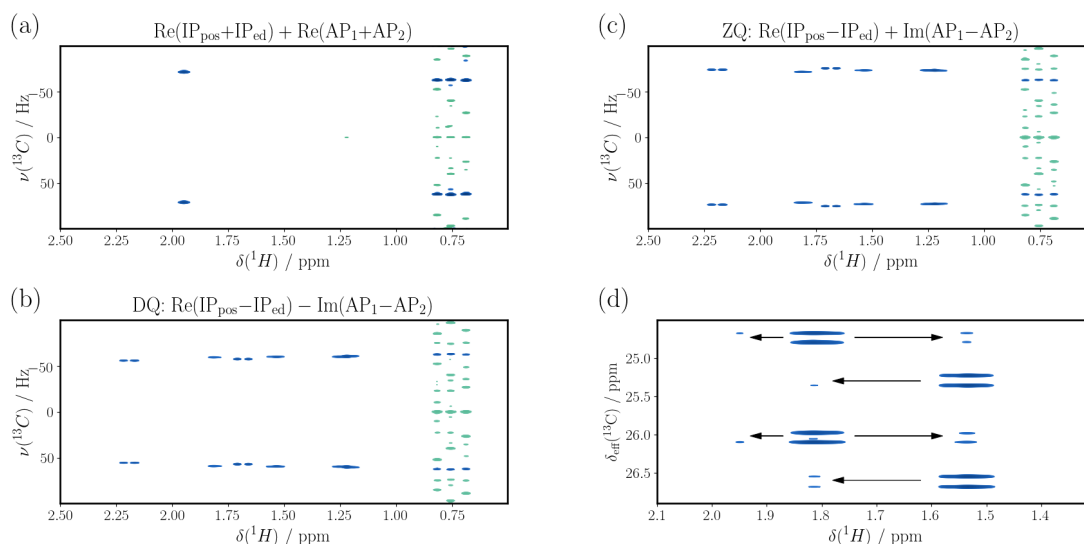


Figure 5.6: The final JRES-HOMQC spectra of camphor after recombination are shown with $\kappa = 0$ in (a) to (c) and $\kappa = 0.2$ in (d). A delay mis-set was purposely introduced in (a) to (c) and $\Delta = 1/(4^1J_{CH})$ with $J_{CH} = 150$ Hz. In (d) the COSY-type coherence transfer can be observed for non-geminal protons. All spectra were acquired with 2 transients and a spectral width of 12 ppm and 512 complex points in the direct dimension. In the indirect dimension a spectral width of 200 Hz and 128 complex points (corresponding to a resolution of ~ 1.56 Hz) were acquired on a 400 MHz spectrometer in 13 min 12 s per spectrum. Calculations are done as indicated above respective spectra.

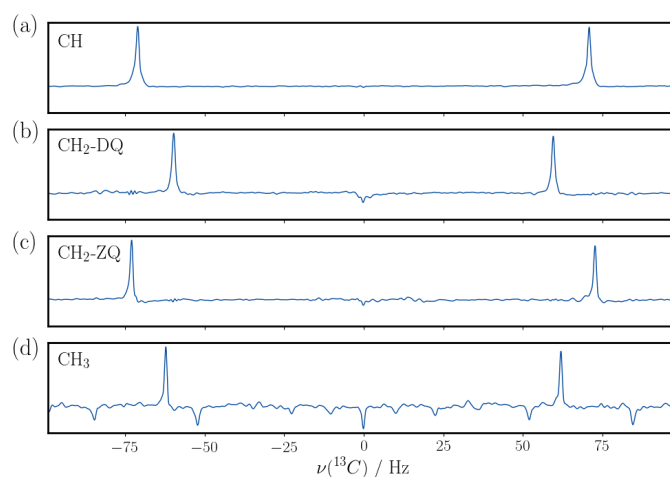


Figure 5.7: Extracted 1D columns from the final JRES-HOMQC spectra of camphor after recombination (Figure 5.6) are shown for CH- (a), DQ- (b), ZQ- (c), and CH₃-signals (d). For given spectra 128 complex points were acquired in the indirect dimension which corresponds to an achievable linewidth of down to ~ 1.56 Hz.

5.3 Homonuclear Decoupling

5.3.1 Experimental Setup and Gradient Calibration for Water Suppression

A step-by-step setup of the BEST-TROSY is described, which should always be used in combination with a gradient optimization discussed below.

Setup of the BEST-TROSY with Pure Shift Acquisition

1. rpar: B.TROSYETF3GPSI
2. getprosol (and calibrate pulses)
3. Set pulse sequence (b_trozy_bbhd_13C) and gpnam8 (SMSQ10.100).
A warning might pop up because chunk length tc (d63) and loop counter n (L0) are not yet set.
4. Increase acquisition time (200ms or more) by increasing TD.
Recall its a TROSY, so no composite pulse decoupling required. For an HSQC acquisition time is limited with respect to power limitations of probehead.
5. Set parameters:

cnst2:	140 Hz	($^1J_{H\alpha,C\alpha}$)
gpz8:	-3.0%	(must be further optimized for water suppression, see following section)
gpz9:	0.1%	(gradient to prevent radiation damping)
NS:	4	
DS:	32	
6. cnst26 gives the offset frequency for carbon inversion pulse. Check that C α s AND COs are covered.
7. It is noticed that the change of preset constants for selective pulse calculation (cnst52-55) has an influence on water suppression.
8. Carbon bound protons need to be inverted for decoupling. Set L0 to even-numbered value and residual magnetization of ^{13}C -bound protons can still be retained for BEST approach.

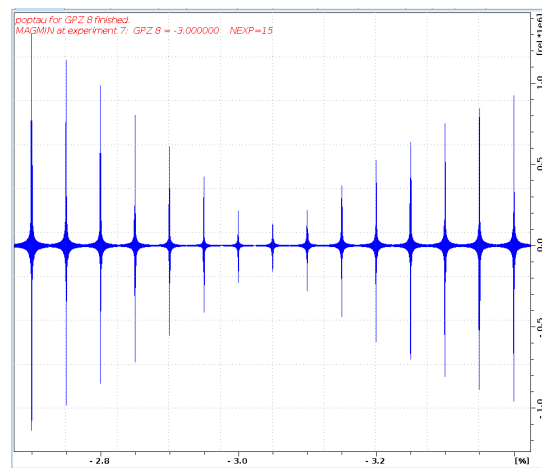
Optimization of Water Suppression (gpz8)

For optimal water suppression we recommend the use of a shigemi tube.

1. Set up the 2D with ALL necessary parameters.
2. Copy the pure-shift experiment and make it a 1D version.
(change parmode in "eda" → there is a button at the top that says "1, 2, ..." → click and choose "1D")
3. Reduce number of scans (NS=1) and dummy scans (DS=2).
(In order to have best reproducibility, keep other parameters as in 2D.)
4. Run a parameter optimization for gpz8. We recommend using "popt", with parameters somewhat like:

PARAMETER	OPTIMUM	STARTVAL	ENDVAL	NEXP	VARMOD	INC
gpz8	MAGMIN	-2.7	-3.4	15	LIN	-0.05

5. Choose gradient strength with the least artifacts. Results should look similar to the figure below:
(Note, for the optimization it can be advisable to choose the HN-area with command "dpl1")
6. Transfer optimal value for gpz8 to 2D.



7. Adjust receiver gain.
8. A second parameter optimization of p1 using "popt" can further improve water suppression if pulses were not calibrated carefully beforehand. Setup can look something like:

PARAMETER	OPTIMUM	STARTVAL	ENDVAL	NEXP	VARMOD	INC
p1	MAGMIN	10.4	10.8	9	LIN	0.05

9. Do not use linear prediction in the indirect dimension if water artifacts reach into the HN area since "noise level" can be increased.

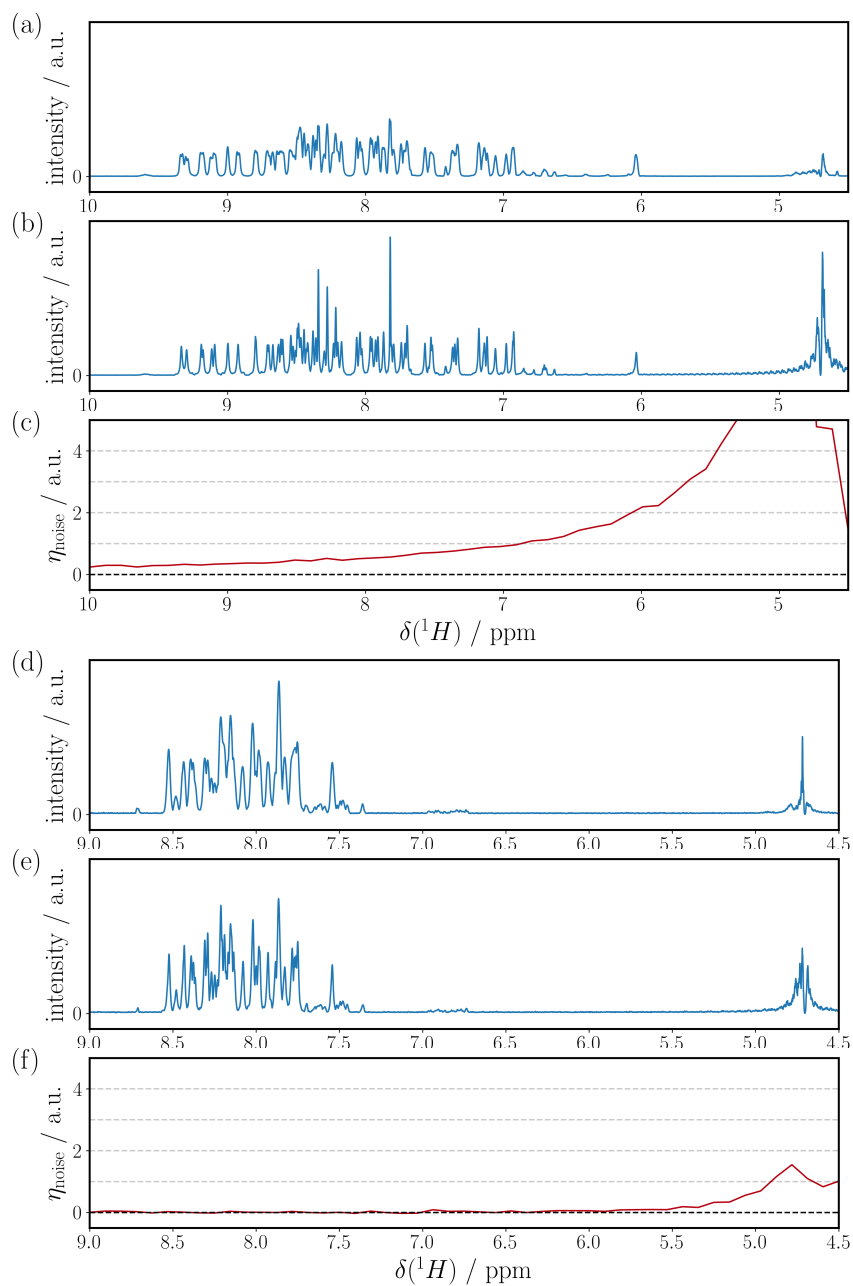


Figure 5.8: Artificial noise level is compared for different BEST-TROSY experiments acquired at 600 MHz with TCI probe for ubiquitin (a-c) and at 700 MHz with liquid nitrogen cooled prodigy probe for p53 (d-f). Absolute value 1D projections along the indirect dimension for standard (a+d) and pure shift acquisition (b+e) are shown in combination with an offset-dependent noise enhancement η_{noise} (c+f) which reflects the increase in noise. It is calculated from: $\eta_{\text{noise}} = N_{\text{HD}}/N_{\text{C}} - 1$ where N_{HD} and N_{C} corresponds to the noise in the homo decoupled and the conventional spectrum, respectively. Clearly, the increase in noise strongly depends on the quality of water suppression and an optimization of gpz8 is, hence, inevitable.

5.3.2 Comparison of FHSQC and BEST-TROSY (Comparable Parameters)

In order to estimate the influence of cross-correlated relaxation on ubiquitin spectra the FHSQC and BEST-TROSY were recorded with similar acquisition parameters of 2048 complex points in 214 ms. While for standard acquisition the reduction in linewidth due to cross-correlated relaxation is covered by broad multiplets, the decrease in linewidth using pure shift acquisition is considerably larger as illustrated in Figure 5.9 (d). This is affirmed by the correlation plot in Figure 5.10 (b) where the average linewidth using pure shift acquisition is reduced by ~ 1.3 Hz for the BEST-TROSY – a decrease of only ~ 0.3 Hz is determined for standard acquisition. Note, the Figure 5.9 (a) and (c) in the appendix are equal to Figure 3.12 (a) and (c) in the main text (Section 3.2.3) which is likewise true for Figure 5.10 (a) and Figure 3.13 (a).

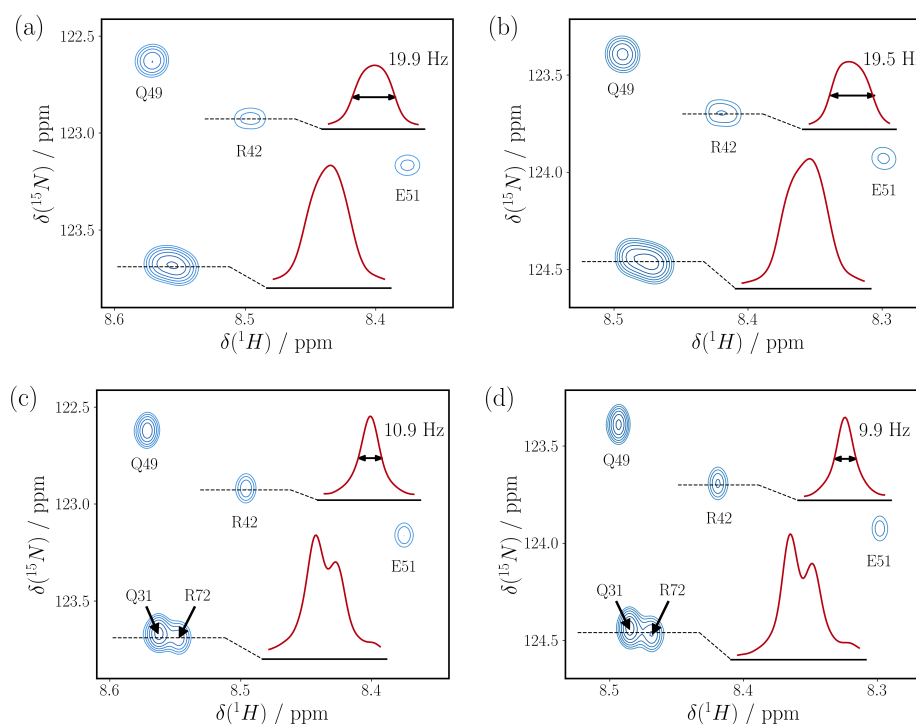


Figure 5.9: Clipped spectra of ubiquitin acquired at 600 MHz using a FHSQC (a+c) and BEST-TROSY (b+d) with standard (a+b) and $^{13}\text{C-BIRD}^{\text{FX}}$ pure shift acquisition (c+d) – a quadratic sine apodization is applied. In both, FHSQC and BEST-TROSY, $n = 6$ chunks were acquired in 214 ms ($\tau_c = 17.8$ ms).

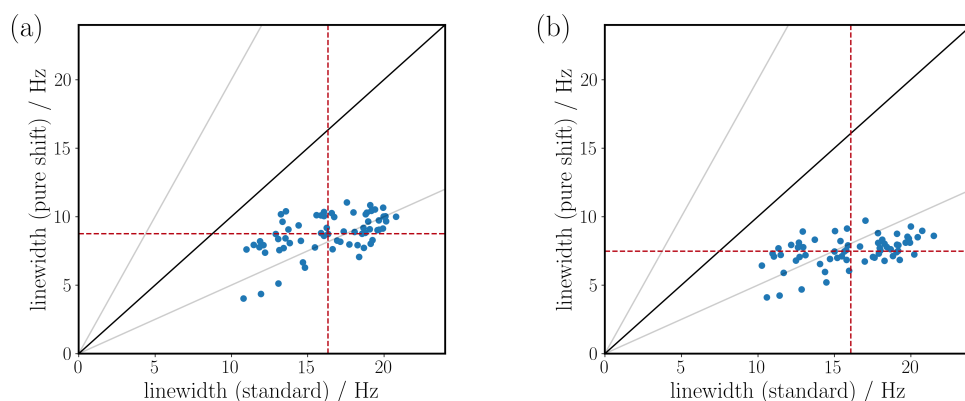


Figure 5.10: The linewidths of amide protons in ubiquitin using a standard and pure shift acquisition are compared in a correlation plot for the FHSQC (a) and BEST-TROSY (b). In both experiments $n = 6$ chunks are acquired in 214 ms ($\tau_c = 17.8$ ms) and no apodization is used. Average values are indicated by red dashed lines which are 16.3 Hz (standard) and 8.8 Hz (pure shift) in (a) and 16.0 Hz (standard) and 7.5 Hz (pure shift) in (b).

5.3.3 Artifact Reduction in Real-Time Pure Shift Acquisition

The present section is affiliated to Section 3.2.3 of the main text and artifacts from real-time pure shift experiments are illustrated in a ^{13}C -BIRD-based pure shift BEST-TROSY. Different methods for artifact suppression are available in literature and exemplary results are illustrated in Figure 5.11.^[305,307] A more detailed discussion on artifacts in real-time homonuclear decoupled experiments is found in Section 3.1.5.

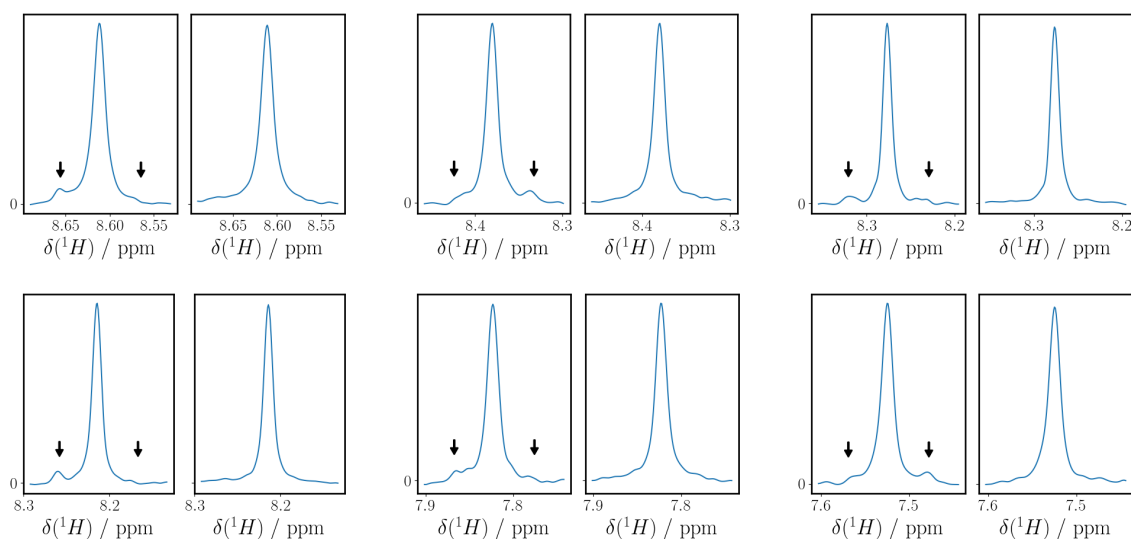


Figure 5.11: Various 1D slices of a BEST-TROSY are shown where artifacts (left images, indicated by arrows) are suppressed (right images) using SAPPHIRE. In the direct dimension $n = 6$ chunks are acquired in 214 ms ($\tau_c = 17.8$ ms) and a quadratic sine apodization is used. For SAPPHIRE the number of scans were doubled.

5.3.4 BEST-TROSY at Fast Repetition Rates (Ubiquitin)

The present section affiliates to the discussion given in Section 3.2.3 and for *ubiquitin* the maximal intensities are illustrated in a correlation plot where BEST-TROSY with and without pure shift is used at $d1 = 0.5$ s.

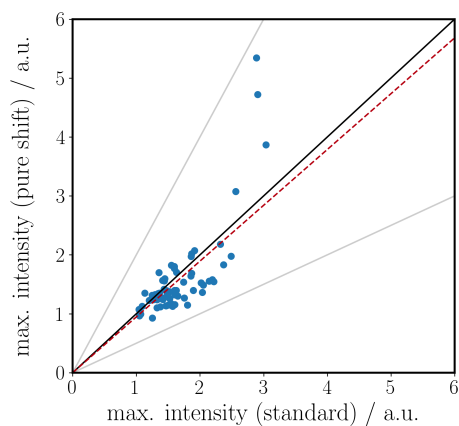


Figure 5.12: The maximal intensities of amide protons in ubiquitin using a standard and pure shift acquisition are compared in a correlation plot for the BEST-TROSY with an interscan delay of $d1 = 0.5$ s. In both experiments $n = 6$ chunks are acquired in 214 ms ($\tau_c = 17.8$ ms) and a quadratic sine apodization is used. The average value is indicated by a red dashed lines which corresponds to a decrease of $\sim 6\%$ when the pure shift acquisition is applied.

5.4 Pulse Sequences

5.4.1 ^{13}C , ^{13}C -PM-TOCSY

```

1
2 #include <Avance.incl>
3 #include <Grad.incl>
4 #include <Delay.incl>
5
6 "p4=p3*2"
7
8 "d6=d4/2"
9 "d11=30m"
10 "in0=inf1/2"
11 "d0=0"
12 "acqt0=0"
13
14 "l2=l1-1"
15 "d5=d4 * 4 * l1"
16
17 ;baseopt_echo
18
19 1 ze
20 2 d11 do:f2
21 20u LOCKH_OFF
22 d1 p10:f1 p12:f2
23 50u UNBLKGRAD
24 (p3 ph1):f2
25 p16:gp5
26 d16
27
28 ; t1 incrementation
29 (p18:sp19 ph3):f1 ;BEBOP
30 d0
31 (p4 ph1):f2
32 d0
33 (p18:sp18 ph10):f1 ;trBEBOP
34
35 ; first zfilter block
36 4u p10:f1
37 4u gron1
38 (p23:sp23 ph8):f1
39 4u groff
40 p16:gp3
41 d16
42
43 ; z to z in-phase planar mixing transfer block
44 (p13:sp13 ph1):f1 ;UR90 or BEBOP
45 d6 rpp22
46 (p17:sp17 ph21+ph22):f1 ;BIBOP180
47 d4
48 (p17:sp17 ph20+ph22):f1 ;BIBOP180
49 d6
50 (p15:sp15 ph20+ph22):f1 ;UR90
51
52 5 d4
53 (p17:sp17 ph21+ph22):f1 ;BIBOP180
54 d4 ipp22
55 d4
56 (p17:sp17 ph20+ph22):f1 ;BIBOP180
57 d4
58 (p15:sp15 ph20+ph22):f1 ;UR90
59 lo to 5 times l2
60
61 d6
62 (p17:sp17 ph21+ph22):f1 ;BIBOP180
63 d4

```

```

64 (p17:sp17 ph20+ph22):f1 ;BIBOP180
65 d6
66 (p13:sp16 ph10):f1 ;UR90 or trBEBOP
67
68 ; second zfilter block
69 4u gron2 pl0:f1
70 (p24:sp24 ph9):f1
71 40u groff
72 p16:gp4 ;gradient to prevent complete refocusing
73 d16
74 4u BLKGRAMP pl12:f2
75
76 ; excitation
77 (p13:sp13 ph1):f1 ;BEBOP
78
79 ; acquisition
80 go=2 ph31 cpd2:f2
81 d11 do:f2 mc #0 to 2
82 F1PH(calph(ph3, +90), caldel(d0, +in0))
83 20u LOCKH_OFF
84 exit
85
86
87
88 ph1 = 0
89 ph2 = 1
90 ;excitation, states, TPPI
91 ph3 = 0 2
92 ;chirp pulse(z-filter)
93 ph8 = 0
94 ph9 = 2
95 ph10= 2
96 ;transfer block phases
97 ph20= 1
98 ph21= 3
99 ; MLEV supercycles
100 ph22=0 0 2 2 2 0 0 2 2 2 0 0 0 2 2 0
101 ;readout/receiver phase
102 ph31= 0 2
103
104 ;p1 : f1 channel - power level for pulse (default)
105 ;p2 : f2 channel - power level for pulse (default)
106 ;p12: f2 channel - power level for CPD/BB decoupling
107 ;p17: f4 channel - power level for CPD/BB decoupling
108 ;sp3 : f2 channel - shaped pulse 180 degree (on resonance)
109 ;sp5 : f2 channel - shaped pulse 180 degree (off resonance)
110 ;sp13: f2 channel - shaped pulse 180 degree (adiabatic)
111 ;p1 : f1 channel - 90 degree high power pulse
112 ;p2 : f1 channel - 180 degree high power pulse
113 ;p3 : f2 channel - 90 degree high power pulse
114 ;p4 : f2 channel - 180 degree high power pulse
115 ;p8 : f2 channel - 180 degree shaped pulse for inversion (adiabatic)
116 ;p14: f2 channel - 180 degree shaped pulse
117 ;p16: homospoil/gradient pulse
118 ;p19: gradient pulse 2
119 ;p13: excitation pulse
120 ;sp13: excitation pulse
121 ;sp16: time reversed excitation pulse
122 ;p15: UR90 pulse (PM)
123 ;sp15: UR90 pulse (PM)
124 ;p17: inversion pulse (PM)
125 ;sp17: inversion pulse (PM)
126 ;d0 : incremented delay (2D) [3 usec]
127 ;d1 : relaxation delay; 1-5 * T1
128 ;d4 : planar mixing delay
129 ;d5 : total planar mixing time
130 ;d11: delay for disk I/O [30 msec]

```

```

131 ;d16: delay for homospoil/gradient recovery
132 ;inf1: 1/SW(X) = 2 * DW(X)
133 ;in0: 1/(2 * SW(X)) = DW(X)
134 ;nd0: 2
135 ;in20: = in0
136 ;ns: 2 * n
137 ;ds: 32
138 ;td1: number of experiments
139 ;cpd2: decoupling according to sequence defined by cpdprg2
140 ;pcpd2: f2 channel - 90 degree pulse for decoupling sequence
141 ;FnMODE: states
142
143
144 ;for z-only gradients:
145 ;gpz1: 10%
146 ;gpz2: -10%
147 ;gpz3: 18%
148 ;gpz4: -15%
149
150 ;use gradient files:
151 ;gpnam1: SMSQ10.100
152 ;gpnam2: SMSQ10.100
153 ;gpnam3: SMSQ10.100
154 ;gpnam4: SMSQ10.100

```

5.4.2 3D (H)CC(CO)NH-TOCSY

```

1
2 prosol relations=<triple>
3
4 #include<Avance.incl>
5 #include<Grad.incl>
6 #include<Delay.incl>
7
8 "p2=p1*2"
9 "p22=p21*2"
10 "d11=30m"
11 "d12=20u"
12 "d13=4u"
13
14 "d3=1.1m"
15 "d4=1.7m"
16 "d21=3.6m"
17 "d22=4.4m"
18 "d23=12.4m"
19 "d25=5.5m"
20 "d26=2.3m"
21
22 "d0=3u"
23 "d10=d23/2-p14/2"
24 "d29=d23/2-p14/2-p26-d25-4u"
25 "d30=d23/2-p14/2"
26
27 "in0=inf1/2"
28 "in10=inf2/4"
29
30 "in29=in10"
31 "in30=in10"
32
33 "td2=tdmax(td2,d30*2,in30)"
34
35 ;"l1=(d15/(p9*115.112))"
36 "l2=l1-1"
37 "d7=d6/2"

```

```

38 "d16=200u"
39
40 "DELTA1=d3+p2+d0*2+larger(p14,p22)-p14-4u"
41 "DELTA2=d23+4u-d22"
42 "DELTA3=d25-p16-d16-4u"
43 "DELTA4=p16+d16+7u"
44
45 ; shaped pulses
46 "cnst23=o2/bf2" ; cnst32 = o2p
47
48 "spoff2=bf2*(cnst21/1000000)-o2"
49 "spoal2=1"
50 "spoff5=bf2*(cnst21/1000000)-o2"
51 "spoal5=0.5"
52 "spoff7=bf2*(cnst22/1000000)-o2"
53 "spoal7=0.5"
54 "spoff8=bf2*(cnst21/1000000)-o2"
55 "spoal8=0"
56
57 "spoff30=bf2*(cnst24/1000000)-o2" ; BIBOP (all carbons off resonance)
58
59 "spoff31=bf2*(cnst24/1000000)-o2" ; BEBOP (all carbons off resonance)
60 "spoal31=1"
61 "spoff32=bf2*(cnst24/1000000)-o2" ; BEBOPtr (all carbons off resonance)
62 "spoal32=0"
63
64 "spoff33=bf2*(cnst24/1000000)-o2" ; UR180 (all carbons off resonance)
65 "spoal33=0.5"
66
67 ; planar mixing
68 "spoff40=0"
69 "spoff41=0"
70 "spoff42=0"
71 "spoff43=0"
72 "spoff44=0"
73
74 aqseq 321
75
76
77 1 ze
78   d11 p116:f3
79 2 d11 do:f3
80 3 d11
81   d1
82   50u UNBLKGRAD
83   d12 p11:f1 p10:f2 p13:f3
84
85   (p1 ph3):f1
86   d4
87   (center (p2 ph1):f1 (p30:sp30 ph1):f2 ) ;BIBOP180
88   d4
89   (p1 ph2):f1
90
91   4u
92   p16:gp1
93   d16
94
95   (p31:sp31 ph4):f2 ;BEBOP 90
96   d0
97   (center (p14:sp5 ph12):f2 (p22 ph1):f3 ) ; selective CO pulse
98   d3
99   (p2 ph1):f1
100  d0
101  (p33:sp33 ph1):f2 ;UR180
102  DELTA1
103  (p14:sp5 ph1):f2 ; selective CO pulse
104  4u p116:f3

```

```

105 (p31:sp32 ph2):f2 ;BEBOPtr 90
106
107 ;first filter block
108 d12
109 20u fq=cnst24(bf ppm):f2 ; center of carbon bandwidth
110 4u gron10
111 (p40:sp40 ph1):f2 ;SmChirp
112 4u groff
113 p16:gp5
114 d16
115
116 ;in-phase transfer block, planar mixing
117 (p41:sp41 ph1):f2 ;BEBOP 90 => spoffs = 0
118 d6
119 (p43:sp43 ph20):f2 ;BURBOP180
120 d6
121 (p44:sp44 ph20):f2 ;UR90
122
123 5 d6
124 d6
125 (p43:sp43 ph21):f2 ;BURBOP180
126 d6
127 d6
128 (p44:sp44 ph20):f2 ;UR90
129 lo to 5 times l2
130
131 d6
132 (p43:sp43 ph20):f2 ;BURBOP180
133 d6
134 (p41:sp42 ph10):f2 ;BEBOPtr 90 => spoffs = 0
135
136 ;second filter block
137 4u
138 4u gron10
139 (p40:sp40 ph1):f2 ;SmChirp
140 4u groff
141 p16:gp5
142 d16 pl19:f1 fq=cnst23(bf ppm):f2 ; C0 frequency
143
144 ; C0 inphase to C0zNz
145 (p13:sp2 ph5):f2 ; C0 90
146 d23 cpds1:f1 ph2
147 (center (p14:sp5 ph1):f2 (p22 pl3 ph8):f3 ) ; C0 180
148 d23
149 (p13:sp8 ph2):f2 ; C0 90 tr
150
151 4u
152 4u do:f1
153 (p26 ph10):f1
154 4u
155 p16:gp2
156 d16
157 (p26 ph2):f1
158 4u cpds1:f1 ph1
159
160 (p21 ph6):f3
161 d30
162 (p14:sp7 ph1):f2 ; decoupling of Calphas
163 d30
164 (center (p14:sp5 ph1):f2 (p22 ph1):f3 ) ; C0 180
165 d10
166 (p14:sp7 ph1):f2 ; decoupling of Calphas
167 d29
168 4u do:f1
169 (p26 ph9):f1
170 4u
171 p16:gp3*EA

```

```
172 d16
173 DELTA3 pl1:f1
174
175 (center (p1 ph1):f1 (p21 ph1):f3 )
176 d26
177 (center (p2 ph1):f1 (p22 ph1):f3 )
178 d26
179 (center (p1 ph2):f1 (p21 ph7):f3 )
180 d26
181 (center (p2 ph1):f1 (p22 ph1):f3 )
182 d26
183 (p1 ph1):f1
184 DELTA4
185 (p2 ph1):f1
186 3u
187 p16:gp4
188 d16 pl16:f3
189 4u BLKGRAD
190 go=2 ph31 cpd3:f3
191 d11 do:f3 mc #0 to 2
192 F1PH(calph(ph4, +90), caldel(d0, +in0))
193 ;F2EA(calgrad(EA) & calph(ph7, +180), caldel(d10, +in10) & caldel(d29, +in29) &
194 caldel(d30, -in30) & calph(ph6, +180) & calph(ph8, +180) & calph(ph31, +180))
195 exit
196
197 ph1=0
198 ph2=1
199 ph3=0 0 0 0 0 0 0 2 2 2 2 2 2 2
200 ph4=0 0 2 2
201 ph5=0 0 0 0 2 2 2 2
202 ph6=0 2
203 ph7=3
204 ph8=0
205 ph9=3
206 ph10=2
207
208 ph12=0 1 ; removal of artifacts created from excitation of CO
209 ph20=1
210 ph21=3
211
212 ph23=0
213 ph25=2
214 ph31=0 2 2 0 2 0 0 2 2 0 0 2 0 2 2 0
215
216
217 ;p10 : 0W
218 ;p11 : f1 channel - power level for pulse (default)
219 ;p13 : f3 channel - power level for pulse (default)
220 ;p115: f2 channel - power level for TOCSY-spinlock
221 ;p116: f3 channel - power level for CPD/BB decoupling
222 ;p119: f1 channel - power level for CPD/BB decoupling
223
224 ;p13: f2: Q5_sebop (C=0 off resonance)
225 ;spnam2: Q5_sebop (C=0 off resonance)
226 ;spnam8: Q5tr_sebop (C=0 off resonance)
227 ;p14: f2: Q5_surbop (sp5->C=0 and sp7->Calpha)
228 ;spnam5: Q5_surbop (C=0 off resonance)
229 ;spnam7: Q5_surbop (Calpha off resonance)
230
231 ;p30: f2: BIBOP (all carbons off resonance)
232 ;spnam30: BIBOP (all carbons off resonance)
233 ;p31: f2: BEBOP (all carbons off resonance)
234 ;spnam31: BEBOP (all carbons off resonance)
235 ;spnam32: BEBOPtr (all carbons off resonance)
236 ;p33: f2: UR180 (all carbons off resonance)
237 ;spnam33: UR180 (all carbons off resonance)
```

```

238 ;p40: f2: Chirp zFilter (planar mixing on resonance)
239 ;spnam40: Chirp zFilter (planar mixing on resonance)
240 ;p41: f2: BEBOP (planar mixing on resonance)
241 ;spnam41: BEBOP (planar mixing on resonance)
242 ;spnam42: BEBOPtr (planar mixing on resonance)
243 ;p43: f2: BIBOP (planar mixing on resonance)
244 ;spnam43: BIBOP (planar mixing on resonance)
245 ;p44: f2: UR90 (planar mixing on resonance)
246 ;spnam44: UR90 (planar mixing on resonance)
247
248 ;sp2: f2 channel - shaped pulse 90 degree (C=0 on resonance)
249 ;sp3: f2 channel - shaped pulse 180 degree (on resonance)
250 ;sp5: f2 channel - shaped pulse 180 degree (C=0 off resonance)
251 ;sp7: f2 channel - shaped pulse 180 degree (Ca off resonance)
252 ;sp8: f2 channel - shaped pulse 90 degree (on resonance)
253 ;
254 ;sp9: f2 channel - shaped pulse 180 degree (Ca on resonance)
255 ;
256 ;p1 : f1 channel - 90 degree high power pulse
257 ;p2 : f1 channel - 180 degree high power pulse
258 ;p9 : f2 channel - 90 degree low power pulse
259 ;p13: f2 channel - 90 degree shaped pulse
260 ;p14: f2 channel - 180 degree shaped pulse
261 ;p16: homospoil/gradient pulse [1 msec]
262 ;p21: f3 channel - 90 degree high power pulse
263 ;p22: f3 channel - 180 degree high power pulse
264 ;p24: f2 channel - 180 degree shaped pulse (sp9)
265 ;p26: f1 channel - 90 degree pulse at p19
266 ;d0 : incremented delay (F1 in 3D) [3 usec]
267 ;d1 : relaxation delay; 1-5 * T1
268 ;d3 : 1/(6J(CH)) [1.1 msec]
269 ;d4: 1/(4J(CH)) [1.7 msec]
270 ;d10: incremented delay (F2 in 3D) = d23/2-p14/2
271 ;d11: delay for disk I/O [30 msec]
272 ;d12: delay for power switching [20 usec]
273 ;d13: short delay [4 usec]
274 ;d15: TOCSY mixing time [12 msec]
275 ;d16: delay for homospoil/gradient recovery
276 ;d21: 1/(2J(CaCO)) [3.6 msec]
277 ;d22: 1/(2Jprime(CaCO)) [4.4 msec]
278 ;d23: constant time delay T(N) = 1/(4Jprime(NCO)) [12.4 msec]
279 ;d25: 1/(2Jprime(NH)) [5.5 msec]
280 ;d26: 1/(4J(NH)) [2.3 msec]
281 ;d29: incremented delay (F2 in 3D) = d23/2-p14/2-p26-d25-4u
282 ;d30: decremented delay (F2 in 3D) = d23/2-p14/2
283 ;cnst21: CO chemical shift (offset, in ppm)
284 ;cnst22: Calpha chemical shift (offset, in ppm)
285 ;cnst24: 100 ppm - center of carbon spectrum
286 ;o2p: Caliphatic chemical shift (cnst23)
287 ;l1: loop for DIPSI2 cycle: ((p6*115.112) * l1) = mixing time
288 ;inf1: 1/SW(Cali) = 2 * DW(Cali)
289 ;inf2: 1/SW(N) = 2 * DW(N)
290 ;in0: 1/(2 * SW(Cali)) = DW(Cali)
291 ;nd0: 2
292 ;in10: 1/(2 * SW(N)) = DW(N)
293 ;nd10: 4
294 ;in29: = in10
295 ;in30: = in10
296 ;ns: 16 * n
297 ;ds: >= 16
298 ;td1: number of experiments in F1
299 ;td2: number of experiments in F2 td2 max = 2 * d30 / in30
300 ;FnMODE: States-TPPI (or TPPI) in F1
301 ;FnMODE: echo-antiecho in F2
302 ;cpds1: decoupling according to sequence defined by cpdprg1
303 ;cpd3: decoupling according to sequence defined by cpdprg3
304 ;pcpd1: f1 channel - 90 degree pulse for decoupling sequence

```

```

305 ;pcpd3: f3 channel - 90 degree pulse for decoupling sequence
306
307
308 ;use gradient ratio:      gp 1 : gp 2 : gp 3 : gp 4
309 ;                          50 :  -30 :  80 :  8.1
310
311 ;for z-only gradients:
312 ;gpz1: 50%
313 ;gpz2: -30%
314 ;gpz3: 80%
315 ;gpz4: 8.1%
316
317 ;use gradient files:
318 ;gpnam1: SMSQ10.100
319 ;gpnam2: SMSQ10.100
320 ;gpnam3: SMSQ10.100
321 ;gpnam4: SMSQ10.100

```

5.4.3 IPE-1-DOSY

```

1
2 #include <Avance.incl>
3 #include <Grad.incl>
4 #include <Delay.incl>
5
6
7 # ifdef TEST
8 define list<gradient> diff={ 1 }
9 # else
10 define list<gradient> diff=<Difframp>
11 # endif /*TEST*/
12
13 define delay bigDELTA
14 define delay littleDELTA
15
16 "p2=p1*2"
17
18 "d26=p30+d16"
19 "l1=l2/2-1"
20 "d21=p1*2/PI"
21 "d22=p10*2/PI"
22 "d23=d21-d22"
23 "d24=larger(d26, d25)-d26+d16"
24 "littleDELTA=p30*2"
25 "bigDELTA=((d25*6+d21*2+p2*3+p1*2)*l1+d25*2+d24*2+p30*2+p2*2+p1*2+8u)*2"
26 "d20=bigDELTA"
27
28
29 1 ze
30   littleDELTA
31   bigDELTA
32
33 2 d1
34   50u UNBLKGRAD
35
36   p10 ph1 rpp21 rpp22
37
38 ;begin IM
39   d23
40   4u
41   p30:gp6*diff
42   d24
43   p2 ph20+ph21
44   4u ipp21

```

```

45 p30:gp6*-1*diff
46 d24
47
48 4 p1 ph20+ph22
49 d25 ipp22
50 p2 ph20+ph21
51 d25 ipp21
52 p1 ph20+ph22
53 d25 ipp22
54 p2 ph20+ph21
55 d25 ipp21
56 d21
57 d21
58 d25
59 p2 ph20+ph21
60 d25 ipp21
61 lo to 4 times l1
62
63 p1 ph20+ph22
64 d25 ipp22
65 p2 ph20+ph21
66 d25 ipp21
67 p1 ph20+ph22
68 4u ;ipp22
69 p30:gp6*diff
70 d24
71 p2 ph20+ph21
72 4u ;ipp21
73 p30:gp6*-1*diff
74 d24
75 d21
76 ;end IM
77
78 ;begin IM
79 d21
80 4u
81 p30:gp6*-1*diff
82 d24
83 p2 ph24+ph21
84 4u dpp21
85 p30:gp6*diff
86 d24
87
88 5 p1 ph24+ph22
89 d25 dpp22
90 p2 ph24+ph21
91 d25 dpp21
92 p1 ph24+ph22
93 d25 dpp22
94 p2 ph24+ph21
95 d25 dpp21
96 d21
97 d21
98 d25
99 p2 ph24+ph21
100 d25 dpp21
101 lo to 5 times l1
102
103 p1 ph24+ph22
104 d25 dpp22
105 p2 ph24+ph21
106 d25 dpp21
107 p1 ph24+ph22
108 4u
109 p30:gp6*-1*diff
110 d24
111 p2 ph24+ph21

```

```

112 4u
113 p30:gp6*diff
114 d24
115 d21 BLKGRAD
116 ;end IM
117
118 go=2 ph31
119 d1 mc #0 to 2 F1QF(calgrad(diff))
120 exit
121
122
123 ph1= 0 0 1 1 2 2 3 3
124 ph20=0 2
125 ph24=2 0
126 ;ph21=2 0 3 1 2 0 2 0 3 1 2 0 3 1 0 2 3 1 3 1 0 2 3 1 0 2 1 3 0 2 0 2 1 3 0 2 1 3 2 0 1
    3 1 3 2 0 1 3
127 ;ph22=2 3 1 0 0 1 3 2 3 0 2 1 1 2 0 3 0 1 3 2 2 3 1 0 1 2 0 3 3 0 2 1
128 ph21=0 0 1 3 0 2 3 3 0 0 3 3 2 0 1 3 0 0 3 3 0 0 3 3
129 ph22=2 3 1 0 2 1 3 0 0 3 1 2 0 1 3 2
130 ph31=0 0 1 1 2 2 3 3
131
132
133 ;p11 : f1 channel - power level for pulse (default)
134 ;p1 : f1 channel - 90 degree high power pulse
135 ;p2 : f1 channel - 180 degree high power pulse
136 ;p10 : f1 channel - Ernst flip angle pulse
137 ;p30: gradient pulse (little DELTA * 0.5)
138 ;d1 : relaxation delay; 1-5 * T1
139 ;d16: delay for gradient recovery
140 ;d20: diffusion time (big DELTA)
141 ;d25: delay for IPE
142 ;ns: 1 * n
143 ;ds: 8
144 ;l2: basic cycles (even numbered)
145 ;td1: number of experiments
146 ;FnMODE: QF
147 ; use xf2 and DOSY processing
148
149 ;use AU-program dosy to calculate gradient ramp-file Difframp

```

5.4.4 IPE-2-DOSY

```

1
2 #include <Avance.incl>
3 #include <Grad.incl>
4 #include <Delay.incl>
5
6
7 # ifdef TEST
8 define list<gradient> diff={ 1 }
9 # else
10 define list<gradient> diff=<Difframp>
11 # endif /*TEST*/
12
13 define delay bigDELTA
14 define delay littleDELTA
15
16 "p2=p1*2"
17 "p31=p30/2"
18
19 "l1=l2/2-1"
20 "d21=p1*2/3.1416"
21 "d22=p10*2/3.1416"
22 "littleDELTA=p30*2"

```

```

23 "bigDELTA=(d25*6+d21*2+p2*3+p1*2)*l1+d25*2+d24*2+p30*2+p2*2+p1*2+8u"
24 "d20=bigDELTA"
25
26
27 "d35=d25/2"
28 "d45=p30+2*d16"
29 "d46=p31+d16"
30 "d24=larger(d45,d25)-d45+2*d16+8u+2*d21"
31 "d34=larger(d46,d35)-d46+d16+4u"
32 "d38=larger(d46,d35)-d46+d16+4u+d21-d22"
33 "d39=d34/2"
34 "d27=d25+2*d21"
35 "d37=d35+d21"
36
37 1 ze
38   littleDELTA
39   bigDELTA
40 2 d1
41
42   50u UNBLKGRAD
43
44
45   p10 ph1 rpp21 rpp22
46
47 ;begin IM
48   4u
49   p31:gp6*diff
50   d38
51   p2 ph20+ph21 ;180
52   4u ipp21
53   p30:gp6*-1*diff
54   d24
55   4u
56   p2 ph20+ph21 ;180
57   4u ipp21
58   p31:gp6*diff
59   d34
60
61 4 p1 ph20+ph22 ;90
62
63   d35 ipp22
64   p2 ph20+ph21 ;180
65   d27 ipp21
66   p2 ph20+ph21 ;180
67   d35 ipp21
68
69   p1 ph20+ph22 ;90
70
71   d35 ipp22
72   p2 ph20+ph21 ;180
73   d27 ipp21
74   p2 ph20+ph21 ;180
75   d37 ipp21
76
77 ;-----
78
79   d37
80   p2 ph20+ph21 ;180
81   d27 ipp21
82   p2 ph20+ph21 ;180
83   d35 ipp21
84   lo to 4 times l1
85
86
87   p1 ph20+ph22 ;90
88
89   d35 ipp22

```

```
90 p2 ph20+ph21 ;180
91 d27 ipp21
92 p2 ph20+ph21 ;180
93 d35 ipp21
94
95 p1 ph20+ph22 ;90
96
97 d35 ;ipp22
98 p2 ph20+ph21 ;180
99 d27 ipp21
100 p2 ph20+ph21 ;180
101 d37 ipp21
102
103 ;-----
104 ; SYMMETRY
105 ;-----
106
107 d37
108 p2 ph20+ph21 ;180
109 d27 ipp21
110 p2 ph20+ph21 ;180
111 d35 ipp21
112
113 5 p1 ph24+ph22 ;90
114
115 d35 dpp22
116 p2 ph20+ph21 ;180
117 d27 ipp21
118 p2 ph20+ph21 ;180
119 d35 ipp21
120
121 p1 ph24+ph22 ;90
122
123 d35 dpp22
124 p2 ph20+ph21 ;180
125 d27 ipp21
126 p2 ph20+ph21 ;180
127 d37 ipp21
128
129 ;-----
130
131 d37
132 p2 ph20+ph21 ;180
133 d27 ipp21
134 p2 ph20+ph21 ;180
135 d35 ipp21
136 lo to 5 times ll
137
138 p1 ph24+ph22 ;90
139
140 d35 dpp22
141 p2 ph20+ph21 ;180
142 d27 ipp21
143 p2 ph20+ph21 ;180
144 d35 ipp21
145
146 p1 ph24+ph22 ;90
147
148 4u
149 p31:gp6*-1*diff
150 d34
151 p2 ph20+ph21 ;180
152 4u ipp21
153 p30:gp6*diff
154 d24
155 4u
156 p2 ph20+ph21 ;180
```

```

157 4u ipp21
158 p31:gp6*-1*diff
159 d39
160 d39 BLKGRAD
161 ;end IM
162
163 go=2 ph31
164 d1 mc #0 to 2 F1QF(calgrad(diff))
165 exit
166
167
168
169
170 ph1= 0
171 ph20=0
172 ph24=2
173
174 ;6460
175 ph21=3 3 0 0 3 3 1 1 2 2 1 1
176 ph22= 2 3 1 0 2 1 3 0 0 3 1 2 0 1 3 2
177 ;ph22=2 3 1 0 2 1 3 0 0 3 1 2 0 1 3 2 0 1 3 2 0 3 1 2 2 1 3 0 2 3 1 0
178
179 ph31=0
180
181 ;p11 : f1 channel - power level for pulse (default)
182 ;p1 : f1 channel - 90 degree high power pulse
183 ;p2 : f1 channel - 180 degree high power pulse
184 ;p10 : f1 channel - Ernst flip angle pulse
185 ;p30: gradient pulse (little DELTA * 0.5)
186 ;d1 : relaxation delay; 1-5 * T1
187 ;d16: delay for gradient recovery
188 ;d20: diffusion time (big DELTA)
189 ;d25: delay for IPE
190 ;ns: 1 * n
191 ;ds: 8
192 ;l2: basic cycles (even numbered)
193 ;td1: number of experiments
194 ;FnMODE: QF
195 ; use xf2 and DOSY processing
196
197 ;use AU-program dosy to calculate gradient ramp-file Difframp

```

5.4.5 JRES-HOMQC

```

1 #include <Avance.incl>
2 #include <Grad.incl>
3 #include <Delay.incl>
4
5 "p2=p1*2"
6 "p4=p3*2"
7 "d4=1s/(cnst2*4)"
8 "d5=1s/(cnst3*4)-4u"
9 "d11=30m"
10
11 "d0=3u"
12 "d10=3u"
13 "in0=inf1/2"
14 "in10=inf1*cnst10/2"
15
16 "DELTA2=d4-larger(p2,p4)/2-4u"
17 "DELTA3=DELTA2-2*d0-p2"
18 "DELTA5=p16+d16+de+8u"
19 "DELTA6=DELTA2-p16-d16"
20

```

```
21 "acqt0=0"
22 baseopt_echo
23
24
25 1 ze
26   d11 p112:f2
27 2 d1 do:f2
28
29   (p1 ph1)
30   DELTA2 p12:f2
31   4u
32   (center (p2 ph1) (p4 ph6):f2 ) ;180
33   4u
34   DELTA2 UNBLKGRAD
35   (p1 ph2)
36   (p3 ph3):f2
37
38 ;t1 evolution
39   d10
40   (p2 ph1)
41   d10
42
43 ;create MQ
44   DELTA3
45   4u
46   (center (p2 ph1) (p4 ph1):f2 ) ;180
47   4u
48   DELTA2
49   (p1 ph1)
50
51
52 ;t1 evolution
53   d0
54
55   ;BIRD
56   (p1 ph8:r)
57   d4
58   d4
59   (center (p2 ph8:r) (p4 ph1):f2 )
60   d4
61   d4
62   (p1 ph8:r)
63
64   d0
65
66 ;back transfer
67   (p1 ph1)
68
69   DELTA6
70   p16:gp1*EA
71   d16
72   4u
73   (center (p2 ph1) (p4 ph1):f2 ) ;180
74   4u
75   DELTA2
76
77   (center (p1 ph1) (p3 ph4):f2 ) ;yy90
78
79   DELTA2
80   4u
81   (center (p2 ph1) (p4 ph1):f2 ) ;180
82   4u
83   DELTA2
84
85 ;z-Filter
86   (p1 ph2)
87   4u gron7 pl=0[Watt]:f1
```

```

88 (p24:sp24 ph1):f1
89 40u groff
90 p15:gp15 pl1:f1
91 d16
92 4u
93 (p1 ph1)
94
95 DELTA5 pl12:f2
96 4u
97 (p2 ph1)
98 p16:gp2
99 4u
100 d16 BLKGRAD
101
102 go=2 ph31 cpd2:f2
103 d1 do:f2 mc #0 to 2
104 F1EA(calgrad(EA), caldel(d0, +in0) & caldel(d10, +in10) & calph(ph3, +180) & calph(
105 ph6, +180) & calph(ph31, +180))
106 exit
107
108 ph1=0
109 ph2=1
110 ph3=0 2
111 ph4=0 0 2 2
112 ;ph4=1 1 3 3
113 ph5=2
114 ph6=0
115 ph7=1
116 ph8=0
117 ph9=0
118 ph31=0 2 2 0
119
120
121 ;p11 : f1 channel - power level for pulse (default)
122 ;p12 : f2 channel - power level for pulse (default)
123 ;p112: f2 channel - power level for CPD/BB decoupling
124 ;p1 : f1 channel - 90 degree high power pulse
125 ;p2 : f1 channel - 180 degree high power pulse
126 ;p3 : f2 channel - 90 degree high power pulse
127 ;p4 : f2 channel - 180 degree high power pulse
128
129 ;p15: homospoil/gradient pulse, z-Filter: 500 us
130 ;p16: homospoil/gradient pulse: 1000 us
131
132 ;d0 : incremented delay (2D) [3 usec]
133 ;d1 : relaxation delay; 1-5 * T1
134 ;d4 : 1/(4J)XH
135 ;d5 : 1/(4J)HH
136 ;d11: delay for disk I/O [30 msec]
137 ;d16: delay for homospoil/gradient recovery
138 ;cnst2: = J(XH)
139 ;cnst10: = kappa
140 ;inf1: 1/SW(X) = 2 * DW(X)
141 ;in0: 1/(2 * SW(X)) = DW(X)
142 ;nd0: 2
143 ;ns: 2 * n
144 ;ds: >= 16
145 ;td1: number of experiments
146 ;FnMODE: echo-antiecho
147
148 ;use gradient ratio: gp 1 : gp 2
149 ; 80 : 20.1 for C-13
150
151 ;for z-only gradients:
152 ;gpz1: 80%
153 ;gpz2: 20.1% for C-13

```

```

154 ;gpz7: 5-7% for z-Filter gradient during echo
155 ;gpz15: 70% for z-Filter gradient pulse after echo
156
157 ;use gradient files:
158 ;gpnam1: SMSQ10.100
159 ;gpnam2: SMSQ10.100
160 ;gpnam13: SMSQ10.100
161 ;gpnam14: SMSQ10.100
162 ;gpnam15: SMSQ10.100

```

5.4.6 HOMQC-TOCSY

```

1
2 #include <Avance.incl>
3 #include <Grad.incl>
4 #include <Delay.incl>
5
6 "p2=p1*2"
7 "p4=p3*2"
8 "d4=1s/(cnst2*4)"
9 "d11=30m"
10
11 "FACTOR1=(d9/(p6*115.112))/2"
12 "l1=FACTOR1*2"
13
14 "d0=3u"
15 "d10=3u"
16 "in0=inf1/2"
17 "in10=inf1*cnst10/2"
18 "DELTA=2*d0+p2+2*d16+2*p14"
19 "DELTA3=d4-2*d10-p2"
20 "DELTA7=d4-p17-d16-10u"
21
22 "acqt0=0"
23 baseopt_echo
24
25
26 1 ze
27   d11
28 2 d1
29
30   50u UNBLKGRAD
31 #   ifdef X13C
32   ; destroy Boltzmann 13C
33   (p3 ph1):f2
34   4u
35   p13:gp13
36   d16
37 #   else
38 #   endif /*X13C*/
39
40   (p1 ph1)
41   d4
42   (center (p2 ph1) (p4 ph1):f2 ) ;180
43   d4
44   (p1 ph2)
45
46 ;destroy 12C-H coherence
47   p16:gp16
48   d16
49
50   (p3 ph3):f2 ;states pulse
51
52 ; CS evolution

```

```

53 d10
54 (p2 ph1)
55 d10
56
57 ;create MQ
58 DELTA3
59 (center (p2 ph1) (p4 ph1):f2 )
60 d4
61 (p1 ph1)
62
63 ;t1 evolution
64 d0
65
66 ;BIRDdX
67 (p1 ph8:r)
68 d4
69 d4
70 (center (p2 ph8:r) (p4 ph1):f2 )
71 d4
72 d4
73 (p1 ph8:r)
74
75 d0
76
77 ;back transfer
78 (p1 ph1)
79 d4
80 (center (p2 ph1) (p4 ph1):f2 )
81 d4
82 (lalign (p1 ph2) (p3 ph4):f2 )
83 d4*0.5
84 (center (p2 ph1) (p4 ph1):f2 )
85 d4*0.5
86
87 ;store along z/zz
88 ;(ralign (p1 ph1) (p3 ph5):f2) ;for in-phase ECOSY pattern
89 (ralign (p1 ph2) (p3 ph5):f2) ;for anti-phase ECOSY pattern
90 p15:gp15
91 d16 pl10:f1
92
93 ;begin DIPSI2
94 4 p6*3.556 ph22
95 p6*4.556 ph24
96 p6*3.222 ph22
97 p6*3.167 ph24
98 p6*0.333 ph22
99 p6*2.722 ph24
100 p6*4.167 ph22
101 p6*2.944 ph24
102 p6*4.111 ph22
103
104 p6*3.556 ph24
105 p6*4.556 ph22
106 p6*3.222 ph24
107 p6*3.167 ph22
108 p6*0.333 ph24
109 p6*2.722 ph22
110 p6*4.167 ph24
111 p6*2.944 ph22
112 p6*4.111 ph24
113
114 p6*3.556 ph24
115 p6*4.556 ph22
116 p6*3.222 ph24
117 p6*3.167 ph22
118 p6*0.333 ph24
119 p6*2.722 ph22

```

```
120 p6*4.167 ph24
121 p6*2.944 ph22
122 p6*4.111 ph24
123
124 p6*3.556 ph22
125 p6*4.556 ph24
126 p6*3.222 ph22
127 p6*3.167 ph24
128 p6*0.333 ph22
129 p6*2.722 ph24
130 p6*4.167 ph22
131 p6*2.944 ph24
132 p6*4.111 ph22
133 lo to 4 times l1
134 ;end DIPSI2
135
136 ;z-Filter
137 4u gron7 pl0:f1
138 (p24:sp24 ph1):f1
139 40u groff
140 p17:gp17 pl1:f1
141 d16
142 4u BLKGRAD
143 (p1 ph1)
144
145 go=2 ph31
146 d1 mc #0 to 2
147 F1PH(caliph(ph3, +90), caldel(d0, +in0) & caldel(d10, +in10))
148 exit
149
150
151 ph1=0
152 ph2=1
153 ph3=0 2
154 ph4=1 1 3 3
155 ph5=0 0 2 2
156 ph6=0
157 ph8=0
158 ph22=3
159 ph24=1
160 ph31=0 2 2 0
161
162
163 ;pl1 : f1 channel - power level for pulse (default)
164 ;pl2 : f2 channel - power level for pulse (default)
165 ;pl3 : f3 channel - power level for pulse (default)
166 ;pl12: f2 channel - power level for CPD/BB decoupling
167 ;p1 : f1 channel - 90 degree high power pulse
168 ;p2 : f1 channel - 180 degree high power pulse
169 ;p3 : f2 channel - 90 degree high power pulse
170 ;p4 : f2 channel - 180 degree high power pulse
171
172 ;p13: destroy Sz: 1000 us
173 ;p15: z-Filter: 2500 us
174 ;p16: 1000 us
175 ;p17: 500 us
176
177 ;d0 : incremented delay (2D) [3 usec]
178 ;d1 : relaxation delay; 1-5 * T1
179 ;d4 : 1/(4J)XH
180 ;d5 : 1/(4J)HH
181 ;d9 : TOCSY mixing time
182 ;d11: delay for disk I/O [30 msec]
183 ;d16: delay for homospoil/gradient recovery
184 ;cnst2: = J(XH)
185 ;cnst10: = kappa
186 ;inf1: 1/SW(X) = 2 * DW(X)
```

```

187 ;in0: 1/(2 * SW(X)) = DW(X)
188 ;nd0: 2
189 ;ns: 2 * n
190 ;ds: 8
191 ;td1: number of experiments
192 ;FnMODE: states
193
194 ;use gradient ratio:  gp 1 : gp 2
195 ;      80 : 20.1      for C-13
196
197 ;for z-only gradients:
198 ;gpz1: 80%
199 ;gpz2: 20.1% for C-13
200 ;gpz7: 5-7% for z-Filter gradient during echo
201 ;gpz13: 40% destroy Sz
202 ;gpz16: 60%
203 ;gpz15: 70% for z-Filter gradient pulse after echo
204
205 ;use gradient files:
206 ;gpnam1: SMSQ10.100
207 ;gpnam2: SMSQ10.100
208 ;gpnam13: SMSQ10.100
209 ;gpnam14: SMSQ10.100
210 ;gpnam15: SMSQ10.100

```

5.4.7 FHSQC Using ^{13}C -BIRD Pure Shift Amide Proton Detection

```

1
2 #include <Avance.incl>
3 #include <Grad.incl>
4 #include <Delay.incl>
5 #include <De.incl>
6
7
8 "p2=p1*2"
9 "p22=p21*2"
10 "d11=30m"
11 "d12=20u"
12 "d13=4u"
13 "d21=1s/(cnst4*2)"
14 "d26=1s/(cnst4*4)"
15
16 "p29=300u"
17
18 "d0=3u"
19
20 "in0=inf1/2"
21
22 "DELTA=d19-p22/2"
23 "DELTA1=d26-p16-d16-p27*3-d19*5-p1*2/PI"
24 "DELTA2=d26-p16-d16-p27*2-p0-d19*5-de-8u"
25 "DELTA3=d0+larger(p2,p14)/2"
26 "DELTA4=p21*2/PI"
27 "DELTA5=d21-larger(p2,p22)/2"
28
29 "TAU=d26-p16-d16-4u"
30
31 ;-----homodecoupled acquisition
32 "d62=aq/10"
33 "d63=d62/2"
34
35 "l1=10-1"
36 "d22=1/(2*cnst2)"
37 "DELTA6=d22-larger(p2,p14)/2"

```

```
38 "d17=d16+p29+10u-8u"
39 ;-----homodecoupled acquisition
40
41
42 "acqt0=0"
43 baseopt_echo
44
45
46 dwellmode explicit
47
48 1 ze
49   d11 p116:f3
50 2 d11 do:f3
51   4u BLKGRAD
52   d1
53   4u p11:f1 p13:f3
54   50u UNBLKGRAD
55
56   (p1 ph1)
57   4u
58   p16:gp1
59   d16
60   TAU
61   (center (p2 ph1) (p22 ph6):f3 )
62   TAU
63   4u
64   p16:gp1
65   d16
66   (p1 ph2)
67
68   4u
69   p16:gp2
70   d16
71
72   (p21 ph3):f3
73   DELTA3
74   (p22 ph3):f3
75   DELTA4
76   d0
77
78   (center (p2 ph5) (p14:sp3 ph1):f2 )
79
80   d0
81   DELTA4
82   (p22 ph4):f3
83   DELTA3
84   (p21 ph4):f3
85
86   4u
87   p16:gp2
88   d16
89
90   (p1 ph7)
91   DELTA1
92   p16:gp3
93   d16 p118:f1
94   p27*0.231 ph2
95   d19*2
96   p27*0.692 ph2
97   d19*2
98   p27*1.462 ph2
99   DELTA
100  (p22 ph1):f3
101  DELTA
102  p27*1.462 ph8
103  d19*2
104  p27*0.692 ph8
```

```

105 d19*2
106 p0*0.231 ph8
107 4u
108 p16:gp3
109 d16
110 DELTA2 pl16:f3
111 4u cpd3:f3
112
113
114
115 ;-----homodecoupled acquisition
116 ACQ_START(ph30,ph31)
117
118 0.1u REC_UNBLK
119 0.05u DWL_CLK_ON
120 d63
121 0.05u DWL_CLK_OFF
122 0.1u REC_BLK
123
124 10u do:f3
125 p29:gp8
126 d16 rpp14 pl1:f1
127
128 ;BIRD rX
129 (p1 ph11+ph14):f1
130 DELTA6
131 (center (p2 ph11+ph14):f1 (p14:sp3 ph11+ph14):f2 )
132 DELTA6
133 (p1 ph13+ph14):f1
134
135 4u gron9
136 d17
137 4u groff
138 4u gron9*-1
139 d17
140 4u groff
141
142 (p2 ph13+ph14):f1
143 p29:gp8*-1
144 d16
145 10u cpd3:f3
146
147 ;loop
148 4 0.1u REC_UNBLK
149 0.05u DWL_CLK_ON
150 d62
151 0.05u DWL_CLK_OFF
152 0.1u REC_BLK
153
154 10u do:f3
155 p29:gp8
156 d16 ipp14
157
158 ;BIRD rX
159 (p1 ph11+ph14):f1
160 DELTA6
161 (center (p2 ph11+ph14):f1 (p14:sp3 ph11+ph14):f2 )
162 DELTA6
163 (p1 ph13+ph14):f1
164
165 4u gron9
166 d17
167 4u groff
168 4u gron9*-1
169 d17
170 4u groff
171

```

```

172 (p2 ph13+ph14):f1
173 p29:gp8*-1
174 d16
175 10u cpd3:f3
176 lo to 4 times l1
177
178 0.1u REC_UNBLK
179 0.05u DWL_CLK_ON
180 d62*2
181 0.05u DWL_CLK_OFF
182 0.1u REC_BLK
183
184 rcyc=2
185
186 d11 do:f3 mc #0 to 2
187     F1PH(calph(ph3, +90) & calph(ph6, +90), caldel(d0, +in0))
188 exit
189
190
191 ph1=0
192 ph2=1
193 ph3=0 2
194 ph4=0 0 0 0 2 2 2 2
195 ph5=0 0 2 2
196 ph6=0
197 ph7=2
198 ph8=3
199
200 ; bbhd
201 ph11=1 1 3 3
202 ph13=3 3 1 1
203 ph14=0 2 2 0 2 0 0 2
204
205 ph29=0
206 ph30=0
207 ph31=0 2 0 2 2 0 2 0
208
209
210 ;p11 : f1 channel - power level for pulse (default)
211 ;p13 : f3 channel - power level for pulse (default)
212 ;p116: f3 channel - power level for CPD/BB decoupling
213 ;p118: f1 channel - power level for 3-9-19-pulse (watergate)
214 ;p132: f1 channel - power level for low power presaturation
215 ;sp3: f2 channel - shaped pulse 180 degree (adiabatic)
216 ;spnam3: Crp60,0.5,20.1 (Crp80,0.5,20.1)
217 ;p0 : f1 channel - 90 degree pulse at p118
218 ;
219 ;p1 : f1 channel - 90 degree high power pulse
220 ;p2 : f1 channel - 180 degree high power pulse
221 ;p14: f2 channel - 180 degree shaped pulse for inversion (adiabatic)
222 ;p16: homospoil/gradient pulse
223 ;p21: f3 channel - 90 degree high power pulse
224 ;p22: f3 channel - 180 degree high power pulse
225 ;p27: f1 channel - 90 degree pulse at p118
226 ;p29: gradient pulse 3 [300 usec]
227 ;d0 : incremented delay (2D) [3 usec]
228 ;d1 : relaxation delay; 1-5 * T1
229 ;d11: delay for disk I/O [30 msec]
230 ;d12: delay for power switching [20 usec]
231 ;d13: short delay [4 usec]
232 ;d16: delay for homospoil/gradient recovery
233 ;d19: delay for binomial water suppression
234 ; d19 = (1/(2*d)), d = distance of next null (in Hz)
235 ;d21 : 1/(2J(YH))
236 ;d26 : 1/(4J(YH))
237 ;d62: length of block between decoupling pulses : = aq/10 [< 20-25 msec]
238 ;d63: = d62/2

```

```

239 ;cnst4: = J(YH)
240 ;l0 : number of blocks during acquisition time
241 ;      adjust to get d62 as required
242 ;inf1: 1/SW(X) = 2 * DW(X)
243 ;in0: 1/(2 * SW(X)) = DW(X)
244 ;nd0: 2
245 ;ns: 8 * n
246 ;ds: 16
247 ;td1: number of experiments
248 ;FnMODE: States-TPPI (or TPPI)
249 ;cpd3: decoupling according to sequence defined by cpdprg3: garp4.p62
250 ;pcpd3: f3 channel - 90 degree pulse for decoupling sequence
251 ;cpdprg3: garp4.p62
252
253 ;for z-only gradients:
254 ;gpz1: 50%
255 ;gpz2: 80%
256 ;gpz3: 30%
257 ;gpz4: 3%
258 ;gpz5: 5%

```

5.4.8 BEST-TROSY Using ^{13}C -BIRD Pure Shift Amide Proton Detection

```

1
2 prosol relations=<triple>
3
4 #include <Avance.incl>
5 #include <Grad.incl>
6 #include <Delay.incl>
7 #include <De.incl>
8
9 define list<gradient> EA3 = { 1.0000 0.8750 }
10 define list<gradient> EA5 = { 0.6667 1.0000 }
11 define list<gradient> EA7 = { 1.0000 0.6595 }
12
13 "p22=p21*2"
14 "d11=30m"
15 "d12=20u"
16
17 "d25=2.7m"
18 "d26=2.7m"
19
20 "p29=250"
21
22 ; Bruker standard values
23 "cnst52=1.426"
24 "cnst53=1.0"
25 "cnst54=8.3"
26 "cnst55=5.0"
27
28 #   ifdef CALC_SP
29 "p42=(bwfac26/(cnst55*cnst52*bf1))*1000000"
30 "spw26=plw1/((p42*90.0)/(p1*totrot26))*((p42*90.0)/(p1*totrot26))*(integfac26*integfac26)"
31 "spoal26=0.5"
32
33 "p43=(bwfac28/(cnst55*cnst53*bf1))*1000000"
34 "spw28=plw1/((p43*90.0)/(p1*totrot28))*((p43*90.0)/(p1*totrot28))*(integfac28*integfac28)"
35 "spw29=plw1/((p43*90.0)/(p1*totrot29))*((p43*90.0)/(p1*totrot29))*(integfac29*integfac29)"
36 "spoal28=1"
37 "spoal29=0"
38 #   endif /*CALC_SP*/

```

```
39 "d0=3u"
40
41
42 "in0=inf1/2"
43
44 "DELTA1=d26-p19-d16-larger(p22,p42)/2"
45 "DELTA6=d25-p29-d16-larger(p22,p42)/2-p43*cnst43"
46 "DELTA7=d26-p16-d16-larger(p22,p42)/2"
47 "DELTA8=de+4u"
48 "DELTA=d0*2+p8+p21*4/PI"
49
50 "spoff13=bf2*(cnst26/1000000)-o2"
51
52 "spoff26=bf1*(cnst54/1000000)-o1"
53 "spoff28=bf1*(cnst54/1000000)-o1"
54 "spoff29=bf1*(cnst54/1000000)-o1"
55
56
57 "acqt0=0"
58 baseopt_echo
59
60 ;-----homodecoupled acquisition
61 "d62=aq/10"
62 "d63=d62/2"
63
64 #   ifdef BILEV
65 "d52=d62/4"
66 define list<delay> Dlist = { d63 d63 d63 d63 d52 d52 d52 d52 }
67 #   else
68 define list<delay> Dlist = { d63 d63 d63 d63 }
69 #   endif /*BILEV*/
70
71 "l1=10-2"
72 "p2=2*p1"
73 "DELTA5=1/(2*cnst2)"
74 "d17=d16+p29-8u"
75 dwellmode explicit
76 ;-----homodecoupled acquisition
77
78
79 1 d11 ze
80 2 d11
81 3 d12
82
83 (p22 ph1):f3
84 20u BLKGRAD
85 d1
86 20u p10:f1
87 50u UNBLKGRAD
88
89 (p43:sp28 ph3)
90 p19:gp1
91 d16
92 DELTA1
93 (center (p42:sp26 ph2) (p22 ph1):f3 )
94 DELTA1
95 p19:gp1
96 d16
97 (p43:sp29 ph2):f1
98
99 p16:gp2
100 d16
101
102 (p21 ph5):f3
103 d0
104 (p8:sp13 ph1):f2
105 d0
```

```

106 (p22 ph1):f3
107 DELTA
108
109 p16:gp3*EA3
110 d16
111
112 (p43:sp29 ph6)
113 p29:gp4
114 d16
115 DELTA6
116 (center (p42:sp26 ph2) (p22 ph2):f3 )
117 DELTA6
118 p29:gp4
119 d16
120 (p43:sp28 ph1)
121
122 p16:gp5*EA5
123 d16
124 DELTA8
125
126 (p21 ph1):f3
127 p16:gp6
128 d16
129 DELTA7
130 (center (p42:sp26 ph2) (p22 ph2):f3 )
131 DELTA7
132 p16:gp6
133 d16
134 (p21 ph7:r):f3
135
136 p16:gp7*EA7
137 d16
138 4u
139
140 ;-----homodecoupled acquisition
141 ACQ_START(ph30,ph31)
142
143 0.1u REC_UNBLK
144 0.05u DWL_CLK_ON
145 Dlist
146 0.05u DWL_CLK_OFF
147 0.1u REC_BLK
148
149 p29:gp8
150 d16 rpp14 pl1:f1
151
152 ;BIRD rX
153 (p1 ph11+ph14):f1
154 DELTA5
155 (center (p2 ph11+ph14):f1 (p8:sp13 ph11+ph14):f2 )
156 DELTA5
157 (p1 ph13+ph14):f1
158
159 4u gron9
160 d17
161 4u groff
162 4u gron9*-1
163 d17
164 4u groff
165
166 (p2 ph13+ph14):f1
167 p29:gp8*-1
168 d16
169
170 ;second acquisition
171 0.1u REC_UNBLK
172 0.05u DWL_CLK_ON

```

```

173 Dlist^
174 d63
175 0.05u DWL_CLK_OFF
176 0.1u REC_BLK
177
178 p29:gp8
179 d16 ipp14
180
181 ;BIRD rX
182 (p1 ph11+ph14):f1
183 DELTA5
184 (center (p2 ph11+ph14):f1 (p8:sp13 ph11+ph14):f2 )
185 DELTA5
186 (p1 ph13+ph14):f1
187
188 4u gron9
189 d17
190 4u groff
191 4u gron9*-1
192 d17
193 4u groff
194
195 (p2 ph13+ph14):f1
196 p29:gp8*-1
197 d16
198
199 ;loop
200 4 0.1u REC_UNBLK
201 0.05u DWL_CLK_ON
202 d62
203 0.05u DWL_CLK_OFF
204 0.1u REC_BLK
205
206 p29:gp8
207 d16 ipp14
208
209 ;BIRD rX
210 (p1 ph11+ph14):f1
211 DELTA5
212 (center (p2 ph11+ph14):f1 (p8:sp13 ph11+ph14):f2 )
213 DELTA5
214 (p1 ph13+ph14):f1
215
216 4u gron9
217 d17
218 4u groff
219 4u gron9*-1
220 d17
221 4u groff
222
223 (p2 ph13+ph14):f1
224 p29:gp8*-1
225 d16
226 lo to 4 times l1
227
228 0.1u REC_UNBLK
229 0.05u DWL_CLK_ON
230 d62
231 d63
232 0.05u DWL_CLK_OFF
233 0.1u REC_BLK
234
235 rcyc=2
236 Dlist.res
237
238 d11 mc #0 to 2
239 F1EA(calgrad(EA3) & calgrad(EA5) & calgrad(EA7) & calph(ph6, +180) & calph(ph7,

```

```

+180), caldel(d0, +in0) & calph(ph5, +180) & calph(ph31, +180))
240
241 4u BLKGRAD
242 exit
243
244
245 ph1=0
246 ph2=1
247 ph3=2
248 ph4=3
249 ph5=0 2
250 ph6=1
251 ph7=1
252 ph11=1 1 3 3
253 ph13=3 3 1 1
254 ph14=0 2 2 0 2 0 0 2
255 ph29=0
256 ph30=0
257 ph31=0 2
258
259
260 ;p11 : f1 channel - power level for pulse (default)
261 ;p13 : f3 channel - power level for pulse (default)
262 ;sp13: f2 channel - shaped pulse 180 degree (Ca and C=0, adiabatic)
263 ;sp26: f1 channel - shaped pulse 180 degree (Reburp.1000)
264 ;sp28: f1 channel - shaped pulse 90 degree (Eburp2.1000)
265 ;sp29: f1 channel - shaped pulse 90 degree (Eburp2tr.1000)
266 ;
267 ;p30 : f2 channel - 180 degree shaped pulse for inversion (BIP)
268 ;p16: homospoil/gradient pulse [1 msec]
269 ;p19: gradient pulse 2 [500 usec]
270 ;p21: f3 channel - 90 degree high power pulse
271 ;p22: f3 channel - 180 degree high power pulse
272 ;p29: gradient pulse 3 [250 usec]
273 ;p42: f1 channel - 180 degree shaped pulse for refocussing
274 ; Reburp.1000 (1.4ms at 600.13 MHz)
275 ;p43: f1 channel - 90 degree shaped pulse for excitation
276 ; Eburp2.1000/Eburp2tr.1000 (1.7ms at 600.13 MHz)
277 ;d0 : incremented delay (F1) [3 usec]
278 ;d1 : relaxation delay; 1-5 * T1
279 ;d11: delay for disk I/O [30 msec]
280 ;d12: delay for power switching [20 usec]
281 ;d16: delay for homospoil/gradient recovery
282 ;d25: 1/(4J(NH)) [2.7 msec]
283 ;d26: 1/(4J(NH))
284 ;d62: chunk length
285 ;d63: half a chunk length
286 ;cnst2: 1J(Ca,Ha) coupling (140 Hz) [2.7 msec]
287 ;cnst26: Call chemical shift (offset, in ppm) [101 ppm]
288 ;cnst43: compensation of chemical shift evolution during p43
289 ; Eburp2.1000: 0.69
290 ;cnst52: scaling factor for p42 to compensate for transition region
291 ; Reburp.1000: 1.426
292 ;cnst53: scaling factor for p43 to compensate for transition region
293 ; Eburp2.1000: 1.000
294 ;cnst54: H(N) chemical shift (offset, in ppm)
295 ;cnst55: H(N) bandwidth (in ppm)
296 ;inf1: 1/SW(N) = 2 * DW(N)
297 ;in0: 1/(2 * SW(N)) = DW(N)
298 ;nd0: 2
299 ;l0: number of chunks (normally 6 or 8)
300 ;ns: 2 * n
301 ;ds: 8
302 ;td1: number of experiments
303 ;FnMODE: echo-antiecho
304
305

```

```

306 ;for z-only gradients:
307 ;gpz1: 2%
308 ;gpz2: 21%
309 ;gpz3: -80%
310 ;gpz4: 5%
311 ;gpz5: 30%
312 ;gpz6: 45%
313 ;gpz7: 30.13%
314 ;gpz8: -3.5% (change and see for best water suppression in 1Ds)
315 ;gpz9: 0.5%
316
317 ;use gradient files:
318 ;gpnam1: SMSQ10.100
319 ;gpnam2: SMSQ10.100
320 ;gpnam3: SMSQ10.100
321 ;gpnam4: SMSQ10.32
322 ;gpnam5: SMSQ10.100
323 ;gpnam6: SMSQ10.100
324 ;gpnam7: SMSQ10.100
325 ;gpnam8: SMSQ10.32

```

5.4.9 SHACA-HSQC Using BASEREX

```

1
2 #include <Avance.incl>
3 #include <Grad.incl>
4 #include <Delay.incl>
5 #include <De.incl>
6
7 "p2=p1*2"
8 "p4=p3*2"
9 "d2=1s/(cnst2*2)"
10 "d4=1s/(cnst2*4)"
11 "d41=1s/(cnst41*4)"
12 "d11=30m"
13 "d12=20u"
14 "p29=300u"
15
16 "d0=3u"
17
18 "in0=inf1/2"
19 "d62=aq/10"
20 "d63=d62/2"
21 "l1=(10-1)/2"
22 "TAU=p43"
23
24 "DELTA1=d4-p16-de+p1*2/PI-8u"
25 "DELTA5=d2-larger(p2,p42)/2"
26 "DELTA=p16+d16-6u"
27
28 "acqt0=0"
29 baseopt_echo
30
31 dwellmode explicit
32
33
34 1 ze
35   d11 p112:f2
36 2 d11 do:f2
37   4u BLKGRAD
38   d12 p19:f1
39   d1 cw:f1 ph29
40   4u do:f1
41   d12 p11:f1

```

```

42
43 3 4u p12:f2
44   (p1 ph1)
45   4u
46   d4
47   (center (p2 ph1) (p4 ph6):f2 )
48   d4 UNBLKGRAD
49   4u p10:f2
50   (p1 ph2)
51   (p40:sp40 ph3):f2
52
53   d0 p10:f2 p110:f3
54
55   (center (p2 ph5) (p41:sp41 ph1):f2 (p50:sp50 ph1):f3)
56   p16:gp1*-1
57   d16 p10:f2
58   (p42:sp42 ph4):f2
59   DELTA p12:f2
60
61   d0
62
63   (p1 ph1)
64   d41
65   (center (p2 ph1) (p4 ph1):f2 )
66   d41
67
68   (ralign (p1 ph8) (p3 ph4):f2 )
69   d4
70   (center (p2 ph2) (p4 ph1):f2 )
71   4u
72   p16:gp2*EA
73   DELTA1 p112:f2
74
75 ;-----homodecoupled acquisition
76
77 4u cpd2:f2
78   ACQ_START(ph30,ph31)
79
80   0.1u REC_UNBLK
81   0.05u DWL_CLK_ON
82   d63
83   0.05u DWL_CLK_OFF
84   0.1u REC_BLK
85
86   10u do:f2
87   p29:gp5
88   d16
89   TAU
90   4u gron4
91   (p1 ph1)
92   DELTA5
93   4u p10:f2
94   (center (p2 ph2) (p42:sp42 ph1):f2 )
95   4u
96   DELTA5
97   (p1 ph10)
98   4u groff p10:f2
99   (p43:sp43 ph1):f2
100  p29:gp5
101  d16 p112:f2
102  20u
103  p29:gp6
104  d16
105  4u gron4
106  (p2 ph1)
107  4u groff
108  p29:gp6

```

```
109 d16
110 10u cpd2:f2
111
112 4 0.1u REC_UNBLK
113 0.05u DWL_CLK_ON
114 d62
115 0.05u DWL_CLK_OFF
116 0.1u REC_BLK
117
118 10u do:f2
119 p29:gp5*-1
120 d16
121 TAU
122 4u gron4
123 (p1 ph1)
124 DELTA5
125 4u p10:f2
126 (center (p2 ph2) (p42:sp42 ph1):f2 )
127 4u
128 DELTA5
129 (p1 ph10)
130 4u groff p10:f2
131 (p43:sp43 ph1):f2
132 p29:gp5*-1
133 d16 p112:f2
134 20u
135 p29:gp6*-1
136 d16
137 4u gron4
138 (p2 ph1)
139 4u groff
140 p29:gp6*-1
141 d16
142 10u cpd2:f2
143
144
145 0.1u REC_UNBLK
146 0.05u DWL_CLK_ON
147 d62
148 0.05u DWL_CLK_OFF
149 0.1u REC_BLK
150
151 10u do:f2
152 p29:gp5
153 d16
154 TAU
155 4u gron4
156 (p1 ph1)
157 DELTA5
158 4u p10:f2
159 (center (p2 ph2) (p42:sp42 ph1):f2 )
160 4u
161 DELTA5
162 (p1 ph10)
163 4u groff p10:f2
164 (p43:sp43 ph1):f2
165 p29:gp5
166 d16 p112:f2
167 20u
168 p29:gp6
169 d16
170 4u gron4
171 (p2 ph1)
172 4u groff
173 p29:gp6
174 d16
175 10u cpd2:f2
```

```

176 lo to 4 times l1
177
178
179 0.1u REC_UNBLK
180 0.05u DWL_CLK_ON
181 d62*2
182 0.05u DWL_CLK_OFF
183 0.1u REC_BLK
184
185 rcyc=2
186
187 d11 do:f2 mc #0 to 2
188     F1EA(calgrad(EA) & calph(ph8, +180), caldel(d0, +in0) & calph(ph3, +180) & calph(
189         ph6, +180) & calph(ph31, +180))
190
191 4u BLKGRAD
192 exit
193
194 ph1=0
195 ph2=1
196 ph3=0 2
197 ph4=0 0 0 0 2 2 2 2
198 ph5=0 0 2 2
199 ph6=0
200 ph8=3
201 ph10=2
202 ph29=0
203 ph30=0
204 ph31=0 2 0 2 2 0 2 0
205
206
207 ;p11 : f1 channel - power level for pulse (default)
208 ;p12 : f2 channel - power level for pulse (default)
209 ;p13 : f3 channel - power level for pulse (default)
210 ;p110 : f3 channel - 0 Watt power level
211 ;p112: f2 channel - power level for CPD/BB decoupling
212 ;p1 : f1 channel - 90 degree high power pulse
213 ;p2 : f1 channel - 180 degree high power pulse
214 ;p3 : f2 channel - 90 degree high power pulse
215 ;p4 : f2 channel - 180 degree high power pulse
216 ;p16: homospoil/gradient pulse
217 ;p22: f3 channel - 180 degree high power pulse
218 ;p40: 1.5 ms pulse length for Eburp2.1000 on f2 (for Gly: 2.5 ms)
219 ;p41: 2 ms pulse length for Burbop-180.1 on f2
220 ;p42: 1.5 ms pulse length for Reburp.1000 on f2 (for Gly: 2.5 ms)
221 ;p43: 160 us pulse length for Bip720,100,10.1 on f2
222 ;p50: 1.6 ms pulse length for Bip720,100,10.1 on f3
223 ;sp40: Eburp2.1000 on f2
224 ;sp41: Burbop-180.1 on f2
225 ;sp42: Reburp.1000 on f2
226 ;sp43: Bip720,100,10.1 on f2
227 ;sp50: Bip720,100,10.1 on f3
228 ;d0 : incremented delay (2D) [3 usec]
229 ;d1 : relaxation delay; 1-5 * T1
230 ;d4 : 1/(4J)CaHa
231 ;d11: delay for disk I/O [30 msec]
232 ;d16: delay for homospoil/gradient recovery
233 ;cnst2: = J(CaHa)
234 ;cnst41: = 290 for Gly and 145 for all others
235 ;inf1: 1/SW(X) = 2 * DW(X)
236 ;in0: 1/(2 * SW(X)) = DW(X)
237 ;nd0: 2
238 ;ns: 1 * n
239 ;ds: >= 16
240 ;td1: number of experiments
241 ;FnMODE: echo-antiecho

```

```

242 ;cpd2: decoupling according to sequence defined by cpdprg2
243 ;pcpd2: f2 channel - 90 degree pulse for decoupling sequence
244
245 ;use gradient ratio: gp 1 : gp 2
246 ;      80 : 20.1      for C-13
247
248 ;for z-only gradients:
249 ;gpz1: 80%
250 ;gpz2: 20.1%
251 ;gpz4: 0.1%
252 ;gpz5: 5%
253 ;gpz6: 7%
254
255 ;use gradient files:
256 ;gpnam1: SMSQ10.100
257 ;gpnam2: SMSQ10.100
258 ;gpnam5: SMSQ10.100
259 ;gpnam6: SMSQ10.100

```

5.4.10 SHACA-SIHSQC for Methyl-Groups Using BASEREX

```

1
2 #include <Avance.incl>
3 #include <Grad.incl>
4 #include <Delay.incl>
5 #include <De.incl>
6
7
8 "p2=p1*2"
9 "p4=p3*2"
10 "d2=1s/(cnst2*2)"
11 "d4=1s/(cnst2*4)-p4/2"
12 "d24=1s/(cnst21*cnst2)-(0.22*p17/2)"
13 "d11=30m"
14 "d12=20u"
15 "p29=300u"
16
17 "d0=3u"
18
19 "in0=inf1/2"
20 "d62=aq/10"
21 "d63=d62/2"
22 #   ifdef BILEV4
23 "d52=d62/4"
24 define list<delay> Dlist = { d63 d63 d52 d52 }
25 #   else
26 define list<delay> Dlist = { d63 d63 d63 d63 }
27 #   endif /*BILEV4*/
28 "l1=10-2"
29 "TAU=p39"
30
31 "DELTA1=p16+d16-p1*0.78+de+8u"
32 "DELTA5=d2-(0.95*p14/2)"
33 "DELTA=p16+d16-6u"
34
35 #   ifdef CALC_SP
36 ;Reburp
37 "p14=(bwfac14/(cnst55*cnst52*bf2))*1000000"
38 "spw14=plw2/((p14*90.0)/(p3*totrot14))*((p14*90.0)/(p3*totrot14))*(integfac14*integfac14)"
39 "spoal14=0.5"
40
41 ; Eburp
42 "p15=(bwfac15/(cnst55*cnst53*bf2))*1000000"

```

```

43 "spw15=plw2/((p15*90.0)/(p3*totrot15))*((p15*90.0)/(p3*totrot15))*(integfac15*integfac15
   )"
44 "spoal15=1"
45
46 ; Q3.1000
47 "p17=(bwfac17/(cnst55*cnst53*bf2))*1000000"
48 "spw17=plw2/((p17*90.0)/(p3*totrot17))*((p17*90.0)/(p3*totrot17))*(integfac17*integfac17
   )"
49 "spoal17=0.5"
50 #   endif /*CALC_SP*/
51
52 "acqt0=0"
53 baseopt_echo
54 dwellmode explicit
55
56
57 1 ze
58   d11 pl12:f2
59 2 d11 do:f2
60   4u BLKGRAD
61   d12 pl9:f1
62   d1  cw:f1 ph29
63   4u do:f1
64   d12 pl1:f1
65   50u UNBLKGRAD
66
67 3 4u
68   (p1 ph1)
69   d4 pl2:f2
70   (center (p2 ph1) (p4 ph6):f2 )
71   d4
72   4u pl0:f2 pl10:f3
73   (p1 ph2)
74   (p15:sp15 ph3):f2
75
76   d0
77
78   (center (p2 ph7) (p13:sp13 ph1):f2 (p27:sp27 ph1):f3)
79   p16:gp1*EA
80   d16 pl0:f2
81   (p14:sp14 ph4):f2
82   DELTA pl2:f2
83
84   d0
85
86   (center (p1 ph1) (p3 ph4):f2 )
87   d24 pl0:f2
88   (center (p2 ph1) (p17:sp17 ph1):f2 ) ; Q3.1000
89   d24 pl2:f2
90
91   (center (p1 ph2) (p3 ph5):f2 )
92   d4
93   (center (p2 ph1) (p4 ph1):f2 )
94   d4 pl0:f2
95   (p1 ph1)
96
97   DELTA1
98   (p2 ph1)
99   4u
100  p16:gp2
101  d16 pl12:f2
102
103 ;-----homodecoupled acquisition
104
105 plusminus.res
106 4u cpd2:f2
107 ACQ_START(ph30,ph31)

```

```
108
109 0.1u REC_UNBLK
110 0.05u DWL_CLK_ON
111 Dlist
112 0.05u DWL_CLK_OFF
113 0.1u REC_BLK
114
115 10u do:f2
116 p29:gp5*plusminus
117 d16
118 TAU
119 4u gron4
120 (p1 ph1)
121 DELTA5
122 4u pl0:f2
123 (center (p2 ph2) (p14:sp14 ph1):f2 )
124 4u
125 DELTA5
126 (p1 ph10)
127 4u groff pl0:f2
128 (p39:sp4 ph1):f2
129 p29:gp5*plusminus
130 d16 pl12:f2
131 20u
132 p29:gp6*plusminus
133 d16
134 4u gron4
135 (p2 ph1)
136 4u groff
137 p29:gp6*plusminus
138 d16
139 igrad plusminus
140 10u cpd2:f2
141
142 0.1u REC_UNBLK
143 0.05u DWL_CLK_ON
144 Dlist^
145 d63
146 0.05u DWL_CLK_OFF
147 0.1u REC_BLK
148
149 10u do:f2
150 p29:gp5*plusminus
151 d16
152 TAU
153 4u gron4
154 (p1 ph1)
155 DELTA5
156 4u pl0:f2
157 (center (p2 ph2) (p14:sp14 ph1):f2 )
158 4u
159 DELTA5
160 (p1 ph10)
161 4u groff pl0:f2
162 (p39:sp4 ph1):f2
163 p29:gp5*plusminus
164 d16 pl12:f2
165 20u
166 p29:gp6*plusminus
167 d16
168 4u gron4
169 (p2 ph1)
170 4u groff
171 p29:gp6*plusminus
172 d16
173 igrad plusminus
174 10u cpd2:f2
```

```

175
176 4 0.1u REC_UNBLK
177   0.05u DWL_CLK_ON
178   d62
179   0.05u DWL_CLK_OFF
180   0.1u REC_BLK
181
182   10u do:f2
183   p29:gp5*plusminus
184   d16
185   TAU
186   4u gron4
187   (p1 ph1)
188   DELTA5
189   4u pl0:f2
190   (center (p2 ph2) (p14:sp14 ph1):f2 )
191   4u
192   DELTA5
193   (p1 ph10)
194   4u groff pl0:f2
195   (p39:sp4 ph1):f2
196   p29:gp5*plusminus
197   d16 pl12:f2
198   20u
199   p29:gp6*plusminus
200   d16
201   4u gron4
202   (p2 ph1)
203   4u groff
204   p29:gp6*plusminus
205   d16
206   igrad plusminus
207   10u cpd2:f2
208
209   lo to 4 times l1
210
211   0.1u REC_UNBLK
212   0.05u DWL_CLK_ON
213   d62*2
214   0.05u DWL_CLK_OFF
215   0.1u REC_BLK
216
217   rcyc=2
218
219
220   d11 do:f2 mc #0 to 2
221       F1EA(calgrad(EA) & calph(ph5, +180), caldel(d0, +in0) & calph(ph3, +180) & calph(
222           ph6, +180) & calph(ph31, +180))
223
224   4u BLKGRAD
225 exit
226
227
228 ph1=0
229 ph2=1
230 ph3=0 2
231 ph6=0
232 ph8=3
233 ph10=2
234 ph29=0
235 ph30=0
236
237 #   ifdef BILEV4
238 ph4=0 0 0 0 2 2 2 2
239 ph5=1 1 1 1 3 3 3 3
240 ph7=0 0 0 0 2 2 2 2

```

```

241 ph31=0 2 0 2 2 0 2 0
242 #   else
243 ph4=0 0 2 2
244 ph5=1 1 3 3
245 ph7=0 0 2 2
246 ph31=0 2 2 0
247 #   endif /*BILEV4*/
248
249
250 ;p11 : f1 channel - power level for pulse (default)
251 ;p12 : f2 channel - power level for pulse (default)
252 ;p13 : f3 channel - power level for pulse (default)
253 ;p112: f2 channel - power level for CPD/BB decoupling
254 ;p1 : f1 channel - 90 degree high power pulse
255 ;p2 : f1 channel - 180 degree high power pulse
256 ;p3 : f2 channel - 90 degree high power pulse
257 ;p4 : f2 channel - 180 degree high power pulse
258 ;p16: homospoil/gradient pulse
259 ;p22: f3 channel - 180 degree high power pulse
260 ;p28: f1 channel - trim pulse
261 ;d0 : incremented delay (2D)           [3 usec]
262 ;d1 : relaxation delay; 1-5 * T1
263 ;d4 : 1/(4J)XH
264 ;d11: delay for disk I/O                [30 msec]
265 ;d16: delay for homospoil/gradient recovery
266 ;cnst2: = J(XH)
267 ;cnst21: = 4 (CH), 8 (CH2 or all multipl.), 12 (CH3)
268 ;cnst52: 1.3636360 Reburp
269 ;cnst53: 1.1538460 Eburp
270 ;cnst55: Bandwidth for selective pulses
271 ;inf1: 1/SW(X) = 2 * DW(X)
272 ;in0: 1/(2 * SW(X)) = DW(X)
273 ;nd0: 2
274 ;ns: 1 * n
275 ;ds: >= 16
276 ;td1: number of experiments
277 ;FnMODE: echo-antiecho
278 ;cpd2: decoupling according to sequence defined by cpdprg2
279 ;pcpd2: f2 channel - 90 degree pulse for decoupling sequence
280
281 ;use gradient ratio:  gp 1 : gp 2
282 ;      80 : 20.1   for C-13
283
284 ;for z-only gradients:
285 ;gpz1: 80%
286 ;gpz2: 20.1% for C-13, 8.1% for N-15
287
288 ;use gradient files:
289 ;gpnam1: SMSQ10.100
290 ;gpnam2: SMSQ10.100

```

5.4.11 CT-SHACA-HSQC Using BASEREX

```

1
2 #include <Avance.incl>
3 #include <Grad.incl>
4 #include <Delay.incl>
5 #include <De.incl>
6
7 "p2=p1*2"
8 "p4=p3*2"
9 "d2=1s/(cnst2*2)"
10 "d4=1s/(cnst2*4)"
11 "d24=1s/(cnst2*cnst21)-0.95*p14/2"

```

```

12 "d11=30m"
13 "d12=20u"
14 "p29=300u"
15
16 "d0=3u"
17
18 "in0=inf1/2"
19 "d62=aq/10"
20 "d63=d62/2"
21 #   ifdef BILEV4
22 "d52=d62/4"
23 define list<delay> Dlist = { d63 d63 d52 d52 }
24 #   else
25 define list<delay> Dlist = { d63 d63 d63 d63 }
26 #   endif /*BILEV4*/
27 "l1=10-2"
28 "TAU=p39"
29
30
31 "DELTA1=p16+d16-p1*0.78+de+8u"
32 "DELTA5=d2-(0.95*p14/2)"
33
34
35 #   ifdef CALC_SP
36 ;Reburp
37 "p14=(bwfac14/(cnst55*cnst52*bf2))*1000000"
38 "spw14=plw2/((p14*90.0)/(p3*totrot14))*((p14*90.0)/(p3*totrot14))*(integfac14*integfac14)"
39 "spoal14=0.5"
40
41 ; Eburp
42 "p15=(bwfac15/(cnst55*cnst53*bf2))*1000000"
43 "spw15=plw2/((p15*90.0)/(p3*totrot15))*((p15*90.0)/(p3*totrot15))*(integfac15*integfac15)"
44 "spoal15=1"
45
46 ;I-burp
47 "p17=(bwfac17/(cnst55*cnst54*bf2))*1000000"
48 "spw17=plw2/((p17*90.0)/(p3*totrot17))*((p17*90.0)/(p3*totrot17))*(integfac17*integfac17)"
49 "spoal17=0.5"
50 #   endif /*CALC_SP*/
51
52 ;CT
53 "d25=1s/(cnst22)"
54 "d23=d25*cnst23/2"
55 "DELTA3=d23-p14+d0"
56 "d20=d23-p16-d16-p14-20u"
57 "in20=in0"
58 "td1=tdmax(td1,d20*2,in20)"
59
60
61 "acqt0=0"
62 baseopt_echo
63 dwellmode explicit
64
65
66 1 ze
67   d11 pl12:f2
68 2 d11 do:f2
69   4u BLKGRAD
70   d12 pl9:f1
71   d1 cw:f1 ph29
72   4u do:f1
73   d12 pl1:f1
74
75 3 4u pl2:f2

```

```
76 (p1 ph1)
77 d4
78 (center (p2 ph1) (p4 ph6):f2 )
79 d4 UNBLKGRAD
80 4u p10:f2 p110:f3
81 (p1 ph2)
82 (p15:sp15 ph3):f2
83
84 d0
85
86 (center (p2 ph7) (p13:sp13 ph1):f2 (p27:sp27 ph1):f3)
87 4u
88 (p17:sp17 ph1):f2 ;I-BURP
89 DELTA3
90
91 (p17:sp17 ph1):f2 ;I-BURP
92 d20
93 p16:gp1*EA*-1
94 d16
95 20u p12:f2
96 (center (p1 ph1) (p3 ph4):f2 )
97 d24 p10:f2
98 (center (p2 ph1) (p14:sp14 ph1):f2 )
99 d24 p12:f2
100
101 (ralign (p1 ph2) (p3 ph5):f2 )
102 d4
103 (center (p2 ph1) (p4 ph1):f2 )
104 d4
105 (p1 ph1)
106
107 DELTA1
108 (p2 ph1)
109 4u
110 p16:gp2
111 d16 p112:f2
112
113 ;-----homodecoupled acquisition
114
115 plusminus.res
116 4u cpd2:f2
117 ACQ_START(ph30,ph31)
118
119 0.1u REC_UNBLK
120 0.05u DWL_CLK_ON
121 Dlist
122 0.05u DWL_CLK_OFF
123 0.1u REC_BLK
124
125 10u do:f2
126 p29:gp5*plusminus
127 d16
128 TAU
129 4u gron4
130 (p1 ph1)
131 DELTA5
132 4u p10:f2
133 (center (p2 ph2) (p14:sp14 ph1):f2 )
134 4u
135 DELTA5
136 (p1 ph10)
137 4u groff p10:f2
138 (p39:sp4 ph1):f2
139 p29:gp5*plusminus
140 d16 p112:f2
141 20u
142 p29:gp6*plusminus
```

```

143 d16
144 4u gron4
145 (p2 ph1)
146 4u groff
147 p29:gp6*plusminus
148 d16
149 igrad plusminus
150 10u cpd2:f2
151
152 0.1u REC_UNBLK
153 0.05u DWL_CLK_ON
154 Dlist^
155 d63
156 0.05u DWL_CLK_OFF
157 0.1u REC_BLK
158
159 10u do:f2
160 p29:gp5*plusminus
161 d16
162 TAU
163 4u gron4
164 (p1 ph1)
165 DELTA5
166 4u p10:f2
167 (center (p2 ph2) (p14:sp14 ph1):f2 )
168 4u
169 DELTA5
170 (p1 ph10)
171 4u groff p10:f2
172 (p39:sp4 ph1):f2
173 p29:gp5*plusminus
174 d16 p112:f2
175 20u
176 p29:gp6*plusminus
177 d16
178 4u gron4
179 (p2 ph1)
180 4u groff
181 p29:gp6*plusminus
182 d16
183 igrad plusminus
184 10u cpd2:f2
185
186 4 0.1u REC_UNBLK
187 0.05u DWL_CLK_ON
188 d62
189 0.05u DWL_CLK_OFF
190 0.1u REC_BLK
191
192 10u do:f2
193 p29:gp5*plusminus
194 d16
195 TAU
196 4u gron4
197 (p1 ph1)
198 DELTA5
199 4u p10:f2
200 (center (p2 ph2) (p14:sp14 ph1):f2 )
201 4u
202 DELTA5
203 (p1 ph10)
204 4u groff p10:f2
205 (p39:sp4 ph1):f2
206 p29:gp5*plusminus
207 d16 p112:f2
208 20u
209 p29:gp6*plusminus

```

```

210 d16
211 4u gron4
212 (p2 ph1)
213 4u groff
214 p29:gp6*plusminus
215 d16
216 igrad plusminus
217 10u cpd2:f2
218
219 lo to 4 times l1
220
221 0.1u REC_UNBLK
222 0.05u DWL_CLK_ON
223 d62*2
224 0.05u DWL_CLK_OFF
225 0.1u REC_BLK
226
227 rcyc=2
228
229 d11 do:f2 mc #0 to 2
230 F1EA(calgrad(EA) & calph(ph5, +180), caldel(d0, +in0) & caldel(d20, -in20) & calph(
    ph3, +180) & calph(ph6, +180) & calph(ph31, +180))
231
232 4u BLKGRAD
233
234 exit
235
236
237 ph1=0
238 ph2=1
239 ph3=0 2
240 ph6=0
241 ph10=2
242 ph29=0
243 ph30=0
244
245 # ifdef BILEV4
246 ph4=0 0 0 0 2 2 2 2
247 ph5=1 1 1 1 3 3 3 3
248 ph7=0 0 0 0 2 2 2 2
249 ph31=0 2 0 2 2 0 2 0
250 # else
251 ph4=0 0 2 2
252 ph5=1 1 3 3
253 ph7=0 0 2 2
254 ph31=0 2 2 0
255 # endif /*BILEV4*/
256
257
258 ;p11 : f1 channel - power level for pulse (default)
259 ;p12 : f2 channel - power level for pulse (default)
260 ;p13 : f3 channel - power level for pulse (default)
261 ;p112: f2 channel - power level for CPD/BB decoupling
262 ;p1 : f1 channel - 90 degree high power pulse
263 ;p2 : f1 channel - 180 degree high power pulse
264 ;p3 : f2 channel - 90 degree high power pulse
265 ;p4 : f2 channel - 180 degree high power pulse
266 ;p16: homospoil/gradient pulse
267 ;p22: f3 channel - 180 degree high power pulse
268 ;p28: f1 channel - trim pulse
269 ;d0 : incremented delay (2D) [3 usec]
270 ;d1 : relaxation delay; 1-5 * T1
271 ;d4 : 1/(4J)XH
272 ;d11: delay for disk I/O [30 msec]
273 ;d16: delay for homospoil/gradient recovery
274 ;cnst2: = J(XH)
275 ;cnst21: = 4 (CH), 8 (CH2 or all multipl.), 12 (CH3)

```

```
276 ;cnst52: 1.3636360 Reburp
277 ;cnst53: 1.1538460 Eburp
278 ;cnst55: Bandwidth for selective pulses
279 ;inf1: 1/SW(X) = 2 * DW(X)
280 ;in0: 1/(2 * SW(X)) = DW(X)
281 ;nd0: 2
282 ;ns: 1 * n
283 ;ds: >= 16
284 ;td1: number of experiments
285 ;FnMODE: echo-antiecho
286 ;cpd2: decoupling according to sequence defined by cpdprg2
287 ;pcpd2: f2 channel - 90 degree pulse for decoupling sequence
288
289 ;use gradient ratio: gp 1 : gp 2
290 ;      80 : 20.1 for C-13
291
292 ;for z-only gradients:
293 ;gpz1: 80%
294 ;gpz2: 20.1% for C-13, 8.1% for N-15
295
296 ;use gradient files:
297 ;gpnam1: SMSQ10.100
298 ;gpnam2: SMSQ10.100
```

5.5 Numerical Simulations

5.5.1 Strong Coupling: Berry-Phase

```

1 #xxyy_sphere_start1_centered_obs1p_rotFr_noabs.py
2
3 import numpy as np
4 import scipy.linalg as scla
5 from pylab import fft, rfft, fftshift, fft2
6 import matplotlib.pyplot as plt
7 import itertools
8
9 # -----
10 #
11 ct = lambda hermi: np.conj(np.transpose(hermi))
12 prop = lambda rho, U: np.dot( np.dot(U, rho), ct(U))
13
14 def prop_op(ops, U):
15     for i in range(len(ops)): ops[i] = np.dot( np.dot(U, ops[i]), ct(U))
16     return ops
17
18 def measure(rho, ops):
19     temp = []
20     for op in ops: temp.append( np.trace(np.dot( op, rho )) / np.trace( np.dot(ct(op), op)
21     ) )
22     return temp
23
24 def Offset(H, spin, offset):
25     H += 2*np.pi * offset * Iz[ spin ]
26     return H
27
28 def J_ZQ0(H, spin1, spin2, J):
29     H += 2*np.pi* J * (np.dot(Iy[ spin1 ], Iy[ spin2 ]) + np.dot(Ix[ spin1 ], Ix[ spin2 ]))
30     return H
31
32 def defpuls(*args):
33     func = lambda pphase, ppow: 2*np.pi* (np.cos(2*np.pi* pphase/4.) * sum([Ix[ n ] for n
34     in args]) + np.sin(2*np.pi* pphase/4.) * sum([Iy[ n ] for n in args]) ) * ppow
35     return func
36
37 def acq_double_rotating(rho, H_t2, pts, dwt, n=10):
38     fid = {}
39     for op in ops: fid[op] = []
40
41     for k in range(pts):
42         for op in ops: fid[op].append( measure(rho, operators[op]) )
43
44         for i in range(n):
45             U_t2 = scla.expm(-1j * H_t2 * dwt/n)
46             rho = prop(rho, U_t2)
47         return fid
48
49 # -----
50 # Define base, which is given by the kronecker product of ExEx(I3x,y,z)xExE...
51 mIx = 0.5 * np.array([[0,1.],[1.,0]])
52 mIy = 0.5 * 1j * np.array([[0,-1.],[1.,0]])
53 mIz = 0.5 * np.array([[1.,0],[0,-1.]])
54 mIp = np.array([[0,1],[0,0]])
55 mIm = np.array([[0,0],[1,0]])
56 mIa = np.array([[1,0],[0,0]])
57 mIb = np.array([[0,0],[0,1]])
58
59 def base(i, mi, nspins):
60     mstart = np.eye(2**i)

```

```

61  mlend = np.eye(2**(nspins-i-1))
62  return np.kron(np.kron(m1start,mi),mlend)
63
64  def init(spins):
65      norder = 2**len(spins)
66
67      global Iu, Ix, Iy, Iz, Ip, Im, Ia, Ib
68      Iu = {}; Ix = {}; Iy = {}; Iz = {}; Ip = {}; Im = {}; Ia = {}; Ib = {};
69
70      for i, spin in enumerate(spins):
71          Iu[spin] = np.eye(norder)
72          Ix[spin] = base(i, mIx, len(spins))
73          Iy[spin] = base(i, mIy, len(spins))
74          Iz[spin] = base(i, mIz, len(spins))
75          Ip[spin] = base(i, mIp, len(spins))
76          Im[spin] = base(i, mIm, len(spins))
77          Ia[spin] = base(i, mIa, len(spins))
78          Ib[spin] = base(i, mIb, len(spins))
79  # -----
80
81
82  # -----
83  # Prepare spinsystem
84  spins = ['H1', 'H2']
85  init(spins)
86
87  Ham = 1j*0
88  Ham = J_ZQ0(Ham, 'H1', 'H2', 10)
89  Ham = Offset(Ham, 'H1', 10)
90  Ham = Offset(Ham, 'H2', -10)
91
92  Hpuls = defpuls('H1', 'H2')
93
94  ppow = 10 * 10**3
95  # -----
96
97
98  # -----
99  # Prepare insilico-experimental data: Parameters
100 pts = 595 # Time domain points
101 dwt = 0.00015 # Dwell time
102 # -----
103
104
105 # -----
106 # Run insilico-experiment
107 rho_init = Ix['H1']
108 # -----
109
110
111
112 # -----
113 # Run insilico-experiment
114 # -----
115 operators = {}
116 operators["x_y_zy"] = [Ix["H1"], Iy["H1"], 2*np.dot(Iz["H1"], Iy["H2"] )]
117 ops = operators.keys()
118
119 rho = rho_init[:]
120 fid = acq_double_rotating(rho, Ham, pts, dwt)
121 # -----
122
123
124
125
126 # -----
127 # Plotting: functions

```

```

128 from matplotlib.patches import FancyArrowPatch
129 from mpl_toolkits.mplot3d import proj3d
130 import matplotlib as mpl
131 from mpl_toolkits.mplot3d import Axes3D
132
133 plt.rcParams.update({
134     "text.usetex": True,
135     "font.family": "serif",
136     "font.serif": ["Computer Modern Roman"]})
137
138 cmap = mpl.cm.get_cmap('viridis')
139
140
141 class Arrow3D(FancyArrowPatch):
142     def __init__(self, xs, ys, zs, *args, **kwargs):
143         FancyArrowPatch.__init__(self, (0,0), (0,0), *args, **kwargs)
144         self._verts3d = xs, ys, zs
145
146     def draw(self, renderer):
147         xs3d, ys3d, zs3d = self._verts3d
148         xs, ys, zs = proj3d.proj_transform(xs3d, ys3d, zs3d, renderer.M)
149         self.set_positions((xs[0],ys[0]),(xs[1],ys[1]))
150         FancyArrowPatch.draw(self, renderer)
151
152 def plot_arrow(ax, z, coord, color, lwd, **kwargs):
153     a = Arrow3D([z[0],coord[0]],[z[1],coord[1]],[z[2],coord[2]], mutation_scale=20, lw=lwd
154               , arrowstyle="->", color=color, **kwargs)
155     ax.add_artist(a)
156
157 def plot_puls(ax, coord, c):
158     X = np.transpose(coord)[0]
159     Y = np.transpose(coord)[1]
160     Z = np.transpose(coord)[2]
161
162     ax.plot(X, Y, Z, color=c, lw=3)
163     ax.set_xlim([-1,1])
164     ax.set_ylim([-1,1])
165     ax.set_zlim([-1,1])
166     return ax
167
168 def kugel():
169     fig = plt.figure(figsize=(6,6))
170     ax = fig.add_subplot(111, projection='3d')
171
172     u = np.linspace(0, 2 * np.pi, 100)
173     v = np.linspace(0, np.pi, 100)
174     x = np.outer(np.cos(u), np.sin(v))
175     y = np.outer(np.sin(u), np.sin(v))
176     z = np.outer(np.ones(np.size(u)), np.cos(v))
177     ax.plot_surface(x, y, z, rstride=4, cstride=4, color='k', alpha = 0.005)
178     ax.plot_wireframe(x, y, z, color="k", alpha = 0.05)
179
180     s=20
181     ax.text(1.55, 0, -0.05, r"$\langle \hat{I}_\mathrm{1x} \rangle$", size=s)
182     ax.text(0, 1.15, -0.05, r"$\langle \hat{I}_\mathrm{1y} \rangle$", size=s)
183     ax.text(0.18, -0.18, 1.1, r"$\langle 2\hat{I}_\mathrm{1z}\hat{I}_\mathrm{2y} \rangle$",
184           , size=s)
185
186     plot_arrow(ax, [-1,0,0], [1,0,0], 'k', 2.5)
187     plot_arrow(ax, [0,-1,0], [0,1,0], 'k', 2.5)
188     plot_arrow(ax, [0,0,-1], [0,0,1], 'k', 2.5)
189
190     ax.set_xlim([-1,1])
191     ax.set_ylim([-1,1])
192     ax.set_zlim([-1,1])
193     return ax

```

```

193 norm = lambda vec: np.array(vec) / np.sqrt(vec[0]**2+vec[1]**2+vec[2]**2)
194 # -----
195
196
197
198
199 FID = np.zeros( [len(fid["x_y_zy"]), 3] )
200 FID[:,0] = np.array(fid["x_y_zy"])[: ,0]
201 FID[:,1] = np.array(fid["x_y_zy"])[: ,1]
202 FID[:,2] = np.array(fid["x_y_zy"])[: ,2]
203
204 # -----
205 # Plotting: draw tracks
206 ax = kugel()
207 color_range = np.linspace(0,1,len(fid["x_y_zy"])-1)
208
209 for i in range(len(FID)-1):
210     temp = [FID[i], FID[i+1]]
211     plot_puls(ax, temp, cmap(color_range[i]))
212
213 plot_arrow(ax, [0,0,0.3], [0,0,1], 'k', 2.5, zorder=102)
214 ax.set_frame_on(False)
215 ax.axes.set_axis_off()
216 plt.tight_layout()
217
218 ax.view_init(elev = 10, azim=40)
219 plt.savefig('Berry_phase.png', dpi=300)
220 plt.show()
221 plt.close('all')
222 # -----
223
224
225 t = []
226 for f in FID:
227     t.append(np.sqrt(np.abs(f[0])**2+np.abs(f[1])**2+np.abs(f[2])**2))
228 plt.plot(t); plt.show()

```

5.5.2 AHT: IPE (Time-Dependence, 1D)

```

1 import numpy as np
2 import itertools
3 import scipy.linalg as scla
4 import matplotlib.pyplot as plt
5
6
7 # -----
8 # Matrix product of multiple matrices
9 ct = lambda hermi: np.conj(np.transpose(hermi))
10
11 def M(*arg):
12     dot = arg[0]
13     for k in range(1,len(arg)):
14         dot = np.dot(dot,arg[k])
15     return dot
16
17 def Offset(H, spin, offset):
18     H += 2*np.pi * offset * Iz[ spin ]
19     return H
20
21 def Jweak(H, spin1, spin2, J):
22     H += 2*np.pi* J * (np.dot(Iz[ spin1 ], Iz[ spin2 ]))
23     return H
24
25 def defpuls(*args):
26     func = lambda pphase, ppow: 2*np.pi* (np.cos(2*np.pi* pphase/4.) * sum([Ix[ n ] for n
27         in args]) + np.sin(2*np.pi* pphase/4.) * sum([Iy[ n ] for n in args]) ) * ppow

```

```

28 # -----
29
30
31
32 # -----
33 # Define base, which is given by the kronecker product of ExEx(I3x,y,z)xExE...
34 mIx = 0.5 * np.array([[0,1.],[1.,0]])
35 mIy = 0.5 * 1j * np.array([[0,-1.],[1.,0]])
36 mIz = 0.5 * np.array([[1.,0],[0,-1.]])
37 mIp = np.array([[0,1],[0,0]])
38 mIm = np.array([[0,0],[1,0]])
39 mIa = np.array([[1,0],[0,0]])
40 mIb = np.array([[0,0],[0,1]])
41
42 def base(i, mi, nspins):
43     m1start = np.eye(2**i)
44     m1end = np.eye(2**(nspins-i-1))
45     return np.kron(np.kron(m1start,mi),m1end)
46
47 def init(spins):
48     norder = 2**len(spins)
49
50     global Iu, Ix, Iy, Iz, Ip, Im, Ia, Ib
51     Iu = {}; Ix = {}; Iy = {}; Iz = {}; Ip = {}; Im = {}; Ia = {}; Ib = {};
52
53     for i, spin in enumerate(spins):
54         Iu[spin] = np.eye(norder)
55         Ix[spin] = base(i, mIx, len(spins))
56         Iy[spin] = base(i, mIy, len(spins))
57         Iz[spin] = base(i, mIz, len(spins))
58         Ip[spin] = base(i, mIp, len(spins))
59         Im[spin] = base(i, mIm, len(spins))
60         Ia[spin] = base(i, mIa, len(spins))
61         Ib[spin] = base(i, mIb, len(spins))
62 # -----
63
64
65
66 # -----
67 # Toggling frame functions
68 def measure(operators, ham, tem):
69     for op in ops:
70         tem[op].append(np.trace(M(operators[op], ham)) / np.trace(M(operators[op], operators
71         [op]))) # since ops are normed, normalization is irrelevant
72     return tem
73
74 def prop(operators, U):
75     for op in ops:
76         operators[op] = M(U, operators[op], ct(U))
77     return operators
78
79 def integrate(xarray, yarray):
80     summe = 0
81     for x0, x1 in zip(range(0,len(xarray)-1), range(1,len(xarray))):
82         dx = xarray[x1]-xarray[x0]
83         dy = yarray[x1]-yarray[x0]
84         summe += yarray[x0] * dx + 0.5 * dy * dx
85     return summe
86
87 def puls(operators, tem, func, hamiltonian, ppow, degree, pphase, pts=20):
88     step = degree/(360*ppow)/(pts-1)
89     propa = scla.expm(-1j * step * (func(pphase, ppow) ))
90
91     tem = measure(operators, hamiltonian, tem)
92     if tem['t'] != []: tem['t'].append(tem['t'][-1])
93     else: tem['t'] = [0.]

```

```

94     for i in range(pts-1):
95         operators = prop(operators, propa)
96         tem = measure(operators, hamiltonian, tem)
97         tem['t'].append(tem['t'][-1]+step)
98
99     return operators, tem
100
101 def delay(operators, tem, hamiltonian, length, pts=20):
102     step = length/(pts-1)
103     propa = scla.expm(-1j * step * Ham1)
104
105     tem = measure(operators, hamiltonian, tem)
106     if tem['t'] != []: tem['t'].append(tem['t'][-1])
107     else: tem['t'] = [0.]
108
109     for i in range(pts-1):
110         operators = prop(operators, propa)
111         tem = measure(operators, hamiltonian, tem)
112         tem['t'].append(tem['t'][-1]+step)
113
114     return operators, tem
115 # -----
116
117
118 # -----
119 # Prepare spin system
120 spins = ['H', 'C']
121 init(spins)
122
123 Ham = 1j*0
124
125 # Offsets
126 Ham = Offset(Ham, 'H', 1)
127 Ham = Offset(Ham, 'C', 1)
128
129 # Coupling
130 Ham = Jweak(Ham, 'H', 'C', 2) # twice as large, since pi*J*(2*IzIz) vs 2*pi*(Iz)
131     # resulting k_maximal is thus 1 and not 0.5
132
133 # Put offset to "St urterm"
134 Ham1 = 1j*0
135 Ham1 = Offset(Ham1, 'H', 0)
136
137 CHpuls = defpuls('H', 'C')
138 Hpuls = defpuls('H')
139 Cpuls = defpuls('C')
140 ppow90 = 2 * 10**3
141 ppow180 = 2 * 10**3
142
143 factor = 1 / (4*ppow90) * 2 / np.pi
144 # -----
145
146
147
148 # -----
149 # insilico-experiment parameters
150 ops = ["".join(item) for item in itertools.product("xyz", repeat=len(spins))]
151
152 def start(ops):
153     operators = {}
154     for op in ops:
155         if op[0] == '1': operators[op] = Iu[spins[0]]
156         elif op[0] == 'x': operators[op] = Ix[spins[0]]
157         elif op[0] == 'y': operators[op] = Iy[spins[0]]
158         elif op[0] == 'z': operators[op] = Iz[spins[0]]
159
160     for o in range(1, len(ops)):

```

```

161     if op[o] == '1': operators[op] = M(operators[op], Iu[spins[o]])
162     elif op[o] == 'x': operators[op] = M(operators[op], Ix[spins[o]])
163     elif op[o] == 'y': operators[op] = M(operators[op], Iy[spins[o]])
164     elif op[o] == 'z': operators[op] = M(operators[op], Iz[spins[o]])
165
166     norm = np.sqrt( np.trace(M( ct(operators[op]), operators[op])) )
167     operators[op] /= norm
168     #print(str(np.real(1/norm))+ ' ',op)
169
170     tem = {'t': []}
171     sumtem = {}
172
173     for op in ops: tem[op] = []
174     for op in ops: sumtem[op] = []
175
176     return operators, tem, sumtem
177 # -----
178
179
180
181 # -----
182 # Run insilico-experiments
183 t = 0.001
184 operators, tem, sumtem = start(ops)
185 operators, tem = delay(operators, tem, Ham, t+factor, pts=2)
186 operators, tem = puls(operators, tem, CHpuls, Ham, ppow180, 180, 0, pts=10)
187 operators, tem = delay(operators, tem, Ham, t, pts=2)
188 operators, tem = puls(operators, tem, CHpuls, Ham, ppow90, 90, 2, pts=10)
189 operators, tem = delay(operators, tem, Ham, t, pts=2)
190 operators, tem = puls(operators, tem, CHpuls, Ham, ppow180, 180, 0, pts=10)
191 operators, tem = delay(operators, tem, Ham, t, pts=2)
192 operators, tem = puls(operators, tem, CHpuls, Ham, ppow90, 90, 3, pts=10)
193 operators, tem = delay(operators, tem, Ham, t, pts=2)
194 operators, tem = puls(operators, tem, CHpuls, Ham, ppow180, 180, 1, pts=10)
195 operators, tem = delay(operators, tem, Ham, t+factor, pts=2)
196
197 operators, tem = delay(operators, tem, Ham, t+factor, pts=2)
198 operators, tem = puls(operators, tem, CHpuls, Ham, ppow180, 180, 3, pts=10)
199 operators, tem = delay(operators, tem, Ham, t, pts=2)
200 operators, tem = puls(operators, tem, CHpuls, Ham, ppow90, 90, 1, pts=10)
201 operators, tem = delay(operators, tem, Ham, t, pts=2)
202 operators, tem = puls(operators, tem, CHpuls, Ham, ppow180, 180, 0, pts=10)
203 operators, tem = delay(operators, tem, Ham, t, pts=2)
204 operators, tem = puls(operators, tem, CHpuls, Ham, ppow90, 90, 0, pts=10)
205 operators, tem = delay(operators, tem, Ham, t, pts=2)
206 operators, tem = puls(operators, tem, CHpuls, Ham, ppow180, 180, 2, pts=10)
207 operators, tem = delay(operators, tem, Ham, t+factor, pts=2)
208 # -----
209
210
211 # -----
212 # Plotting
213 for op in ops:
214     sumtem[op] = integrate(tem['t'], np.real(tem[op]))
215     fac = tem['t'][-1] * 2. * np.pi
216     print('    k average ( '+op+' ): ', int(sumtem[op]/fac *10000)/10000)
217 # -----
218
219
220
221 from mpl_toolkits.axes_grid.inset_locator import (inset_axes, InsetPosition, mark_inset)
222 import matplotlib as mpl
223 plt.rcParams.update({
224     "text.usetex": True,
225     "font.family": "serif",
226     "font.serif": ["Computer Modern Roman"]})
227

```

```

228 plt.rcParams['axes.linewidth'] = 2
229 plt.rcParams['font.size'] = 18
230 plt.rcParams['xtick.labelsize'] = 16
231 plt.rcParams['ytick.labelsize'] = 16
232
233 # -----
234 # Plotting
235 fig, ax = plt.subplots(9, 1, sharex=True, sharey=True, figsize=(8, 7*1.5))
236
237 ax[0].plot(np.array(tem['t']) / tem['t'][-1], np.array(tem['xx']) / (2*np.pi) , label=op
, color='#b6000f', lw=2.)
238 ax[1].plot(np.array(tem['t']) / tem['t'][-1], np.array(tem['yy']) / (2*np.pi) , label=op
, color='#b6000f', lw=2.)
239 ax[2].plot(np.array(tem['t']) / tem['t'][-1], np.array(tem['zz']) / (2*np.pi) , label=op
, color='#b6000f', lw=2.)
240 ax[3].plot(np.array(tem['t']) / tem['t'][-1], np.array(tem['xy']) / (2*np.pi) , label=op
, color='#b6000f', lw=2.)
241 ax[4].plot(np.array(tem['t']) / tem['t'][-1], np.array(tem['xz']) / (2*np.pi) , label=op
, color='#b6000f', lw=2.)
242 ax[5].plot(np.array(tem['t']) / tem['t'][-1], np.array(tem['yz']) / (2*np.pi) , label=op
, color='#b6000f', lw=2.)
243 ax[6].plot(np.array(tem['t']) / tem['t'][-1], np.array(tem['ix']) / (2*np.pi) , label=op
, color='#b6000f', lw=2.)
244 ax[7].plot(np.array(tem['t']) / tem['t'][-1], np.array(tem['iy']) / (2*np.pi) , label=op
, color='#b6000f', lw=2.)
245 ax[8].plot(np.array(tem['t']) / tem['t'][-1], np.array(tem['iz']) / (2*np.pi) , label=op
, color='#b6000f', lw=2.)
246
247 ax[0].set_xlim([0,1.01])
248 ax[0].set_ylim([-1.4,1.4])
249
250 ax[0].set_ylabel(r"$\hat{\mathcal{H}}^{\mathrm{x}}\mathrm{x}\mathrm{z}$", rotation
=0)
251 ax[1].set_ylabel(r"$\hat{\mathcal{H}}^{\mathrm{y}}\mathrm{y}\mathrm{z}$", rotation
=0)
252 ax[2].set_ylabel(r"$\hat{\mathcal{H}}^{\mathrm{z}}\mathrm{z}\mathrm{z}$", rotation
=0)
253 ax[3].set_ylabel(r"$\hat{\mathcal{H}}^{\mathrm{x}}\mathrm{y}\mathrm{z}$", rotation
=0)
254 ax[4].set_ylabel(r"$\hat{\mathcal{H}}^{\mathrm{x}}\mathrm{z}\mathrm{z}$", rotation
=0)
255 ax[5].set_ylabel(r"$\hat{\mathcal{H}}^{\mathrm{y}}\mathrm{z}\mathrm{z}$", rotation
=0)
256 ax[6].set_ylabel(r"$\hat{\mathcal{H}}^{\mathrm{x}}\mathrm{T,z}$", rotation=0)
257 ax[7].set_ylabel(r"$\hat{\mathcal{H}}^{\mathrm{y}}\mathrm{T,z}$", rotation=0)
258 ax[8].set_ylabel(r"$\hat{\mathcal{H}}^{\mathrm{z}}\mathrm{T,z}$", rotation=0)
259
260 for i in range(9): ax[i].yaxis.set_label_coords(-0.1,0.3)
261 for i in range(9): ax[i].plot([0,1.01], [1,1], "k--", lw = 0.5, zorder=0)
262 for i in range(9): ax[i].plot([0,1.01], [-1,-1], "k--", lw = 0.5, zorder=0)
263 for i in range(9): ax[i].xaxis.set_visible(False)
264 for i in range(9): ax[i].spines['top'].set_visible(False)
265 for i in range(9): ax[i].spines['bottom'].set_visible(False)
266 for i in range(9): ax[i].spines['right'].set_visible(False)
267 for i in range(9): ax[i].spines['left'].set_visible(False)
268 for i in range(9): ax[i].arrow(0, -1.4, 0, 2.8, color='k', lw=1, linestyle="-",
head_width=0.009, head_length=0.3, length_includes_head = True, jointstyle="round",
clip_on=False, zorder=10)
269 for i in range(9): ax[i].arrow(0, 0, 1.01, 0, color='k', lw=1, linestyle="-", head_width
=0.2, head_length=0.015, length_includes_head = True, jointstyle="round", clip_on=
False, zorder=10)
270
271 plt.text(0.45, 0.02, r"pulse sequence", fontsize=20, transform=plt.gcf().transFigure)
272
273 plt.tight_layout(pad=0.3, rect=(0,0.04,1,1))
274 plt.savefig("TF_IM_6echoes_9.png")
275 plt.show()

```

```
276 plt.close('all')
277 # -----
```

5.5.3 AHT: Case 1 and 2 for Shaped Pulses (Offset-Dependence, 1D)

```
1 import numpy as np
2 import itertools
3 import scipy.linalg as scla
4 import matplotlib.pyplot as plt
5
6 # -----
7 # Matrix product of multiple matrices
8 ct = lambda hermi: np.conj(np.transpose(hermi))
9
10 def Offset(H, spin, offset):
11     H += 2*np.pi * offset * Iz[ spin ]
12     return H
13
14 def Jweak(H, spin1, spin2, J):
15     H += 2*np.pi * J * (np.dot(Iz[ spin1 ], Iz[ spin2 ]))
16     return H
17
18 def defpuls(*args):
19     func = lambda pphase, pamp: 2*np.pi * (np.cos(2*np.pi * pphase/4.) * sum([Ix[ n ] for n
20         in args]) + np.sin(2*np.pi * pphase/4.) * sum([Iy[ n ] for n in args]) ) * pamp
21     return func
22
23 def load_shape(path_to_file, separator):
24     data = []; comments = []
25     tmp = open(path_to_file, 'r')
26     load_data = tmp.read()
27     load_data = load_data.split('\n')
28
29     for line in load_data:
30         if '##' in line or line == '': pass
31         else:
32             line = line.split(separator)
33             try: line = [float(slic) for slic in line]
34             except: line = [slic.replace(' ', '') for slic in line]
35             data.append(line)
36     return data
37
38 # -----
39
40 # -----
41 # Define base, which is given by the kronecker product of ExEx(I3x,y,z)xExE...
42 mIx = 0.5 * np.array([[0,1.],[1.,0]])
43 mIy = 0.5 * 1j * np.array([[0,-1.],[1.,0]])
44 mIz = 0.5 * np.array([[1.,0],[0,-1.]])
45 mIp = np.array([[0,1],[0,0]])
46 mIm = np.array([[0,0],[1,0]])
47 mIa = np.array([[1,0],[0,0]])
48 mIb = np.array([[0,0],[0,1]])
49
50 def base(i, mi, nspins):
51     m1start = np.eye(2**i)
52     m1end = np.eye(2**(nspins-i-1))
53     return np.kron(np.kron(m1start,mi),m1end)
54
55 def init(spins):
56     norder = 2**len(spins)
57
58     global Iu, Ix, Iy, Iz, Ip, Im, Ia, Ib
```

```

59 Iu = {}; Ix = {}; Iy = {}; Iz = {}; Ip = {}; Im = {}; Ia = {}; Ib = {};
60
61 for i, spin in enumerate(spins):
62     Iu[spin] = np.eye(norder)
63     Ix[spin] = base(i, mIx, len(spins))
64     Iy[spin] = base(i, mIy, len(spins))
65     Iz[spin] = base(i, mIz, len(spins))
66     Ip[spin] = base(i, mIp, len(spins))
67     Im[spin] = base(i, mIm, len(spins))
68     Ia[spin] = base(i, mIa, len(spins))
69     Ib[spin] = base(i, mIb, len(spins))
70 # -----
71
72
73
74 # -----
75 # Toggling frame functions
76 def measure(basis, ham, traj):
77     for op in ops: traj[op].append(np.trace(np.dot(ct(basis[op]), ham)) / np.trace(np.dot(
78         ct(basis[op]), basis[op])))
79     return traj
80 measureU = lambda operator, base: np.trace( np.dot( ct(operator), base ) ) / np.trace(
81     np.dot( ct(base), base ) )
82
83 def prop(basis, U):
84     for op in ops:
85         basis[op] = np.dot(U, np.dot(basis[op], ct(U)))
86     return basis
87 diffT = lambda a: np.matrix(a[1:]) - np.matrix(a[:-1]) # get time steps from strand
88             (-> length is reduced by 1)
89 interH = lambda a: np.array( np.matrix(a[1:]) + np.matrix(a[:-1]) ) / 2 # interpolate
90             time-dependent Hamiltonian (-> length is reduced by 1)
91
92 def integrate(xarray, yarray):
93     dT = diffT(xarray)
94     iH = interH(yarray)
95     return np.sum( np.multiply(iH, dT) )
96
97 def puls(basis, traj, func, hamiltonian, Z, pamp, degree, pphase, pts=100):
98     step = degree/(360*pamp)/(pts-1)
99     propa = scla.expm(-1j * step * (func(pphase, pamp) + Z))
100
101     traj = measure(basis, hamiltonian, traj)
102     if traj['t'] != []: traj['t'].append(traj['t'][-1])
103     else: traj['t'] = [0.]
104
105     for i in range(pts-1):
106         basis = prop(basis, propa)
107         traj = measure(basis, hamiltonian, traj)
108         traj['t'].append(traj['t'][-1]+step)
109
110     return basis, traj
111
112 def delay(basis, traj, hamiltonian, Z, length, pts=100):
113     step = length/(pts-1)
114     propa = scla.expm(-1j * step * Z)
115
116     traj = measure(basis, hamiltonian, traj)
117     if traj['t'] != []: traj['t'].append(traj['t'][-1])
118     else: traj['t'] = [0.]
119
120     for i in range(pts-1):
121         basis = prop(basis, propa)
122         traj = measure(basis, hamiltonian, traj)

```

```

122     traj['t'].append(traj['t'][-1]+step)
123
124     return basis, traj
125
126 def shaped_puls(basis, traj, func, hamiltonian, Z, shape, pamp, pulslen, pphase):
127     step = pulslen / len(shape)
128
129     traj = measure(basis, hamiltonian, traj)
130     if traj['t'] != []: traj['t'].append(traj['t'][-1])
131     else: traj['t'] = [0.]
132
133     for pul in shape:
134         propa = scla.expm(-1j * step * (func(pul[1]/90+pphase, pul[0]/100*pamp) + Z) )
135         basis = prop(basis, propa)
136         traj = measure(basis, hamiltonian, traj)
137         traj['t'].append(traj['t'][-1]+step)
138
139     return basis, traj
140 # -----
141
142
143
144 # -----
145 # Prepare spin system
146 spins = ['H', 'C']
147 init(spins)
148
149 Ham = 1j*0
150
151 # Coupling
152 J = 300
153 Ham = Jweak(Ham, 'H', 'C', J) # twice as large, since pi*J*(2*IzIz) vs 2*pi*(Iz)
154     # resulting k_maximal is thus 1 and not 0.5
155 omega = J*np.pi
156
157 Hpuls = defpuls( 'H' )
158 Cpuls = defpuls( 'C' )
159
160 Hxx = 2* np.dot( Ix['H'], Ix['C'] )
161 Hyx = 2* np.dot( Iy['H'], Ix['C'] )
162 Hzx = 2* np.dot( Iz['H'], Ix['C'] )
163
164 Hxy = 2* np.dot( Ix['H'], Iy['C'] )
165 Hyy = 2* np.dot( Iy['H'], Iy['C'] )
166 Hzy = 2* np.dot( Iz['H'], Iy['C'] )
167
168 Hxz = 2* np.dot( Ix['H'], Iz['C'] )
169 Hyz = 2* np.dot( Iy['H'], Iz['C'] )
170 Hzz = 2* np.dot( Iz['H'], Iz['C'] )
171 # -----
172
173
174
175
176 # -----
177 # insilico-experiment parameters
178 ops = ["".join(item) for item in itertools.product("XYZ", repeat=len(spins))]
179 basis = {}
180
181 def start(ops):
182     for op in ops:
183         if op[0] == '1': basis[op] = Iu[spins[0]]
184         elif op[0] == 'X': basis[op] = Ix[spins[0]]
185         elif op[0] == 'Y': basis[op] = Iy[spins[0]]
186         elif op[0] == 'Z': basis[op] = Iz[spins[0]]
187
188     for o in range(1, len(op)):

```

```

189     if op[o] == '1': basis[op] = np.dot(basis[op], Iu[spins[o]])
190     elif op[o] == 'X': basis[op] = 2*np.dot(basis[op], Ix[spins[o]])
191     elif op[o] == 'Y': basis[op] = 2*np.dot(basis[op], Iy[spins[o]])
192     elif op[o] == 'Z': basis[op] = 2*np.dot(basis[op], Iz[spins[o]])
193
194     traj = {'t': []}
195     sumtraj = {}
196
197     for op in ops: traj[op] = []
198
199     return basis, traj
200 # -----
201
202
203
204 # -----
205 # Run insilico-experiments
206
207 i2 = {"11": (0,0), "1X": (0,1), "1Y": (0,2), "1Z": (0,3),
208       "X1": (1,0), "XX": (1,1), "XY": (1,2), "XZ": (1,3),
209       "Y1": (2,0), "YX": (2,1), "YY": (2,2), "YZ": (2,3),
210       "Z1": (3,0), "ZX": (3,1), "ZY": (3,2), "ZZ": (3,3),}
211
212 def loga(A):
213     E = np.linalg.eig(A)[1]
214     invE = np.linalg.inv(E)
215     B = np.dot(invE, np.dot(A, E))
216     for i in range(len(B)): B[i,i] = np.log(B[i,i])
217     C = np.dot(E, np.dot(B, invE))
218     return C
219
220 def interpolate(shape, N):
221     xp = np.linspace(0,1,len(shape))
222     x = np.linspace(0,1,N)
223     a = np.transpose(shape)
224     b = np.interp(x, xp, a[0])
225     c = np.interp(x, xp, a[1])
226     shape = np.transpose(np.vstack([b,c]))
227     return shape
228
229
230 SP_name = 'Reburp.1000'
231
232 # -----
233 directory = ""
234
235 SP = {'puls': load_shape(directory+SP_name, ","),
236      'pulslen': 1000 * 10**(-6),
237      'pulsamp': (6264.9),
238      "offset": 7000,
239      'opt': [True, 2000],
240      }
241
242 offsets = np.linspace(-SP["offset"], SP["offset"], 51)
243 zero = int(len(offsets)/2)
244 # -----
245
246
247 avham = 1j*np.zeros( [4, 4, len(offsets)] )
248 logmU = 1j*np.zeros( [4, 4, len(offsets)] )
249
250 for o, off in enumerate(offsets):
251
252     Zpuls = 1j*0
253     Zpuls = Offset(Zpuls, 'H', 0)
254     Zpuls = Offset(Zpuls, 'C', off)
255

```

```

256 ECHO = True # calculate shaped pulse in heteronuclear echo
257
258 if not ECHO:
259     basis, traj = start(ops)
260     basis, traj = shaped_puls(basis, traj, Cpuls, Ham, Zpuls, SP['puls'], SP['pulsamp'],
261                               SP['pulslen'], 0)
262
263 else:
264     pause = int(len(SP['puls'])/2)
265     basis, traj = start(ops)
266     basis, traj = shaped_puls(basis, traj, Cpuls, Ham, Zpuls, SP['puls'][:pause], SP['
267                               pulsamp'], SP['pulslen']/2, 0)
268     basis, traj = puls(basis, traj, Hpuls, Ham, Zpuls, pamp, 180, 0)
269     basis, traj = shaped_puls(basis, traj, Cpuls, Ham, Zpuls, SP['puls'][pause:], SP['
270                               pulsamp'], SP['pulslen']/2, 0)
271
272 T = traj['t'][-1]
273
274 if o==zero: traj0 = traj
275
276 for op in ops: avham[i2[op]+(o,)] = integrate(traj['t'], traj[op] ) / T / omega
277 print(o)
278
279 U_MIX = Iu[spins[0]]
280 dT = diffT(traj['t'])
281
282 XX = interH(traj['XX'])[0] / omega
283 XY = interH(traj['XY'])[0] / omega
284 XZ = interH(traj['XZ'])[0] / omega
285
286 YX = interH(traj['YX'])[0] / omega
287 YY = interH(traj['YY'])[0] / omega
288 YZ = interH(traj['YZ'])[0] / omega
289
290 ZX = interH(traj['ZX'])[0] / omega
291 ZY = interH(traj['ZY'])[0] / omega
292 ZZ = interH(traj['ZZ'])[0] / omega
293
294 for i, t in enumerate(np.array(dT)[0]):
295
296     HamX = 1j*0
297
298     HamX += XX[i] * (np.pi*J) * Hxx
299     HamX += XY[i] * (np.pi*J) * Hxy
300     HamX += XZ[i] * (np.pi*J) * Hxz
301
302     HamX += YX[i] * (np.pi*J) * Hyx
303     HamX += YY[i] * (np.pi*J) * Hyy
304     HamX += YZ[i] * (np.pi*J) * Hyz
305
306     HamX += ZX[i] * (np.pi*J) * Hzx
307     HamX += ZY[i] * (np.pi*J) * Hzy
308     HamX += ZZ[i] * (np.pi*J) * Hzz
309
310 # create effective propagator
311 U_t = scla.expm(-1j * t * HamX)
312 U_MIX = np.dot(U_t, U_MIX)
313
314 # extract effective hamiltonian
315 logU = 1j*np.zeros([4,4])
316 #V_MIX = scla.logm(U_MIX) / (-1j) / omega / T
317 V_MIX = loga(U_MIX) / (-1j) / omega / T
318
319 logmU[i2["XX"]+(o,)] += measureU( V_MIX, Hxx )
320 logmU[i2["YX"]+(o,)] += measureU( V_MIX, Hyx )
321 logmU[i2["ZX"]+(o,)] += measureU( V_MIX, Hzx )

```

```

320
321     logmU[i2["XY"]+(o,)] += measureU( V_MIX, Hxy )
322     logmU[i2["YY"]+(o,)] += measureU( V_MIX, Hyy )
323     logmU[i2["ZY"]+(o,)] += measureU( V_MIX, Hzy )
324
325     logmU[i2["XZ"]+(o,)] += measureU( V_MIX, Hxz )
326     logmU[i2["YZ"]+(o,)] += measureU( V_MIX, Hyz )
327     logmU[i2["ZZ"]+(o,)] += measureU( V_MIX, Hzz )
328
329 # -----
330
331
332
333
334 plt.rcParams['axes.linewidth'] = 2
335 plt.rcParams['font.size'] = 28
336 plt.rcParams['xtick.labelsize'] = 20
337 plt.rcParams['ytick.labelsize'] = 20
338 plt.rcParams.update({
339     "text.usetex": True,
340     "font.family": "serif",
341     "font.serif": ["Computer Modern Roman"]})
342
343 offsets /= 1000
344 fig, ax = plt.subplots(3,3, sharex=True, sharey=True, figsize=(10,10))
345
346 ax[0,0].plot(offsets, avham[i2['XX']] , color='#b6000f', lw=3.)
347 ax[0,0].plot(offsets, logmU[i2['XX']] , linestyle=":", color='#00499e', lw=3.)
348 ax[0,0].hlines([0], offsets[0], offsets[-1], color='k', linestyle="--", lw=1.)
349 ax[0,0].text(-6, -1, "XX", color='#b6000f')
350
351 ax[0,1].plot(offsets, avham[i2['XY']] , color='#b6000f', lw=3.)
352 ax[0,1].plot(offsets, logmU[i2['XY']] , linestyle=":", color='#00499e', lw=3.)
353 ax[0,1].hlines([0], offsets[0], offsets[-1], color='k', linestyle="--", lw=1.)
354 ax[0,1].text(-6, -1, "XY", color='#b6000f')
355
356 ax[0,2].plot(offsets, avham[i2['XZ']] , color='#b6000f', lw=3.)
357 ax[0,2].plot(offsets, logmU[i2['XZ']] , linestyle=":", color='#00499e', lw=3.)
358 ax[0,2].hlines([0], offsets[0], offsets[-1], color='k', linestyle="--", lw=1.)
359 ax[0,2].text(-6, -1, "XZ", color='#b6000f')
360
361 ax[1,0].plot(offsets, avham[i2['YX']] , color='#b6000f', lw=3.)
362 ax[1,0].plot(offsets, logmU[i2['YX']] , linestyle=":", color='#00499e', lw=3.)
363 ax[1,0].hlines([0], offsets[0], offsets[-1], color='k', linestyle="--", lw=1.)
364 ax[1,0].text(-6, -1, "YX", color='#b6000f')
365
366 ax[1,1].plot(offsets, avham[i2['YY']] , color='#b6000f', lw=3.)
367 ax[1,1].plot(offsets, logmU[i2['YY']] , linestyle=":", color='#00499e', lw=3.)
368 ax[1,1].hlines([0], offsets[0], offsets[-1], color='k', linestyle="--", lw=1.)
369 ax[1,1].text(-6, -1, "YY", color='#b6000f')
370
371 ax[1,2].plot(offsets, avham[i2['YZ']] , color='#b6000f', lw=3.)
372 ax[1,2].plot(offsets, logmU[i2['YZ']] , linestyle=":", color='#00499e', lw=3.)
373 ax[1,2].hlines([0], offsets[0], offsets[-1], color='k', linestyle="--", lw=1.)
374 ax[1,2].text(-6, -1, "YZ", color='#b6000f')
375
376 ax[2,0].plot(offsets, avham[i2['ZX']] , color='#b6000f', lw=3.)
377 ax[2,0].plot(offsets, logmU[i2['ZX']] , linestyle=":", color='#00499e', lw=3.)
378 ax[2,0].hlines([0], offsets[0], offsets[-1], color='k', linestyle="--", lw=1.)
379 ax[2,0].text(-6, -1, "ZX", color='#b6000f')
380
381 ax[2,1].plot(offsets, avham[i2['ZY']] , color='#b6000f', lw=3.)
382 ax[2,1].plot(offsets, logmU[i2['ZY']] , linestyle=":", color='#00499e', lw=3.)
383 ax[2,1].hlines([0], offsets[0], offsets[-1], color='k', linestyle="--", lw=1.)
384 ax[2,1].text(-6, -1, "ZY", color='#b6000f')
385
386 ax[2,2].plot(offsets, avham[i2['ZZ']] , color='#b6000f', lw=3.)

```

```

387 ax[2,2].plot(offsets, logmU[i2['ZZ']], linestyle=":", color='#00499e', lw=3.)
388 ax[2,2].hlines([0], offsets[0], offsets[-1], color='k', linestyle="--", lw=1.)
389 ax[2,2].text(-6, -1, "ZZ", color='#b6000f')
390
391 for i in range(3):
392     ax[0,i].set_xlim([offsets[0],offsets[-1]])
393     ax[0,i].set_ylim([-1.1,1.1])
394     ax[0,i].set_yticks([-1,0,1])
395
396 ax[2,0].set_xlabel(r"offset $\nu_S$ / kHz", size=22)
397 ax[2,1].set_xlabel(r"offset $\nu_S$ / kHz", size=22)
398 ax[2,2].set_xlabel(r"offset $\nu_S$ / kHz", size=22)
399
400 plt.tight_layout(pad=0.8)
401 plt.savefig("TF_"+SP_name+"_offset.png")
402 plt.close('all')

```

5.5.4 AHT: Case 4 for Shaped Pulses (Fast, Offset-Dependence, 2D)

```

1 import numpy as np
2 import scipy.linalg as scla
3 import matplotlib.pyplot as plt
4 import matplotlib.patches as patches
5 from matplotlib import cm
6 import itertools
7 import time
8 from mpl_toolkits.axisartist.axislines import SubplotZero
9
10 print(time.ctime())
11
12
13 # -----
14 # define base
15 mIx = 0.5 * np.array([[0,1],[1,0]])
16 mIy = 0.5 * 1j * np.array([[0,-1],[1,0]])
17 mIz = 0.5 * np.array([[1,0],[0,-1]])
18 mIp = np.array([[0,1],[0,0]])
19 mIm = np.array([[0,0],[1,0]])
20 mIa = np.array([[1,0],[0,0]])
21 mIb = np.array([[0,0],[0,1]])
22
23 def base(i, mi, nspins):
24     m1start = np.eye(2**i)
25     m1end = np.eye(2**(nspins-i-1))
26     return np.kron(np.kron(m1start,mi),m1end)
27
28 def init(spins):
29     norder = 2**len(spins)
30
31     global Iu, Ix, Iy, Iz, Ip, Im, Ia, Ib
32     Iu = {}; Ix = {}; Iy = {}; Iz = {}; Ip = {}; Im = {}; Ia = {}; Ib = {};
33
34     for i, spin in enumerate(spins):
35         Iu[spin] = np.eye(norder)
36         Ix[spin] = base(i, mIx, len(spins))
37         Iy[spin] = base(i, mIy, len(spins))
38         Iz[spin] = base(i, mIz, len(spins))
39         Ip[spin] = base(i, mIp, len(spins))
40         Im[spin] = base(i, mIm, len(spins))
41         Ia[spin] = base(i, mIa, len(spins))
42         Ib[spin] = base(i, mIb, len(spins))
43 # -----
44
45

```

```

46
47 # -----
48 # standard functions
49 ct = lambda hermi: np.conj(np.transpose(hermi))
50 proj = lambda base, Op: np.trace(np.dot( ct(base), Op )) / np.trace(np.dot( ct(base),
    base ))
51
52 def Offset(H, spin, offset):
53     H += 2*np.pi * offset * Iz[ spin ]
54     return H
55
56 def defpuls(*args):
57     func = lambda pphase, pamp: 2*np.pi* (np.cos(2*np.pi* pphase/4.) * sum([Ix[ n ] for n
    in args]) + np.sin(2*np.pi* pphase/4.) * sum([Iy[ n ] for n in args]) ) * pamp
58     return func
59
60 def prop0(operators, U):
61     for op in operators.keys(): operators[op] = np.dot( np.dot(ct(U), operators[op]), U )
62     return operators
63
64 def propB(basis, U):
65     for b in basis.keys(): basis[b] = np.dot( np.dot(U, basis[b]), ct(U) )
66     return basis
67
68 def measure(operators, basis, traj):
69     for op in operators.keys():
70         x = proj( basis[0], operators[op] )
71         y = proj( basis[1], operators[op] )
72         z = proj( basis[2], operators[op] )
73         traj[op].append( [x, y, z] )
74     return traj
75 # -----
76
77
78 # -----
79 # functions for Average Hamiltonian Theory
80 diffT = lambda a: np.matrix(a[1:]) - np.matrix(a[:-1]) # get time steps from strand
    (-> length is reduced by 1)
81 interH = lambda a: np.array( np.matrix(a[1:]) + np.matrix(a[:-1]) ) / 2 # interpolate
    time-dependent Hamiltonian (-> length is reduced by 1)
82
83 def integrate(dT, iH):
84     return np.sum( np.multiply(iH, dT) )
85
86 def integrate2(dT, iHs):
87     summe = 0
88     for iH1, iH2 in iHs:
89         # We want to end up in something like [Hx, Hy]*tx*ty (with x < y).
90         # This corresponds to (H1[x] * H2[y] * dT[x] * dT[y]) in the code (commutator is
    taken care of when "integrate2" is called).
91         # Expansion of two vectors to matrix calculates all correlation terms, including the
    ones for anti-symmetric term.
92         # [IySy, IzSy] = iIx and [IzSy, IySy] = -iIx
93         # The diagonal is not needed in the second order Hamiltonian (since x=y). It is
    removed in the second line.
94         M12 = np.transpose( np.multiply( iH1, dT ) ) * np.multiply( iH2, dT )
95         summe += np.sum( np.tril(M12) ) - np.sum( np.triu(M12) )
96     return summe
97 # -----
98
99
100
101 # -----
102 # define functions for toggling frame
103 def puls(basis, traj, operators, func, pamp, degree, pphase=0, z=0, steps=20):
104
105     pulslen = 1 / pamp * degree / 360

```

```

106 steplength = pulslen / steps
107
108 Ham_zee = 2*np.pi * z * Iz['1']
109 propa = scla.expm(-1j * steplength * (func(pphase, pamp) + Ham_zee) )
110
111 traj = measure(operators, basis, traj)
112 if traj['t'] != []: traj['t'].append(traj['t'][-1])
113 else: traj['t'] = [0.]
114
115 for i in range(steps):
116     basis = propB(basis, propa) # propagate basis
117     traj = measure(operators, basis, traj)
118     traj['t'].append(traj['t'][-1]+steplength)
119
120 return basis, traj
121
122 def delay(basis, traj, operators, length, z=0, steps=1000):
123
124     steplength = length/steps
125
126     Ham_zee = 2*np.pi * z * Iz['1']
127     propa = scla.expm(-1j * steplength * Ham_zee)
128
129     traj = measure(operators, basis, traj)
130     if traj['t'] != []: traj['t'].append(traj['t'][-1])
131     else: traj['t'] = [0.]
132
133     for i in range(steps):
134         basis = propB(basis, propa) # propagate basis
135         traj = measure(operators, basis, traj)
136         traj['t'].append(traj['t'][-1]+steplength)
137
138     return basis, traj
139
140 def load_shape(path_to_file, separator):
141     data = []; comments = []
142     tmp = open(path_to_file, 'r')
143     load_data = tmp.read()
144     load_data = load_data.split('\n')
145
146     for line in load_data:
147         if '##' in line or line == '': pass
148         else:
149             line = line.split(separator)
150             try: line = [float(slic) for slic in line]
151             except: line = [slic.replace(' ', '') for slic in line]
152             data.append(line)
153     return data
154
155 def shaped_puls(basis, traj, operators, func, SP, pphase=0, z=0):
156
157     shape = SP['puls']
158     pulslen = SP['pulslen']
159     pamp = SP['pulsamp']
160
161     steplength = pulslen / len(shape)
162
163     Ham_zee = 2*np.pi * z * Iz['1']
164
165     traj = measure(operators, basis, traj)
166     if traj['t'] != []: traj['t'].append(traj['t'][-1])
167     else: traj['t'] = [0.]
168
169     for pul in shape:
170         propa = scla.expm(-1j * steplength * (func(pul[1]/90+pphase, pul[0]/100*pamp) +
171         Ham_zee) )
172         basis = propB(basis, propa) # propagate basis

```

```

172     traj = measure(operators, basis, traj)
173     traj['t'].append(traj['t'][-1]+steplength)
174
175     return basis, traj
176 # -----
177
178
179
180 # -----
181 # Prepare spinsystem
182 spins = ['1']
183 init(spins)
184
185 Hpuls = defpuls( '1' )
186
187 i1 = {"x": (0,), "y": (1,), "z": (2,), "X": (0,), "Y": (1,), "Z": (2,)}
188
189 i2 = {"11": (0,0), "1X": (0,1), "1Y": (0,2), "1Z": (0,3),
190       "X1": (1,0), "XX": (1,1), "XY": (1,2), "XZ": (1,3),
191       "Y1": (2,0), "YX": (2,1), "YY": (2,2), "YZ": (2,3),
192       "Z1": (3,0), "ZX": (3,1), "ZY": (3,2), "ZZ": (3,3),}
193 # -----
194
195
196
197
198 # -----
199 # load pulses
200 directory = ""
201 SP_name = 'Reburp.1000'
202
203 # -----
204 #
205 if SP_name == 'Reburp.1000':
206     SP = {'puls': load_shape(directory+SP_name, ","),
207          'pulslen': 1000 * 10**(-6),
208          'pulsamp': (6264.9),
209          'offset': 7000,
210          'opt': [True, 2000],
211          }
212 # -----
213
214
215 offsets = np.linspace(-SP["offset"], SP["offset"], 11)
216 # -----
217
218
219
220 # -----
221 # insilico-experiment
222 temp = {}
223
224 for o1, offset in enumerate(offsets):
225
226     print(time.ctime(), o1)
227
228     basis = {0: Ix['1'], 1: Iy['1'], 2: Iz['1']}
229     operators = {'x': Ix['1'], 'y': Iy['1'], 'z': Iz['1']}
230     traj = {'x': [], 'y': [], 'z': [], 't': []}
231
232     basis, traj = shaped_puls(basis, traj, operators, Hpuls, SP, z=offset)
233
234 # -----
235 # extracting
236 for n, op in enumerate(operators.keys()): temp[(o1,)+(n,)] = traj[op]
237 # -----
238 # -----

```

```

239
240
241 # -----
242 # 1D to 2D
243 results = 1j*np.zeros([len(offsets), 3, 3, len(traj[op])-1])
244 avham = 1j*np.zeros( [4, 4, len(offsets), len(offsets)] )
245
246 T = traj['t'][-1]
247 dT = diffT(traj['t'])
248
249 for o, offset in enumerate(offsets):
250     for n, op in enumerate(operators.keys()):
251         results[o, i1['X'], i1[op], :] = interH( np.transpose(temp[(o,)+i1[op]])[0] )
252         results[o, i1['Y'], i1[op], :] = interH( np.transpose(temp[(o,)+i1[op]])[1] )
253         results[o, i1['Z'], i1[op], :] = interH( np.transpose(temp[(o,)+i1[op]])[2] )
254
255
256 for o1, offset in enumerate(offsets):
257     print("calculate: ", time.ctime(), o1)
258     for o2, offset2 in enumerate(offsets):
259
260         X1x = results[o1, i1['X'], i1['x']] [0]
261         Y1x = results[o1, i1['Y'], i1['x']] [0]
262         Z1x = results[o1, i1['Z'], i1['x']] [0]
263
264         X1y = results[o1, i1['X'], i1['y']] [0]
265         Y1y = results[o1, i1['Y'], i1['y']] [0]
266         Z1y = results[o1, i1['Z'], i1['y']] [0]
267
268         X1z = results[o1, i1['X'], i1['z']] [0]
269         Y1z = results[o1, i1['Y'], i1['z']] [0]
270         Z1z = results[o1, i1['Z'], i1['z']] [0]
271
272         X2x = results[o2, i1['X'], i1['x']] [0]
273         Y2x = results[o2, i1['Y'], i1['x']] [0]
274         Z2x = results[o2, i1['Z'], i1['x']] [0]
275
276         X2y = results[o2, i1['X'], i1['y']] [0]
277         Y2y = results[o2, i1['Y'], i1['y']] [0]
278         Z2y = results[o2, i1['Z'], i1['y']] [0]
279
280         X2z = results[o2, i1['X'], i1['z']] [0]
281         Y2z = results[o2, i1['Y'], i1['z']] [0]
282         Z2z = results[o2, i1['Z'], i1['z']] [0]
283
284
285 # -----
286 # Create time-dependent Hamiltonian in interaction frame (upper case X,Y,Z)
287 # based on a strong coupling (time-independent) Hamiltonian in rotating frame (lower
288 # case x,y,z).
289
290 ## weak coupling terms
291 #XX = X1z*X2z
292 #XY = X1z*Y2z
293 #XZ = X1z*Z2z
294
295 #YX = Y1z*X2z
296 #YY = Y1z*Y2z
297 #YZ = Y1z*Z2z
298
299 #ZX = Z1z*X2z
300 #ZY = Z1z*Y2z
301 #ZZ = Z1z*Z2z
302
303 # strong coupling terms
304 XX = X1x*X2x + X1y*X2y + X1z*X2z
305 XY = X1x*Y2x + X1y*Y2y + X1z*Y2z

```

```

305 XZ = X1x*Z2x + X1y*Z2y + X1z*Z2z
306
307 YX = Y1x*X2x + Y1y*X2y + Y1z*X2z
308 YY = Y1x*Y2x + Y1y*Y2y + Y1z*Y2z
309 YZ = Y1x*Z2x + Y1y*Z2y + Y1z*Z2z
310
311 ZX = Z1x*X2x + Z1y*X2y + Z1z*X2z
312 ZY = Z1x*Y2x + Z1y*Y2y + Z1z*Y2z
313 ZZ = Z1x*Z2x + Z1y*Z2y + Z1z*Z2z
314 # -----
315
316
317
318 # -----
319 # First order average Hamiltonian
320 avham[i2['XX']+(o1,o2)] = integrate(dT, XX ) / T
321 avham[i2['XY']+(o1,o2)] = integrate(dT, XY ) / T
322 avham[i2['XZ']+(o1,o2)] = integrate(dT, XZ ) / T
323
324 avham[i2['YX']+(o1,o2)] = integrate(dT, YX ) / T
325 avham[i2['YY']+(o1,o2)] = integrate(dT, YY ) / T
326 avham[i2['YZ']+(o1,o2)] = integrate(dT, YZ ) / T
327
328 avham[i2['ZX']+(o1,o2)] = integrate(dT, ZX ) / T
329 avham[i2['ZY']+(o1,o2)] = integrate(dT, ZY ) / T
330 avham[i2['ZZ']+(o1,o2)] = integrate(dT, ZZ ) / T
331 # -----
332
333
334
335 ## -----
336 ## Second order average Hamiltonian.
337 ## Normally, division by (1j * 2 * T) would be correct, but by removing 1j in
338 ## commutators the calculation stays real.
339 ## Commutator rules are needed (first line): [IySy,IzSy] = [IySz,IzSz] = [IySx,IzSx]
340 = iIx !
341 ## It should be noted that: [IzSy,IySy] = [IzSz,IySz] = [IzSx,IySx] = -iIx
342 ## This anti-symmetry of commutator is accounted for in function integrate2.
343 #avham[i2['X1']+(o1,o2)] = integrate2(dT, [ [YY, ZY], [YZ, ZZ], [YX, ZX] ] )/(2*T)
344 #avham[i2['Y1']+(o1,o2)] = integrate2(dT, [ [ZX, XX], [ZZ, XZ], [ZY, XY] ] )/(2*T)
345 #avham[i2['Z1']+(o1,o2)] = integrate2(dT, [ [XX, YX], [XY, YY], [XZ, YZ] ] )/(2*T)
346
347 #avham[i2['1X']+(o1,o2)] = integrate2(dT, [ [YY, YZ], [ZY, ZZ], [XY, XZ] ] )/(2*T)
348 #avham[i2['1Y']+(o1,o2)] = integrate2(dT, [ [XZ, XX], [ZZ, ZX], [YZ, YX] ] )/(2*T)
349 #avham[i2['1Z']+(o1,o2)] = integrate2(dT, [ [XX, XY], [YX, YY], [ZX, ZY] ] )/(2*T)
350 # -----
351
352
353
354 plt.rcParams['axes.linewidth'] = 2
355 plt.rcParams['font.size'] = 28
356 plt.rcParams['xtick.labelsize'] = 17
357 plt.rcParams['ytick.labelsize'] = 17
358 plt.rcParams.update({
359 "text.usetex": True,
360 "font.family": "serif",
361 "font.serif": ["Computer Modern Roman"]})
362
363
364 from mpl_toolkits.axes_grid1 import ImageGrid
365
366 fig = plt.figure(figsize=(12, 10))
367 ax = ImageGrid(fig, 111, # as in plt.subplot(111)
368 nrows_ncols=(3,3),
369 axes_pad=0.23,

```

```

370     share_all=True,
371     #aspect=False,
372     cbar_location="right",
373     cbar_mode="edge",
374     cbar_size="7%",
375     cbar_pad=0.2,
376     )
377
378 offs = offsets/1000
379 ax[0].contourf(offs, offs, avham[i2['XX']], levels=np.linspace(-1, 1, 12), cmap=cm.RdBu)
380 ax[0].tick_params("both", labelsize = 17, width=2)
381
382 ax[1].contourf(offs, offs, avham[i2['XY']], levels=np.linspace(-1, 1, 12), cmap=cm.RdBu)
383 ax[1].tick_params("both", labelsize = 17, width=2)
384
385 cb1 = ax[2].contourf(offs, offs, avham[i2['XZ']], levels=np.linspace(-1, 1, 12), cmap=cm.
    RdBu)
386 ax[2].tick_params("both", labelsize = 17, width=2)
387
388 ax[3].contourf(offs, offs, avham[i2['YX']], levels=np.linspace(-1, 1, 12), cmap=cm.RdBu)
389 ax[3].tick_params("both", labelsize = 17, width=2)
390
391 ax[4].contourf(offs, offs, avham[i2['YY']], levels=np.linspace(-1, 1, 12), cmap=cm.RdBu)
392 ax[4].tick_params("both", labelsize = 17, width=2)
393
394 cb2 = ax[5].contourf(offs, offs, avham[i2['YZ']], levels=np.linspace(-1, 1, 12), cmap=cm.
    RdBu)
395 ax[5].tick_params("both", labelsize = 17, width=2)
396
397 ax[6].contourf(offs, offs, avham[i2['ZX']], levels=np.linspace(-1, 1, 12), cmap=cm.RdBu)
398 ax[6].tick_params("both", labelsize = 17, width=2)
399
400 ax[7].contourf(offs, offs, avham[i2['ZY']], levels=np.linspace(-1, 1, 12), cmap=cm.RdBu)
401 ax[7].tick_params("both", labelsize = 17, width=2)
402
403 cb3 = ax[8].contourf(offs, offs, avham[i2['ZZ']], levels=np.linspace(-1, 1, 12), cmap=cm.
    RdBu)
404 ax[8].tick_params("both", labelsize = 17, width=2)
405
406 for i in range(9):
407     ax[i].set_xlim([-SP["offset"]/1000, SP["offset"]/1000])
408     ax[i].set_ylim([-SP["offset"]/1000, SP["offset"]/1000])
409
410 if SP['opt'][0]:
411     for i in range(9):
412         ax[i].vlines([-SP['opt'][1]/1000, SP['opt'][1]/1000], -SP['opt'][1]/1000, SP['opt']
            ] [1]/1000, color='k', linestyle="--", lw=2.)
413         ax[i].hlines([-SP['opt'][1]/1000, SP['opt'][1]/1000], -SP['opt'][1]/1000, SP['opt']
            ] [1]/1000, color='k', linestyle="--", lw=2.)
414
415 labels = [r"$2I_{\mathrm{1x}}I_{\mathrm{2x}}$", r"$2I_{\mathrm{1x}}I_{\mathrm{2y}}$", r"$2I_{\mathrm{1x}}I_{\mathrm{2z}}$",
416     r"$2I_{\mathrm{1y}}I_{\mathrm{2x}}$", r"$2I_{\mathrm{1y}}I_{\mathrm{2y}}$", r"$2I_{\mathrm{1y}}I_{\mathrm{2z}}$",
417     r"$2I_{\mathrm{1z}}I_{\mathrm{2x}}$", r"$2I_{\mathrm{1z}}I_{\mathrm{2y}}$", r"$2I_{\mathrm{1z}}I_{\mathrm{2z}}$"]
418 x = -SP['offset']/1000 * 0.88
419 y = SP['offset']/1000 * 0.7
420 w = SP['offset']/1000 * 0.61
421 h = SP['offset']/1000 * 0.25
422 x_off = 0.265*SP['offset']/1000
423 y_off = 0.09*SP['offset']/1000
424 for i in range(9):
425     rect = patches.Rectangle((x-w/2+x_off, y-h/2+y_off), w, h, linewidth=1, edgecolor='k',
        facecolor='w', zorder=8)
426     ax[i].add_patch(rect)
427     ax[i].text(x, y, labels[i], size=20, ha="left", va="baseline", zorder=9)

```

```
428
429 ax[6].set_xlabel(r"frequency $\nu_2$ / kHz", size=19)
430 ax[7].set_xlabel(r"frequency $\nu_2$ / kHz", size=19)
431 ax[8].set_xlabel(r"frequency $\nu_2$ / kHz", size=19)
432
433 ax[0].set_ylabel(r"frequency $\nu_1$ / kHz", size=19)
434 ax[3].set_ylabel(r"frequency $\nu_1$ / kHz", size=19)
435 ax[6].set_ylabel(r"frequency $\nu_1$ / kHz", size=19)
436
437
438 cbar1 = ax[2].cax.colorbar(cb1)
439 cbar1.ax.tick_params(labelsize=17)
440 cbar1.ax.set_ylim([-1,1])
441 cbar1.ax.set_yticks([-1,-0.5,0.,0.5,1])
442
443
444 cbar2 = ax[5].cax.colorbar(cb2)
445 cbar2.ax.tick_params(labelsize=17)
446 cbar2.ax.set_ylim([-1,1])
447 cbar2.ax.set_yticks([-1,-0.5,0.,0.5,1])
448
449
450 cbar3 = ax[8].cax.colorbar(cb3)
451 cbar3.ax.tick_params(labelsize=17)
452 cbar3.ax.set_ylim([-1,1])
453 cbar3.ax.set_yticks([-1,-0.5,0.,0.5,1])
454
455
456 plt.tight_layout(pad=0.6)
457 for i in range(9): ax[i].set_yticks(ax[i].get_xticks())
458 for i in range(9): ax[i].set_ylim(ax[i].get_xlim())
459 for i in range(9): ax[i].set_xticks(ax[i].get_yticks())
460 for i in range(9): ax[i].set_xlim(ax[i].get_ylim())
461 plt.savefig("TF_"+SP_name+"_offset_2D_narrow.png")
462 plt.close('all')
```


List of Publications

1. “Amplitudes and time scales of picosecond-to-microsecond motion in proteins studied by solid-state NMR: a critical evaluation of experimental approaches and application to crystalline ubiquitin.”
J. D. Haller, P. Schanda. *Journal of Biomolecular NMR* **2013**, *57*, 263.
2. “Probing transient conformational states of proteins by solid-state R(1 ρ) relaxation-dispersion NMR spectroscopy.”
P. Ma, J. D. Haller, J. Zajakala, P. Macek, A. C. Sivertsen, D. Willbold, J. Boisbouvier, P. Schanda. *Angewandte Chemie* **2014**, *53*, 4312.
3. “Observing the overall rocking motion of a protein in a crystal.”
P. Ma, Y. Xue, N. Coquelle, J. D. Haller, T. Yuwen, I. Ayala, O. Mikhailovskii, D. Willbold, J.-P. Colletier, N. R. Skrynnikov, P. Schanda. *Nature Communications* **2015**, *6*, 8361.
4. “Boosting the NMR Assignment of Carbohydrates with Clean In-Phase Correlation Experiments.”
T. Gyöngyösi, I. Timári, J. Haller, M. R.M. Koos, B. Luy, K. E. Kövér. *ChemPlusChem* **2018**, *83*, 53.
5. “Real-time pure shift measurements for uniformly isotope-labeled molecules using X-selective BIRD homonuclear decoupling.”
J. D. Haller, A. Bodor, B. Luy. *Journal of Magnetic Resonance* **2019**, *302*, 64.
- 5'. The publication was awarded with the *Ernst Prize* 2020 by the German Chemical Society.
6. “Power of Pure Shift H α C α Correlations: A Way to Characterize Biomolecules under Physiological Conditions.”
A. Bodor, J. D. Haller, C. Bouguechtouli, F. X. Theillet, L. Nyitray, B. Luy. *Analytical Chemistry* **2020**, *92*, 12423.

List of Tables

1.1	Commutators for a Two-Spin System.	18
2.1	Eigenfunctions and Eigenvalues of Strongly Coupled Two-Spin System.	142
2.2	Transition Frequencies and Intensities in Spectrum of Strongly Coupled Two-Spin System.	142
3.1	Comparing Resolution for ^1H , ^{15}N -HSQC, CON and SHACA-HSQC.	194

List of Figures

1.1	Zeeman Splitting for Nuclear Spin $I = \frac{1}{2}$ with Positive Gyromagnetic Ratio.	2
1.2	Bloch Sphere for Nuclear Spins with Positive Gyromagnetic Ratio.	5
1.3	General Rotation in the Product Operator Formalism.	17
1.4	Detection in the <i>Pulse Frame</i> or the <i>On-Resonant Frame</i>	24
1.5	Effect of a Weak Off-Resonant Pulse ($\Delta = 1$ Hz)	25
1.6	Effect of a Weak Off-Resonant Pulse ($\Delta = 2$ Hz)	26
1.7	Pulse Sequence for the So-Called Perfect Echo.	32
1.8	Non-Zero Operators in the Toggling Frame of the Perfect Echo – Part 1.	35
1.9	Non-Zero Operators in the Toggling Frame of the Perfect Echo – Part 2.	36
1.10	The Time-Dependence of the Second Order Dyson Series.	40
1.11	The Time-Dependence of the First Order Average Hamiltonian $\bar{\mathcal{H}}_1$	43
1.12	Trajectory for an Off-Resonant Pulse Using the Suzuki-Trotter Approximation.	46
1.13	The Dependency of the Suzuki-Trotter Approximants on n and θ	46
1.14	Auto-Correlation Function $G(\tau)$ and Spectral Density $J(\omega)$	51
1.15	T_1 and T_2 Relaxation Rates and NOE Enhancement ϵ	53
1.16	Non-Decoupled ^{15}N -HSQC Exhibiting Cross Correlated Relaxation.	54
2.1	Comparison of Planar and Isotropic Mixing in 5-Spin Chain.	60
2.2	Pulse Sequence of the Relayed CLIP-COSY.	60
2.3	Comparison of Relayed Transfer in TOCSY and CLIP-COSY.	61
2.4	Relayed CLIP-COSY Spectra for α -Glucose.	62
2.5	Pulse Sequence for $^{13}\text{C},^{13}\text{C}$ -PM-TOCSY.	64
2.6	Numerical Simulations for FLOPSY and PM-TOCSY.	65
2.7	FLOPSY and PM-TOCSY of Amino Acid Mixture Recorded at a 1.0 GHz Spectrometer.	67
2.8	PM-TOCSY of TauF4 and Human Ubiquitin Recorded at a 1.0 GHz Spectrometer.	68
2.9	Pulse Sequence for PM-based 3D (H)CC(CO)NH Experiment.	70
2.10	$^1\text{H},^{13}\text{C}$ -Plane of the 3D (H)CC(CO)NH Experiment for Ubiquitin.	72
2.11	Ernst Angle Excitation in DOSY.	76
2.12	Time-Dependent Hamiltonian in the Toggling Frame of IPE-1.	79
2.13	Time-Dependent Hamiltonian in the Toggling Frame of IPE-2.	80
2.14	DIPSI and IPE-1 in Conventional TOCSY.	81
2.15	Spin State Preservation from IPE-1 with 2 Basic Cycles (Numerical Simulations).	82
2.16	Spin State Preservation from IPE-2 with 2 Basic Cycles (Numerical Simulations).	82
2.17	Spin State Preservation from IPE-1: Experimental Verification for Strychnine.	83
2.18	Spin State Preservation from IPE-1 and IPE-2: Dependence on Mixing Time.	84
2.19	Basic Conception of DOSY.	86
2.20	DOSY Pulse Sequences Using IPEs.	87
2.21	Comparison of 1D-IPE-DOSY to Conventional STE-DOSY with and without Convection Compensation.	88
2.22	Comparison of fast 2D IPE-DOSY to Conventional STE-DOSY with Convection Compensation.	89
2.23	Classification of 180° Pulses by Normalized Effective Rotation Axis.	93

2.24	Classification of 90° Pulses by Normalized Effective Rotation Axis.	94
2.25	Three Cases Used for the Investigation of Coupling Evolution during Shaped Pulses.	99
2.26	Q3 – Selective 180° Pulse.	100
2.27	Q3 – Average Hamiltonian $\bar{\mathcal{H}}_{0,J}(\nu_S)$ for Heteronuclear Spins (Case 1).	100
2.28	Q3 – Average Hamiltonian $\bar{\mathcal{H}}_{0,J}(\nu_S)$ for Heteronuclear Echo (Case 2).	101
2.29	Q3 – Average Hamiltonian $\bar{\mathcal{H}}_{0,J}(\nu_1, \nu_2)$ for Homonuclear Spins (Case 4).	101
2.30	RE-BURP – Selective 180° Pulse.	102
2.31	RE-BURP – Average Hamiltonian $\bar{\mathcal{H}}_{0,J}(\nu_S)$ for Heteronuclear Spins (Case 1).	102
2.32	RE-BURP – Average Hamiltonian $\bar{\mathcal{H}}_{0,J}(\nu_S)$ for Heteronuclear Echo (Case 2).	103
2.33	RE-BURP – Average Hamiltonian $\bar{\mathcal{H}}_{0,J}(\nu_1, \nu_2)$ for Homonuclear Spins (Case 4).	103
2.34	r-SNOB – Selective 180° Pulse.	104
2.35	r-SNOB – Average Hamiltonian $\bar{\mathcal{H}}_{0,J}(\nu_S)$ for Heteronuclear Spins (Case 1).	104
2.36	r-SNOB – Average Hamiltonian $\bar{\mathcal{H}}_{0,J}(\nu_S)$ for Heteronuclear Echo (Case 2).	105
2.37	r-SNOB – Average Hamiltonian $\bar{\mathcal{H}}_{0,J}(\nu_1, \nu_2)$ for Homonuclear Spins (Case 4).	105
2.38	I-BURP-2 – Selective 180° Pulse.	106
2.39	I-BURP-2 – Average Hamiltonian $\bar{\mathcal{H}}_{0,J}(\nu_S)$ for Heteronuclear Spins (Case 1).	106
2.40	I-BURP-2 – Average Hamiltonian $\bar{\mathcal{H}}_{0,J}(\nu_S)$ for Heteronuclear Echo (Case 2).	107
2.41	I-BURP-2 – Average Hamiltonian $\bar{\mathcal{H}}_{0,J}(\nu_1, \nu_2)$ for Homonuclear Spins (Case 4).	107
2.42	Q5 – Selective 90° Pulse.	108
2.43	Q5 – Average Hamiltonian $\bar{\mathcal{H}}_{0,J}(\nu_S)$ for Heteronuclear Spins (Case 1).	108
2.44	Q5 – Average Hamiltonian $\bar{\mathcal{H}}_{0,J}(\nu_1, \nu_2)$ for Homonuclear Spins (Case 4).	109
2.45	E-BURP-2 – Selective 90° Pulse.	110
2.46	E-BURP-2 – Average Hamiltonian $\bar{\mathcal{H}}_{0,J}(\nu_S)$ for Heteronuclear Spins (Case 1).	111
2.47	E-BURP-2 – Average Hamiltonian $\bar{\mathcal{H}}_{0,J}(\nu_1, \nu_2)$ for Homonuclear Spins (Case 4).	111
2.48	e-SNOB – Selective 90° Pulse.	112
2.49	e-SNOB – Average Hamiltonian $\bar{\mathcal{H}}_{0,J}(\nu_S)$ for Heteronuclear Spins (Case 1).	113
2.50	e-SNOB – Average Hamiltonian $\bar{\mathcal{H}}_{0,J}(\nu_1, \nu_2)$ for Homonuclear Spins (Case 4).	113
2.51	BURBOP-180 – Broadband 180° Pulse.	114
2.52	BURBOP-180 – Average Hamiltonian $\bar{\mathcal{H}}_{0,J}(\nu_S)$ for Heteronuclear Spins (Case 1).	114
2.53	BURBOP-180 – Average Hamiltonian $\bar{\mathcal{H}}_{0,J}(\nu_S)$ for Heteronuclear Echo (Case 2).	115
2.54	BURBOP-180 – Average Hamiltonian $\bar{\mathcal{H}}_{0,J}(\nu_1, \nu_2)$ for Homonuclear Spins (Case 4).	115
2.55	Adiabatic Chirp – Broadband 180° Pulse.	116
2.56	Adiabatic Chirp – Average Hamiltonian $\bar{\mathcal{H}}_{0,J}(\nu_S)$ for Heteronuclear Spins (Case 1).	116
2.57	Adiabatic Chirp – Average Hamiltonian $\bar{\mathcal{H}}_{0,J}(\nu_S)$ for Heteronuclear Echo (Case 2).	117
2.58	Adiabatic Chirp – Average Hamiltonian $\bar{\mathcal{H}}_{0,J}(\nu_1, \nu_2)$ for Homonuclear Spins (Case 4).	117
2.59	BURBOP-90 – Broadband 90° Pulse.	118
2.60	BURBOP-90 – Average Hamiltonian $\bar{\mathcal{H}}_{0,J}(\nu_S)$ for Heteronuclear Spins (Case 1).	118
2.61	BURBOP-90 – Average Hamiltonian $\bar{\mathcal{H}}_{0,J}(\nu_1, \nu_2)$ for Homonuclear Spins (Case 4).	119
2.62	BEBOP – Broadband 90° Pulse.	120
2.63	BEBOP – Average Hamiltonian $\bar{\mathcal{H}}_{0,J}(\nu_S)$ for Heteronuclear Spins (Case 1).	121
2.64	BEBOP – Average Hamiltonian $\bar{\mathcal{H}}_{0,J}(\nu_1, \nu_2)$ for Homonuclear Spins (Case 4).	121
2.65	Echo – 180° Hard Pulse.	122
2.66	Echo – Average Hamiltonian $\bar{\mathcal{H}}_{0,J}(\nu_S)$ for Heteronuclear Spins (Case 1 and 2).	123
2.67	Echo – Average Hamiltonian $\bar{\mathcal{H}}_{0,J}(\nu_1, \nu_2)$ for Homonuclear Spins (Case 4).	123
2.68	IMP – Shaped 180° Pulse.	124
2.69	IMP – Average Hamiltonian $\bar{\mathcal{H}}_{0,J}(\nu_S)$ for Heteronuclear Spins (Case 1).	125
2.70	IMP – Average Hamiltonian $\bar{\mathcal{H}}_{0,J}(\nu_1, \nu_2)$ for Homonuclear Spins (Case 4).	125
2.71	BUBU – Shaped 180° Pulse Sandwich.	126
2.72	BUBU – Average Hamiltonian $\bar{\mathcal{H}}_{0,J}(\nu_1, \nu_S)$ for Heteronuclear Spins (Case 3).	127
2.73	BUBU – Homonuclear Average Hamiltonian $\bar{\mathcal{H}}_{0,J}(\nu_1, \nu_2)$ for ¹ H-Shape (Case 4).	128
2.74	BUBU – Homonuclear Average Hamiltonian $\bar{\mathcal{H}}_{0,J}(\nu_1, \nu_2)$ for X-Shape (Case 4).	128

2.75	BUBI – Shaped 180° Pulse Sandwich.	129
2.76	BUBI – Average Hamiltonian $\bar{\mathcal{H}}_{0,J}(\nu_1, \nu_S)$ for Heteronuclear Spins (Case 3).	130
2.77	BUBI – Homonuclear Average Hamiltonian $\bar{\mathcal{H}}_{0,J}(\nu_1, \nu_2)$ for ¹ H-Shape (Case 4).	131
2.78	BUBI – Homonuclear Average Hamiltonian $\bar{\mathcal{H}}_{0,J}(\nu_1, \nu_2)$ for X-Shape (Case 4).	131
2.79	BE ^{tr} BE – Shaped 180° Pulse Sandwich.	132
2.80	BE ^{tr} BE – Average Hamiltonian $\bar{\mathcal{H}}_{0,J}(\nu_1, \nu_S)$ for Heteronuclear Spins (Case 3).	133
2.81	BEBE ^{tr} – Average Hamiltonian $\bar{\mathcal{H}}_{0,J}(\nu_1, \nu_S)$ for Heteronuclear Spins (Case 3).	133
2.82	BUBU – Homonuclear Average Hamiltonian $\bar{\mathcal{H}}_{0,J}(\nu_1, \nu_2)$ for ¹ H-Shape (Case 4).	134
2.83	BUBU – Homonuclear Average Hamiltonian $\bar{\mathcal{H}}_{0,J}(\nu_1, \nu_2)$ for X-Shape (Case 4).	134
2.84	Spectrum of Strongly Coupled Two-Spin System.	135
2.85	Spectrum of Strongly Coupled Two-Spin System in Zeeman Product Basis.	136
2.86	Evolution of Strong Coupling During a Delay in the Double Rotating Frame.	137
2.87	Spectrum of Strongly Coupled Two-Spin System in Double Rotating Frame.	138
2.88	Spectrum of Zero-Quantum Coupled Two-Spin System.	139
2.89	Comparison of Geometric Phase Induced by Off-Resonant Irradiation and Strong Coupling ZQ-terms.	140
2.90	Average Hamiltonian of Strong Coupling in the Double Rotating Frame.	144
2.91	Numerical Simulations of Double- and Zero-Quantum Correlations.	147
2.92	Pulse Sequence of the JRES-HOMQC.	148
2.93	JRES-HOMQC Spectra of Camphor.	150
2.94	JRES-HOMQC Spectra of Camphor After Recombination.	151
2.95	JRES-HOMQC Spectra of Camphor After Recombination (1D Columns).	151
2.96	Pulse Sequence of the HOMQC-TOCSY.	153
2.97	Numerical Simulations of the Reduced Multiplet in the HOMQC-TOCSY.	155
2.98	Numerical Simulations of the Frequency Discrimination in the HOMQC-TOCSY.	155
2.99	HOMQC-TOCSY Spectra of Camphor.	156
2.100	HOMQC-TOCSY Spectra of Vincamine.	157
3.1	Pseudo-2D Chunked Acquisition Scheme.	161
3.2	Selective Element Used for Chunked Acquisition.	162
3.3	Real-Time Pure Shift Acquisition.	163
3.4	Selective Averaging in Homonuclear Decoupling.	165
3.5	Chunk Artifacts From Transverse Relaxation and Anti-Phase Coherence.	166
3.6	Typical Spin Network of an Amide Proton.	167
3.7	Pulse Sequence for Pure Shift Acquisition of Amide Protons Using a ¹³ C-BIRD-Filter.	168
3.8	Effective Rotations of Real-Time Pure Shift Acquisition Using a ¹³ C-BIRD-Filter.	169
3.9	The Effect of Radiation Damping During Pure Shift Acquisition.	171
3.10	Comparison of Water Suppression for Different Pure Shift Methods.	172
3.11	BEST-TROSY Spectra of Ubiquitin with and without Pure Shift Acquisition.	173
3.12	Pure Shift FHSQC and BEST-TROSY of Ubiquitin Using ¹³ C-BIRD Filter (Clipped).	174
3.13	Linewidth Correlation Plot for FHSQC and BEST-TROSY with and without Pure Shift Acquisition.	175
3.14	Impact of Proton Carbon Long-Range Couplings on Linewidth.	176
3.15	Maximum Intensity Correlation Plot for FHSQC and BEST-TROSY with and without Pure Shift Acquisition.	178
3.16	Magnetization Recovery for Pure Shift Acquisition.	179
3.17	BEST-TROSY Spectra of p53TAD with and without Pure Shift Acquisition.	180
3.18	Correlation Plot for Signal Widths and Maximal Intensities in BEST-TROSY with and without Pure Shift Acquisition (p53TAD).	181
3.19	Pulse Sequence for BASEREX Acquisition.	182
3.20	Effective Rotations of BASEREX Acquisition.	183
3.21	Numerical Simulations of Real-Time Pure Shift Acquisition Using Different BIRD-Filters.	185
3.22	BASEREX Acquisition Tested on Anomeric Center of Uniformly ¹³ C-Labeled Glucose.	186

3.23	BASEREX Acquisition Tested on Uniformly ^{13}C , ^{15}N -Labeled Amino Acid Mixture. . . .	187
3.24	Typical Coupling Network of an $\text{H}\alpha$, $\text{C}\alpha$ -Spin Pair.	189
3.25	Pulse Sequence for the Selective $\text{H}\alpha$, $\text{C}\alpha$ -HSQC.	191
3.27	Selective $\text{H}\alpha$, $\text{C}\alpha$ -HSQC Comparison of 1D Rows for Various Samples.	193
3.28	Selective $\text{H}\alpha$, $\text{C}\alpha$ - HSQC for α -Synuclein.	194
3.29	Isotope-Shifted Peaks, Water Suppression and Acquisition of Glycines and Serines for the SHACA-HSQC.	195
3.30	Pulse Sequences of Sensitivity Improved SHACA-HSQC.	197
3.31	Transfer Efficiency for CH -, CH_2 - and CH_3 -Groups in Sensitivity Improved HSQC Experiments.	198
3.32	H_{Methyl} , C_{Methyl} -Correlations for Amino Acid Mixture and Human Ubiquitin.	199
3.33	Pulse Sequences of Constant Time SHACA-HSQC.	201
3.34	$\text{H}\alpha$, $\text{C}\alpha$ -Correlations of Amino Acid Mixture from SHACA-HSQC, CT-SHACA-HSQC and Standard CT-HSQC.	202
3.35	$\text{H}\alpha$, $\text{C}\alpha$ -Correlations of Ubiquitin from CT-SHACA-HSQC.	203
3.36	Signal Intensity Correlation Plot for CT-SHACA-HSQC and Conventional CT-HSQC. . . .	204
5.1	The Dependency of the Suzuki-Trotter Approximants on n Considering Large Values for θ	216
5.2	Spin State Preservation from IPE-1 with 2 Basic Cycles and Using the IMP Shape.	217
5.3	Spin State Preservation from IPE-1 with 4 Basic Cycles.	217
5.4	Evolution of Strong Coupling During a Spin Echo in the Double Rotating Frame.	218
5.5	Average Hamiltonian of Strong Coupling During a Spin Echo in the Double Rotating Frame. . . .	219
5.6	Artifacts of JRES-HOMQC Spectra of Camphor After Recombination and Mis-Set.	220
5.7	Artifacts of JRES-HOMQC Spectra of Camphor After Recombination and Mis-Set (1D Columns).	220
5.8	Increase in Artificial Noise from Incomplete Water Suppression.	223
5.9	Pure Shift FHSQC and BEST-TROSY of Ubiquitin (Comparable Conditions).	224
5.10	Linewidth Correlation Plot for FHSQC and BEST-TROSY (Comparable Conditions).	225
5.11	Artifact Reduction in Real-Time Pure Shift Acquisition.	225
5.12	Correlation Plot of BEST-TROSY with and without Pure Shift Acquisition.	226

List of References

- [1] I. I. Rabi, J. R. Zacharias, S. Millman and P. Kusch. *Physical Review* **1938**, *53*, 318–318. (cit. on pp. III, 13).
- [2] F. Bloch, W. W. Hansen and M. Packard. *Physical Review* **1946**, *69*, 127. (cit. on p. III).
- [3] E. M. Purcell, H. C. Torrey and R. V. Pound. *Physical Review* **1946**, *69*, 37–38. (cit. on p. III).
- [4] J. S. Waugh, L. M. Huber and U. Haeberlen. *Physical Review Letters* **1968**, *20*, 180–182. (cit. on pp. III, 27, 38, 41, 56, 92).
- [5] L. Braunschweiler and R. R. Ernst. *Journal of Magnetic Resonance* **1983**, *53*, 521–528. (cit. on pp. III, 55, 74, 75).
- [6] K. Takegoshi, K. Ogura and K. Hikichi. *Journal of Magnetic Resonance* **1989**, *84*, 611–615. (cit. on pp. III, 32, 58).
- [7] E. O. Stejskal and J. E. Tanner. *The Journal of Chemical Physics* **1965**, *42*, 288–292. (cit. on pp. IV, 85, 86).
- [8] K. F. Morris and C. S. Johnson. *Journal of the American Chemical Society* **1992**, *114*, 3139–3141. (cit. on pp. IV, 85).
- [9] M. M. Maricq and J. S. Waugh. *The Journal of Chemical Physics* **1979**, *70*, 3300–3316. (cit. on pp. IV, 3, 38, 165).
- [10] A. Bax, A. F. Mehlkopf and J. Smidt. *Journal of Magnetic Resonance* **1979**, *35*, 167–169. (cit. on pp. V, 160, 190, 200).
- [11] A. Bodor, J. D. Haller, C. Bouguechtouli, F. X. Theillet, L. Nyitray and B. Luy. *Analytical Chemistry* **2020**, *92*, 12423–12428. (cit. on pp. V, 164, 173, 182, 189, 191, 209).
- [12] J. D. Haller, A. Bodor and B. Luy. *Journal of Magnetic Resonance* **2019**, *302*, 64–71. (cit. on pp. V, 92, 103, 164, 204, 208).
- [13] M. H. Levitt. *Spin dynamics: Basics of Nuclear Magnetic Resonance, Second Edition*. John Wiley & Sons, 2009 (cit. on pp. 1, 10, 13, 15, 23, 135).
- [14] F. Bloch. *Physical Review* **1946**, *70*, 460–474. (cit. on pp. 1, 50).
- [15] S. Yun, M. F. Lightstone and M. J. Thomson. *International Journal of Thermal Sciences* **2005**, *44*, 421–428. (cit. on p. 1).
- [16] J. Keeler. *Understanding NMR spectroscopy*. John Wiley & Sons, 2010 (cit. on pp. 1, 51, 52).
- [17] R. R. Ernst, G. Bodenhausen and A. Wokaun. *Principles of Nuclear Magnetic Resonance in One and Two Dimensions*. Oxford University Press, 1987 (cit. on pp. 1, 6–8, 10, 38, 41, 50, 75, 135, 139, 143).
- [18] F. Schwabl. *Quantenmechanik (QM I)*. Springer Berlin Heidelberg, 2007 (cit. on pp. 1, 19, 39).
- [19] P. Zeeman. *Verhandlungen der Physikalischen Gesellschaft zu Berlin* **1896**, *15*, 128–130. (cit. on p. 1).
- [20] E. Schrödinger. *Physical Review* **1926**, *28*, 1049–1070. (cit. on p. 2).
- [21] A. G. Redfield. *Advances in Magnetic and Optical Resonance* **1965**, *1*, 1–32. (cit. on p. 2).

- [22] W. Pauli. *Zeitschrift für Physik* **1927**, *43*, 601–623. (cit. on p. 4).
- [23] J. VON Neumann. *Nachrichten von der Gesellschaft der Wissenschaften zu Göttingen* **1927**, 245–278. (cit. on p. 6).
- [24] L. Landau. *Zeitschrift für Physik* **1927**, *45*, 430–441. (cit. on p. 6).
- [25] K. Packer and K. Wright. *Molecular Physics* **1983**, *50*, 797–813. (cit. on p. 8).
- [26] S. A. Smith, W. E. Palke and J. T. Gerig. *Concepts in Magnetic Resonance* **1992**, *4*, 107–144. (cit. on pp. 10, 12, 213).
- [27] E. Wigner. *Zeitschrift für Physik* **1927**, *43*, 624–652. (cit. on p. 12).
- [28] U. Haeberlen. *High Resolution NMR in Solids - Selective Averaging*. Academic Press, 1976 (cit. on pp. 12, 25, 41, 43, 56, 78, 212).
- [29] S. A. Smith, W. E. Palke and J. T. Gerig. *Concepts in Magnetic Resonance* **1992**, *4*, 181–204. (cit. on p. 12).
- [30] S. A. Smith, W. E. Palke and J. T. Gerig. *Concepts in Magnetic Resonance* **1993**, *5*, 151–177. (cit. on p. 12).
- [31] W. E. Lamb. *Physical Review* **1941**, *60*, 817–819. (cit. on p. 12).
- [32] N. F. Ramsey. *Physical Review* **1950**, *78*, 699–703. (cit. on p. 12).
- [33] I. I. Rabi, N. F. Ramsey and J. Schwinger. *Reviews of Modern Physics* **1954**, *26*, 167–171. (cit. on pp. 13, 22).
- [34] N. F. Ramsey and E. M. Purcell. *Physical Review* **1952**, *85*, 143–144. (cit. on p. 14).
- [35] N. F. Ramsey. *Physical Review* **1953**, *91*, 303–307. (cit. on p. 14).
- [36] M. Karplus. *Journal of the American Chemical Society* **1963**, *85*, 2870–2871. (cit. on pp. 14, 74, 145).
- [37] C. A. Haasnoot, F. A. DE Leeuw and C. Altona. *Tetrahedron* **1980**, *36*, 2783–2792. (cit. on pp. 14, 74, 145).
- [38] O. Sørensen, G. Eich, M. Levitt, G. Bodenhausen and R. Ernst. *Progress in Nuclear Magnetic Resonance Spectroscopy* **1984**, *16*, 163–192. (cit. on p. 16).
- [39] I. I. Rabi, S. Millman, P. Kusch and J. R. Zacharias. *Physical Review* **1939**, *55*, 526–535. (cit. on p. 22).
- [40] G. B. Furman and I. M. Kadzhaya. *Journal of Magnetic Resonance* **1993**, *A105*, 7–9. (cit. on p. 24).
- [41] F. Bloch and A. Siegert. *Physical Review* **1940**, *57*, 522–527. (cit. on pp. 24, 57).
- [42] M. V. Berry. *Proceedings of the Royal Society of London. A. Mathematical and Physical Sciences* **1984**, *392*, 45–57. (cit. on pp. 24, 57, 135).
- [43] M. Sattler, J. Schleucher and C. Griesinger. *Progress in Nuclear Magnetic Resonance Spectroscopy* **1999**, *34*, 93–158. (cit. on pp. 25, 69).
- [44] F. J. Dyson. *Physical Review* **1949**, *75*, 486–502. (cit. on pp. 38, 39).
- [45] W. Magnus. *Communications on Pure and Applied Mathematics* **1954**, *7*, 649–673. (cit. on pp. 38, 39, 41, 56).
- [46] U. Haeberlen and J. S. Waugh. *Physical Review* **1968**, *175*, 453–467. (cit. on pp. 38, 41, 56).
- [47] J. H. Shirley. *Physical Review* **1965**, *B138*, 979–987. (cit. on p. 38).
- [48] R. Garg and R. Ramachandran. *Journal of Chemical Physics* **2020**, *153*, 034106. (cit. on p. 38).
- [49] M. M. Maricq. *Physical Review* **1982**, *B25*, 6622–6632. (cit. on p. 38).
- [50] P.-L. Giscard and C. Bonhomme. *Physical Review Research* **2020**, *2*, 023081. (cit. on p. 38).
- [51] P. L. Giscard, K. Lui, S. J. Thwaite and D. Jaksch. *Journal of Mathematical Physics* **2015**, *56*, 053503. (cit. on p. 38).

- [52] S. J. Glaser. *Journal of Magnetic Resonance* **1993**, *A104*, 283–301. (cit. on pp. 39, 59).
- [53] A. Brinkmann. *Concepts in Magnetic Resonance Part A: Bridging Education and Research* **2016**, *45A*, (cit. on pp. 41, 92).
- [54] P. Mansfield. *Physics Letters A* **1970**, *32*, 485–486. (cit. on p. 43).
- [55] C. H. Wang and J. D. Ramshaw. *Physical Review* **1972**, *B6*, 3253–3262. (cit. on p. 43).
- [56] M. M. Maricq. *The Journal of Chemical Physics* **1987**, *86*, 5647–5651. (cit. on p. 45).
- [57] M. Suzuki. *Communications in Mathematical Physics* **1976**, *51*, 183–190. (cit. on p. 45).
- [58] G. Bodenhausen, R. Freeman and G. A. Morris. *Journal of Magnetic Resonance* **1976**, *23*, 171–175. (cit. on pp. 46, 160).
- [59] N. Bloembergen, E. M. Purcell and R. V. Pound. *Physical Review* **1948**, *73*, 679–712. (cit. on pp. 50, 52).
- [60] I. Solomon. *Physical Review* **1955**, *99*, 559–565. (cit. on p. 52).
- [61] A. Gupta, T. Stait-Gardner, M. J. Moghaddam and W. S. Price. *Concepts in Magnetic Resonance Part A: Bridging Education and Research* **2015**, *44*, 74–113. (cit. on p. 52).
- [62] A. W. Overhauser. *Physical Review* **1953**, *92*, 411–415. (cit. on pp. 52, 63).
- [63] F. A. Anet and A. J. Bourn. *Journal of the American Chemical Society* **1965**, *87*, 5250–5251. (cit. on pp. 52, 63).
- [64] J. Jeener, B. H. Meier, P. Bachmann and R. R. Ernst. *The Journal of Chemical Physics* **1979**, *71*, 4546–4553. (cit. on p. 52).
- [65] K. Pervushin, R. Riek, G. Wider and K. Wüthrich. *Proceedings of the National Academy of Sciences* **1997**, *94*, 12366–12371. (cit. on p. 53).
- [66] C. N. Banwell and H. Primas. *Molecular Physics* **1963**, *6*, 225–256. (cit. on p. 54).
- [67] H. J. Hogben, M. Krzystyniak, G. T. Charnock, P. J. Hore and I. Kuprov. *Journal of Magnetic Resonance* **2011**, *208*, 179–194. (cit. on p. 54).
- [68] J. Jeener and G. Alewaeters. *Progress in Nuclear Magnetic Resonance Spectroscopy* **2016**, *94-95*, 75–80. (cit. on p. 55).
- [69] R. R. Ernst. *Chimia* **1975**, 179. (cit. on p. 55).
- [70] W. P. Aue, E. Bartholdi and R. R. Ernst. *The Journal of Chemical Physics* **1976**, *64*, 2229–2246. (cit. on p. 55).
- [71] S. R. Hartmann and E. L. Hahn. *Physical Review* **1962**, *128*, 2042–2053. (cit. on p. 55).
- [72] R. D. Bertrand, W. B. Moniz, A. N. Garroway and G. C. Chingas. *Journal of the American Chemical Society* **1978**, *100*, 5227–5229. (cit. on pp. 55, 63).
- [73] M. Ernst, C. Griesinger, R. R. Ernst and W. Bermel. *Molecular Physics* **1991**, *74*, 219–252. (cit. on p. 55).
- [74] T. Carlomagno, B. Luy and S. J. Glaser. *Journal of Magnetic Resonance* **1997**, *126*, 110–119. (cit. on p. 55).
- [75] R. Konrat, I. Burghardt and G. Bodenhausen. *Journal of the American Chemical Society* **1991**, *113*, 9135–9140. (cit. on p. 55).
- [76] A. Allerhand. *The Journal of Chemical Physics* **1966**, *44*, 1. (cit. on pp. 55, 75).
- [77] D. G. Davis and A. Bax. *Journal of the American Chemical Society* **1985**, *107*, 2820–2821. (cit. on pp. 55, 74).
- [78] G. A. Morris and R. Freeman. *Journal of the American Chemical Society* **1979**, *101*, 760–762. (cit. on pp. 55, 63).
- [79] D. P. Burum and R. R. Ernst. *Journal of Magnetic Resonance* **1980**, *39*, 163–168. (cit. on pp. 55, 63).

- [80] A. A. Maudsley and R. R. Ernst. *Chemical Physics Letters* **1977**, *50*, 368–372. (cit. on p. 55).
- [81] A. A. Maudsley, L. Moller and R. R. Ernst. *Journal of Magnetic Resonance* **1977**, *28*, 463–469. (cit. on p. 55).
- [82] G. Bodenhausen and D. J. Ruben. *Chemical Physics Letters* **1980**, *69*, 185–189. (cit. on pp. 55, 145).
- [83] L. Müller. *Journal of the American Chemical Society* **1979**, *101*, 4481–4484. (cit. on pp. 55, 145).
- [84] A. Bax, R. H. Griffey and B. L. Hawkins. *Journal of Magnetic Resonance* **1983**, *55*, 301–315. (cit. on pp. 55, 145).
- [85] H. Kessler, C. Griesinger, J. Zarbock and H. R. Loosli. *Journal of Magnetic Resonance* **1984**, *57*, 331–336. (cit. on p. 55).
- [86] H. Kessler, W. Bermel and C. Griesinger. *Journal of the American Chemical Society* **1985**, *107*, 1083–1084. (cit. on p. 55).
- [87] A. Bax and M. F. Summers. *Journal of the American Chemical Society* **1986**, *108*, 2093–2094. (cit. on pp. 55, 145).
- [88] A. Bax and D. Marion. *Journal of Magnetic Resonance* **1988**, *78*, 186–191. (cit. on pp. 55, 145).
- [89] D. P. Burum, M. Linder and R. R. Ernst. *Journal of Magnetic Resonance* **1981**, *44*, 173–188. (cit. on p. 56).
- [90] M. R. Koos, G. Kummerlöwe, L. Kaltschnee, C. M. Thiele and B. Luy. *Angewandte Chemie - International Edition* **2016**, *55*, 7655–7659. (cit. on pp. 56, 58).
- [91] T. Gyöngyösi, I. Timári, J. Haller, M. R. Koos, B. Luy and K. E. Kövér. *ChemPlusChem* **2018**, *83*, 53–60. (cit. on pp. 56, 58, 61, 73).
- [92] A. Lingel, A. Vulpetti, T. Reinsperger, A. Proudfoot, R. Denay, A. Frommlet, C. Henry, U. Hommel, A. D. Gossert, B. Luy and A. O. Frank. *Angewandte Chemie - International Edition* **2020**, *59*, 14809–14817. (cit. on pp. 56, 62, 63, 65, 92, 114, 118).
- [93] S. Grzesiek, J. Anglister and A. Bax. *Journal of Magnetic Resonance* **1993**, *B101*, 114–119. (cit. on pp. 56, 69, 70).
- [94] H. Kovacs and A. Gossert. *Journal of Biomolecular NMR* **2014**, *58*, 101–112. (cit. on pp. 56, 62, 69, 70).
- [95] A. Bax and D. G. Davis. *Journal of Magnetic Resonance* **1985**, *65*, 355–360. (cit. on pp. 56, 59, 74).
- [96] A. J. Shaka, C. J. Lee and A. Pines. *Journal of Magnetic Resonance* **1988**, *77*, 274–293. (cit. on pp. 56, 59, 62).
- [97] S. P. Rucker and A. J. Shaka. *Molecular Physics* **1989**, *68*, 509–517. (cit. on pp. 56, 59).
- [98] M. Kadkhodaie, O. Rivas, M. Tan, A. Mohebbi and A. J. Shaka. *Journal of Magnetic Resonance* **1991**, *91*, 437–443. (cit. on pp. 56, 59, 62, 63, 66, 67).
- [99] I. C. Felli, R. Pierattelli, S. J. Glaser and B. Luy. *Journal of Biomolecular NMR* **2009**, *43*, 187–196. (cit. on pp. 56, 59).
- [100] R. R. Ernst and W. A. Anderson. *Review of Scientific Instruments* **1966**, *37*, 93–102. (cit. on pp. 56, 74, 75).
- [101] A. M. Torres, G. Zheng and W. S. Price. *Magnetic Resonance in Chemistry* **2010**, *48*, 129–133. (cit. on pp. 56, 58).
- [102] J. A. Aguilar, R. W. Adams, M. Nilsson and G. A. Morris. *Journal of Magnetic Resonance* **2014**, *238*, 16–19. (cit. on pp. 56, 58, 85, 88, 90).
- [103] S. Ehni and B. Luy. *Journal of Magnetic Resonance* **2013**, *232*, 7–17. (cit. on pp. 56, 63, 64, 70, 92, 94, 99, 100, 104, 112, 129, 132, 190).
- [104] S. Ehni and B. Luy. *Journal of Magnetic Resonance* **2014**, *247*, 111–117. (cit. on pp. 56, 92).

- [105] C. Griesinger, O. W. Sørensen and R. R. Ernst. *Journal of the American Chemical Society* **1985**, *107*, 6394–6396. (cit. on pp. 57, 146).
- [106] C. Griesinger, O. W. Sørensen and R. R. Ernst. *The Journal of Chemical Physics* **1986**, *85*, 6837–6852. (cit. on pp. 57, 146).
- [107] C. Griesinger, O. W. Sørensen and R. R. Ernst. *Journal of Magnetic Resonance* **1987**, *75*, 474–492. (cit. on p. 57).
- [108] E. L. Hahn. *Physical Review* **1950**, *80*, 580–594. (cit. on pp. 58, 85, 122).
- [109] P. C. M. VAN Zijl, C. T. W. Moonen and M. VON Kienlin. *Journal of Magnetic Resonance* **1990**, *89*, 28–40. (cit. on p. 58).
- [110] T. Schulte-Herbrüggen, Z. Mádi, O. Sørensen and R. R. Ernst. *Molecular Physics* **1991**, *72*, 847–871. (cit. on p. 58).
- [111] Z. Mádi, B. Brutscher, T. Schulte-Herbrüggen, R. Brüschweiler and R. Ernst. *Chemical Physics Letters* **1997**, *268*, 300–305. (cit. on pp. 58, 59).
- [112] D. Sinnaeve. *Journal of Magnetic Resonance* **2014**, *245*, 24–30. (cit. on p. 58).
- [113] A. Verma, S. Bhattacharya and B. Baishya. *RSC Advances* **2018**, *8*, 19990–19999. (cit. on p. 58).
- [114] J. Ilgen, L. Kaltschnee and C. M. Thiele. *Magnetic Resonance in Chemistry* **2018**, *56*, 918–933. (cit. on pp. 58, 162).
- [115] L. Kaltschnee, A. Kolmer, I. Timári, V. Schmidts, R. W. Adams, M. Nilsson, K. E. Kövér, G. A. Morris and C. M. Thiele. *Chemical Communications* **2014**, *50*, 15702–15705. (cit. on pp. 58, 145, 162).
- [116] J. A. Aguilar, M. Nilsson, G. Bodenhausen and G. A. Morris. *Chemical Communications* **2012**, *48*, 811–813. (cit. on p. 58).
- [117] T. Parella. *Magnetic Resonance in Chemistry* **2019**, *57*, 13–29. (cit. on pp. 58, 90).
- [118] M. Rance. *Journal of Magnetic Resonance* **1987**, *74*, 557–564. (cit. on pp. 59, 60).
- [119] M. J. Thrippleton and J. Keeler. *Angewandte Chemie - International Edition* **2003**, *42*, 3938–3941. (cit. on pp. 59, 60, 63, 64, 70, 148, 153, 159).
- [120] P. W. Howe. *Journal of Magnetic Resonance* **2006**, *179*, 217–222. (cit. on pp. 59, 60).
- [121] J. J. Koivisto. *Chemical Communications* **2013**, *49*, 96–98. (cit. on pp. 59, 60).
- [122] O. Schedletzky, B. Luy and S. J. Glaser. *Journal of Applied Physics* **1998**, *130*, 27–32. (cit. on p. 59).
- [123] B. Luy and S. J. Glaser. *Journal of Magnetic Resonance* **2001**, *153*, 210–214. (cit. on p. 59).
- [124] B. Luy and S. J. Glaser. *Journal of Magnetic Resonance* **2003**, *164*, 304–309. (cit. on p. 59).
- [125] L. Müller and R. R. Ernst. *Molecular Physics* **1979**, *38*, 963–992. (cit. on p. 59).
- [126] U. Piantini, O. W. Sørensen and R. R. Ernst. *Journal of the American Chemical Society* **1982**, *104*, 6800–6801. (cit. on p. 60).
- [127] M. Rance, O. Sørensen, G. Bodenhausen, G. Wagner, R. Ernst and K. Wüthrich. *Biochemical and Biophysical Research Communications* **1983**, *117*, 479–485. (cit. on p. 60).
- [128] G. Eich, G. Bodenhausen and R. R. Ernst. *Journal of the American Chemical Society* **1982**, *104*, 3731–3732. (cit. on p. 60).
- [129] D. Marion, M. Ikura, R. Tschudin and A. Bax. *Journal of Magnetic Resonance* **1989**, *85*, 393–399. (cit. on pp. 60, 70).
- [130] K. Kövér, O. Prakash and V. Hruby. *Journal of Magnetic Resonance* **1993**, *A103*, 92–96. (cit. on pp. 61, 152).
- [131] K. E. Kövér, V. J. Hruby and D. Uhrín. *Journal of Magnetic Resonance* **1997**, *129*, 125–129. (cit. on p. 61).

- [132] S. W. Fesik, H. L. Eaton, E. T. Olejniczak, E. R. P. Zuiderweg, L. P. McIntosh and F. W. Dahlquist. *Journal of the American Chemical Society* **1990**, *112*, 886–888. (cit. on pp. 62, 73).
- [133] A. E. Bennett, J. D. Gross and G. Wagner. *Journal of Magnetic Resonance* **2003**, *165*, 59–79. (cit. on p. 62).
- [134] D. Ban, A. D. Gossert, K. Giller, S. Becker, C. Griesinger and D. Lee. *Journal of Magnetic Resonance* **2012**, *221*, 1–4. (cit. on p. 62).
- [135] H. Kovacs, D. Moskau and M. Spraul. *Progress in Nuclear Magnetic Resonance Spectroscopy* **2005**, *46*, 131–155. (cit. on p. 62).
- [136] K. Kobzar, S. Ehni, T. E. Skinner, S. J. Glaser and B. Luy. *Journal of Magnetic Resonance* **2012**, *225*, 142–160. (cit. on pp. 63, 64, 70, 92, 93, 114, 190).
- [137] A. Bax, G. Clore and A. M. Gronenborn. *Journal of Magnetic Resonance* **1990**, *88*, 425–431. (cit. on pp. 65, 73).
- [138] N. Sibille, I. Huvent, C. Fauquant, D. Verdegem, L. Amniai, A. Leroy, J. M. Wieruszkeski, G. Lippens and I. Landrieu. *Proteins: Structure, Function and Bioinformatics* **2012**, *80*, 454–462. (cit. on p. 66).
- [139] J. A. Pople. *The Journal of Chemical Physics* **1956**, *24*, 1111–1111. (cit. on p. 66).
- [140] G. T. Montelione, B. A. Lyons, S. D. Emerson and M. Tashiro. *Journal of the American Chemical Society* **1992**, *114*, 10974–10975. (cit. on p. 69).
- [141] B. Lyons and G. Montelione. *Journal of Magnetic Resonance* **1993**, *B101*, 206–209. (cit. on p. 69).
- [142] R. Clowes, W. Boucher, C. Hardman, P. Domaille and E. Laue. *Journal of Biomolecular NMR* **1993**, *3*, 349–354. (cit. on p. 69).
- [143] L. Emsley and G. Bodenhausen. *Journal of Magnetic Resonance* **1992**, *97*, 135–148. (cit. on pp. 70, 92, 100, 108).
- [144] A. J. Shaka, J. Keeler, T. Frenkiel and R. Freeman. *Journal of Magnetic Resonance* **1983**, *52*, 335–338. (cit. on pp. 70, 160, 182).
- [145] A. J. Shaka, P. B. Barker and R. Freeman. *Journal of Magnetic Resonance* **1985**, *64*, 547–552. (cit. on pp. 70, 160).
- [146] A. G. Palmer, J. Cavanagh, P. E. Wright and M. Rance. *Journal of Magnetic Resonance* **1991**, *93*, 151–170. (cit. on pp. 70, 197).
- [147] L. Kay, P. Keifer and T. Saarinen. *Journal of the American Chemical Society* **1992**, *114*, 10663–10665. (cit. on pp. 70, 197).
- [148] K. Pervushin, R. Riek, G. Wider and K. Wüthrich. *Journal of the American Chemical Society* **1998**, *120*, 6394–6400. (cit. on p. 71).
- [149] P. Allard and T. Härd. *Journal of Magnetic Resonance* **1997**, *126*, 48–57. (cit. on p. 73).
- [150] W. Bermel, I. C. Felli, R. Kümmerle and R. Pierattelli. *Concepts in Magnetic Resonance Part A* **2008**, *32A*, 183–200. (cit. on pp. 73, 189, 194).
- [151] E. T. Olejniczak, R. X. Xu and S. W. Fesik. *Journal of Biomolecular NMR* **1992**, *2*, 655–659. (cit. on p. 73).
- [152] A. Majumdar, H. Wang, R. Morshausser and E. Zuiderweg. *Journal of Biomolecular NMR* **1993**, *3*, 387–397. (cit. on p. 73).
- [153] J. S. Waugh. *Journal of Magnetic Resonance* **1986**, *68*, 189–192. (cit. on p. 74).
- [154] M. H. Levitt, R. Freeman and T. Frenkiel. *Journal of Magnetic Resonance* **1982**, *50*, 157–160. (cit. on pp. 74, 122).
- [155] P. Caravatti, L. Braunschweiler and R. R. Ernst. *Chemical Physics Letters* **1983**, *100*, 305–310. (cit. on pp. 74, 77).

- [156] D. P. Weitekamp, J. R. Garbow and A. Pines. *The Journal of Chemical Physics* **1982**, *77*, 2870–2883. (cit. on pp. 74, 77).
- [157] D. P. Burum and W. K. Rhim. *The Journal of Chemical Physics* **1979**, *71*, 944–956. (cit. on pp. 74, 77).
- [158] J. Klages, H. Kessler, S. J. Glaser and B. Luy. *Journal of Magnetic Resonance* **2007**, *189*, 217–227. (cit. on p. 74).
- [159] M. R. Hansen, M. Rance and A. Pardi. *Journal of the American Chemical Society* **1998**, *120*, 11210–11211. (cit. on p. 74).
- [160] F. Kramer, W. Peti, C. Griesinger and S. J. Glaser. *Journal of Magnetic Resonance* **2001**, *149*, 58–66. (cit. on p. 74).
- [161] A. Garon, R. Zeier and S. J. Glaser. *Physical Review* **2015**, *A91*, 042122. (cit. on p. 74).
- [162] E. J. Wells and H. S. Gutowsky. *The Journal of Chemical Physics* **1965**, *43*, 3414–3415. (cit. on p. 75).
- [163] M. R. Koos and B. Luy. *Journal of Magnetic Resonance* **2019**, *300*, 61–75. (cit. on p. 75).
- [164] H. Y. Carr and E. M. Purcell. *Physical Review* **1954**, *94*, 630–638. (cit. on pp. 85, 122).
- [165] A. G. Anderson, R. L. Garwin, E. L. Hahn, J. W. Horton, G. L. Tucker and R. M. Walker. *Journal of Applied Physics* **1955**, *26*, 1324–1338. (cit. on p. 85).
- [166] J. E. Tanner. *The Journal of Chemical Physics* **1970**, *52*, 2523–2526. (cit. on p. 85).
- [167] S. J. Gibbs and C. S. Johnson. *Journal of Magnetic Resonance* **1991**, *93*, 395–402. (cit. on p. 85).
- [168] D. H. Wu, A. Chen and C. S. Johnson. *Journal of Magnetic Resonance* **1995**, *A115*, 260–264. (cit. on p. 85).
- [169] K. F. Morris and C. S. Johnson. *Journal of the American Chemical Society* **1992**, *114*, 776–777. (cit. on p. 85).
- [170] A. Jerschow and N. Müller. *Journal of Magnetic Resonance* **1997**, *125*, 372–375. (cit. on p. 85).
- [171] A. Jerschow and N. Müller. *Journal of Magnetic Resonance* **1998**, *132*, 13–18. (cit. on p. 85).
- [172] C. Johnson. *Progress in Nuclear Magnetic Resonance Spectroscopy* **1999**, *34*, 203–256. (cit. on p. 85).
- [173] G. Pagès, V. Gilard, R. Martino and M. Malet-Martino. *The Analyst* **2017**, *142*, 3771–3796. (cit. on p. 85).
- [174] X. Guo, K. S. Wetzels, S. C. Solleder, S. Spann, M. A. R. Meier, M. Wilhelm, B. Luy and G. Guthausen. *Macromolecular Chemistry and Physics* **2019**, *220*, 1900155. (cit. on p. 85).
- [175] D. Sinnaeve. *eMagRes* **2016**, *5*, 967–980. (cit. on p. 86).
- [176] D. Sinnaeve. *Concepts in Magnetic Resonance Part A* **2012**, *40A*, 39–65. (cit. on p. 86).
- [177] Y. Shrot and L. Frydman. *Journal of Magnetic Resonance* **2008**, *195*, 226–231. (cit. on p. 90).
- [178] D. Burstein. *Concepts in Magnetic Resonance* **1996**, *8*, 269–278. (cit. on p. 90).
- [179] J. Frahm, K. D. Merboldt, W. Hänicke and A. Haase. *Journal of Magnetic Resonance* **1985**, *64*, 81–93. (cit. on p. 90).
- [180] W. Sattin, T. H. Mareci and K. N. Scott. *Journal of Magnetic Resonance* **1985**, *65*, 298–307. (cit. on p. 90).
- [181] Ě. Kupče and R. Freeman. *Magnetic Resonance in Chemistry* **2007**, *45*, 2–4. (cit. on p. 90).
- [182] D. Schulze-Sünninghausen, J. Becker and B. Luy. *Journal of the American Chemical Society* **2014**, *136*, 1242–1245. (cit. on pp. 90, 177).
- [183] D. Schulze-Sünninghausen, J. Becker, M. R. M. Koos and B. Luy. *Journal of Magnetic Resonance* **2017**, *281*, 151–161. (cit. on pp. 90, 177).
- [184] M. H. Levitt and R. Freeman. *Journal of Magnetic Resonance* **1979**, *33*, 473–476. (cit. on p. 92).

- [185] A. J. Shaka. *Chemical Physics Letters* **1985**, *120*, 201–205. (cit. on p. 92).
- [186] J. Baum, R. Tycko and A. Pines. *Physical Review* **1985**, *A32*, 3435–3447. (cit. on pp. 92, 116).
- [187] Ě. Kupče and R. Freeman. *Journal of Magnetic Resonance* **1995**, *A117*, 246–256. (cit. on p. 92).
- [188] M. A. Smith, H. Hu and A. J. Shaka. *Journal of Magnetic Resonance* **2001**, *151*, 269–283. (cit. on pp. 92, 168, 182, 190).
- [189] K. Kobzar, T. E. Skinner, N. Khaneja, S. J. Glaser and B. Luy. *Journal of Magnetic Resonance* **2004**, *170*, 236–243. (cit. on pp. 92, 182, 190).
- [190] K. Kobzar, T. E. Skinner, N. Khaneja, S. J. Glaser and B. Luy. *Journal of Magnetic Resonance* **2008**, *194*, 58–66. (cit. on pp. 92, 182, 190).
- [191] T. E. Skinner, K. Kobzar, B. Luy, M. R. Bendall, W. Bermel, N. Khaneja and S. J. Glaser. *Journal of Magnetic Resonance* **2006**, *179*, 241–249. (cit. on pp. 92, 120).
- [192] T. E. Skinner, N. I. Gershenzon, M. Nimbalkar, W. Bermel, B. Luy and S. J. Glaser. *Journal of Magnetic Resonance* **2012**, *216*, 78–87. (cit. on pp. 92, 114, 190).
- [193] D. L. Goodwin, M. R. M. Koos and B. Luy. *Physical Review Research* **2020**, *2*, 33157. (cit. on p. 92).
- [194] L. Emsley and G. Bodenhausen. *Chemical Physics Letters* **1990**, *165*, 469–476. (cit. on p. 92).
- [195] H. Geen and R. Freeman. *Journal of Magnetic Resonance* **1991**, *93*, 93–141. (cit. on pp. 92, 93, 102, 106, 110, 182).
- [196] Ě. Kupče and R. Freeman. *Journal of Magnetic Resonance* **1993**, *A102*, 122–126. (cit. on p. 92).
- [197] Ě. Kupče, J. Boyd and I. D. Campbell. *Journal of Magnetic Resonance* **1995**, *B106*, 300–303. (cit. on pp. 92, 104, 112).
- [198] N. Khaneja, T. Reiss, C. Kehlet, T. Schulte-Herbrüggen and S. J. Glaser. *Journal of Magnetic Resonance* **2005**, *172*, 296–305. (cit. on pp. 92, 114, 124).
- [199] P. Coote, C. Anklin, W. Masefski, G. Wagner and H. Arthanari. *Journal of Magnetic Resonance* **2017**, *281*, 94–103. (cit. on p. 92).
- [200] P. W. Coote, S. A. Robson, A. Dubey, A. Boeszoermyeni, M. Zhao, G. Wagner and H. Arthanari. *Nature Communications* **2018**, *9*, 3014. (cit. on p. 92).
- [201] J. E. Power, M. Foroozandeh, R. W. Adams, M. Nilsson, S. R. Coombes, A. R. Phillips and G. A. Morris. *Chemical Communications* **2016**, *52*, 2916–2919. (cit. on p. 92).
- [202] E. Lescop, T. Kern and B. Brutscher. *Journal of Magnetic Resonance* **2010**, *203*, 190–198. (cit. on pp. 92, 100).
- [203] R. D. Boyer, R. Johnson and K. Krishnamurthy. *Journal of Magnetic Resonance* **2003**, *165*, 253–259. (cit. on pp. 92, 116).
- [204] Ě. Kupče and R. Freeman. *Journal of Magnetic Resonance* **2007**, *187*, 258–265. (cit. on pp. 92, 116).
- [205] M. H. Levitt. *Progress in Nuclear Magnetic Resonance Spectroscopy* **1986**, *18*, 61–122. (cit. on pp. 93, 94).
- [206] B. Luy, K. Kobzar, T. E. Skinner, N. Khaneja and S. J. Glaser. *Journal of Magnetic Resonance* **2005**, *176*, 179–186. (cit. on p. 96).
- [207] A. A. Marchione and E. L. Diaz. *Journal of Magnetic Resonance* **2018**, *286*, 143–147. (cit. on p. 115).
- [208] S. Meiboom and D. Gill. *Review of Scientific Instruments* **1958**, *29*, 688–691. (cit. on p. 122).
- [209] J. W. Jacobs, J. W. Van Os and W. S. Veeman. *Journal of Magnetic Resonance* **1983**, *51*, 56–66. (cit. on pp. 122, 160).

- [210] C. R. Harris, K. J. Millman, S. J. VAN DER Walt, R. Gommers, P. Virtanen, D. Cournapeau, E. Wieser, J. Taylor, S. Berg, N. J. Smith, R. Kern, M. Picus, S. Hoyer, M. H. VAN Kerkwijk, M. Brett, A. Haldane, J. F. DEL RÍO, M. Wiebe, P. Peterson, P. Gérard-Marchant, K. Sheppard, T. Reddy, W. Weckesser, H. Abbasi, C. Gohlke and T. E. Oliphant. *Nature* **2020**, *585*, 357–362. (cit. on p. 124).
- [211] P. Virtanen, R. Gommers, T. E. Oliphant, M. Haberland, T. Reddy, D. Cournapeau, E. Burovski, P. Peterson, W. Weckesser, J. Bright, S. J. VAN DER Walt, M. Brett, J. Wilson, K. J. Millman, N. Mayorov, A. R. J. Nelson, E. Jones, R. Kern, E. Larson, C. J. Carey, I. Polat, Y. Feng, E. W. Moore, J. VanderPlas, D. Laxalde, J. Perktold, R. Cimrman, I. Henriksen, E. A. Quintero, C. R. Harris, A. M. Archibald, A. H. Ribeiro, F. Pedregosa and P. VAN Mulbregt. *Nature Methods* **2020**, *17*, 261–272. (cit. on p. 124).
- [212] J. D. Hunter. *Computing in Science and Engineering* **2007**, *9*, 90–95. (cit. on p. 124).
- [213] M. J. Thrippleton, R. A. E. Edden and J. Keeler. *Journal of Magnetic Resonance* **2005**, *174*, 97–109. (cit. on pp. 135, 160).
- [214] A. Kumar and R. R. Ernst. *Journal of Magnetic Resonance* **1976**, *24*, 425–447. (cit. on p. 143).
- [215] W. P. Aue, P. Bachmann, A. Wokaun and R. R. Ernst. *Journal of Magnetic Resonance* **1978**, *29*, 523–533. (cit. on p. 145).
- [216] H. Günther. *NMR Spectroscopy - Basic Principles, Concepts, and Applications in Chemistry*. Wiley-VCH, 2013 (cit. on p. 145).
- [217] B. Mulloy, T. A. Frenkiel and D. B. Davies. *Carbohydrate Research* **1988**, *184*, 39–46. (cit. on p. 145).
- [218] W. Thomas. *Progress in Nuclear Magnetic Resonance Spectroscopy* **1997**, *30*, 183–207. (cit. on p. 145).
- [219] T. Parella and J. F. Espinosa. *Progress in Nuclear Magnetic Resonance Spectroscopy* **2013**, *73*, 17–55. (cit. on p. 145).
- [220] G. Kummerlöwe and B. Luy. *Trends in Analytical Chemistry* **2009**, *28*, 483–493. (cit. on p. 145).
- [221] P. Tzvetkova, U. Sternberg, T. Gloge, A. Navarro-Vázquez and B. Luy. *Chemical Science* **2019**, *10*, 8774–8791. (cit. on p. 145).
- [222] A. Enthart, J. C. Freudenberger, J. Furrer, H. Kessler and B. Luy. *Journal of Magnetic Resonance* **2008**, *192*, 314–322. (cit. on p. 145).
- [223] T. Reinsperger and B. Luy. *Journal of Magnetic Resonance* **2014**, *239*, 110–120. (cit. on pp. 145, 162).
- [224] I. Timári, L. Kaltschnee, A. Kolmer, R. W. Adams, M. Nilsson, C. M. Thiele, G. A. Morris and K. E. Kövér. *Journal of Magnetic Resonance* **2014**, *239*, 130–138. (cit. on pp. 145, 162).
- [225] M. Ottiger, F. Delaglio and A. Bax. *Journal of Magnetic Resonance* **1998**, *131*, 373–378. (cit. on p. 145).
- [226] P. Andersson, A. Annala and G. Otting. *Journal of Magnetic Resonance* **1998**, *133*, 364–367. (cit. on p. 145).
- [227] P. Andersson, J. Weigelt and G. Otting. *Journal of Biomolecular NMR* **1998**, *12*, 435–441. (cit. on p. 145).
- [228] A. Rexroth, P. Schmidt, S. Szalma, T. Geppert, H. Schwalbe and C. Griesinger. *Journal of the American Chemical Society* **1995**, *117*, 10389–10390. (cit. on p. 145).
- [229] T. Carlomagno, H. Schwalbe, A. Rexroth, O. Sørensen and C. Griesinger. *Journal of Magnetic Resonance* **1998**, *135*, 216–226. (cit. on p. 145).
- [230] E. Miclet, D. C. Williams, G. M. Clore, D. L. Bryce, J. Boisbouvier and A. Bax. *Journal of the American Chemical Society* **2004**, *126*, 10560–10570. (cit. on p. 145).

- [231] L. Castañar, M. Garcia, E. Hellemann, P. Nolis, R. R. Gil and T. Parella. *The Journal of Organic Chemistry* **2016**, *81*, 11126–11131. (cit. on p. 146).
- [232] N. Marcó, P. Nolis, R. R. Gil and T. Parella. *Journal of Magnetic Resonance* **2017**, *282*, 18–26. (cit. on p. 146).
- [233] N. Marcó, A. Souza, P. Nolis, R. Gil and T. Parella. *Journal of Magnetic Resonance* **2017**, *276*, 37–42. (cit. on p. 146).
- [234] N. Marcó, R. R. Gil and T. Parella. *Magnetic Resonance in Chemistry* **2017**, *55*, 540–545. (cit. on p. 146).
- [235] T. Fäcke and S. Berger. *Journal of Magnetic Resonance* **1995**, *A113*, 114–116. (cit. on p. 146).
- [236] N. Giraud, L. Béguin, J. Courtieu and D. Merlet. *Angewandte Chemie - International Edition* **2010**, *49*, 3481–3484. (cit. on p. 146).
- [237] D. Pitoux, B. Plainchont, D. Merlet, Z. Hu, D. Bonnaffé, J. Farjon and N. Giraud. *Chemistry - A European Journal* **2015**, *21*, 9044–9047. (cit. on p. 146).
- [238] J. E. Herbert Pucheta, D. Pitoux, C. M. Grison, S. Robin, D. Merlet, D. J. Aitken, N. Giraud and J. Farjon. *Chemical Communications* **2015**, *51*, 7939–7942. (cit. on p. 146).
- [239] D. Sinnaeve, J. Ilgen, M. E. Di Pietro, J. J. Primožic, V. Schmidts, C. M. Thiele and B. Luy. *Angewandte Chemie - International Edition* **2020**, *132*, 5354–5358. (cit. on p. 146).
- [240] P. Tzvetkova, S. Simova and B. Luy. *Journal of Magnetic Resonance* **2007**, *186*, 193–200. (cit. on p. 146).
- [241] O. Sørensen, M. H. Levitt and R. Ernst. *Journal of Magnetic Resonance* **1983**, *55*, 104–113. (cit. on p. 147).
- [242] D. Uhrín, T. Liptaj and K. Kövér. *Journal of Magnetic Resonance* **1993**, *A101*, 41–46. (cit. on pp. 148, 160, 162, 168).
- [243] M. Foroozandeh, R. W. Adams, N. J. Meharry, D. Jeannerat, M. Nilsson and G. A. Morris. *Angewandte Chemie - International Edition* **2014**, *53*, 6990–6992. (cit. on pp. 152, 162, 163).
- [244] L. Lerner and A. Bax. *Journal of Magnetic Resonance* **1986**, *69*, 375–380. (cit. on p. 152).
- [245] B. L. Marquez, W. H. Gerwick and R. Thomas Williamson. *Magnetic Resonance in Chemistry* **2001**, *39*, 499–530. (cit. on p. 152).
- [246] T. Parella and J. F. Espinosa. *Progress in Nuclear Magnetic Resonance Spectroscopy* **2013**, *73*, 17–55. (cit. on p. 152).
- [247] K. Ding and A. M. Gronenborn. *Journal of Magnetic Resonance* **2003**, *163*, 208–214. (cit. on p. 153).
- [248] J. E. Herbert Pucheta, D. Pitoux, C. M. Grison, S. Robin, D. Merlet, D. J. Aitken, N. Giraud and J. Farjon. *Chemical Communications* **2015**, *51*, 7939–7942. (cit. on p. 159).
- [249] D. Pitoux, B. Plainchont, D. Merlet, Z. Hu, D. Bonnaffé, J. Farjon and N. Giraud. *Chemistry - A European Journal* **2015**, *21*, 9044–9047. (cit. on p. 159).
- [250] D. Sinnaeve, M. Foroozandeh, M. Nilsson and G. A. Morris. *Angewandte Chemie - International Edition* **2016**, *55*, 1090–1093. (cit. on pp. 159, 162).
- [251] K. Zangger. *Progress in Nuclear Magnetic Resonance Spectroscopy* **2015**, *86-87*, 1–20. (cit. on pp. 159, 161).
- [252] L. Castañar and T. Parella. *Magnetic Resonance in Chemistry* **2015**, *53*, 399–426. (cit. on p. 159).
- [253] W. P. Aue, J. Karhan and R. R. Ernst. *The Journal of Chemical Physics* **1976**, *64*, 4226–4227. (cit. on p. 159).
- [254] K. Nagayama, P. Bachmann, K. Wüthrich and R. R. Ernst. *Journal of Magnetic Resonance* **1978**, *31*, 133–148. (cit. on p. 159).

- [255] A. Bax, R. Freeman and G. A. Morris. *Journal of Magnetic Resonance* **1981**, *43*, 333–338. (cit. on p. 159).
- [256] A. Martinez, F. Bourdreux, E. Riguet and J. M. Nuzillard. *Magnetic Resonance in Chemistry* **2012**, *50*, 28–32. (cit. on p. 159).
- [257] A. J. Shaka, J. Keeler and R. Freeman. *Journal of Magnetic Resonance* **1984**, *56*, 294–313. (cit. on p. 159).
- [258] S. Simova, H. Sengstschmid and R. Freeman. *Journal of Magnetic Resonance* **1997**, *124*, 104–121. (cit. on p. 159).
- [259] B. Luy. *Journal of Magnetic Resonance* **2009**, *201*, 18–24. (cit. on p. 159).
- [260] A. J. Pell and J. Keeler. *Journal of Magnetic Resonance* **2007**, *189*, 293–299. (cit. on p. 159).
- [261] J. R. Garbow, D. P. Weitekamp and A. Pines. *Chemical Physics Letters* **1982**, *93*, 504–509. (cit. on pp. 160, 162, 168).
- [262] O. W. Sørensen, C. Griesinger and R. R. Ernst. *Journal of the American Chemical Society* **1985**, *107*, 7778–7779. (cit. on pp. 160, 162).
- [263] H. Oschkinat, A. Pastore, P. Pfändler and G. Bodenhausen. *Journal of Magnetic Resonance* **1986**, *69*, 559–566. (cit. on pp. 160, 162).
- [264] A. J. Pell, R. A. E. Edden and J. Keeler. *Magnetic Resonance in Chemistry* **2007**, *45*, 296–316. (cit. on pp. 160, 162).
- [265] K. Furihata, M. Tashiro and H. Seto. *Magnetic Resonance in Chemistry* **2010**, *48*, 179–183. (cit. on p. 160).
- [266] B. Görling, S. Bräse and B. Luy. *Magnetic Resonance in Chemistry* **2012**, *50*, S58–S62. (cit. on p. 160).
- [267] P. Sakhaii, B. Haase and W. Bermel. *Journal of Magnetic Resonance* **2013**, *228*, 125–129. (cit. on p. 160).
- [268] A. L. Bloom and J. N. Shoolery. *Physical Review* **1955**, *97*, 1261–1265. (cit. on p. 160).
- [269] W. A. Anderson and R. Freeman. *The Journal of Chemical Physics* **1962**, *37*, 85–103. (cit. on p. 160).
- [270] T. Parella and P. Nolis. *Concepts in Magnetic Resonance Part A: Bridging Education and Research* **2010**, *36*, 1–23. (cit. on p. 160).
- [271] J. P. Jesson, P. Meakin and G. Kneissel. *Journal of the American Chemical Society* **1973**, *95*, 618–620. (cit. on p. 160).
- [272] A. Hammarström and G. Otting. *Journal of the American Chemical Society* **1994**, *116*, 8847–8848. (cit. on p. 160).
- [273] J. Weigelt, A. Hammarström, W. Bermel and G. Otting. *Journal of Magnetic Resonance* **1996**, *B110*, 219–224. (cit. on p. 160).
- [274] Ě. Kupče and G. Wagner. *Journal of Magnetic Resonance* **1995**, *B109*, 329–333. (cit. on pp. 160, 173).
- [275] P. Király, R. W. Adams, L. Paudel, M. Foroozandeh, J. A. Aguilar, I. Timári, M. J. Cliff, M. Nilsson, P. Sándor, G. Batta, J. P. Waltho, K. E. Kövér and G. A. Morris. *Journal of Biomolecular NMR* **2015**, *62*, 43–52. (cit. on pp. 161, 167, 173, 178).
- [276] K. Zangger and H. Sterk. *Journal of Magnetic Resonance* **1997**, *124*, 486–489. (cit. on pp. 161, 188).
- [277] P. Sakhaii, B. Haase, W. Bermel, R. Kerssebaum, G. E. Wagner and K. Zangger. *Journal of Magnetic Resonance* **2013**, *233*, 92–95. (cit. on p. 161).
- [278] G. E. Wagner, P. Sakhaii, W. Bermel and K. Zangger. *Chemical Communications* **2013**, *49*, 3155–3157. (cit. on p. 161).

- [279] L. Castañar, P. Nolis, A. Virgili and T. Parella. *Chemistry - A European Journal* **2013**, *19*, 15472–15475. (cit. on p. 161).
- [280] M. Foroozandeh, P. Giraudeau and D. Jeannerat. *Magnetic Resonance in Chemistry* **2013**, *51*, 808–814. (cit. on p. 161).
- [281] R. Brüschweiler, C. Griesinger, O. W. Sørensen and R. R. Ernst. *Journal of Magnetic Resonance* **1988**, *78*, 178–185. (cit. on pp. 161, 190).
- [282] M. Nilsson and G. A. Morris. *Chemical Communications* **2007**, 933–935. (cit. on p. 161).
- [283] G. A. Morris, J. A. Aguilar, R. Evans, S. Haiber and M. Nilsson. *Journal of the American Chemical Society* **2010**, *132*, 12770–12772. (cit. on p. 161).
- [284] J. A. Aguilar, S. Faulkner, M. Nilsson and G. A. Morris. *Angewandte Chemie - International Edition* **2010**, *49*, 3901–3903. (cit. on p. 161).
- [285] J. A. Aguilar, M. Nilsson and G. A. Morris. *Angewandte Chemie - International Edition* **2011**, *50*, 9716–9717. (cit. on p. 162).
- [286] I. Timári, T. Z. Illyés, R. W. Adams, M. Nilsson, L. Szilágyi, G. A. Morris and K. E. Kövér. *Chemistry - A European Journal* **2015**, *21*, 3472–3479. (cit. on p. 162).
- [287] M. Foroozandeh, G. A. Morris and M. Nilsson. *Chemistry - A European Journal* **2018**, *24*, 13988–14000. (cit. on pp. 162, 163).
- [288] M. Foroozandeh, R. W. Adams, M. Nilsson and G. A. Morris. *Journal of the American Chemical Society* **2014**, *136*, 11867–11869. (cit. on p. 162).
- [289] M. Foroozandeh, L. Castañar, L. G. Martins, D. Sinnaeve, G. D. Poggetto, C. F. Tormena, R. W. Adams, G. A. Morris and M. Nilsson. *Angewandte Chemie - International Edition* **2016**, *55*, 15579–15582. (cit. on p. 162).
- [290] J. M. Lopez, R. Cabrera and H. Maruenda. *Scientific Reports* **2019**, *9*, 1–8. (cit. on p. 162).
- [291] M. Foroozandeh, R. W. Adams, P. Király, M. Nilsson and G. A. Morris. *Chemical Communications* **2015**, *51*, 15410–15413. (cit. on p. 162).
- [292] P. Sakhaii, B. Haase and W. Bermel. *Journal of Magnetic Resonance* **2009**, *199*, 192–198. (cit. on p. 163).
- [293] I. E. Ndukwe, A. Shchukina, V. Zorin, C. Cobas, K. Kazimierczuk and C. P. Butts. *ChemPhysChem* **2017**, *18*, 2081–2087. (cit. on p. 163).
- [294] A. Shchukina, M. Kaźmierczak, P. Kasprzak, M. Davy, G. R. Akien, C. P. Butts and K. Kazimierczuk. *Chemical Communications* **2019**, *55*, 9563–9566. (cit. on p. 163).
- [295] A. Lupulescu, G. L. Olsen and L. Frydman. *Journal of Magnetic Resonance* **2012**, *218*, 141–146. (cit. on pp. 163, 168, 182).
- [296] L. Paudel, R. W. Adams, P. Király, J. A. Aguilar, M. Foroozandeh, M. J. Cliff, M. Nilsson, P. Sándor, J. P. Waltho and G. A. Morris. *Angewandte Chemie - International Edition* **2013**, *52*, 11616–11619. (cit. on pp. 163, 173, 175, 182).
- [297] Y. Liu, M. D. Green, R. Marques, T. Pereira, R. Helmy, R. Thomas Williamson, W. Bermel and G. E. Martin. *Tetrahedron Letters* **2014**, *55*, 5450–5453. (cit. on p. 163).
- [298] M. Pérez-Trujillo, L. Castañar, E. Monteagudo, L. T. Kuhn, P. Nolis, A. Virgili, R. T. Williamson and T. Parella. *Chemical Communications* **2014**, *50*, 10214–10217. (cit. on p. 163).
- [299] I. Timári, L. Kaltschnee, M. H. Raics, F. Roth, N. G. A. Bell, R. W. Adams, M. Nilsson, D. Uhrín, G. A. Morris, C. M. Thiele and K. E. Kövér. *RSC Advances* **2016**, *6*, 87848–87855. (cit. on p. 163).
- [300] N. H. Meyer and K. Zangger. *Angewandte Chemie - International Edition* **2013**, *52*, 7143–7146. (cit. on p. 163).
- [301] S. Glanzer and K. Zangger. *Chemistry - A European Journal* **2014**, *20*, 11171–11175. (cit. on p. 163).

- [302] N. H. Meyer and K. Zangger. *Chemical Communications* **2014**, *50*, 1488–1490. (cit. on pp. 164, 173, 188).
- [303] L. Castañar, P. Nolis, A. Virgili and T. Parella. *Chemistry - A European Journal* **2013**, *19*, 17283–17286. (cit. on pp. 164, 188).
- [304] J. Ying, J. Roche and A. Bax. *Journal of Magnetic Resonance* **2014**, *241*, 97–102. (cit. on pp. 164, 166, 173–175, 181, 188).
- [305] J. Mauhart, S. Glanzer, P. Sakhaii, W. Bermel and K. Zangger. *Journal of Magnetic Resonance* **2015**, *259*, 207–215. (cit. on pp. 166, 183, 192, 225).
- [306] Ě. Kupče, R. Freeman, G. Wider and K. Wüthrich. *Journal of Magnetic Resonance* **1996**, *A122*, 81–84. (cit. on p. 166).
- [307] P. Moutzouri, Y. Chen, M. Foroozandeh, P. Király, A. R. Phillips, S. R. Coombes, M. Nilsson and G. A. Morris. *Chemical Communications* **2017**, *53*, 10188–10191. (cit. on pp. 166, 183, 192, 225).
- [308] P. Király, M. Nilsson and G. A. Morris. *Journal of Magnetic Resonance* **2018**, *293*, 19–27. (cit. on p. 166).
- [309] J. C. Barna and E. D. Laue. *Journal of Magnetic Resonance* **1987**, *75*, 384–389. (cit. on p. 167).
- [310] V. Y. Orekhov, I. Ibraghimov and M. Billeter. *Journal of Biomolecular NMR* **2003**, *27*, 165–173. (cit. on p. 167).
- [311] D. Rovnyak, D. P. Frueh, M. Sastry, Z. Y. J. Sun, A. S. Stern, J. C. Hoch and G. Wagner. *Journal of Magnetic Resonance* **2004**, *170*, 15–21. (cit. on p. 167).
- [312] S. Hiller, C. Wasmer, G. Wider and K. Wüthrich. *Journal of the American Chemical Society* **2007**, *129*, 10823–10828. (cit. on p. 167).
- [313] S. Mori, C. Abeygunawardana, M. Johnson and P. Vanzijl. *Journal of Magnetic Resonance* **1995**, *B108*, 94–98. (cit. on pp. 167, 169, 176, 177, 179).
- [314] P. Schanda, H. Van Melckebeke and B. Brutscher. *Journal of the American Chemical Society* **2006**, *128*, 9042–9043. (cit. on pp. 167, 176, 177).
- [315] J. Farjon, J. Boisbouvier, P. Schanda, A. Pardi, J.-P. Simorre and B. Brutscher. *Journal of the American Chemical Society* **2009**, *131*, 8571–8577. (cit. on pp. 167, 177).
- [316] R. S. Molday, S. W. Englander and R. G. Kallen. *Biochemistry* **1972**, *11*, 150–158. (cit. on pp. 167, 177).
- [317] Y. Bai, J. S. Milne, L. Mayne and S. W. Englander. *Proteins: Structure, Function, and Genetics* **1993**, *17*, 75–86. (cit. on pp. 167, 177, 179, 189).
- [318] D. Neri, G. Wider and K. Wüthrich. *Proceedings of the National Academy of Sciences* **1992**, *89*, 4397–4401. (cit. on p. 168).
- [319] N. Bloembergen and R. V. Pound. *Physical Review* **1954**, *95*, 8–12. (cit. on p. 170).
- [320] A. Vlassenbroek, J. Jeener and P. Broekaert. *The Journal of Chemical Physics* **1995**, *103*, 5886–5897. (cit. on p. 170).
- [321] Y. Y. Lin, N. Lisitza, S. Ahn and W. S. Warren. *Science* **2000**, *290*, 118–121. (cit. on p. 170).
- [322] P. L. Weber, S. C. Brown and L. Mueller. *Biochemistry* **1987**, *26*, 7282–7290. (cit. on p. 174).
- [323] A. C. Wang, S. Grzesiek, R. Tschudin, P. J. Lodi and A. Bax. *Journal of Biomolecular NMR* **1995**, *5*, 376–382. (cit. on pp. 174, 189, 203).
- [324] J. Becker and B. Luy. *Magnetic Resonance in Chemistry* **2015**, *53*, 878–885. (cit. on p. 177).
- [325] Z. Solyom, M. Schwarten, L. Geist, R. Konrat, D. Willbold and B. Brutscher. *Journal of Biomolecular NMR* **2013**, *55*, 311–321. (cit. on p. 177).
- [326] H. Roder, G. Wagner and K. Wuethrich. *Biochemistry* **1985**, *24*, 7407–7411. (cit. on p. 179).
- [327] A. D. Robertson and R. L. Baldwin. *Biochemistry* **1991**, *30*, 9907–9914. (cit. on p. 179).

- [328] Y. Pérez, M. Gairí, M. Pons and P. Bernadó. *Journal of Molecular Biology* **2009**, *391*, 136–148. (cit. on p. 179).
- [329] M. G. Murrall, M. Schiavina, V. Sainati, W. Bermel, R. Pierattelli and I. C. Felli. *Journal of Biomolecular NMR* **2018**, *70*, 167–175. (cit. on p. 179).
- [330] P. E. Wright and H. J. Dyson. *Journal of Molecular Biology* **1999**, *293*, 321–331. (cit. on p. 189).
- [331] N. Rezaei-Ghaleh, M. Blackledge and M. Zweckstetter. *ChemBioChem* **2012**, *13*, 930–950. (cit. on p. 189).
- [332] I. C. Felli and R. Pierattelli. *Intrinsically Disordered Proteins Studied by NMR Spectroscopy*. Vol. 870. Advances in Experimental Medicine and Biology. Springer International Publishing, 2015 (cit. on p. 189).
- [333] H. J. Dyson and P. E. Wright. *Chemical Reviews* **2004**, *104*, 3607–3622. (cit. on p. 189).
- [334] S. Kosol, S. Contreras-Martos, C. Cedeño and P. Tompa. *Molecules* **2013**, *18*, 10802–10828. (cit. on p. 189).
- [335] F.-X. Theillet, L. Kalmar, P. Tompa, K.-H. Han, P. Selenko, A. K. Dunker, G. W. Daughdrill and V. N. Uversky. *Intrinsically Disordered Proteins* **2013**, *1*, e24360. (cit. on pp. 189, 204).
- [336] V. N. Uversky. *Frontiers in Physics* **2019**, *7*, 8–23. (cit. on p. 189).
- [337] B. Mateos, C. Conrad-Billroth, M. Schiavina, A. Beier, G. Kontaxis, R. Konrat, I. C. Felli and R. Pierattelli. *Journal of Molecular Biology* **2019**, (cit. on p. 189).
- [338] W. Bermel, I. Bertini, L. Duma, I. C. Felli, L. Emsley, R. Pierattelli and P. R. Vasos. *Angewandte Chemie - International Edition* **2005**, *44*, 3089–3092. (cit. on p. 189).
- [339] W. Bermel, I. Bertini, J. Chill, I. C. Felli, N. Haba, V. Kumar M. V. and R. Pierattelli. *ChemBioChem* **2012**, *13*, 2425–2432. (cit. on p. 189).
- [340] I. C. Felli and R. Pierattelli. *Journal of Magnetic Resonance* **2014**, *241*, 115–125. (cit. on p. 189).
- [341] J. Lopez, R. Schneider, F.-X. Cantrelle, I. Huvent and G. Lippens. *Angewandte Chemie - International Edition* **2016**, *128*, 7544–7548. (cit. on p. 189).
- [342] S. Sukumaran, S. A. Malik, S. S. R., K. Chandra and H. S. Atreya. *Chemical Communications* **2019**, *55*, 7820–7823. (cit. on p. 189).
- [343] V. Kanelis, L. Donaldson, D. R. Muhandiram, D. Rotin, J. D. Forman-Kay and L. E. Kay. *Journal of Biomolecular NMR* **2000**, *16*, 253–259. (cit. on p. 189).
- [344] S. Mäntylähti, O. Aitio, M. Hellman and P. Permi. *Journal of Biomolecular NMR* **2010**, *47*, 171–181. (cit. on p. 189).
- [345] S. Mäntylähti, M. Hellman and P. Permi. *Journal of Biomolecular NMR* **2011**, *49*, 99–109. (cit. on p. 189).
- [346] A. S. Maltsev, J. Ying and A. Bax. *Journal of Biomolecular NMR* **2012**, *54*, 181–191. (cit. on p. 196).
- [347] J. Schleucher, M. Sattler and C. Griesinger. *Angewandte Chemie - International Edition* **1993**, *32*, 1489–1491. (cit. on p. 197).
- [348] G. W. Vuister and A. Bax. *Journal of Magnetic Resonance* **1992**, *98*, 428–435. (cit. on p. 200).
- [349] R. Paquin, P. Pelupessy, L. Duma, C. Gervais and G. Bodenhausen. *The Journal of Chemical Physics* **2010**, *133*, 034506. (cit. on p. 212).